274
10/20/66

MASTER

ORNL-3970
UC-25 – Metals, Ceramics, and Materials

METALS AND CERAMICS DIVISION
ANNUAL PROGRESS REPORT
FOR PERIOD ENDING JUNE 30, 1966

RELEASED FOR ANNOUNCEMENT
IN NUCLEAR SCIENCE ABSTRACTS

OAK RIDGE NATIONAL LABORATORY
operated by
UNION CARBIDE CORPORATION
for the
U.S. ATOMIC ENERGY COMMISSION

THIS DOCUMENT HAS BEEN REVIEWED.
NO INVENTIONS OF PATENT INTEREST
TO THE A.E.C. ARE DISCLOSED THEREIN.
10/25/66

DISCLAIMER

Printed in USA. Price $6.00 . Available from the Clearinghouse for Federal
Scientific and Technical Information, National Bureau of Standards,
U.S. Department of Commerce, Springfield, Virginia 22151

ORNL-3970

[illegible]

H. C. $ 6.00; MN 1.50

Contract No. W-7405-eng-26

METALS AND CERAMICS DIVISION ANNUAL PROGRESS REPORT

for Period Ending June 30, 1966

J. H Frye, Jr., Director
J. E. Cunningham, Assistant Director

RELEASED FOR ANNOUNCEMENT
IN NUCLEAR SCIENCE ABSTRACTS

Section Heads

G. M. Adamson, Jr.
B. S. Borie
D. A. Douglas, Jr.
C. J. McHargue
P. Patriarca

Compiled and Edited by Sigfred Peterson

OCTOBER 1966

OAK RIDGE NATIONAL LABORATORY
Oak Ridge, Tennessee
operated by
UNION CARBIDE CORPORATION
for the
U. S. ATOMIC ENERGY COMMISSION

Reports previously issued in this series are as follows:

ORNL-28	Period Ending March 1, 1948
ORNL-69	Period Ending May 31, 1948
ORNL-407	Period Ending July 31, 1949
ORNL-511	Period Ending October 31, 1949
ORNL-583	Period Ending January 31, 1950
ORNL-754	Period Ending April 30, 1950
ORNL-827	Period Ending July 31, 1950
ORNL-910	Period Ending October 31, 1950
ORNL-987	Period Ending January 31, 1951
ORNL-1033	Period Ending April 30, 1951
ORNL-1108	Period Ending July 31, 1951
ORNL-1161	Period Ending October 31, 1951
ORNL-1267	Period Ending January 31, 1952
ORNL-1302	Period Ending April 30, 1952
ORNL-1366	Period Ending July 31, 1952
ORNL-1437	Period Ending October 31, 1952
ORNL-1503	Period Ending January 31, 1953
ORNL-1551	Period Ending April 10, 1953
ORNL-1625	Period Ending October 10, 1953
ORNL-1727	Period Ending April 10, 1954
ORNL-1875	Period Ending October 10, 1954
ORNL-1911	Period Ending April 10, 1955
ORNL-1988	Period Ending October 10, 1955
ORNL-2080	Period Ending April 10, 1956
ORNL-2217	Period Ending October 10, 1956
ORNL-2422	Period Ending October 10, 1957
ORNL-2632	Period Ending October 10, 1958
ORNL-2839	Period Ending September 1, 1959
ORNL-2988	Period Ending July 1, 1960
ORNL-3160	Period Ending May 31, 1961
ORNL-3313	Period Ending May 31, 1962
ORNL-3470	Period Ending May 31, 1963
ORNL-3670	Period Ending June 30, 1964
ORNL-3870	Period Ending June 30, 1965

Contents

PART I. FUNDAMENTAL PROGRAMS

PART II. HIGH-TEMPERATURE MATERIALS PROGRAM

PART III. GENERAL FUELS AND MATERIALS RESEARCH

PART IV. REACTOR DEVELOPMENT SUPPORT

PART V. OTHER PROGRAM ACTIVITIES

PAPERS AND PUBLICATIONS

Summary

PART I. FUNDAMENTAL PROGRAMS

1. Crystal Physics

Our analysis of the effect of interrelated process variables on the growth of UO_2 single crystals by our centrifugal floating-zone technique was continued. The hydrothermal conditions favorable for the growth of crystals of lanthanide oxyhydroxides, ferrates, and hydroxides were studied. A split autoclave incorporating disposable liners and Bridgman seals was devised. From molten-salt solutions we grew crystals of CeO_2, hexagonal and tetragonal GeO_2, ThO_2, and Y_2GeMoO_8, and we investigated the temperature dependence of the lattice constants of Y_2GeMoO_8, ThO_2, and CeO_2 over the temperature range 50 to 350°C. In collaboration with the Solid State Division, we studied electron-spin resonance of the lanthanides in our crystals. Apparatus for the spectrophotometric study of small crystals was developed.

2. Deformation and Annealing of Metals

Grain-boundary migration rates during annealing of dilute alloys appear to be determined by the drag of a segregated impurity atmosphere, whereas the rate-controlling process in zone-refined metals is the transfer of single atoms across the boundary. In aluminum-gold alloys the migration rate for a given composition appeared to vary inversely as the degree of supersaturation.

Mechanical twinning does not contribute significantly to the formation of preferred orientation at high levels of deformation in niobium. The reorientation of niobium single crystals during cold rolling was accompanied by deformation-band formation. The presence or absence of such bands strongly influenced the tendency for recrystallization during annealing.

3. Deformation of Crystalline Solids

Our program of basic studies of the deformation of metals and alloys is aimed at a better understanding of the controlling processes during deformation, of the resulting structure, and of the changes due to annealing. Such knowledge contributes to the utilization of existing materials and the development of better ones.

During the past year the orientation dependence of storage of energy during deformation of copper crystals was studied. These results should have an important bearing on the theories of work hardening. For the first time, sheet-texture data could be transformed into a complete three-dimensional inverse pole figure, which is required for the complete representation. The method has resulted in a very much more complete texture determination for copper, aluminum, and brass. Studies have been continued on the rate-controlling mechanisms in deformation of tantalum and tantalum-alloy crystals. We analyzed the problem of irradiation hardening and the overshoot in single crystals.

4. Diffusion in Solids

By use of radioactive-tracer techniques, diffusion coefficients were obtained for Cr in Cr, Cr–20% Ni, and Cr–44% Ni; Ag and Sc in β-Ti; Mn in bcc δ-Mn; and V and Ti in V-Ti alloys at 10% increments over the entire composition range. The mathematical models for diffusion in grain boundaries were reviewed to compare their derivations. Boundary conditions, mathematical statements, and methods of solutions for three published models were considered.

5. Direct Observation of Lattice Defects

An etch-pit technique showed the distribution of dislocations near cracks and in slip bands for tungsten deformed at room temperature. A model was developed for correlating cross slip in bcc metals with stress and temperature. The derived expressions suggested that the sudden onset of brittleness as the temperature is lowered may be the result of a sudden decrease in ability to slip on any plane other than the most highly stressed {110}.

We are analyzing the bend-yield stress and the brittle-fracture morphology in tungsten. Some results are reported on the microstructure of SAP. A new process for the rapid preparation of transmission-electron-microscopy specimens is briefly described.

6. Electronic Properties of Metals and Alloys

The large increase in the electronic specific heat coefficient and the superconducting transition temperature with content of alloyed transition metals Nb, Mo, Re, and Ru depends upon the atomic concentration and not on the electron-to-atom ratio and whether the matrix crystal structure is cubic or hexagonal. This behavior contrasts with alloying from other regions of the transition metals, where the electron-to-atom ratio is a useful parameter, and suggests that a special effect occurs, such as phonon-electron enhancement of the electronic specific heat coefficient.

Interstitial impurity additives increased the critical current density of precipitation-enhanced transition-metal superconductors in the systems Nb-Zr, Nb-Hf, and Nb-Ti. Precipitation enhancement of critical current density was observed in systems Ti-Ta and Zr-Ta.

By mass spectroscopy of the gas over molten zirconium during zone refining, we sought methods to prepare crystals of greater purity for galvanomagnetic investigations. Hydrogen removal, carbon removal through methane and other hydrocarbons, and a limited amount of oxygen removal through CO_2 and CO would be indicated by the pressures observed. Oxygen pressure dropped below 10^{-13} torr, so we were able to zone refine from oxygen and obtain a resistance ratio of 1160 after 25 passes.

Galvanomagnetic tests had shown earlier that the Fermi surface of zirconium is closed and compensated. New voltage measurements show leading terms linear in magnetic field and oscillating in sign with field rotation, inconsistent with theory. We are seeking greater purity and larger magnetic fields to resolve this discrepancy.

Experiments with Mössbauer effect following Coulomb excitation were continued with isotopes of germanium and nickel. We established that for germanium the recoiless fraction in the target is about one-tenth that in the absorber. Investigations of electronic properties of copper-nickel alloys by measurements of hyperfine splitting and isomer shift were started.

7. Physical Ceramics Studies

The compressive-creep deformation of thoria exhibited three modes: brittle fracture at high stress, a macroscopically ductile viscous creep at low stress, and an intermediate mode that exhibits some ductility on a macroscopic scale. Ledge and pore formation at grain boundaries during compressive creep have been investigated. Study of the densification kinetics of sintering powder compacts has been extended to five additional oxides. As in the case of ThO_2, the densification kinetics indicated that the initial sintering is not compatible with diffusion-controlled processes. The progressive geometric changes occurring in a sintering powder mass are being studied, and a mathematical model to describe the process is being constructed.

8. Physical Properties

The thermal conductivity of single and polycrystalline silicon was measured from 91 to 1280°K. The thermal resistivity is linear with temperature below 1050°K, but the slope changes near the Debye temperature (650°K). Above 1050°K an electronic contribution was observed and agreed in magnitude with values calculable from the electrical resistivity. Analysis of our tungsten results led to a Lorenz number greater than the classical limit of 2.443×10^{-8} $(v/°C)^2$; this value can be qualitatively explained by inclusion of a nonnegligible third term in the Lorenz-number series expansion. This third term is proportional to the cubic temperature dependency of the electrical resistivity. Based on the behavior of neighboring lanthanides and metallic melts and existing theories, the thermal conductivity of promethium was estimated to 2000°C. Work to broaden the temperature limits of physical-property measurement capacity and measurements on Cr, W, Fe, Al, Pt, and Mo were initiated. Thermal-conductivity measurements below 140°C were completed on Al_2O_3, MgO, Y_2O_3, ThO_2, ThO_2-UO_2, SAP, W-Ta and W-Re alloys, Hastelloy X, and Inconel 626. A hot-cell thermal-conductivity apparatus is being constructed for testing of irradiated specimens.

9. Solid State and Molecular Theory

Progress has been made in our continuing studies of applications of ligand-field theory, calculations on atoms and molecules, and investigations of the electronic states of disordered systems. In addition, a new program of band-theory calculations has been started.

10. Spectroscopy of Ionic Media

Topics investigated by means of optical spectroscopy included vibrational-electronic transitions in ionic crystals, coordination geometry, and unusual electronic structures in ionic melts.

11. Superconducting Materials

We are studying the effects of metallurgical variables on the properties of superconducting materials. These variables include transformation products and morphologies, mechanical strain, aging reactions, and fabrication and heat-treatment procedures. We have determined the time-temperature-transformation curves for the transformation of the bcc solid-solution alloys of niobium and zirconium to two bcc phases of different compositions at temperatures between 600 and 950°C as functions of composition, temperature, and oxygen contamination. Critical current density measurements as functions of applied magnetic field on transformed specimens indicate that a broad maximum occurs between 40 and 60 vol % transformation, that is, when the grain boundaries are completely occupied by a pearlitic transformation product. The maximum critical current densities are greater by a factor of 10 to 15 than those obtained in severely cold-worked alloys.

Electrical resistivity was measured on purified technetium at just above its critical temperature (7.8°K) and from 77 to 1700°K. Lattice and electronic thermal conductivities were calculated, and a Debye temperature of 411°K was obtained.

Monoband interference filters producing monochromatic light were used to make black and white photomicrographs that show most of the information given by colors in microstructures anodized for color contrast. Several black and white photomicrographs are made of the same field in wavelengths of light selected to emphasize different features of the colored microstructure. These then allow presentation in technical journals of information derived from color without the prohibitive cost of color reproduction.

12. Surface Reactions of Metals

Our major responsibility continues to be to investigate the fundamentals of the oxidation mechanisms of metals and alloys. Emphasis is shifting to alloy oxidation. X-ray and electron-microscopic techniques were used to compare surface topography, mosaic spread, average strain, and other structural details of the oxide on several dilute copper-base alloys (notably Cu-Ni) with the corresponding parameters for the oxide on pure copper. Oxidation-rate changes were correlated with changes in the extent of the paths of easy diffusion in the oxide.

Our studies of the aqueous corrosion of aluminum alloys in high-temperature water were extended to include binary aluminum alloys containing Zr, Mg, Cu, Fe, and Be. All reduced the corrosion rate of aluminum. Pronounced corrosion-rate minima were observed in the aluminum-yttrium and aluminum-zinc systems, the increase in rate at the higher concentrations being related to renewed intergranular attack.

The technique of thermally oxidizing a previously anodized specimen proved useful in studying oxygen-solution effects in tantalum and niobium. Additional measurements of the flexure of oxidizing niobium and tantalum were rationalized in terms of stresses associated with oxygen solution in the metal followed by a stage in the oxidation process in which stresses within the oxide layer itself control flexure. Finally, a suitable technique was developed for removing anodic films from niobium-tantalum alloys and for preparing other refractory-alloy oxide films. These specimens should be useful for studies of oxide-phase stability and of the influence of alloying elements on the oxidation of refractory metals.

13. X-Ray Diffraction

The crystal structure of Y_2BeO_4 was described. We found the same unusual threefold oxygen coordination about beryllium as in the previously reported $Ca_{12}Be_{17}O_{29}$. Analyses of structures of other beryllates are in progress.

Refinements to both theory and experiment were made in the low-angle x-ray-scattering program. Analysis of space-charge effects in proportional counters and of slit-height corrections to low-angle scattering data has been completed. A relation has been found between the apparently disparate theories of low-angle scattering from precipitating systems proposed by Gerold and by Cowley.

Experiments illustrating the advantages of x-ray monochromation by bent pyrolytic graphite with a high degree of basal-plane orientation are reported. Preliminary results predict eventual realization of a monochromator that places as much or more useful power at the experimental sample as may be obtained with an unmonochromated beam.

PART II. HIGH-TEMPERATURE MATERIALS PROGRAM

14. High-Temperature Materials Development

This program is concerned with materials problems associated with high-temperature high-performance reactors for advanced propulsive and power applications, especially for space devices. Particular emphasis is placed on those problems stemming from systems that use alkali metals as thermodynamic working fluids and heat-transfer media in refractory-alloy systems.

The capability for extrusion of tungsten and tungsten-base alloys was demonstrated, and floating-mandrel techniques obviating the use of glass-type lubricants were developed. A secondary fabrication method for production of thin-walled tubing by duplex extrusion with molybdenum jacketing was developed.

Weldability studies were conducted on a variety of niobium- and tantalum-base alloys, and mechanical properties of these welds were determined to 1300°C. Time-temperature parameters for aging and overaging were defined. Brazing alloys were developed for joining refractory alloys to themselves and to oxide ceramics. Procedures were established for welding a variety of loops and other components. Unique techniques were devised for field-welding refractory-metal tubes, for seal-welding corrosion capsules in vacuum, and for penetrating thin-walled thermocouple wells through thick-walled pipes.

The evaporation rates of a complex commercial cobalt-base alloy decreased with time but were independent of pressure between 870 and 1150°C in the pressure range 6×10^{-10} to 6×10^{-7} torr. The effects of aging on the mechanical behavior of tantalum-base alloys were determined. An ultrahigh-vacuum technique for measuring gas-metal reactions revealed that 1% Zr in niobium increases the solubility of nitrogen in niobium by a factor of 4.

Creep-rupture properties of Nb-, Ta-, Mo-, and W-base alloys – including effects of heat treatment – were investigated. Of special interest are alternating-stress situations for the D-43 alloy. Effects of pretest annealing on creep-rupture behavior of niobium-base alloys were determined.

A total of 38,500 hr was accumulated in refluxing capsule tests involving refractory alloys with boiling potassium, with very little evidence of dissolutive attack. Results of thermal-convection-loop and forced-convection-loop tests substantiated results from capsule tests. Mass-transfer effects were observed in refractory-alloy–lithium systems studied in the approximate temperature range 1000 to 1300°C, and some interesting conclusions from this work are reported.

Nondestructive evaluation techniques were developed and applied for Nb-, Ta-, and W-base alloys in the form of tubing. Preparation of reference standards by electrical discharge machining constituted the principal developmental effort in this work.

Thermophysical properties of Nb-, Ta-, and W-base alloys were evaluated in tests developed for thermal conductivity, electrical resistivity, thermoelectric effects, specific heat, and total hemispherical emittance.

15. Materials Compatibility

Corrosion in the niobium-oxygen-potassium system at 1000 and 1250°C is controlled by solid-state diffusion of oxygen from the niobium. The driving force seems to be the tendency to form mixed metal oxides, in agreement with previous results at lower temperatures.

At 815°C Nb–1% Zr specimens containing an oxygen-to-zirconium atom ratio less than 2 took up oxygen, while specimens with a ratio greater than 2 lost oxygen. Thus the direction of oxygen movement appears to depend on whether the atom ratio of oxygen is less than or greater than that corresponding to ZrO_2.

A unique fast-neutron activation analysis facility suitable for handling highly active alkali metals without protective capsulation was designed and is under construction. We are assembling a molecular distillation rig capable of refining alkali metals to higher purity than has been possible with other methods.

16. Tungsten Metallurgy

Thermochemical deposition (TCD) of tungsten has continued to produce sheet material for complete metallurgical evaluation. The effects of basic deposition parameters on deposit morphology were studied in an effort to optimize the process. The texture of TCD tungsten rolled at 1200°C was found to approach the $\{100\}\langle 011\rangle$ ideal texture with increasing reduction up to 80%. The ductile-to-brittle transition temperature (DBTT) in tungsten was examined as a function of annealing treatment and grain size. Annealing lowered the DBTT of TCD tungsten but raised that of stress-relieved powder-metallurgy material. Fracture in tungsten appears to be initiated at grain boundaries and probably at impurities segregated there. Creep-rupture properties were measured on TCD and powder-metallurgy tungsten, W–2% ThO_2, and Sylvania A.

17. Uranium Nitride

Research and development on uranium nitride as a nuclear fuel for high-temperature reactors with high power densities has included studies of synthesis with high purity, pellet fabrication, effects of Mo, W, Th, O, and C on the structure of UN, and the vaporization of UN at low temperatures. Pertinent data and interpretations are presented.

PART III. GENERAL FUELS AND MATERIALS RESEARCH

18. Dispersions in Solids

A unique colloid chemical method was developed for effecting oxide particle dispersion hardening in the refractory metals and alloys. Forming a simultaneous colloid between the dispersant and a salt of the matrix assures fineness and uniformity of dispersion in the final alloy.

We sought stable fissile compounds for fueling thorium fuels and means for dispersion strengthening their matrix. Uranium diboride was the only compound stable at 1000°C, although US and UP were unreactive at 800°C. "Splat-cooling" of throium containing 1.3% Be was a new method for promoting substantial elevated-temperature hardening in fabricated alloys.

19. Fuel Element Development

Thermochemical deposition processes are being utilized to prepare fuel compounds and refractory alloys from volatile halides. We prepared UO_2 powder from UF_6 in continuing studies and from UCl_5 as a method of direct conversion of the product of the chloride volatility process. Solid UO_2 coatings were deposited on ThO_2 pellets to form a fissile-fertile combination having a potential reprocessing advantage.

Deposition of tungsten-rhenium alloys has continued. Greatly improved uniformity of composition was achieved by deposition at higher temperatures than used previously.

The intermetallic compound UAl_3 was successfully fabricated into aluminum-base fuel elements for irradiation to high burnup in the Oak Ridge Research Reactor. Swelling that occurred during vacuum degassing of UAl_3-Al compacts for Advanced Test Reactor (ATR) elements was related to UAl_3 content and degassing temperature. Aluminum-base miniature test plates containing U_3O_8 or niobium-coated UO_2–15% ZrO_2 fuel particles were irradiated to burnups up to 1.7×10^{21} fissions/cm^3 at cladding-film interface temperatures of 240 to 265°C without evidence of failure.

20. Mechanical Properties

Our investigations have continued to emphasize the effects of neutron irradiation on the mechanical properties of structural alloys. We have outlined the potential solutions to the problem of elevated temperature radiation damage. These involve modifying the metallurgical structure by decreasing the grain size, producing the optimum carbide distribution, and introducing small amounts of titanium to the basic type 304 stainless steel composition.

Studies of radiation damage to welds and brazes in austenitic stainless steels and nickel-base alloys show that these are also affected by high-temperature radiation damage.

Limited data on stainless steels irradiated in a fast reactor (LAMPRE) show that the ductility of type 316L stainless steel is significantly reduced at temperatures above 600°C, whereas the ductility of 17-4 PH steel is reduced only at a temperature around 700°C. Another ferritic alloy whose properties are less sensitive to irradiation is the composition Fe–15% Cr–4% Al–1% Y.

Also, the displacement type of damage that is very pronounced in stainless steels at about 250°C results from clusters of defects that are visible in the electron microscope. A reasonable correlation exists between the mechanical properties after irradiation and the structures observed in the electron microscope.

21. Nondestructive Test Development

In our continued development of computer calculation of parameters of an induced electromagnetic field, we calculated the forces generated in a specimen by eddy currents and obtained good correlation with experimental results. We also calculated and measured the impedance of a family of coils under varied operating conditions with excellent results. We developed a prototype beat-frequency eddy-current instrument, which offers high sensitivity for measuring conductivity variations. The phase sensitivity instrument was further improved for temperature stability, and development of a portable model began.

Our work on nonbond detection using ultrasonics has been directed toward development of a device for hot-cell examination of fuel tubes of the type used for PM-1 and proposed for HWOCR. We have developed techniques and calibration curves for electrical discharge machining of reference discontinuities for inspection of sheet, plate, and tubing. Techniques are being developed for observing ultrasonic energy in transparent liquids and solids using schlieren and photoelastic effects.

Our penetrating radiation work has emphasized scintillation detection methods, including use of attenuation to monitor variations in fuel content in vibratorily compacted fuel rods. Fiber optics were superior light pipes for applications in which scintillators and photomultipliers must be separated. We completed development and evaluation of a monitoring system for assaying ^{235}U in core blanks for fuel plate fabrication.

22. Sintered Aluminum Products Development

Sintered aluminum products (SAP) material is the prime candidate for the construction material of the fuel rods and pressure tubes of the Heavy-Water Organic-Cooled Reactor (HWOCR). Previously available sintered aluminum products exhibit erratic behavior in the form of poor process yield, structural inhomogeneity, gas fissuring and blistering, anisotropic properties, premature fracture, and low creep ductility. Since most of the erratic behavior is either process or material related, a thorough study is being conducted to determine the material and processing parameters necessary to produce a desired end product consistently and economically. The study may also improve our understanding of the mechanical behavior of sintered aluminum products so that maximum benefit may be derived from proper control of the material and processing parameters.

Characterization of various forms of aluminum powder has revealed that use of metal flakes within a controlled size range produces a stronger and more homogeneous final product. The oxide morphology can be controlled and agglomeration prevented by exposing the powders to vacuum at 600°C. Fractograph studies have revealed that sintered aluminum products fail in a ductile manner at low strain rates above 400°C, even though total uniform elongation is less than 0.5%. Electron microscopy studies indicate that strengthening in SAP is not related to stabilization of a cold-worked structure at high temperatures. The as-milled flake is completely recrystallized with a very low dislocation density. Hot working of SAP compacts significantly improves the rupture strength of the material.

A process flowsheet has been developed, and process variables are being investigated at each important step. Quality control techniques are under investigation to monitor the product at selected stages of fabrication.

23. Zirconium Metallurgy

In our study of the metallurgy of zirconium-base alloys, we continued the examination of the effects of preferred orientation and hydrogen content on the directional precipitation of hydride, the anisotropy of mechanical properties, the development of texture during fabrication, oxidation-corrosion mechanisms, and the anisotropy of oxidation. We developed techniques for determining the approximate basal pole figure for Zircaloy-2 by Knoop microhardness measurements, the determination of the orientation in space of the basal pole of any single grain of a polycrystalline close-packed hexagonal specimen by polarized light microscopy, and the determination of the hydride and basal pole figures in hexagonal metals by quantitative metallography.

PART IV. REACTOR DEVELOPMENT SUPPORT

24. BONUS Fuel Element Development

We successfully rebuilt a 32-rod BONUS fuel assembly using manufacturing procedures that provided significant improvements over those used by the manufacturer of the original core loading. Technical assistance was given to ORGDP concerning the fabrication of eight advanced fuel assemblies to be fabricated for the BONUS Reactor. We decided to use Incoloy 800 as the fuel cladding material for these assemblies, primarily because it resists corrosion by superheated steam better than the Inconel 600 used for core I.

Mechanical properties studies have concentrated on the collapse behavior of fuel tubes made from alloys being considered for advanced BONUS applications. Nondestructive testing studies are being conducted to develop improved techniques for testing the fuel elements. The problem areas include evaluation of the fuel cladding, the spacer-to-cladding braze bonds, and the welds in the fuel, coolant, and pressure tubes. Brazing studies on Incoloy-800 tubing have shown the influence of temperature and time upon grain growth of material in the annealed and cold-worked conditions.

25. Desalination

The desalination program consists of two main areas of interest. One concerns the reactor and the other the distillation plant. The problems relating to the heat source are under the cognizance of the AEC, while the evaporator-condenser is under the direction of the Office of Saline Water in the Department of the Interior. In the past year we have analyzed the cost of fabricating a number of different fuel elements in an effort to develop the optimum design for producing low-cost steam. We also developed specially shaped tubing for heat-transfer tests in an attempt to reduce the cost of the evaporation and condensing steps in converting salt water to fresh water.

26. Gas-Cooled Reactor Program

All-ceramic nuclear fuels consisting of pyrolytic-carbon-coated $(Th,U)O_2$ and $(Th,U)C_2$ fuel particles offer considerable advantages as fission-product-retaining fuel for high-temperature gas-cooled converter reactors. Much of our support for the Program consisted in developing techniques for fluidized-bed coating of particles and preparing and testing pyrolytic-carbon-coated particles and fueled-graphite elements containing such particles. Our technology for deposition of coatings from methane was extended to larger equipment and to the coating of larger (~ 500-μ-diam) fuel particles. We also developed techniques for depositing and characterizing low-density (<1 g/cm^3) coatings from acetylene.

Under heat treatment and irradiation, coated oxide fuels were stable and performed at least as well as if not better than coated carbides. Predictions based on our mathematical model for coated-particle behavior agreed well with actual results of a recent survey irradiation experiment. The model has also been valuable for planning further irradiation experiments and for optimizing the thickness ratios of two-layer coatings. We developed techniques for depositing an optimum coating on oxide fuel particles and prepared about 1.5 kg of coated $(Th,U)O_2$ microspheres for a cooperative irradiation experiment in the Dragon Reactor in England. We also performed heat-transfer analyses of the recent series of irradiation experiments on 6-cm-diam fueled-graphite spheres to correlate heat-generation rates with measured temperatures. Two processes for fabricating fission-product-emitting fueled-graphite elements are being evaluated as well.

Our other supporting activities included two experiments at higher temperatures on the creep behavior of graphite under irradiation. Results were consistent with a model for irradiation-induced creep and indicated that if the creep-rate coefficient is such that the stress level does not exceed the fracture stress, very large creep strains (>2%) may be accommodated. The available thermodynamic data for ceramic nuclear fuels were analyzed and correlated. The metallurgical behavior of stainless steel and Inconel nozzles designed for temperature measurement in the EGCR was monitored in a series of mockup tests. In addition, the failure of a 42-in.-diam stainless steel bellows at the EGCR was analyzed.

27. High Flux Isotope Reactor

The procedures previously developed at ORNL for fabricating HFIR fuel elements have been successfully transferred to industry. Metals and Controls, Inc., has now fabricated 11 fuel assemblies consisting of inner and outer annuli. Assistance from ORNL was required by the fabricator in working out the production problems, especially in the area of assembly and welding. Over 9000 fuel plates have been produced according to the HFIR specifications. The plate rejection rate has been reduced from more than 20% to about 10%.

The final density of an HFIR U_3O_8 dispersion fuel plate is not a function of the compact pressing pressure, since high final densities are being obtained even with pressures as low as 15 tons/in.^{2}. The final core dimensions varied with pressing pressures below 25 tons/in.^{2}.

Two procedures are being developed for adding wire spacers to the HFIR elements. In one, we draw either a steel wire or carbide balls with a diameter larger than the channel spacing through the channel, cutting grooves in both plates. The spacing wire, also larger than the channel, is then drawn into the grooves. In the second method, wires are ultrasonically welded to flat plates before they are curved and assembled into a fuel element. Small subassemblies were made by both techniques and used for flow testing.

Two additional sets of HFIR control plates were fabricated by slight modifications of procedures previously developed. The first set was then assembled into complete control cylinders meeting specifications.

Hot-cell examinations were made of miniature control plate samples after irradiation to doses of 2.9×10^{21} neutrons/cm^2 (thermal) and 1.1×10^{21} neutrons/cm^2 (fast). No evidence of any reaction, swelling, or plate deformation was found. The irradiated samples were cut to expose the dispersions and exposed to boiling water. The irradiated samples of the europium oxide dispersion swelled considerably but less than the controls. As expected, the europium molybdate dispersion did not swell.

28. High Flux Isotope Reactor Target Development

The Transuranium Project is to produce gram quantities of the heavier transuranium elements by successive neutron captures in ^{239}Pu. This nuclide has been converted to ^{242}Pu, ^{243}Am, and ^{244}Cm at Savannah River. Facilities and equipment at ORNL will be used to further irradiate these products and recover the isotopes produced. Target elements containing principally these three nuclides will be fabricated and then irradiated in the HFIR at a flux of approximately 3×10^{15} neutrons cm^{-2} sec^{-1}. The target elements will be reprocessed in the Transuranium Processing Facility (TRU) to recover the product actinides and to recycle the target actinides to the HFIR. Recycle target elements must be remotely manufactured because of the high gamma and neutron radiation associated with the contained nuclides.

Our tasks have involved the development of suitable targets, the development of procedures for fabricating these target elements under various conditions, and the testing and confirmation of design of the HFIR target element. We have almost completed the irradiation program for confirmation of the HFIR target element design, we have fabricated the necessary ^{242}Pu targets, and we have completed the development of the target fabrication equipment for the TRU. This equipment is now undergoing final testing prior to "hot" operation in the TRU.

29. Medium-Power Reactor Experiment

Tests using forced-circulation loops with boiling potassium have continued. The erosion damage of mockup turbine blades increased with decreasing vapor quality and was reduced by the addition of a hot trap.

In natural-circulation boiling-potassium loops chromium was transferred by high-purity potassium when TZM and stainless steel were both present in the condenser. The only attack found after 3000 hr of operation was an intergranular attack to 2 mils in a very limited area adjacent to boiling nucleation sites. A second all-stainless-steel loop with 3400 ppm oxygen added to the potassium in the boiler showed a similar but much heavier attack near the nucleation sites. Material was removed from inserts in the top of the condenser and deposited on those lower down, especially near the liquid level.

The compatibility of six high-temperature brazing alloys with boiling potassium at 1500 to 1600°F for times up to 6500 hr was studied. The alloys were tested as joints between type 316 stainless steel tubing and are rated in order of increasing attack: Coast Metals 50 and 52, General Electric J8100 and J8300, and Nicrobraz 50 and 10. Nicrobraz 10 was not recommended for use in boiling potassium at these times and temperatures.

Welds in type 304 stainless steel were cycled to failure by fatigue testing. Welds that had been heat treated at 1800°F had properties comparable to base metal, while the as-welded specimens had a shorter life expectancy.

Cermet bearings of tungsten carbide were brazed with an Ni-Si-B alloy to refractory metal pumps of a variety of sizes and configurations. Joints of tungsten carbide brazed to TZM were successfully carburized in methane. The high carburizing temperatures required higher-melting brazing alloys, these alloys were found in the Ni-Cr-Si system.

Coatings have been found that will increase the thermal emittance of both aluminum and stainless steel. One on aluminum appears stable to 600°F and one on stainless steel to 1500°F.

30. Molten-Salt Reactor Program

Surveillance specimens of Hastelloy N and grade CGB graphite have been assembled, placed in both the MSRE and the control test system, and exposed to molten fluorides for more than 1350 hr. The first sampling of these is scheduled for the early part of August 1966.

A reduction in ductility reduces the stress-rupture life of Hastelloy N. This reduction is sensitive to neutron dose, and a stress level exists below which no embrittlement is observed.

Welds in commercial Hastelloy N had poorer stress-rupture properties than did the base metal. Properties could be improved by postweld heat treatments. The welds were, however, degraded less than the base metal when exposed to neutrons.

Dynamic corrosion studies with fused salts and liquid lead have continued. Salt loops are still circulating successfully after several years of operation. Difficulties are still being encountered with plugging of the lead loops. A loop of Nb–1% Zr operated with lead at 1400°F for 4300 hr, however, niobium crystals were found in the cold leg.

A new brazing alloy, Pd–35% Ni–5% Cr, has been developed and has successfully brazed graphite to molybdenum. The joints have withstood thermal cycling and exposures of 1000 hr to molten fluoride salts at 700°C. A special joint brazed with a gold-nickel alloy successfully contained molten fluoride salts at 700°C and 150 psig for 500 hr.

Six new grades of graphite are being evaluated to determine their potential for use in molten-salt breeder reactors. Four are isotropic and two are anisotropic needle-coke graphite. Initial data indicate that they would have to be modified to be useful in the MSBR.

31. Reactor Evaluation

As part of the Laboratory's assistance to AEC in analyzing the potential of various reactor systems, we are evaluating the fuel fabrication costs and performance for potential reactor systems. Our library of computer programs for estimating fuel fabrication costs has continued to expand to cover added types of fuel elements. Fuel costs were estimated and performance was predicted for various fuel elements proposed for heavy-water-moderated organic-cooled reactors.

32. Thorium Utilization

Oak Ridge National Laboratory has been assigned the responsibility for evaluating the feasibility of utilizing thorium as a source of energy. To transform this potentially valuable resource into an economic fuel, it is necessary to completely characterize its physical and chemical nature. In addition, we must develop processes that will recover the valuable products bred during irradiation and reconstitute the new fuel into a form suitable for additional irradiation. Thus, the program in its entirety is a multidiscipline problem. The Metals and Ceramics Division's responsibilities involve characterization of the fuel, testing of the fuel under irradiation, and the development of processes for fabricating fuel elements prototypic of designs useful for power reactors.

Since the ^{233}U bred from thorium carries alpha and gamma activity, personnel must be shielded during processing steps. An $8,000,000 research facility in which pilot-scale processes can be demonstrated was designed and will be completed in December 1966. Remotely operated equipment is under development by the Chemical Technology and Metals and Ceramics Divisions and will be installed and jointly operated. The equipment will be designed to prepare and encapsulate uranium and thorium compounds in a graphite matrix for use in high-temperature gas-cooled reactors. In the past year we have endeavored to optimize the most critical step in the fabrication process, that of placing a carbon coating on microspheres of urania and thoria. The pyrolytically deposited carbon must meet several density and anisotropy requirements in addition to specifications for sphericity and thickness. The significant process variables in a fluidized-bed coater have been identified and are being quantified so that a completely automatic system can be designed. As an alternate approach to the problem a heated rotating drum could be employed as a coating system. Much larger charges of particles are possible in such a device, but the low efficiency of the gas-solid contact is a major obstacle that has not yet been solved. Although our concept of using carbon-coated oxides has proven very satisfactory, the desire to use part of the fuel in the carbide form persists. Although the carbide can be made by mixing of sols, a higher density product can be achieved by the process of solid-solid conversion we demonstrated last year. A pilot-scale version of the process has been designed and fabricated.

The irradiation program has two objectives. One is to explore the capabilities of thoria-base fuels so that their full potentialities can be utilized by designers, and the second is to proof test the products from the processes and equipment designed for remote operation. Most of the accomplishments are related to the first objective. Thoria-base fuels are stable in performance at exposures of over 1000 reactor full-power days. Successful tests were completed with heat ratings of 1000 w/cm. We conclude that thoria-base fuels have marked superiority to urania fuels in reactivity control and structural stability at very high heat ratings.

Irradiation of coated microspheres of sol-gel-derived fuel is a joint undertaking with the ORNL Gas-Cooled Reactor Program. Results indicate that sol-gel-prepared fuels perform equivalently to ceramics processed by older methods. Carbon-coated oxide fuels have performed satisfactorily despite thermodynamic instability.

Sol-gel techniques provide extra degrees of flexibility in the forming of ceramic bodies. In the gel state, extrusion without the use of plasticizers has been demonstrated. Packing of preselected sized microspheres to 85% of theoretical density in small-diameter tubes has been accomplished with very low-energy vibration.

A basic study of the sintering and grain growth of thoria and urania produced by the sol-gel process uses differential thermal analyses and hot stage microscopy. Although no simple law seems to describe the rate effects observed, shrinkage and crystal growth are evidently related to crystallite size.

PART V. OTHER PROGRAM ACTIVITIES

33. Isotopic Heat Source Development

A program was inaugurated with the Isotopes Division to investigate materials of current and future interest for encapsulating isotopes to be used as heat sources. Isotopic heat sources are of considerable value in thermoelectric and thermionic power technology because they offer the ability to operate unattended for relatively long periods of time at elevated temperature. The main effort has been associated with development of remote electron-beam welding techniques for refractory alloys and studies of the creep resistance of the tantalum-base alloys T-111 and T-222, particularly applied as pressure-vessel materials for alpha-emitting isotopes. The compatibility of platinum as a braze metal between iridium and tungsten-base alloys for high-temperature application was examined. Thermal conductivity of solid and liquid promethium and of a bed of PuO_2 spheroids in inert atmospheres was calculated.

34. Metallography

Vacuum evaporation of oxide films on polished metal surfaces provided a new means of revealing microstructures; we have worked out experimental techniques this past year to enable us to use this method routinely. The present state of metallography was thoroughly reviewed and presented as a paper. We discovered that curing stresses in our metallographic mounting material were damaging some braze samples; we investigated this phenomenon and developed a means of minimizing it. We examined the effect of specimen preparation on electron-beam microprobe analysis.

We continued to extend and refine our techniques of handling ceramic materials. A successful method of polishing and etching CeC_2, which is quite reactive with moisture, was developed. The procedure was similar to that employed for thorium and thorium-uranium dicarbides. We discovered that the appearance of the pyrolytic carbon coating on microspheres was greatly affected by the method of final polishing. Using alumina in silicone oil revealed the general structure of the coating but made it appear to have low density. Using $0.5\text{-}\mu$ diamond paste in water showed less marked structure but higher apparent density.

35. Rover Rocket Nozzle Materials

The short-time tensile properties and joinability of eight alloys were investigated. These are Inconel X-750, Inconel 718, René 62, Hastelloy X, Hastelloy N, Inconel 625, IN-102, and type 347 stainless steel. In addition, the thermal conductivities of Hastelloy X, Hastelloy N, Inconel 625, and Inconel 702 were estimated. These materials are all candidates for nuclear rocket nozzle fabrication. Also, a method for nondestructively testing tapered thin-wall tubes was developed.

36. SNAP-8 and SNAP-50 Corrosion Studies

Corrosion support programs for the SNAP-8 and SNAP-50 reactor systems were continued. Studies on the former were completed, and a summary report was issued. The most pronounced performance-deteriorating corrosion phenomenon found was carbon migration from the Croloy 9M to the other structural materials in the system (chromized Hastelloy N, types 347 and 316 stainless steel, and Hastelloy C) in contact with the eutectic NaK. The bimetallic heat-rejection loop, made from type 316 stainless steel and Nb–1% Zr alloy, studied in support of SNAP-50 completed its scheduled 6000-hr operation with eutectic NaK, was dismantled, and is being examined. Removable and permanent specimens of both structural metals located in the heated section showed very small or no weight change.

37. Thermonuclear Project

Failures in copper tubing subjected to extreme conditions were analyzed, lead alloys with increased lithium content were developed, and tungsten probes with BN insulation were fabricated. The last of these required unique extension of thermochemical deposition processes.

Part I.

Fundamental Programs

page blank

1. Crystal Physics

G. W. Clark

Material technology of tomorrow is dependent upon improved understanding of presently known materials and upon insight into new and novel materials. The use of single crystals is often required to characterize unambiguously many physical phenomena. Suitable crystals are frequently difficult to obtain, particularly of refractory substances. Thus, we are conducting a continuing program to provide crystals needed in research, to devise and improve methods of crystal growth, and to develop increased understanding of crystal-growth processes and kinetics. Crystals are being grown by several methods: by a floating-zone scheme, from molten-salt solvents, from supercritical aqueous systems, and by the general Verneuil method. More than ten compounds have been synthesized in single-crystal form within the past year. Some of these crystals have been used by other groups in investigations of electron-spin resonance, optical properties, deformation, fission-gas release, and magnetic properties and in x-ray analysis of neutron damage. Also, we are investigating selected physical properties, both those related to the crystal-growth process and those important for characterizing new compounds.

GROWTH OF UO_2 SINGLE CRYSTALS BY A CENTRIFUGAL FLOATING-ZONE TECHNIQUE

D. E. Hendrix A. T. Chapman[1]
G. W. Clark

We have continued the study of crystal growth in UO_2 by a modified zone-melting technique[2] in which a preheated UO_2 rod moves slowly through a radiofrequency induction coil, causing progressive melting (2800°C) and recrystallization inside a solid UO_2 shell. Thermal gradients favorable to the formation of a single crystal along the rod axis are promoted by rotation of the rod.

Our problem is to analyze the effect of the interrelated variables (frequency, power level, coil design, electrical and thermal properties of the material to be melted, and the chemical and mechanical controls) on the process. With an understanding of the interrelation, we can apply this technique more effectively to other refractory materials.

We have redesigned and built a system providing smoother control of rotary and vertical movement, preheating of the rod, and better control of the temperature and oxygen-to-uranium ratio of the rod. This apparatus now permits routine crystal growth. We have thus grown UO_2 crystals, both from green powder compacts and from single-crystal seeds, with no indication of a strongly preferred growth direction.

As a measure of the effect of given variables, the perfection of the UO_2 crystals has been studied by a modified Berg-Barrett technique. Typical crystals show subgrains with minimum dimensions of about 1 mm (generally elongated in the direction of growth) and with rocking curve widths between 0.1 and 0.2°. In a crystal roughly 1 cm in diameter and 4 cm long, the maximum variation of orientation among the subgrains is about 1°. A preliminary look at etch-pit densities has not given a clear correlation with the x-ray-determined quality of the crystals. The problem of cracking of the UO_2 crystals still persists.

---

[1] Consultant from Georgia Institute of Technology, Atlanta.

[2] A. T. Chapman and G. W. Clark, *Metals and Ceramics Div. Ann. Progr. Rept. June 30, 1965*, ORNL-3870, p. 3.

The technique of preheating followed by direct inductive coupling and eddy-current heating has been applied with promising results to $BaTiO_3$, TiO_2, NiO, and $(Th,U)O_2$.

HYDROTHERMAL GROWTH

O. C. Kopp[3] G. W. Clark

Lanthanide Oxyhydroxides, Ferrates, and Hydroxides

The system Ln_2O_3-H_2O has been studied in the temperature range 380 to 560°C and the pressure range 350 to 1100 kg/cm^2 for the sesquioxides of lutetium (ionic radius 0.85 A), erbium (0.89 A), europium (0.98 A), and neodymium (1.04 A). The experiments were performed in type 347 stainless steel liners by the split-autoclave technique reported below. The dominant phases obtained were the oxyhydroxide LnOOH, the ferrate $LnFeO_3$, and the trihydroxide $Ln(OH)_3$. We focused our attention on the synthesis of the oxyhydroxide phase, which becomes more difficult with increasing radius of the trivalent lanthanide ion, and the NdOOH compound was not successfully grown. The other oxyhydroxides were grown as single crystals in the size range 1 to 2.5 mm in a three-week growth period. Single-crystal x-ray photographs revealed that the oxyhydroxide phase was monoclinic rather than orthorhombic as previously reported. The same result was obtained independently by Christensen.[4]

Although yttrium is not a lanthanide, the YOOH phase is very similar to the LnOOH phases. Single crystals of YOOH were obtained at 400 to 450°C in the pressure range 350 to 1000 kg/cm^2. The largest crystals were obtained at the higher temperatures and pressures and exceeded 1 mm after three weeks growth. We are now doping the YOOH phase with lanthanide ions for electronic-state studies of these ions in a dilute state in this crystal environment.

Split Autoclave for Hydrothermal Experiments[5]

We designed a split autoclave that uses disposable liners prepared from seamless tubing of a wide range of materials. This permits the use of solvents other than aqueous solutions. Incorporated into each end of the tube liner is a Bridgman seal. An autoclave supporting a $\frac{3}{4}$-in.-OD liner has been used at pressures up to 2000 kg/cm^2 at a temperature of 450°C without deformation of the autoclave halves or bolts.

GROWTH OF CRYSTALS FROM MOLTEN-SALT SOLUTIONS

C. B. Finch G. W. Clark

Conditions were ascertained for thermal-gradient growth of fair-quality hexagonal GeO_2 crystals up to 3 mm from $Li_2O \cdot 2MoO_3$ at 1050 to 1080°C. Single crystals of tetragonal GeO_2, the modification stable below a 1033°C transformation,[6] were grown to 1 mm by slow cooling of a GeO_2-PbO solution from 1030 to 960°C. Growth of single-crystal ThO_2, both pure and lanthanide-doped, was continued by the described method.[7] ThO_2 was also grown from two other solvents, PbF_2 and $7BaO \cdot 2B_2O_3$, neither of which appears as suitable for growth as does $Li_2O \cdot 2WO_3$.

Crystals of Y_2GeMoO_8 doped with several lanthanides were grown for electron-spin-resonance investigation. The crystal chemistry of the scheelite $LnABO_8$-type compounds (Ln = any lanthanide; A = Si, Ti, Ge, Zr, or Sn; B = Mo or W) is being studied. The ion radius limits for formation of the scheelite structure are being delineated by x-ray examination of appropriate stoichiometric pellets fired at 1300°C.

Single-Crystal Growth of Cerium Dioxide from Lithium Ditungstate Solvent[8]

Single crystals of CeO_2 were grown as octahedra up to 2 mm on edge from $Li_2O \cdot 2WO_3$ solvent.

---

[3] Consultant from the University of Tennessee, Knoxville.

[4] A. N. Christensen, *Acta Chem. Scand.* **19,** 1391 (1965).

[5] Summarized from *Rev. Sci. Instr.* **37,** 372 (1966).

[6] A. W. Laubengayer and D. S. Morton, *J. Am. Chem. Soc.* **54,** 2303–20 (1932).

[7] C. B. Finch and G. W. Clark, *J. Appl. Phys.* **36**(7), 2143–45 (1965).

[8] Summarized from note submitted for publication in *Joumal of Applied Physics.*

Growth occurred by solution transfer from CeO_2 nutrient at 1100°C to nuclei in regions 25 to 30°C cooler. Optically clear crystals contained 200 ppm W and less than 50 ppm Li. Crystals of CeO_2 doped with various lanthanides, including Nd^{3+}, Gd^{3+}, Dy^{3+}, Fr^{3+}, and Yb^{3+}, were grown by the same method.

TEMPERATURE DEPENDENCE OF LATTICE CONSTANTS

C. B. Finch G. W. Clark

The coefficients of linear thermal expansion α were determined for Y_2GeMoO_8, ThO_2, and CeO_2 over the temperature range 50 to 350°C with an interferometric dilatometer described by Peters and Cragoe.[9] A slit, a microphotometer, and an *X-Y* recorder were incorporated into the apparatus to enable automatic registry of the passage of interference fringes. Mean values of α were $13.4 \pm 0.3 \times 10^{-6}/°C$ for single-crystal tetragonal Y_2GeMoO_8 ([001] direction), $9.0 \pm 0.3 \times 10^{-6}/°C$ for single-crystal ThO_2, and $11.3 \pm 0.2 \times 10^{-6}/°C$ for single-crystal CeO_2. No discontinuities were evident in the expansion of any of the above compounds for the temperature interval studied.

ELECTRON SPIN RESONANCE OF RARE-EARTH IONS IN CeO_2: Yb^{3+} AND Er^{3+} (Ref. 10)

M. M. Abraham[11] G. W. Clark
R. A. Weeks[11] C. B. Finch

The paramagnetic resonance spectrum of Yb^{3+} and Er^{3+} in single crystals of CeO_2 has been measured at 10 Gc/sec and 4°K. In sites of cubic symmetry, the ground states in both cases are found to be isotropic Γ_7 doublets with $g = 3.424 \pm 0.001$ for Yb^{3+} and $g = 6.747 \pm 0.006$ for Er^{3+}. Hyperfine structures for the odd isotopes were resolved with $A(^{171}Yb) = (877.1 \pm 1.0) \times 10^{-4}$ cm^{-1}, $A(^{173}Yb) = (242.0 \pm 0.3) \times 10^{-4}$ cm^{-1}, and $A(^{167}Er) = (232.1 \pm 0.3) \times 10^{-4}$ cm^{-1}. Nearby charge compensation produces sites of axial symmetry. For Yb^{3+}, one set of axes is along the four $\langle 111 \rangle$ crystal directions with $g_{\parallel} = 4.733 \pm 0.004$ and $g_{\perp} = 2.744 \pm 0.002$. For Er^{3+} two different axial spectra were measured, also with trigonal symmetry about the $\langle 111 \rangle$ directions. For one set $g_{\parallel} = 10.25 \pm 0.05$ and $g_{\perp} = 4.847 \pm 0.005$, and for the other set $g_{\parallel} = 4.539 \pm 0.005$ and $g_{\perp} = 7.399 \pm 0.007$. In most crystals the linewidths were 20 Oe; however, in some crystals in which no cubic sites were found, the axial linewidths were greater than 50 Oe. Comparisons of the axial g-tensor traces with the cubic g tensor and the magnitude and sign of $\Delta g = g_{\parallel} - g_{\perp}$ are the basis for a discussion of the possible nature of the charge compensation producing the axial symmetry.

APPARATUS FOR THE SPECTROPHOTOMETRIC STUDY OF SMALL CRYSTALS[12]

J. P. Young[13] G. W. Clark

We developed auxiliary equipment for the model 14M Cary recording spectrophotometer to obtain absorption spectra of 0.3- to 0.4-mm-diam crystals of appropriate thickness. Also, we can obtain spectra of 0.1-mm crystals over the range of wavelengths of the Cary high-intensity-source accessory.

---

[9] C. G. Peters and C. H. Cragoe, *Natl. Bur. Std. (U.S.), Sci. Papers* **16**, 449 (1920).

[10] Abstract of *Phys. Rev.* **148**, 350–52 (1966).

[11] Solid State Division.

[12] Summarized from *Rev. Sci. Instr.* **37**, 234 (1966).

[13] Analytical Chemistry Division.

2. Deformation and Annealing of Metals

C. J. McHargue

Our studies are directed toward finding the principles underlying the atom movements that occur during deformation, annealing, and phase transformation in solids. We use these principles to correlate the physical and mechanical properties with the microstructure and to obtain specific properties by suitable thermal and mechanical treatments that modify the microstructure. During this report period we continued to study migration of grain boundaries during annealing and the deformation of body-centered cubic metals.

GRAIN-BOUNDARY MIGRATION-RATE STUDIES

R. A. Vandermeer

Grain-Boundary Migration[1]

Paul Gordon[2] R. A. Vandermeer

We reviewed and analyzed recent advances in the understanding of grain-boundary migration behavior in zone-refined metals and dilute alloys. The effect of orientation and boundary structure factors and their interdependence with impurity effects were considered in detail. A new theory was advanced to explain the high mobility of Kronberg-Wilson coincident lattice boundaries in all but the highest-purity materials, where random boundaries are predicted to have the higher mobility.

Investigations aimed at the quantitative understanding of the drastic effect dissolved impurities have on boundary migration were also examined, and the results were compared with the predictions of migration-rate theories. Such comparisons lead to the conclusion that in dilute alloys impurity atmospheres that are segregated about the boundaries can act as a drag when the boundaries move. In zone-refined metals the rate-controlling process for boundary migration appears to be the transfer of single atoms across the boundary.

A Transient Effect in Grain-Boundary Migration During Recrystallization in Aluminum[3]

R. A. Vandermeer

The experimental findings that indicated a transient growth of some grains during the early stages of recrystallization in aluminum rods extruded at sub-zero temperatures have already been given.[4] Two explanations have been proposed. One involves the role residual impurities may play during the transient growth period. The migrating grain boundary undergoes a transition from a high nearly impurity-independent velocity to a low impurity-dependent velocity. This transition is brought about by a decrease in driving force due to recovery in the cold-worked matrix. The alternative interpretation assumes that a large excess of vacancies is generated during deformation and is effectively frozen in as either single vacancies or vacancy clusters, due to the low deformation temperature. The presence of this vacancy field is postulated to enhance the mobility of migrating

---

[1] Summarized from paper published in *Recrystallization Grain Growth and Textures*, American Society for Metals, Metals Park, Ohio (in press).

[2] Professor of Metallurgical Engineering at Illinois Institute of Technology, Chicago.

[3] Summarized from paper submitted to *Acta Metallurgica*.

[4] R. A. Vandermeer, *Metals and Ceramics Div. Ann. Progr. Rept. June 30, 1964*, ORNL-3670, pp. 61–62.

grain boundaries. Annealing these vacancy defects out decreases the boundary mobility until the vacancy excess is eliminated.

Grain-Boundary Migration During Recrystallization of Aluminum Alloys Dilute in Gold

We measured the migration rates of grain boundaries during recrystallization of dilute alloys of gold in zone-refined aluminum. Metallographic examination revealed that second-phase particles, presumably the intermetallic compound Al_2Au, are present in some of the alloys. Furthermore, the migration rates in these alloys depend on the thermal history of the test pieces. Typical results are shown in Fig. 2.1, where the migration rates of an alloy containing 45 ppm Au, rolled 40% at 0°C, and annealed at 111°C are plotted as a function of the volume fraction recrystallized for strips of different thermal histories prior to deformation. Table 2.1 lists (1) the thermal histories of the strips as well as (2) notes regarding the state of precipitation as determined by visual examination at 100× in a light microscope (see Fig. 2.2).

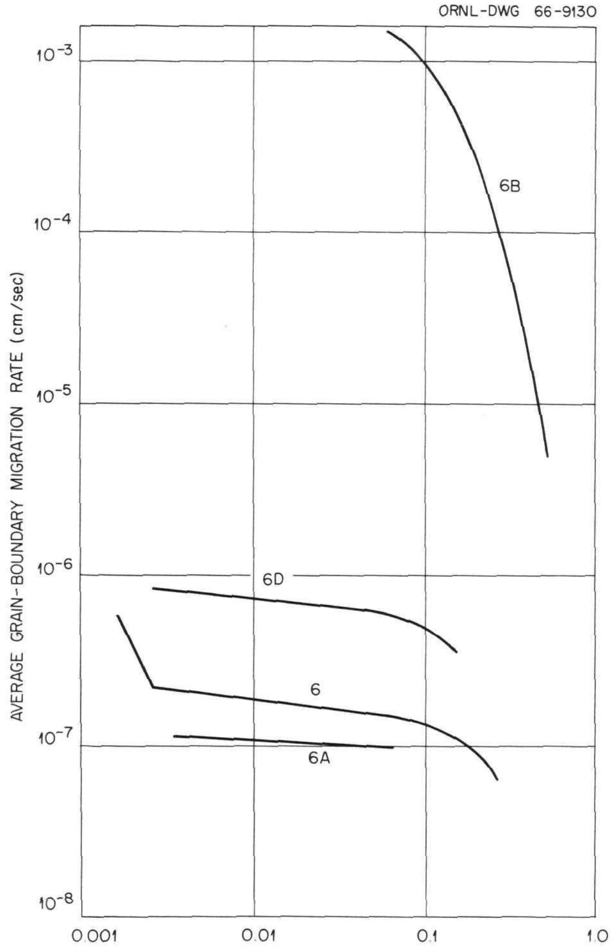

Fig. 2.1. Variation of Average Grain-Boundary Migration Rate as a Function of Volume Fraction Recrystallized at 111°C for Specimens with Different Thermal Histories of an Alloy of Zone-Refined Aluminum Containing 45 ppm Au. Thermal histories are given in Table 2.1.

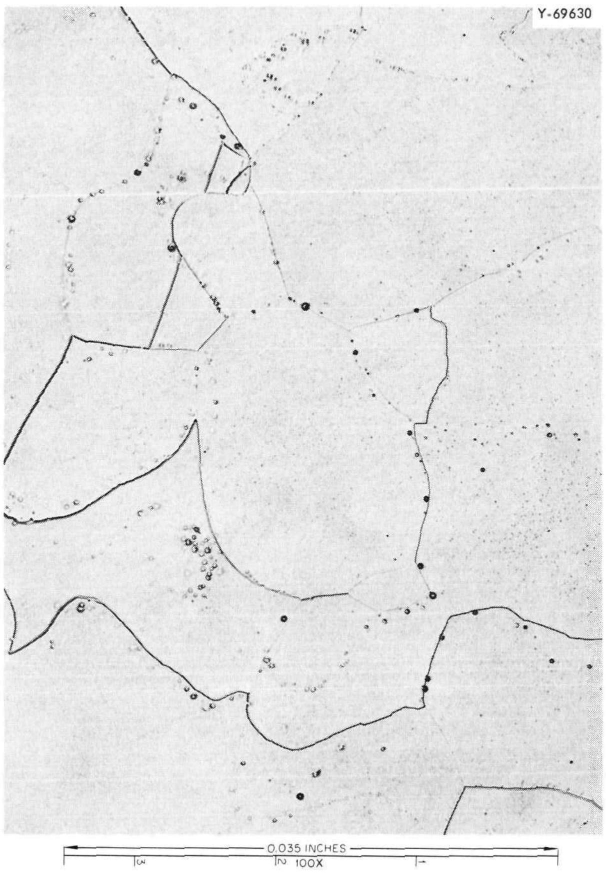

Fig. 2.2. Photomicrograph Depicting the Penultimate Grain Size and the State of Precipitation in an Alloy of Zone-Refined Aluminum Containing 45 ppm Au. Reduced 27.5%. Details of thermal history are given under 6B in Table 2.1.

These data indicate that the migration rates are highest when the solid solution is the least supersaturated with respect to the gold; impurities (i.e.,

Table 2.1. Relationship Between Thermal History Before Rolling and State of Precipitation[a]

Designation	Thermal History	State of Precipitation
6	Penultimate anneal: 3 hr 415°C, cooled rapidly in air	No precipitate visible
6A	Penultimate anneal: 2 hr 415°C, quenched into ice water	No precipitate visible
6B	Penultimate anneal: 44 hr 415°C, slow cool to 300°C, held 48 hr, slow cool to 200°C, held 170 hr, slow cool to 100°C, held 1 week, slow cool to 24°C, held 2.5 months	Many precipitate particles present, large spherical particles in grain boundaries, small black dots within grains, see Fig. 2.2
6D	Same as 6, but reheated to 300°C and held for 25.5 hr, slow cool to 200°C, held 50 hr, slow cool to 100°C, held 71 hr, slow cool to 24°C, held 2 weeks	Some detectable precipitation

[a] Specimens were given final anneal at 111°C after rolling.

most of the gold atoms) are tied up with the precipitate particles. Conversely, the migration rates are lowest when the solid solution is the most supersaturated (i.e., most of the gold atoms are in solution). This seems to be in qualitative agreement at least with the impurity-drag theories of boundary migration. Furthermore, the precipitate particles themselves seem to have little effect on the migration rates and act only as disposals for purification of the matrix. The specimens containing the most precipitate particles gave rates of boundary migration about the same as that of zone-refined aluminum, where no impurities and hence no precipitate particles were present.

THE ANNEALING OF DEFORMATION TWINS IN COLUMBIUM[5]

J. C. Ogle C. J. McHargue

Lightly deformed columbium single crystals which contain only parallel twins or parallel and intersecting twins were annealed at 1000° and 1600°C. No recrystallization occurred in specimens having only parallel twins. Only noncoherent twin boundaries migrated at 1000°C but both coherent and noncoherent ones moved at 1600°C. Recrystallization occurred within a few minutes at twin intersections at 1000°C. The orientation of the recrystallized grains differed from that of both the matrix and deformation twins, but could be derived by ⟨110⟩ and/or ⟨112⟩ rotations.

PREFERRED ORIENTATION OF NIOBIUM

J. C. Ogle R. A. Vandermeer

We are investigating the development of preferred orientation in cold-rolled electron-beam-melted niobium, starting with a fine-grained randomly oriented aggregate. X-ray-diffraction pole figures of the (110), (200), and (222) planes were obtained from specimens rolled to 20, 40, 60, 80, and 95% reduction in thickness at temperatures near −196°C. The high-intensity regions of the pole figures of the specimen that was reduced 95% are ridges which, as the (200) and (222) pole figures in Fig. 2.3 indicate, run from {001}⟨110⟩ towards the {112}⟨110⟩ and then to the {111}⟨211⟩ ideal orientations. Of these ideal orientations, the {001}⟨110⟩ appears to be the strongest. The ridge-like nature of the texture is already evident after 80% reduction, but the highest intensity seems to be associated with an orientation near {112}⟨110⟩. The results on specimens deformed

---

[5] Abstract of *Trans. Met. Soc. AIME* **236**, 686 (1966).

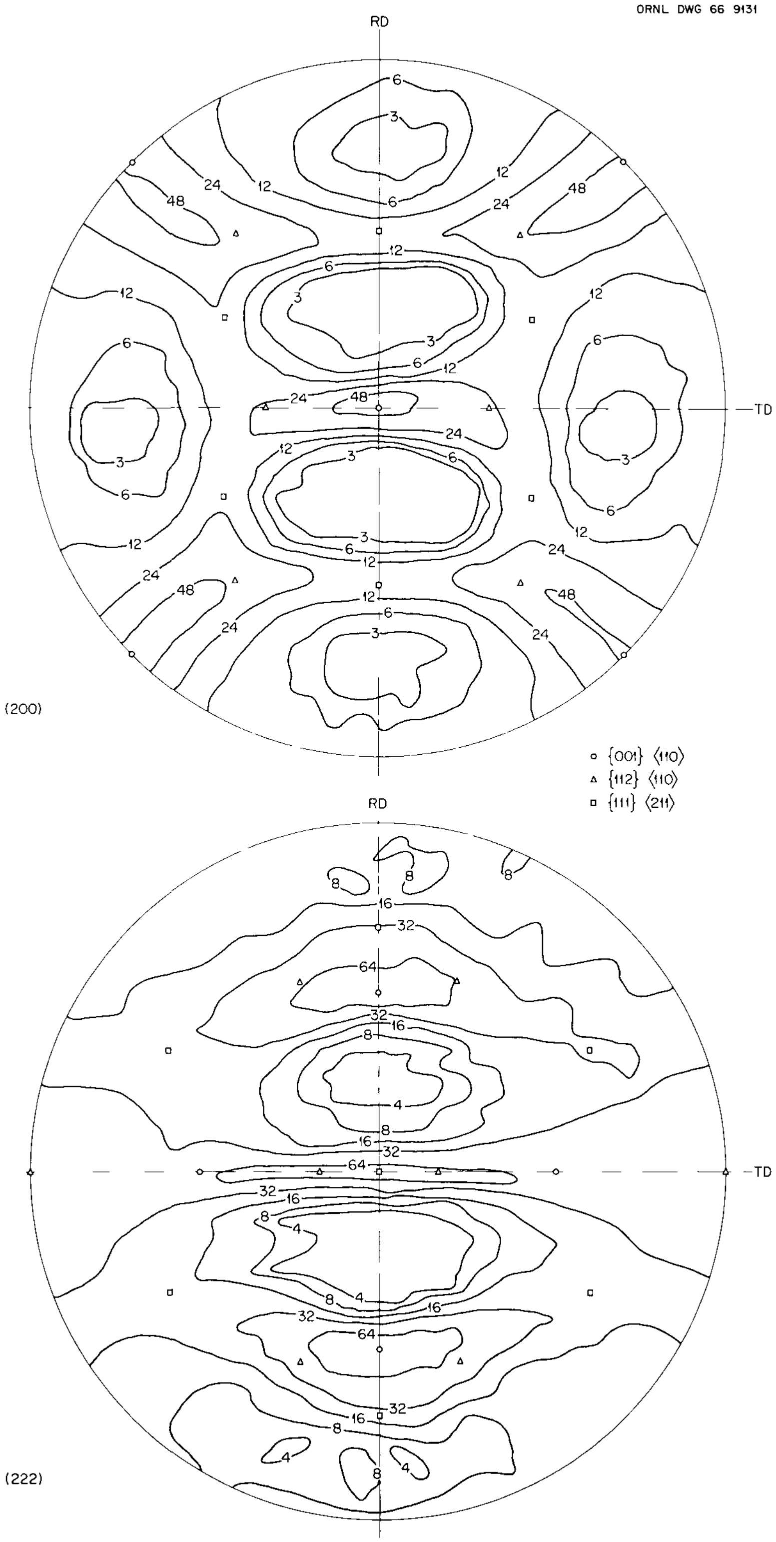

Fig. 2.3. The (200) and (222) Pole Figures of Polycrystalline Niobium Rolled 94% at Subzero Temperatures. The circle points show the $\{001\}\langle 110\rangle$, the triangles the $\{112\}\langle 110\rangle$, and the squares the $\{111\}\langle 211\rangle$ ideal orientations.

lesser amounts suggest that, in the early stages of deformation, material tends first to accumulate near the {544}⟨225⟩ orientation. This is followed by reorientation toward the {112}⟨110⟩ and ultimately to the {001}⟨110⟩ orientation. This later reorientation, from the {112}⟨110⟩ to the {001}⟨110⟩, has been predicted on theoretical grounds by Dillamore and Roberts,[6] but the apparent stability of the {544}⟨225⟩ at the lower reductions has not been predicted. We are presently investigating specimens deformed up to 99% reduction in thickness to see if further reorientation takes place.

We also examined the microstructures of niobium specimens deformed to 5, 10, 20, 40, 60, 80, and 95% reductions to assess the role of mechanical twinning on the overall deformation behavior of this material. Twinning, as observed in the light microscope, occurred only up to about 10 or 20% reduction, and then only very few twins were noted. We believe that these twins make no significant contribution in a direct way to the final rolling texture. The density of twins seemed to be a function of their position in the strip. Grains at the rolling-plane surface and those near the midplane of the strip were devoid of twins, whereas most of the twins were found in grains just below the rolling-plane surface.

The texture of niobium rolled 95% at room temperature was redetermined on the fine-grained randomly oriented starting stock. It was less sharp than the texture of niobium rolled at the lower temperature but otherwise differed very little.

We also determined the recrystallization textures of the niobium sheets rolled to 95% reduction in thickness. Both the recrystallization temperature and the resulting texture were identical in specimens rolled at both temperatures. The most intense regions of the pole figures of recrystallized specimens annealed 1 hr at 1115°C were centered on the {544}⟨225⟩ ideal orientation with some spread toward the transverse direction. Thus, the weak component of the rolling texture became the dominating component of the subsequent recrystallization texture.

We are studying the reorientation of single crystals of electron-beam-zone-refined niobium during rolling 94% near −196°C and recrystallization. Table 2.2 lists the initial orientations and the rolling textures in the interior of the crystals. Our results show that of the three crystals studied only the (101)[010] undergoes significant reorientation in its interior during rolling. In agreement with this is the metallographic observation on transverse sections that only this crystal contained deformation bands *in the central regions* of the strip after rolling. All of these strips, however, were heavily banded *at the surface regions*. These observations suggest a possible texture variation from the surface to the center in the two crystals that showed no reorientation in their interiors. Experiments are now under way to confirm this suggested variation.

The recrystallization tendencies of these rolled single crystals seemed to depend on whether or not deformation bands were formed on rolling. Thus, the (101)[010] crystal recrystallized readily in the strip interior, whereas the others recrystallized reluctantly (i.e., higher temperatures were required to induce recrystallization). However, at the surface regions where deformation bands were present, all of the crystals recrystallized rather readily. We will examine this question more fully.

The center recrystallization texture of a rolled (101)[101] crystal annealed 1 hr at 922°C was determined and can best be described as an approximate fiber texture about a [111] parallel to the normal direction of the strip. Both the center and surface recrystallization of the other crystals will also be determined.

Table 2.2. Initial Orientations and Rolling Textures of Niobium Single Crystals

Crystal	Rolling Plane	Rolling Direction	Texture at Strip Interior
5000	(101)	[010]	$(111)[\bar{1}2\bar{1}]$ $(111)[1\bar{2}1]$ $(001)[\bar{1}10]$
5100	(001)	$[\bar{1}00]$	$(001)[\bar{1}00]$
5200	(001)	$[\bar{1}10]$	$(001)[\bar{1}10]$

---

[6] I. L. Dillamore and W. T. Roberts, *Acta Met.* 12, 281 (1964).

3. Deformation of Crystalline Solids

Our program of basic studies of the deformation of metals and alloys is aimed at a better understanding of the controlling processes during deformation, of the resulting structure, and of the changes due to annealing. Such knowledge contributes to the utilization of existing materials and the development of better ones.

WORK HARDENING AND DISLOCATION STRUCTURE IN TANTALUM AND TANTALUM-BASE ALLOYS[1]

R. J. Arsenault   A. Lawley[2]

The work hardening characteristics of tantalum and tantalum-alloy single crystals were investigated as a function of temperature, orientation, and interstitial concentration; associated dislocation structures were characterized parallel and perpendicular to the primary slip vector. The presence or absence of stage II hardening can be related to the magnitude of the effective stress τ^*. When $\tau^* \cong 0$, stage II hardening occurs and the work-hardening slope θ_{II} is a maximum. As τ^* increases, θ_{II} decreases, and in the limit only stage I is observed. In comparison to fcc metals, there is a large degree of overshoot (approximately 10°), and it appears that secondary slip is a necessary condition for the existence of stage II hardening. An explanation for the dependency of stage II and the magnitude of θ_{II} on the level of τ^* is advanced, based on two factors: the probability that the stable reaction

$$\frac{a}{2}[11\bar{1}] + \frac{a}{2}[1\bar{1}1] = a[100]$$

would occur increases with decreasing τ^*, and the increase in internal stress required for secondary slip is lower at small effective stresses. These concepts are shown to be consistent with the associated structures.

Increasing the solute concentration either eliminates the three stages of work hardening or reduces the rate of work hardening in stage II. Interstitial impurities lock the grown-in dislocations and/or lead to precipitates; both give rise to barriers and induce secondary slip at low strains with an associated parabolic form of the stress-strain curve. Similarly, substitutional atoms can lock the grown-in dislocations such that these act as barriers (e.g., tungsten additions) or reduce the number of operative sources on secondary-slip systems (e.g., niobium additions).

DISLOCATION DYNAMICS APPLIED TO THE PROBLEM OF OVERSHOOT[3]

R. J. Arsenault

In general, single-crystal samples in tension should deform on only one slip system until the orientation of the tensile axis reaches a symmetry position in which the resolved shear stress on a second slip system is the same as on the original slip system. Then deformation should occur on both slip systems. For face-centered cubic metals these conditions of deformation generally apply.[4,5] However, face-centered cubic solid solutions,[6] body-centered cubic metals,[7] and body-centered

---

[1] Abstract of paper submitted for publication to *The Philosophical Magazine*.

[2] The Franklin Institute Research Laboratories, Philadelphia.

[3] Summarized from paper accepted for publication in *Acta Metallurgica*.

[4] R. Karnop and G. Sachs, *Z. Physik* **41**, 116 (1927).

[5] F. von Göler and G. Sachs. *Z. Physik* **55**, 581 (1929).

[6] T. E. Mitchell and P. R. Thornton, *Phil. Mag.* **8**, 1127 (1963).

[7] R. E. Reed, Solid State Division, private communication.

cubic solid solutions do not deform in this manner. When the orientation of the tensile axis reaches the symmetry position, the sample continues to deform on the original (primary) slip system. The extent to which the orientation of tensile axis rotates beyond the symmetry line is defined as "overshoot."

By a theoretical analysis, we conclude that the effect due to the differences in the densities of mobile dislocations on the primary and secondary slip systems can be a major factor contributing to the degree of overshoot. The temperature dependence of dislocation dynamic contribution will vary as the parameter temperature divided by the activation volume.

THE APPARENT TEMPERATURE DEPENDENCE OF THE ACTIVATION ENERGY OF SLIP IN NEUTRON-IRRADIATED COPPER[8]

R. J. Arsenault

From an investigation of the activation energy of slip in neutron-irradiated copper, it has been concluded that the activation energy was temperature dependent, but this conclusion is in contradiction with the results of an investigation of the temperature dependence of the activation energy at constant stress. The latter found the activation energy to be independent of temperature. The apparent contradiction was explained in terms of the stress dependence of the pre-exponential term; that is, the effective distance moved by a dislocation in a successful thermal fluctuation is a function of stress.

SOME NOTES ON THE STRENGTHENING MECHANISM IN NEUTRON-IRRADIATED COPPER SINGLE CRYSTALS[9]

T. J. Koppenaal[10] R. J. Arsenault

Discussions are presented in some of the controversial areas regarding the interpretation of the strengthening mechanism in neutron-irradiated copper single crystals. The specific topics that are discussed include the following: the correction of cross-head speed changes to strain-rate changes, the strain-rate dependence of the flow stress, the temperature dependence of the pre-exponential factor, the free energy and the enthalpy of activation, the defect and obstacle size spectrum, and the nature of the force-distance behavior for the interaction of mobile dislocations with irradiation-produced obstacles.

It is shown that many of the recent arguments made against our previously published explanation of the strengthening mechanism can be readily explained without changing our interpretation.

THE POSSIBILITY OF IRRADIATION DAMAGE AFFECTING THE RATE-CONTROLLING MECHANISM FOR SLIP IN BODY-CENTERED CUBIC METALS AND SOLID SOLUTIONS[11]

R. J. Arsenault

There have been numerous investigations of the rate-controlling mechanism for deformation in neutron-irradiated face-centered cubic metals; there have been only a few preliminary experiments employing body-centered cubic metals. These experiments indicate that the neutron damage does not appear to change the rate-controlling mechanism for deformation in body-centered cubic metals. The reason for the absence of change is due to the intrinsic rate-controlling mechanism of body-centered cubic metals and the particular experimental conditions employed.

These reasons are examined in detail, and the probable experimental condition necessary for the observation of a detectable change in the rate-controlling mechanism is explored.

METHODS OF REDUCTION OF TEXTURE DATA TO INVERSE POLE FIGURES[12]

R. O. Williams

Several methods have been devised to facilitate the inversion of texture data to inverse pole figures, which give the distribution of a physical direction over the crystallographic triangle. Graph-

---

[8] Abstract of paper submitted for publication to *The Philosophical Magazine*.

[9] Abstract of paper submitted for publication to *Physica Status Solidi*.

[10] Metallurgy Division, Argonne National Laboratory, Argonne, Ill.

[11] Abstract of ORNL-3993 (in press).

[12] Abstract of ORNL-3979 (in press).

ical integration is replaced by summing the distribution over a set of points. The coordinates of these sets are given for seven planes in the cubic system. A graphical method is presented which gives an improved starting distribution and will give an adequate inversion for simple textures.

SHEET INVERSE POLE FIGURES

R. O. Williams

For materials having cylindrical symmetry (fiber textures), all orientations of the crystallites can be completely described by a density function defined over the unit triangle for the crystal system. This density function gives the probability that any given point will show that orientation. This representation has been known for many years, and the complete mathematical definition was worked out about ten years ago.[13]

For materials with textures of less symmetry, the corresponding representation requires a third angular variable. Whereas the method has been worked out more or less satisfactorily for fiber textures, this is not true for sheet textures. The mathematical definition and representation have been derived,[14,15] but no actual inversions have been carried out. The problem has been redefined, and our method for expediently carrying out the inversion is outlined below.

The basic concept is shown in Fig. 3.1 for the cubic system. One of the sheet directions, such as the normal direction, is located within the basic unit triangle, as for a fiber texture. A second direction, such as the rolling direction, is located by the angle β relative to the equator measured in a counter-clockwise direction. All possible orientations are represented with the first axes located within the unit triangle and the second located by β within a range of 180°. This corresponds to the angular volume shown in Fig. 3.1*b*.

The relation between all possible diffraction data and the above definition is shown in Fig. 3.2. Figure 3.2*a* defines the angles for the diffraction data, and Fig. 3.2*b* shows how these angles are related to the definition, assuming that the intensity data are from the (200) plane. The value

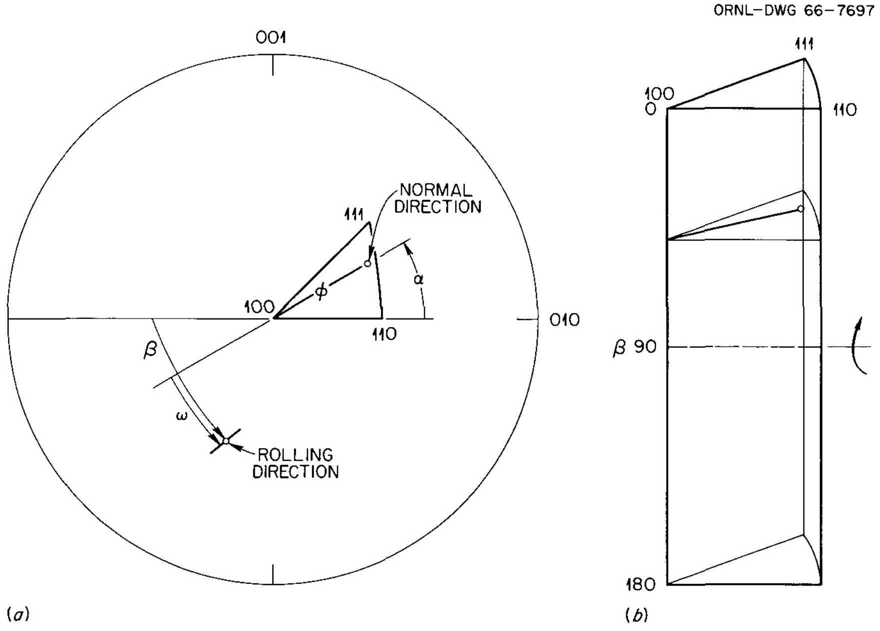

Fig. 3.1. Definition of the Inverse Pole Figure for Sheet Textures. (*a*) Definition of coordinates, (*b*) angular volume containing all possible orientations.

---

[13] L. K. Jetter, C. J. McHargue, and R. O. Williams, *J. Appl. Phys.* **27**, 368 (1956).

[14] H. J. Bunge, *Z. Metallk.* **56**, 872–74 (1965).

[15] R. J. Roe, *J. Appl. Phys.* **36**, 2024 (1965).

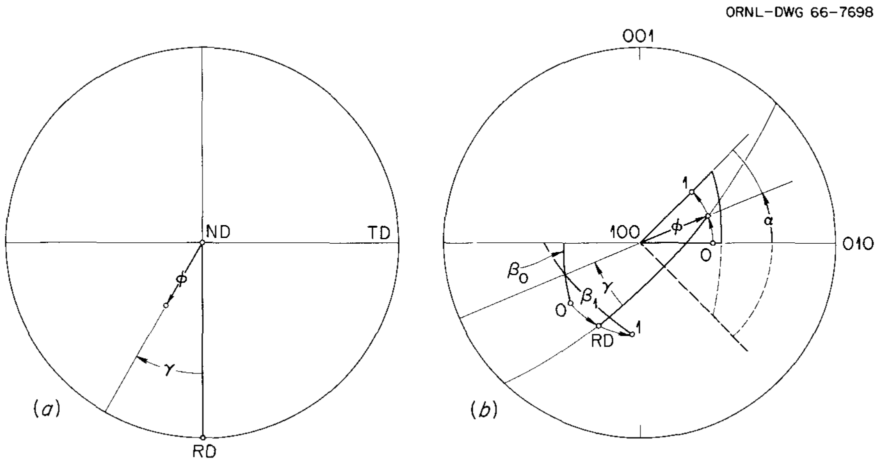

Fig. 3.2. The Relation Between Intensity and Inverse Pole Figure. (a) Angular coordinates for the normal pole figure. (b) Angular ranges of orientations that contribute to the intensity at the given values of ϕ and γ for the (200) plane.

of the normalized diffraction intensity I at particular values of ϕ and γ is equal to the sum of all possible orientations that have these values of γ and ϕ, divided by the angular arc over which these orientations may be spread. All such orientations are defined for the material on the arc ϕ degrees from (100) and for those values of β that lie between β_0 and β_1. This corresponds to α going from 0 to 45°. Mathematically, this is given by

$$I(hkl, \phi, \gamma) = \alpha^{-1} \int_0^{45^\circ} T(\phi, \alpha, \beta)\, d\alpha \; , \qquad (1)$$

where T is the density function, since the arc over which the orientations are spread is also α. The problem is slightly more complicated than this, since a set of orientations within the dotted triangle of the opposite hand must also be included so that α from -45° to 0° is also included. For this set of orientations, β is measured in a clockwise direction by the original definition. In addition, as ϕ becomes larger, the unit-triangle boundary is intercepted, such that the path is folded back. But we do not need to cover the details here. For other planes, ϕ and α are measured relative to the pole of that plane. It should be noticed that this relation is the same as for fiber textures but includes an additional dimension.[13]

Our problem is, then, to obtain the density function in this angular volume that best agrees with the experimental data. While this problem is more difficult than for fibers, a method was found that fits the data in the least-squares sense while permitting no negative values of the density function (such negative values have no physical meaning and must be excluded even though they are mathematically permissible).

We consider the inverse volume to be composed of a set of points for which the density function is required. If one considers in detail the definition of the problem, in particular Fig. 3.2, one should realize that each point in the inverse volume corresponds to only a few sets of ϕ's and α's in each intensity plane, in particular, three such points for the (100) plane and four for the (111) plane for the cubic system. The value of the density function at this point can only contribute to the intensity at these sets of points. This is a most important fact. Consider now an iterative solution where each inverse point is considered as the sole variable in sequence. The change of the residual, $I - \hat{I}$ (the experimental intensity less the presently calculated intensity), at each point is related to the change of the density function ΔT by the relation

$$\Delta(I - \hat{I}) = (I - \hat{I}) - a\Delta T \; , \qquad (2)$$

where a is the fraction of the path for Eq. (1) that is assignable to that density point. Equation (2) is based on the one additional approximation that an integral can be replaced by a sum. The variance of the inverse point is thus defined to be

$$V(I) = \Sigma\, \Delta(I - \hat{I})^2$$

$$= \Sigma\,[(I - \hat{I})^2 - 2a(I - \hat{I})\Delta T + a^2T^2]\ , \quad (3)$$

where the summing is carried out for all points corresponding to the inverse point. The least-squares solution corresponds to $dV(I)/dT = 0$, so that the required ΔT, which gives minimum variance, is just

$$\Delta T = \Sigma\, a(I - \hat{I})/\Sigma\, a^2\ . \quad (4)$$

If the process can be repeated as often as necessary such that ΔT approaches zero, then clearly a least-squares solution is approached. It does not follow that the estimated change given by Eq. (4) is necessarily the optimum value; and indeed, the use of twice this value makes the solution converge more rapidly. Since negative values of T are not permitted, it is set to zero at points where the best fit would make it negative. For such points Eq. (4) need not hold, and thus we have a least-squares solution in a special sense that $T \geqq 0$. Because of this restriction we will not have a strictly unbiased solution, since the error of the points of zero value cannot be negative. The iterative solution is initiated with $T = 1.0$ so that initially $\hat{I} = 1.0$.

In the basic solution, 1300 points in the inverse volume are calculated, and six iterations are normally used. The solution requires 5 min on the CDC 1604-A computer; each additional iteration adds 45 sec. Solutions have been obtained for rolled copper, brass, and aluminum.

The major texture for rolled copper is shown in Fig. 3.3. It consists of a high-intensity region ($T = 15$) that runs from (211), $\beta = 40°$ to (110), $\beta = 55°$. By conventional notation these correspond to $(\bar{2}11)[111]$ and $(\bar{1}10)[112]$ textures. All orientations between these terminal textures appear to be uniformly populated. A second weaker texture continuous with the above texture is (110) [001] ($\beta = 90°$), which is shown in the bottom of this figure. Another still weaker texture exists as a shell around the (100)[010] ($\beta = 0°$ and 90°). A suggestion of this texture can be seen in Fig. 3.3. The last two textures are relatively poorly developed compared to the major texture, and all three textures overlap somewhat.

ORNL-DWG 66-5986

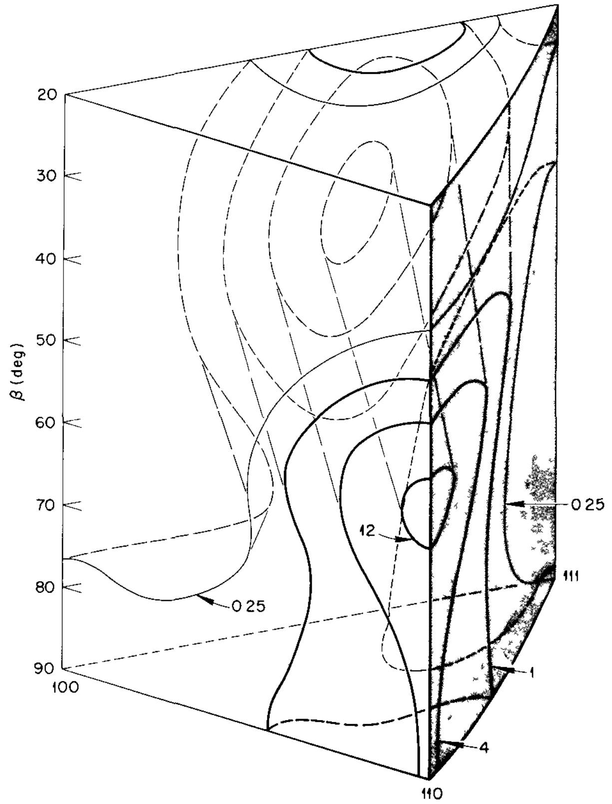

Fig. 3.3. A Partial Inverse Pole Figure for Copper Rolled 95%. The main feature consists of the rod starting on the back face at $(\bar{2}11)[111]$, passing to $(\bar{1}10)[112]$ in the front edge, and then passing along this edge to $(\bar{1}10)[001]$ in the bottom plane.

This method of analysis is much more powerful than the usual ones. The results show that the previous ideal textures for copper are not particularly accurate, and some details were not recognized. This method is the only possible way in which minor textures can be identified. For the first time the experimental data are quantitatively reproduced from a texture analysis.

IMPACT CALORIMETER

A. Wolfenden[16]

Work has continued on the impact calorimeter designed to measure the energy relations involved

---

[16] Noncitizen employee from England.

in the plastic deformation of metals as a function of deformation temperature and strain and to measure the immediate and subsequent energy releases on heating the samples. The apparatus and its mode of operation have been reported previously.[17] Some trouble has been encountered in connection with the use of the vacuum system to hold the piston down on the compressed-air chamber prior to firing. The electronic components have been installed with the rig and await testing. A magnetic pickup has been mounted on the hammer guide rails to facilitate measurement of the hammer velocity (and hence energy) before and after deformation. An accelerometer mounted on top of the inertial block will allow the energy losses due to vibration to be evaluated. Amplifiers and a multichannel chart recorder have been wired to measure simultaneously the outputs from the magnetic pickup, the accelerometer, and a thermocouple attached to the sample.

TENSILE CALORIMETER

A. Wolfenden[16]

The study was initiated of the energy relations involved in the tensile deformation of copper single crystals as functions of orientation at room temperature. To cover adequately the orientations in the standard stereographic triangle, 22 crystals were grown. The samples have been pulled in the calorimeter designed and reported by Williams.[18] Of the samples pulled, 11 provided useful data, and the data from another 4 await analysis. The stored energy as a function of orientation and strain is presented in Fig. 3.4. Typical scatter is shown on one curve.

The figure shows that for all orientations the initial rates of energy storage are low, agreeing with the observation of Williams,[18] but the rates rise at different strains for differently oriented samples, eventually becoming approximately linear. The three samples with initial orientations closest to the (110) pole exhibited the lowest stored-energy values at given strains above about 0.06. Below strains of 0.06, the curves for all the samples converge, and differences cannot be resolved readily. The samples of orientations nearest the (100)–(111) symmetry line tend to have the highest stored-energy values at all strains covered in the tests.

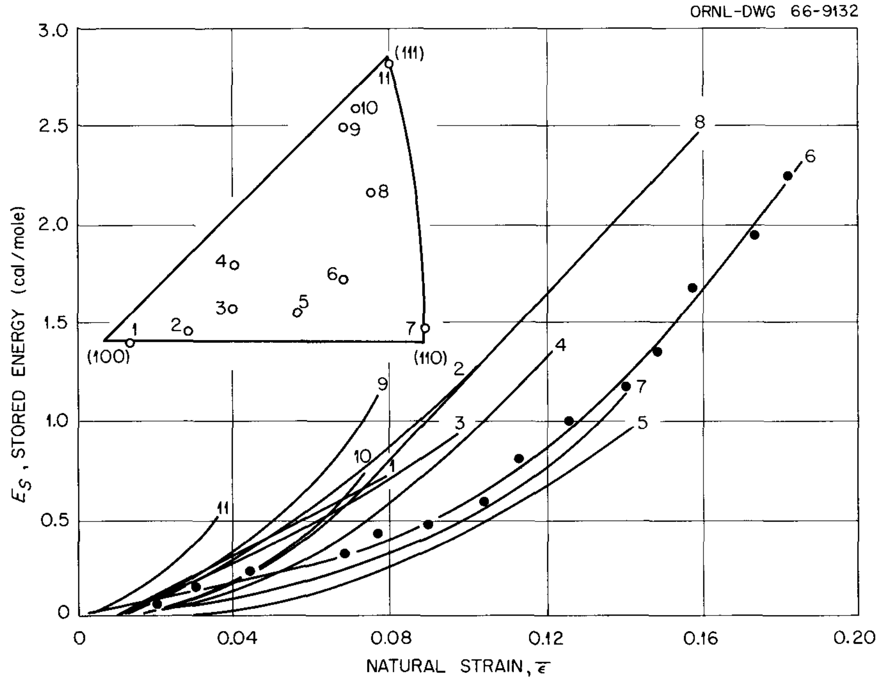

Fig. 3.4. Stored Energy as a Function of Strain.

---

[17] A. Wolfenden, *Metals and Ceramics Div. Ann. Progr. Rept. June 30, 1965*, ORNL-3870, pp. 13–14.

[18] R. O. Williams, *Acta Met.* **12**, 745 (1964).

Theories of work hardening in face-centered cubic metals predict the stored energy E_s as a function of the square of the flow stress $\bar{\sigma}$ or of the square of the shear stress τ. To elucidate these theories, the present data were plotted as E_s vs $(\bar{\sigma})^2$ and E_s vs τ^2. The former plots were approximately linear though with orientation-dependent gradients. The four samples with orientations near the (100)–(111) symmetry line had the lowest slopes, agreeing qualitatively with the data of Wolfenden[19] on copper and aluminum single crystals deformed at −195°C. Since in terms of dislocation motion and multiplication the shear stress is probably more relevant here than the flow stress, we felt that the observed orientation dependence of the E_s vs τ^2 curves may be significant. As a test of this significance, E_s was plotted vs τ^2. These curves are again linear, though still orientation dependent, but with less spread in slope. Therefore, we tentatively assert that the linear curves of E_s vs τ^2 are orientation dependent, but a full analysis of the theoretical significance of this observation cannot be made at this time.

---

[19] A. Wolfenden, Ph.D. thesis, University of Liverpool, 1965.

4. Diffusion in Solids

T. S. Lundy

Studies were continued of diffusion in body-centered cubic metals with emphasis placed on alloy diffusion. Models for grain-boundary diffusion were surveyed to obtain perspective on the problem of short-circuit diffusion. Experiments to explain the very small diffusion coefficient in regions very near the metal surface in silver were started. An attempt will be made in future experiments to clarify the effect of this region on the overall diffusion properties.

DIFFUSION OF ^{51}Cr IN CHROMIUM-NICKEL ALLOYS

J. Askill[1]

Diffusion of ^{51}Cr in pure chromium, Cr–20% Ni, and Cr–44% Ni was measured from 1000 to 1850°C. Nonlinear log activity vs x^2 (x = penetration depth) penetration plots were found at temperatures within 150°C of the melting point for pure chromium,[2] within 115°C for the 20% alloy, and within 75°C for the 44% alloy. The nonlinear penetration plots were analyzed into two straight-line components, which yielded two diffusion coefficients. By comparison with a penetration plot obtained for a single-crystal sample, we showed that the higher diffusion coefficient is due to some form of high-temperature grain-boundary-diffusion effect. Supporting x-ray data for pure chromium and the alloys eliminated the possibility of a phase transformation at 1755°C.

The nonlinear behavior in the Arrhenius plot for the volume diffusion coefficients is similar to that found for self-diffusion in vanadium, although the change in slope of the plot occurs 400°C higher in temperature. The position of the change in slope of the Arrhenius plot for chromium can be explained quantitatively, as that for vanadium and the unusual diffusion behavior in Ti, Zr, and U, by a simple vacancy/divacancy model of diffusion. The results obtained for pure chromium and the 20 and 44% Ni alloys are shown in Fig. 4.1.

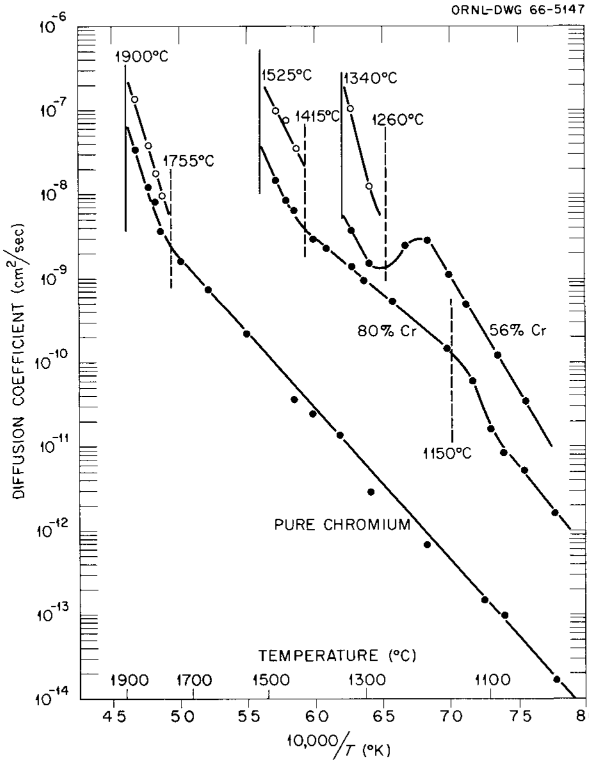

Fig. 4.1. Diffusion of ^{51}Cr in Chromium-Nickel Alloys.

---

[1] Noncitizen employee from England.

[2] J. Askill, *Metals and Ceramics Div. Ann. Progr. Rept. June 30, 1965*, ORNL-3870, pp. 16–18.

DIFFUSION OF ^{110}Ag AND ^{46}Sc IN β-TITANIUM

J. Askill[1]

The diffusion of ^{110}Ag and ^{46}Sc was measured in β-titanium from 950 to 1650°C. Unlike previous data on the diffusion of Mo, Nb, Ta, Fe, V, Cr, Mn, Ni, Co, P, and Sn as well as self-diffusion, all of which exhibit curved Arrhenius plots, the plots for both scandium and silver were linear over the complete temperature range. The data gave the relations

$$D_{\mathrm{Ag}} = 3 \times 10^{-2} \exp(-43000/RT)$$

and

$$D_{\mathrm{Sc}} = 4 \times 10^{-3} \exp(-32400/RT) .$$

Interestingly, both silver and scandium are electronegative with respect to Ti, whereas all the other solute elements investigated are electropositive.

SELF-DIFFUSION IN MANGANESE

J. Askill[1]

Some preliminary results were obtained for the diffusion of ^{54}Mn in polycrystalline body-centered cubic δ-manganese from 1170 to 1210°C. In this temperature range the diffusion coefficient varied from 1×10^{-7} to 4×10^{-7} cm^2/sec.

MATHEMATICAL MODELS OF DIFFUSION IN GRAIN BOUNDARIES[3]

Lida K. Barrett[4]

Mathematical analysis of diffusion in solids containing grain boundaries is necessary for the quantitative interpretation of experimental results. Mathematical models by Fisher,[5] Whipple,[6] and Suzuoka[7] were reviewed, and the derivations (physical assumptions, mathematical statements, and methods of solution) were compared. The results contained in various commentary and comparison papers[8–12] were summarized.

DIFFUSION OF ^{44}Ti AND ^{48}V IN TITANIUM-VANADIUM ALLOYS

J. F. Murdock

The study of diffusion of titanium and vanadium in titanium-vanadium alloys at 10% increments over

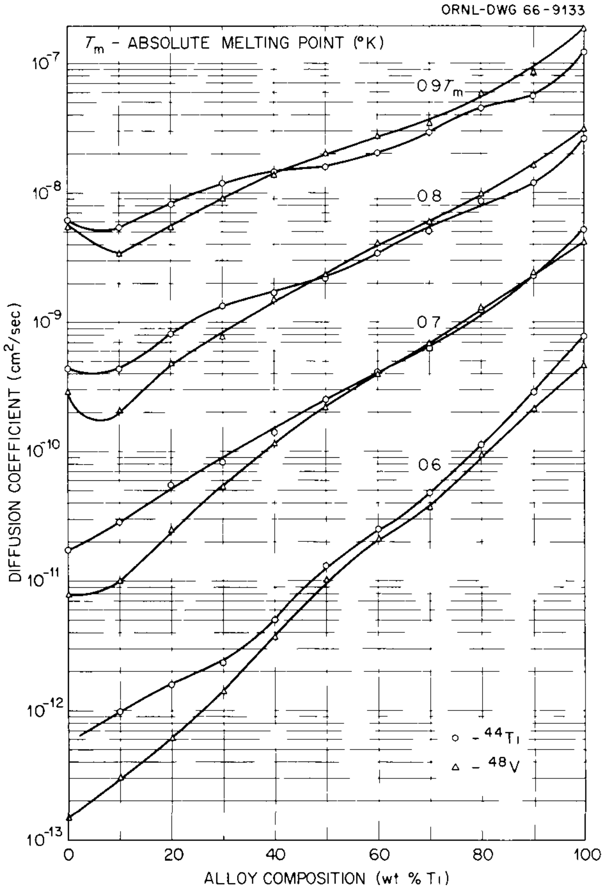

Fig. 4.2. Diffusion of ^{44}Ti and ^{48}V in Titanium-Vanadium Alloys. Values are plotted for temperatures equal to four different fractions of the absolute melting point.

---

[3] Abstracted from ORNL-TM-1224 (August 1965).

[4] Consultant from the University of Tennessee.

[5] J. C. Fisher, *J. Appl. Phys.* **22**, 74–77 (1951).

[6] R.T.P. Whipple, *Phil. Mag.* **45**, 1225–36 (1954).

[7] T. Suzuoka, *Trans. Japan Inst. Metals* **2**, 25–33 (1961).

[8] C. C. Maneri and F. J. Milford, *A Discussion of Theories of Grain Boundary Diffusion*, ARL-48 (July 1961).

[9] V. E. Wood *et al.*, *J. Appl. Phys.* **33**, 3574 (1962).

[10] A. D. LeClair, *Brit. J. Appl. Phys.* **14**, 351 (1963).

[11] T. Suzuoka, *J. Phys. Soc. Japan* **19**, 839 (1964).

[12] H. S. Levine and C. J. MacCallum, *J. Appl. Phys.* **31**, 595 (1960).

the entire composition range was completed. Arrhenius-type plots were determined for both elements in each of the alloys to within 50 to 75°C of the melting point. The data appeared in most cases to be best fitted on a $\ln D$ vs $1/T$ plot by a straight line up to 1300 to 1400°C and by a curved line from there to near the melting point.

The most significant results are illustrated in Fig. 4.2. Diffusional properties are usually correlated with the absolute melting point of the material. The figure shows the diffusion coefficient at a given fraction of the absolute melting point as a function of alloy composition. Of particular interest is the observation that adding 40% Ti to vanadium changes the diffusion coefficient of either species at a given fraction of the melting point by a factor of only 4 to 5, but adding 40% V to titanium gives a factor of 100 to 200 change.

5. Direct Observation of Lattice Defects

J. O. Stiegler

We are using optical- and electron-microscopy techniques in a research program aimed at understanding the mechanisms involved in deformation and fracture of metals and alloys. Principal emphasis is on the direct observation of lattice defects by transmission electron microscopy, but complementary studies involve fractography and etch-pitting techniques. In addition to our own research program we are working closely with other groups in the Division on the SAP, tungsten, and high-temperature-materials programs and on studies of irradiation damage to stainless steels and of high-temperature fracture of nickel-base alloys. A study of recrystallization, grain growth, and the ductile-to-brittle transition in tungsten sheet is presented in Part II, Chap. 16 of this report.

ETCH-PITTING EXPERIMENTS ON BODY-CENTERED CUBIC METALS AND ALLOYS

B.T.M. Loh

From the atomistic point of view, the bulk mechanical behavior of crystals may generally be thought of as a statistical result of activities of all dislocations in the crystal. Therefore, it is essential that we understand all the dislocation mechanisms that contribute to plastic deformation and their dependencies on external and internal variables. The etch-pitting technique has been used extensively to study the dislocation activities, and in some respects it is more useful than transmission electron microscopy. Hence, we are also doing etch-pitting experiments on body-centered cubic metals and alloys to supplement electron microscopy.

We tried three etching methods to bring out dislocation pits in tungsten: (1) Wolff solution (2 parts saturated $CuSO_4$ and 1 part concd. NH_4OH), (2) 15% $K_3Fe(CN)_6$–5% NaOH–80% H_2O, and (3) electrolytic etching in 2% NaOH. Judging from the pit densities, the first method seems to give a more realistic picture of dislocation density. Transmission electron microscopy was used on thin samples to check the correlation between pits and dislocations. Based on a few observations, the correlation is poor, but we suspect that the specimen-preparation procedures may play a role here. The pits are bounded by $\{110\}$ and $\{100\}$ crystallographic planes. Therefore, by examining the shape of the pit, we can determine the orientation of specimen surface. A computer program has been written for this purpose.

Five polycrystalline tungsten specimens, compressed at room temperature to different plastic strains ranging from 0.2 to 6.8%, were all cracked longitudinally. Optical microscopy revealed that the intergranular cracks branched heavily in the specimen strained 6.8% and branched less as the amount of strain decreased. Most twins were associated with the cracks, but there were isolated patches of twinned grains, the number and thickness of twins decreasing with decreasing strain. Slip steps were not easily observed by optical microscopy, but many fine steps were revealed by replica electron microscopy. The pit density showed a general increase near grain-boundary triple points and twin–grain-boundary intersection points, but no well-defined slip bands were observed. The flow stresses were lower for specimens tested at 250°C, about one-half that of those tested at room temperature. Such specimens showed no cracking or twinning at the highest plastic strain studied, about 11%; wavy surface steps were readily revealed by optical microscopy, and curved pit bands formed after polishing and etching. For single crystals of tungsten tested at room temperature, straight slip bands first formed at one end; then more bands formed along the specimen as the stress increased. Four orientations of these bands have been found. Further work is being done to show the nature of these bands.

Since slip-band formation is the unit process in plastic deformation, at least during the initial yielding, a more systematic study will be done in the near future on tungsten and silicon-iron to examine the origin and nature of slip bands, the distribution of slip bands, and their dependences on stress, temperature, strain rate, and orientation.

CRYSTALLOGRAPHY OF SLIP IN BODY-CENTERED CUBIC CRYSTALS

J. O. Stiegler

The $\langle 111 \rangle$ slip direction is well documented for body-centered cubic crystals, but much uncertainty and confusion exists over the identity of the active slip plane or planes. Views have ranged from the most highly stressed plane, regardless of its crystallographic identification, to specific low-index planes ($\{110\}$, $\{211\}$, and $\{321\}$, for example). In some elaborate etch-pitting studies Sestak and Libovicky[1,2] showed that at low temperatures or high strain rates slip was crystallographic (along well-defined $\{110\}$ planes) but that at elevated temperatures or low strain rates it became noncrystallographic.

We have analyzed the crystallography of slip in terms of Dorn and Rajnak's[3] model of dislocation motion, in which thermal fluctuations help dislocations to overcome the Peierls stress. In the absence of a stress, a screw dislocation lies in a potential valley along a close-packed $\langle 111 \rangle$ direction; thermal fluctuations attempt to throw loops over the Peierls hill in both directions on each of the three $\{110\}$ planes. Application of a stress upsets this equilibrium by expanding loops in the forward direction and closing them in the backward direction, the frequency of successful fluctuations on a given $\{110\}$ plane depending on the component of stress resolved on that plane. Dorn and Rajnak[3] give the following expression for the frequency of nucleation of successful loops in a dislocation of length L:

$$\nu_n = (\nu_0 L/W) \exp\,(-U_n/kT)\,, \qquad (1)$$

where ν_0 is the Debye frequency, W the length of a critical-size loop, U_n the energy to nucleate the pair of kinks making up the loop (stress dependent), k the Boltzmann constant, and T the absolute temperature. Dorn and Rajnak's expression for U_n as a function of the shear stress τ is a complex integral equation that may be approximated analytically by

$$U_n \approx 2U_k(1 - \tau/\tau_p)^2\,, \qquad (2)$$

where U_k is the energy to nucleate a kink and τ_p is the Peierls stress.

To determine the path of a dislocation, we need to calculate the relative frequency of formation of successful loops on each of the three $\{110\}$ planes belonging to a common $\langle 111 \rangle$ zone containing the dislocation. Consider the ratio on two of these planes. Let $\alpha_1\tau$ be the shear stress on plane 1, and $\alpha_2\tau$ that on plane 2. In Eq. (1) ν_0 and L are constants, and W is only weakly stress dependent. Thus, the relative frequencies are given by

$$\frac{\nu_1}{\nu_2} = \exp\left\{ -\frac{2U_k}{kT}\left[\frac{2\tau}{\tau_p}(\alpha_2 - \alpha_1) - \frac{\tau^2}{\tau_p^2}(\alpha_2^2 - \alpha_1^2)\right]\right\}. \qquad (3)$$

A similar expression may be derived for the ratio ν_1/ν_3. We see that this ratio depends on both stress and temperature. At high stresses or low temperatures loop expansion is favored on the most highly stressed $\{110\}$ plane, while at elevated temperatures or low stresses the relative frequency of motion on a less highly stressed $\{110\}$ plane increases.

From Eq. (3) we can calculate relative ν values for the three $\{110\}$ planes containing a common $\langle 111 \rangle$ direction in terms of the temperature and the stress acting on each, and from this we get a vector describing the displacement of the dislocation. For example, the dislocation will move in a

---

[1] B. Sestak and S. Libovicky, *Czech. J. Phys.* **B12**, 131 (1962).

[2] S. Libovicky and B. Sestak, *J. Appl. Phys.* **34**, 2919 (1963).

[3] J. E. Dorn and S. Rajnak, *Trans. Met. Soc. AIME* **230**, 1052 (1964).

⟨112⟩ direction normal to its Burgers vector in each of the three {110} planes, the distance in each direction being proportional to the frequency in that plane. The displacement vector **S** is given by

$$\mathbf{S} = \sum_{i=1}^{3} \nu_i \mathbf{d}_i \,, \tag{4}$$

where $\mathbf{d}_i$ is the vector slip distance in the ith ⟨112⟩ direction. The slip plane (P) is normal to the vector [**P**] given by

$$[\mathbf{P}] = \mathbf{S} \times \mathbf{b} \,, \tag{5}$$

where **b** is the Burgers vector. The Miller indices of [**P**] are equivalent to those of (P).

Since the relative ν_i values change with temperature and with magnitude and direction of the local stress, the identity of the slip plane also will change with these variables. In inhomogeneous or locally varying stress fields, curved slip surfaces will result. This analysis indicates that at low temperatures or high stresses (strain rates) slip will occur on the most highly stressed {110} plane. Identically oriented crystals deformed at high temperatures or low stresses will show slip lines lying near the arbitrary plane of maximum resolved shear stress. This is in agreement with the limited observations of Sestak and Libovicky,[1,2] Erickson,[4] and Noble and Hull.[5]

In standard tensile tests the yield or flow stress increases sharply as the deformation temperature is lowered. The increase often appears to be exponential. Since both increasing stress and decreasing temperature increase the exponent in Eq. (3), slip character can change strongly with a relatively small decrease in temperature. We are considering the possibility that the sudden onset of brittleness that is observed as the test temperature is lowered is a result of this abrupt decrease in ability to slip on planes other than the most highly stressed {110} plane.

BEND-YIELD-STRESS–GRAIN-SIZE–TEMPERATURE RELATIONSHIPS IN TUNGSTEN SHEET

K. Farrell A. C. Schaffhauser[6]
J. O. Stiegler

Load-deflection curves obtained from bend tests on recrystallized tungsten sheet display similar discontinuous yielding to that observed in other body-centered cubic metals in tensile tests. The bend-yield stresses have the same dependence on test temperature as do reported tensile-flow stresses. We are trying to apply a Hall-Petch-type analysis to the grain-size dependence of the bend-yield stresses and to relate the ensuing Hall-Petch parameters to the ductile-to-brittle transition behavior of the tungsten sheet.

BRITTLE-FRACTURE MORPHOLOGY OF TUNGSTEN

K. Farrell J. T. Houston

Our earlier studies of the brittle behavior of powder-metallurgy tungsten have shown that fine-grained primary recrystallized tungsten fractures mainly along the grain boundaries. Where cleavage occurs, it is initiated by a grain-boundary crack. The intergranular fracture is thought to be associated with impurities. Tungsten produced by plasma-arc melting has a much higher purity, and it fractures mainly by cleavage. We are studying whether the morphology of brittle fracture in the high-purity tungsten can be changed from cleavage to intergranular by suitable thermal treatments that would induce movement of impurities to grain boundaries. The kinetics of such a process might shed light on the nature of the impurities responsible for intergranular separation.

Many brittle fractures in body-centered cubic metals occur with little or no apparent plastic deformation. Examination of cleavage fractures in tungsten shows little evidence of slip or twinning in the matrix adjacent to the fracture. However, the fracture surfaces display river markings and other markings that may result from twins. Dislocations associated with these features can be revealed by etch pitting. This technique is being used to identify fracture surfaces and to study the cleavage-fracture process.

MICROSTRUCTURE OF SAP

K. Farrell J. T. Houston

Sintered aluminum products (SAP) consist of finely dispersed aluminum oxide particles in an

---

[4] J. S. Erickson, *J. Appl. Phys.* 33, 2499 (1962).

[5] F. W. Noble and D. Hull, *Phil. Mag.* 12, 777 (1965).

[6] Physical Metallurgy Group.

aluminum matrix. Optical metallography cannot resolve the fine-scale detail of these microstructures, but transmission electron microscopy readily reveals oxide size, shape, and distribution, matrix grain size, inclusions, etc. These observations are being made on commercial SAP and on ORNL experimental products to assist in control of the production process and improvement of the mechanical properties of the products.

All stages of production are followed from examination of the starting material through the processed billets to extruded bars and tubes. Foils from bulk material are prepared by our recently developed jet-thinning technique, reported below, using perchloric-alcohol solutions. The oxide particles are found to be small (<0.1 μ) and may have the form of needles, platelets, or rosettes, depending on the manufacturing procedure. The matrix grain size appears to be determined by the amount and distribution of the oxide phase and is usually less than 1 μ for a finely dispersed phase but may be very much larger where oxide clustering depletes the matrix. These structures are quite stable at temperatures up to 600°C.

We are also investigating the nature and causes of the large voids and fissures that can be introduced into SAP by heating at elevated (600°C) temperatures.

SEMIAUTOMATIC PREPARATION OF SPECIMENS FOR TRANSMISSION ELECTRON MICROSCOPY[7]

C.K.H. DuBose J. O. Stiegler

A rapid expansion in the use of transmission electron microscopy in our laboratory led to the development of new equipment to produce usable specimens of a variety of materials, often after neutron irradiation, in a quick and reliable manner. Specimens are cut, in a hot cell if necessary, to a thickness of about 18 mils and a maximum diameter of $\frac{1}{8}$ in. These are first "dimpled" on both sides by an electrolytic jet technique to reduce the thickness of the center of the specimen to about 2 mils. The shape of the dimple bottom is controlled by varying the current density, and under appropriate conditions large flat-bottomed dimples can be formed. Final polishing is accomplished in a standard electrolytic polishing cell, in which breakthrough in the dimpled region is detected by an extremely sensitive photocell device. Incident light is piped to the specimen, and light transmitted through the hole is delivered to the photocell by a fiber-optics system. The fiber optics provides a small intense light beam and also eliminates interference from thermal fluctuations of the polishing solution and radiation effects on the photocell. Activation of the photocell stops the polishing action in the final step.

With this technique, extremely small holes can be detected, which usually are surrounded by reasonably large areas transparent to electrons. The technique is rapid compared to standard techniques using large foils, and it does not require close attention of the operator. We can now go from a bulk sample to a finished specimen in about 30 min. An ORNL report giving full details on design of the equipment and operation of the technique is being prepared.

---

[7] Abstract of paper presented at the 20th AEC Metallography Group Meeting, Denver, Colo., May 18–20, 1966.

6. Electronic Properties of Metals and Alloys

J. O. Betterton, Jr.

The investigations of electronic properties of metals and alloys have continued by means of low-temperature specific heats, galvanomagnetic properties, and Mössbauer-effect studies. Experimental techniques were extended by developing better methods of purification by zone refining and of heat treating and quenching, superior wires for carrying critical superconducting current, and new Mössbauer techniques that yield information on impurities and defects.

LOW-TEMPERATURE SPECIFIC HEATS OF ZIRCONIUM ALLOYS

J. O. Betterton, Jr. J. O. Scarbrough

When transition-metal solutes to the right of zirconium in the periodic table are alloyed with zirconium, the electronic specific heat coefficient and the superconducting transition temperature invariably increase, and the Debye temperature always decreases. We have continued investigation of the specific heats with new measurements on pure zirconium, zirconium-niobium alloys, and zirconium-rhenium alloys. The results are plotted in Fig. 6.1 along with earlier data[1] from quenched Zr-Nb, Zr-Mo, and Zr-Ru alloys. The increases in electronic specific heat and in transition temperature and the decrease in Debye temperature were nearly independent of solute group number and of crystal structure. The correlation in terms of atom fraction zirconium in the alloy is not perfect but is much better than the alternate correlation in terms of electron-to-atom ratio. X-ray studies of these quenched alloys show that the structure shifted from close-packed hexagonal to body-centered cubic at 5% Mo, 2.8% Re, and 2.8% Ru and that niobium alloys up to 5% are still close-packed hexagonal. The indifference of the properties and their rates of change to crystal structure implies that entropy differences between the hexagonal and cubic phases have their origin in processes that occur at higher temperatures and that changes are from localized alloying effects, which do not see the influence of crystal symmetry or the effects of average number of electrons in the alloys.

As an illustration of the large rate of change of the electronic specific heat in these alloys, and to contrast the results to earlier work, the density of electronic states derived for zirconium-niobium alloys (assuming a rigid band, independent electrons, and one additional electron per niobium atom) is plotted in Fig. 6.2 along with the density of electronic states for zirconium-scandium alloys[2] (assuming a deficiency of one electron per scandium atom) and for zirconium–B-subgroup alloys[3] (assuming that the filled d shell takes no part in alloying and that solutes Ag, Cd, In, Sn, and Sb contribute 1, 2, 3, 4, and 5 electrons, respectively, to the zirconium band structure). Although this figure represents portions of the density of states of pure scandium and pure zirconium only approximately because of the necessary assumptions, it does show the large increase in electronic specific heat coefficient with the niobium-type addition.

---

[1] J. O. Betterton and J. O. Scarbrough, *Metals and Ceramics Div. Ann. Progr. Rept. June 30, 1965*, ORNL-3870, pp. 27–31.

[2] J. O. Betterton, Jr., and J. O. Scarbrough, *Metals and Ceramics Div. Ann. Progr. Rept. June 30, 1964*, ORNL-3670, pp. 49–52.

[3] G. D. Kneip, J. O. Betterton, Jr., and J. O. Scarbrough, *Phys. Rev.* **131**, 2425–32 (1963).

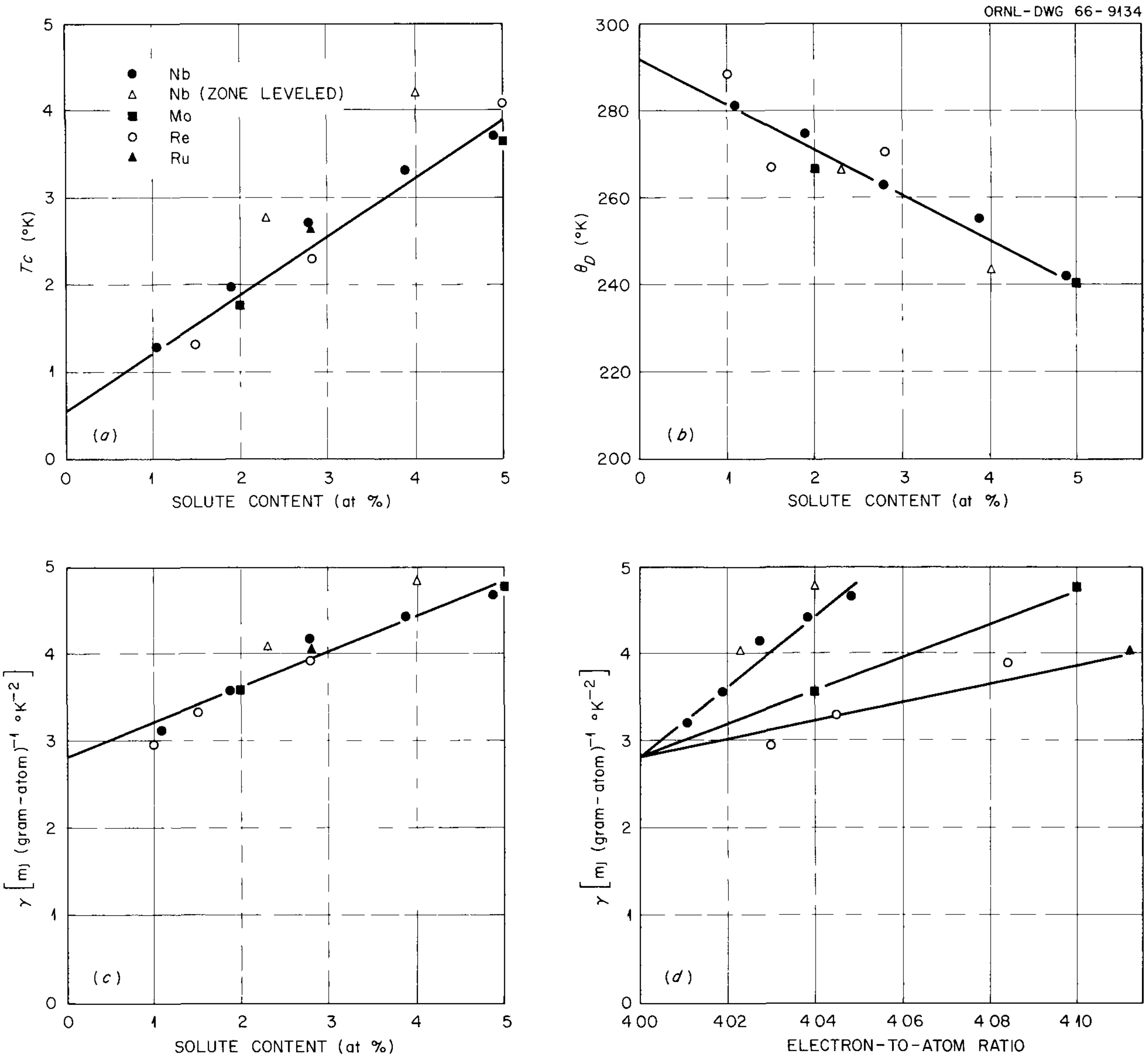

Fig. 6.1. Properties Derived from Low-Temperature Specific Heat Measurements on Zirconium Alloys. (*a*) Superconducting transition temperature T_c, (*b*) Debye temperature θ_D, and (*c*) electronic specific heat coefficient γ plotted as function of atomic percentage of solute. (*d*) γ plotted as a function of electron-to-atom ratio.

Bucher has determined[4] that the superconducting transition temperature of zirconium varies with isotopic mass as $M^{-0.05}$, so a critical balance must exist between the attractive electron-phonon interaction and the repulsive Coulomb interaction, with the electron-phonon interaction dominating. The rapid rise in superconducting transition temperature with Nb, Mo, Re, and Ru solutes might be associated with a lessening of the Coulomb interaction, except that both electronic specific heat and the transition temperature follow a parallel increase. More likely, some other effect, such as the phonon enhancement of the electronic specific heat coefficient proposed by Clogston,[5]

---

[4] E. Bucher *et al.*, *Phys. Letters* **15**, 303 (1965).

[5] A. M. Clogston, as cited by E. Bucher *et al.*, footnotes 6 and 7.

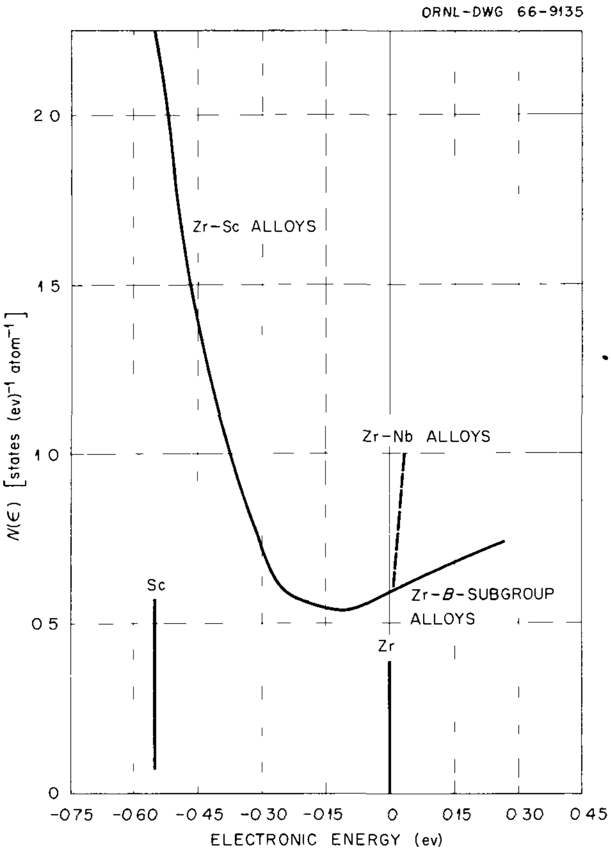

Fig. 6.2. Density of Electronic States for Zr-Sc and Zr–B-Subgroup Alloys Compared with That for Zr-Nb Alloys. Crystal structure: close-packed hexagonal.

is responsible for the large effects we observe. Bucher[6,7] has also suggested that this mechanism may be responsible for the high values of the electronic specific heat coefficient in similar superconducting alloys.

EFFECTS OF HEAT TREATMENT AND IMPURITIES ON CRITICAL CURRENT DENSITY OF TRANSITION-METAL SUPERCONDUCTORS

J. O. Betterton, Jr. D. S. Easton
J. O. Scarbrough

A large transport current can be sustained in a mixed-state type II superconductor in a magnetic field when the superconducting parts of the sample are pinned against the action of the Lorentz forces.[8] This can be accomplished by introducing localized strains in the lattice of the superconductor by cold working,[9] cooling finely divided composite samples,[10] or precipitation.[11,12] With these strains the sample will have a lower free energy when the superconducting parts of the mixed state are in certain regions. The sample is thus able to withstand the Lorentz forces, which increase as the current increases in the presence of a magnetic field.

Our method[13] of increasing the effectiveness of the precipitation heat treatment is the addition of interstitial elements that are chemically electronegative to one of the other alloying components in the superconductor. The interstitial solution expands the atomic volume of the precipitating phase relative to the volume of the superconductor, and the precipitation with interstitial elements then generates more local strain. The chemical condition has the effect of reducing the solid-solubility limit of the superconductor for the phase enriched by the additive. Both conditions act together when oxygen, nitrogen, and carbon are added to transition-metal superconductors, and the critical current density would be expected to be

---

[6] E. Bucher, F. Heiniger, and J. Muller, "Low Temperature Specific Heat of Solid Solutions of the Third Transition Series," p. 1059 in *Proc. Ninth Intern. Conf. Low Temp. Phys., Columbus, Ohio, Aug. 31–Sept. 4, 1964*, ed. by J. G. Daunt *et al.*, Plenum, New York, 1965.

[7] E. Bucher *et al.*, "Experimental Relations for Electron Interactions in Transition Metals, Determined from Superconductivity Data," p. 616 in *Proc. Ninth Intern. Conf. Low Temp. Phys., Columbus, Ohio, Aug. 31–Sept. 4, 1964*, ed. by J. G. Daunt *et al.*, Plenum, New York, 1965.

[8] C. J. Gorter, *Phys. Letters* **1**, 69 (1962).

[9] J. E. Kunzler, *Bull. Am. Phys. Soc.* **6**, 278 (1961).

[10] C. P. Bean and R. W. Schmit, *Science* **140**, 26 (1963).

[11] G. D. Kneip, Jr., J. O. Betterton, Jr., D. S. Easton, and J. O. Scarbrough, p. 603 in *High Magnetic Fields*, ed. by H. Kolm *et al.*, MIT Press, Cambridge, Mass., and Wiley, New York, 1962.

[12] G. D. Kneip, Jr., J. O. Betterton, Jr., D. S. Easton, and J. O. Scarbrough, *Method for Increasing the Critical Current Density of Superconducting Alloys*, U.S. Patent No. 3,215,569 (Nov. 2, 1965).

[13] J. O. Betterton, Jr., G. D. Kneip, Jr., D. S. Easton, and J. O. Scarbrough, *Method of Increasing the Critical Current Density of Hard Superconducting Alloys, and the Products Thereof*, French Patent No. 1,371,338 (PV-942594) (July 27, 1964).

increased. This was first observed experimentally[14] for oxygen and carbon additions to the alloys Nb–25 at. % Zr. We measured the effect of oxygen additions to Ti-Nb, Zr-Nb, and Ti-Ta alloys and nitrogen additions to Hf-Nb alloys on the critical current density. The results are given in Table 6.1 for one field strength, 30 kilogauss. Figure 6.3 shows the effect of oxygen addition and field strength on critical current density of one example, Ti–30 at. % Nb. Oxygen increased the critical current density of cold drawn and precipitated titanium-niobium superconductors, and nitrogen increased the critical current density of cold drawn and precipitated hafnium-niobium. We were able to repeat the critical current enhancement by oxygen in Nb–25 at. % Zr and to observe the effect in Nb–50 at. % Zr. The precipitation heat treatment did increase the critical current density in titanium-tantalum significantly, but no significant effect of 0.08 to 0.27 at. % O occurred in these alloys. We think titanium-tantalum alloy is unaffected by oxygen either because the oxygen additive was not soluble during homogenization at

Table 6.1. Effect of Interstitial Impurities and Heat Treatment on Superconducting Critical Current Density

Alloy Composition (at. %)							Critical Current Density[a] (amp/cm^2)	
Major Components					Impurities		Heat Treated[b]	Not Heat Treated
Ti	Nb	Hf	Zr	Ta	O	Other		
							$\times 10^3$	$\times 10^3$
70	30						31	8
70	30				0.08		63	5
70	30				0.16	0.1 Fe	50	2
45	55						6	2
45	55				0.2		8	4
45	55					0.52 Fe	15	7
45	55				0.13	0.52 Fe	17	7
	50	50					5	2
	50	50				0.02–0.2 N	11	2
	50		50				160	8
	50		50		0.1		202	11
	50		50			0.24 Sc	130	9
	50		50		0.09	0.24 Sc	190	10
	75		25				152	30
	75		25		0.02		215	31
	75		25			0.02 Fe	180	34
	75		25		0.02	0.02 Fe	164	23
40				60			27	14
40				60	0.08		26	14
40				60			34	12
40				60	0.27		33	7
			50	50			11	2

[a] Measured at 4.2°K in a transverse magnetic field of 30 kilogauss.

[b] Treated for various times and temperatures, usually selected to give optimum response.

---

[14] J. O. Betterton, Jr., G. D. Kneip, Jr., D. S. Easton, and J. O. Scarbrough, p. 61 in *Superconductors*, ed. by M. Tanenbaum and W. V. Wright, Interscience, New York, 1962.

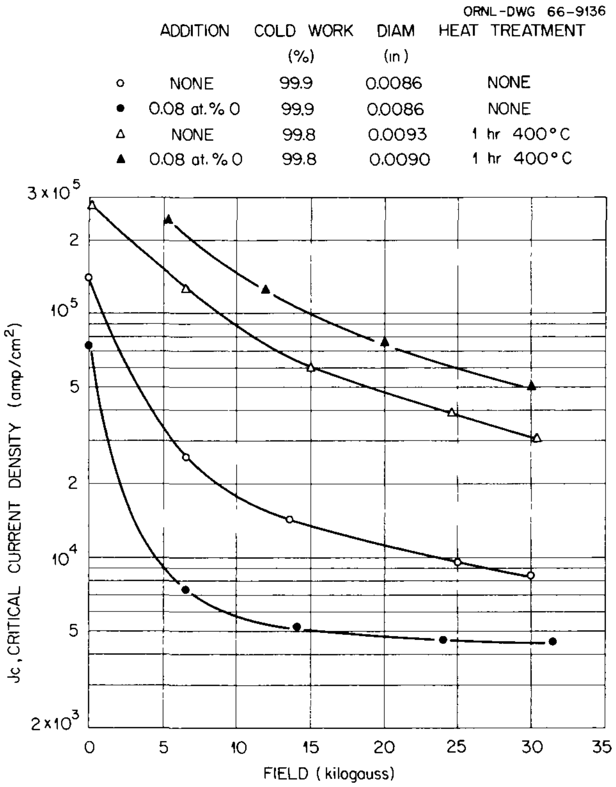

Fig. 6.3. Effects of Oxygen Addition and Heat Treatment on the Critical Current Density at Various Field Strengths for Arc-Cast Ti–30 at. % Nb Swaged to 0.220 in., Homogenized 1 hr at 1250°C, and Cold Drawn to the Indicated Diameter. The current is measured perpendicular to the field at 4.2°K.

1250 to 1500°C or because the increased strain did not occur because the precipitate was not enriched in oxygen.

Quaternary iron and scandium additives, as shown in Table 6.1, were not beneficial. Scandium formed larger compound-like particles in both the cast and homogenized Nb–50 at. % Zr. These particles were too large to enhance the current density and only served to deplete the system of oxygen during the heat treatment to develop a fine precipitate. A new superconductor, Zr–50 at. % Ta alloy, had appreciable critical current density at 30 kilogauss at 4.2°K and showed precipitation-heat-treatment enhancement in agreement with the form of the phase diagram.[15] Zone leveling in a high vacuum was necessary to obtain this alloy sufficiently ductile to fabricate at room temperature.

PURIFICATION OF ZIRCONIUM

D. S. Easton J. O. Betterton

By zone refining in a baked 10^{-10}-torr apparatus, we are able to produce 99.98 at. % zirconium crystals with impurities 0.004 at. % O, 0.002 at. % Hf, <0.004 at. % C, <0.004 at. % N, <0.009 at. % H, and less than 1 at. ppm other impurities. The zoned samples exhibit crystalline imperfections as a result of solidification and solid-state beta-to-alpha transformation. Annealing below the transformation temperature eliminated these imperfections. The anneal, however, has the adverse effect of a reduced resistance ratio $R_{300°\mathrm{K}}/R_{4°\mathrm{K}}$ as a result of what seems to be disordering of clusters of oxygen atoms.

Seeking methods of reducing the oxygen content, we have studied the partial pressures of various gases over molten zirconium by means of a quadrupole mass spectrometer. Typical results are shown in Fig. 6.4. Background pressures prior to melting are shown on the left, and background pressures after solidifications are shown on the right side of the figure. The gases that arise from the liquid zirconium are hydrogen, methane, nitrogen, ethane, propane, carbon monoxide, and carbon dioxide. The presence of methane and carbon oxides suggests that doping of zirconium with carbon and then with hydrogen during zone refining could lead to greater purity. The oxygen pressure was low at 10^{-13} to 10^{-14} torr, so no appreciable contamination from this gas during zone refining should occur. The particular sample of zirconium shown in Fig. 6.4 reached the highest resistance ratio yet reported for zirconium, 1160. This occurred after 25 passes in the end that froze last, so this sample appears to have been purified from oxygen both by vaporization and by oxygen transport by the liquid zones.

GALVANOMAGNETIC PROPERTIES OF ZIRCONIUM

J. O. Betterton D. S. Easton

The magnetoresistance of zirconium[16] previously reported was approximately isotropic for various

---

[15] R. P. Elliott, *Constitution of Binary Alloys – First Supplement*, McGraw, New York, 1965.

[16] J. O. Betterton and D. S. Easton, *Metals and Ceramics Div. Ann. Progr. Rept. June 30, 1965*, ORNL-3870, pp. 44–49.

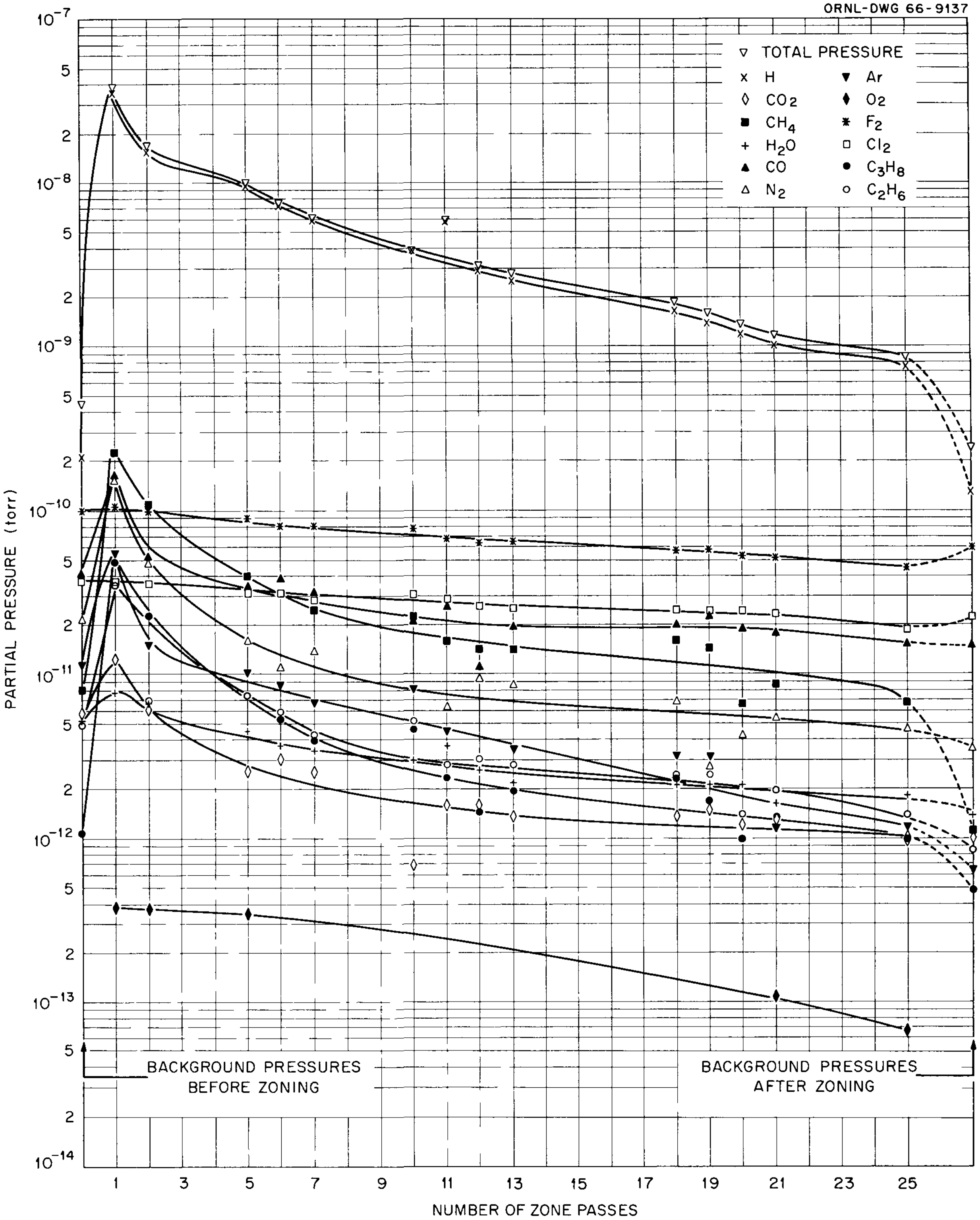

Fig. 6.4. Partial Pressures of Various Gases over Zirconium During Zone Refining.

current directions and was nearly quadratic in magnetic-field dependence. These results showed that the Fermi surface of zirconium is closed and compensated in terms of the Lifshitz theory of high-field galvanomagnetic properties.[17,18] However, voltages observed transverse to both current and magnetic field and also parallel to magnetic field but transverse to current are predominantly linear in field strength and oscillating in sign. According to extensions of the Lifshitz theory by Korringa,[19] these linear terms of alternating sign are neither consistent with high-field behavior for a closed and compensated metal nor with a similar case with breakdown of compensation due to impurities. We plan further investigation by increasing the magnetic field, since the effect may be due to failure to achieve the classical high-field limit.

The closed and compensated behavior of zirconium agrees with the electronic structure that might be expected by analogy with the energy-band calculations[20] of titanium by Matthiess for one direction $\langle 21\bar{1}0\rangle$ in **k**-space. These calculations show that the *d* bands overlap only slightly. With two electrons in each band and two atoms in the unit cell, the eight electrons of the two zirconium atoms almost completely fill the lower four bands, leaving as many electrons in the overlapping bands as there are holes in the lower bands. This situation is consistent with the minimum in density of states indicated by the specific heat of alloys in Fig. 6.2.

OBSERVATION OF THE MÖSSBAUER EFFECT FOLLOWING COULOMB EXCITATION

Gordon Czjzek J.L.C. Ford, Jr.[21]
J. C. Love[22]

The observation of the Mössbauer effect in ^{73}Ge following Coulomb excitation of the 67.0-kev level of this nucleus was reported previously.[23,24] In the first experiment, in which we used a 136-mg/cm^2-thick absorber, an unexpectedly small effect was observed. In a new series of experiments under otherwise similar conditions, the effect was observed with absorber thicknesses of 68 and 272 mg/cm^2 (Fig. 6.5). The thickness dependence of

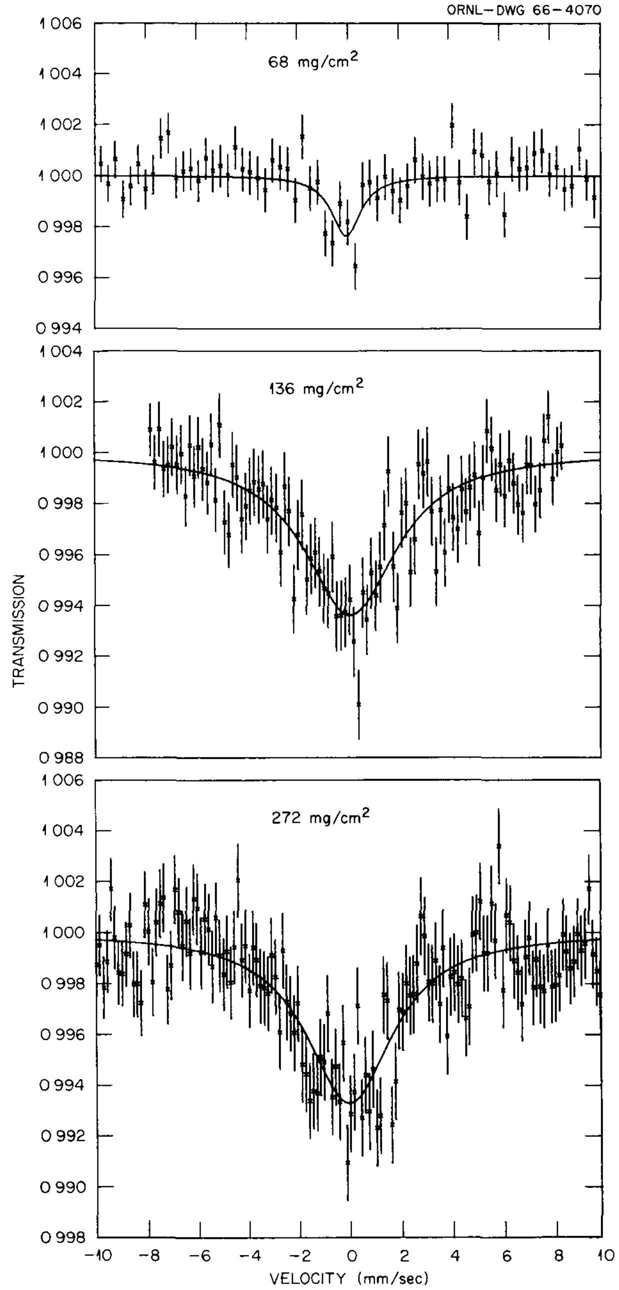

Fig. 6.5. Mossbauer Spectra of ^{73}Ge. The target was isotopically enriched ^{73}Ge and the absorber natural germanium of the thicknesses indicated.

---

[17] I. M. Lifshitz, M. Ia. Azbel', and M. I. Kaganov, *Soviet Phys. JETP (English Transl.)* **4**, 41–54 (1957).

[18] I. M. Lifshitz and V. G. Peschanskii, *Soviet Phys. JETP (English Transl.)* **8**, 875–83 (1959).

[19] Jan Korringa, private communication, April 14, 1966.

[20] L. F. Mattheiss, *Phys. Rev.* **134**, 4970 (1964).

[21] Physics Division.

[22] National Science Foundation Cooperative Fellow from the Ohio State University.

[23] G. Czjzek, F. E. Obenshain, D. Seyboth, and J.L.C. Ford, Jr., *Metals and Ceramics Div. Ann. Progr. Rept. June 30, 1965*, ORNL-3870, pp. 35–37.

[24] G. Czjzek, J.L.C. Ford, Jr., F. E. Obenshain, and D. Seyboth, *Phys. Letters* **19**, 673–75 (1966).

the observed line width and of the maximum absorption allows a separation of the recoilless fractions of target and absorber. We found that the recoilless fraction of the absorber must lie in the range 0.10 to 0.17, in agreement with the value 0.125 derived from the Debye formula. The recoilless fraction in the target is then between 0.008 and 0.013. This strong reduction of the recoilless fraction in the target is probably caused by the ion bombardment. It is not yet clear which of the possible mechanisms is responsible for this reduction.

In another experiment, the first of a longer series, the Mössbauer effect of ^{61}Ni was observed with a pure nickel target and a Cu–2.5% Ni absorber. The purpose of this series of experiments is to investigate the hyperfine splitting and isomer shift of ^{61}Ni in copper-nickel alloys as a function of the nickel concentration. These alloys constitute a case of great interest for the theory of alloys, and the measurement of these quantities will give valuable information on the electronic structure of the alloys.

The spectrum obtained in the first experiment is shown in Fig. 6.6. The observed spectrum agrees with the assumption of hyperfine splitting in the target and an unsplit absorption line, as expected. The value of the internal field in nickel derived from the spectrum, $H_{\mathrm{eff}} = 77 \pm 10$ kilogauss, agrees with previous measurements. The measured isomer shift is zero, but the statistical uncertainty (±0.1 mm/sec) is about twice the expected shift. These results establish that the investigation can be done in principle, but the resolution has to be improved by a factor of about 10. Work is in progress to achieve this goal, using an unsplit target and improved equipment.

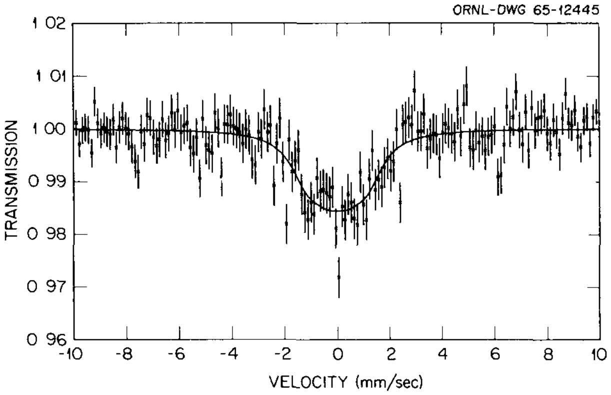

Fig. 6.6. Mössbauer Spectrum of Isotopically Enriched ^{61}Ni Target. Absorber: Cu–2.5% Ni alloy.

7. Physical Ceramics Studies

C. S. Morgan

Increasing use of high-temperature processes has greatly increased the importance of ceramic components. With this development the need for knowledge of sintering, which is required to make most ceramic parts, and of high-temperature deformation properties of ceramic materials has increased. Sintering and deformation studies designed to advance our understanding of basic phenomena in ceramic materials are being carried out. Study of self-diffusion in thoria is being initiated and will be coordinated with thoria deformation studies.

GRAIN-BOUNDARY REACTIONS DURING DEFORMATION[1]

C. S. Yust L. E. Poteat[2]

Recent studies of the creep deformation of thorium dioxide and uranium dioxide have revealed a variation in deformation mode with strain rate and indicated that grain-boundary sliding is associated with the viscous-creep mode. Compression tests on bicrystal and very-large-grain polycrystal UO_2 specimens have been used to study the grain-boundary sliding process in greater detail. The data are presented in Fig. 7.1. The large-grain polycrystalline specimens, which typically contain six to ten grains, yielded results comparable to those for fine-grain material at stresses in excess of 6000 psi but not at stresses less than 6000 psi. This is interpreted to mean that the diffusional transport of material is a process associated with grain boundaries.

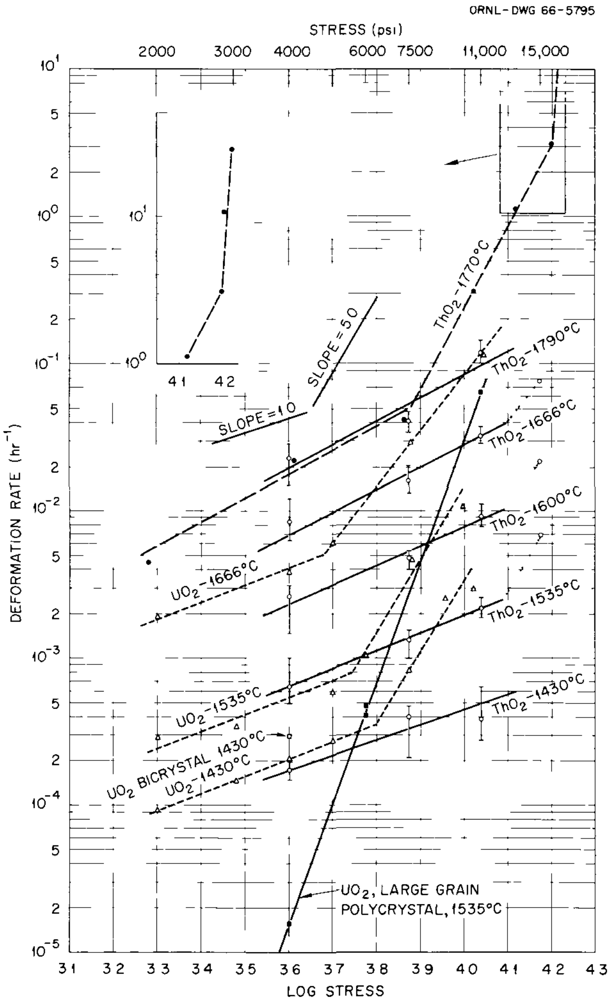

Fig. 7.1. Summary of Deformation Data for ThO_2 and UO_2 Polycrystalline and Bicrystal Specimens.

---

[1] Abstract of a paper presented before the Third International Materials Symposium, University of California, Berkeley, June 13–17, 1966.

[2] Consultant and summer employee from Clemson University, Clemson, S.C.

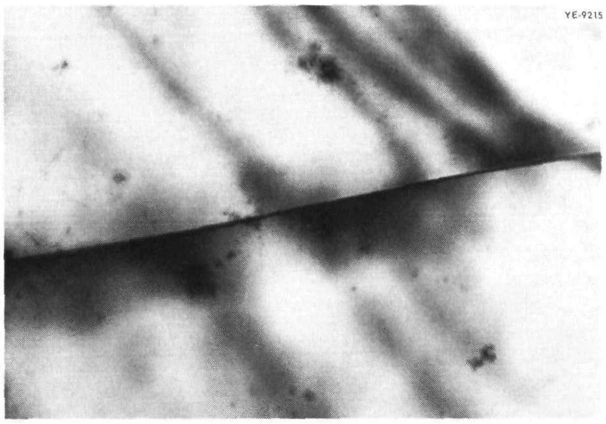

Fig. 7.2. Electron Micrograph of a Typical UO_2 Bicrystal Boundary Before Grain-Boundary Sliding Occurred. 45,000×. Reduced 52%.

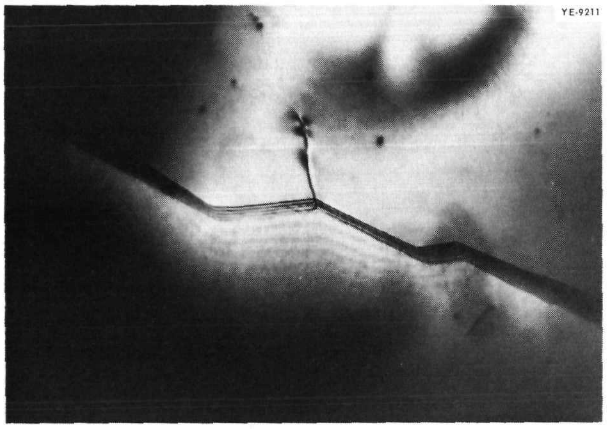

Fig. 7.3. Ledges in a UO_2 Bicrystal Boundary After a Small Amount of Grain-Boundary Sliding. 69,000×. Reduced 52%.

Electron microscopy (Fig. 7.2) of a bicrystal boundary prior to sliding showed it to be straight and free of gross impurities. After a very small displacement, the boundary contained large ledges, shown in Fig. 7.3. Such ledges have long been considered to be the source of boundary cavities formed during boundary sliding. Gifkins[3] has suggested that such ledges are formed by the intersection of slip with the boundary; Chen and Machlin[4] have suggested that they are "grown-in." These ledges were formed under conditions such that dislocation motion would not be expected to contribute to the sliding process; hence, the Gifkins mechanism does not seem the likely mechanism for ledge formation here. The grain boundary may be visualized as consisting of atomic-size ledges, resulting because the grain lattices are not atomically smooth where they meet the boundary. The application of shear stress to the boundary may cause the small ledges to migrate along the boundary and coalesce to form the large ledges observed in this work.

DEFORMATION MECHANISMS IN THORIA AT ELEVATED TEMPERATURES[5]

L. E. Poteat[2]   C. S. Yust

The compressive-creep characteristics of thorium dioxide were studied over a wide range of strain rates. The specimens tested were prepared from 99.99% thoria powder by cold pressing and sintering, were 97.5% dense, and had an average grain diameter of 10 μ. The creep deformation of thoria exhibited three modes: brittle fracture at high stress, a macroscopically ductile viscous creep mode at low stress, and an intermediate mode that exhibits some ductility on a macroscopic scale. The data are summarized in Fig. 7.1. The slope of approximately 1.0 for the viscous range implies that material is transported by diffusion, while the slope of approximately 5.0 for the intermediate range indicates that material is transported by the climb of dislocations. Similar effects are noted in polycrystalline uranium dioxide, and the data for the viscous and intermediate creep ranges for this material are also presented in Fig. 7.1. Intergranular voids are generated in these materials during deformation, although the tendency to do so is diminished in UO_2. In UO_2 and ThO_2, which both have the fluorite structure, grain-boundary sliding appears to be associated with the viscous-creep process.

---

[3] R. C. Gifkins, *Acta Met.* 4(1), 98 (1956).

[4] C. W. Chen and E. S. Machlin, *Acta Met.* 4(11), 655 (1956).

[5] Abstract of paper presented before the Annual Meeting of the American Ceramic Society, Washington, D.C., May 7–12, 1966.

INITIAL SINTERING OF OXIDES

C. S. Morgan L. L. Hall

The study of the densification kinetics of sintering powder compacts has been extended to five additional oxides. Studies of the initial sintering (i.e., as the temperature is being raised) permit the observation of densification kinetics that may not be diffusion controlled. The initial densification kinetics of ThO_2 exhibits three distinctive effects:[6]

1. a temperature-dependent densification end point,
2. a disproportionate increase in the densification rate with increase in temperature as compared with that expected from volume-diffusion processes, and
3. a maximum and minimum in the densification rate as the temperature is being increased at a uniform rate.

The oxides tested during this report period, ZrO_2-CaO, CeO_2, MgO, CaO, and SiO_2, exhibited some or all of these distinctive phenomena.

An explanation of these effects by a diffusion sintering process, either volume or grain-boundary diffusion, is not evident; however, a qualitative explanation based on dislocation transport of material can be proposed. This explanation depends on the premise that as the temperature is increased the stress required for motion and generation of dislocations steadily decreases. As the temperature is raised, a rush of dislocation motion causes a burst of densification, which overrides the effect of diffusion-controlled processes (i.e., volume diffusion, grain-boundary diffusion, or dislocation movement with diffusion support). The result is that the densification kinetics during nonisothermal sintering is not consistent with diffusion processes. On the other hand, under isothermal conditions all material-transport mechanisms resulting in densification are diffusion controlled.

A TOPOLOGICAL STUDY OF SINTERING

L. K. Barrett[7] C. S. Yust

This work is an effort to understand the progressive geometric changes occurring in a sintering mass and to construct a mathematical model that will describe the process. Relatively large particle-size copper powders are being used to study the void-solid interface. The observations to date indicate that the removal of void space is a continuous process, beginning with the elimination of the smallest voids, which are usually those associated with the individual particles. The formation of necks between particles results in the formation of a continuous highly interconnected void space in the solid, and continued densification leads to the pinching of some continuous channels, which then begin to shrink and fill. Individual pores are not frequently isolated, but "trees" of isolated porosity are possible at the late stages of sintering. Also, the local sintering behavior is evidently very dependent on the broader structure.

---

[6] C. S. Morgan and C. S. Yust, "Sintering of Materials with the Fluorite Structure," *J. Nucl. Mater.* 10(3), 182 (1963).

[7] Consultant from the University of Tennessee, Knoxville.

8. Physical Properties

D. L. McElroy

Our work emphasizes the development of accurate methods of measuring the physical properties of solids at high temperatures so that we may gain insight into heat-transport phenomena. By critical evaluation of a series of interrelated physical-property measurements obtained on carefully selected and well-characterized specimens, one can interpret the behavior of a material with respect to existing theories and test the theories for adequacy. From an understanding of heat transport we may make reliable predictions outside the range of available data, as well as possibly alter a material's properties by control of physical and chemical variables. The lack of physical-property data at high temperatures directly limits adequate design of high-temperature systems. Thus, the present program serves a practical purpose, since needed high-temperature data and extensive measurement capacities are natural consequences of our studies.

Although accurate measurements of physical properties are rare and obtaining experimental competence at high temperatures is a gradual process, we have attained the following measurement capacity: thermal conductivity λ from -200 to 1000°C, and work is progressing to extend this to 1600°C; electrical resistivity ρ and Seebeck coefficient S from -269 to 1400°C, and extension to 2200°C is imminent; specific heat C_p from 100 to 900°C with a planned extension to cover the range -200 to 1400°C; and total hemispherical emittance E_t from 100 to 1600°C. As the following material indicates, this capacity is being applied to a variety of materials chosen to illustrate particular heat-transport mechanisms.

RADIAL HEAT FLOW METHODS FOR MEASUREMENT OF THERMAL CONDUCTIVITY OF SOLIDS

D. L. McElroy   J. P. Moore

This chapter[1] reviews and contrasts the steady-state radial heat flow methods that have been used to measure the thermal conductivity of solids. The mathematical models and error sources of five classifications are treated, including: unguarded cylindrical methods, guarded cylindrical methods, spherical and ellipsoidal methods, comparative concentric cylindrical methods, and direct-heating methods. Measurement results on five materials generated by these methods provide a comparison of the quality of each method. Recommended techniques are given for the use of radial systems to cover broad limits of thermal conductivity (0.01 to 1.6 w cm^{-1} $°\text{C}^{-1}$) and temperature (270 to 3900°K).

TEMPERATURE MEASUREMENT AND CONTROL

D. L. McElroy   W. Fulkerson

This chapter[2] deals with the natural phenomena used to measure and control temperature in metals

---

[1] Modified abstract prepared for publication in a book entitled *Thermal Conductivity*, ed. by R. P. Tye, Academic, London, 1966.

[2] Modified abstract prepared for publication in a book entitled *Techniques in Metals Research*, ed. by R. F. Bunshah, Wiley, New York, 1966.

research. Each method is treated by presenting the theory and physical principle, the technology of construction, acceptable measurement practices, examples of applications, relative merits, and likely error sources. Although major emphasis is placed on thermoelectric and optical methods, other thermometry topics are covered, including the ideal thermodynamic temperature scale, the International Practical Temperature Scale, expansion thermometry, resistance thermometry, new thermometers, and modern control methods. Thus, this chapter presents the state of available knowledge, the areas of current research, and the problem areas that still plague temperature measurement and control.

PHYSICAL PROPERTIES OF SILICON

W. Fulkerson J. P. Moore
R. S. Graves

For single-crystal and polycrystalline silicon, we measured λ from 91 to 1330°K, ρ from 300 to 1273°K, and S from 350 to 1270°K. The thermal-conductivity data for both polycrystalline and single-crystal specimens were essentially the same to within experimental error (~2%). The thermal resistivity, $W = 1/\lambda$, could be expressed by two linear relations:

$$W = -0.169 + 3.005 \times 10^{-3}T,\ 130 \leqq T \leqq 680°\mathrm{K}\ , \quad (1)$$

and

$$W = -1.115 + 4.37 \times 10^{-3}T,\ 680 \leqq T \leqq 1050°\mathrm{K}\ . \quad (2)$$

The break at 680°K shown in Fig. 8.1 is close to the Debye temperature (650°K) for silicon. Glassbrenner and Slack[3] have suggested that the increased resistivity indicated by the data above 690°K is due to four-phonon scattering processes, and they show that this added resistivity term should be proportional to T^2. The plot of our data in Fig. 8.2 as $(W - W_I)/T$ vs T is essentially linear only above 680°K. This linearity would be

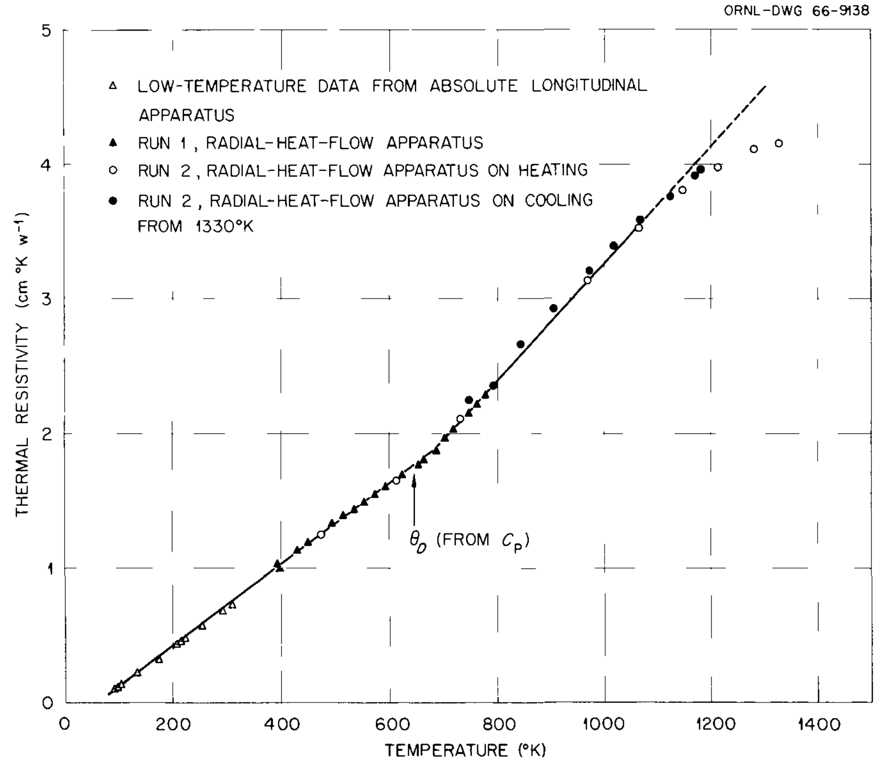

Fig. 8.1. Thermal Resistance of Single-Crystal Silicon.

---

[3] C. S. Glassbrenner and G. A. Slack, *Phys. Rev.* **134**, 1058 (1964).

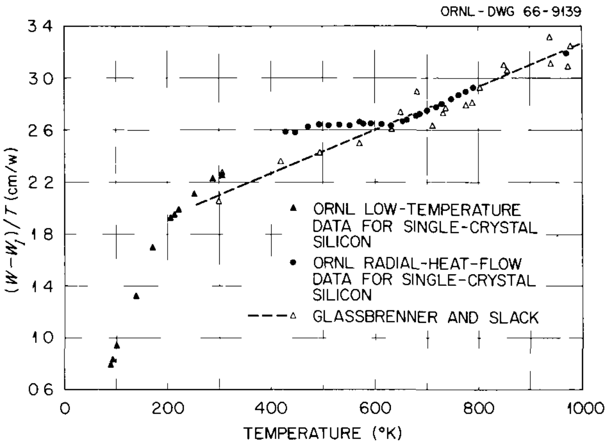

Fig. 8.2. Modified Thermal-Resistance Plot to Show Possible Four-Phonon Scattering in Single-Crystal Silicon.

expected if there were a T^2 term; however, Eq. (2) also fits the data in this temperature range. Thus, the evidence for a T^2 term is not conclusive. The term W_I is the resistivity due to isotope scattering and is taken[3] to be 0.033 cm °K w^{-1}.

Above 1050°K W deviates from the linear relation (2), as shown in Fig. 8.1, due to an increasing electronic contribution, most of which is due to ambipolar diffusion. The theoretically calculated excess conductivity due to this mechanism agrees within the experimental error with measured values. The high-temperature data agree closely (within 2%) with that obtained by Glassbrenner and Slack and not that of Shanks *et al.*[4]

The electrical-resistivity data for both polycrystalline and single-crystal specimens agreed well with the values reported for intrinsic silicon by Morin and Maita,[5] and the data were used in calculating the electronic portion of the thermal conductivity. The specimens were extrinsic *n*-type below about 250°C, and the value of the resistivity in the extrinsic range was sensitive to the specimen heat treatment.

The Seebeck coefficients of the polycrystalline and single-crystal silicon specimens were identical in the intrinsic temperature range and decreased rapidly with temperature. Both specimens were *n*-type in the extrinsic range.

FURTHER RESULTS ON HIGH-PURITY IRON

J. P. Moore T. G. Kollie
W. Fulkerson D. L. McElroy

Eleven λ data points between 754 and 775°C on the ORNL high-purity iron confirmed our previous measurements[6] and did not confirm the anomalous λ deviations reported by Richter and Kohlhaas[7] at the Curie point. On an ultrahigh-purity iron ($\rho_{300}/\rho_{4.2} = 226$), we completed measurements of S to 1050°C, ρ to 1500°C, and λ between -200 and 0°C. Measurements of C_p to 850°C with this material are progressing with an improved pulse-heating system to study further the 35% discontinuity in C_p previously reported at the Curie point.[8] The literature on the energetics of ferromagnetic materials is being surveyed to select other materials likely to show this behavior.

ELECTRONIC HEAT TRANSPORT

W. Fulkerson R. K. Williams
J. P. Moore

Analysis of our previously reported λ data[9] on tungsten, using the first two terms of the Lorenz-number series, revealed an anomalous temperature dependence for the lattice portion of λ. We recently showed that inclusion of a nonnegligible third term in the Lorenz expansion reduces this anomaly. Carrying the expansion of the Lorenz number L two terms past that given by Ziman[10] yields

$$L = L_0 - S^2 - \frac{16}{5} L_0 \frac{\Delta\rho}{\rho} , \qquad (3)$$

where $\Delta\rho$ is the T^3 dependence of ρ and L_0, the classical limit, is 2.443×10^{-8} $(\mathrm{v}/°\mathrm{C})^2$. Our

---

[4] H. R. Shanks *et al.*, *Phys. Rev.* **130**, 1743 (1963).

[5] F. J. Morin and J. P. Maita, *Phys. Rev.* **96**, 28 (1954).

[6] W. Fulkerson, J. P. Moore, and D. L. McElroy, *J. Appl. Phys.* **37**, 2639–53 (1966).

[7] V. F. Richter and R. Kohlhaas, *Z. Naturforsch.* **19a**, 1632–34 (1964).

[8] T. G. Kollie, *The Development of a Pulse Heating Calorimeter Technique for Measuring the Specific Heat of Electrical Conductors and Its Application to Pure Iron from 100° to 1200°C*, ORNL-TM-1187 (August 1965).

[9] W. Fulkerson, J. P. Moore, and R. S. Graves, *Metals and Ceramics Div. Ann. Progr. Rept. June 30, 1965*, ORNL-3870, pp. 45–48.

[10] J. M. Ziman, *Electrons and Phonons, the Theory of Transport Phenomena in Solids*, 3d ed., p. 383, Clarendon Press, Oxford, 1963.

tungsten ρ data to 1400°C has a cubic temperature dependency that yields a Lorenz number that increases with temperature and is larger than L_0. This Lorenz-number correction is too large, but it is in the proper direction to remove the disturbing lattice portion behavior. From measurements on dilute tungsten-tantalum alloy we derived a Lorenz number that also indicates that the classical limit is too small for tungsten. Furthermore, if one can write λ as the sum of its electronic and lattice components

$$\lambda = LT/\rho + 1/(A + BT) , \tag{4}$$

and if $BT >> A$, then

$$\lambda T \cong LT^2/\rho + 1/B . \tag{5}$$

If L is a constant, then a plot of λT vs T^2 should yield a straight line of slope L and intercept $1/B$. Such a plot for tungsten yields $L = 1.115\ L_0$, which tends to confirm the alloy work. This approach has worked well for molybdenum, iron above the Curie temperature, Inconel 702, Pt–40% Rh, Nb–10% W, and T-111 but fails for platinum and aluminum, either because BT is not always much greater than A or because L is changing with temperature.

ESTIMATED THERMAL-CONDUCTIVITY VALUES FOR SOLID AND LIQUID PROMETHIUM[11]

R. K. Williams D. L. McElroy

Elemental promethium is a potential isotopic power source, but its properties are largely unknown, and its melting point has only recently been determined to be 1080 ± 10°C. We have used the theory of heat conduction in solids and liquids and the known behavior of other rare-earth elements and metallic melts to estimate the thermal conductivity of promethium to 2000°C. The thermal conductivity of liquid promethium is estimated to lie between 0.1 and 0.25 w cm^{-1} °C^{-1} at the melting point and between 0.1 and 0.36 w cm^{-1} °C^{-1} at 2000°C. The electrical resistivity and thermal conductivity of solid promethium and the self-diffusion coefficient and atomic volume of liquid promethium were also estimated.

EQUIPMENT DEVELOPMENT

New Electrical Resistivity and Radial Heat Flow Apparatus

T. G. Kollie R. K. Williams
W. Fulkerson

To expedite property measurements on a number of solids to 1400°C we duplicated our electrical-resistivity–Seebeck-coefficient apparatus. This second apparatus allowed ρ measurements on (1) Hastelloy X and Inconel 625, which were needed to estimate their thermal conductivity from −273 to 1000°C (see Part V, Chap. 35 of this report); (2) a molybdenum specimen to 1400°C on which λ and ρ were previously measured[12] at another laboratory; (3) a series of commercial sintered aluminum products; (4) the iron and silicon specimens mentioned above; and (5) a number of graphite specimens to supplement analysis of λ measurements.[13] We obtained a check on the accuracy of our electrical-resistivity measurements by submitting our tungsten specimen for independent ρ measurements at the National Research Council, Ottawa, Canada. The maximum deviation of their results[14] from ours was ±0.4% to 1200°C, which is well inside the combined estimated error bands for both laboratories.

Accurate high-temperature ρ data are required for analysis of λ data on the transition metals and for the prediction of the thermal conductivities of pure metals and alloys. An ultrahigh-vacuum furnace (5×10^{-9} torr at 2200°C) was designed and ordered to obtain the required ρ and S measurements on ultrahigh-purity materials. This apparatus should obtain data about as accurate as those presently obtained at lower temperatures.

A high-temperature guarded radial heat flow apparatus is being tested to obtain λ data to 1500°C. Current tests are restricted to below 1000°C, where the λ of the tungsten specimen is known.[9] This system can be operated with a high vacuum or an inert atmosphere. Results obtained to date

---

[11] Abstracted from ORNL-TM-1424 (March 1966).

[12] A. D. Feith, *Measurement of the Thermal Conductivity and Electrical Resistivity of Molybdenum*, GETM-65-10-1 (October 1965).

[13] "Physical Properties Group, Progress Report: Oak Ridge National Laboratory," *Proceedings of Fifth Conference on Thermal Conductivity, Denver, Colorado, Oct. 20–22, 1965* (limited distribution).

[14] M. J. Laubitz, private communication, 1966.

indicate that vacuum operation will not be practical below 1200°C, but at 750°C acceptable data can be obtained with helium introduced at a reduced pressure (10 to 20 torrs).

Guarded Longitudinal Apparatus

J. P. Moore

A guarded longitudinal heat flow apparatus that uses absolute power measurements was constructed for simultaneous λ, ρ, and S measurements between -195 and 70°C. This apparatus has been used to study the properties of high-purity samples of Fe, W, Mo, Pt, and Al. The platinum results are compared to previous studies in Fig. 8.3. According to Powell and Tye,[15] the use of platinum as a λ standard is enhanced by its near-constant value between room temperature and 1000°C. The disagreement among the results of Powell and Tye, Bode,[16] Holm and Stormer,[17] and Laubitz[18] created doubt about Powell and Tye's results on their specimen. Subsequently, we obtained their specimen, and our results indicate that Powell and Tye are in error. Although this apparatus was not designed for measurements on poor thermal conductors, it has been used on Inconel 625 and Hastelloy X (see Part V, Chap. 35 of this report).

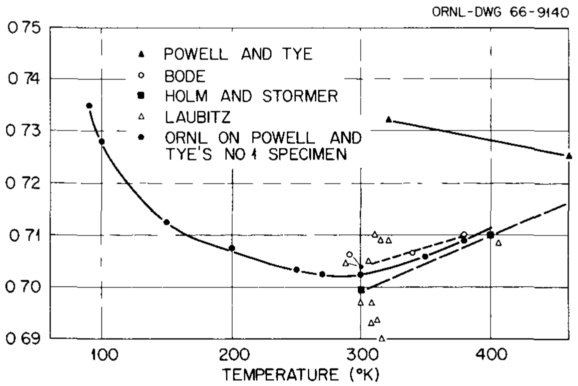

Fig. 8.3. Thermal Conductivity of Platinum.

Comparative Longitudinal Heat Flow Apparatus

J. P. Moore R. S. Graves

This apparatus measures λ of small uninstrumented specimens from about 20 to 150°C for studies of effects of controlled specimen variables such as impurity level, mixture ratios in two-phase materials such as cermets, porosity, and neutron irradiation. An outline of the specific work with this apparatus follows.

1. We studied the effect of porosity on the λ of ThO_2 and the effect of UO_2 addition and sintering atmosphere on the λ of ThO_2 (see Part IV, Chap. 32 of this report).
2. We studied λ variation of Al-UO_2 cermets, with emphasis on the effect of varying amounts and particle-size distribution of UO_2 (see Part III, Chap. 28).
3. We determined the Lorenz number of tungsten using tungsten-tantalum alloys.
4. We measured λ of W–26% Re with subsequent extrapolation to 1400°C using measured ρ values (see Part II, Chap. 14).
5. We measured interfacial resistance on indium, gold, and lead foils.
6. We measured λ of sintered aluminum products with various Al_2O_3 concentrations.
7. We determined λ of control specimens for irradiation testing. The results of Y_2O_3, Al_2O_3, NbC, TiC, TaC, WC, and ZrC are reported in Part II, Chap. 14. Measurements on MgO specimens with densities between 3.17 and 3.59 g/cm^3 showed that λ varied with density according to

$$\frac{\lambda_{TD}}{\lambda_M} = \frac{1 - \rho'}{1 + \beta\rho'}, \qquad (6)$$

where λ_M is the measured thermal conductivity, λ_{TD} is the λ of theoretically dense material, ρ' is the pore volume fraction, and β is an empirical constant, which is unity for MgO.

8. Measurements of λ on chromium indicated a large decrease in the lattice portion of λ at the Néel temperature (311°K). This corresponds to an increase in the electronic portion, as indicated by the electrical-resistivity data of Arajs[19] if $L = L_0$ is assumed.

---

[15] R. W. Powell and R. P. Tye, *Brit. J. Appl. Phys.* **14**, 662 (1963).

[16] K. H. Bode "Measurement of the Thermal Conductivity of Pure Platinum Between 0°C and 100°C," *PTB-Mitteilungen* Nr 5/1964, p. 416 (in German).

[17] R. Holm and R. Stormer, *Wiss. Veroeffentl. Siemens-Konzern* **9**, 312–22 (1930).

[18] M. J. Laubitz, private communication, 1965.

[19] S. Arajs, *J. Less-Common Metals* **4**, 46–51 (1962).

This apparatus was so useful that a duplicate has been constructed for use in the High-Radiation-Level Examination Laboratory.

RELATED WORK

Our radial heat flow apparatus was used to measure λ of Nb–10% W (approximately the composition of D-43) to 1000°C and λ of T-111 to 450°C (see Part II, Chap. 14). Special specimens were included to permit simultaneous measurements of S and ρ, and the technique appeared to be satisfactory. The specific-heat apparatus was used to measure the emittance of W–26% Re (see Chap. 14) and several high-emittance coatings (see Part IV, Chap. 29).

We performed a series of studies for the Isotopes Division (see Part V, Chap. 33) including (1) estimation of λ of PuO_2 microspheres in helium and in vacuum at various void fractions of solids, (2) heat-transfer analysis to achieve temperature control of a furnace to be used to hot press isotopic heat sources, and (3) supervision of a development program on an unproven commercially available thermal-conductivity apparatus for eventual use in the Isotopes Division hot-cell work.

9. Solid-State and Molecular Theory

J. S. Faulkner

Our research interests are reasonably well illustrated by the summaries that appear in this report. The primary purpose is to carry out quantum-theoretical investigations of the properties of solids and molecules, but we have also been able to furnish some needed theoretical help for other groups and individuals in the Division.

BAND THEORY

J. S. Faulkner H. L. Davis
H. W. Joy

Computer programs for calculating the electronic states of ordered crystalline solids by the Green's function or KKR method[1–4] have been written and checked out. This latter method is known to give accurate and rapidly convergent results for crystal potentials of the muffin-tin type. Many of the early band-theory calculations were done with rather crude methods, and even some of the more recent ones treat so few points in k-space that they are not very useful. Well-written programs and the availability of a very high-speed computer enable us to carry out useful calculations with reasonable facility, and this capability will aid our investigations of the electronic properties of real solids.

HARTREE-FOCK-ROOTHAAN WAVE FUNCTIONS FOR LITHIUM

H. W. Joy

We demonstrated that we can indeed obtain analytic Hartree-Fock wave functions by means of the minimum-energy orthogonalization technique[5] instead of the more usual methods.[6] All of the Bagus-Gilbert[7] functions for the lithium atom, including their minimal, marginal, nominal, and accurate basis set functions, were duplicated and then improved upon by a straightforward and systematic application of the method.

VALENCE-STATE WAVE FUNCTIONS FOR CARBON

H. J. Silverstone[8] H. W. Joy

We obtained a new $2p\pi$ atomic orbital for π-electron theory by minimizing the energy of the carbon atom in a valence state appropriate for alternate hydrocarbon ground states. When the molecular wave function is described in part by molecular-orbital theory, new terms appear in the valence-state energy in addition to those in the standard valence-bond formula of Van Vleck.[9]

---

[1] J. Korringa, *Physica* **13**, 392 (1947).

[2] W. Kohn and N. Rostoker, *Phys. Rev.* **94**, 1111 (1954).

[3] P. M. Morse, *Proc. Natl. Acad. Sci. U.S.* **42**, 276 (1956).

[4] F. S. Ham and B. Segall, *Phys. Rev.* **124**, 1786 (1961).

[5] H. W. Joy, L. J. Schaad, and G. S. Handler, *J. Chem. Phys.* **41**, 2026 (1964).

[6] C.C.J. Roothaan and P. S. Bagus, p. 47 in *Methods in Computational Physics*, vol. 2, ed. by B. Alder, S. Fernbach, and M. Rotenberg, Academic, New York, 1963.

[7] P. S. Bagus *et al.*, *Bull. Am. Phys. Soc.* **9**, 624 (1964).

[8] Johns Hopkins University, Baltimore.

[9] J. H. Van Vleck, *J. Chem. Phys.* **2**, 20 (1934).

The resulting $2p\pi$ orbital gives a value for the one-center Coulomb repulsion integral of 12.4 ev, compared to the semiempirical value of approximately 11 ev and the old theoretical value of 16.9 ev.

We also calculated valence states appropriate for ions and excited states of alternate hydrocarbons and found that the $2p\pi$ atomic orbitals do not remain invariant under such excitations in the smaller molecules, contrary to what has generally been assumed in this field.

STABILITY AND STRUCTURE OF H_3O

C. E. Melton[10] H. W. Joy

We are carrying out one-center expansion calculations on the electronic wave function of H_3O to lend a measure of theoretical support to its recent experimental discovery.[11] The calculations so far have shown H_3O to be stable relative to H_3O^+ (which, in turn, has been computed[12,13] to be stable relative to $H_2O + H^+$). However, they have not yet shown it to be stable relative to $H_2O + H$, nor have they reached an adequate prediction of the presumably nonplanar geometry of the molecule.

COMPUTER CODES FOR THE APPLICATION OF LIGAND-FIELD THEORY

H. L. Davis

In the study of the paramagnetic, optical, and microwave properties of predominantly ionic crystals, it is quite generally recognized that a vast amount of experimental data can be explained by the application of ligand-field theory, since the relevant physical properties usually arise from the effects of the crystalline electrostatic field on an unfilled *p*-, *d*-, or *f*-electron shell. To correlate such experimental data with ligand-field theory, one is confronted with an involved fitting procedure, entailing the variation of parameters representing electrostatic repulsion between electrons, spin-orbit coupling, and the crystalline electrostatic field. To minimize such tedium, a rather extensive library of computer codes has been developed over the last year and is essentially completed. These codes are quite general and have been written so they can be applied to the study of *p*-, *d*-, or *f*-electron configurations in positions of arbitrary symmetry. We anticipate that these codes will find frequent future use in our program for the theoretical interpretation of magnetic and optical data arising from ionic crystals, solutions, and molten salts that contain either transition metal ions, lanthanide ions, or actinide ions.

THEORETICAL INTERPRETATION OF SPECTRA DUE TO A Bi^+ COMPLEX

H. L. Davis

The $Bi^+(6p^2)$ ion is a product of the reaction between bismuth metal and dilute solutions of $BiCl_3$ in liquid $AlCl_3$-NaCl and $ZnCl_2$-KCl mixtures.[14,15] These experiments are the first isolation of an ion having an unfilled *p*-electron shell in a nongaseous environment, and they also provided absorption spectra of a complex containing the Bi^+ ion in the respective solutions. We provided a detailed theoretical interpretation for such spectra by showing that ligand-field theory of a p^2 configuration adequately rationalizes both the relative intensities and the positions of the bands of the spectra. This interpretation is analogous to the familiar interpretations given spectra due to transitions between ligand-field states of d^N and f^N configurations. Thus, the theoretical work lends added support to the identification of Bi^+ in the solutions and should be of value for any future work on Bi^+ in other environments. Finally, this theoretical interpretation also has the novelty of being the first quantitatively successful comparison of ligand-field theory for a p^N configuration with observed spectra.

ELECTRONIC STATES OF DISORDERED SYSTEMS

J. S. Faulkner

The method for calculating the density of states of liquid metals put forth by Klauder[16] and Matsu-

---

[10] Chemistry Division.

[11] C. E. Melton and P. S. Rudolph, *J. Catalysis* **5**, 387 (1966).

[12] D. M. Bishop, *J. Chem. Phys.* **43**, 4453 (1965).

[13] R. Moccia, *J. Chem. Phys.* **40**, 2186 (1964).

[14] N. J. Bjerrum, C. R. Boston, G. P. Smith, and H. L. Davis, *Inorg. Nucl. Chem. Letters* **1**, 141 (1965).

[15] See also chap. 10 of this report.

[16] J. R. Klauder, *Ann. Phys. (N.Y.)* **14**, 43 (1961).

bara and Toyozawa[17] has been extended to include three-body scattering terms self-consistently and to infinite order. The resulting integral equation has so far proved unsolvable. If half of the three-body terms are ignored, an approximation suggested, but not investigated, by Klauder[16] is obtained. Calculations on this integral equation have been carried out, but the resulting density of states is clearly wrong.

---

[17] T. Matsubara and Y. Toyozawa, *Progr. Theoret. Phys. (Kyoto)* **26**, 739 (1961).

10. Spectroscopy of Ionic Media

G. P. Smith

Spectroscopic investigations of the structure and chemistry of molten salts have been a prime concern of this group for several years. Most of the research reports that follow deal with this topic. Recently, however, work was initiated on crystalline salts, and this is described in the terminal report of this chapter.

Research currently in progress, but not reported here, includes the development of quantitative procedures for sorting out mixtures of coordination geometries in molten salts, an extension of the work reported here on bismuth to cover other ions with novel electronic structures, an investigation of chemical kinetics in molten salts, and a substantial broadening of the work on ionic crystals.

THE MOLTEN $NiCl_2$-CsCl SYSTEM[1]

G. P. Smith C. R. Boston

Optical absorption spectra (5 to 26 kK) of fused mixtures of CsCl and $NiCl_2$ containing 2 to 60 mole % $NiCl_2$ were measured at about 860°C, and a mixture containing 20 mole % $NiCl_2$ was studied at 560–862°C. Up to 20 mole % $NiCl_2$, the Bouguer-Beer law was accurately obeyed, and each nickel was tetrahedrally coordinated to four chlorides. At higher $NiCl_2$ contents nickel coordination was partitioned between tetrahedral and other (unidentified) geometries. The fraction with tetrahedral coordination progressively decreased with increasing $NiCl_2$ content but was still appreciable at 60 mole % $NiCl_2$. The most prominent feature of the spectrum associated with the unidentified geometries was a band between 18 and 19 kK. These results indicate that nickel has very similar coordination geometries in the liquid and crystalline phases of Cs_3NiCl_5 but very different coordination geometries in crystalline and liquid $CsNiCl_3$.

OPTICAL SPECTRA AND DENSITIES OF MOLTEN ORGANIC SALTS CONTAINING LARGE NICKEL CHLORIDE CONCENTRATIONS[2]

G. P. Smith S. von Winbush[3]

The optical absorption spectra of nickel chloride–tri-*n*-butylbenzylphosphonium chloride melts and glasses were measured over the wavelength range of 350–1650 mμ, at compositions of 0.1–33.3 mole % $NiCl_2$, at temperatures of 22–174°C, and with path lengths of 0.007–1.00 cm. It was concluded that the nickel in these melts was present almost exclusively as approximately tetrahedral $NiCl_4^{2-}$ anions under all conditions studied. The internal absorbance, *A*, at all wavelengths was found to be proportional to the molar concentration of $NiCl_2$ to within a small error over the entire composition range at 174°C. Furthermore, *A* was a linear

---

[1] Abstract of "Electronic Spectra and Coordination Geometry in Molten Mixtures of CsCl and $NiCl_2$ Containing Up to 60 Mole Percent $NiCl_2$," paper to be published in *The Journal of Chemical Physics*.

[2] Abstract of "Optical Spectra and Densities of Molten Chloride Salts Having Large Nickel Chloride Concentration. Nickel Chloride–Tri-*n*-butylbenzylphosphonium Chloride Systems Up to 33.3 Mole % Nickel Chloride," *J. Am. Chem. Soc.* **88**, 2127 (1966).

[3] Summer Research Participant in 1965 from the Agricultural and Technical College of North Carolina, Greensboro.

function of temperature over the range 22–172°C at a fixed composition of 33.3 mole % $NiCl_2$. In order to interpret absorption intensities in terms of volume concentrations, the densities of molten mixtures containing 5.03–33.44 mole % $NiCl_2$ were measured as functions of temperature. The molar volume at a fixed temperature was found to be a linear function of the mole per cent composition.

THE SIGNIFICANCE OF THERMALLY GENERATED ISOSBESTIC POINTS[4]

J. Brynestad G. P. Smith

The significance of isosbestic points formed by a set of absorption spectra measured at a series of temperatures is overstressed in the literature. It has been supposed that such isosbestic points can occur only under a specified set of highly restrictive conditions. We find, however, that there are various other conditions, quite different from those previously specified, under which temperature-generated isosbestic points may occur. We conclude that the mere presence or absence of thermally generated isosbestic points for a closed system does not, of itself, provide any useful information about the nature of the system.

PRODUCTS OF THE Bi^{3+}-Bi REACTION IN ACIDIC CHLORIDE MEDIA[5]

N. J. Bjerrum[6] C. R. Boston
G. P. Smith

The spectra of Bi^+ and Bi_5^{3+} in molten $AlCl_3$-NaCl have been measured. These unusual oxidation states of bismuth result from the reaction between bismuth metal and dilute solutions of bismuth trichloride in liquid $AlCl_3$-NaCl and $ZnCl_2$-KCl eutectic mixtures. The formulas Bi^+ and Bi_5^{3+} were determined from mass-action equations using concentrations measured spectrophotometrically. Equilibrium constants were measured for the following equilibria:

$$6Bi^+(soln) \rightleftharpoons Bi_5^{3+}(soln) + Bi^{3+}(soln) ,$$

$$2Bi(liq) + Bi^{3+}(soln) \rightleftharpoons 3Bi^+(soln) ,$$

and

$$4Bi(liq) + Bi^{3+}(soln) \rightleftharpoons Bi_5^{3+}(soln) .$$

The Bi^+ spectrum is probably due to transitions within *p*-type orbitals, whereas the origin of the Bi_5^{3+} spectrum is less certain. Interaction effects due to the existence of bismuth in two oxidation states (+1 and +3) were observed. The present measurements in dilute bismuth trichloride solutions have been correlated with earlier measurements in pure bismuth trichloride. The possibility of metal-metal bonding in the Bi_5^{3+} entity has been considered.

EVIDENCE FOR Bi_8^{2+} AS A PRODUCT OF THE Bi-Bi^{3+} REACTION IN $AlCl_3$-NaCl MELTS[7]

N. J. Bjerrum[6] G. P. Smith

In addition to the Bi^+ and Bi_5^{3+} entities described above, a third species having the formula Bi_8^{2+} resulted from the Bi-Bi^{3+} reaction in $AlCl_3$-NaCl melts. Conditions that favored the formation of this higher polymer were excess bismuth metal and solvent compositions of less than 50 mole % $AlCl_3$. Both the oxidation number and degree of polymerization were determined by techniques similar to those used in identifying Bi^+ and Bi_5^{3+}.

TEMPERATURE DEPENDENCE OF THE ABSORPTION SPECTRUM OF NICKEL(II)-DOPED $KMgCl_3$ AND THE CRYSTAL STRUCTURE OF $KMgCl_3$[8]

J. Brynestad H. L. Yakel[9]
G. P. Smith

Temperature dependence from 80 to 763°K was measured for the intraconfigurational $3d^8 \longleftrightarrow 3d^8$ transitions of octahedrally coordinated $NiCl_6^{4-}$ in single crystals of $K(Mg_{1-x},Ni_x)Cl_3$ with small

---

[4] Abstract of a paper to be submitted for publication.

[5] Abstracted from a paper to be submitted for publication. Also, reported in part in *Inorg. Nucl. Chem. Letters* 1, 141 (1965).

[6] Visitor from Denmark, now at Technical University of Denmark.

[7] Preliminary report.

[8] Abstract of paper to be submitted to *The Journal of Chemical Physics*.

[9] X-Ray Diffraction Group.

x. The crystal structure of the host material, $KMgCl_3$, was determined at 298, 383, and 448°K. Band energies were treated in terms of the Liehr-Ballhausen model of $d^{2,8}$ electronic systems with Dq, B, C, and λ used as empirical parameters. At all temperatures the data are satisfactorily represented by $B = 850$ cm^{-1}, $C/B = 3.986$ (free-ion value), and $\lambda = -275$ cm^{-1}. Thus B, C, and λ are all reduced to about 82% of their free-ion values. The parameter λ is estimated from band splittings at 80°K. The parameter Dq varies between -570 cm^{-1} at 80°K and -500 cm^{-1} at 763°K. Oscillator strengths of the $^3A_{2g} \to {}^3T_{1g}$(F) and $^3A_{2g} \to {}^3T_{1g}$(P) transitions increase by a large factor between 80 and 763°K, while that of $^3A_{2g} \to {}^3T_{2g}$ increases by a small factor. The compound $KMgCl_3$ has a cubic perovskite-type structure at 448°K. At lower temperatures it has an orthorhombically distorted perovskite-type structure in which the distortion is small and magnesium retains approximately O_h coordination.

11. Superconducting Materials

M. L. Picklesimer

We are studying the effects of metallurgical variables on the properties of superconducting materials. Of concern are the effects on current-carrying capacity as a function of magnetic field of such things as morphology, compositions, and spacings of two-phase structures; mechanical strain; preferred orientation; aging and transformation reactions; and fabrication and heat-treatment procedures. For the studies to be meaningful, we must have a considerable knowledge of the physical metallurgy and phase diagrams of the systems of interest. Few of these have been studied, and those that have have not been studied in sufficient detail. Consequently, much of the effort is devoted to establishing a background of information on the transformation kinetics and products, morphologies, phase diagrams, precipitation and aging reactions, and rates of formation of intermetallic compounds. The alloy systems of present interest are those based on niobium and technetium.

THE KINETICS OF THE BETA-PHASE DECOMPOSITION IN NIOBIUM (COLUMBIUM)-ZIRCONIUM[1]

G. R. Love M. L. Picklesimer

Above 950°C the Nb-Zr system consists of a completely miscible bcc solid solution, commonly called the β phase. Between 950 and 600°C, and between 20 and 85% Nb, the β phase decomposes, after sufficiently long times, into two bcc solid solutions. The kinetics of the decomposition in fine-grained Nb-33 at. % Zr alloys are conveniently described with T-T-T (time-temperature-transformation) curves having a "nose" at about 2 hr at 700°C. The reaction rate varies only slowly with zirconium content and negligibly with oxygen contamination; it is speeded up by a factor of 10 to 15 by 90% cold work and slowed by a factor of 10 to 20 by a two-hundredfold increase in grain size.

NEAR-SURFACE EFFECTS IN SUPERCONDUCTING NIOBIUM-ZIRCONIUM ALLOYS[2]

G. R. Love

At a given magnetic field, critical currents may be induced to flow in the surface layers of a superconductor by the application of a relatively small-amplitude alternating-current field. Many measurements of this induced current have been made as a function of the intensity of the direct-current field. The results of these measurements may be interpreted by assuming that there is a near-surface layer of a few hundred angstroms thickness which is able to carry extraordinary current densities, from 3 to 20 times the bulk current densities at a given field. Current densities calculated for this surface layer exceed 10^7 amp/cm^2 at low fields. Details of the observations vary with sample history, but the general features of these measurements have been observed in all samples tested.

---

[1] Abstract, *Trans. Met. Soc. AIME* **236**, 430–35 (1966).

[2] Abstract of paper accepted for publication in *Journal of Applied Physics*. An earlier version of this paper was presented as ORNL-TM-1276 (December 1965).

EFFECT OF DECOMPOSITION OF THE BETA PHASE ON SUPERCONDUCTING CRITICAL CURRENTS IN NIOBIUM-ZIRCONIUM[3]

G. R. Love M. L. Picklesimer

The alternating-current magnetization technique described by Bean,[4] modified to take account of the near-surface effects, was used to conveniently and rapidly determine superconducting critical currents in relatively massive samples. Use of this technique coupled with transformation kinetics data[1] established a broad maximum in critical current density at applied fields below 40 kilogauss for samples heat treated to produce 40 to 60% decomposition of the beta phase at temperatures between 650 and 800°C. In this range of transformation, there is complete transformation in the grain boundaries to a pearlitic structure having a mean lamellar spacing of between 800 and 2000 A. This spacing approximates the estimated London depth in niobium-zirconium alloys. The magnitude of the critical current at the maximum in critical current density is 10 to 15 times the critical current density observed in severely cold-worked niobium-zirconium alloys. However, decomposition of the beta phase into the pearlitic structure is accompanied by an increase in the incidence and severity of flux jumping at all fields tested (40 kilogauss max).

THE ELECTRICAL RESISTIVITY OF TECHNETIUM FROM 8.0 TO 1700°K[5]

C. C. Koch G. R. Love

The electrical resistivity of purified technetium has been determined at just above its superconducting critical temperature (7.8°K) and continuously in two overlapping experiments from 77 to 370°K and from 300 to 1700°K. The effect of cold work on the resistivity was noted. Using thermal-conductivity data of Baker, values were calculated for the lattice and electronic thermal conductivities. These values were consistent with a Debye temperature for technetium of 411°K in comparison to the range of values of 351 to 422°K reported by Gschneider.

COLOR METALLOGRAPHY IN BLACK AND WHITE[6]

G. R. Love M. L. Picklesimer

Selective use of color, as in polarized-light examination and in anodizing for microstructural contrast by color, helps the revelation and interpretation of metallurgical microstructures. However, the economics of color reproduction for technical publications has essentially prohibited color printing, making it difficult to communicate the information readily visible in the colored microstructure. By correctly choosing monoband interference filters for the light source, one can emphasize the contrast within a colored microstructure on black and white photomicrographs. Multiple photographs of the same field in several wavelengths of illumination can then record the essence of all of the color information of the specimens in readily publishable black and white prints.

---

[3] Abstracted from paper to be submitted for publication.

[4] C. P. Bean, *Rev. Mod. Phys.* **36**, 31 (1964).

[5] Abstract of paper accepted for publication in *Journal of the Less-Common Metals.*

[6] Abstracted from paper accepted for publication in *Transactions of the Metallurgical Society of AIME.*

12. Surface Reactions of Metals

J. V. Cathcart

We are investigating the fundamental mechanisms of the oxidation and corrosion of metals and alloys. Our studies of gaseous oxidation are concerned with the investigation of stress generation during oxidation and the manner in which such stresses influence material transport across the oxide film and otherwise affect the oxidation process. For example, stresses arising during oxidation appear to manifest themselves in the creation of certain "paths of easy diffusion" in the oxide. These paths determine, to a great degree, the effectiveness of an oxide film as a barrier against further oxidation and, thus, are important factors in setting limits to the technological usefulness of a metal.

The emphasis in our program is being shifted to studies of alloy oxidation. We are attempting to apply the principles developed in our previous work on the thin-film stage of oxidation of pure copper to studies of the corresponding stage for dilute copper alloys. Similarly, some of the techniques worked out in our research on niobium and tantalum promise to be useful in studying the oxidation of refractory-metal alloys. In addition, we are investigating the corrosion mechanisms operative in aluminum and aluminum alloys in high-temperature water.

ALLOY OXIDATION

Copper-Base Alloys

J. V. Cathcart G. F. Petersen

Studies of the oxidation of single crystals of copper-base alloys containing from 0.1 to 5.0 at. % additives were undertaken in an effort to understand the influence of the alloying elements on the thin-film stage of alloy oxidation. Systems studied included Cu-Ag, Cu-Ni, and Cu-Al. Surprisingly, the valence of the added element did not have much effect on the oxidation rate. Instead, for all the alloys studied, the crystal planes that in pure copper exhibit a relatively high rate of oxidation [e.g., the (100) and (111)] oxidized considerably more slowly. On the other hand, the rate of oxidation of the (110) for the alloys increased. In general, the alloy crystals showed substantial oxidation-rate anisotropy, although not to the same extent as does pure (99.999%) copper.

The fact that the oxidation rates for some planes were reduced while those for others increased suggests that some factor other than a change in the concentration of the diffusing species in the oxide was responsible for the oxidation behavior of the alloys. For this reason, we tried to correlate the rate changes with corresponding changes in the structural details of the oxide. X-ray and electron-microscopic examination of the oxide on several copper-nickel alloys is in progress. These studies show the oxide on the alloys to be generally highly oriented, as is the case for the oxide on pure copper. For both pure copper and the alloys, the size of the mosaic blocks in the oxide was approximately 100 A. Both the mosaic spread and the average strain in the oxide lattice (measured normal to the specimen surface) also proved to be essentially the same. An important difference was noted, however, in the oxide formed on the (111) of Cu–0.4 at. % Ni. Here, the normal 1 : 1 ratio of parallel and antiparallel orientations in the oxide was altered to 1 : 2, thus reducing the area of incoherent twin boundaries in the oxide and thereby limiting the extent of paths of easy diffusion through the oxide. Similar measurements on the (100) of Cu–0.4 at. % Ni were inconclusive because the oxide was not sufficiently well oriented to permit an accurate determination of the distribution of twins in the oxide.

Preliminary indications are that the increase in oxidation rate of the (110) observed for copper-nickel alloys is associated with an increased tendency for the oxide to recrystallize to a more random orientation. Unless considerable grain growth also occurred at the same time, recrystallization of the oxide would be expected to increase the extent of grain-boundary diffusion through the oxide and thus increase the rate of oxidation of the specimen.

The results of this study indicate that a change in oxidation rate for the alloy may be correlated with a change in the extent of lattice disarray in the oxide. Thus, the data are consistent with the hypothesis that paths of easy diffusion through the oxide can have an appreciable effect on the oxidation rate of a metal.

Aluminum-Alloy Corrosion

J. V. Cathcart J. J. Campbell

The chief purpose of this research is to study the fundamental mechanisms of aluminum-alloy corrosion in high-temperature water. Specimens were tested in static distilled water at 200 to 300°C and at pressures of 170 to 500 psi. Testing times ranged from one to several hundred hours. Systems studied included binary alloys of aluminum containing Zn, Mg, Cu, Fe, Y, and Be.

Within certain concentration ranges, all additives tested greatly improved the corrosion resistance of aluminum. Characteristically, the very severe intergranular attack, so evident in the corrosion of pure aluminum, was repressed in the alloys. Exceptions to this rule sometimes occurred at high alloy concentrations. Thus, small additions of zinc improved the corrosion resistance of aluminum and repressed grain-boundary attack, whereas an Al–30% Zn specimen suffered such extensive intergranular attack that the specimen tended to disintegrate into its individual grains. Such behavior produced a marked corrosion-rate minimum as a function of zinc concentration in aluminum-zinc alloys (see Fig. 12.1). A somewhat similar behavior was noted in the aluminum-yttrium system, where the corrosion minimum occurred at approximately 2% Y.

Most aluminum binary alloys exhibit only a very limited region of solid solubility, the second phase usually appearing at concentrations considerably less than 1% at temperatures of approximately 200°C. The possibility seemed to exist that the beneficial effect of alloying agents was essentially an electrochemical one associated with the presence of the two phases in the alloy, and, therefore, an important aim of our investigation was to study the effect on the corrosion rate of the presence of a second metallic phase.

We found, however, that the observed reduction in corrosion rate of several alloys appeared to be virtually independent of whether or not the second phase was anodic or cathodic with respect to the aluminum matrix. Furthermore, we were able to check directly the effect of the appearance of the second phase in the case of the aluminum-zinc system, which is one of the few binary aluminum systems having an extensive region of solid solubility at the aluminum-rich end of the phase diagram. As indicated in Fig. 12.1, the second phase

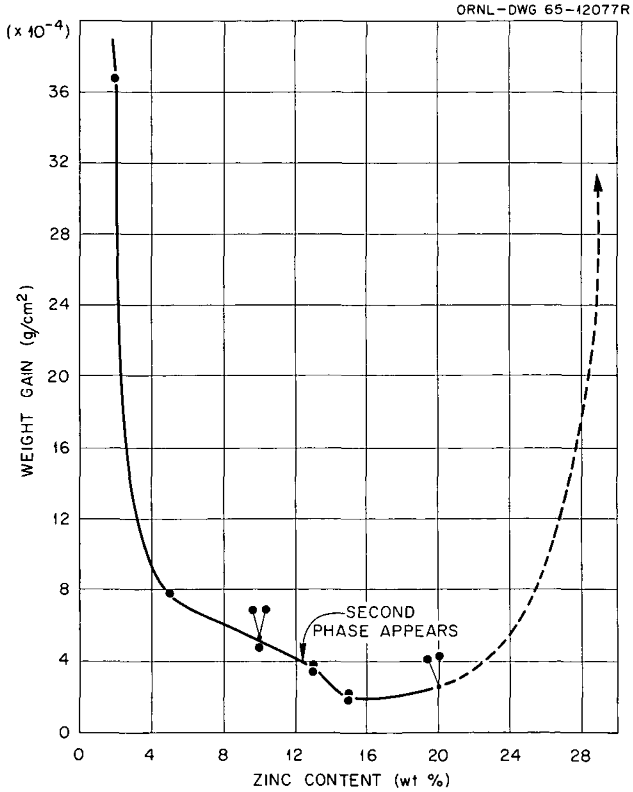

Fig. 12.1. Corrosion of Zinc-Aluminum Alloys in Distilled Water at 200°C. Weight gains are all for 6-hr tests.

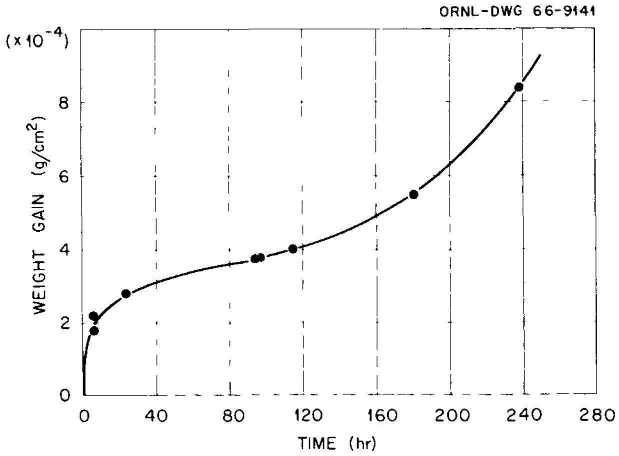

Fig. 12.2. Corrosion of Al–15% Zn in Distilled Water at 200°C.

precipitates at approximately 13% Zn. Small additional increases in zinc content reproducibly reduced the corrosion rate; however, it is evident that the greatest effect of the zinc occurred in the single-phase region.

The corrosion rate of a set of Al–15% Zn samples was determined in 200°C water. The resulting rate curve in Fig. 12.2 indicates that a breakaway corrosion behavior occurs for this alloy.

REFRACTORY-METAL OXIDATION

R. E. Pawel J. V. Cathcart

Our previous studies of the early stages of gaseous oxidation of tantalum and niobium have pointed to oxygen-solution effects with attendant stress generation in the metal as being important in determining the overall course of the reaction. We have also shown that stresses exist in the oxide products and that such stresses become dominant during the breakaway increase in the oxidation rate typical of these metals. The potentially large effect of such stresses upon oxidation mechanisms generally makes these studies important from both theoretical and technological points of view. Thus, we are continuing to examine the sources of stress during oxidation and the resulting influence on the protective nature of oxide films. In addition, the properties of thin oxide films themselves, both in place and removed from the metal, are being investigated.

Stress Measurements During the Oxidation of Tantalum and Niobium[1]

The flexure technique was used to characterize the development of stresses during the gaseous oxidation of tantalum in the temperature range 350 to 550°C and of niobium at 400 and 425°C. Bending stresses in the rectangular specimens were calculated and their presence rationalized on the basis of surface stresses due to both oxygen-solution and oxide-film effects. In the early stages of oxidation, stresses of the order of the yield stress arise in the surface layers due to the solution of oxygen into the metal. Later, as thicker oxide layers develop, film stresses substantially control the gross flexure behavior.

The Effect of Anodic Films on the Gaseous Oxidation of Tantalum[2]

The influence of anodic films up to 3000 A thick on the subsequent high-temperature oxidation characteristics of tantalum was studied. At a given temperature, the anodic films decreased the gross oxygen-consumption rate to an extent dependent upon their thickness and also delayed the onset of the breakaway increase in the oxidation rate common to this metal. The result that very thin anodic films pass comparatively large quantities of oxygen to the metal while postponing the appearance of the crystalline oxide phases permitted some oxygen-solution effects during the early stages of oxidation to be observed.

Annealing of Stripped Anodic Oxide Films

We have continued our studies of the annealing characteristics of thin anodic oxide films stripped from tantalum surfaces. The films were stripped mechanically, mounted on copper or stainless steel support screens, and annealed in vacuum at temperatures up to 1200°C. After annealing at temperatures above 800°C, the films were generally crystallized completely to β-Ta_2O_5. However, in several instances specimens annealed in the temperature range 1000 to 1100°C showed a small

---

[1] Abstract of paper accepted by *Acta Metallurgica*.

[2] Abstract of paper submitted to the *Journal of the Electrochemical Society*.

proportion of a second phase. Annealing of composite films of oxide and vapor-deposited carbon produced this phase in sufficient quantity for accurate transmission-electron-diffraction measurements. The phase was indexed as face-centered cubic with a cell constant of 4.38 A. This value suggested that the material was either TaO or TaC, indicating that the β-Ta_2O_5 was unexpectedly reduced during such treatments.

Alloy Oxide Films

The technique of separating anodically formed pentoxide films from the surface of refractory metals may prove particularly suitable for providing electron-microscope and diffraction specimens of alloy oxides. Preliminary experiments along two lines of approach have been made satisfactorily. First, alloy oxide films have been stripped from tantalum-niobium alloys without difficulty, and the as-stripped films exhibited the same general character as those formed on the pure metals. Secondly, strippable anodic films containing large quantities of impurities may be formed in concentrated electrolytes. For example, films formed on tantalum in concentrated phosphoric acid contain several percent phosphorus; other electrolytes can lead to incorporation of other elements. Both of the above methods are presently being used to produce alloy oxide specimens for further treatment and observation by electron microscopy of the phase stability and structure.

13. X-Ray Diffraction

H. L. Yakel

The ability of x-ray diffraction experiments to serve both as an adjunctive analytic tool and as a self-contained research technique is utilized in our laboratory. A relatively complete array of equipment is maintained and operated at the request of other groups to provide needed data on lattice parameters, phase identification, crystal orientation and perfection, phase transitions, and crystal structure.

Basic studies include the determination of average crystal structures of mixed oxide phases containing BeO and investigations of diffraction effects caused by lack of perfection (e.g. due to solid-solution formation, radiation damage, or precipitation) in real crystalline substances of known structure.

ROUTINE ANALYSES

O. B. Cavin R. M. Steele
L. A. Harris H. L. Yakel

More than 1100 problems that might be classified as routine were processed during the report period. Results of the analyses, where pertinent, appear in other sections of this report. Several, which by their nature are of special interest from a structural viewpoint, are described below.

The investigation of the minor phase whose appearance coincides with the embrittlement of the alloy INOR-8 suggested that its crystal structure must resemble that of the complex face-centered cubic carbides of composition M_6C. The lattice parameter of the phase is strongly dependent on the manner of sample preparation, however, and the rather strict compositional control of the alloy makes identification of the phase as a pure carbide questionable. The role of other interstitial impurities in stabilizing an M_6C-type structure may be critical.

The determination of the atom positions in $KMgCl_3$ at room temperature and at two elevated temperatures has been completed and is abstracted in Chap. 10 of this report.

In cooperation with the Crystal Physics Group, we undertook a study of the parameters delimiting the areas of stability of a scheelite-type solid solution with general formula Ln_2AMoO_8, where Ln is a lanthanide and A is a group IVA or IVB element. While the broad outline of the progress made in this program is given in Chap. 1 of this report, we may note here the absence, in the systems studied to date, of long-range ordering on the (A,Mo) atom sites and the appearance in compounds where Ln = Eu, Sm, and Nd and A = Ge of satellite diffraction maxima at the low -2θ side of reflections *hkl* with *h* or *k* nonzero. The second phase that these satellites suggest cannot be distinguished optically. The appearance of the satellites is also strongly dependent on the sample history; they are observed from as-grown crystals but vanish when the crystals are crushed.

Crystallographic data for previously unreported compounds and alloys appear in Table 13.1.

CRYSTAL STRUCTURE OF MIXED OXIDE COMPOUNDS CONTAINING BeO

L. A. Harris H. L. Yakel

Calcium Beryllate

We tried to prove that gases may be diffused into and trapped by the large isolated voids in the

Table 13.1. Crystallographic Data for New Alloys and Compounds

Composition (at. %)	Crystal System	Lattice Parameter (A)	Remarks
90 Tb–10 Y	Hexagonal	$a_0 = 3.607 \pm 0.001$ $c_0 = 5.702 \pm 0.002$	hcp[a]
75 Tb–25 Y	Hexagonal	$a_0 = 3.620 \pm 0.001$ $c_0 = 5.708 \pm 0.001$	hcp
70 Tb–30 Y	Hexagonal	$a_0 = 3.627 \pm 0.001$ $c_0 = 5.715 \pm 0.002$	hcp
30 Tb–70 Y	Hexagonal	$a_0 = 3.639 \pm 0.001$ $c_0 = 5.724 \pm 0.001$	hcp
90 Tb–10 Sc	Hexagonal	$a_0 = 3.584 \pm 0.001$ $c_0 = 5.669 \pm 0.001$	hcp
80 Tb–20 Sc	Hexagonal	$a_0 = 3.559 \pm 0.001$ $c_0 = 5.614 \pm 0.001$	hcp
71 Tb–29 Sc	Hexagonal	$a_0 = 3.518 \pm 0.001$ $c_0 = 5.580 \pm 0.001$	hcp
51 Tb–49 Sc	Hexagonal	$a_0 = 3.479 \pm 0.001$ $c_0 = 5.511 \pm 0.002$	hcp
25 Tb–75 Sc	Hexagonal	$a_0 = 3.392 \pm 0.001$ $c_0 = 5.686 \pm 0.001$	hcp
90 La–10 Tb	Hexagonal	$a_0 = 3.757 \pm 0.001$ $c_0 = 12.11 \pm 0.01$	dhcp[b]
80 La–20 Tb	Hexagonal	$a_0 = 3.736 \pm 0.001$ $c_0 = 12.02 \pm 0.01$	dhcp
VF_2	Tetragonal	$a_0 = 4.79 \pm 0.01$ $c_0 = 3.235 \pm 0.003$	Rutile-type

[a] hcp = hexagonal close-packed ABAB... sequence.

[b] dhcp = double hexagonal close-packed ABAC... sequence.

crystal structure[1] of $Ca_{12}Be_{17}O_{29}$. Samples of $Ca_{12}Be_{17}O_{29}$ weighing 100 to 350 mg were exposed to argon and to helium in a bomb apparatus at pressures near 1500 psi and at temperatures up to 500°C for periods of 24 hr. Together with untreated control samples, the test specimens were analyzed for gas content by mass spectrometry. Only the helium-treated sample gave a positive result; a significant burst of helium was observed from the test sample at about 600°C.

A complete set of Mo Kα diffraction data was collected from a $Ca_{12}Be_{17}O_{29}$ crystal and is being analyzed to further refine the atom positional and thermal parameters.

Yttrium Beryllate[2]

The crystal structure of an yttrium beryllium oxide compound has been determined by three-dimensional Patterson and difference Fourier

---

[1] L. H. Harris and H. L. Yakel, *Acta Cryst.* **20,** 295 (1966).

[2] Abstract of paper accepted for publication in *Acta Crystallographica.*

methods and refined by iterative least-squares calculations. The composition for the compound was shown to be Y_2BeO_4 as a result of the structure analysis. The unit-cell dimensions are a_0 = 3.5315 ± 0.0005 A, b_0 = 9.8989 ± 0.0010 A, and c_0 = 10.4000 ± 0.0010 A; the cell contains four formula weights of Y_2BeO_4 with an x-ray density $\rho = 4.582 \pm 0.002$ g·cm^{-3}. Within the limits of a linear least-squares refinement of x-ray data the space group is Pmcn.

The structure of Y_2BeO_4 is described as consisting of ribbons of interconnected octahedra formed from two pseudo close-packed layers of oxygen atoms between which yttrium atoms occupy octahedral interstices. The ribbons are five oxygen atoms (four octahedra) wide and extend without limit parallel to the **a** direction. The intersections of these ribbons form channels that contain beryllium atoms trigonally coordinated to oxygen atoms in a coplanar group.

Lanthanum Beryllium Oxide

Crystals of a lanthanum beryllium oxide of uncertain composition near 60 mole % BeO have been prepared and analyzed by diffraction methods. Their symmetry has been assigned as monoclinic, space group C2/c or Cc, with lattice parameters a_0 = 7.53 ± 0.01 A, b_0 = 7.35 ± 0.01 A, c_0 = 7.44 ± 0.01 A, and β = 91.5 ± 0.1°. Intensities of diffraction maxima will be measured and the structure of this phase analyzed.

SMALL-ANGLE SCATTERING EXPERIMENTS AND THEORY

Space-Charge Effects in Proportional Counters[3]

R. W. Hendricks

The space charge in a gas-filled proportional counter, resulting from the slowly moving positive ions as they drift towards the anode, significantly shifted in position and broadened the energy peak created by monoenergetic x rays. A quantitative theory for both the mean shift and the broadening was developed and confirmed experimentally.

Calculation of Weighting Functions for Collimation Corrections in Small-Angle X-Ray Scattering[4]

R. W. Hendricks P. W. Schmidt[5]

Weighting functions are used for collimation corrections in small-angle x-ray scattering to specify the range of angles passed by the collimating system for a given nominal scattering angle and also to describe the relative emphasis given to different angles within this range. A method was developed for calculating weighting functions for most collimating systems employing slits to define the x-ray beam. We found explicit forms for the slit-width and slit-length weighting functions for the Kratky Kamera[6] and for the four-slit system developed by Anderegg *et al.*[7]

On the Determination of the Metastable Miscibility Gap from Integrated Small-Angle X-Ray Scattering Data[8]

R. W. Hendricks B. S. Borie

The metastable miscibility gap is believed to control the formation of Guinier-Preston zones in quenched Al-Ag, Al-Zn, and NaCl-AgCl solid solutions. Gerold has shown that the phase boundaries of such a metastable miscibility gap may be calculated from integrated small-angle x-ray scattering data. His theory appears, at first sight, to be in disagreement with the integrated intensity calculated from the order-modulated Laue monotonic scattering based on the general result of Cowley, which indicates that the phase boundaries and the integrated intensity are unrelated.

In order to resolve the apparent discrepancy, an expression is derived for the total intensity scattered by a binary alloy which has segregated into

---

[3] Abstract of paper to be submitted for publication in *The Review of Scientific Instruments.*

[4] Abstract of paper to be submitted for publication in *Acta Physica Austriaca.*

[5] Department of Physics, University of Missouri, Columbia.

[6] O. Kratky and Z. Skala, *Z. Elektrochem.* **62,** 73 (1958).

[7] J. W. Anderegg *et al., J. Am. Chem. Soc.* **77,** 2927–37 (1955).

[8] Abstract of paper accepted for publication in *The Proceedings of the Syracuse Conference on Small-Angle X-ray Scattering,* to be published by Gordon and Breach, New York, fall 1966.

coherent zones in a uniform matrix. The two-phase model of the zones is assumed for the calculation, with the atoms in the zones and in the matrix having any degree of local order. It is found that the Cowley description of that portion of the total intensity which is sensitive to the local atomic arrangements consists of four physically distinguishable parts, two of which are often not observable in small-angle scattering experiments. On eliminating these unobservable terms from the Cowley equation, the remaining intensity is related to the composition of the metastable miscibility gap in the same manner as given by Gerold.

X-RAY MONOCHROMATORS

C. J. Sparks

Crystals are used to monochromate polychromatic sources of x rays for many applications in diffraction analysis and for the determination of a wavelength in terms of the Bragg angle in fluorescence analysis. A wider usage of monochromators in diffraction experiments has been hampered by the idea that large intensity losses invariably accompany monochromation and that the use of balanced filters or β-filtered characteristic radiation directly from the x-ray-tube source is, therefore, preferable.

This expected intensity decrease is not realized, however, if certain strongly diffracting crystals are used as monochromators. In particular, we found that hot-pressed pyrolytic graphite obtained from the Carbon Products Division of Union Carbide Corporation is an outstandingly strong diffractor of x rays from its basal planes and is thus a potentially important monochromator crystal.

We wish to know the fraction of the incident beam power P_0 that will diffract from a crystal that is set at the Bragg angle. The integrated power of the reflection may be calculated theoretically from the formula

$$\int P_a \, d\alpha = \langle P \rangle \frac{\Delta\alpha}{57.3}$$

$$= P_0 \frac{F^2 e^{-2M}}{2\mu V_a^2} \cdot K\lambda^3 \frac{(1 + \cos^2 2\theta_s)}{2 \sin 2\theta_s},$$

where $\langle P \rangle$ is the average power of the diffracted beam over the angular reflecting range of the crystal $\Delta\alpha$, V_a is the unit-cell volume, θ_s is the Bragg angle for the reflection, $K = e^4/m^2c^4$, and the other terms have their usual significance. For the 00.2 reflection of Cu Kα radiation from graphite, neglecting extinction one can calculate that $\langle P \rangle / P_0 \cong 0.47/\Delta\alpha$, where $\Delta\alpha$ is given in degrees and the divergence of the incident x-ray beam is comparable to the mosaic spread ($\Delta\alpha$) of the crystal.

The ratio $\langle P \rangle / P_0$ cannot, of course, exceed unity, but if $\Delta\alpha$ is about 0.5° or less, we could hope to approach a condition for which virtually no intensity is lost when highly oriented graphite is used as a monochromator. In practice, secondary extinction reduces the ratio to about $\frac{1}{3}$ for the most highly oriented graphite available ($\Delta\alpha$ = 0.55°). But use of curved monochromators, such as that described by Warren,[9] would permit a larger solid angle of radiation from the tube target to be intercepted by the monochromator. This would, in turn, provide more useful intensity at the experimental sample (at the monochromator focus) than is now available in the diverging beams directly from the x-ray-tube target.

We showed both experimentally and theoretically that pyrolytic graphite diffracts about five times more strongly in its basal reflection than does the most widely used monochromator crystal, mosaic LiF in its 200 reflection. In Fig. 13.1 we plot

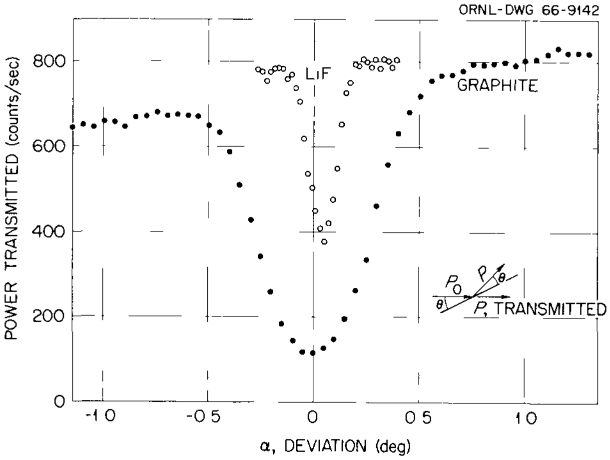

Fig. 13.1. Transmitted Power Through LiF and Pyrolytic Graphite Crystals as a Function of the Deviation, α, from the Bragg Angle.

---

[9] B. E. Warren, *J. Appl. Phys.* **25**, 814 (1954).

the power transmitted *through* a crystal of LiF and one of pyrolytic graphite as a function of angular rotation about the Bragg angle θ. These data emphasize the very strong reflecting power of both crystals by the large decreases in transmitted power at the Bragg position caused by the diffraction of a large part of the incident beam.

Because graphite contains imperfections on a small scale compared to the large mosaic blocks in bent LiF, the distribution of intensity in the monochromated beam is more uniform. This is also a desirable feature for many diffraction applications.

Part II.

High-Temperature Materials Program

page blank

14. High-Temperature Materials Development

W. O. Harms

This program centers on materials problems associated with high-temperature high-performance reactors for advanced propulsive and power applications, especially for space devices. Particular emphasis is placed on those problems stemming from systems that use alkali metals as thermodynamic working fluids and heat-transfer media in refractory-metal systems.

The effort is broadly based and includes such specific topics as (1) fabrication studies and procurement of refractory alloys; (2) development and evaluation of procedures for joining advanced refractory alloys; (3) assessment of the physical metallurgical behavior of advanced refractory alloys in terms of recrystallization, grain growth, interstitial contamination, aging response, and strengthening mechanisms; (4) determination and evaluation of long-time creep-rupture properties of advanced refractory alloys; (5) compatibility studies in alkali-metal–refractory-alloy systems, including engineering-scale forced-circulation loops; (6) application of nondestructive testing techniques to refractory-alloy mill products and fabricated components; and (7) measurement of key thermophysical properties of refractory metals and alloys.

In the text that follows, frequent reference is made to commercial refractory-metal alloys by their trade designations. The nominal compositions of these alloys are listed in Table 14.1.

Table 14.1. Compositions of Refractory-Metal Alloys

Designation	Base	Alloying Elements (wt %)
B-66	Niobium	5 Mo, 5 V, 1 Zr
C-129Y	Niobium	10 Hf, 10 W, 0.1 Y
Cb-752	Niobium	10 W, 2.5 Zr
Cb-753	Niobium	5 V, 1.25 Zr
D-43	Niobium	10 W, 1 Zr, 0.1 C
FS-85	Niobium	27 Ta, 10 W, 1 Zr
T-111	Tantalum	8 W, 2 Hf
T-222	Tantalum	9.6 W, 2.4 Hf, 0.01 C
TZM	Molybdenum	0.5 Ti, 0.08 Zr, 0.02 C
TZC	Molybdenum	1.2 Ti, 0.25 Zr, 0.15 C

FABRICATION DEVELOPMENT

C. F. Leitten

Our objectives are to develop fabrication techniques directed primarily toward the production of refractory-metal tubing; to provide special alloys that cannot be procured commercially because of cost, quantity involved, or general unavailability; and to procure from commercial sources those well-developed refractory alloys required for the program.

Fabrication development concentrates on devising new or improved techniques for the manufacture of refractory-alloy tubing. Also, facilities must be maintained and updated to keep pace with the support service required for numerous other facets of the program.

Extrusion of Refractory Alloys

R. E. McDonald G. A. Reimann

The ORNL 1250-ton press was modified for extrusion of refractory alloys. The press, billet heater, and redesigned tooling have functioned

Table 14.2. Conditions and Results of Tungsten and Tungsten-Alloy Extrusions[a]

Extrusion	Billet Dimensions (in.)		Billet Weight (lb)	Extrusion Conditions						Tube Shell Dimensions (in.)	
	Outside Diameter	Inside Diameter		Temperature (°C)	Reduction Ratio[b]	Force (tons) Maximum	Force (tons) Minimum	Speed (in./sec)	Extrusion Index, K (psi)	Outside Diameter	Inside Diameter
									$\times 10^3$		
Unalloyed Tungsten Billets											
1631	2.981	Solid	23.1	1760	5.4	695	685	5.0	111.7	1.321	
1632	2.985	Solid	22.8	1760	5.8	680	530	4.5	104.9	1.278	
1636	2.982	Solid	22.1	1760	5.6	530	520	3.8	83.0	1.306	
0003	2.990	0.875	20.3	1750	6.4	700	*c*	*c*	*c*	*c*	*c*
0004	2.992	0.875	20.2	1750	6.4	690	665	0.7	100.0	1.410	*d*
0031	2.985	0.875	14.9	1770	4.0	550	465	1.0	90.0	1.707	0.735
W–2% Mo Billets											
1633[e]	2.985	Solid	23.3	1870	5.7	575	560	4.0	89.1	1.285	
1634[e]	2.981	Solid	23.2	1870	4.4	460	440	5.0	83.8	1.470	
1635[e]	2.986	Solid	23.6	1870	4.4	475	445	4.5	82.9	1.475	
W–25 at. % Re Billets											
1559[f]	2.950	Solid	15.0	2150	5.5	530	520	4.0	85.7	1.913 × 0.920[f]	
1560[f]	2.939	Solid	17.8	2200	5.3	550	475	10.5	89.0	1.915 × 0.930[f]	
1592[e]	2.876	1.000	17.2	2100	4.9	550	510	9.5	95.1	1.639	0.978
1593[e]	2.831	1.000	17.4	2250	4.8	530	495	10.3	97.3	1.653	0.981
W–30 at. % Re–30 at. % Mo Billets											
0034	2.990	1.063	17.6	2200	4.0	695	*c,d*	0.6	*c,d*	1.693	*c,d*
Molybdenum-Clad Tungsten Duplex Billets											
1637	2.987	0.815	14.8	1650	8.8	435	425	5.5	57.4	1.252	0.774
0037[c]	2.985	0.747	14.2	1900	8.8	505	395	1.1	63.0	1.257	0.740

---

[a] Billets prepared by powder-metallurgy technique except as noted.

[b] Based on ratio of cross-sectional areas of billet container and extrusion.

[c] Incomplete extrusion.

[d] Mandrel failed.

[e] Arc-cast billets.

[f] Sheet bar extrusions.

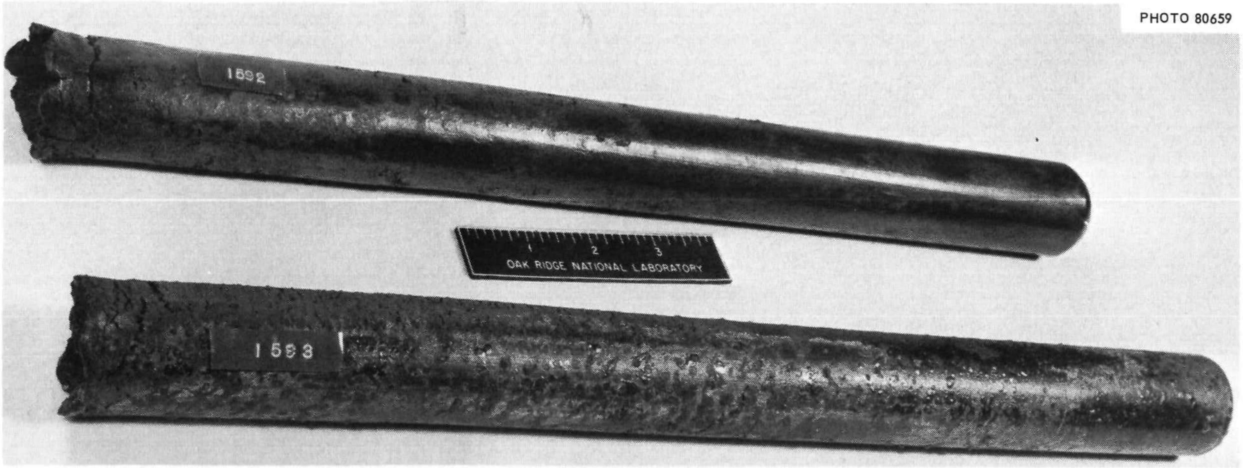

Fig. 14.1. Extruded Tube Shells of W–25 at. % Re. Billets were heated to 2100°C (1592) and 2250°C (1593) and extruded at ratios of 4.9 and 4.8. Lubrication was provided by the oxidation of a 10-mil layer of thermochemically deposited tungsten.

satisfactorily.[1] Tungsten and tungsten-alloy billets are extruded by the floating-mandrel technique to produce tube shells for subsequent processing into large- and small-diameter thin-walled tubing.

Extrusion data for tungsten and tungsten-alloy billets are summarized in Table 14.2. The base-metal oxide lubrication technique was used in all cases. In this technique the volatile tungsten oxide (molybdenum oxide in the case of the duplex billet), formed during transfer of the billet in air from the billet furnace to the container, serves as an adequate lubricant during extrusion.

The oxide formed on the W–25 at. % Re alloy billets did not provide satisfactory lubrication.[2] Thus, for this alloy and for the ternary W-Re-Mo alloy, a layer of unalloyed tungsten was thermochemically deposited on each billet surface prior to extrusion, and the surface was then finish-ground to a uniform 10-mil thickness. The large amount of oxide generated by the tungsten deposit provided satisfactory lubrication for these billets. The two W–25 at. % Re shells extruded in this manner are shown in Fig. 14.1. Note the generally good surface quality with only minor cracking. The application of thermochemically deposited coatings to refractory-metal billets is a significant development in extrusion lubrication, since niobium- and tantalum-base billets may be similarly coated, giving sufficient oxide-forming tungsten to protect the base metal from oxidation during heating as well as to provide a lubricating film during extrusion.[1]

The development of the duplex billet was another significant accomplishment. The billet design and a partially assembled billet are shown in Fig. 14.2. This approach to obtaining thin-walled tungsten tubing was required because the cross sections of the as-extruded tube shells, as shown in Fig. 14.1, were too heavy for drawing except by high-capacity drawbenches. Existing drawbench technology would not permit sufficient heating to perform initial drawing on as-extruded sections without danger of breakage. By jacketing sections of as-extruded tube shells with molybdenum and extruding the resulting duplex billet over a floating mandrel, thin-walled tungsten tubing can be produced with minimal change in internal diameter. After extrusion the molybdenum jacket is leached from the thin-walled tungsten tube, and the tube can then be finish-drawn to final size. The as-extruded section from the duplex billet is shown in Fig. 14.3 alongside the thin-walled tungsten tube from

---

[1] W. O. Harms (compiler), "A Summary of Progress by Metals and Ceramics Division, Oak Ridge National Laboratory," to be published in *Proceedings of Tungsten and Tungsten Alloy Tubing Development Meeting, May 26, 1966, AEC, Germantown, Md.*

[2] R. E. McDonald and G. A. Reimann, *Metals and Ceramics Div. Ann. Progr. Rept. June 30, 1965*, ORNL-3870, pp. 102–4.

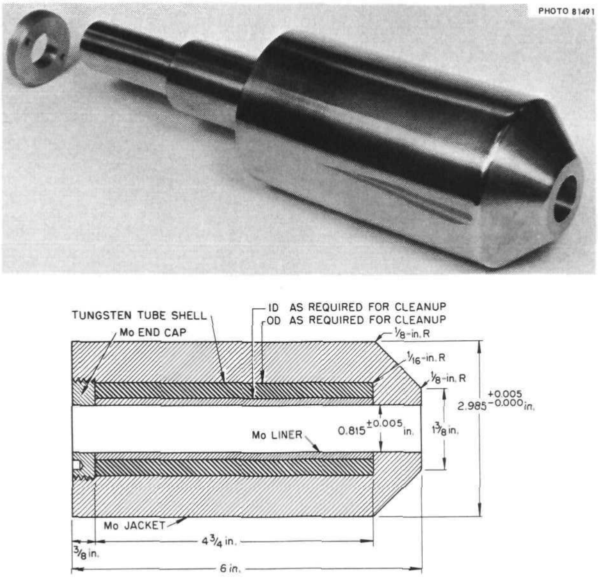

Fig. 14.2. Duplex Billet for Producing Thin-Walled Tungsten Tubing by Reextrusion over a Floating Mandrel.

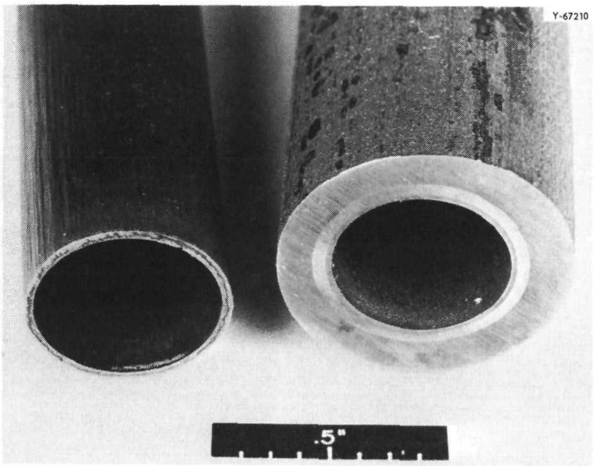

Fig. 14.3. As-Extruded Cross Section from Duplex Billet (*Right*) and *Portion of Thin-Walled Tungsten Tubing* from Same Extrusion After Dissolution of Molybdenum Covering (Left).

which the molybdenum covering had been dissolved. A second duplex billet, similar to those just described except that the inner molybdenum sleeve was omitted, was also extruded. The tungsten tube shell was deformed directly against the mandrel, improving the tubing surfaces and producing a wrought microstructure.[1]

Service Activity

R. E. McDonald

In addition to the extrusion mentioned above, a substantial amount of service work was performed. It included press-forging of Nb–1% Zr and D-43 domed end caps at room temperature; swaging of tungsten, molybdenum, and tantalum alloy rods; rolling of molybdenum, tantalum, and niobium alloy sheet; and drawing of T-111 and D-43 tubing. The service activity also included monitoring and expediting all subcontracted refractory-metal machining for the program.

JOINING OF REFRACTORY MATERIALS

G. M. Slaughter

Welding of Advanced Refractory Alloys

R. G. Donnelly

We are continuing to investigate the weldability of advanced refractory alloys and the effects of aging on the properties of weldments involving these alloys. An additional niobium-base alloy (FS-85) and an additional tantalum-base alloy (T-222) were included in our studies on 0.5-in.-thick plates. Two promising sheet alloys (Cb-752 and Cb-753) have also been evaluated for general weldability and propensity toward embrittling aging reactions.

The plate welds were evaluated by radiographic, fluorescent-penetrant, and metallographic techniques as well as by chemical analysis for interstitial impurities. Sound welds with no porosity or cracks were made in each of these alloys. The properties of the weldments were determined by room-temperature testing of side-bend specimens and by transverse tensile tests at elevated temperatures. The bend specimens were bent around a 2*T* radius, where *T* is the thickness of the specimen. The T-222 specimens exhibited almost no ductility at room temperature; the angle of bend sustained was essentially 0°. The FS-85 welds, however, sustained bends of 20 and 45° before fracture. A 2-hr anneal at 1315°C improved the ductility of both alloys; the annealed FS-85 survived a full 105° bend and the T-222 failed at 45°

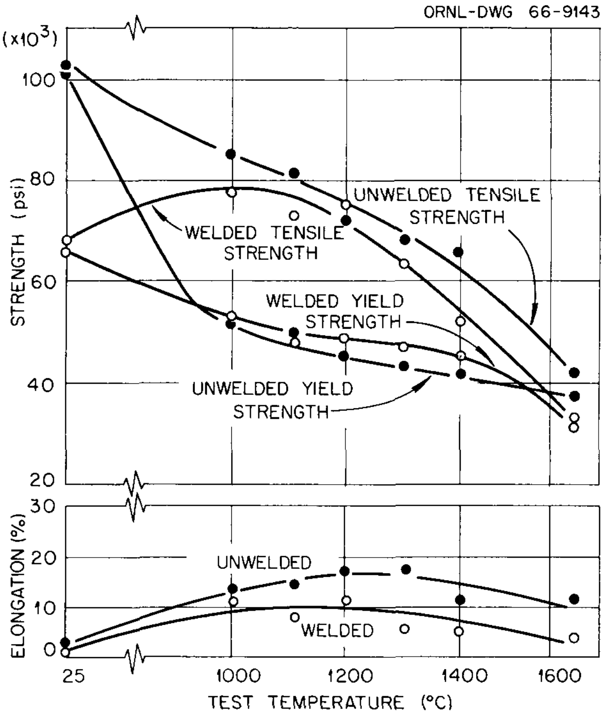

Fig. 14.4. Results of Transverse Tensile Tests on T-222 Plate.

The results of transverse tensile tests on specimens from T-222 plate along with unwelded specimen data are presented in Fig. 14.4. Although the welded specimen exhibited relatively low strength at room temperature, the strength properties at higher temperatures were quite comparable to those of the unwelded material. In general, the ductilities exhibited by both welded and unwelded specimens were low, particularly at room temperature.

Only welded specimens of the FS-85 alloy were tested. Unlike T-222, this alloy exhibited good room-temperature strength and ductility in the welded condition as well as better ductility throughout the testing range. As expected, T-222 was about 50% stronger than FS-85 in the high-temperature range. Tensile failures in FS-85 generally occurred in the base metal or heat-affected zone, while the T-222 specimens always failed in the weld metal, even though chemical analysis showed no contamination of the weld metal by interstitials. This is the same pattern of failure noted previously[3] for other niobium- and tantalum-base alloys.

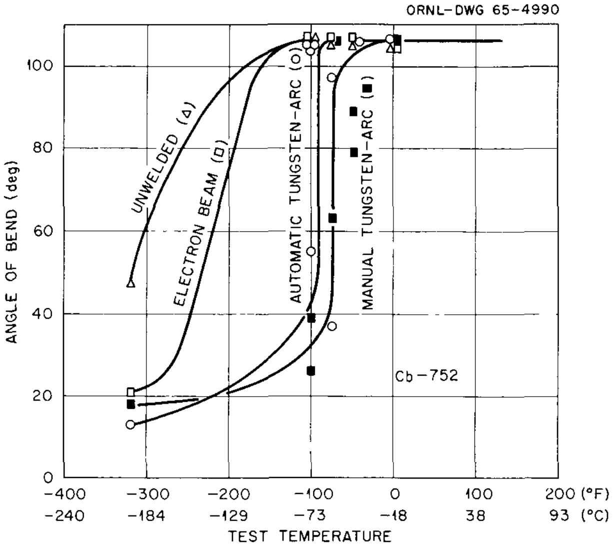

Fig. 14.5. Ductile-to-Brittle Transition Temperature Curves for Cb-752 Alloy Sheet Weld Specimens.

For sheet welds of Cb-752 and Cb-753, we determined the ductile-to-brittle transition temperatures in bending at room temperature. The results of 4*T* bend tests on 0.030-in.-thick Cb-752 specimens welded by the electron-beam and gas tungsten-arc techniques are shown in Fig. 14.5; data for unwelded specimens are included for comparison. The general effects exhibited by these alloys are similar to those observed for other refractory alloys evaluated in this series; that is, the transition temperatures were raised somewhat by electron-beam welding but much more by the gas tungsten-arc techniques. On an absolute basis, the results for the Cb-752 alloy welds were very similar to those obtained previously[4] on FS-85 specimens, and the Cb-753 compared closely with C-129Y. Both C-129Y and Cb-753 have the lowest ductile-to-brittle transition temperatures of any of the niobium-base alloys investigated.

The effects of aging on the longitudinal bend ductility of welded Cb-752 and Cb-753 were also determined, and the results for Cb-752 are plotted in Fig. 14.6. These results show the now typical behavior of niobium alloy welds, that is, embrittlement and subsequent overaging. Although both alloys exhibit the same type of reaction, the temperature range over which these reactions take place differs. In fact, while the Cb-752 alloy does

---

[3] R. G. Donnelly, *Metals and Ceramics Div. Ann. Progr. Rept. June 30, 1965*, ORNL-3870, pp. 108–9.

[4] R. G. Donnelly, *Metals and Ceramics Div. Ann. Progr. Rept. June 30, 1964*, ORNL-3670, pp.77–79.

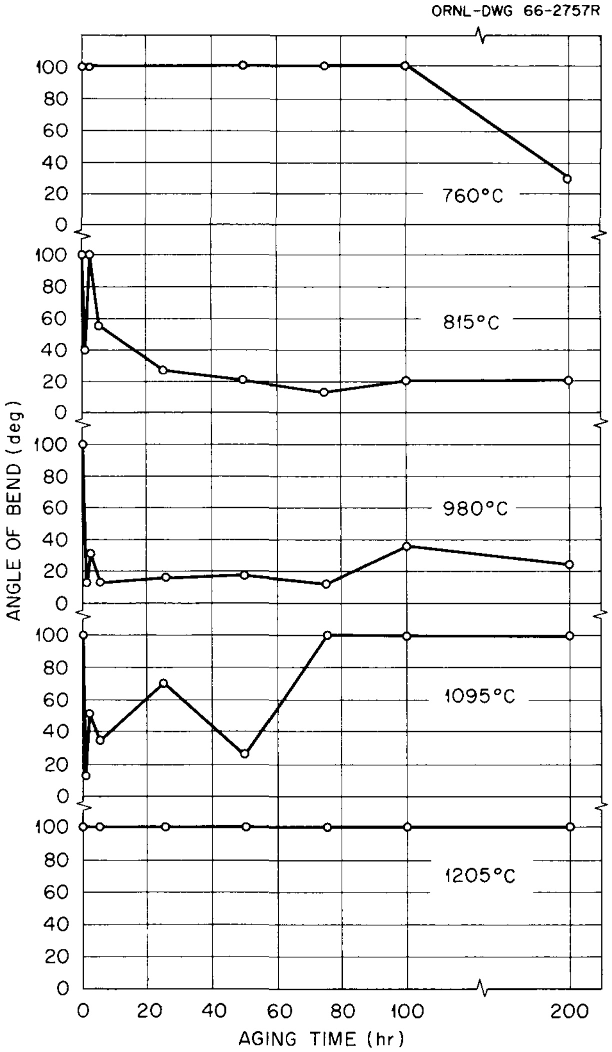

Fig. 14.6. Results of Room-Temperature Bend Tests on Cb-752 Welds Aged at Various Temperatures.

not overage until 1095°C for the times investigated, the Cb-753 alloy overages at 815°C. Thus far, the Cb-753 has exhibited weld-metal aging to a lower degree than any of the alloys investigated. A possible explanation of this is found in the vanadium content, since diffusion and diffusion-controlled reactions can occur at lower temperatures by the addition of vanadium to niobium.[5,6]

Brazing Alloy Development

D. A. Canonico

The development of brazing alloys for joining ceramics as well as refractory metals has been emphasized. The brazing temperatures of interest have included lower temperatures (about 1300°C) as well as those previously reported[7] for higher temperature requirements.

Several ternary alloy systems have been investigated, and the specific compositions selected for further study were, for the most part, concentrated in the vertical ternary section originating at liquidus minima in binary alloy systems (such as titanium-zirconium or titanium-vanadium) and arbitrarily selected 50-50 compositions in the titanium-tantalum and titanium-niobium systems. The third element was added in all instances to depress the melting temperature. For those systems studied, Table 14.3 lists the minimum melting temperature, the type of system that produced that minimum (eutectic or liquidus minimum), and the approximate composition at which the minimum values occurred.

Melting-point determinations conducted on tantalum coupons provided information pertaining to the wettability (on a refractory metal) of several ternary and quaternary experimental brazing alloys. Tests using inverted T-sections were completed on a number of these alloys; those alloys that exhibited adequate wetting were subjected to a bend test (the vertical leg of the T was bent 90°) to determine the ability of the brazement to withstand deformation. Table 14.4 lists the alloys that satisfied the flowability test and the results of the bend tests on joints made on them.

The brazing of Al_2O_3 has constituted an important part of this study. Electron microprobe investigations on ceramic–braze-metal interfaces were initiated in an attempt to determine which metals are most beneficial to wetting. On a molybdenum-to-aluminum oxide joint brazed with the 48% Ti–48% Zr–4% Be alloy previously developed,[8] a definite reaction zone can be seen in Fig. 14.7. The reaction zone varied in aluminum content from essentially none on the braze side to about 11% on the Al_2O_3 side and in molybdenum

---

[5] C. S. Hartley, J. E. Steedly, Jr., and L. D. Parsons, *Binary Interdiffusion in Body-Centered Cubic Transition Metal Systems*, ML-TDR-64-316 (December 1964).

[6] H. E. McCoy, Jr., *An Evaluation of the Creep Properties of Cb-753 and a Comparison of This Alloy with Several Other Niobium-Base Alloys*, ORNL-TM-1347 (January 1966); *Am. Soc. Metals Trans. Quart.* **59**, 277–87 (1966).

[7] R. G. Gilliland, *Metals and Ceramics Div. Ann. Progr. Rept. June 30, 1965*, ORNL-3870, pp. 110–11.

[8] C. W. Fox, R. G. Gilliland, and G. M. Slaughter, *Welding J.* **42**, 535-s–40-s (1963).

Table 14.3. Approximate Composition and Temperatures of Eutectics or Liquidus Minima in Experimental Ternary Brazing Alloys

Approximate Composition (wt %)					Type of System	Approximate Melting Temperature (°C)
Ti	Zr	V	Nb	Other		
44	44			12 Ta	Liquidus minimum	1550
48.5	48.5			3 Si	Eutectic	1220
42.5	42.5		15		Liquidus minimum	1450
45	45			10 Ge	Eutectic	1250
39	39			22 Cr	Eutectic	1020
49.3	49.3			1.4 B	Eutectic	1200
64		26	10		Liquidus minimum	1560
68		27		5 Mo	Liquidus minimum	1530
54		21		25 Cr	Eutectic	1375
47				47 Ta 6 Si	Eutectic	1520
46.5			46.5	7 Si	Eutectic	1475

Table 14.4. Results of Brazing Studies with Experimental Alloys

Composition (wt %)					Brazing Temperature (°C)	Approximate Melting Temperature of Alloy (°C)	Results of Room-Temperature Bend Test[a]
Ti	Zr	Mo	Al	Other			
49	49			2 Si	1400	1260	Passed
46	46			8 Ge	1400	1250	Passed
35	35			30 Cr	1300	1060	Passed
49	49			2 B	1500	1250–1350	Passed
30	15	15		40 Cr	1900	<1500	Failed
48	37 5	7.5	7		1600	1450	Passed
50	40	8	2		1600	1450	Failed
50	40	2	8		1600	1450	Failed
50	40	9	1		1600	1450	Failed

[a] A brazement passed the test if the vertical leg could undergo a 90° bend without fracture.

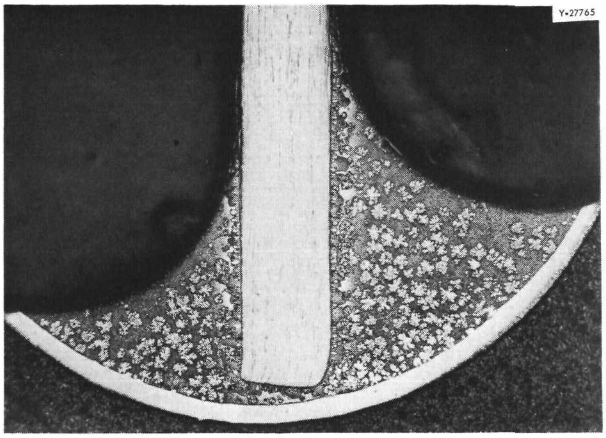

Fig. 14.7. **Molybdenum-to-Aluminum Oxide Brazed Joint.** Vertical member, molybdenum; brazing alloy, 48% Ti–48% Zr–4% Be; base material, aluminum oxide. A reaction zone between the brazing alloy and ceramic is evident. Etchant: concd NH_4OH + 30% H_2O_2. 60×. Reduced 52%.

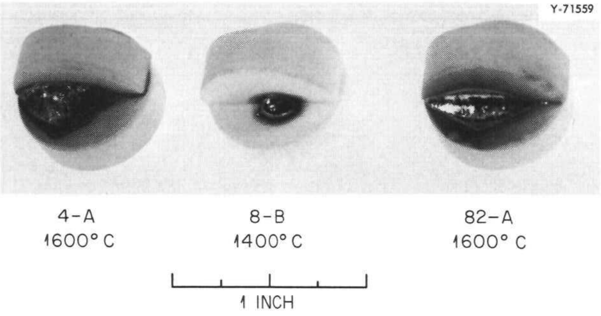

Fig. 14.8. **Experimental Brazements of Al_2O_3 to Al_2O_3.**

content from 11% on the braze side to none on the Al_2O_3 side. The zirconium and titanium contents were essentially constant across the zone, at approximately 38 and 45% respectively.

Figure 14.8 shows the results of additional investigations. Alloys 4-A (45% Ti–45% Zr–10% Ta) and 82-A (48% Ti–37.5% Zr–7.5% Mo–7% Al) successfully wet and brazed a ceramic composite, while alloy 8-B (46% Ti–46% Zr–8% Ge) did not.

Field Welding of Refractory Alloys

E. A. Franco-Ferreira

A field welding apparatus was successfully developed and used for welding of refractory-metal pumped forced-circulation loops into their test stands. The apparatus is shown in Fig. 14.9. In Fig. 14.9*a* the tubing to be welded passes vertically through the 1½-in.-ID glass cross, the welding torch is in the right leg, and the evacuation line is attached to the ball valve on the left leg. The entire assembly is rotated around the tubing to be welded by a tachometer-controlled direct-current motor through a flexible shaft and roller-chain drive. Welding current is supplied through the slip ring at the bottom of the cross.

Figure 14.9*b* shows the apparatus in position during pumpdown prior to the first field weld. This weld joined the boiler leg of the loop to the pump cell. The other two joints to be welded are covered with rubber tubing and are at the right of the welding device in the photograph. Before the glass was broken, the welds were radiographically inspected in case an additional pass was required. The first weld had to be cut out and rewelded due to excessive push-through. The reweld was successful. The other two welds were successfully made with no problem.

Electron-Beam Brazing of a Tantalum Pump Cell

R. G. Donnelly

The Lewis Research Center of NASA asked us for assistance in brazing a tantalum pump cell for liquid-metal studies. An extensive search by NASA of both industrial and government facilities and experience failed to produce a competent source that would undertake the work.

Although tantalum-base alloys T-222 or T-111 were selected originally as the materials of construction, difficulties were encountered by NASA in obtaining high-quality tubing. Consequently, pure tantalum was substituted. The cell consisted of a helical coil of eight turns of 0.25-in.-diam by 0.015-in.-wall tubing. The turns of the coil were to be brazed together to form a solid cylinder, and a Ta–10% W ring was to be brazed to each end. Two Ta–10% W shorting bars also were to be joined to the tube leads.

The brazing alloy 35% Ta–35% V–30% Ti was selected from our previous work because of its good brazing characteristics, its low tendency to erode tantalum, and its adequately high melting point (1650°C). At the maximum operating temperature of 1100°C, brazing alloys of this general

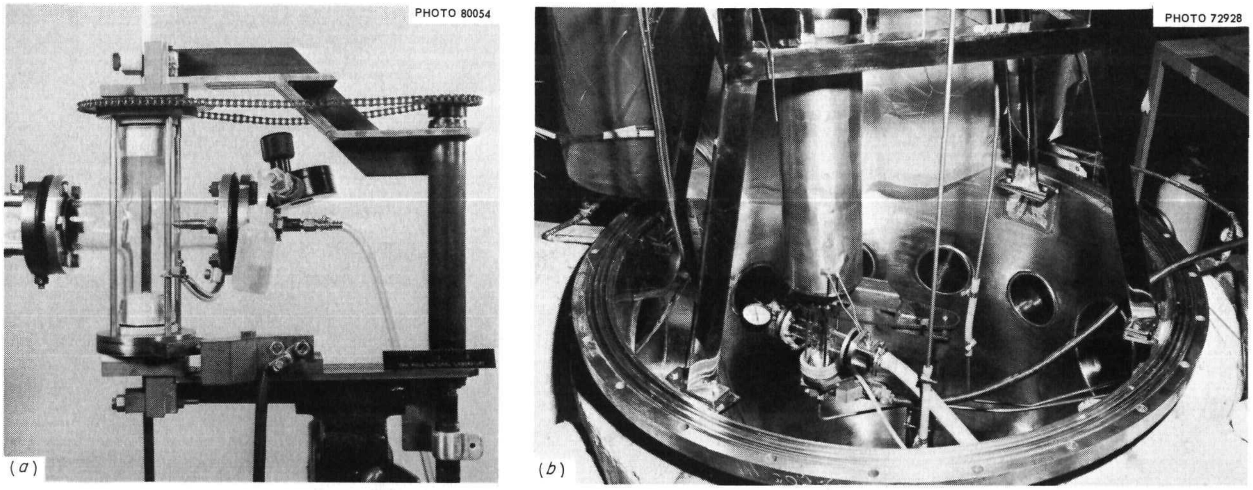

Fig. 14.9. Demountable Rotating Field Welding Apparatus for Joining Refractory-Alloy Tubes. (*a*) Closeup in the laboratory. (*b*) In position for weld on Nb–1% Zr tubes in a boiling potassium loop.

type possess shear strengths of approximately 20,000 psi.

The initial plan was to vacuum braze the assembly in a furnace heated with tantalum or tungsten elements, but this posed very difficult alloy preplacement problems. Electron-beam brazing was selected as a more practical approach, and feasibility experiments verified its suitability. To braze a joint, alloy wire was placed on it and then fused in place with a defocused beam while the coil was slowly rotated. This procedure was repeated until all joints were brazed. Close control over the heat input was necessary because of the thin wall of the tubing and was easily maintained in the tube-to-tube joint. However, where the tubes were to be joined to the relatively heavy end plates, control was somewhat more difficult. By preferentially centering the beam on the heavier member, this joint was also successfully completed.

The amount of heat used was deliberately kept to a minimum to limit solution of the tantalum. Consequently, the alloy did not flow completely through the joint and fillet on the other side. Since only electrical conductivity and slight mechanical rigidity were necessary (and not leak-tightness between the tubes), the technique was quite satisfactory. The assembly is shown in Fig. 14.10. This coil was shipped to NASA Lewis Research Center for installation in their pump loop.

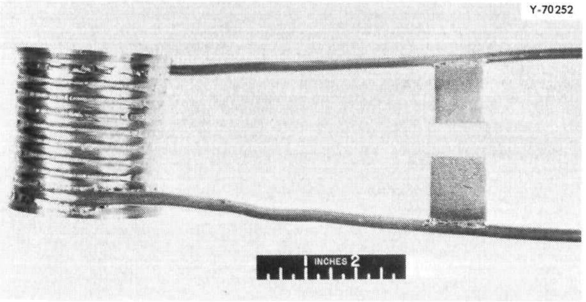

Fig. 14.10. Tantalum Coil After Electron-Beam Brazing.

PHYSICAL METALLURGY OF HIGH-TEMPERATURE ALLOYS

H. Inouye

Vaporization of Haynes Alloy No. 25 to 1150°C

D. T. Bourgette

The evaporation behavior of Haynes alloy No. 25 (Co–20% Cr–15% W–10% N–3% Fe–1% Si–1% Mn) was investigated at 870, 930, 980, 1040, 1090, and 1150°C over a pressure range of 6×10^{-10} to 5×10^{-7} torr. The evaporation rates at constant temperature decreased with time, as shown in Fig. 14.11, but were independent of pressure in the range investigated. This behavior suggests that the surfaces of the specimens were quickly

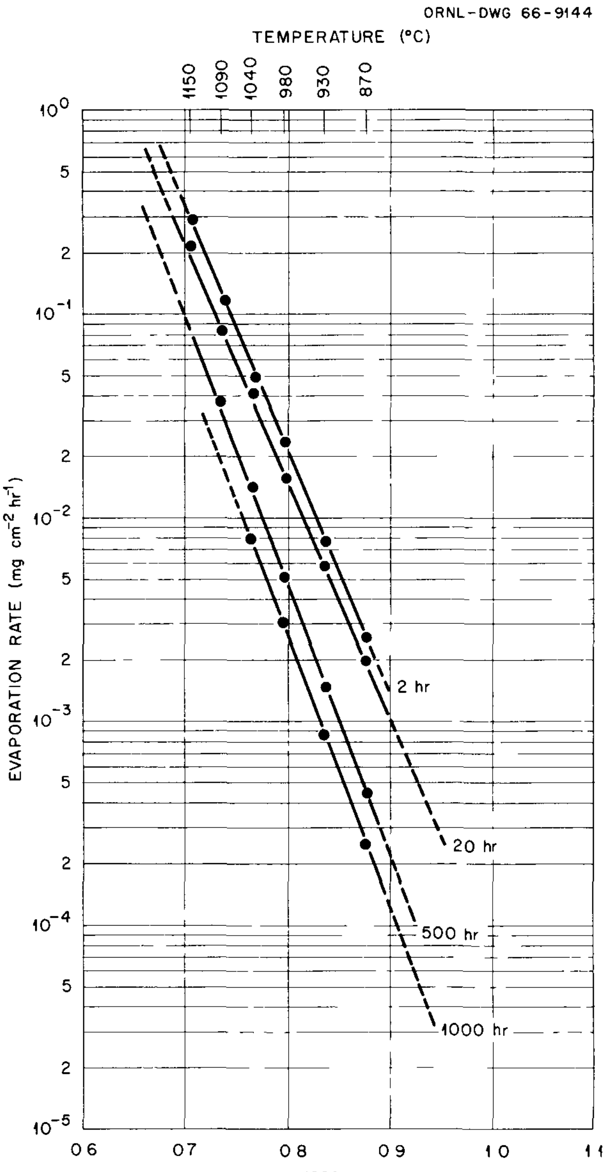

Fig. 14.11. Variation of the Evaporation Rate of Haynes Alloy No. 25 with Temperature and Time.

depleted of the more volatile elements and their further loss became diffusion-rate dependent. The parallel lines of this plot indicate that little change occurs in the evaporation mechanism with changes in the surface concentrations of the more volatile elements.

Electron probe microanalysis showed that the more volatile elements Cr, Mn, Fe, Ni, and Si were selectively evaporated from the alloy surfaces. In addition, surface roughening, void formation, and microstructural variations occurred as illustrated in Fig. 14.12. The loss of Cr, Mn, Fe, and Ni increased the tungsten concentration at the specimen surfaces and resulted in the formation of the Laves phase $(Co, Ni)_2W$. Normally this phase does not exist in this alloy above 900°C. In Fig. 14.12, the surface structure in (*a*), (*b*), and (*c*) and the honeycomb structure in (*d*), (*e*), and (*f*) were identified as the Laves phase.

This investigation has been completed and a final report will be issued.[9]

Aging Behavior in T-111

D. T. Bourgette

In this investigation, we are concerned with the influence of heat treatment and carbon content on the room-temperature tensile properties of T-111. Sheet specimens of commercial T-111 containing 70 ppm carbon were solution annealed at temperatures of 1700 to 2000°C and subsequently aged at 900 to 1400°C for times to 1600 hr. In addition, specimens of T-111 doped with carbon to levels of 190, 340, and 570 ppm were similarly heat treated. All heat treatments were conducted in high vacuum.

The results of room-temperature tensile tests showed that maximum strength is obtained after a 1-hr anneal in the temperature range 1700 to 1850°C followed by a rapid quench. Annealing above 1850°C resulted in excessive grain growth and a corresponding deterioration of mechanical properties. The loss of mechanical strength due to aging treatments at 1100, 1260, and 1400°C for extended times is illustrated in Fig. 14.13 as a function of carbon content. Aging treatments up to 200 hr at 1100°C also resulted in some loss of mechanical strength at room temperature, as illustrated in Table 14.5. This behavior was also typical for aging temperatures of 900, 1260, and 1400°C.

Overaging also occurred in specimens that were slowly cooled from solution-annealing temperatures of 1700 to 1900°C. Because of this behavior and the fact that duplex heat treating in the range of 900 to 1400°C always resulted in overaging at the

---

[9] D. T. Bourgette, *Vaporization of Haynes Alloy No. 25 to 1150°C*, report in preparation.

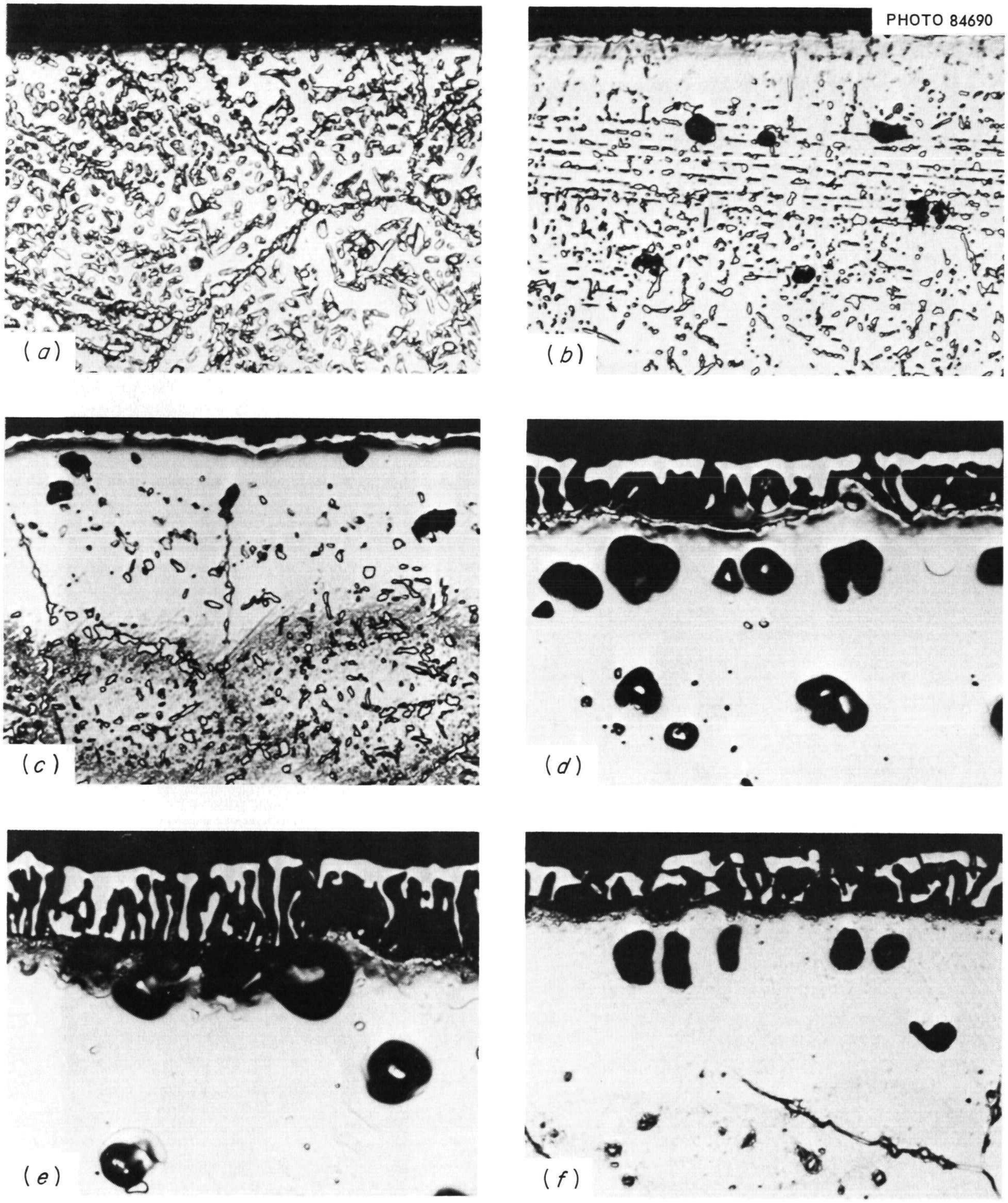

Fig. 14.12. Haynes Alloy No. 25 After Evaporation Tests in High Vacuum for the Indicated Times and Temperatures. 500×. (*a*) 1182 hr, 870°C, weight loss 0.707 mg/cm^2. (*b*) 2181 hr, 930°C, 3.51 mg/cm^2. (*c*) 2158 hr, 980°C, 8.72 mg/cm^2. (*d*) 2672 hr, 1040°C, 21.89 mg/cm^2. (*e*) 644 hr, 1090°C, 27.10 mg/cm^2. (*f*) 164 hr, 1150°C, 23.46 mg/cm^2.

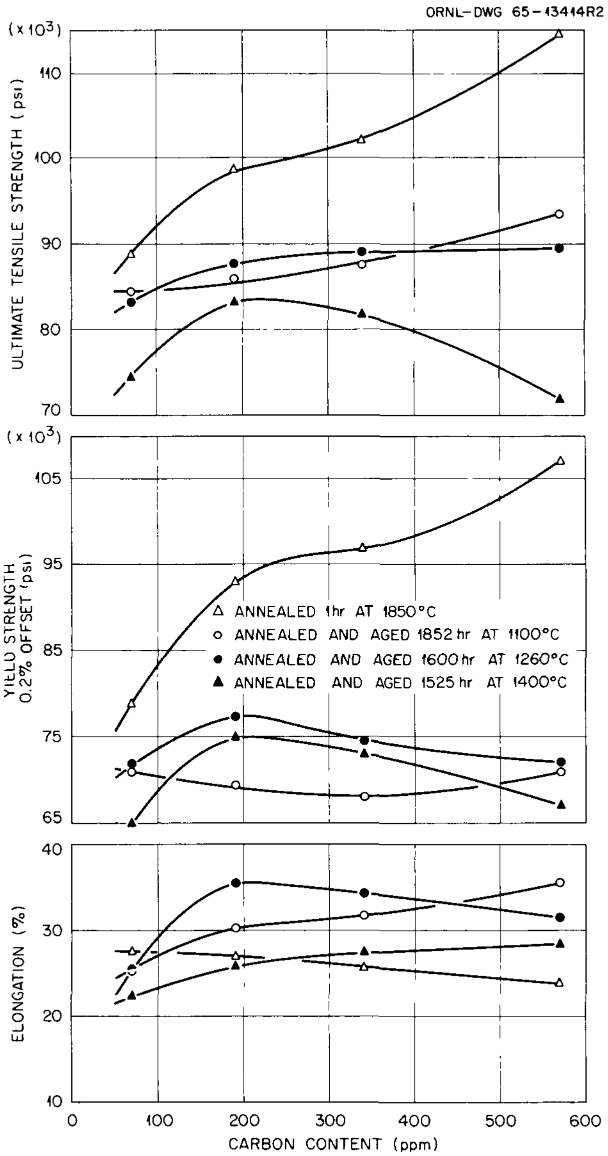

Fig. 14.13. Room-Temperature Tensile Properties of T-111 Doped to Four Different Carbon Levels, Solution Annealed at 1850°C for 1 hr, Quenched in Silicone Oil at −70°C, and Aged as Indicated.

carbon levels investigated, we conclude that T-111 ages on fast cooling from the solutioning temperature, although the effects of the aging reaction are not serious. We further conclude that submicroscopic precipitates formed on dislocations during quenching, thus decreasing the number of dislocations participating in the deformation process. Since the precipitates were too small to be observed optically, the material would appear as a single phase, as was the case for the solution-annealed T-111.

Gas-Metal Equilibria in the System N_2/Nb–1% Zr

H. Inouye

We have continued our studies to elucidate the role of the interstitials oxygen, carbon, and nitrogen on the physical metallurgy of refractory metals. To this end we have developed a highly sensitive ultrahigh-vacuum technique to measure the reaction kinetics and equilibria in gas-metal systems.[10,11]

In the Nb-Zr-N system we have determined that 1% Zr lowers the partial pressure of nitrogen over niobium by a factor as high as 40; or, for a given nitrogen pressure, the amount of nitrogen in solution at equilibrium is higher by a factor of 4 in the alloy than in the unalloyed niobium.

The solubility limit of nitrogen in the alloy is in excess of 278 ppm, and the solid solutions obey Sieverts' law. We determined that ΔH for the reaction $\frac{1}{2}N_2 \rightleftharpoons N$ (dissolved) depended on the temperature, the nitrogen content of the alloy, and the presence or absence of oxidizing gases in the test apparatus. Based on these observations and the effect of zirconium noted above, we tentatively concluded that the oxygen solubility in the alloy was increased by the dissolved nitrogen. At 1400°C the oxygen solubility appears to be about 70 ppm when the nitrogen content of the alloy is less than 100 ppm.

MECHANICAL PROPERTIES OF REFRACTORY ALLOYS

J. R. Weir, Jr.

Creep-Rupture Properties of Refractory Alloys

R. L. Stephenson

Our objective is to provide creep-rupture data to 1000 hr for meaningful comparison of the properties of promising refractory alloys. As previously

---

[10] H. Inouye, *Equilibrium Solid Solutions of Nitrogen in Cb–1% Zr Between 1200–1800°C*, ORNL-TM-1355 (February 1966).

[11] H. Inouye, *Metals and Ceramics Div. Ann. Progr. Rept. June 30, 1965*, ORNL-3870, pp. 112–16.

Table 14.5. Room-Temperature Tensile Properties of Commercial T-111, Solution Annealed at 1850°C for 1 hr, Quenched, and Aged at 1100°C

Aging Time (hr)	Strength (psi)		Elongation (%)
	Ultimate Tensile	Yield, 0.2% Offset	
0	88,800	78,000	25.5
0.50	86,800	74,200	25.4
1	86,300	73,100	25.9
5	86,900	73,700	26.4
10	86,000	75,100	26.9
25	85,700	75,600	24.6
50	84,300	72,000	25.1
100	84,100	67,600	27.3
200	85,100	71,000	25.2

reported,[12] significant improvements in the short-time creep-rupture properties of FS-85 and Cb-752 can be produced by pretest annealing at elevated temperatures. We have demonstrated that these improvements are stable for at least 1000 hr, as shown in Figs. 14.14 and 14.15.

We have concerned ourselves with the effect of fabrication variables on the creep-rupture properties of molybdenum-base alloys. Stress-relieved and recrystallized TZM, fabricated according to current mill practice, was tested to provide reference data. A portion of the same heat was recrystallized at 1540°C, and some was warm worked 50%. The 1000-hr rupture stresses of material in these three conditions are compared in Fig. 14.16. Additional work is in progress on TZM along with work on niobium-modified TZM and TZC.

Behavior of Refractory Alloys Under Dynamic Loads

R. W. Swindeman

An understanding of material behavior under dynamic loads is essential to minimize the risk of premature failure of nuclear reactor components at stress levels lower than those defined in terms of constant load conditions. In spite of the vast work on fatigue, very few data are available for refractory metals and alloys at high temperatures. Accordingly, we have initiated a program to provide such information.

The program is in the equipment development phase. One machine is operational, and testing is under way to evaluate its performance and to incorporate modifications that may be necessary to optimize vacuum, temperature, and mechanical performance. The testing chamber is shown in Fig. 14.17. The rod-type specimen with a $\frac{1}{2}$-in. gage length is mounted in heavy T-111 grips and is centered within a tungsten mesh furnace capable of temperatures of 2000°C. The vacuum system is capable of less than 5×10^{-7} torr at room temperature and achieves less than 2×10^{-6} torr after a few hours at 1100°C. The loading system consists of a 10,000-lb hydraulic actuator and servo-controller designed for alternating stress work and is capable of operating from near static conditions to 10 cps.

While developing a suitable grip design, we have limited our maximum temperature to 1100°C. Some typical data obtained on D-43 during this phase of the program are given in Table 14.6.

---

[12] R. L. Stephenson, *Metals and Ceramics Div. Ann. Progr. Rept. June 30, 1965*, ORNL-3870, p. 123.

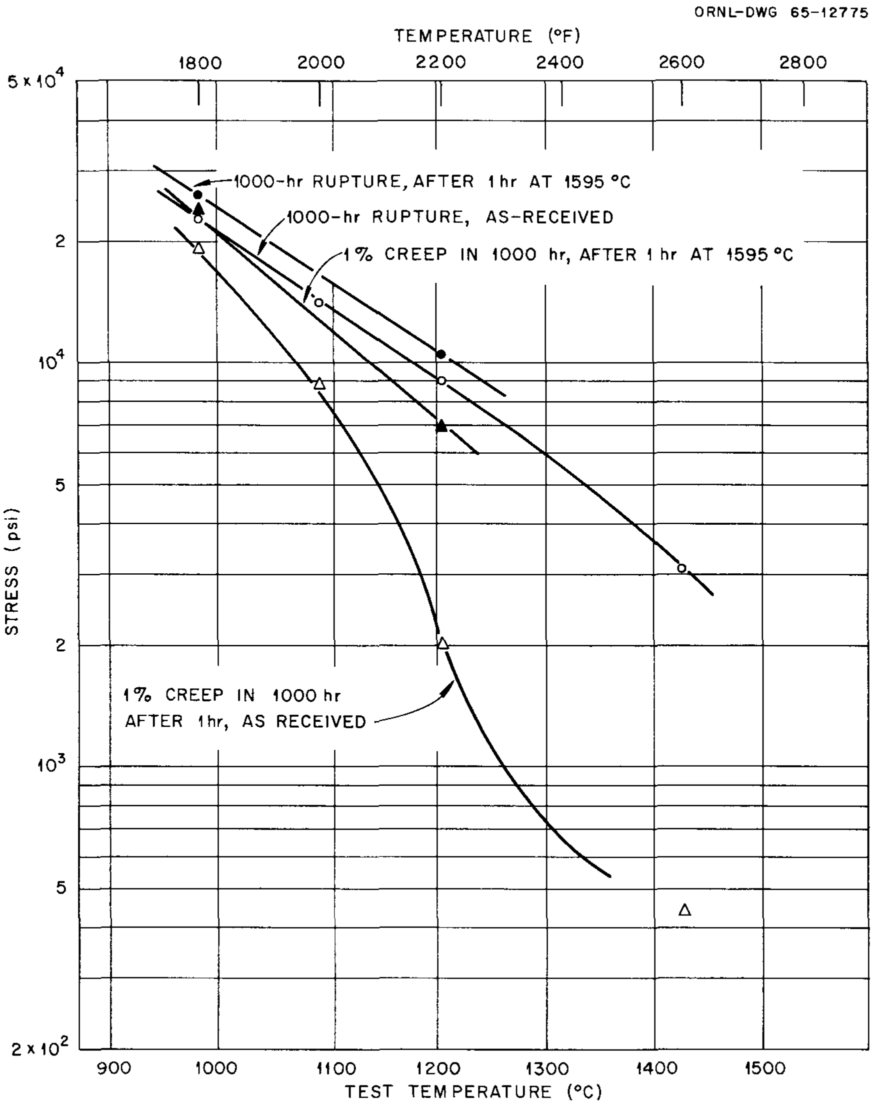

Fig. 14.14. Effect of Pretest Annealing on Long-Time Creep Properties of FS-85.

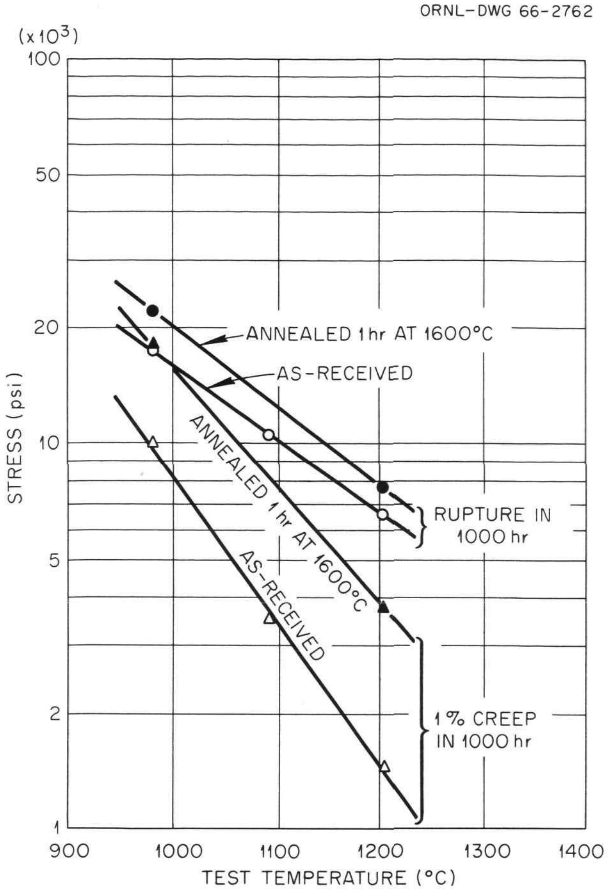

Fig. 14.15. Effect of Pretest Annealing on Creep-Rupture Properties of Cb-752.

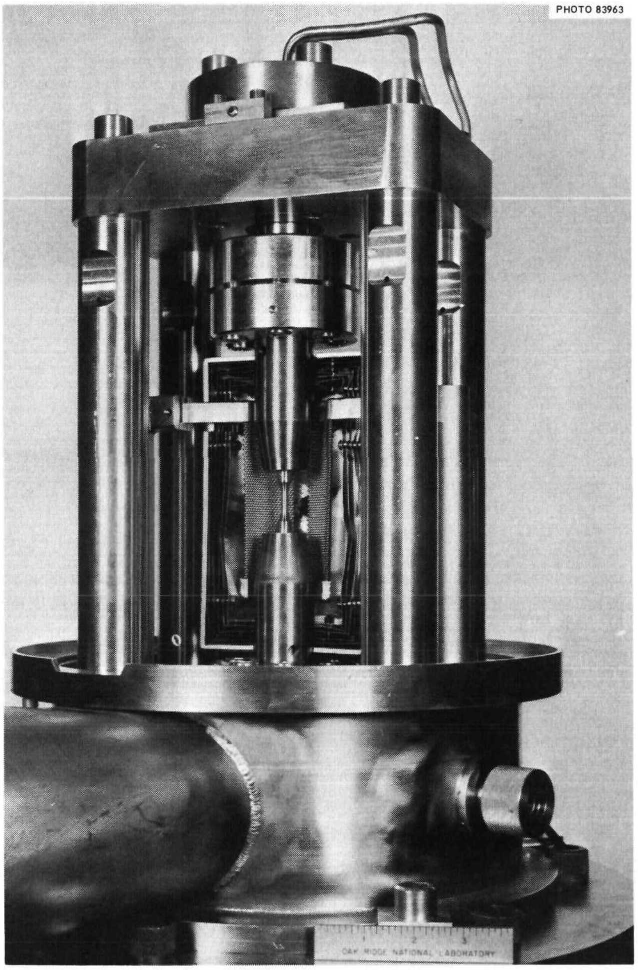

Fig. 14.17. Refractory Alloy Specimen Mounted in the Testing Chamber of High-Temperature Fatigue-Testing Apparatus.

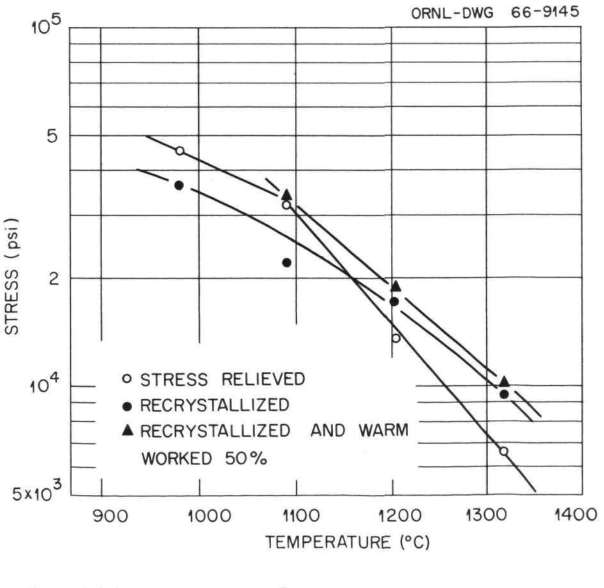

Fig. 14.16. Stress to Rupture TZM Alloy in 1000 hr at Various Temperatures.

Table 14.6. Low-Cycle Fatigue Data for D-43[a]

Temperature (°C)	Stress Range[b] (psi)	Cycles to Failure
Room	145,000	1195
870	76,500	3635
980	73,200	2750

[a] Based on tests at 1 cps and triangular extension-time patterns. Plastic strain range 0.96%.

[b] Values listed are twice the stress amplitude.

COMPATIBILITY OF ALKALI METALS WITH STRUCTURAL MATERIALS

J. H. DeVan

Compatibility of Boiling Alkali Metals with Refractory Alloys

J. R. DiStefano D. H. Jansen
B. Fleischer

Auxiliary electrical or ion-propulsion requirements for space vehicles necessitate power plants of high efficiency that will operate at high temperatures. Systems consisting of a nuclear reactor and a Rankine-cycle turbine generator have been proposed in which an alkali metal would be used to cool the reactor, power the turbine, and lubricate the turbine, generator, and pump.[13] Above 1000°C refractory metals and alloys are being considered for use as structural materials, nozzles, turbine blades, and fuel-element cladding. To evaluate the compatibility of these metals with boiling alkali metals, a three-phase corrosion program involving refluxing capsules, natural-circulation loops, and forced-circulation loops has been undertaken.[14] Tests are being conducted at 1100 to 1400°C with durations ranging from 100 to 5000 hr. Materials under investigation include Nb–1% Zr, D-43, C-129Y, FS-85, T-111, TZM, and tungsten.

Each refluxing capsule contains machined and weighed insert specimens in the condenser section to provide quantitative data on the rate of dissolutive attack. Natural-circulation loops contain similar inserts in the liquid region below the condenser as well as in the condenser. Pumped loops have test sections designed to provide data on the corrosion-erosion resistance of potential nozzle and turbine blade materials.

Table 14.7 summarizes the conditions and results of the tests that have been operated during the past year. A total of 38,500 hr has been accumulated in refluxing capsule tests with very little evidence of dissolutive attack. Weight changes on insert specimens have largely reflected the pickup or migration of oxygen in the system. Traces of zirconium dioxide have been found in the boiler section of some Nb–1% Zr capsules and could be indicative of zirconium mass transfer; however, results are inconclusive thus far.

Results from natural-circulation loop tests have been in good agreement with results from refluxing capsule tests. Metallographic examinations of boiler and condenser sections revealed negligible dissolutive attack, and weight changes of condenser and subcooler inserts have generally correlated with changes in oxygen concentration.

A forced-circulation boiling-potassium loop (FCL-6) was fabricated of Nb–1% Zr to test the erosion characteristics of TZM nozzle and blade specimens against potassium vapor. The loop is scheduled for 3000 hr and is currently operating at a maximum temperature of 1100°C. A similar loop (FCL-8) using D-43 as the basic containment alloy is presently under construction and will be used to test D-43 nozzle and blade specimens at 1200°C.

Corrosion of Refractory Alloys by Lithium

C. E. Sessions

The mass transfer rates of refractory metals in high-temperature lithium have been under study in thermal-convection loops.[15,16] Alloy compositions tested to date include Nb–1% Zr, D-43, FS-85, and TZM. Loop operating conditions are summarized in Table 14.8.

Mass transfer rates in these systems were determined by weight-change measurements of 58 insert specimens placed end-to-end around each loop. Specimens at the same temperature experienced the same weight change irrespective of whether they were in the hot or cold leg. Accordingly, the concentration changes that occurred in the lithium on moving through the loop appeared to be small relative to the total concentration driving force for corrosion. Subsequent mass balance calculations showed the total change in solute concentration around the loop to be on the order of a few parts per billion. Deposition rate constants derived from these studies were notably higher than solution

---

[13] A. P. Fraas, *Nucleonics* **22**(1), 72 (1964).

[14] J. H. DeVan, J. R. DiStefano, and D. H. Jansen, *Metals and Ceramics Div. Ann. Progr. Rept. June 30, 1965*, ORNL-3870, pp. 124–29.

[15] J. H. DeVan and C. E. Sessions, *Trans. Am. Nucl. Soc.* **8**(2), 394–95 (1965).

[16] C. E. Sessions and J. H. DeVan, *Metals and Ceramics Div. Ann. Progr. Rept. June 30, 1965*, ORNL-3870, pp. 129–31.

Table 14.7. Summary of Boiling Alkali Metals–Structural Materials Compatibility Tests

Material		Fluid	Temperature (°C)		Test Duration (hr)	Condensing Rate (g min^{-1} cm^{-2})	Weight Change (mg/cm^2)	Results
Insert Specimen	Container		Boiler	Condenser				
				Refluxing Capsules				
Nb–1% Zr	Nb–1% Zr	Na	1230	1190	5000	0.18	+0.1 to +1.3	No evidence of penetration by sodium. Oxygen pickup in both capsule and inserts.
Nb–1% Zr	Nb–1% Zr	Rb	1280	1265	1800	0.60	−0.1 to +0.2	No evidence of penetration. Oxygen pickup less than in sodium.
Nb–1% Zr	Nb–1% Zr	Cs	1220	1190	5000	0.65	+0.02 to +0.3	Same as above.
Nb–1% Zr	Nb–1% Zr	K	1190	1170	5000	0.35		Examination in progress.
C-129Y	C-129Y	K	1325	1250	560	0.36		Test in progress.
W	W	K	1315	1240	1000	0.33		Test in progress.
				Natural-Circulation Loops				
T-111	T-111	K	1250		3000	0.47	−0.4 to +2.5	No attack. C and O pickup by loop material.
TZM	D-43	K	1320		3000	0.35	+0.3	No attack. O pickup in loop material in areas of decarburization.
FS-85	FS-85	K	1320			0.26		Test in progress.
TZM	TZM	K	Under construction					
				Forced-Circulation Loops				
TZM	Nb–1% Zr	K	1200			165 g/min		Test in progress.
D-43	D-43	K	1300		Under construction			

Table 14.8. Operating Conditions for 3000-hr Thermal-Convection Loop Tests on Refractory Alloys in Lithium

Loop	Alloy		Temperature (°C)		Lithium Flow Rate (fpm)
	Loop Tubing	Inserts	Maximum Hot Leg	Minimum Cold Leg	
TCL-1R	Nb–1% Zr	Nb–1% Zr	1190	1080	10.6
TCL-2R	Nb–1% Zr	Nb–1% Zr and TZM	1210	1060	7.5
TCL-3R	D-43	D-43	1200	1030	7.5
TCL-4R[a]	FS-85	FS-85	1220	~980	~4.5
TCL-5R[b]	Nb–1% Zr	Nb–1% Zr	1315	1115	4.8

[a] Terminated after 502 hr by leak in expansion tank.

[b] Test loop currently operating.

rate constants. This was concluded because no more than one-third as much loop surface underwent deposition as underwent dissolution.

Niobium-base alloys showed a consistent loss of oxygen during exposure to lithium at 1050 to 1200°C. Chemical analyses also showed a tendency for zirconium and nitrogen to migrate from high- to low-temperature loop regions. A dissimilar-alloy loop system (Nb–1% Zr/TZM) also showed a migration of unlike alloying constituents.

NONDESTRUCTIVE EVALUATION OF REFRACTORY ALLOYS

R. W. McClung K. V. Cook

We have nondestructively evaluated tubing, sheet, and plate of several refractory alloys, including Nb–1% Zr, FS-85, D-43, W–26% Re, TZM, T-111, and T-222. The specific techniques employed were selected according to the materials and their configurations. Fluorescent penetrants were used to evaluate the outer surfaces of the alloys, and very few significant discontinuities were detected by this procedure. At least one ultrasonic technique was used for the detection of internal flaws, and in some instances radiography and eddy currents were also applied.

A large portion of our work was devoted to the preparation of appropriate reference standards and subsequent evaluation of materials under study. For the ultrasonic evaluation of sheet, plate, bar, and tubing, we have found that electrical discharge machining yields the most accurate and reproducible reference notches, as reported in Part III, Chap. 21 of this report.

Brief feasibility studies[17] were made on eddy-current, ultrasonic, and x-ray techniques for the measurement of thickness of TCD tungsten deposited on the inner surface of copper tubes. The x-ray approach was selected for further development because it seemed to offer the quickest solution. A through-transmission x-ray attenuation technique was used in which the radiation detector was placed in the bore of the tube. The x rays were attenuated principally by the tungsten as they passed through the duplex wall. Calibration curves for attenuation vs tungsten thickness were established using thin foils of tungsten and copper.

PHYSICAL PROPERTIES

D. L. McElroy

This phase of the program is concerned with the measurement and correlation of high-temperature thermophysical properties of refractory materials.

---

[17] W. O. Harms (compiler), "A Summary of Progress by Metals and Ceramics Division, Oak Ridge National Laboratory," to be published in *Proceedings of Tungsten and Tungsten Alloy Tubing Development Meeting, May 26, 1966, AEC, Germantown, Md.*

Table 14.9. Physical Properties of Niobium-, Tantalum-, and Tungsten-Base Alloys as a Function of Temperature

Temperature (°C)	Thermal Conductivity (w cm^{-1} $°C^{-1}$)			Total Hemispherical Emittance
	Nb–10% W	T-111	W–26% Re[a]	W–26% Re
0			0.310	
100	0.4844	0.420	0.359	0.26
200	0.5099	0.446	0.402	0.28
300	0.5307	0.469	0.440	0.30
400	0.5468	0.487	0.473	0.32
500	0.5625	0.500	0.501	0.35
600	0.5782		0.525	0.37
700	0.5920		0.548	
800	0.6062		0.569	
900	0.6175		0.588	
1000	0.6264		0.605	
1100			0.621	
1200			0.634	
1300			0.648	0.52[b]
1400			0.660	
1500			0.671	

[a] Estimated values.

[b] Based on linear extrapolation.

An understanding of the behavior of these materials is sought from property measurements including thermal conductivity λ, electrical resistivity ρ, Seebeck coefficient S, specific heat C_p, and total hemispherical emittance E_t.

Physical Properties of D-43 and T-111

J. P. Moore R. S. Graves

The radial heat flow apparatus was used to measure λ between 50 and 1000°C of Nb–10% W alloy, which is quite similar to D-43. Smoothed λ values for this alloy are given in Table 14.9 and are precise to ±0.5% and accurate to ±1.5%. Results on T-111 completed to 450°C are included in this table and are being extended to 1000°C. The T-111 assembly includes a special disk of the Nb–10% W alloy to allow measurements of ρ and S in the radial heat flow apparatus. This apparatus has worked satisfactorily thus far. Tests are in progress that will allow a statement of precision and accuracy for the T-111 values obtained on a limited supply of material. An analysis, given in Part I, Chap. 8 of this report, of the λ and ρ data on the Nb–10% W alloy indicated that the Lorenz number L is 2.584×10^{-8} $(v/°C)^2$, whereas for T-111 L is 2.436×10^{-8} $(v/°C)^2$.

Physical Properties of W–26% Re

J. P. Moore T. G. Kollie
W. Fulkerson

Thermal conductivity was measured on a sample of W–26% Re over the temperature range 20 to

140°C. These low-temperature results were used with ρ values obtained to 1500°C in an auxiliary experiment to estimate the values of λ from 0 to 1500°C given in Table 14.9. This analysis indicated L to be 2.695×10^{-8} $(\mathrm{v}/{}^\circ\mathrm{C})^2$. Values of E_t measured on a tube of W–26% Re to 650°C are also given in Table 14.9. A linear extrapolation of these measurements yielded a value of 0.52 for E_t at 1300°C. This high value is indicative of the surface roughness of the tube used.

Thermocouple Calibrations

W. Fulkerson

Two Mo/W–26% Re thermocouples were calibrated against a W–5% Re/W–26% Re thermocouple to 1400°C, and excellent agreement was obtained with values calculated from integrated absolute Seebeck coefficient results. This agreement was sufficiently good that the calculated values were used to extrapolate the measured curve to 2100°C by the following equation:

$$E = 2.010 + 1.752 \times 10^{-2}t - 5.329 \times 10^{-6}(t - 1100)^2 ,$$

where E is the thermal emf in millivolts and t is temperature in °C and ranges from 1100 to 2100°C. This particular thermocouple adhered better to specimens exposed to rapid thermal cycling than did other high-temperature thermocouples.

Thermal Conductivity of Refractory Compounds

J. P. Moore R. S. Graves

The longitudinal heat flow apparatus (Part I, Chap. 8) was used to complete λ measurements on control specimens for a series of irradiation experiments. The results on unirradiated MgO are presented in Chap. 8. The results on Y_2O_3 and Al_2O_3 are given in Table 14.10. These results are in agreement with literature values for these materials.

Measurements on refractory metal carbides NbC, TaC, TiC, ZrC, and WC, which had been prepared by explosion pressing, hot pressing, and slip casting, could not be correlated with the preparation procedure. The λ values for these carbides appear to be related to the metal involved in the sense that if the λ of the metal increases with temperature, then so does the carbide. For these carbides the electronic portion of λ is dominated by the lattice portion. A more detailed specimen characterization will be required for these measurements to be considered significant.

Table 14.10. Thermal Conductivity of Y_2O_3 and Al_2O_3

Temperature (°C)	Thermal Conductivity (w cm^{-1} °C^{-1})	
	Y_2O_3	Al_2O_3
30	0.126	0.341
75	0.107	0.285
120	0.092	0.243

15. Materials Compatibility

J. H. DeVan

Studies of the effects of impurities in alkali metal–refractory metal systems have continued. We are presently investigating the mechanism of the corrosion processes in the Nb-O-K and (Nb–1% Zr)-O-K systems. Concurrently, we are studying new methods for the determination of oxygen and its removal from alkali metals as an aid to the corrosion studies and to the use of engineering systems employing alkali metals.

EFFECT OF OXYGEN IN THE NIOBIUM-POTASSIUM SYSTEM

A. P. Litman

Previously we reported on the behavior of unalloyed niobium in static liquid potassium at temperatures up to 815°C when oxygen was present in the system.[1–3] These studies revealed that oxygen rapidly migrated out of the niobium at rates controlled by solid-state diffusion[4] to form complex corrosion products. To determine if a similar mechanism holds at higher temperatures, we conducted analogous tests at 1000 and 1250°C.

Oxygen-doped niobium specimens heated in potassium for various times at 1000 and 1250°C lost oxygen as shown in Table 15.1. Oxygen appeared to reach a steady-state level after 1 hr at 1250°C and after 5 hr at 1000°C. At both temperatures the specimen weight losses were about twice the weight of the oxygen lost, indicating a substantial uptake of niobium by the potassium. At 1000°C, a hardness gradient was induced in the niobium in 1 hr but disappeared by 2 hr; at 1250°C any hardness gradient had disappeared even after the shortest exposure. These data are in agreement with previous studies at lower temperature, which indicated that migration of oxygen is controlled by solid-state diffusion.

Table 15.1. Loss of Oxygen from Niobium at High Temperatures

Temperature (°C)	Oxygen Content (ppm) for Various Exposures						
	0 hr	0.5 hr	1 hr	2 hr	5 hr	16 hr	100 hr
1000	2600		500	250	150	160	140
1250	3300	230	190		180	170	180

---

[1] A. P. Litman, *Metals and Ceramics Div. Ann. Progr. Rept. June 30, 1965*, ORNL-3870, pp. 136–38.

[2] A. P. Litman, *The Effect of Oxygen on the Corrosion of Niobium by Liquid Potassium*, ORNL-3751 (July 1965).

[3] A. P. Litman, "Interactions in the Niobium-Oxygen-Potassium System," presented at AEC-NASA Liquid Metals Information Meeting, Gatlinburg, Tenn., Apr. 21–23, 1965; CONF-65041 (in press).

[4] A. P. Litman, *Phys. Status Solidi* 11, K47–48 (1965).

COMPATIBILITY IN THE Nb-Zr-O-K SYSTEM AT 815°C

A. P. Litman

Substitutional alloying additions, especially stable oxide formers such as zirconium and hafnium, are important in modifying the refractory metal–alkali metal corrosion process. Our investigations of the behavior of Nb-Zr-O alloys in lithium[5] have shown that effects of oxygen on corrosion are minimized if oxygen in the alloy is converted to stable ZrO_2 by heat treatment before exposure to lithium. To examine the effect in potassium, two groups of Nb–0.86% Zr alloy specimens were heated for 100 hr at 815°C in potassium containing approximately 1500 ppm dissolved oxygen. The specimens were exposed in Nb–1.05% Zr capsules containing 170 ppm oxygen.

Those specimens containing an oxygen-to-zirconium atom ratio less than 2 (2100 ppm O) gained weight, and chemical analysis showed that the weight change was due to oxygen uptake. Specimens with an oxygen-to-zirconium ratio greater than 2 (4400 ppm O) lost weight as a result of oxygen depletion. A pretest 1200°C heat treatment given to some of the specimens had no effect on oxygen exchange. A dark tightly adherent scale less than 0.001 in. thick partially covered all specimens after test, and electron diffraction analysis tentatively identified the scale as NbO_2.

Chemical analysis of the Nb–1% Zr containers used in these experiments revealed a significant increase in oxygen in the zone of the capsules exposed to liquid. Hardness measurements given in Fig. 15.1 showed the oxygen to be restricted to the innermost 0.010-in. layer of the capsule wall. Interaction with the capsule and, in some cases, the specimens reduced the oxygen level of the potassium from 1500 ppm to less than 50 ppm.

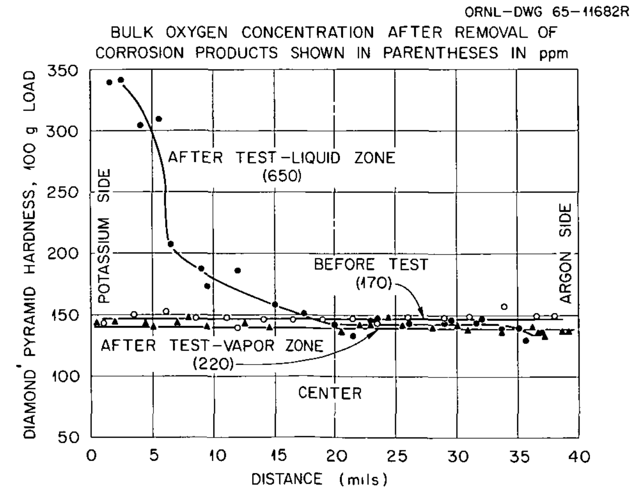

Fig. 15.1. Microhardness Profiles Across Nb–1.05% Zr–0.017% O Capsule After Exposure to Argon and Potassium Containing 1500 ppm O for 100 hr at 815°C.

DETERMINATION OF OXYGEN IN ALKALI METALS

A. P. Litman J. E. Strain[6]

The gettering–vacuum fusion (GVF) analytical technique, which was developed to measure oxygen in potassium,[7] is currently being applied to the determination of oxygen in sodium. The analysis relates the oxygen uptake of a zirconium specimen in potassium (sodium) to the oxygen content originally in the liquid metal. This analytical procedure proved to be accurate in potassium despite variations in the thermal and environmental history of the alkali metal. The production of various oxide species when hot potassium contacts different container materials has always compromised oxygen analyses by conventional methods such as amalgamation and vacuum distillation.

Albeit the GVF method is accurate, it is nevertheless time-consuming and expensive. A nondestructive analytical method, fast-neutron activation analysis,[8] which does not have the disadvantages of the GVF procedure, was investigated this past year. The nuclear method involves counting the decay of radioactive ^{16}N produced by the reaction of ^{16}O with 14-Mev neutrons. We analyzed in replicate a sample of pure potassium, a sample of potassium previously contaminated with a relatively large quantity of oxygen, and a control capsule, using an existing fast-neutron

---

[5] J. R. DiStefano, *Corrosion of Refractory Metals by Lithium*, ORNL-3551 (March 1964).

[6] Analytical Chemistry Division.

[7] A. P. Litman and J. W. Prados, *Electrochem. Technol.* 3, 9–10 (September–October 1965).

[8] E. L. Steele and W. W. Meinke, *Anal. Chem.* 32(2), 185–87 (1962).

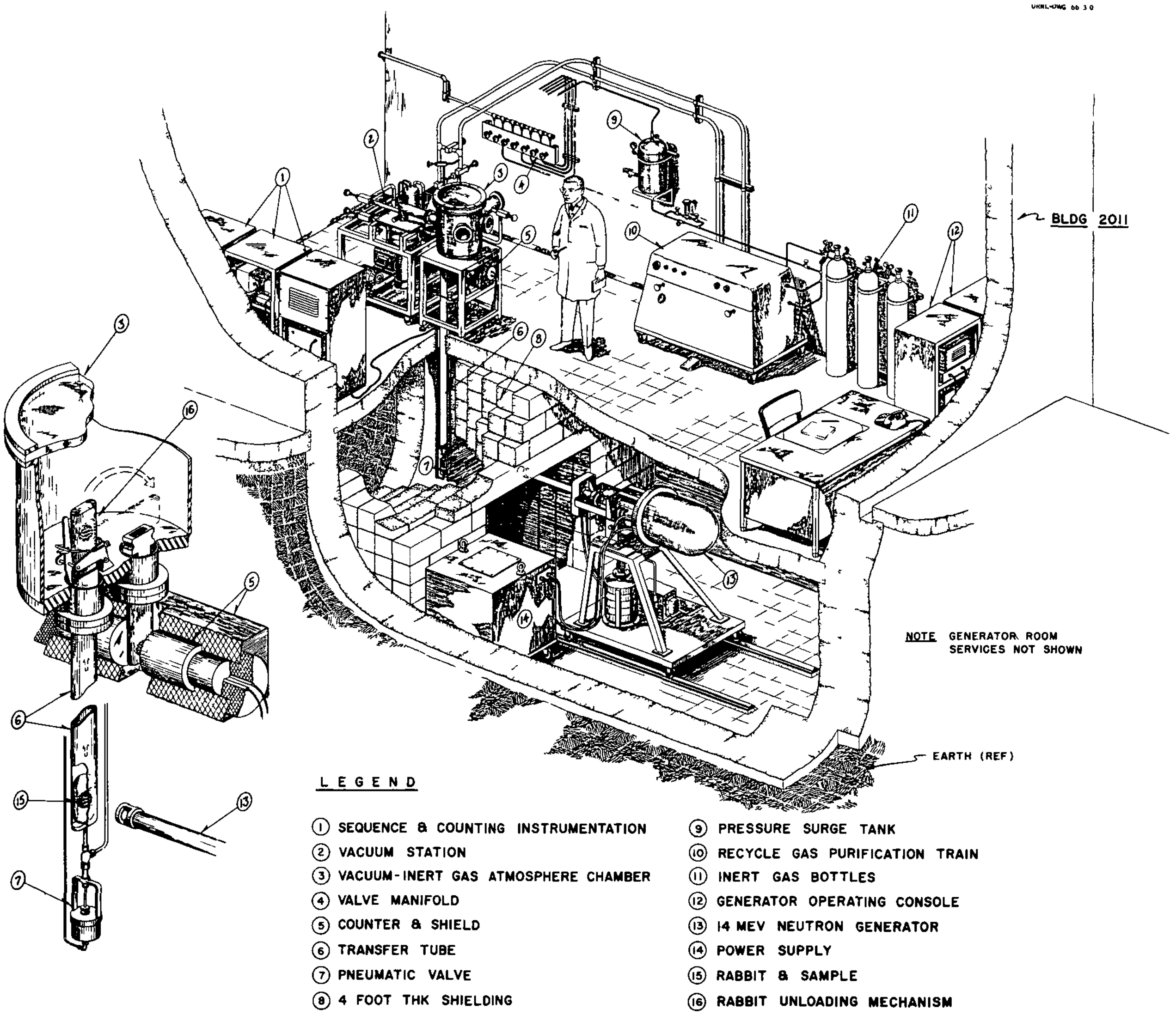

Fig. 15.2. Fast-Neutron Activation Analysis Facility.

generator facility at ORNL and systems at other sites. Maximum sensitivity (1975 counts/mg O) and the best oxygen recovery (115%) were found for the system having the largest NaI detectors, designed for 4π geometry, and using nitrogen rather than air to propel the sample rabbit. The use of nitrogen avoided the ^{16}N recoil effect encountered by other workers.[9]

In the demonstration studies, the relatively high oxygen blank of the sample container clouded the practical limits of detection and accuracy. To circumvent this problem, we are constructing a unique fast-neutron activation analysis facility, ORNL Mark II, specifically designed for handling highly active alkali metals without protective capsulation. This facility, shown in isometric view in Fig. 15.2, incorporates certain desirable features of other fast-neutron activation systems and should be an important aid to research and engineering studies on alkali metals. We plan to be routinely analyzing samples in this facility by fall 1966.

---

[9] O. U. Anders and D. W. Briden, *Anal. Chem.* **37**(4), 530–33 (1965).

PURIFICATION OF ALKALI METALS

A. P. Litman L. R. Trotter

Studies of refractory metal–alkali metal couples have shown the serious effects only a few parts per million foreign impurities, such as oxygen, can have on system stability. Both hot trapping and vacuum distillation are generally effective in improving the purity of alkali metals available for use in test systems. In this vein, we have acquired an experimental molecular distillation unit that should be capable of refining and producing very high-purity alkali metals. The test unit, Fig. 15.3, fabricated from type 304 stainless steel, contains approximately 2 ft^2 evaporating surface and a hollow condenser containing an evaporative coolant chamber. This single-stage unit, which has already been used at the Oak Ridge Gaseous Diffusion Plant to separate potassium isotopes,[10] is presently being modified so that the condensate can be recycled and samples can be taken for chemical analysis during operation. Use of this rig is scheduled to begin in summer 1966.

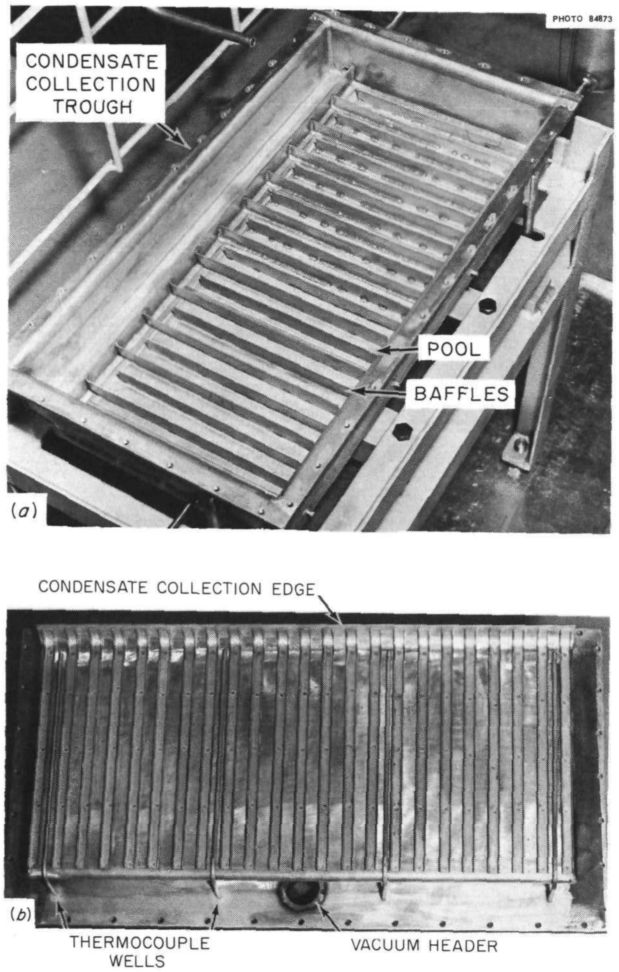

Fig. 15.3. Molecular Distillation Apparatus. (*a*) Evaporator. (*b*) Condenser.

---

[10] R. M. McGill *et al.*, "The Separation of Potassium Isotopes by Molecular Distillation," K-1650, pp. 32–43 (Sept. 29, 1965).

16. Tungsten Metallurgy

W. O. Harms

Thermochemical deposition (TCD) of tungsten and tungsten alloys is being developed as a fabrication method for high-temperature reactor components. An important advantage of the process is the ability to fabricate tubing and objects with diverse and intricate shapes at lower temperatures and with simpler equipment than is required for more conventional procedures. We are defining the optimum conditions for deposition, studying the effect of warm working on TCD tungsten, and evaluating the TCD materials in terms of ductile-to-brittle transition temperatures and creep-rupture properties.

As an adjunct to this work, the basic problem of brittleness in tungsten is being investigated on more conventionally prepared tungsten-base materials through correlation of low-temperature ductility with electron microscope studies. More fundamental studies of the deformation of tungsten are reported in Part I, Chap. 5 of this report. Experiments on the extrusion of tungsten-base alloys and results of physical property measurements on tungsten-base materials are presented in Chap. 14. Studies on thermochemical deposition of tungsten-rhenium alloys are described in Part III, Chap. 19.

THERMOCHEMICAL DEPOSITION OF TUNGSTEN

C. F. Leitten, Jr.

Thermochemically deposited tungsten in the form of sheet was prepared for metallurgical evaluation. In addition, a major effort involved empirical and statistical investigations of deposition parameters as related to deposit morphology. The effect of warm rolling on the microstructure, texture, and properties of TCD tungsten was also investigated.

Production of Tungsten Sheet

F. H. Patterson

Tungsten sheet stock was produced by thermochemical deposition (TCD) for complete metallurgical evaluation, including deformation studies. Sheet material up to 145 mils thick was deposited on the inside flat surfaces of octagonal molybdenum mandrels.[1] Each mandrel provided flat substrates for the production of eight 1.5 × 16 in. sheets. A multiple-heating-zone tube furnace overcame the problem of thickness nonuniformity reported previously.[2] The conditions used to deposit the sheet material are listed below.

H_2 gas flow	3000 cm^3/min
WF_6 gas flow	200 cm^3/min
Chamber pressure	5 torrs
Chamber temperature	
Zone 1 (inlet)	585°C
Zone 2	540°C
Zone 3	530°C
Zone 4	560°C
Zone 5	595°C

---

[1] F. H. Patterson and C. F. Leitten, Jr., *Thermochemical Deposition of High-Purity Tungsten Sheet* (forthcoming ORNL publication).

[2] F. H. Patterson, W. C. Robinson, Jr., and C. F. Leitten, Jr., *Metals and Ceramics Div. Ann. Progr. Rept. June 30, 1965*, ORNL-3870, pp. 155–59.

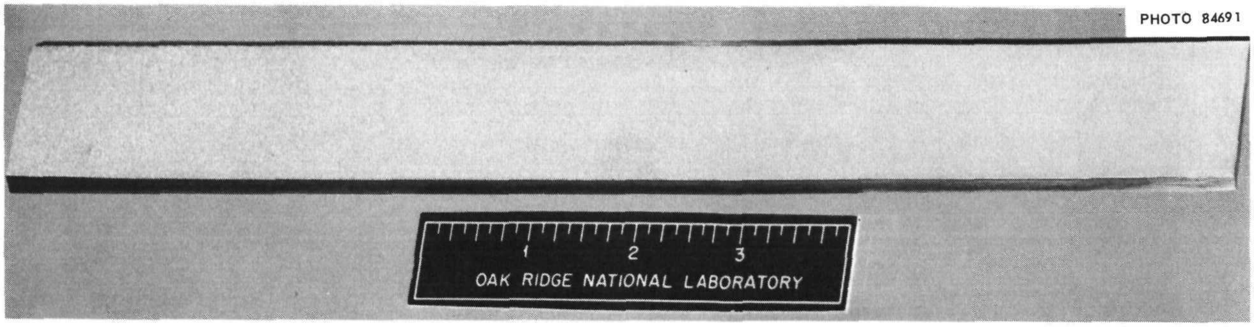

Fig. 16.1. Sheet of TCD Tungsten 145 Mils Thick.

An unprecedentedly thick 145-mil deposit is shown in Fig. 16.1. This material contained less than 5 ppm O, 8 ppm F, and 5 ppm C. An average deposition rate of 3.5 mils/hr was realized at an efficiency of about 70%.

Parametric Studies

F. H. Patterson W. C. Robinson, Jr.

Irregular or nodular growths that have been observed in TCD tungsten deposits were tentatively attributed to occlusion of tungsten particles precipitated in the gas phase, localized high concentrations of HF, and oxidizing contaminants. These nodular growths have a more random grain orientation than the bulk deposit and contribute to lower bulk purity. Studies were conducted, therefore, to provide an understanding of the effects of basic deposition parameters on the grain morphology of the deposits. Tungsten was deposited in ⅞-in.-diam copper tubes uniformly heated over a 16-in. length. An H_2/WF_6 ratio of 15 and a pressure of 5 torrs were used.

The effect of air contamination was examined in a set of experiments at 580°C. No irregularities in the deposit were observed when a few parts per million air was added, but nodular growths were observed when 10 cm^3/min air was added. Presumably, oxyfluorides and oxides of tungsten disrupted the normal growth habit and nucleated the formation of nodules.

In a second series of experiments temperature was varied from 460 to 840°C. Nodular growths were not observed below a temperature of about 740°C and were observed at higher temperatures under these experimental conditions.

The effect of total mass flow was examined at 580°C by varying the flow rate from 778 to 6210 cm^3/min (H_2/WF_6 ratio of 15). The purpose was to determine whether the transition from smooth to nodular deposit could be induced by a change from turbulent to laminar flow in the deposition tube. No changes in deposit morphology were observed for the range of flow rates employed. In a series of experiments at 580°C the WF_6 and H_2 were held constant at 200 and 3000 cm^3/min and argon was used to vary the gas velocity in the deposition chamber. Again no effect on the character of the deposit was found within the range 4700 to 6700 ft^3/min. Thus, air contamination and increasing temperature caused nodular growths in tungsten deposits, and mass flow and velocity had no effect under the conditions of these experiments. Air contamination, which is minimized during normal deposition, probably can be discounted as a prime cause for nodular growth. Accordingly, the effect of gas concentration as influenced by temperature, pressure, and flow rate and measured by deposition rate is being examined. A further possible benefit of this study is the determination of the rate-controlling mechanism for metal deposition. A statistical program has been prepared to systematically examine the effects of deposition parameters on deposition rate and to correlate the associated gas-phase composition (including by-product HF) with deposit morphology.[3]

---

[3] Joint effort includes T. L. Hebble of the Mathematics Division and J. D. Fleming, consultant from the Georgia Institute of Technology.

The range of parameters being studied is listed below.

Temperature	450 to 820°C
Pressure	9 to 20 torrs
Flow rates	
WF_6	60 to 370 cm^3/min
H_2	750 to 5200 cm^3/min

The experimental program involves 81 separate experiments, all of which have been completed. The results are presently being analyzed.

Deformation Studies

F. H. Patterson J. E. Spruiell[4]
B. F. Shuler[5]

Some effects of rolling and annealing on the microstructure and texture of TCD tungsten sheet were investigated. The sheet was prepared under previously established deposition conditions. The as-deposited material possessed a coarse columnar

ORNL-DWG 66-9146

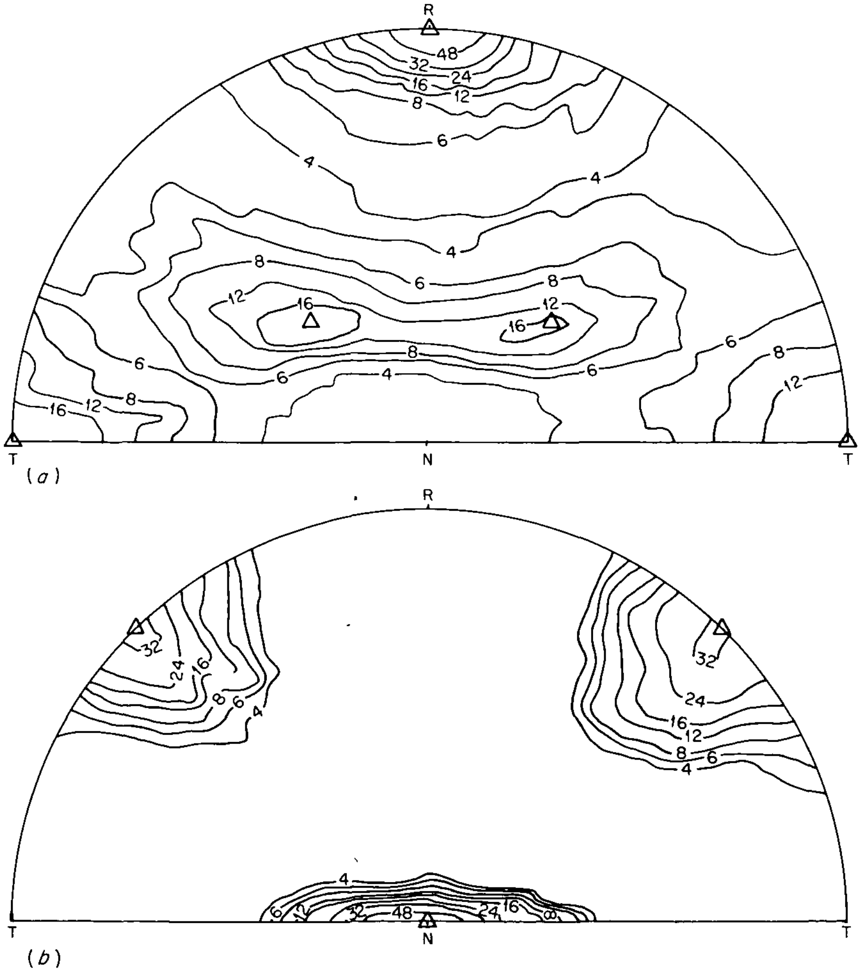

Fig. 16.2. Pole Figures for TCD Tungsten Rolled 80% at 1200°C and Stress Relieved at 1200°C for 1 hr. The ideal {100}⟨110⟩ texture is indicated by triangles. *R, T,* and *N* indicate rolling, transverse, and normal directions respectively. (*a*) ⟨110⟩ pole figure. (*b*) ⟨200⟩ pole figure.

---

[4] Consultant from the University of Tennessee.

[5] Summer employee from the University of Tennessee.

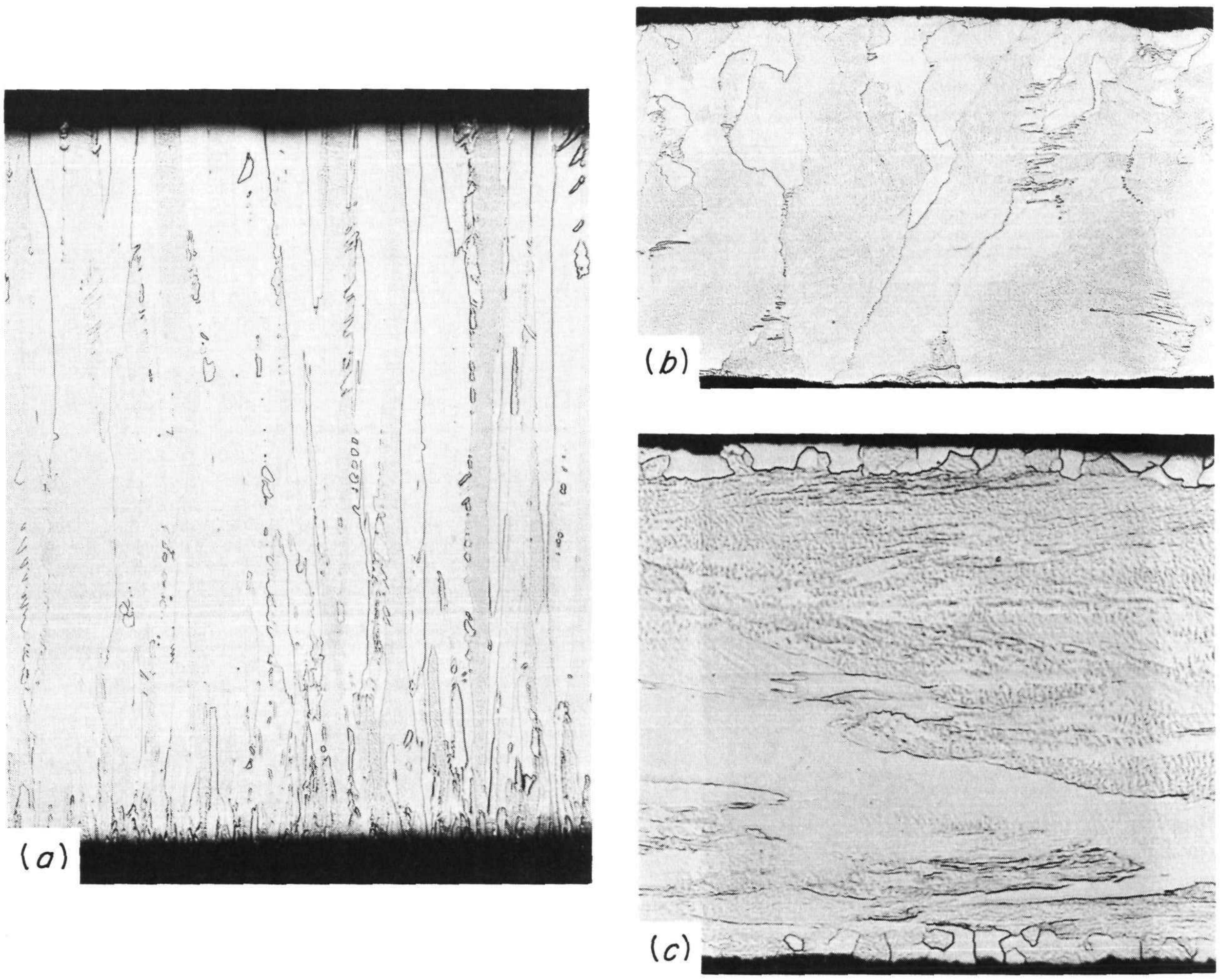

Fig. 16.3. Microstructure of TCD Tungsten Sheet Used in Deformation Studies. (*a*) As deposited (initial deposition surface at top); 50×. (*b*) Reduced 60% by rolling at 1200°C and stress relieved at 1200°C 1 hr; 75×. (*c*) Reduced 80% by rolling at 1200°C and stress relieved at 1200°C for 1 hr; 250×. Etchant: 50 parts concd NH_4OH and 50 parts 30% H_2O_2.

grain structure[6] with $\{100\}$ planes parallel to the deposition substrate; individual grains, however, were randomly rotated about $\langle 001 \rangle$. Microstructure and texture changes were examined after rolling at 1200°C to various reductions up to 80%. Some specimens were subjected to different heat treatments at intermediate stages of the rolling operation, and all specimens received some form of final heat treatment, either a stress relief at 1200°C for 1 hr or an annealing treatment at 2000°C for 30 min.

Rolling textures were determined by an x-ray diffraction technique that used spherical samples.[7] Thin sheets of the rolled material were cemented together and electrical-discharge machined to a spherical shape. A $\{100\}$ $\langle 011 \rangle$ texture was approached after reductions in thickness up to 60%. After 80% reduction, this texture was more pronounced and is best described as $\{100\}$ $\langle 011 \rangle$ spread ±15° about the rolling direction. Typical $\langle 110 \rangle$ and $\langle 200 \rangle$ pole figures for the material

---

[6] R. L. Heestand, J. I. Federer, and C. F. Leitten, Jr., *Preparation and Evaluation of Vapor-Deposited Tungsten*, ORNL-3662 (August 1964).

[7] L. K. Jetter and B. S. Borie, Jr., *J. Appl. Phys.* **24**, 232–35 (1953).

reduced 80% are shown in Fig. 16.2, wherein the contour lines represent regions of constant diffraction intensity and the triangles indicate the positions of the ideal $\{100\}\langle 011\rangle$ texture. Although the 80%-reduced material recrystallized when annealed for 30 min at 2000°C, no change in texture was observed.

The columnar grain structure of the as-deposited sheet was not destroyed until reductions near 80% were reached. Figure 16.3 shows the microstructures of the as-deposited material and the same material after 60 and 80% reduction. After 60% reduction the columnar structure had just begun to break down (Fig. 16.3*b*), although many grains still spanned the width of the specimen. The microstructure of the sample reduced 80% exhibits the fibrous appearance characteristic of heavily worked metals (Fig. 16.3*c*). Complete recrystallization did not occur during the 30-min anneals at 2000°C except for samples reduced 80% in thickness.

Rolling experiments are being conducted at temperatures successively lower than 1200°C to ascertain the feasibility of drawing TCD tungsten tubing.

LOW-TEMPERATURE BEND DUCTILITY AND STRENGTH OF TCD TUNGSTEN[8]

A. C. Schaffhauser

We have determined the ductile-to-brittle transition temperature[9] (DBTT) and low-temperature strength of TCD tungsten sheet. These properties were compared with those of high-purity powder-metallurgy-produced (PM) wrought tungsten sheet, and the factors controlling these properties are discussed.

The DBTT of as-deposited TCD sheet was 270 to 300°C regardless of the orientation or grain structure of the sheet. A 1-hr anneal in the temperature range of 1000 to 2000°C lowered the DBTT by 100°C or more due to relief of nonhomogeneous microstrain. This behavior is contrasted with that of the PM material, for which the DBTT ranged between 120 and 160°C in the stress-relieved condition but was raised by 150°C or more by annealing above the recrystallization temperature (1350°C).

The difference in the ductile-to-brittle transition behavior of the two materials is attributed to the quantity of impurities segregated at the grain boundaries as described below. Due to the higher purity and grain stability of TCD tungsten, it is less susceptible to grain-boundary segregation on annealing at high temperatures and thus has a lower DBTT.

The low-temperature yield strength of as-deposited TCD tungsten is about half that of wrought PM tungsten. However, after annealing both materials above the recrystallization temperature of the wrought sheet, the strengths are comparable. For annealing temperatures over 2000°C, TCD tungsten has a definite strength advantage due to its grain-growth resistance.

RECRYSTALLIZATION, GRAIN GROWTH, AND THE DUCTILE-TO-BRITTLE TRANSITION IN TUNGSTEN SHEET[10]

K. Farrell A. C. Schaffhauser
J. O. Stiegler

The ductile-to-brittle transition temperature (DBTT) in bending has been examined in wrought and in recrystallized powder-metallurgy tungsten sheet as a function of annealing treatment and grain size. Wrought-and-recovered sheet consisting of small subgrains had the lowest DBTT of 70°C, but this was raised to 225°C by the onset of primary recrystallization at 1150°C. Primary grain growth was inhibited at annealing temperatures between 1300 and 2200°C. Secondary recrystallization started at 2000°C from one surface, and the new grains grew readily. All recrystallized specimens had DBTT's in the range 235 to 280°C, irrespective of annealing temperature, grain size, and fracture mode. Primary recrystallized specimens fractured mainly along the grain boundaries, but secondary recrystallized specimens fractured mainly by transgranular cleavage initiated from a

---

[8] Summarized from "Low Temperature Ductility and Strength of Vapor-Deposited Tungsten," presented at 1965 Winter Meeting of the American Nuclear Society, Washington, D. C., Nov. 11–14, 1965.

[9] Defined as the lowest temperature at which a 90° bend could be obtained without cracking. $4T$ punch radius, 0.1 in./min deflection rate.

[10] Abstract of paper to be submitted for publication.

grain-boundary source. These results are consistent with a picture of grain growth and embrittlement involving impurities segregated at the grain boundaries. We suggest that the high DBTT in the recrystallized tungsten is determined by the initiation of a brittle crack at a grain boundary. The influence of segregated impurities at the grain boundaries on the initiation and subsequent behavior of the mobile dislocations involved in the formation of the crack is considered important.

CREEP-RUPTURE PROPERTIES OF TUNGSTEN AND TUNGSTEN ALLOYS

H. E. McCoy

The primary objective of this program is to obtain adequate creep-rupture data on tungsten and tungsten alloys for designing engineering systems for long-term operation at elevated temperatures.[11] The materials studied have included wrought powder-metallurgy tungsten, several lots of TCD tungsten, W–2% ThO_2, and Sylvania A (W–0.5% Hf–0.02% C). The creep-rupture properties of these four materials are summarized in Fig. 16.4 for test temperatures of 1650 and 2200°C. Within the scatter of the experimental data we concluded that the powder-metallurgy and the TCD tungsten exhibited equivalent stress-rupture properties. The rupture ductilities of the four materials are compiled in Table 16.1.

At 1650°C all four materials were structurally stable. However, at 2200°C several significant changes occurred: the grain size of the powder-metallurgy tungsten became very large; the Sylvania A and the W–2% ThO_2 both exhibited only slight grain growth; and the TCD tungsten formed an extensive network of intergranular voids. We think this void formation is due to the presence of some as-yet unidentified impurity.

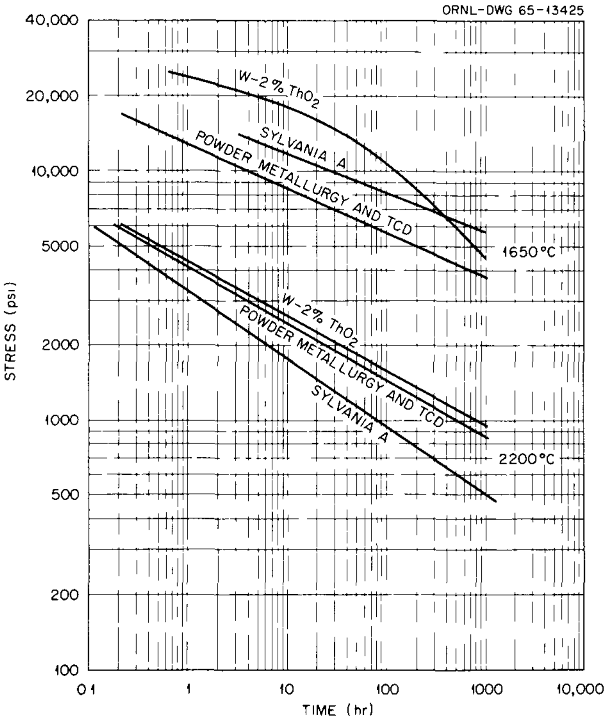

Fig. 16.4. Creep-Rupture Properties of Tungsten and Tungsten-Base Alloys.

Table 16.1. Elongations of Tungsten and Tungsten-Base Alloys

Material	Elongation at 100-hr Rupture Life (%)	
	1650°C	2200°C
Wrought powder-metallurgy tungsten	32	12–19
TCD tungsten	3–5	17–35
Sylvania A (W–0.5% Hf–0.02% C)	9	20–25
W–2% ThO_2	9	8

---

[11] H. E. McCoy, *Creep-Rupture Properties of Tungsten and Tungsten Alloys*, ORNL-3992 (to be published).

17. Uranium Nitride

J. L. Scott W. O. Harms

Uranium mononitride has increasing interest as a nuclear fuel because it offers potential advantages over UC, a similar but more extensively developed fuel. Because of their higher densities and much higher thermal conductivities, metal-clad elements of either UN or UC can potentially be operated without central melting at heat ratings that produce gross melting in the more standard fuel UO_2. Unlike UC, however, the stoichiometry of UN is easily controlled within very narrow limits. Since stoichiometry affects both fuel-cladding reactions and fuel swelling rates, these problems should be less severe with the mononitride than with the monocarbide. In addition, UN has a higher melting point (2800°C) than the monocarbide (2450°C) and is harder at high temperatures, so the threshold for breakaway swelling for UN should occur at a somewhat higher temperature than for UC. For example, existing data[1] indicate that enhanced swelling of UC occurs above 1100°C. If one assumes equivalent properties for UN and UC at the same fraction of the absolute melting temperature, enhanced swelling of UN would be expected at about 1300°C. The improvement in linear heat rating of a fuel rod associated with this increase in central operating temperature is about 700 w/cm.

The potential advantages cited above should also apply to the mixed uranium-plutonium compounds, which are of interest for fast-reactor fuels. Although compatibility limits and swelling thresholds will be different for plutonium-containing materials, the relative positions of the nitride and carbide should remain unchanged. One drawback to the nitride as a fast-reactor fuel is the higher neutron-absorption cross section of nitrogen than of carbon. Our studies have indicated that in view of this effect the breeding gain for (U,Pu)N will be somewhat lower than for (U,Pu)C. This disadvantage must be weighed against the higher specific power that can be achieved in the nitride fuel. The problem may also be circumvented by use of ^{15}N, which on a large scale can be produced for about $1.00 per gram. Since the anion weight is only 5% of the total and recycle of nitrogen is feasible, the cost of the ^{15}N isotope can be made small relative to the cost of plutonium.

Our work on UN includes studies of sintering kinetics and pellet fabrication, the effects of impurities on structure and properties, the development of improved structures through controlled precipitation, and thermodynamic studies. Other portions of the program have been summarized in appropriate progress reports.[2–6]

SYNTHESIS OF UN POWDER AND PELLET FABRICATION

R. A. Potter J. M. Leitnaker
T. G. Godfrey

The production of low-oxygen-content UN pellets for basic property measurements has been emphasized during the present report period. We developed techniques for synthesizing UN powder with a low oxygen content and with a low surface activity so that oxygen would not be absorbed during exposure to air. We also studied the range

---

[1] Atomics International, *Annual Technical Progr. Rept. AEC Unclassified Programs Fiscal Year 1964*, NAA-SR-9999 (Aug. 31, 1964).

[2] ORNL-TM-1200 (classified).

[3] ORNL-TM-1270 (classified).

[4] ORNL-TM-1300 (classified).

[5] ORNL-TM-1400 (classified).

[6] ORNL-TM-1455 Part 2 (classified).

of fabrication conditions that would permit us to produce UN free of metallic uranium.

Uranium nitride powders obtained from commercial sources normally contain 1000 to 5000 ppm O. This material is generally made[7] by alternately hydriding and dehydriding uranium and then nitriding to $UN_{1.75}$ in an atmosphere of nitrogen and reducing to UN by vacuum treatment at about 1200°C.

We found that an additional heat treatment at about 2000°C will decrease the final oxygen content to below 500 ppm. The reduction in oxygen content arises partly from the preferential sublimation of oxygen as UO_2 and partly from the reduction of surface area of the powder. As a result of the reduced surface area, the oxygen pickup upon subsequent exposure to air, such as during the pressing operation, is reduced. The sinterability of the powder is also reduced by the additional heat treatment, but pellets of low oxygen content can be made routinely with a density 95% of theoretical. For fast-reactor fuel applications there is some advantage to a product with a controlled intermediate density.

In addition to pure UN powders, we synthesized solid solutions of (U,2% Th)N and (U,5% Th)N for internal oxidation studies, both in powder form. We synthesized these powders from uranium-thorium alloys by the same process as UN. At 2000°C equilibrium was attained for the solid solution containing 2% Th after approximately 1 hr but not for the material with 5% Th; cold-pressed specimens of both compositions reached equilibrium when heat treated for 1 hr at 2300°C, as indicated by sharp x-ray diffraction peaks and lattice parameter measurements. Sintering UN at high temperatures requires an overpressure of nitrogen to prevent the appearance of a liquid uranium phase; at low temperatures a vacuum is required to prevent rapid formation of higher nitrides. A series of experiments was performed to determine the temperature above which a nitrogen overpressure must be maintained to prevent formation of liquid uranium during the sintering cycle. Liquid uranium did not form at changeover temperatures of 1650°C and below. In these experiments the nitrogen was admitted or removed in approximately 20 min.

DISTRIBUTION OF SECOND-PHASE MATERIAL IN URANIUM NITRIDE

T. G. Godfrey J. M. Leitnaker
R. A. Potter

We are continuing our efforts to improve the irradiation performance of UN by producing a finely dispersed stable precipitate in it. Second-phase materials under study include tungsten, molybdenum, uranium dioxide, and thorium dioxide. An important aspect of this work is the synthesis of high-purity uranium nitride powder of closely controlled composition, as reported in the previous section. Also inherent in this investigation is the development and evaluation of experimental and analytical techniques for determining the presence of fine precipitates and their effects on the properties of the nitride.

Tungsten and Molybdenum

Both tungsten and molybdenum were investigated as possible precipitate formers. We found that tungsten was only very slightly soluble in UN at high temperature but that molybdenum was soluble to the extent of about 0.1 at. % at room temperature, as indicated by lattice parameter contraction. When specimens containing 0.1% Mo were annealed at 2625°C and rapidly cooled, electron microscopy revealed that the molybdenum was present as a rather fine precipitate (1000 to 2000 A) within the UN grains. While the density of precipitate particles (10^9 to $10^{10}/cm^3$) was not as high as is generally desired, we are encouraged by this result and are continuing the heat-treatment studies.

Uranium Dioxide

The first precipitate observed in this study was deduced to be UO_2, and a hypothesis was presented to explain its presence.[8] Additional experiments have not refuted the earlier work. A sample of UN with 2000 ppm O heated 8 hr at 2300°C in N_2 showed, by electron microscopy, a high density (approximately $10^{15}/cm^3$) of fine precipitate

---

[7] R. A. Potter, *Metals and Ceramics Div. Ann. Progr. Rept. June 30, 1965*, ORNL-3870, pp. 164–66.

[8] T. G. Godfrey and J. O. Stiegler, *Metals and Ceramics Div. Ann. Progr. Rept. June 30, 1965*, ORNL-3870, pp. 168–69.

particles near the surface but none toward the center. Metallography revealed no UO_2 in the grain boundaries near the outside but an increasing amount toward the center. Weight-loss measurements indicated that oxygen had been lost through volatilization of UO_2 and that the process was diffusion controlled. These observations are open to two interpretations. First, the cooling rate may have been rapid enough at the outside region that a precipitate formed but did not have sufficient time to agglomerate, while further in it did. Alternatively, one can postulate that the oxygen content of the outer region was reduced by the vaporization process to the extent that the solubility limit was reached at a temperature too low for gross agglomeration of the precipitate to occur.

In other experiments, carbon was added to UN in the form of UC_2. This procedure led to an inhomogeneous structure with regions high and low in carbon. Electron microscopy showed that a fine precipitate was also nonuniformly distributed, in keeping with our ideas[8] concerning the role of carbon in precipitation of oxide in UN.

Thorium Dioxide

Incorporation of thorium in UN appears attractive from the standpoint of precipitate formation. A ThO_2 precipitate should coalesce more slowly at a given temperature than UO_2, since for ThO_2 the coalescence would involve the simultaneous diffusion of two ion species through the UN matrix rather than only one for UO_2. To this end we are studying the solubility and phase relationships in the Th-U-N-O-C system. We have shown that the addition of ThO_2 to UN leads to a thorium-rich oxide phase and a uranium-rich nitride phase. Current experiments are concerned with determining the optimum way of incorporating thorium and oxygen in the starting materials and the heat treatments necessary to develop the desired composition and distribution of the phases.

Techniques for Evaluation of Precipitates

We are exploring possible techniques for determining the presence of precipitates in UN and for assessing their effects on the properties of the material. Electron microscopy is considered to be the most promising method of examination, but the more standard techniques are not applicable in the present work. Since our specimens are pressed and sintered compacts that contain 5 to 10% porosity, preparation of thin sections for transmission electron microscopy is extremely difficult. Our examinations to date have been made on replicas of fractured surfaces, but this technique is often subject to uncertainty because of artifacts that may arise during replication. Therefore we are attempting variations in techniques, such as fracturing the sample under a liquid and then removing the liquid from the sample in the vacuum evaporator prior to shadowing and replicating.

A precision lattice-parameter computer program[9] has been modified for determination of phase compositions in conjunction with chemical analysis and optical metallography. We are also developing a computer program to aid in the analysis of x-ray diffraction line broadening as a measure of lattice strain arising from the presence of fine precipitates. This technique might yield information about the degree of coherency of the precipitate and how it changes with heat treatment and coalescence.

Additional techniques under study are room-temperature and hot hardness measurements, as well as high-temperature compressive creep. We have previously shown[10] that microhardness reflects compositional variations in UN, although the relationships are not straightforward. Compressive creep may be a more meaningful test, since it is essentially a test of the bulk material and is not so dependent on localized variations.

THERMODYNAMIC STUDIES ON UN

Vaporization Behavior of UN

J. M. Leitnaker R. A. Potter
H. Inouye

Since all reactions of UN with its environment either involve or can be derived from the equations describing its vaporization behavior, we have

---

[9] R. E. Vogel and C. P. Kempter, *Acta Cryst.* 14, 1130 (1961) and private communication from R. E. Vogel, Los Alamos Scientific Laboratory, October 1965.

[10] T. G. Godfrey and G. Hallerman, *Metals and Ceramics Div. Ann. Progr. Rept. June 30, 1965*, ORNL-3870, pp. 166–68.

attempted to obtain a better understanding of this behavior. The equilibrium nitrogen pressures reported by several investigators[11–13] for the reaction

$$\mathrm{UN}(s) \rightleftharpoons \mathrm{U}(l\text{, saturated with } \mathrm{N}_2) + \tfrac{1}{2}\mathrm{N}_2(g) \qquad (1)$$

show good agreement for the approximate temperature range 1600 to 2800°C. We calculated ΔH°_{298} for reaction (1) from available data, using a consistent set of assumptions, to be 69.6 ± 0.5 kcal/mole.

The vaporization behavior of UN at temperatures less than 1600°C has not been previously investigated. We derived a thermodynamic relationship showing that below some temperature T_{cr}, UN instead of losing nitrogen preferentially will vaporize congruently, according to the equation

$$\mathrm{UN}(s) \rightleftharpoons \mathrm{U}(g) + \tfrac{1}{2}\mathrm{N}_2(g) \ . \qquad (2)$$

Assuming the Langmuir vaporization law, we derived the condition for congruent vaporization:

$$\tfrac{1}{2}\,\Delta F^\circ_{\text{vaporization U}} + 1.7T < -\Delta F^\circ_{\text{formation UN}} \ . \qquad (3)$$

Calculations based on careful analysis of available thermodynamic data indicate that UN will vaporize congruently below about 1300°C. We found that T_{cr} is less than 1400°C by observing metallic uranium at the pellet surface after a 300-hr anneal of UN at 1400°C and a pressure of 2×10^{-10} atm (the equilibrium pressure of nitrogen is calculated to be 4×10^{-9} atm). The precise determination of T_{cr} will be useful in establishing the relationship between the free energy of formation of UN and the free energy of vaporization of uranium.

Present reactor designs involve the use of UN at much lower temperatures than those for which equilibrium nitrogen pressure data are available. Accordingly, we are attempting to make measurements in the low-temperature region. Figure 17.1 shows the preliminary results obtained for nitrogen pressures over UN. The apparatus used has been previously described.[14]

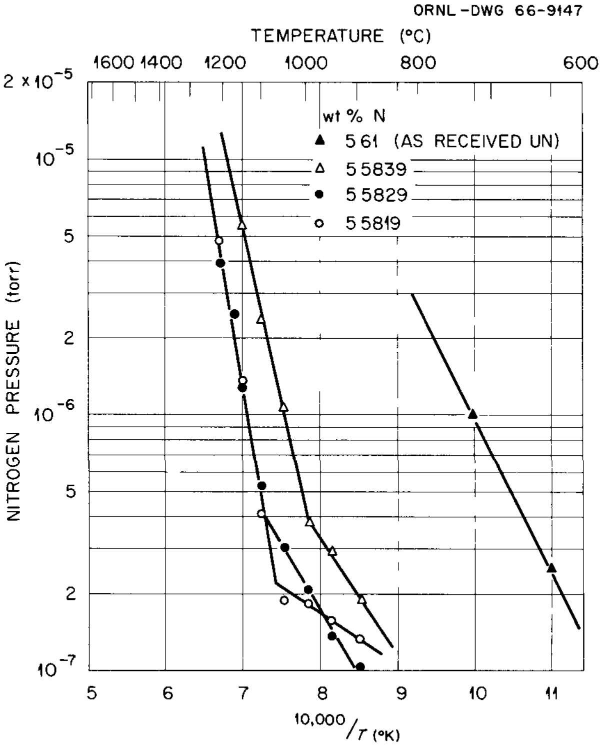

Fig. 17.1. The Nitrogen Pressure over UN as a Function of Temperature.

The data indicate that the nitrogen pressure measured can be extremely sensitive to small changes in composition of the nitride phase. A UN composition change of 10 ppm N changes the observed pressure by a factor of about 4. Although the composition of the UN at the UN-U_2N_3 boundary has not been established, our data show that the homogeneity range of UN is at least 260 ppm N.

The fact that the observed nitrogen pressure did not change after the last 10 ppm N was removed suggests that a fixed point may have been reached in the system. This fixed point could correspond

---

[11] P. A. Vozzella and M. A. DeCrescente, *Thermodynamic Properties of Uranium Mononitride*, PWAC-479 (October 1965).

[12] J. Bugl and A. A. Bauer, Battelle Memorial Institute, unpublished data and D. L. Keller, *Development of Uranium Mononitride, Quarterly Progress Report, January–March 1964*, BMI-X-10083 (April 1964).

[13] R. W. Bonham *et al.*, *High Temperature Vaporization Studies with the Bendix Time-of-Flight Mass Spectrometer*, NLCO-880 (1963).

[14] H. Inouye, *Equilibrium Solid Solutions of Nitrogen in Cb–1% Zr Between 1200–1800°C*, ORNL-TM-1355 (February 1966).

either to the congruent vaporization composition, as suggested by the above analysis, or to the presence of two phases, U(*l*) and UN.

Not shown are the carbon monoxide pressures, which were also measured. These values ranged from nearly equal to double the nitrogen pressure. The presence of the carbon monoxide can be accounted for by the presence of second-phase UO_2 and 1300 ppm C dissolved in the nitride phase. These impurities could explain the fact that the observed nitrogen pressure was three orders of magnitude higher than one would calculate based on our analysis of previous data.

The high-vacuum apparatus used in these studies is limited to about 10^{-5} torr N_2, which is also the limit of detection by the mass spectrometer. A new apparatus has been constructed to extend these measurements to higher pressures.

The U-C-N System

J. M. Leitnaker

The use of solid solutions of UC and UN may have attractive advantages, particularly with regard to chemical reactivity and ease of preparation. Our purpose is to determine the thermodynamic stability of these solid solutions as a function of composition.

An apparatus to determine equilibrium pressures of nitrogen over solid solutions of UC and UN in equilibrium with graphite was built, and preliminary tests were performed. While the precision with which the measurement can be made has not been determined, the pressure of nitrogen can be measured to ±0.05 torr and the temperature to ±2° at 1500°C.

page blank

Part III.

General Fuels and Materials Research

page blank

18. Dispersions in Solids

J. P. Hammond

In recognition of the long-range importance of fine-particle dispersion strengthening and "whisker" reinforcement to the advancement of nuclear fuels and structural materials, an applied research program was instituted to give exclusive attention to this vital area.

Dispersion hardening studies on thorium fuels[1] were transferred to this activity, and an investigation was initiated on dispersion strengthening of molybdenum, selected as representative of the family of refractory metals. We are trying to introduce stable ultrafine dispersions in aluminum and thorium by the SLIS principle.[2] Studies on controlled precipitation in uranium mononitride are described in Part II, Chap. 17 of this report.

DISPERSION HARDENING OF MOLYBDENUM

K. K. Sinha[3]   J. P. Hammond

As a result of extended explorations of methods for introducing dispersions in molybdenum, a unique chemical process was evolved for incorporating uniform and ultrafine dispersions of stable oxides in the tungsten family of metals and alloys; for example, ThO_2 or ZrO_2 in molybdenum, tungsten, molybdenum-rhenium alloys, or tungsten-rhenium alloys.

For best mechanical properties structures were sought with dispersant particles below 0.1 μ in size and interspaced less than 1 μ apart. The standard methods for effecting dispersions, such as mechanical blending of fine metal and oxide powders, decomposition of coprecipitated salts, selective reduction of mixed oxides, and oxide coating of metal powders, were examined, but these yielded coarse dispersions or failed in other ways to give desired properties. The problem was solved in an approach involving colloid chemistry. By forming a simultaneous colloid of the oxide dispersant and a salt of the matrix, fineness and uniformity of dispersions were assured.

Whereas sols of the dispersoid, ThO_2 or ZrO_2, were readily prepared by conventional techniques, sols of adequate concentration in the matrix were achieved only after novel adaptation of the supersaturation principle. Rapid introduction of a saturated aqueous ammonium molybdate solution into 190-proof ethyl alcohol triggered the formation of a thick colloid of the molybdate. Sols of the dispersant and matrix were then mixed together and centrifuged to form an ammonium molybdate–metal oxide cake. After selective reduction in hydrogen, the now metal-matrix dispersion was fabricable to fully dense forms by hot pressing and extrusion.

In the as-sintered state molybdenum dispersions containing 5% ThO_2 showed an impressive 300% improvement in hardness at 1000°C over molybdenum compacts containing no dispersant. After extrusion at 1850°C, the improvement was 140%. Figure 18.1 illustrates the microstructure of the extruded material.

---

[1] J. A. Burka and J. P. Hammond, *Metals and Ceramics Div. Ann. Progr. Rept. June 30, 1964*, ORNL-3670, pp. 249–50; R. G. Wymer and D. A. Douglas, Jr. (compilers), *Status and Progress Report for Thorium Fuel Cycle Development Dec. 31, 1964*, ORNL-3831, p. 137.

[2] Consists of quenching molten particles of an alloy having a solute that is *soluble* in the *liquid* state but *insoluble* in the *solid* state. Nuclear Metals, Inc., has prepared Th–1.3% Be alloy powder for us by this method.

[3] Exchange student from India, now with Atomic Energy Establishment, Trombay, Bombay, India.

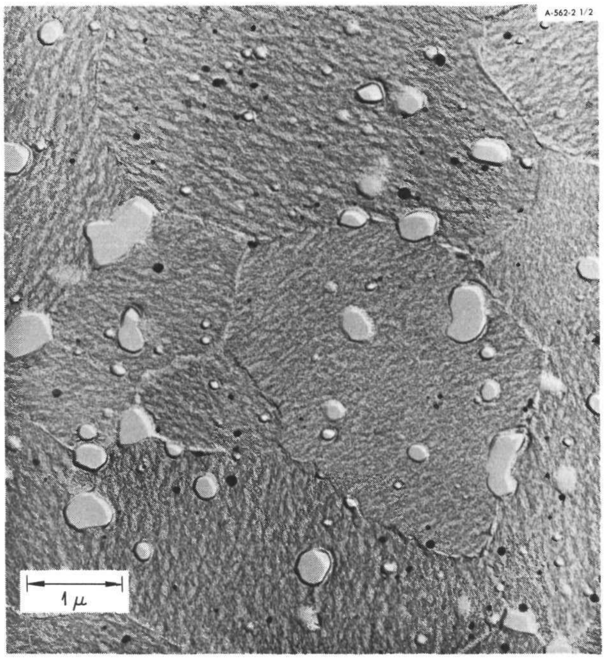

Fig. 18.1. Electron Micrograph of Mo–5% ThO_2 Alloy Processed by the Colloidal Powder Route, Cold Pressed, Sintered at 1900°C, and Extruded at 1850°C. Two-stage replication. 28,000×. Reduced 56.5%.

THORIUM-MATRIX FUELS

Fuels of continuing interest for both epithermal and fast reactors are of the dispersion design[4] using fertile thorium as the matrix and compounds based on ^{233}U or plutonium for the dispersoid. Calculations show that for levels of burnup appropriate for fast reactors, the matrix (by breeding ^{233}U) would contribute about 30% to the total fissioning. Two considerations are important in developing such fuels: chemical compatibility of the dispersoid with the matrix and improvement of permissible temperature and burnup potential of the thorium through enhancement of elevated-temperature strength and introduction of stable ultrafine dispersions for retarding swelling through surface tension-restraint of the fission gases.[5]

Compatibility of Uranium Compounds in Thorium

M. McIlwain[6] J. P. Hammond

Earlier tests on the compatibility of UC, UO_2, and niobium- and graphite-coated UO_2 in thorium

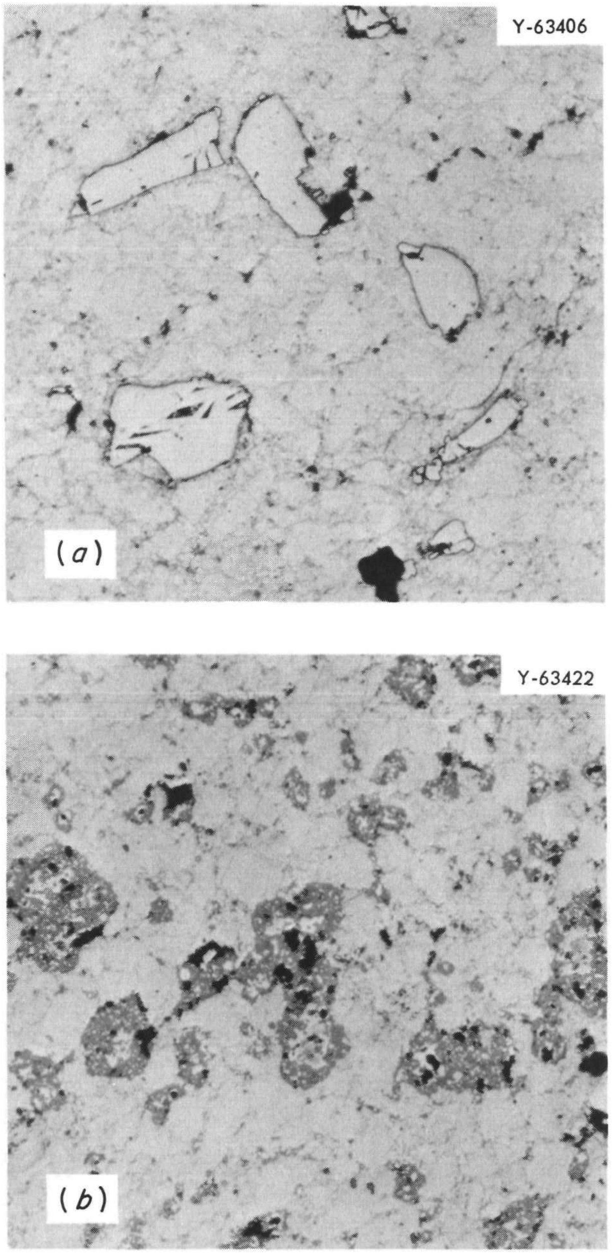

Fig. 18.2. Microstructure of Thorium-Matrix Dispersions After 100 hr at 1000°C Containing (*a*) UB_2 and (*b*) UP. No evidence of reaction is seen for the UB_2 structure, but substantial reaction product formed in the UP particles. Oxalic acid 10% in alcohol. Polish etch. 200×.

---

[4] C. E. Weber, "Progress on Dispersion Elements," *Progr. Nucl. Energy, Ser. V* **2**, 295 (1959).

[5] R. S. Barnes, *A Theory of Swelling and Gas Release for Reactor Materials*, AERE-R-4429 (October 1963).

[6] Now at Spaco, Inc., Huntsville, Ala.

Table 18.1. Chemical Compatibility of Uranium-Bearing Fuel Compounds with Thorium at Elevated Temperatures[a]

Compound	Compound Preparation Method	Reaction Observed After Heating with Thorium for 100 hr		
		600°C	800°C	1000°C
UB_2	Fusion	None	None	None
UB_4	Fusion	None	None	Very slight
US	$H_2S + U$	None	None	Extensive
UP	$PH_3 + U$	None	None	Extensive
(U,Th)C[b]	Fusion	Slight	Extensive	Extensive
$(U,Th)O_2$[b]	Sol microsphere	None	Slight	Extensive
$(U,Th)O_2$[c]	Sol microsphere	None	None	Slight

[a] Samples were fabricated by obliquely blending powders of the compound and thorium ½ hr, cold pressing as ¼-in. pellets, vacuum annealing 8 hr at 300°C to remove lubricants, and cold swaging in Zircaloy-2 tubing. Sections cut from the resulting rod were wrapped in tantalum foil and encapsulated in quartz preparatory to heating 100 hr at temperature.

[b] One atom thorium per atom uranium.

[c] Three atoms thorium per atom uranium.

showed only graphite-coated UO_2 to resist reaction, and its compatibility was marginal.[7] In the interim numerous additional uranium fuel materials became available and were tested. Evaluation was based on degree of reaction observed by metallographic inspection after 100 hr at test temperatures. The results are summarized in Table 18.1.

Although UB_2 was the only compound completely stable at 1000°C, US and UP, attractive from the point of view of uranium density and refractoriness, showed no reaction at 800°C and warrant further consideration. Figure 18.2 illustrates microstructures for the UB_2- and UP-containing samples after the 1000°C heating. Although use of the diboride would require separation of the ^{10}B isotope, this compound is easily prepared from elemental ingredients by fusion, has high uranium density (11.75 g/cm^3) and melting temperature (2440°C), and is expected to show good thermal conductivity.

Dispersion Hardening of Thorium

J. P. Hammond

Thorium-matrix dispersions displaying satisfactory microstructures (<0.1 μ dispersant size and 0.2 to 0.4 μ interspacing)[8] and good creep properties[1] were produced earlier by dry ball-milling ultrafine Vitro thoria in thorium hydride followed by vacuum hot pressing (during which hydrogen was removed) and extrusion. However, milling times of three days and longer were required to achieve needed fineness in the powders, and the hot pressing step, conducted at 1000°C, proved burdensome. Refinements to this process now make it attractive. Improved grinding techniques reduced milling time to one day, and substitution of a sintering operation at 800°C instead of hot pressing contributed to additional control and economy.

---

[7] J. A. Burka and J. P. Hammond, *Metals and Ceramics Div. Ann. Progr. Rept. May 31, 1962*, ORNL-3313, pp. 95–98.

[8] J. A. Burka and J. P. Hammond, *Metals and Ceramics Div. Ann. Progr. Rept. May 31, 1963*, ORNL-3470, pp. 210–12.

Table 18.2. Hot Hardness of Dispersion-Hardened Thorium Alloys

Specimen Number	Method of Hardening	Composition	Hardness[a] (DPHN) at Temperatures (°C) of									
			25	100	200	300	400	500	600	700	750	800
1	None	Thorium[b]	85	45	41	35	33	30	22	15	11	c
2[d]	Alloying	Th–5% Zr	104	93	83	90	77	71	60	42	37	c
3[e]	SLIS	Th–1.3% Be	139	140	105	105	114	86	71	45	37	28
4[f]	SLIS	Th–1.3% Be	108	c	c	c	63	61	56	47	c	29

[a] Values reported represent average of two measurements.

[b] Chemical analysis: 99.8% Th, 340 ppm C, 2000 ppm O, and 180 ppm N.

[c] Not determined.

[d] Thorium has the same chemical content as that used in specimen 1; alloy was prepared by arc-casting.

[e] Thorium same as in specimen 1; alloy prepared by horizontal-jet SLIS method and hot upset extrusion at 600°C.

[f] Same as in specimen 3 and annealed in vacuum 24 hr at 800°C.

A promising alternate method was explored for dispersion strengthening thorium: forming SLIS powder in a Th–1.3% Be alloy by "splat-cooling." Table 18.2 compares hot-hardness results for this dispersion with data for unalloyed thorium and an arc-melted alloy (Th–5% Zr) found to be attractive in earlier work.[9] The alloy prepared by the SLIS method (specimen 3) was as hard as the promising thorium-zirconium alloy (specimen 2) in the temperature range of interest (600 to 800°C). Annealing at 800°C did not appreciably soften this alloy (specimen 4).

---

[9] J. A. Burka and J. P. Hammond, *Evaluation of Thorium-Base Alloys for High Temperature Strength*, ORNL-3777 (April 1965).

19. Fuel Element Development

G. M. Adamson, Jr.

Our objective is to develop the fabrication technology for fuel, cladding, and structural materials with immediate or potential application. Thermochemical deposition of UO_2 and other fuel compounds is being investigated as a possible one-step conversion either from UF_6 or from UCl_5 derived from a fuel recycle process. Potential advantages of low processing temperature, high product purity, and ability to produce various shapes are also incentives for thermochemical deposition of refractory metal alloys. A fuel element fabricated by this technique is a long-range goal of the program.

Also, we are concerned with aluminum-base fuel elements, including the fabrication characteristics and irradiation behavior of UAl_3 dispersions and the performance of UO_2 and U_3O_8 dispersions under conditions of high temperature and burnup.

THERMOCHEMICAL DEPOSITION OF URANIUM DIOXIDE

R. L. Heestand C. F. Leitten, Jr.

A process for direct conversion of UF_6 to UO_2 by a high-temperature reduction-hydrolysis reaction has been reported previously.[1] The UO_2 may be obtained as a solid uniform deposit approaching theoretical density, a dendritic crystalline deposit, or as a submicron powder. Parameters for obtaining the different types of deposit and controlling the stoichiometry of the solid have been published;[2] however, additional experiments on synthesizing UO_2 powders have been conducted due to increasing interest in fabrication behavior of the material.

As-reduced powders generally have an oxygen-to-uranium ratio of approximately 2.080 and fluorine contents as high as 5%. The high fluorine levels suggest the presence of fluorides such as UF_4 or UO_2F_2; however, neither of these compounds has been detected by x-ray or chemical analysis. We believe the high fluorine content is related to the high surface area of the powder (approximately 0.05 μ in diameter), which is shown in Fig. 19.1. Heating to 1000°C for 1 hr in wet hydrogen reduces the fluorine content to less than 100 ppm and adjusts the oxygen-to-uranium ratio to 2.005. During this treatment, the particle size increases to approximately 9 μ in diameter, as shown in Fig. 19.2. Pellets that were cold pressed from the hydrogen-fired material and sintered at 1700°C exhibited a density of 93%, a small grain size, and uniform shrinkage. We are characterizing the sintering behavior of the material further, and UF_6 enriched 2.5% in ^{235}U has been obtained for preparation of irradiation specimens.

Solid coatings of UO_2 have been deposited on thoria pellets in thicknesses up to 0.020 in. Figure 19.3 shows pellets of this type, in which a fertile thoria body bears a thin layer of fissile material. After irradiation, the UO_2 coating can be readily removed to simplify reprocessing. Fully enriched UF_6 has been obtained for preparation of irradiation specimens to demonstrate the behavior of this type of fuel.

---

[1] R. L. Heestand and C. F. Leitten, Jr., *Metals and Ceramics Div. Ann. Progr. Rept. June 30, 1965*, ORNL-3870, pp. 85–88.

[2] R. L. Heestand and C. F. Leitten, Jr., *Nucl. Appl.* 1, 584–88 (1965).

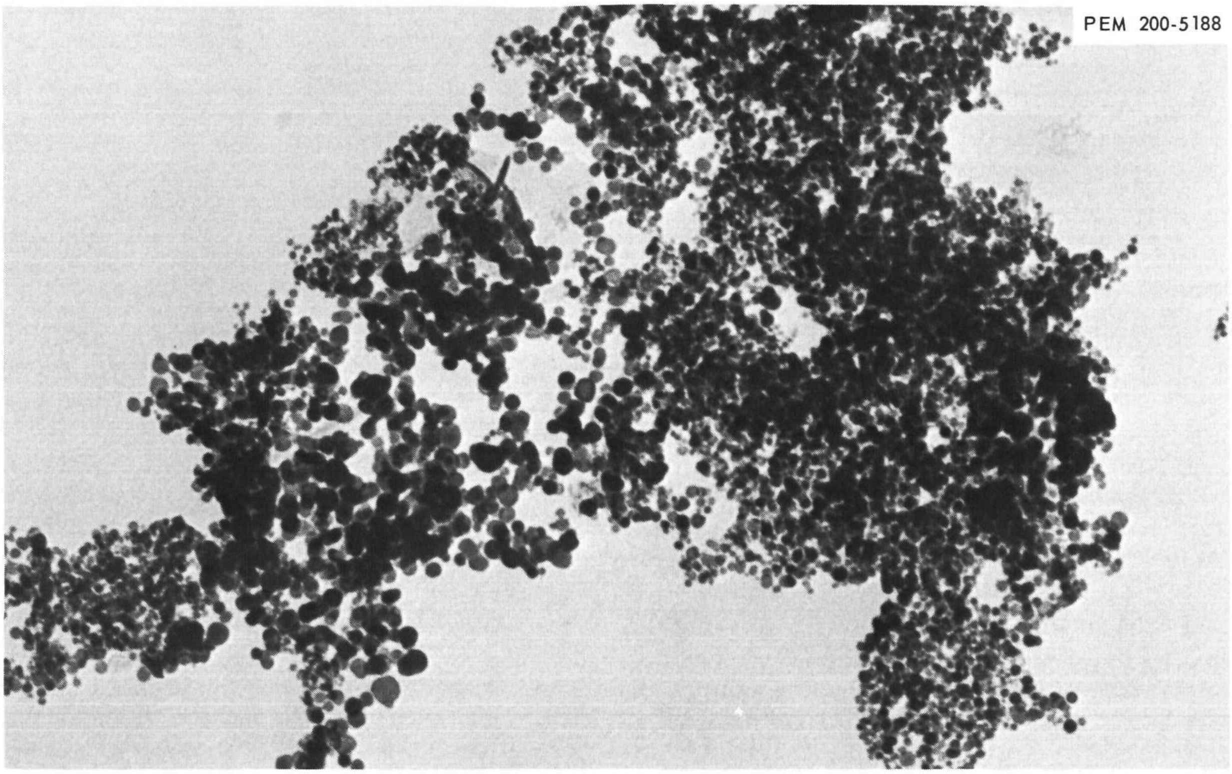

Fig. 19.1. As-Produced Uranium Dioxide Powder. Particle size approximately 0.05 μ. 165,000×.

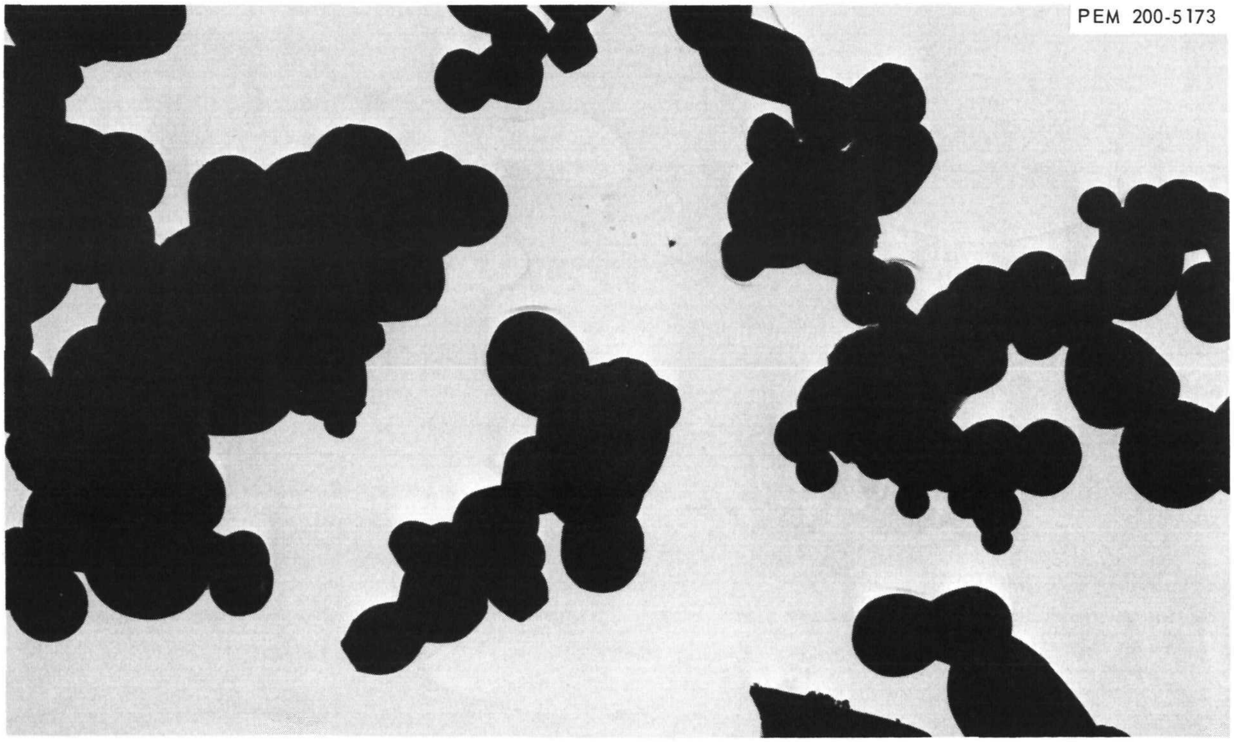

Fig. 19.2. Uranium Dioxide Powder Reduced 1 hr at 1000°C in Wet Hydrogen. Particle size approximately 9 μ. 25,000×.

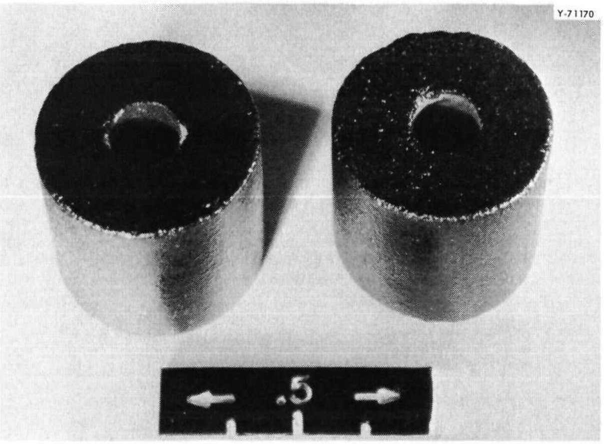

Fig. 19.3. Thoria Pellets 0.400 in. in Diameter by 0.400 in. High, Thermochemically Coated with 0.020 in. UO_2.

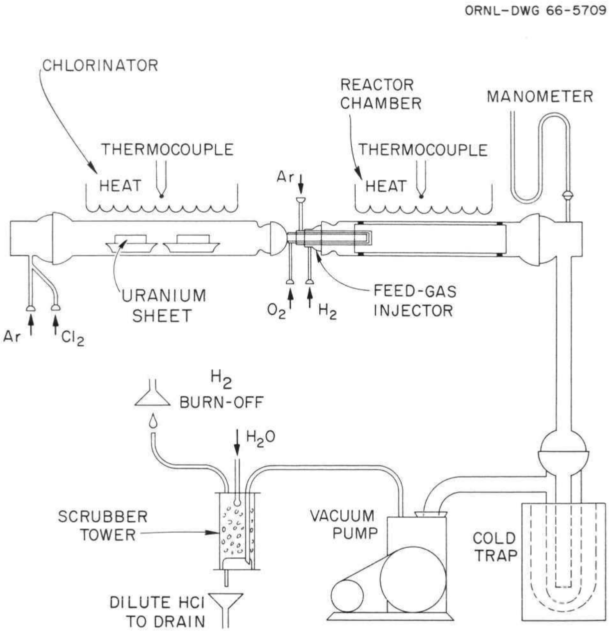

Fig. 19.4. Schematic of Thermochemical Deposition System for Direct Conversion of UCl_5 to UO_2.

CONVERSION OF URANIUM CHLORIDES TO URANIUM DIOXIDE

F. H. Patterson W. C. Robinson, Jr.
C. F. Leitten, Jr.

Our purpose was to demonstrate the feasibility of converting uranium chlorides, obtained from the chloride volatilization process developed for Zircaloy-clad fuels,[3] to uranium dioxide powder by a simultaneous reduction and hydrolysis. To simplify material handling in these experiments, the uranium chlorides were obtained by "in place" chlorination of depleted uranium sheet. The experimental apparatus is shown schematically in Fig. 19.4. Chlorine diluted with argon carrier was passed over uranium sheet at 450°C and a pressure less than 4 torrs. The resulting uranium chlorides (mostly UCl_5) were delivered through an injector to the reaction chamber and mixed with oxygen. An argon blanket minimized reaction at the injector tip. In a series of experiments, the reaction chamber was maintained at temperatures in the range 660 to 960°C and pressures of 1 to 6 torrs. X-ray diffraction showed that the powder deposited at temperatures below 815°C consisted mostly of U_3O_8 with a small amount of UO_2. Above this temperature mostly microfine UO_2 powder and a small amount of U_3O_8 were obtained. The U_3O_8 was readily reduced to UO_2 by heating at 1000°C in wet hydrogen.

These studies established the feasibility of reconverting the product of the chloride volatility process to fuel material by thermochemical deposition. A topical report[4] is being prepared and includes detailed thermodynamic calculations for the reactions involved.

DEPOSITION OF REFRACTORY ALLOYS

J. I. Federer C. F. Leitten, Jr.

Thermochemical deposition studies of tungsten-rhenium alloys have continued for the purpose of developing an alternate fabrication process for refractory-metal cladding for high-temperature fuel elements. Other applications are source

---

[3] R. K. Steunenberg and R. C. Vogel, chap. 6 in *Reactor Handbook*, 2d ed., vol. 2, *Fuel Reprocessing* (ed. by S. M. Stoller and R. B. Richards), Interscience, New York, 1961.

[4] F. H. Patterson, W. C. Robinson, Jr., and C. F. Leitten, Jr., *Conversion of Uranium Chlorides to Urania by Gas-Phase Reduction Hydrolysis*, in preparation.

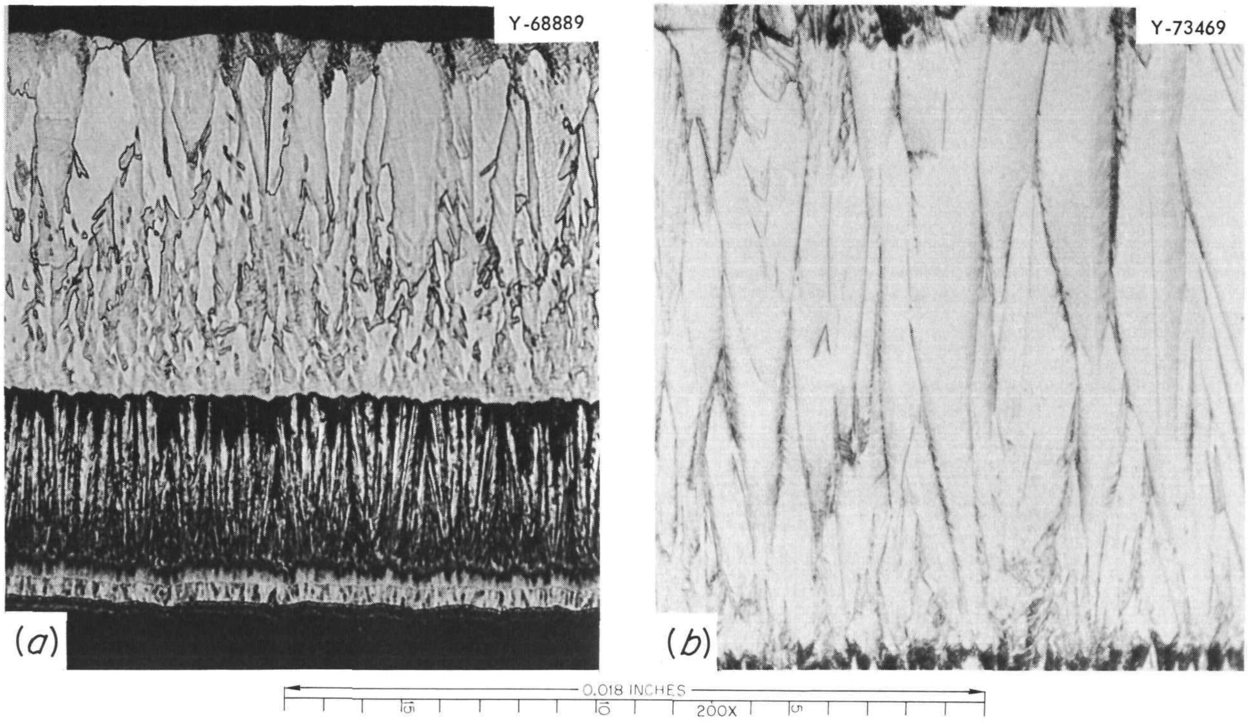

Fig. 19.5. Alloy W–25% Re Deposited in a Moving Hot Zone. Etchant: 50 parts concd NH_4OH and 50 parts 30% H_2O_2. (*a*) Deposited at 800°C without a WF_6-ReF_6 injector. (*b*) Deposited at 900°C with an injector.

material for mechanical working, such as refractory alloy tube shells and thermionic converter components.[5] Thermochemical deposition of tungsten is reported in Part II, Chap. 16 of this report.

The principal effort during the past year was directed toward improvement of the compositional uniformity of the alloy deposits. The deposition process, hydrogen reduction of WF_6 and ReF_6, has been conducted in a 1-in.-long moving hot zone to avoid axial nonuniformity of composition, which characterized tubular deposits prepared in a 12-in.-long stationary hot zone.[6] Alloys of different composition, however, deposited in the temperature gradient leading to the hot zone, and movement of the hot zone resulted in a layered structure, compared in Fig. 19.5 with alloy deposited more uniformly as described below. The layers shown in Fig. 19.5*a* have different rhenium contents as evidenced by vastly different etching rates. This structure emphasizes that the ratio of WF_6 to ReF_6 must remain constant during reduction to yield homogeneous alloys.

Thermodynamic equilibrium calculations indicate that the composition of the deposits will correspond to the metal content of the WF_6-ReF_6 mixture if the correct combination of temperature, pressure, and gas composition is used. Therefore, we are studying reaction at higher temperatures (700 to 1000°C) in an apparatus similar to that used previously except that an injector delivers the WF_6-ReF_6 mixture directly into the hot zone of $\frac{5}{8}$-in.-ID tubular steel mandrels. Smooth surface textured W–25% Re alloys were deposited with an axial variation in rhenium content of ±1% and metal recoveries of 100%. The microstructure of one of these deposits is shown

---

[5] J. I. Federer, R. L. Heestand, F. H. Patterson, and C. F. Leitten, Jr., "Thermochemical Deposition of Refractory Metals, Alloys, and Compounds for Application in Thermionic Devices," paper No. 18 presented at the International Conference on Thermionic Electrical Power Generation, London, England, Sept. 20–24, 1965.

[6] J. I. Federer and C. F. Leitten, Jr., *Metals and Ceramics Div. Ann. Progr. Rept. June 30, 1965*, ORNL-3870, pp. 88–91.

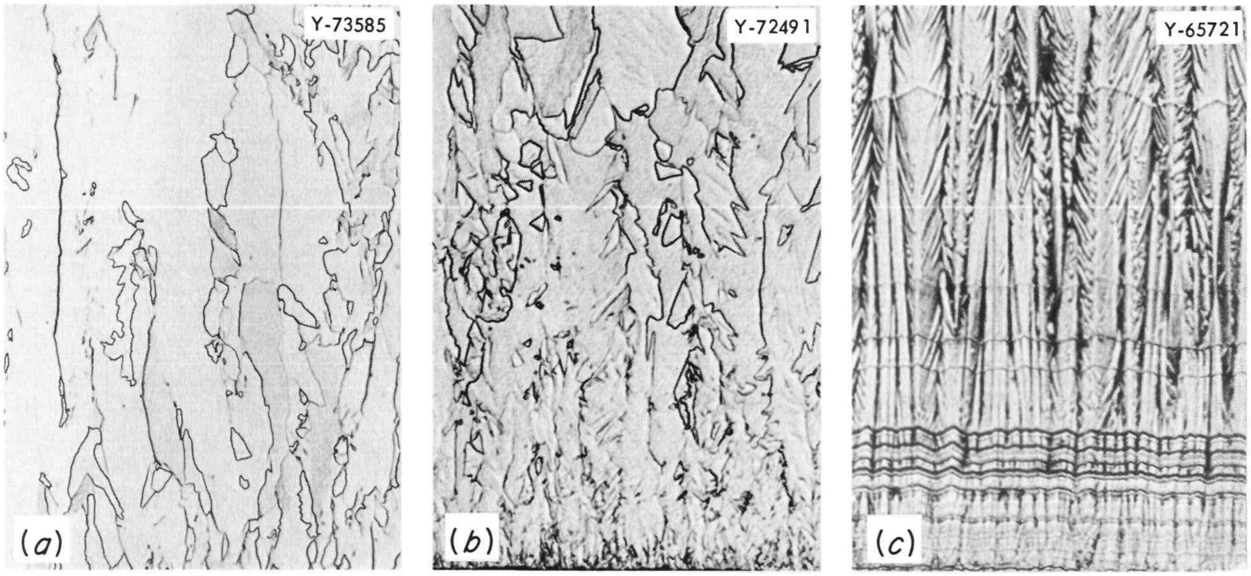

Fig. 19.6. Tungsten-Rhenium Alloys Deposited at 600°C in the External Coating Apparatus. (*a*) 2.4% Re; 200×. (*b*) 8.2% Re, 250×. (*c*) 23.3% Re, 250×. Etchant: 50 parts concd NH_4OH and 50 parts 30% H_2O_2.

in Fig. 19.5*b*. The columnar structure still shows slight evidence of layers of different composition, but it represents a significant improvement over the deposit prepared at a lower temperature without an injector (Fig. 19.5*a*). The moving-hot-zone–injector technique is now sufficiently developed that sheet specimens can be prepared for evaluation of mechanical properties.

Another technique being investigated for preparing tungsten-rhenium alloys is deposition on the outer surface of a heated mandrel that is contained in a relatively large mixing chamber. This design is intended to minimize the nonuniform depletion of ReF_6, which occurs at low temperatures during deposition on the inner wall of a relatively long narrow tube. Tungsten alloys containing up to 25% Re and rhenium alloys containing about 10% W were deposited at 600°C. The alloy containing nominally 25% Re averaged $25.2^{+1.2}_{-1.9}\%$ over a 10-in. length. These results indicate that satisfactory alloys for evaluation of mechanical properties can be deposited by the external coating technique.

Microstructural differences among the tungsten alloys are shown in Fig. 19.6. The grain structure of the alloy containing 2.4% Re is similar to that of unalloyed tungsten except that the columnar structure is less well defined. Further disruption of the columnar structure is evident in the alloy containing 8.2% Re. The alloy containing 23.3% Re has a mainly columnar grain structure, but it has layer lines, which are often observed in externally deposited alloys of high rhenium content. The change in microstructure with increasing rhenium content may be associated with an increasing amount of the beta-tungsten structure.[6,7] This structure coexists with the tungsten-rhenium solid solution in alloys deposited at temperatures to at least 1000°C. Conditions of occurrence and properties of the beta-tungsten structure are being studied because of probable effects on mechanical properties.

FABRICATION OF ENRICHED UAl_3 DISPERSION FUEL PLATES

W. J. Werner M. M. Martin
J. H. Erwin

The uranium-aluminum intermetallic fissile material UAl_3 was fabricated successfully into four fuel elements for the Oak Ridge Research Reactor.[8]

---

[7] J. I. Federer and C. F. Leitten, Jr., *Nucl. Appl.* 1, 575–80 (1965).

[8] Previous work reported by W. J. Werner, J. H. Erwin, M. M. Martin, and C. F. Leitten, Jr., *Metals and Ceramics Div. Ann. Progr. Rept. June 30, 1965*, ORNL-3870, pp. 96–98.

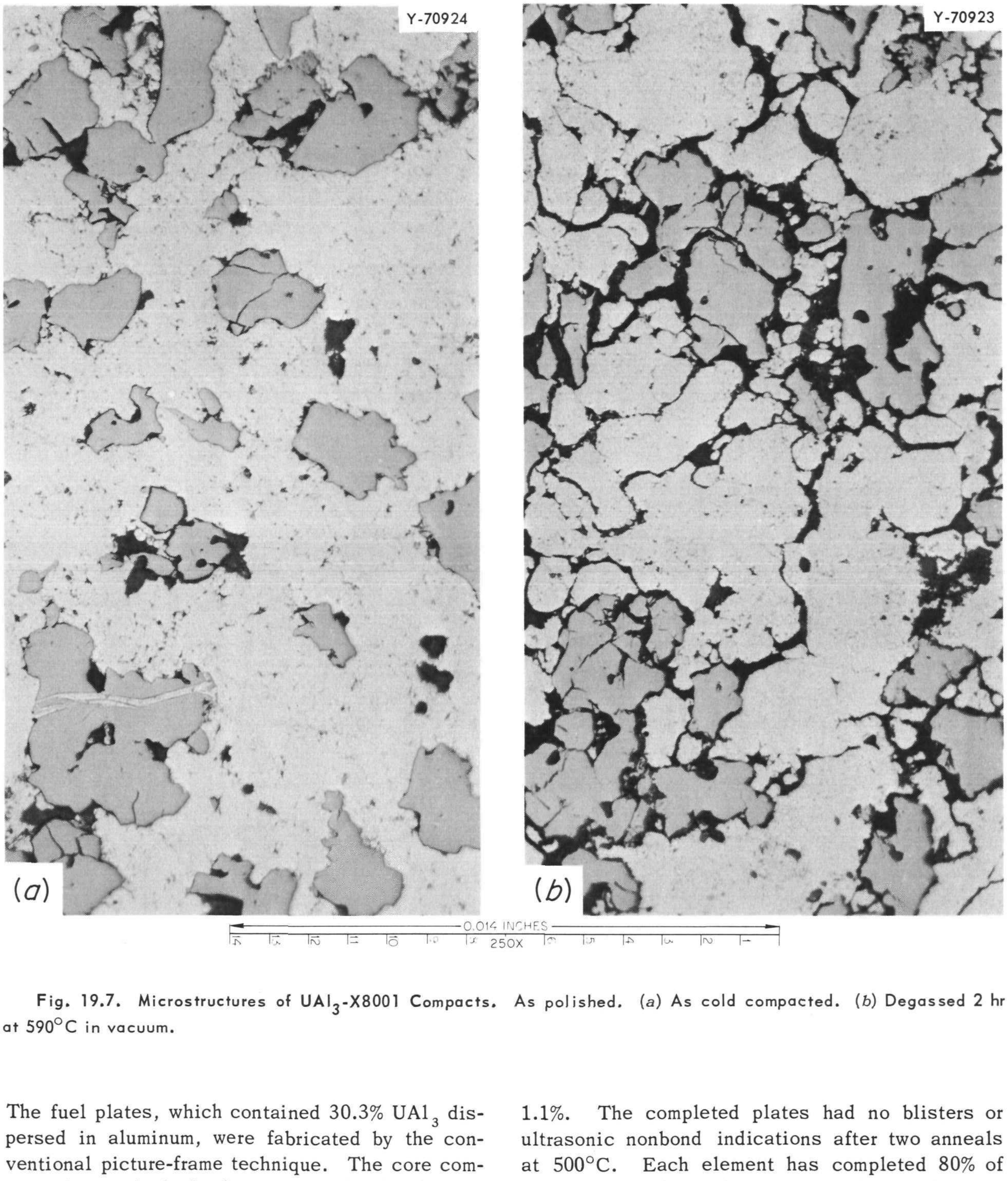

Fig. 19.7. Microstructures of UAl_3-X8001 Compacts. As polished. (*a*) As cold compacted. (*b*) Degassed 2 hr at 590°C in vacuum.

The fuel plates, which contained 30.3% UAl_3 dispersed in aluminum, were fabricated by the conventional picture-frame technique. The core compact for each fuel plate was individually prepared by dry blending UAl_3 and aluminum powders, cold compacting the mixture at 22.5 tons/in.^{2}, and degassing the dense rectangular shape at a pressure less than 5×10^{-2} torr for 2 hr at 590°C. Average growth during degassing was 1.1%. The completed plates had no blisters or ultrasonic nonbond indications after two anneals at 500°C. Each element has completed 80% of the planned 60 at. % burnup without indication of failure. Postirradiation examination of one spent element will begin soon.

Five special ATR fuel elements containing UAl_3 as the fissionable material have been fabricated. The plates have a split fuel core with

Table 19.1. Comparison of Average Growth of Fuel-Aluminum Compacts During Vacuum Degassing at 590°C

Type of Compact	Composition (wt %)	Volume Change (%)
ATR UAl_3-Al-B_4C	51.1 UAl_3, 48.7 X8001 Al, 0.2 B_4C	14.44
ATR U_3O_8-Al-B_4C	44.7 U_3O_8, 55.1 X8001 Al, 0.2 B_4C	0.84
ORR UAl_3-Al	30.3 UAl_3, 69.7 101 Al	1.12

provision for inserting a thermocouple in the aluminum section between the core layers. Stoichiometric UAl_3 for these elements was produced according to procedures developed for the four ORR fuel elements mentioned above, and plate fabrication techniques were similar to those used for production of HFIR-ATR irradiation test miniature plates.[9] The fuel compacts swelled during vacuum degassing prior to billet assembly. Figure 19.7 compares the structure of an as-cold-pressed compact with a compact that was vacuum degassed for 2 hr at 590°C. The latter exhibited a volume change of about 14% and considerable grain-boundary separation or cracking. Table 19.1 compares the average growth of these compacts with ORR fuel element compacts and other ATR compacts in which U_3O_8 was the fissile material. The difference in volume change is not attributed to UAl_3 concentration alone but to differences in the two batches of UAl_3 used for ORR and ATR compacts. Compacts having the ORR composition but containing UAl_3 prepared for the ATR fuel elements swelled several times more than had been observed previously. In addition, the predicted overall growth for conversion of UAl_3 to a phase of composition $UAl_{4.5}$ is only 0.65%.

The cause of swelling in ATR UAl_3 compacts during degassing is unknown. A study of all variables indicates that the amount of swelling decreases with decreasing temperature and UAl_3 content. Studies are continuing to determine the swelling mechanism through the use of gas chromatography, the electron microprobe, x-ray diffraction, and the hot-stage metallograph. Meanwhile, swelling was decreased in a batch of experimental fuel compacts by degassing at 525°C, at which temperature about 4% growth occurred. Compacts processed in this manner were successfully rolled to the desired configuration with no evidence of blistering or nonbond indications.

IRRADIATION TESTING OF ALUMINUM-BASE MINIATURE FUEL PLATES

A. E. Richt M. M. Martin

In cooperation with the Phillips Petroleum Company, a series of aluminum-base miniature test plates were fabricated for determining the influence of high-temperature irradiation to high burnups on the dimensional and chemical stability of U_3O_8 and UO_2 dispersions. The fissile materials were particles of U_3O_8 and niobium-coated UO_2–15% ZrO_2 dispersed in a matrix of X8001 aluminum and roll bonded at 500°C with Alclad 6061 aluminum. The design of the miniatures, which included instrumented as well as standard plates, and the fabrication results were previously reported.[9]

Testing of the fuel specimens began in the later part of 1964 and was completed by mid-1965. The miniatures received maximum burnups in the range of 16 to 17 $\times$ 10^{20} fissions/cm^3 at cladding-film interface temperatures of 240 to 265°C without indication of failure.

Examination of the U_3O_8-bearing fuel specimens (the reference HFIR and ATR fuel material) revealed no evidence of unexpected microstructural changes. Reaction between the U_3O_8 fuel particles and the aluminum matrix was apparent in all specimens; however, the extent of reaction appeared to be primarily a function of the irradiation temperature, not fuel burnup. This effect is clearly shown in Fig. 19.8, where a specimen irradiated to 6.3 $\times$ 10^{20} fissions/cm^3 at 110°C reacted less than an identical specimen irradiated to 3.9 $\times$ 10^{20} fissions/cm^3 at 165°C. Significantly greater reaction occurred in a specimen irradiated to 9.4 $\times$ 10^{20} fissions/cm^3 at 180°C, and complete reaction occurred after 16.1 $\times$ 10^{20} fissions/cm^3 at 240°C, as shown in Fig. 19.9.

---

[9] M. M. Martin, W. J. Werner, and C. F. Leitten, Jr., *Fabrication of Aluminum-Base Irradiation Test Plates*, ORNL-TM-1377 (February 1966).

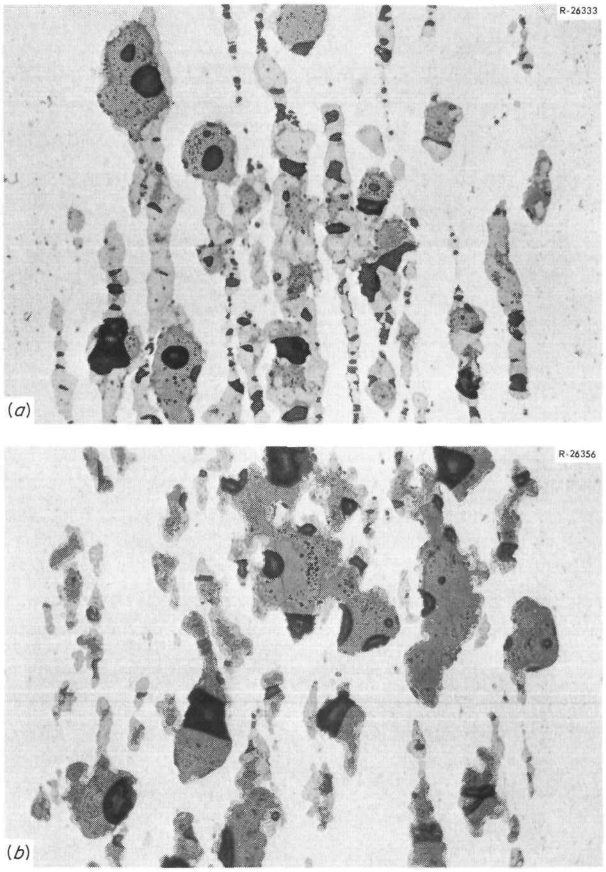

Fig. 19.8. Effect of Temperature upon the Reaction of U_3O_8 with Aluminum During Irradiation. 250×. (*a*) Irradiated to 3.9×10^{20} fissions/cm^3 at 165°C. (*b*) Irradiated to 6.3×10^{20} fissions/cm^3 at 110°C. Reduced 50%.

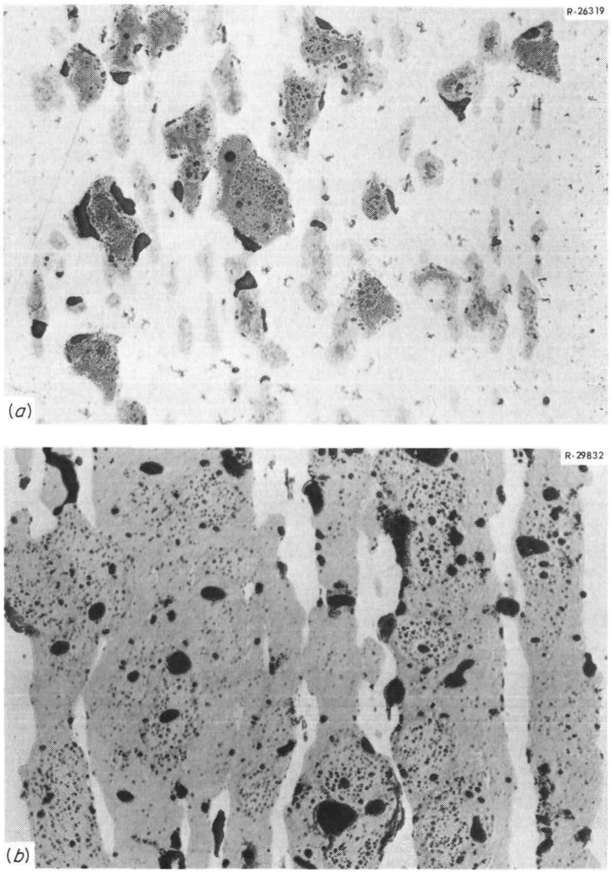

Fig. 19.9. Microstructures of Al–41% U_3O_8 Fuel Specimens After Irradiation. As polished. 250×. (*a*) To 9.4×10^{20} fissions/cm^3 at 180°C. (*b*) To 16.1×10^{20} fissions/cm^3 at 240°C. Reduced 50%.

The burnup level and test temperature achieved by the latter test specimen without evidence of gross failure are both significantly higher than the maximum conditions expected in HFIR.

The specimens fueled with the niobium-coated UO_2-ZrO_2 fuel particles (a substitute material for HFIR) exhibited a number of interesting microstructural changes. Figure 19.10 shows that the niobium coating successfully prevented reaction between the fuel particles and the aluminum matrix during irradiation. The extent of fission-gas porosity in the fuel particles was directly proportional to the fuel burnup. Some reaction between the niobium coating and the aluminum matrix was evident in the higher performance specimens; however, this effect is attributed to the higher irradiation temperatures and not to a burnup effect. Measurements of the fuel particle diameter showed that the UO_2-ZrO_2 particles increased in volume at a rate of 1.3% per atom percent of ^{235}U fissioned. The particles did retain the fission products and remain spherical with this degree of severe swelling, but they offer no major advantage over the reference fuel. Compared to other fuels, fabrication costs also make the use of this fuel unattractive.

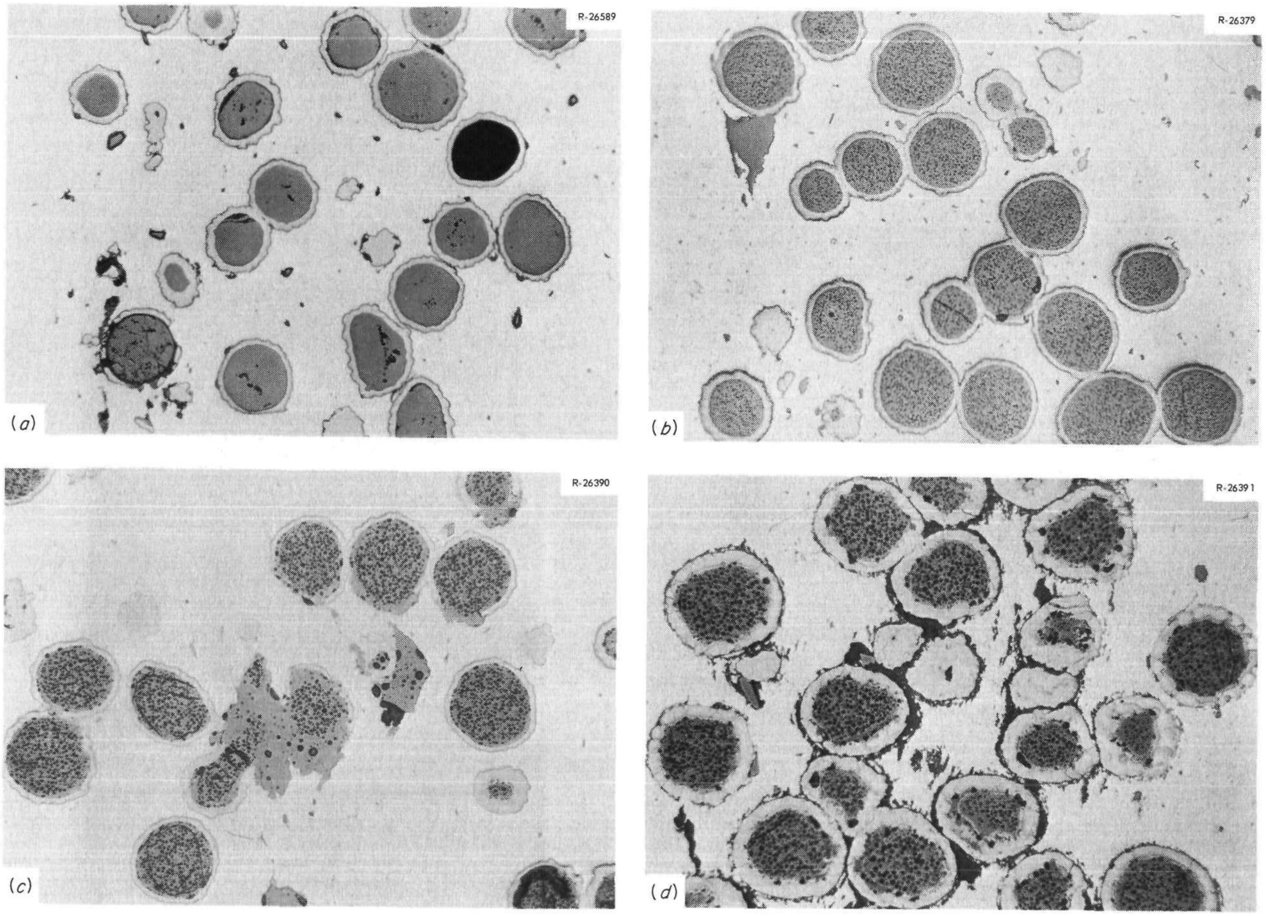

Fig. 19.10. Typical Appearance of Niobium-Coated UO_2-ZrO_2 Fuel Particles in HFIR Irradiation Test Plates. As polished. 250×. (*a*) As fabricated. (*b*) After 6.9×10^{20} fissions/cm^3 at 215°C. (*c*) After 8.8×10^{20} fissions/cm^3 at 390°F. (*d*) After 17.0×10^{20} fissions/cm^3 at 270°C. Reduced 49%.

20. Mechanical Properties

J. R. Weir, Jr.

Our general objectives center around studies of the effects reactor service environments have on the engineering mechanical properties of materials. Our work is so oriented that when we observe important effects on the properties of materials we then investigate potential ways to eliminate the deleterious effects. Our research in the past year has continued to emphasize the elevated-temperature radiation-induced embrittlement of engineering alloys.

Investigations of the mechanical properties of materials for specific applications are reported in Chaps. 14, 16, 22, 24, 30, 33, and 35 of this report.

SOLUTIONS TO THE PROBLEMS OF HIGH-TEMPERATURE IRRADIATION EMBRITTLEMENT[1]

W. R. Martin J. R. Weir, Jr.

The irradiation of stainless steels at temperatures in the range of 600°C and above results in an embrittlement of the alloy that is significantly different from the neutron displacement damage that is of principal importance at temperatures below 600°C. This embrittlement at elevated temperatures does not necessarily affect the strength of an alloy, measured as the stress necessary to produce a given value of strain. The embrittlement can be severe, and ductilities less than 1% have been observed for creep conditions.

Irradiation affects the ability of the alloy to resist intergranular fracture, and most experiments point to the principal cause as one related to the production of helium from two sources. The first one is the $^{10}\mathrm{B}(n,\alpha)$ reaction with neutrons having thermal energies, and the second is reactions between the major alloy constituents and fast neutrons having energies near 3 Mev. Solutions to the problem of embrittlement are then related to (1) alterations of the unirradiated alloy that affect the process of intergranular fracture and (2) modifications of the alloy that reduce the amount of helium that is located in the grain boundaries of the irradiated alloy.

Grain size and whether the structure is annealed or cold worked are two metallurgical variables that greatly affect the ductility of alloys in the temperature range in which they fracture intergranularly. After irradiation, a fine-grained alloy can be an order of magnitude more ductile than the coarse grained. Grain sizes in the range ASTM 8 to 11 are preferred.[2]

To reduce the amount of helium at the grain boundary, one must produce the helium at sites other than the grain boundary and prevent the movement of helium to the grain boundary. A reduction in boron content[3] can reduce the amount of helium produced but is not a complete solution because of the helium generated from Ni, Fe, Cr, N, and other elements. Thus, a more suitable approach would appear to be a desegregation of boron and the production of helium sinks within the matrix of the grains; these will greatly reduce the quantity of helium moving to the grain boundary. Titanium additions to stainless steel are believed to form complex metal borides dispersed homogeneously within the matrix, and the

---

[1] Abstract of paper presented at the Third International Symposium on the Effects of Radiation on Structural Metals, June, 1966, Atlantic City, N.J.

[2] W. R. Martin and J. R. Weir, *J. Nucl. Mater.* 18(2), 108–18 (1966).

[3] W. R. Martin, J. R. Weir, R. E. McDonald, and J. C. Franklin, *Nature* 208(5005), 73 (1965).

precipitate-matrix interfaces serve as a depository for helium.[4] Other approaches for improving high-temperature ductility are available, such as proper aging of existing grades of stainless steels (see next section).

Garofalo[5] has enumerated the conditions for a grain-boundary precipitate to be beneficial for creep-rupture properties. A 100-hr heat treatment at 800°C following a 1-hr solution anneal at 1036°C produces the desired grain-boundary carbide distribution in type 304 stainless steel. The postirradiation creep rupture time and ductility of the aged material at 650°C are improved by factors of approximately 40 and 3, respectively, over those of the unaged material.

IRRADIATION EMBRITTLEMENT OF LOW- AND HIGH-CARBON STAINLESS STEELS AT 700, 800, AND 900°C[6]

W. R. Martin J. R. Weir, Jr.

Reactors, such as the nuclear superheat, gas cooled, and liquid metal, require structural and cladding material applications in the temperature range of 500 to 900°C. We have previously shown that the postirradiation ductility of type 304 stainless steel at elevated temperature is practically independent of irradiation temperature up to 700°C. Our studies of irradiation temperature have now been extended into the temperature range of 700 to 900°C.

In general, the ductility of the irradiated alloy decreases with increasing irradiation temperature when these ductilities are determined at tensile test temperatures within the 650 to 842°C temperature range. A marked difference in the ductility of low- and high-carbon irradiated stainless steels was observed which appears to be related to the quantity of grain-boundary carbides.

These data are interpreted as indicating that grain-boundary carbides formed in irradiated material in this temperature range are capable of increasing the stress at which wedge-type grain-boundary cracks are nucleated and also reducing the rate of crack propagation. Thus, it appears that agglomerated carbides in the grain boundary are capable of reducing the magnitude of irradiation embrittlement.

CREEP AND STRESS-RUPTURE PROPERTIES OF TITANIUM-MODIFIED TYPE 304 STAINLESS STEEL

E. E. Bloom W. R. Martin

Stress-rupture data have been accumulated for two commercial heats of type 304 stainless steel containing 0.15% Ti. The carbon levels of the two heats are 0.014 and 0.05%. After annealing for 1 hr at 1036°C, strengths at 704 and 815°C were increased over those of regular type 304 stainless steel. Ductilities, as measured by total elongation at fracture, were increased by the addition of titanium when the rupture life was less than 1000 hr. However, for rupture lives greater than 1000 hr, ductilities of regular and titanium-modified stainless steels were approximately equal.

The effect of aging for 1000 hr at 600 and 700°C upon the stress-rupture properties at 704°C is shown in Table 20.1. In general, aging decreases the rupture life, increases the minimum creep rate, and increases the ductility. Metallography indicated that when tested in the solution-annealed condition the fracture was intergranular, with numerous triple-point voids present in the area adjacent to the fracture and little evidence of deformation within the matrix. An aged specimen, tested at the same stress, failed transgranularly with a large amount of strain occurring in the matrix. Also, fewer and smaller voids were formed in the aged specimen.

IRRADIATION EMBRITTLEMENT OF WELDS AND BRAZES AT ELEVATED TEMPERATURES[7]

W. R. Martin G. M. Slaughter[8]

Type 304 stainless steel and Inconel 600 welded and brazed joints were irradiated in the Oak Ridge

---

[4] W. R. Martin, *Metals and Ceramics Div. Ann. Progr. Rept. June 30, 1965*, ORNL-3870, pp. 143–44.

[5] F. Garofalo, *Fundamentals of Creep and Creep-Ruptures in Metals*, p. 224, Macmillan, New York, 1965.

[6] Abstract of ORNL-TM-1516 (June 1966).

[7] Abstract of ORNL-TM-1526 (July 1966); accepted for publication in the *Welding Journal*.

[8] Welding and Brazing Group.

Table 20.1. Creep-Rupture Properties of Titanium-Modified[a] Type 304 Stainless Steel Tested at 704°C in Argon

Carbon (%)	Condition	Stress (psi) $\times 10^3$	Rupture Life (hr)	Minimum Creep Rate (%/hr)	Elongation (%)	Reduction in Area (%)
0.05	As solution annealed	15	2150	0.0063	22.7	31.3
		20	302	0.043	36.3	44.5
	Aged 1000 hr at 600°C	15	>2000	0.0055		
		20	60.1	0.452	60.3	89.1
	Aged 1000 hr at 700°C	15	126.8	0.226	69.6	49.2
		20	13.2	2.82	58.9	71.3
0.014	As solution annealed	15	362.4	0.0425	39.1	44.3
		20	19.0	2.30	69.9	69.4
	Aged 1000 hr at 600°C	15	252.0	0.143	54.6	47.9
		20	14.1	3.40	75.1	95.5
	Aged 1000 hr at 700°C	15	151.5	0.257	66.2	65.0
		20	11.3	3.46	59.8	62.9

[a] Containing 0.15% Ti. Two heats are distinguished by different carbon contents.

Research Reactor and then tested in short-time tests at several deformation temperatures ranging from 20 to 900°C. The welds were made with the gas tungsten-arc process using type 308 stainless steel and ERN 62 filler metals. The brazes were made using AWS BNi-7 filler metal (Ni-Cr-P).

The base metal and welds in both materials were embrittled by irradiation but to a lesser degree in stainless steel than in Inconel. In general, the welds in both materials behaved in a manner equal to or better than the corresponding base metals. Irradiation embrittlement was also observed in the brazed joints. The toughness of the braze joints is greatly reduced at temperatures of 270°C and above for the Inconel and 470°C and above for the stainless steel.

FAST-REACTOR IRRADIATION EFFECTS ON TYPES 316L AND 17-4 PH STEELS[9]

W. R. Martin	J. A. Basmajian[10]
J. R. Weir, Jr.	L. D. Kirkbride[10]

The effect of irradiation on the elevated-temperature mechanical properties[11,12] of the stainless steels is primarily one associated with a reduction in tensile ductility without significant change in yield strength. Postirradiation and in-reactor creep properties of these alloys are affected because the embrittlement reduces the time to rupture without a significant change in secondary creep rate. This irradiation embrittlement has been generally attributed[3,12,13] to (n,α) reactions due to both thermal and fast neutrons. The $^{10}B(n,\alpha)$ reaction with thermal neutrons generates the largest portion of the helium produced during irradiation of commercial heats of

---

[9] Summary of paper presented at the American Nuclear Society meeting, Denver, Colo., June 20–23, 1966.

[10] Los Alamos Scientific Laboratory.

[11] W. R. Martin and J. R. Weir, "The Effect of Irradiation Temperature on the Postirradiation Stress-Strain Behavior of Stainless Steel," p. 251 in *Flow and Fracture of Metals and Alloys in Nuclear Environments, Spec. Tech. Publ. No. 380*, American Society for Testing and Materials, Philadelphia, Pa., 1965.

[12] P. C. L. Pheil and D. R. Harries, "Effect of Irradiation in Austenitic Steels and Other High-Temperature Alloys," p. 187 in *Flow and Fracture of Metals and Alloys in Nuclear Environments, Spec. Tech. Publ. No. 380*, American Society for Testing and Materials, Philadelphia, Pa., 1965.

[13] P. R. B. Higgins and A. C. Roberts, *Nature* 206(4900), 1250 (1965).

Table 20.2. Comparison of Fast-Reactor Irradiation Effects on an Austenitic Stainless Steel and Age-Hardening Steel[a]

Deformation Temperature (°C)	Yield Strength[b] (psi)		True Uniform Strain[b] (%)		Total Elongation[b] (%)	
	316L	17-4 PH	316L	17-4 PH	316L	17-4 PH
	$\times 10^3$	$\times 10^3$				
25	34.2 (33.1)	148.0 (162.0)	51.7 (51.0)	7.8 (6.9)	75.6 (72.2)	12.6 (10.2)
400	19.6 (19.0)	113.2 (158.0)	33.1 (33.5)	5.7 (4.4)	43.7 (43.6)	9.9 (6.3)
500	20.5 (17.8)	89.5 (109.8)	34.0 (33.5)	3.1 (2.7)	44.4 (44.8)	8.0 (8.2)
600	19.7 (19.8)	51.3 (70.5)	29.3 (29.7)	4.2 (3.1)	38.8 (40.8)	18.1 (18.8)
700	18.6 (15.6)	33.5 (23.1)	17.7 (18.3)	(4.1)	27.0 (42.7)	16.2 (33.4)
800	15.0 (13.2)	15.2 (15.9)	4.5 (14.0)	4.8	7.3 (42.3)	37.8 (44.0)
900	10.8 (11.3)	10.3 (13.8)	1.8 (14.6)	3.9 (3.4)	3.7 (59.3)	18.3 (16.3)

[a] Irradiated specimens were exposed to a total neutron dose of 2×10^{21} neutrons/cm^2 at approximately 525 ±25°C in LAMPRE.

[b] Values for unirradiated specimens are in parentheses.

structural alloys in thermal reactors. Since most of the boron generally segregates to the grain boundary, the helium is produced at the grain boundaries, where it affects the process of intergranular fracture. However, all the elements undergo an (n, α) reaction at some rate, and in the absence of thermal neutrons the helium generated by the fast neutrons is produced throughout the grains. Therefore, the distribution of helium in a material irradiated in a thermal reactor could be different from that of the same material irradiated in a fast-neutron spectrum only.

It is of great interest, therefore, to determine the postirradiation tensile properties of alloys irradiated in a fast-neutron spectrum. Type 316L and 17-4 PH steels were irradiated at Los Alamos in the LAMPRE at approximately 400°C to a total dose of 2×10^{21} neutrons/cm^2. The strength and ductility of the two alloys are given in Table 20.2. The 17-4 PH is much more ductile than the type 316L stainless steel at 800 and 900°C. Although the unirradiated 17-4 PH samples did not undergo the identical thermal history as the irradiated samples, no significant change in strength of either type 316L or 17-4 PH was observed. The ductilities of the type 316L stainless steel at 700, 800, and 900°C were reduced, while a significant reduction occurred only at 700°C for the 17-4 PH. The effect of irradiation was therefore less for the 17-4 PH than for the type 316L stainless steel.

The improved properties of the age-hardening alloy compared with those of the solid-solution alloy might be due to the intergranular precipitates present in the 17-4 PH. Those precipitates may serve as sinks to which the helium would migrate and hence remain away from the grain boundaries. A solid-solution alloy or an alloy in which precipitates are intergranular will have fewer obstacles to the movement of helium to the grain boundaries. Thus, the grain-boundary concentration of helium generated from the threshold reactions is larger in the type 316L than in 17-4 PH.

IRRADIATION EFFECTS AT HIGH TEMPERATURES FOR Fe-Cr-Al-Y ALLOYS

W. R. Martin

We are investigating the irradiation behavior of Fe-Cr-Al alloys because they fracture transgranularly more readily than austenitic stainless steels. Since irradiation embrittlement at elevated temperature affects intergranular fracture, we are studying the effect of irradiation on the high-temperature ductilities of these ferritic steels.

Table 20.3. Strain Rate Sensitivity of Irradiated[a] and Unirradiated[b] Fe–15% Cr–4% Al–1% Y Alloy[a]

Deformation Temperature (°C)	Strain Rate (%/min)	Strength (psi)		Ductility (%)	
		0.2% Yield	Engineering Ultimate	True Uniform Strain	Total Elongation
		$\times 10^3$	$\times 10^3$		
500	20.0	32.2 (28.0)	45.4 (37.9)	8.8 (8.1)	22.5 (17.9)
	2.0	34.6 (30.7)	41.6 (34.5)	10.8 (4.2)	14.9 (19.7)
	0.2	30.8 (20.1)	35.8 (24.8)	6.0 (7.1)	23.2 (26.3)
600	20.0	29.7 (24.4)	34.8 (28.1)	6.3 (4.1)	32.7 (25.4)
	2.0	27.2 (19.8)	29.9 (21.4)	4.5 (4.3)	30.3 (31.1)
	0.2	21.8 (15.3)	22.8 (17.1)	4.0 (3.5)	30.4 (27.2)
700	20.0	18.5 (13.8)	20.3 (14.6)	6.5 (2.6)	39.0 (62.0)
	2.0	14.2 (9.8)	15.6 (9.9)	4.4 (3.2)	51.9 (51.0)
	0.2	11.4 (8.2)	12.3 (8.5)	2.6 (2.0)	37.8 (44.3)
800	20.0	12.0 (7.6)	12.4 (7.9)	4.4 (2.3)	50.9 (75.7)
	2.0	7.9 (4.3)	8.1 (4.5)	3.5 (3.3)	64.0 (74.1)
	0.2	3.9 (3.5)	4.7 (3.7)	1.9 (1.8)	78.1 (76.4)
871	20.0	6.2 (6.8)	6.5 (6.9)	2.1 (1.0)	58.3 (82.5)
	2.0	4.3 (4.0)	4.8 (4.2)	2.6 (3.3)	76.4 (79.3)
	0.2	2.8 (2.2)	3.2 (2.5)	3.5 (4.1)	93.1 (92.7)

[a] First entries are data from samples irradiated at 50°C to a dose of 1×10^{20} neutrons/cm^2 (thermal) and 1.5×10^{19} neutrons/cm^2 (>1 Mev).

[b] Given in parentheses.

Pre- and postirradiation tensile ductilities at several strain rates are given in Table 20.3. The difference in ductility between irradiated and unirradiated alloys appears greatest at the highest temperatures and strain rates. This behavior is in contrast to that normally observed for austenitic steels, whose ductility is reduced most at the lower strain rates. The irradiated ferritic steel is much more ductile than austenitic steels irradiated at equivalent conditions. The irradiated ferritic material also appears substantially stronger than the unirradiated material at temperatures less than 871°C. This effect may be due to displacement damage, since the alloy was irradiated at approximately 50°C.

COMPARISON OF DISPLACEMENT DAMAGE AND STRENGTH FOR STAINLESS STEEL IRRADIATED AT INTERMEDIATE TEMPERATURES[14]

E. E. Bloom J. O. Stiegler[15]
W. R. Martin J. R. Weir, Jr.

The effects of irradiation at temperatures between 93 and 454°C upon the room-temperature

---

[14] Abstract of ORNL-TM-1535 (June 1966); paper presented at the US/UK Libby-Cockcroft Irradiation Effects Meeting held at Brookhaven National Laboratory, June 23–24, 1966.

[15] Electron Microscopy Group.

mechanical properties and electron microstructures of AISI type 304 stainless steel have been determined. Irradiation at temperatures between 93 and 300°C produces a high density of defect clusters on the order of 100 A in diameter. These defects are responsible for the increased yield stress, for when the irradiation temperature was increased to 371°C, no defect clusters were observed and the yield stress decreased by a factor of 2. At irradiation temperatures of 371°C and higher, precipitates formed within the grains. Deformation (10% by rolling) in a specimen containing the defect clusters was concentrated in very narrow slip bands, while in the specimen containing precipitate particles, the deformation was homogeneous.

21. Nondestructive Test Development

R. W. McClung

Our program is designed to develop new and improved methods of evaluating reactor materials and components. To achieve this we study the various physical phenomena, develop instrumentation and other equipment, devise application techniques, and design and fabricate reference standards. Among the phenomena being actively pursued are electromagnetics (with major emphasis on eddy currents), ultrasonics, and penetrating radiation.

The extension of our ultrasonic technique to the inspection of tapered tubing is described in Part V, Chap. 35 of this report.

ELECTROMAGNETIC TEST METHODS

C. V. Dodd

We have continued both analytical and empirical research and development concerning electromagnetic phenomena. As part of the program, we are studying the mathematical determination of the vector potential of a coil as a function of coil dimensions, frequency, specimen conductivity, and coil-to-specimen spacing (lift-off).[1] This electromagnetic boundary value problem is solved by a relaxation technique on a digital computer. The differential equation for the vector potential is approximated by finite difference terms. By making a number of correcting calculations, we can make the value of the vector potential converge to agreement with the differential equation at every point. Once the vector potential has been determined, any physically observable electromagnetic induction phenomenon can be calculated. One phenomenon we have investigated is the forces produced by eddy currents. These forces produced in the interior of a conducting specimen can be resolved into an alternating force and a steady force. The axial component of the steady force was both measured and calculated for a coil in a ferrite cup above a conducting ring, as shown in Fig. 21.1. The calculated and normalized contours of the force density inside the ring are also shown. The calculated values of the net force were 0.5 to 17% greater than measured values. However, this type of error could result from the value of the permeability used in the calculations, which was 17% higher than the permeability of the ferrite cup used in the measurements. These calculations can be used to study the noncontact generation of ultrasonic pulses by eddy currents and can be applied to many other areas of technology, such as magna-forming, induction pumping, and magnetohydrodynamic generation of electricity.

We have also used our program to calculate the impedance of a coil in the presence of a conductor. Figure 21.2 compares calculated to measured coil impedance. We constructed four coils of the same shape but different sizes and measured impedance as a function of frequency and lift-off. The measured points are the average of measurements from each of the four coils, weighted according to the standard deviation of each coil at each point. There was a large standard deviation at the two lower frequencies and a small standard deviation at the four higher frequencies at each lift-off value. The agreement is very good in the calculated and measured values of $R\sqrt{\omega\mu\sigma}$ (see Fig. 21.2). The error in lift-off arises from the fact that our relaxation process only defines the location of the coil within one-half of a lattice spacing. The difference between measured and calculated lift-off

---

[1] C. V. Dodd, *A Solution to Electromagnetic Induction Problems*, ORNL-TM-1185 (August 1965).

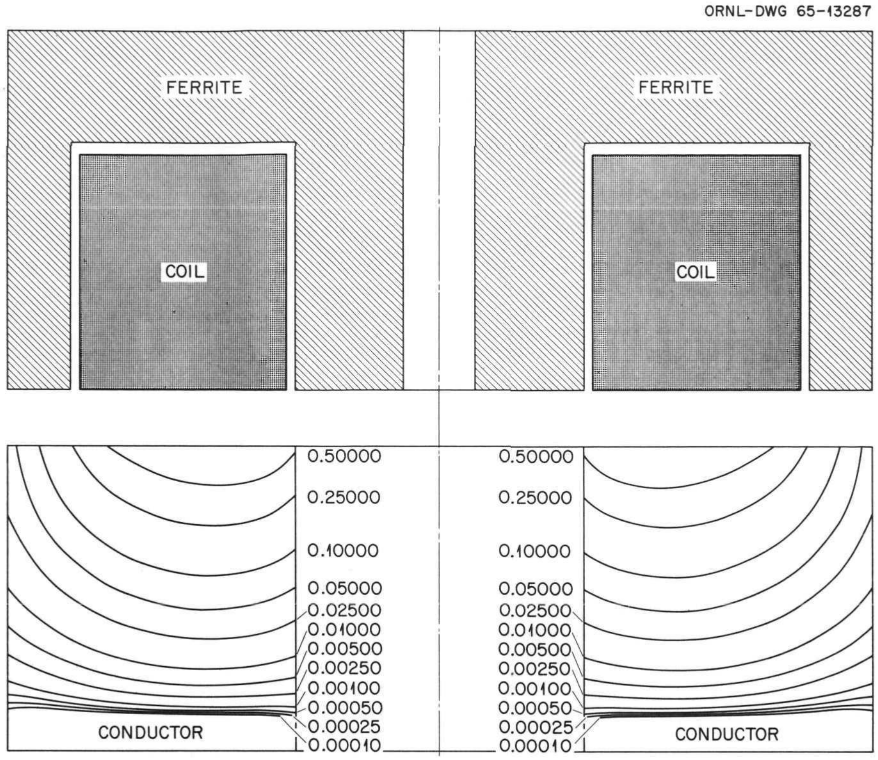

Fig. 21.1. Determination of Axial Eddy-Current Forces in a Conducting Ring.

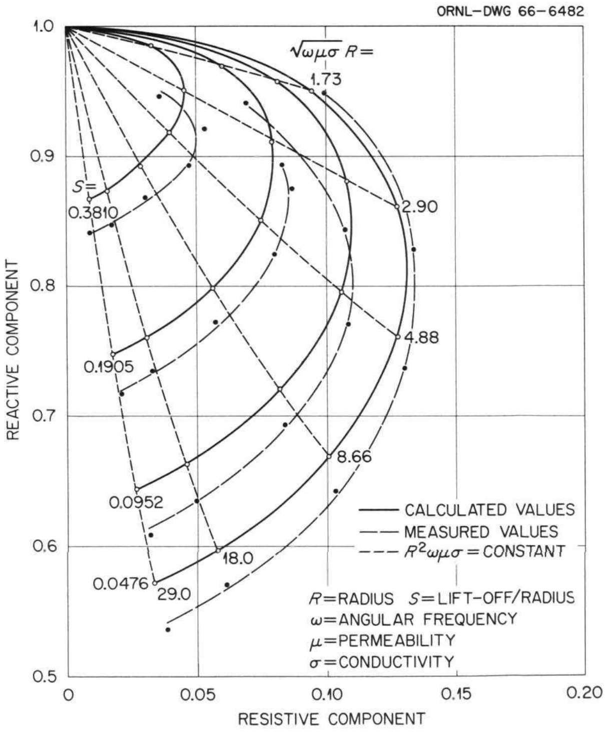

Fig. 21.2. Calculated and Measured Values of Coil Impedance (Normalized Impedance).

is within the range and could be reduced by use of a finer lattice but at an increased computation cost. Overall, the agreement between measured and calculated impedance is very good.

We have developed and constructed a prototype beat-frequency eddy-current instrument to measure conductivity variations in metals. The instrument has two *L*-*C* oscillators. One oscillator is tuned by the impedance of the test coil as it is affected by the metal specimen. The second oscillator is tuned by a variable piston capacitor to track the first oscillator. We shaped the capacitor to give linear dial readings directly in microhm-centimeters. The two frequencies are beat together, and the output is fed into a speaker, giving an audible indication of the frequency difference of the two oscillators. While the instrument does not have lift-off compensation, it does have the advantages of high resolution, direct readings, portability, and inexpensive components.

We are continuing the development and applications of our phase sensitive eddy-current instrument. We have improved the stability of the instrument so that the overall drift measured at

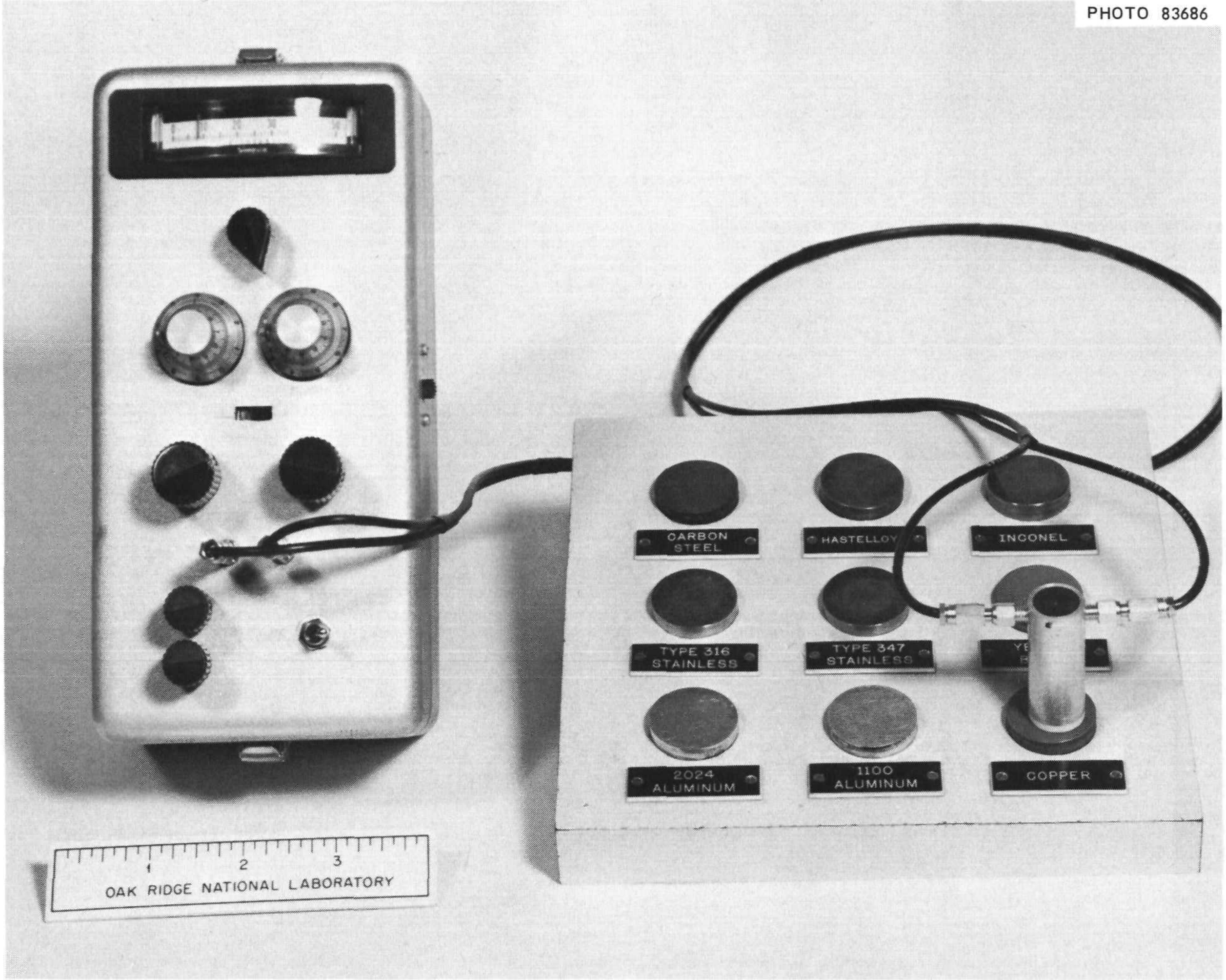

Fig. 21.3. Prototype Portable Phase-Sensitive Eddy-Current Instrument.

the output of the instrument is less than 0.2 v for a 30°C temperature change. This will allow us to measure metal conductivity and thickness with fewer recalibrations. A new discriminator and flip-flop, which will work at 20 Mc, will allow us to measure the thickness of very thin metal specimens. We have also increased the lift-off insensitivity by improving the discriminator circuits of the instrument.

A new portable phase-sensitive instrument, shown in Fig. 21.3, was constructed. It operates either on batteries or 60 cycles ac and may be used to measure conductivity, cladding thickness, and thickness at frequencies of 50 and 500 kc.

ULTRASONIC TEST METHODS

K. V. Cook

We have continued our studies on the behavior of ultrasound in thin sections; the principal effort is the detection of nonbond in clad structures. An immersed through-transmission reflection technique,[2] capable of detecting nonbonds equivalent to a $\frac{1}{16}$-in.-diam reference hole, was developed and applied to remote inspection of fuel tubes

---

[2] K. V. Cook and R. W. McClung, *Metals and Ceramics Div. Ann. Progr. Rept. June 30, 1965*, ORNL-3870, p. 149.

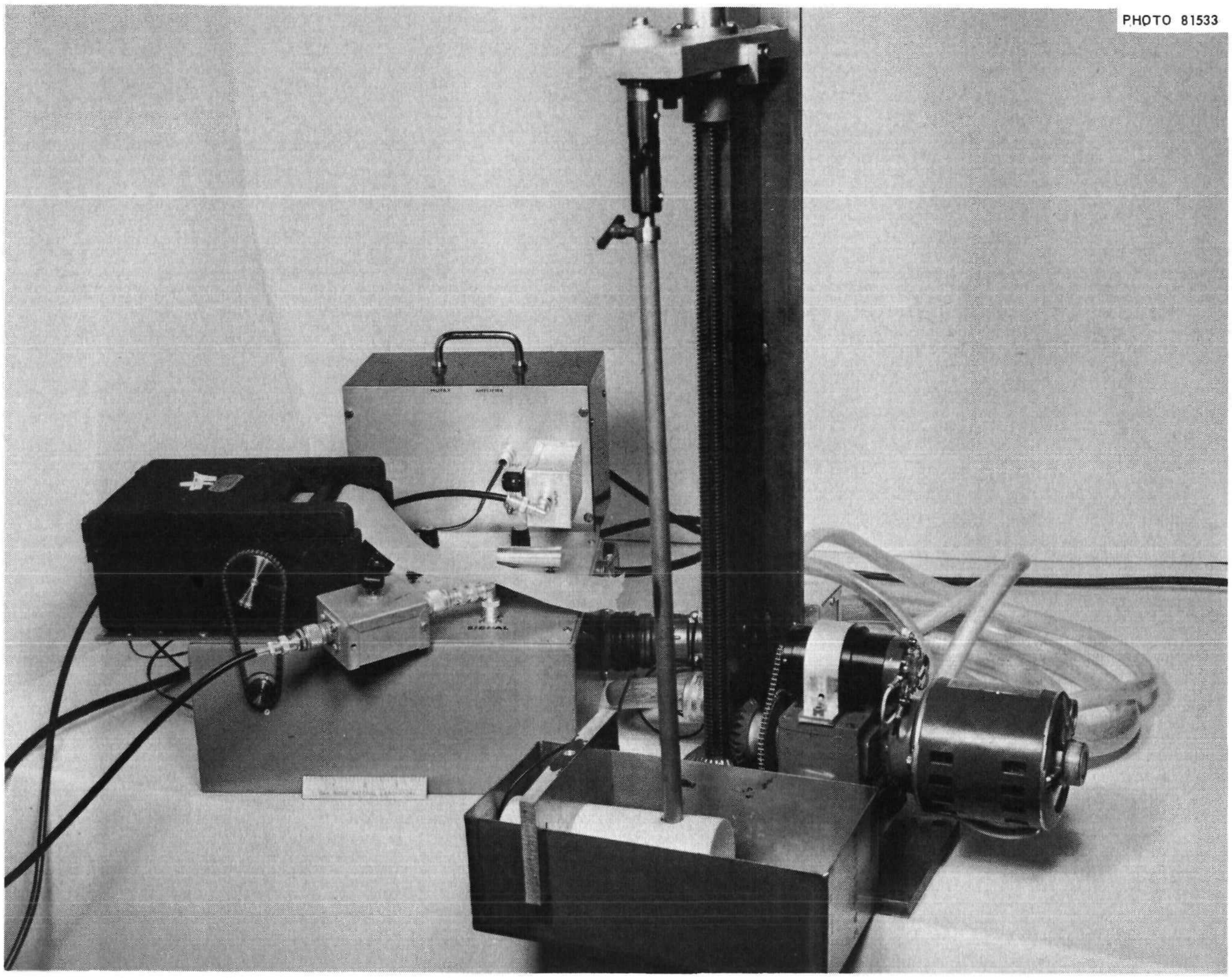

Fig. 21.4. Mechanical System for Helically Scanning Fuel Tubes in a Hot Cell.

containing a cylindrical core of enriched UO_2 dispersed in stainless steel. Figure 21.4 shows the mechanical system for helical scanning of the fuel tubes inside a hot cell. The Teflon-guide-block and transducer assembly is in the small immersion tank with a fuel tube in position for scanning. In actual operation, the motor-driven scanning device (shown on the right) is inside the cell. The controller and recorder, which are outside the cell, are on the left.

We are studying ways to make realistic reproducible reference notches and thus far have used electrical discharge machining (EDM). We have described[3] some of the difficulties overcome in machining longitudinal and transverse EDM notches of nominal depths along with the differential focusing and replication techniques used to determine their depths.

We assembled an optical system for viewing and photographing ultrasound as it travels in a transparent medium. The schlieren method is of principal interest and has been used to view continuous-wave beams emerging from the transducer face and also to view pulsed-ultrasonic packets with a 0.2-μsec light flash. One of these packets is shown in Fig. 21.5.

We can also view pulses of ultrasound in transparent solids with a method involving the photoelastic effect. With the aid of polarized light, interference patterns generated by ultrasonic

---

[3] K. V. Cook and R. W. McClung, "Electrodischarge Machined Reference Discontinuities," submitted for publication in *Materials Evaluation*.

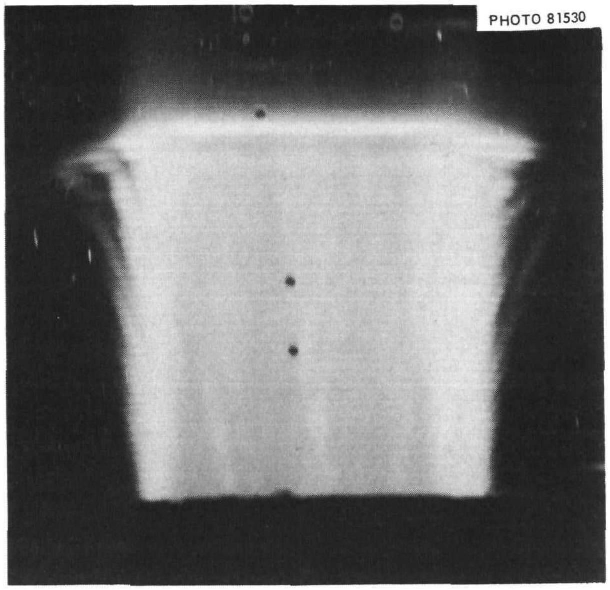

Fig. 21.5. Pulse of Ultrasound as Seen with a Schlieren System.

energy propagating through transparent epoxy sheets were observed. The optical system (as used for schlieren) is shown in Fig. 21.6 along with the ultrasonic oscillator and transducer assembly. The triangular base is an optical bench, which is used to align the required components for ultrasonic photography.

PENETRATING RADIATION

B. E. Foster S. D. Snyder

We are continuing the study of x- and gamma-ray attenuation for the evaluation of fuel elements. Variation in transmitted intensity is readily monitored with a scintillation detector and then related through proper calibration to the fuel loading homogeneity within the area of interest. We completed the data analysis on the two vibratorily compacted $\frac{1}{2}$-in.-diam (Th–3% U)O_2 fuel rods, six $\frac{1}{2}$-in.-diam ThO_2 pellets, and eight $\frac{3}{4}$-in.-diam ThO_2 pellets. These samples were scanned at several longitudinal speeds from 2 to 24 in./min with collimation of $\frac{1}{8} \times \frac{1}{8}$ in. and

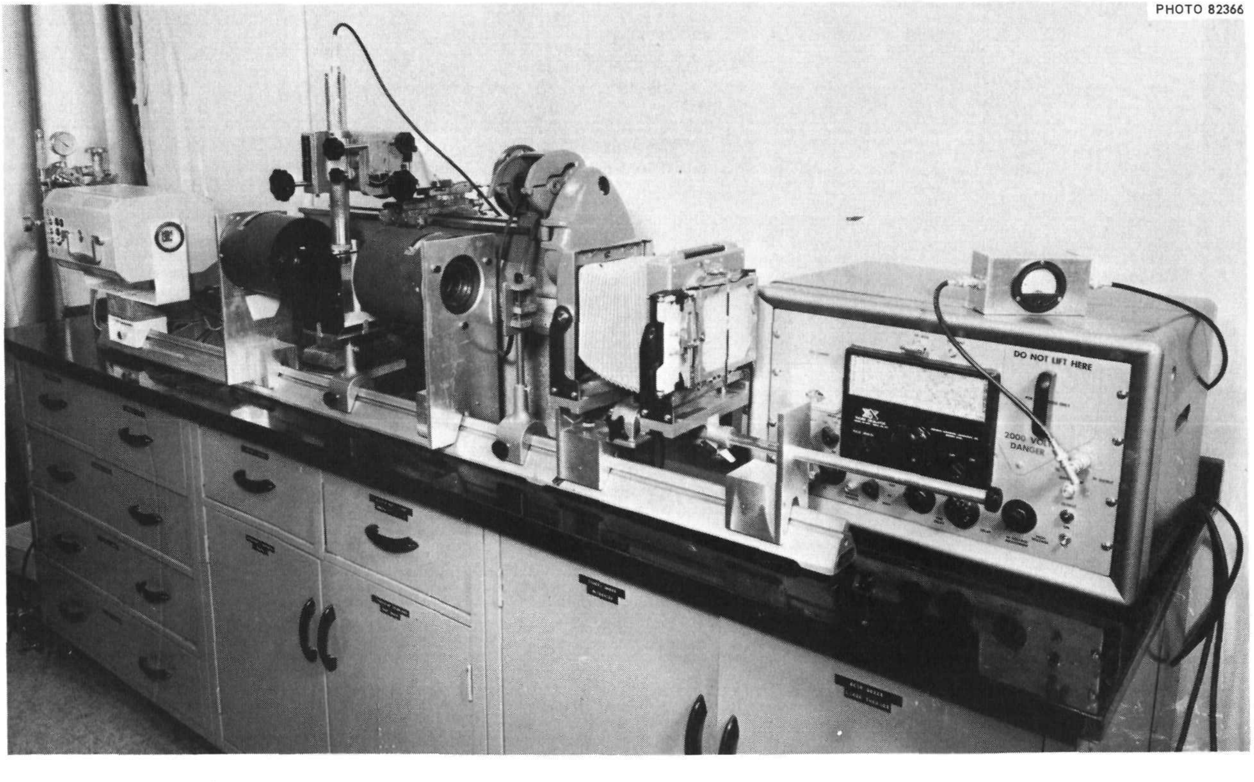

Fig. 21.6. Schlieren System for Viewing Ultrasound.

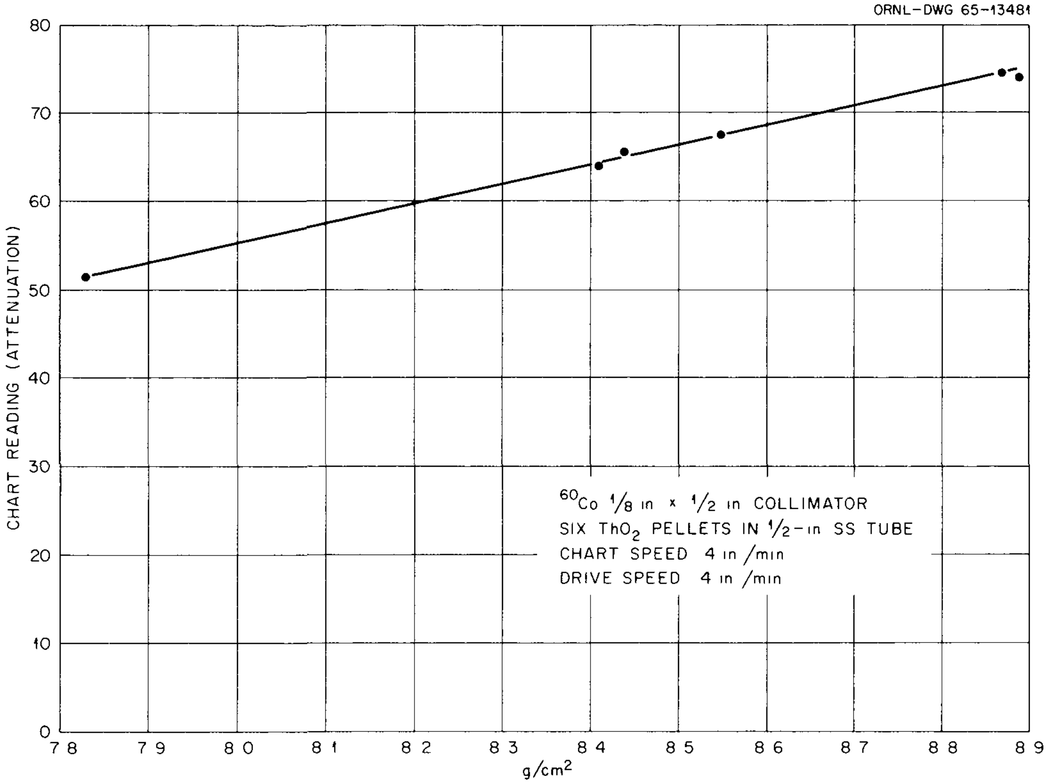

Fig. 21.7. Typical Calibration Chart Relating Fuel Content to Gamma Attenuation.

⅛ × ½ in. and with ^{60}Co and ^{137}Cs as the radiation sources. Radiation attenuation (chart reading) was plotted against longitudinal scan speed and specimen thickness-density product for both types of collimation, both sources, and all speeds. Figure 21.7 shows typical data for the use of ^{60}Co.

We define the calibration of the system as the average response to a given change in fuel concentration. This should not be confused with resolution, which defines the size of the smallest detectable inhomogeneity. When ^{60}Co was used as the radiation source, the average response remained essentially constant for both rod sizes and both collimator sizes at scan speeds of 2 through 24 in./min. The same parameters were varied with ^{137}Cs as the radiation source. The average response remained constant for the ½-in.-diam rods, but the calibration on the ¾-in.-diam rods shifted. This indicates that the radiation energy of ^{137}Cs is too soft for efficient homogeneity evaluation on ¾-in.-diam rods. In addition, the scan traces indicated some degree of smoothing of the small-spot inhomogeneities with the use of larger collimation. This is not an improvement in spot homogeneity but merely an averaging or smoothing over a larger area.

We are further evaluating the system for fuel-rod homogeneity measurements by determining the effect on calibration of changes in the wall thickness of the tube that houses the fuel material. Stainless steel shims from 0.001 to 0.010 in. thick were placed on the ½- and ¾-in.-diam ThO_2 pellets during scanning. This portion will provide useful guideline information for specifying wall thickness tolerances of tubing used to house fuel pellets or vibratorily compacted fuel powders. A topical report is being prepared.[4]

We continued the development of scintillation detector probes for insertion into hollow cylindrical specimens for determination of fuel homogeneity or wall thickness by x-ray attenuation. Since these probes use light pipes to transmit the light produced by a scintillated NaI(Tl) crystal

---

[4] B. E. Foster, S. D. Snyder, and R. W. McClung, *Evaluation of Variables in the Measurement of Fuel Concentration Variations in Fuel Rods*, in preparation.

to a photomultiplier, we compared efficiency and sensitivity of various light-transmitting materials, for example Lucite, quartz, and fiber optics bundles.

First we compared $\frac{5}{16}$-in.-diam 20-in.-long Lucite and quartz rods that were coupled between a $\frac{1}{4}$-in.-diam $\frac{1}{2}$-in.-long NaI(Tl) crystal and an RCA 6342A photomultiplier tube. These were inserted into stainless steel tubing with a 0.020-in. wall thickness. Variations in thickness as small as 0.2% were detectable. Since light-transmission efficiency differed very little between the Lucite and the quartz, we do not intend to pursue the use of quartz, which requires considerably more effort to prepare. A $\frac{1}{4}$-in.-diam by 36-in.-long commercial fiber optics bundle was much more sensitive to aluminum thickness changes than a similar length and diameter of Lucite, we compared the photomultiplier output signal as indicated by a digital voltmeter with 6061 aluminum attenuating a 50-kvcp 0.078-in.-diam collimated x-ray beam. Use of this same fiber optics bundle, NaI(Tl) crystal, and photomultiplier combination to measure the thickness of vapor-deposited tungsten on the inside wall of copper tubing is reported in Part II, Chap. 14 of this report

We are continuing the program for nondestructively determining the uranium content in rectangular uranium-aluminum alloy blanks. The equipment consists of an NaI(Tl) crystal, photomultiplier tube, linear amplifier, single-channel analyzer, high-voltage supply, scaler, and timer connected in the conventional spectrometer arrangement. We monitored the count rate of the 184-kev gamma ray from the decay of ^{235}U. The count rate was determined for 5-min periods at frequent intervals over several days as a check on instrument stability. The equipment proved quite stable, and reproducible data were obtained. To establish a relationship between count rate and uranium content, we measured the count rate from several core blanks, each with a different uranium loading. Then the cores were analyzed chemically for uranium content. Of course, as the uranium content increases, self-absorption of the 184-kev gamma ray increases. The observed counting rates were corrected for self-absorption and instrument resolving time, and the corrected count rate was plotted against uranium content. Subsequent cores can be counted and their uranium contents read directly from the plot. A topical report is being prepared on this work.[5]

---

[5] B E Foster, *Determination of ^{235}U Content in Uranium-Aluminum Fuel Core Blanks*, in preparation

22. Sintered Aluminum Products Development

D. A. Douglas, Jr.

Sintered aluminum products (SAP) material is the prime candidate construction material for the fuel rods and pressure tubes of the Heavy-Water Organic-Cooled Reactor (HWOCR). Previously available SAP exhibit erratic behavior in the form of poor process yield, structural inhomogeneity, gas fissuring and blistering, anisotropic properties, premature fracture, and low creep ductility. Since most of the erratic behavior is either process or material related, a thorough study is being conducted to determine the material and processing parameters necessary to produce a desired end product consistently and economically.

POWDER CHARACTERIZATION

R. S. Mateer[1] W. J. Werner
W. C. Robinson D. S. Cowgill[2]

The dual purpose of powder characterization is to develop specifications that will assure a uniform reproducible starting material and to determine powder characteristics that affect fabricability or final properties. We characterized 13 commercially available aluminum powders according to size, shape, surface area, topography, density, composition, and microstructure. The characteristics of the initial powders used in SAP were parameters usually ignored by previous researchers with the exception of Hérenguel,[3] who related the subsequent SAP mechanical properties to the initial powder thickness.

Atomized powders have the characteristics of chill castings of very fine structure, while the flake materials have a highly recovered or recrystallized structure with low dislocation density. Both flake and atomized powder show unusual resistance to softening (measured by microhardness), and these powder characteristics may be directly related to the elevated-temperature behavior of wrought SAP. None of the powders examined has been specifically treated by the manufacturers for the purpose of fabricating SAP. Therefore, a prime objective of the SAP program is to determine optimum methods for increasing the oxide content and controlling morphology.

Fabrication steps employed following material characterization are delineated in the flowsheet shown in Fig. 22.1. Operations performed in each step are covered in the following sections.

DISPERSION PREPARATION

G. L. Copeland R. L. Heestand
W. J. Werner C. F. Leitten, Jr.

We are seeking a procedure that will produce a flake product of controlled oxide content and thickness with a minimum of contamination. Starting materials have been commercial high-purity partially spherical atomized powders with nominal sizes of 3 to 15 μ. Aluminum and stainless steel mills have been used with aluminum or stainless steel balls with and without internal lifter bars. Lubricants have been stearic acid, oleic acid, and dimethyl silicone fluid with Varsol as the milling vehicle, a wide range of proportions and amounts of these materials has been

---

[1] Consultant from the University of Kentucky.

[2] On loan from Atomics International.

[3] J. Hérenguel and J. Boghen, "Propriétés des demi-produits en aluminium fritté," vol. 1, pp. 341–46 in *Congrès International de l'Aluminium, Paris, June 14–19, 1954*, Société d'Édition et de Documentation des Alliages Légers, Paris, 1955.

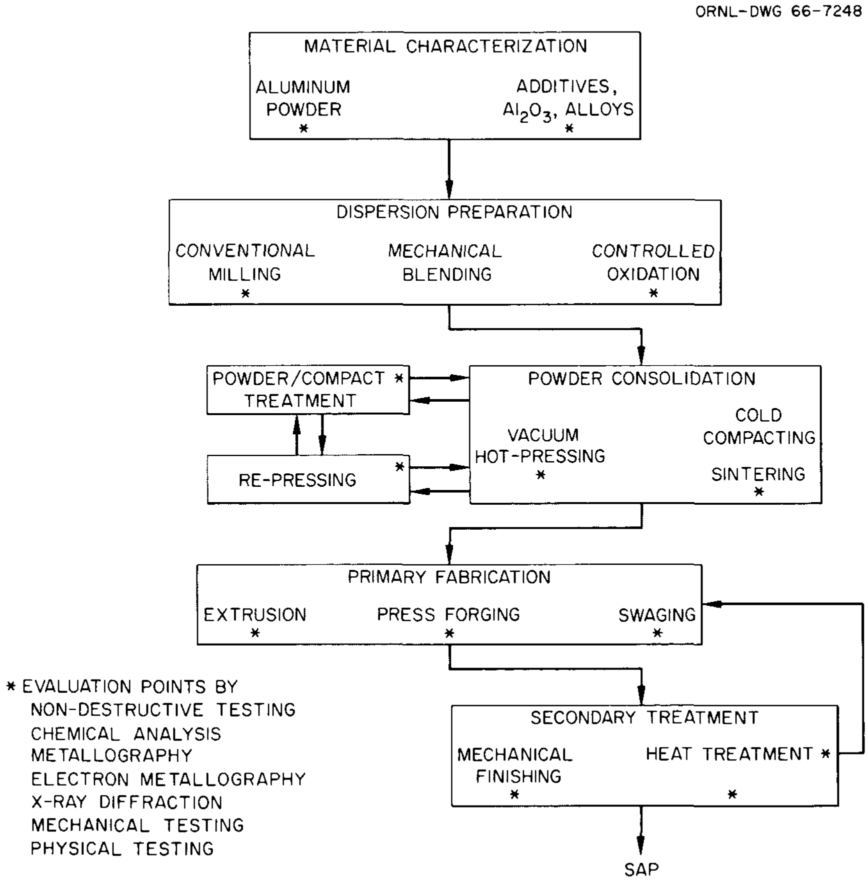

Fig. 22.1. Flowsheet for Sintered Aluminum Products.

studied. All milling has been done in air with no attempt to control temperature (<35°C). Milling times ranged from 5 to 72 hr and milling speeds from approximately 30 to 100% of the speed of maximum energy input (just short of centrifuging). Milling conditions of some typical batches are given in Table 22.1.

Internal lifter bars increase the reproducibility of the process and increase the milling action, thus decreasing the time required to produce a given oxide content. The use of stainless steel rather than aluminum balls required approximately one-third less time and gave a more reproducible product. Under constant milling conditions, the reproducibility of the oxide contents produced with steel balls and internal lifter bars was within the reproducibility of the chemical analysis for oxide content. Spectrographic analysis indicated no additional iron contamination from the use of type 302 stainless steel mills and balls over that from the use of an all-aluminum mill.

Stearic acid appears to be preferable to oleic acid in that it produced a lower oxide content for a given surface area (and flake thickness), thus giving a closer interparticle spacing for a given oxide content. The flake powders produced with these lubricants contained around 1% C with 2 to 3% total organic material and produced extruded rods with less than 0.5% C. The silicone fluid produced a still lower oxide content for a given flake thickness, but the silicone is more difficult to remove from the powders. Typical batches contained approximately 2% C with approximately 4% total organic. Chemical analysis results of these powders after vacuum compacting and extrusion are not available at this time.

Two distinct types of inclusions have been noted in rods produced from commercial ball-milled flake powder; one is metallic or alloy-like in appearance and the other is ceramic-like in appearance. Microprobe analysis indicated that the "metallic" inclusions consist of iron, iron-

Table 22.1. Conditions of Typical Ball-Milling Experiments

Grinding Medium	Lubricant		Amount of Varsol[a] (ml)	Milling Time (hr)	Product Analysis (%)	
	Type	Amount (% of powder)			Al_2O_3[b]	Carbon[c]
Stainless steel	Stearic acid	3	500	9	9.33	1.4
Stainless steel	Stearic acid	3	500	7	8.73	
Stainless steel	Stearic acid	3	500	6	7.49	
Stainless steel	Oleic acid	3	500	7	9.77	1.3
Stainless steel	Silicone fluid	63	None	7	6.90	8.2
Stainless steel	Silicone fluid	63	300	7	12.8	
Stainless steel	Stearic acid	1.25	375	7	6.92	1.8
Aluminum	Stearic acid	1.25	375	7	2.76	0.9
Aluminum	Stearic acid	3	500	7	2.25	0.8

[a] For 300 g of powder.

[b] Average of several batches in most cases.

[c] These powders after vacuum treatment produce extruded rods containing 0.1 to 0.5% C

aluminum, or iron-aluminum-oxygen. The ceramic inclusions seem to be aluminum carbide, probably Al_4C_3. The particles of almost pure iron indicate a pickup during commercial ball milling in steel mills. Some small iron-containing inclusions are present in atomized powder. The carbide is probably a result of carbon pickup from the milling. Rod produced from ORNL ball-milled flake showed considerably fewer and smaller metallic inclusions than commercial alloys.

Aside from the reduction in the metallic inclusions, the ORNL flake appears similar to commercial products. Nominal flake is produced with thicknesses near 0.5 μ and oxide contents from 1 to 35%. Transmission electron microscopy reveals a recrystallized structure in the flake immediately after ball milling with no evidence of tangled dislocation cells but consisting of well-defined grains with a diameter of approximately 0.5 μ.

It would be desirable to obtain the desired oxide content by blending to avoid contamination during milling. Materials used thus far have been Linde B (0.05-μ γ-alumina) blended with commercial high-purity atomized aluminum powder in the nominal size range 3 to 10 μ. In all tests to date, the oxide has been agglomerated, producing an inhomogeneous mixture. Additional studies on dispersing oxides are under way.

A limited amount of effort was devoted to controlled oxidation of spherical aluminum powders by reaction with water, using both large quantities of distilled water and limiting the time of exposure to control oxide content and by adding small quantities of water to yield a high moisture content before reaction. The latter method offered more successful control with levels up to 6% oxide, however, the alpha monohydrate is in the form of fanlike crystals, and smaller aluminum particles are completely consumed to oxide. As an alternate route, we are studying high-temperature oxidation, wherein gamma oxide may be formed directly by exposure of the powder to oxygen at low pressures.

POWDER CONSOLIDATION

G. L. Copeland D. S. Cowgill[2]
C. F. Leitten, Jr.

A second major deviation from past practice in the manufacture of SAP is our substitution of vacuum for air during the conversion of the oxide hydrate to anhydrous oxide. We felt that the use of flake powders and a vacuum outgassing treatment would prevent the formation of large oxide agglomerates in the consolidated product. Our studies show that both are essential and serve to provide a homogeneous distribution of fine stable oxide particles.

Vacuum hot pressing has been done in graphite dies at pressures from 1.6 to 2.6 tons/in.^{2}. The procedure includes holding the powder at 600°C for 2 hr under vacuum, then pressing for 30 min at 600°C under vacuum. This procedure produces compacts with density greater than 95% of theoretical. The final density is independent of pressing load in the range tested. This procedure is sometimes followed by coining at 50 tons/in.^{2} at room temperature, which yields close to theoretical density.

Compacts have been cold pressed at pressures of 20 to 45 tons/in.^{2}. This is followed by a vacuum anneal at 600°C for 20 hr. The compacts are then coined at room temperature at 50 tons/in.^{2}. Final density, generally 94 to 99% of theoretical, does not depend on the initial pressing pressure in this pressure range.

There has been considerable controversy whether the oxide phase was continuous or discontinuous. The morphology of the oxide phase can be varied from a continuous oxide network in the aluminum matrix to discrete oxide particles in the metal matrix by proper selection of outgassing and compaction parameters. A 20-hr vacuum anneal at 600°C, whether of the powder or of the compact after pressing, is sufficient to stabilize 6 to 9% oxide and prevent agglomeration during extrusion. The 2.5-hr anneal during vacuum hot pressing is insufficient to prevent agglomeration of the oxide during extrusion. Further work in this area is in progress.

FABRICATION

G. L. Copeland W. J. Werner
D. S. Cowgill[2] C. F. Leitten, Jr.

The prepared SAP powder is being fabricated by swaging and extrusion to determine the effects of working on the material and to provide specimens for mechanical property measurement, nondestructive testing, and physical metallurgical evaluation.

Swaging

Some XAP-001 rods were hot swaged at 500°C for subsequent tensile tests. Creep-rupture strength appears to be improved by hot swaging.

Hot swaging was used to fabricate 20 compacts including flake, spherical, and blended powders. All swaging was done at 500°C starting temperature, and the first 10% reduction was in Inconel sheathing to provide suitable size for swaging and to prevent spalling from the compacts. Some tests were made using aluminum sheathing, but the sheathing ruptured before sufficient reduction was obtained. All swaged rods attained greater than 98% of theoretical density and showed no strong orientation metallographically. X-ray diffraction, however, revealed distinct ⟨100⟩ and ⟨111⟩ fiber texture of the aluminum.

Cold swaging and wire drawing were used to produce 0.010-in.-diam wire for x-ray analyses. In 1% oxide material no intermediate annealing was required, but in 6% oxide material several intermediate anneals were required. In 6% oxide dispersions 0.030-in.-diam wire could be cold drawn.

Extrusion

Several compacts were extruded as the cores of type 6061 aluminum billets. Extrusion at ratios of 10, 20, and 30 at 500°C was used to evaluate the effects of starting density and reduction ratio on final density and to provide material for mechanical testing and annealing studies.

Primarily compacts were extruded bare, using shear dies in a 500-ton laboratory extrusion press. Reduction ratios of 10, 20, and 30 at 400, 500, and 600°C were used to prepare samples for mechanical testing. Even though all extruded rods were denser than 99% of theoretical, some increase in tensile ductility and strength was found with increasing reduction ratio. Temperature effects have not yet been defined.

Extrusion experiments indicated that density is an inadequate measure of primary fabrication effectiveness, since essentially full density is achieved when reduction ratio is 10 or greater, starting density is 70% or greater, and temperature is 400°C or greater. Also, SAP rod is readily extruded with 80 to 90% recovery with standard tooling and fairly low loads.

EVALUATION OF MATERIALS

All the standard evaluation techniques were applied to the SAP produced and procured by ORNL. These techniques include metallography, electron microscopy, x-ray diffraction, radiography, microprobe analysis, chemical analysis, and mechanical properties evaluation.

X-Ray Diffraction

W. C. Robinson J. E. Spruiell[4]
R. S. Mateer[1] C. F. Leitten, Jr.

The x-ray diffraction line-broadening technique was used to determine grain size in the initial powders and the fiber textures of both swaged and extruded SAP rods. The reduction ratios were 15.7 for the swaged rods and 20 for the extruded rods. The swaged SAP rods had a duplex aluminum fiber texture consisting of $\langle 111 \rangle$ and $\langle 100 \rangle$ components, while extruded flake material had only a $\langle 111 \rangle$ component. The texture of extruded rods is much stronger than that of swaged rods.

X-ray diffraction also has been applied in the determination of the type of oxide present in the fabricated SAP rods and on the powder after various processing steps. The problem is particularly difficult because of the existence of numerous oxides and hydrates, the small amount of oxide present in most SAP materials, and the extremely fine size and homogeneous distribution of the oxide particles. It has not been possible to identify with certainty the oxide species present in the SAP materials. The difficulty appears to be due to the simultaneous existence of several oxide species and small amounts of aluminum carbide.

Metallography and Electron Microscopy

W. C. Robinson K. Farrell
G. L. Copeland

Metallographic examination of commercial SAP reveals oxide agglomerates arranged in "stringers," which run parallel to the extrusion direction. Electron photomicrographs revealed that these oxide agglomerates were as large as 4 μ in diameter and bordered areas of oxide-free aluminum. Light microscopy is insufficient to resolve the oxide phase in SAP prepared directly from ORNL flake, from nontreated atomized powder, or in XAP-005, an Alcoa product. The difference

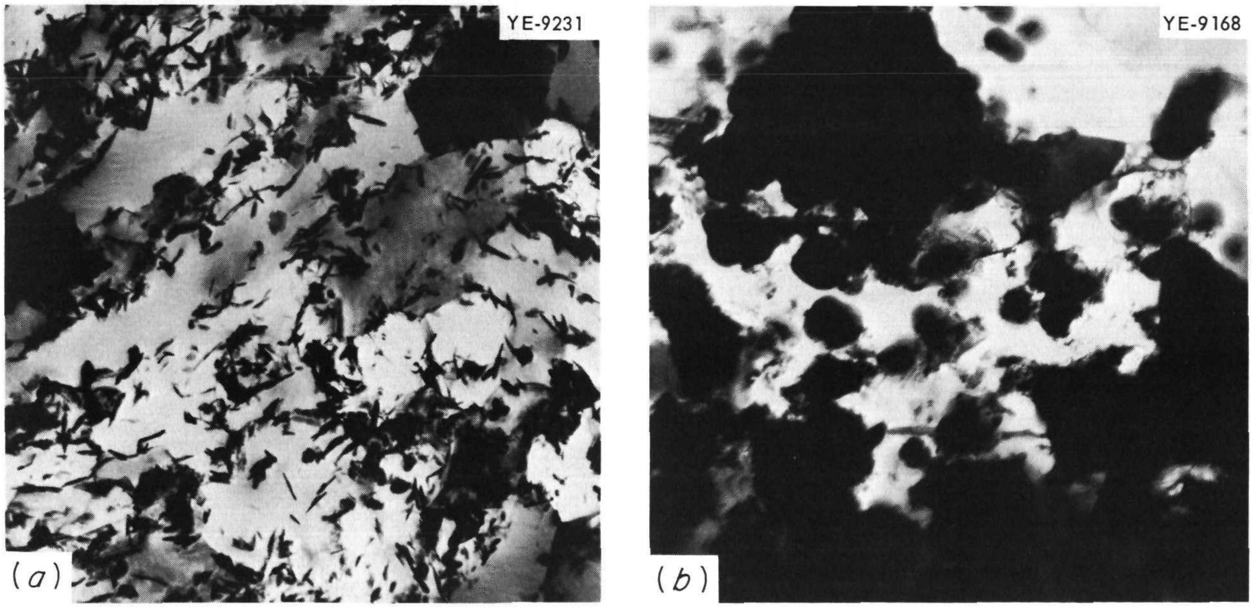

Fig. 22.2. Microstructures of Sintered Aluminum Products. (*a*) ORNL material containing 6% Al_2O_3. 21,000×. (*b*) Commercially produced material containing 7.8% Al_2O_3. 18,000×.

---

[4]Consultant from the University of Tennessee.

in the type of oxide dispersions obtained by these products and other commercial materials is illustrated in Fig. 22.2, which shows electron micrographs of an ORNL SAP and SAP-ISML 930.

The agglomeration of oxide that occurred during blending studies at ORNL could be observed by metallographic examination. Metallographic examination was used also to check for macroscopic porosity and to observe inclusions, which were subsequently examined by microprobe analysis.

Electron microscopy was used to examine flake powders in the initial powder characterization and later to examine flake prepared at ORNL. Flakes stored in liquid nitrogen immediately after milling had well-defined grains with a diameter of about $\frac{1}{2}$ μ. Since there was no evidence of tangled dislocation cells characteristic of the cold-worked state, the flakes had undergone extensive recovery or recrystallization during the ball-milling operation. Since considerable difficulty was encountered in obtaining consistent reliable oxide analysis of SAP materials, chemical analysis is currently not used as a process control. More accurate techniques are being studied.

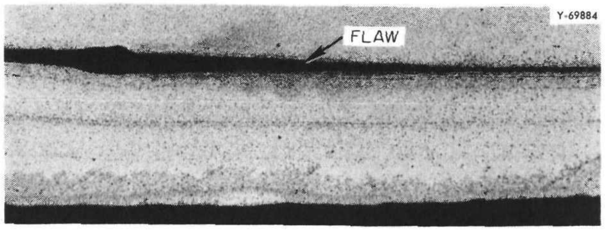

Fig. 22.3. Annular Flaw in a 2-in.-diam SAP Billet. 100×. *Reduced 47%.*

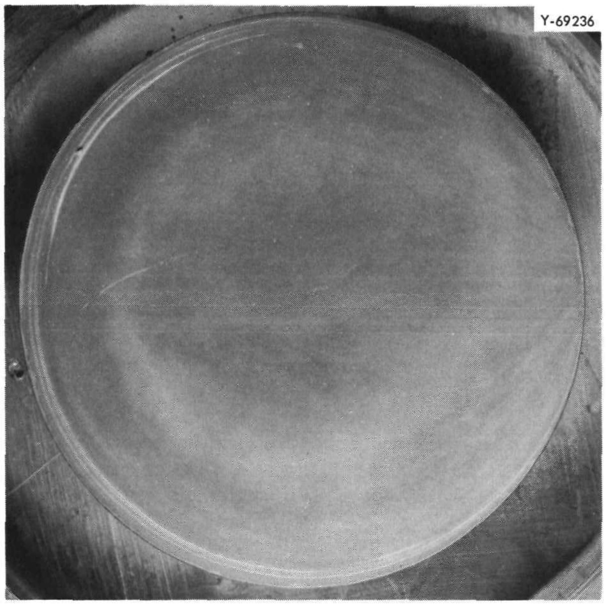

Fig. 22.4. Inhomogeneities in a 2-in.-diam SAP Billet, Shown as Near-Annular Light Streaks and Variations in Darkness.

Nondestructive Testing

R. W. McClung

The nondestructive testing phase of the program is intended to develop necessary methods, techniques, and equipment to evaluate SAP materials at various stages of fabrication. Thus, it will be beneficial during the material development stages as well as applicable to evaluation of finished products.

At the beginning of the program several small pieces of SAP materials were received from Atomics International. The shapes included billets, pressure tubing, and finned tubing. The preliminary investigations were to determine applicability of existing techniques to these items. Ultrasonic techniques seem to be applicable with a sensitivity range similar to that for wrought aluminum. Figure 22.3 shows an annular discontinuity detected near the surface of a 2-in.-diam billet. This was associated with inhomogeneities such as are shown in Fig. 22.4. Low-voltage radiography[5] was applied to detect discontinuities, low-density areas, and high-density inclusions. Liquid-penetrant techniques are applicable to all shapes, and eddy currents have been investigated for inspection of the finned tubing. Conventional encircling-coil eddy-current practice seems to be applicable and sensitive to linear cracks, inclusions, and voids. Figure 22.5 shows discontinuities detected in finned tubing. Advanced technique development using the phase-sensitive eddy-current instrument[6] is under way for more sensitive detection of flaws and measurement of wall thickness.

---

[5] R. W. McClung, *Nondestructive Testing* **20**(4), 248–53 (1962).

[6] C. V. Dodd, *Mater. Evaluation* **22**, 260–62, 272 (1964).

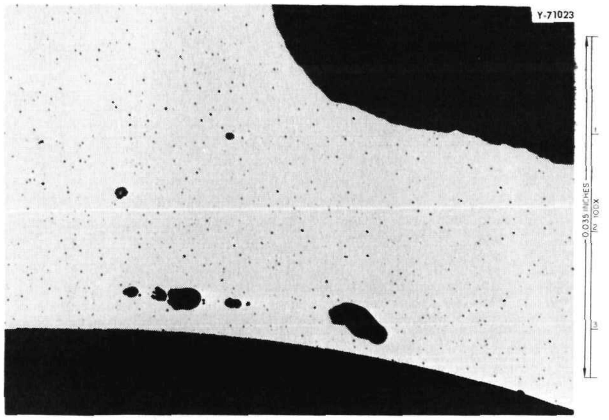

Fig. 22.5. Flaws Detected by Eddy Currents in SAP Finned Tubing.

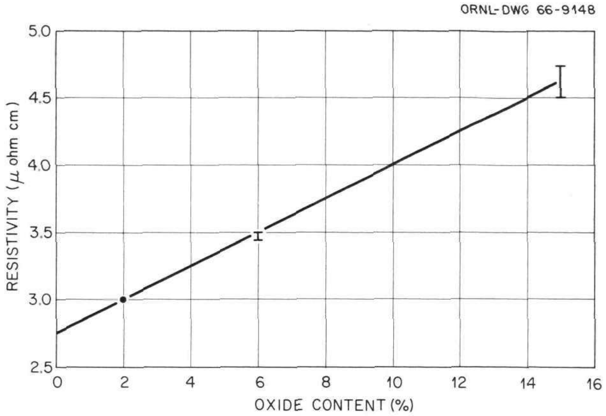

Fig. 22.6. Variation in Electrical Resistivity with Oxide Content in a SAP Billet as Determined by Eddy Currents.

Since processing of SAP materials has begun at ORNL our emphasis has changed to development of methods of process control. Included among the problem areas are measurement and classification of the submicron particles and determination of the oxide content in both powder and billet forms. We are currently surveying commercial equipment capabilities for particle sizing to determine potential applicability and areas in which work needs to be done. Preliminary work has indicated that eddy currents can measure oxide content in the hot-pressed billets. Figure 22.6 shows the relative electrical resistivity as determined by eddy currents on several samples. Extensive calibration will be required for this technique, and differentiation must be made for the response due to density variations.

Mechanical Properties Evaluation

D. G. Harmon K. Farrell

Our mechanical properties investigations regarding the SAP program can be stated as three major efforts. First, we have under way general deformation studies on both commercial and experimental materials. Second, we are evaluating the effects of material and process parameters on the strength properties of our experimental SAP. Third, because of its relative importance, we are pursuing extensive fractographic analysis by replicating and then photographing the fracture surfaces of failed test specimens.

Our general deformation program has led to a better appreciation of the behavior of SAP under various testing conditions. One observation is the effect of extrusion ratio as shown by our own data as well as that of Atomics International.[7] The higher extrusion ratio improves the strength and ductility to some extent. Another important finding has been the strain-rate dependence of mechanical properties at high temperatures. As a matter of fact, much of the relatively large scatter in reported SAP data can be attributed to differences in testing conditions. Figure 22.7 shows our data on commercial XAP-001 superimposed on a scatter band obtained from the literature.[8–16] The change in strain rate

---

[7] D. B. Ferry, *Effects of Fabrication on the Mechanical Properties of SAP*, AI-CE-1032 (Jan. 11, 1966).

[8] E. A. Bloch, *Met. Rev.* 6(22), 193–239 (1961).

[9] R. J. Towner, *Alcoa's APM Alloys*, ALCOA Research Laboratories, New Kensington, Pa., Sept. 15, 1960.

[10] E. G. Kendall and W. H. Friske, *Met. Soc., Am. Inst. Mining, Met. Petrol. Engrs., Inst. Metals Div., Spec. Rept. Ser.* 10, 39–45 (1960).

[11] D. G. Boxall and S. Mocarski, *The Present Status of SAP in the Canadian Organic Cooled Reactor Program*, R61CAP30, Canadian General Electric (June 1961) (limited distribution).

[12] D. M. Guy, *Alcoa's Aluminum Powder Metallurgy (APM) Alloys, Alcoa Green Letter*, ALCOA Research Laboratories, New Kensington, Pa., March 1959 (not released for publication).

[13] W. H. Friske, *Interior Report on the Aluminum Powder Metallurgy Product Development Program*, NAA-SR-4233 (1960).

[14] N. Hansen, *Tensile Properties at Room Temperature and at 400°C of Commercial Sintered Aluminum Products*, RISÖ-96 (December 1964).

[15] Atomics International, *SAP Materials Handbook*, AI-CE-Memo-24 (Mar. 23, 1966).

[16] D. G. Boxall and J. W. Standish, *Mechanical Properties of Dispersion-Strengthened Aluminum Alloys*, AECL-1532 (January 1962).

from 0.2 to 0.002 min^{-1} has a large effect on high-temperature properties and covers a good portion of the scatter band. A strain-rate dependence is not unique to SAP but is significant for many alloy systems, including austenitic stainless steels and nickel-base superalloys.

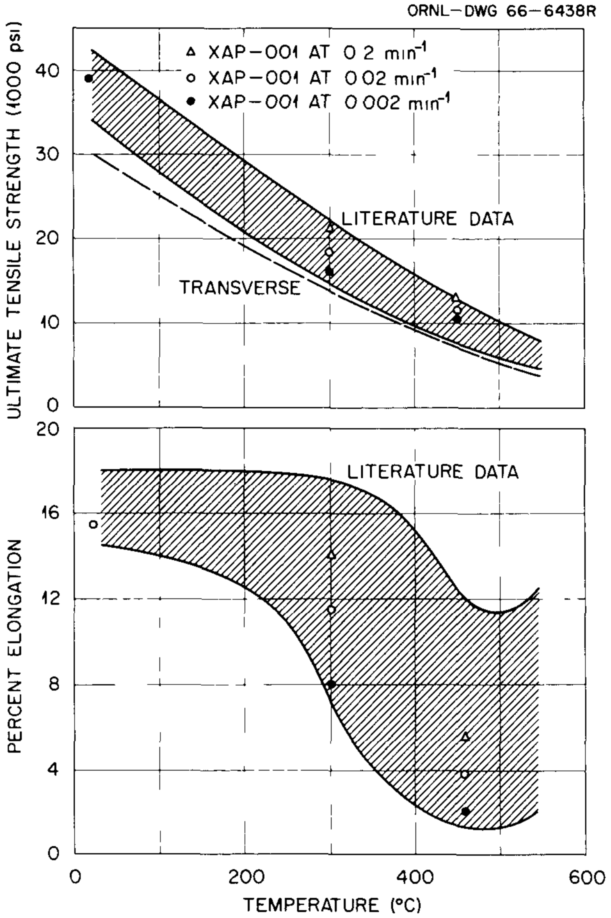

Fig. 22.7. Short-Time Tensile Strength and Ductility of XAP-001.

The strain rate $\dot{\epsilon}$ in SAP is an exponential function of the stress σ: $\dot{\epsilon} = A\sigma^n$. This relationship gives a straight line with slope n on log-log coordinates, as shown in Fig. 22.8. The filled symbols represent 450°C data on an experimental 5% oxide material; the filled triangles are tensile data at three strain rates, and the filled circles are creep rates. The open circles are Battelle data[17] on XAP-001 (previously called M-257) at 427°C. The straight line drawn through the data has a slope of 40. This value of n is unusually high; TD nickel has also shown this high n value.[18]

This very high value for n is significant in both the tensile and creep situations. Any small amount of area change during a tensile test, by internal voiding or tensile necking, gives rise to locally increasing strain rates, which result in curtailed total elongation. Figure 22.9 shows the local neck observed for a high-temperature tensile test.

The high n value affects the creep test by the curtailment of third-stage creep. At the termination of second-stage or linear creep some slight reduction in cross-sectional area has occurred either through actual necking or more likely through internal void formation. Because the load on the specimen is remaining constant this reduction in area increases the stress level. As previously pointed out, because of the high n value, only a small increase in stress provides a significant increase in strain rate, which causes immediate rupture via high-strain-rate shear. This type of rupture is shown in Fig. 22.10. Here we see essentially no necking on the portion that

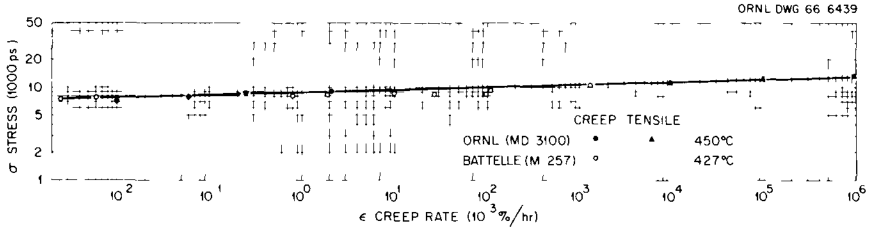

Fig. 22.8. Stress vs Creep Rate for Two Sintered Aluminum Products.

---

[17] J. A. Van Echo and S. W. Porembka, *Long-Term Creep Rupture of Sintered Aluminum Powder and Zircaloy-2 Alloys*, BMI-X-10 113 (Jan. 25, 1965).

[18] L. P. Rice, *Metallurgy and Properties of Thoria-Strengthened Nickel*, DMIC-210 (Oct. 1, 1965).

failed by the growing and linking of the internal voids, a process commonly called ductile tearing. A good deal of necking is seen on the portion that failed by the high-strain-rate shear.

The observations just described and other observations have led to a procedure for the evaluation of any particular experimental SAP rod with a given powder and fabrication history. Because of the limited amount of material available per SAP rod we are using the small button-head specimen design that has been so successful for our irradiation damage studies. Each specimen requires only 2 in. of rod length. To date tensile testing coupled with a modest creep testing schedule has been adequate for the qualitative comparison required. More extensive testing will be added as the field of candidate materials is narrowed. At least four tensile tests are performed on each rod: one tensile test at room temperature for base-line comparison and at least three tensile tests at 450°C covering a wide range of strain rates. This strain rate variation not only provides good tensile data but also allows one to predict the long-time stress-rupture behavior.

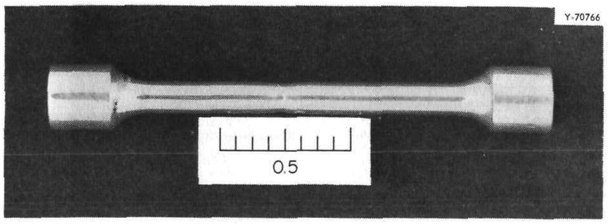

Fig. 22.9. Interrupted 450°C Tensile Test on XAP-001 Showing Local Necking Just Prior to Rupture. Specimen was electropolished before test.

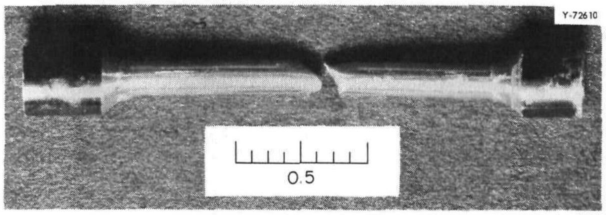

Fig. 22.10. Creep Rupture of XAP-001 at 450°C Showing Local Necking at Shear Lip. No neck is evident on that portion that failed by tearing.

This stress-rupture treatment of tensile data is shown in Fig. 22.11. Plotted on log-log coordinates is the applied stress vs the time to rupture. This particular stress-rupture plot is for one of our rods with 5% oxide tested at 450°C. The open circles are the ultimate tensile strength plotted against the total test time, while the filled circles are actual dead-load stress-rupture tests. One can see the good prediction made by the extension of the tensile data. Data like these have been collected on many of the experimental alloys, including all of the powders being considered and with many process variables already being evaluated. Oxide contents have ranged from 1 to 10%. High-temperature–low-strain-rate ductility has ranged from less than 1% total elongation for the higher oxide contents to as high as 17% for the lower oxide contents.

Another very important aspect of SAP behavior is the mode of fracture. Perhaps our most startling finding has been that under all testing conditions, including high-temperature creep, SAP fracture in a very ductile manner. This ductility is confined to a small portion of the

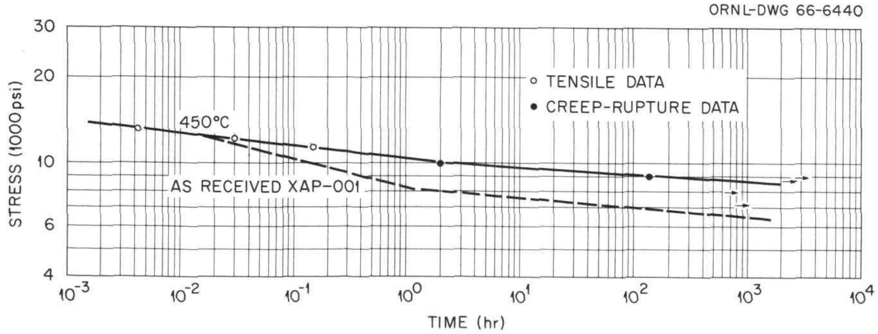

Fig. 22.11. Stress Rupture of an ORNL Experimental SAP Material at 450°C, Compared with a Commercial Material.

PHOTO 84692

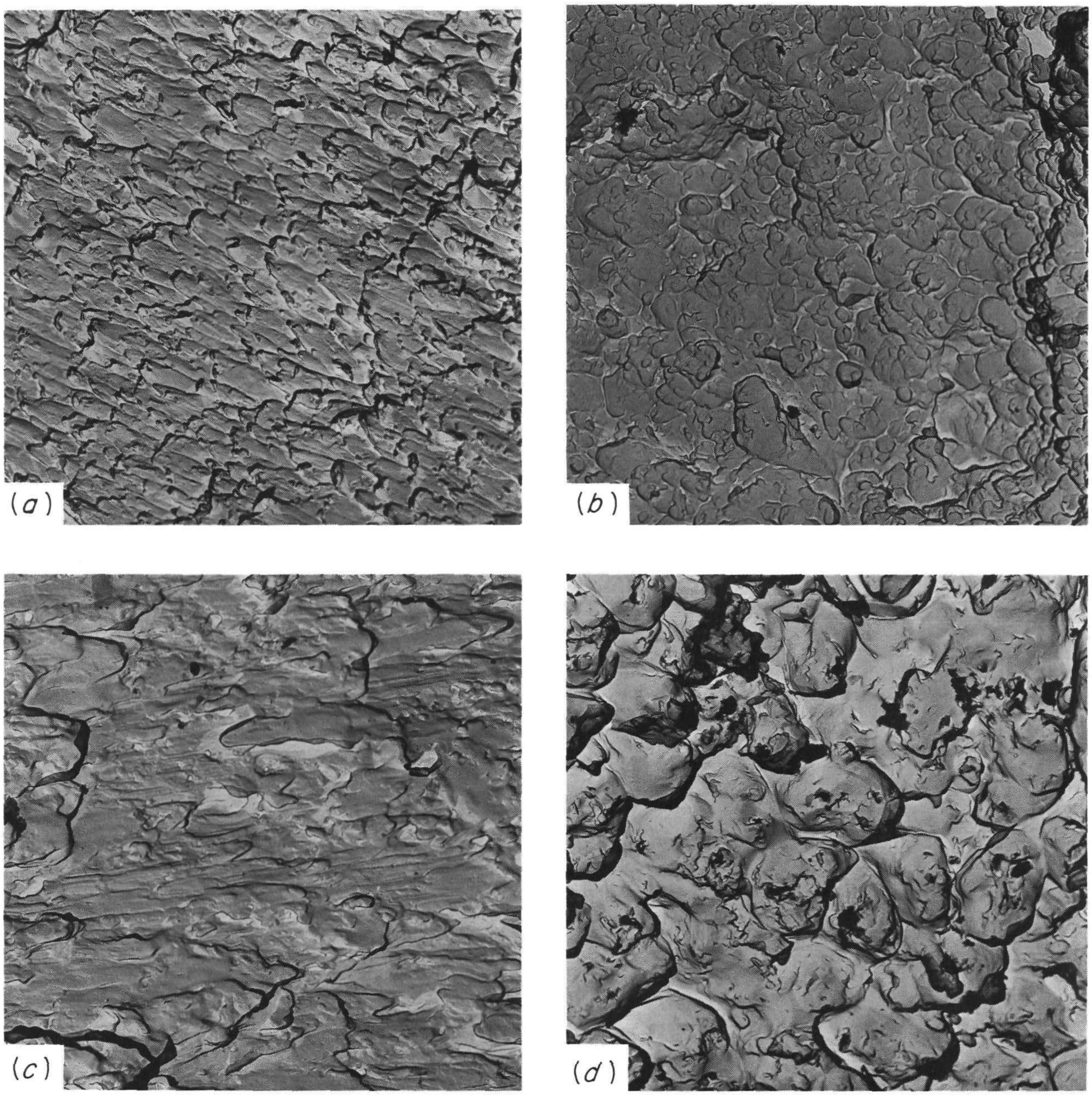

Fig. 22.12. Fracture of Experimental SAP. 6500×. (*a*) Room-temperature shear. (*b*) Room-temperature tearing. (c) 450°C shear. (*d*) 450°C tearing. Replication and fractography by T. A. Nolan, Physics Department, ORGDP.

specimen and thus provides very little overall extension.

Ductile fracture is generally categorized as separation, tearing, or shear. All three of these modes have been found in SAP. Figure 22.12 shows typical low-temperature and high-temperature fractographs. The actual fracture surfaces of the specimens were replicated with a plastic film and subsequently viewed and photographed in the electron microscope. The very fine-scale low-temperature fractures are in contrast to the coarser high-temperature fractures. We now have very good evidence that these high-temperature voids, which initiate fracture, form very early in the tensile test at strains as low as 0.5% and that fracture initiates at the aluminum-Al_2O_3

boundary. The room-temperature shear fractographs are being used routinely to show the oxide distribution within the material. Another technique being used is to anodize the fracture surface for direct replication. Figure 22.13 shows an anodized high-temperature fracture. The platelets of oxide can be seen over the entire surface and are now available for further study, including diffraction analysis and stereophotography.

Another method of fracture analysis that is being used involves conventional microscopy. Examination of tested creep specimens has revealed two types of voids in commercial and experimental SAP. The first type is found only in the gage length near the point of fracture. These voids are rounded, tend to be interconnected parallel to the fracture face, and are connected with the tensile dimples in the fracture process. The second type of void occurs even in the heads of specimens and is elongated in the extrusion direction. Such voids appear on heating alone but grow under an applied load. In some cases these voids link up to form radial fissures. The relationship between the two types of observations and the fracture process has not been established.

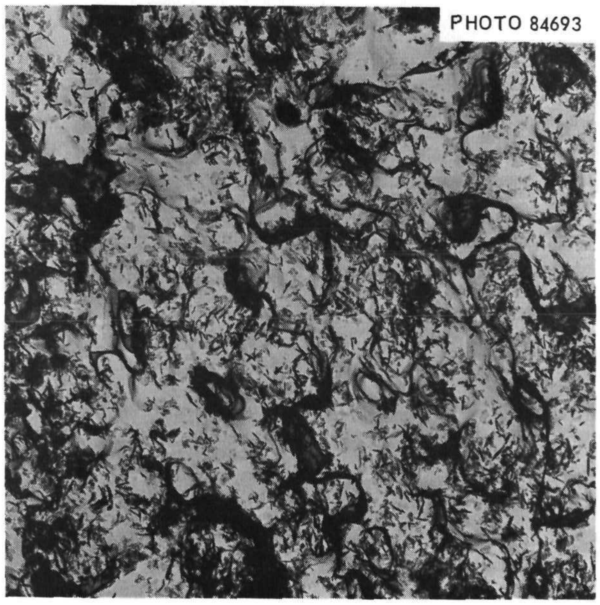

Fig. 22.13. Direct Replication of Anodized Fracture Surface of Experimental SAP Tested at High Temperature. Black needle-shaped particles are oxide platelets viewed on edge. 6500×. Replication and fractography by T. A. Nolan, Physics Department, ORGDP.

DISCUSSION OF RESULTS

The SAP investigation has progressed sufficiently so that we will be able to write detailed specifications for the production of a consistent economical material within the next year. The material produced by these specifications should be as good as the best presently available from any known commercial vendor. Sufficient data are available to enable us to control the oxide content to within 0.5% Al_2O_3 with any of the three investigated lubricants. The resulting flake can be compacted to greater than 95% of theoretical density by methods involving either hot or cold pressing. Finally, the existing extrusion facilities with standard tooling were sufficient to produce rods up to 2 in. in diameter without difficulty.

A large amount of basic information has also resulted from the program. The compositions of the inclusions in the fabricated product have been identified. The atomized powders have been shown to be chill castings of very fine structure. Controlled oxidation of these atomized castings has been difficult because all commercially atomized powder has a very large amount of extremely fine particles that readily convert completely to oxide. These particles, which are less than 1 μ in diameter, occur in all commercial atomized material regardless of nominal size. Finally, we demonstrated that the tensile strength of SAP does not result from the oxide stabilizing a cold-worked structure in aluminum to high temperatures. On the contrary, SAP never possess a cold-worked structure, even the flake coming directly from the mill. The powders always have a highly recovered or recrystallized structure and a very low dislocation density.

23. Zirconium Metallurgy

M. L. Picklesimer

We are investigating zirconium-base alloys of potential use as structural materials in water-cooled or -moderated reactor systems. The principal projects are: (1) studies of the physical metallurgy, consisting of transformation kinetics and morphologies, mechanical properties, phase diagrams, and heat treatment; (2) the development, evaluation, and utilization of preferred orientation and strain anisotropy in α-zirconium alloys during both fabrication and service; (3) the determination of the effects of composition, temperature, and environment on the oxidation-corrosion rates in the thin-film stages of oxide growth; (4) a study of the effects of alloy composition and oxidation environment on the structural properties of thin oxide films in situ; and (5) investigation of the stress orientation of precipitated hydride in Zircaloy-2. A joint effort with the Metallography Group on the effect of specimen preparation on electron microprobe analysis is reported in Part V, Chap. 34 of this report.

STRAIN BEHAVIOR IN ZIRCALOY-2 SHEET-TYPE TENSILE SPECIMENS[1]

P. L. Rittenhouse M. L. Picklesimer

Rolling and transverse direction sheet-type tensile specimens of highly textured Zircaloy-2 were prepared and tested to study strain behavior as a function of specimen geometry. The results of these tests are compared with those obtained from round tensile specimens of the same material.

Nonuniform strain is exhibited in the necked region of the sheet specimens. This adds to the difficulty of using this type of specimen as a measure of strain anisotropy through ratios of contractile to axial strains. Some peculiarities in necking behavior are also discussed.

THE EFFECT OF PREFERRED ORIENTATION AND STRESS ON THE DIRECTIONAL PRECIPITATION OF HYDRIDES IN ZIRCALOY-2[2]

P. L. Rittenhouse M. L. Picklesimer

Hydrogen pickup associated with water and steam corrosion of α-zirconium alloys is one of the major deterrents to their use as reactor materials. The modest solubility of hydrogen in these alloys results in the precipitation of platelets of zirconium hydride. The effect of these platelets on ductility is of prime importance and is dependent on their orientation relative to the stress axis.

Specimens of several lots of Zircaloy-2 plate of known preferred orientation were examined to determine the effects of preferred orientation on the directional precipitation of hydrides. The orientation of the hydrides in unstressed material seems to be associated more with fabrication direction than with preferred orientation. The orientations observed in the unstressed specimens, assuming that fabrication by rolling is a compressive stress state, were consistent with the orientation of hydrides precipitated after plastic deformation by bending.

Elastic stresses applied during precipitation cause a realignment of hydrides that seems to be

---

[1] Abstract of ORNL-TM-1226 (September 1965).

[2] Abstract of paper published in *Papers Presented at the X-Ray Preferred Orientation Meeting Held at National Lead Company of Ohio, Dec. 5 and 6, 1963*, NLCO-946, pp. 79–107 (Dec. 15, 1965).

dependent on the relationship between the stress axis and crystallographic axes. The only significant redistribution of hydrides occurred when the stress axis was parallel to a density of basal poles much greater than random.

DETERMINATION OF THE BASAL POLE ORIENTATION IN ZIRCONIUM BY POLARIZED LIGHT MICROSCOPY[3]

L. T. Larson[4] M. L. Picklesimer

The relationship between the apparent angle of rotation of monochromatic plane-polarized light and the tilt of the basal pole from the surface normal was experimentally determined for zirconium over the wavelength range of 500 to 655 mμ. This relationship allows us to determine the spatial orientation of the basal pole of an individual grain in a polycrystalline zirconium specimen to within ±3° by three simple measurements with a polarized light metallurgical microscope. The method of measurement is discussed in detail.

COMPARISON OF POLE-FIGURE DATA OBTAINED BY X-RAY DIFFRACTION AND MICROHARDNESS MEASUREMENTS ON ZIRCALOY-2[5]

P. L. Rittenhouse M. L. Picklesimer

A rapid and semiquantitative method of determining preferred orientation on large numbers of Zircaloy-2 specimens was desired. Knoop microhardness measurements were investigated as a solution to this problem. The variation of Knoop microhardness measurements on selected planes as a function of indenter axis relative to crystallographic or fabrication directions was determined for four lots of polycrystalline Zircaloy-2, on which both conventional and inverse pole figures had been determined, and on seven Zircaloy-2 single crystals. Data from the single crystals were used to construct a polar coordinate hardness contour map. With use of an empirical relationship between the single-crystal hardnesses and those of the polycrystalline material, conventional pole figures could be constructed which compare favorably with those determined by X-ray diffraction. A quantitative relationship with inverse pole-figure data was also obtained. To determine preferred orientation qualitatively from hardness data requires a minimum of twelve measurements per plane on three, preferably orthogonal, planes. The exact procedure requires attention to grain size, specimen preparation, and indenter load. The time required for preparation, measurement, and analysis is about 45 to 60 min.

RESEARCH ON THE MECHANICAL ANISOTROPY OF ZIRCALOY-2[6]

P. L. Rittenhouse M. L. Picklesimer

The preferred orientation developed in α-zirconium alloys during fabrication causes a strong anisotropy of plastic properties. A reliable system of evaluating and characterizing this anisotropy is a prerequisite to the use of zirconium alloys as materials of construction. Studies of the mechanical properties, strain behavior, and preferred orientation of Zircaloy-2 sheet were performed with the purpose of developing such a system. A method was developed which uses only the natural strain data from orthogonal pairs of tensile and compression specimens to describe the plastic anisotropy and preferred orientation.

DEFORMATION, CREEP, AND FRACTURE IN ALPHA-ZIRCONIUM ALLOYS[7]

M. L. Picklesimer

The anisotropy of mechanical properties observed in α-zirconium alloys can be related to the preferred orientation of the material. The influence of preferred orientation on anisotropy of yield strengths, plastic flow, creep, fracture, their strain rate and temperature sensitivities,

---

[3] Abstract of paper accepted for publication in *Transactions of the Metallurgical Society of AIME*.

[4] Associate Professor of Geology, University of Tennessee; Consultant

[5] Abstract of *Trans. Met. Soc. AIME* **236**, 496–501 (1966).

[6] Abstract of *Electrochem Technol.* **4**, 322–29 (1966).

[7] Abstract of *Electrochem. Technol.* **4**, 289–300 (1966).

and the stability of such textures to further deformation are discussed in terms of the deformation systems observed in single crystals. It is concluded that other deformation systems operate because of the restraint of neighboring grains in polycrystalline materials.

EFFECTS OF NEUTRON IRRADIATION AND VACUUM ANNEALING ON OXIDE FILMS ON ZIRCONIUM[8]

J. C. Banter

Neutron-irradiated, anodized zirconium and thermally oxidized specimens were vacuum annealed. Reflection and transmission spectra of these specimens indicate that irradiation affected neither the oxide films nor their rate of dissolution. However, the annealed films absorb light across the visible and ultraviolet spectral regions, apparently resulting from the production of defects by the film dissolution. Vigorous attack of the zirconium through annealed films by a solution of bromine in ethyl acetate supports the presence of defects. Unannealed specimens are not so attacked. Other results indicate that estimates of film thicknesses on annealed specimens, based on visual observation of interference colors, may be in error. The importance of both film formation and oxygen dissolution to the overall oxidation mechanism is discussed.

ELECTRICAL DISCHARGE MACHINING IN THE METALLURGICAL LABORATORY[9]

J. C. Wilson

Electrical discharge machining (EDM) has proved invaluable for preparing metallurgical specimens at ORNL. The design, construction, and operation of simple, inexpensive EDM units will be described. We will show the capabilities of these machines for such operations as: (1) cutting single crystals to specific orientations with a minimum of deformation, (2) machining spherical, single-crystal oxidation specimens, and (3) cutting cylindrical and flat tensile bars.

ANISOTROPY OF OXIDATION IN ZIRCONIUM[10]

J. C. Wilson

The effect of crystallographic orientation on the oxidation of zirconium was determined semiquantitatively for all orientations by observing the patterns of interference colors on single-crystal spheres oxidized in air (350 to 400°C) and anodically in KOH solutions.

The pattern of oxidation is clearly visible in less than 1 hr at 360°C when the oxide films are less than 700 A (1 mg/dm^2) thick. Under these conditions the ratio of thickest to thinnest films is greater than 2. After 200 hr at 400°C the ratio is about 4, and the thickest film is about 7000 A (10 mg/dm^2). Very roughly, the regions of greatest oxide thickness may be described as narrow bands going from (0001) to $(11\bar{2}2)$, from $(11\bar{2}2)$ to $(31\bar{4}4)$, and from $(31\bar{4}4)$ to $(10\bar{1}0)$. The patterns will be illustrated by color photographs of the oxidized spheres.

In anodized films (1% KOH) up to 2500 A thick (4 mg/dm^2), the thickest films are only about 25% thicker than the thinnest. The pattern of oxidation is plainly visible, and there is a general resemblance to the results from air oxidation. However, the relative rates on certain planes apparently change at higher (30 to 50 v) anodizing potentials. As a result there are distinct differences between air-oxidized and anodized films.

We conclude: (1) To obtain reproducible oxidation results on specific planes in zirconium requires precise control of orientation, because on certain planes an error of a few degrees can result in a factor of 2 difference in oxide thickness, and (2) from the observed oxidation anisotropy and the strong tendency of polycrystalline zirconium to develop strong working and annealing textures, we would expect oxidation rates to depend measurably on the specific textures. For instance, the texture differences between rolled and rolled-and-annealed zirconium might give oxidation rates differing by a factor of 2.

---

[8] Abstract of *Electrochem. Technol.* 4(5–6), 237–39 (1966).

[9] Abstract of paper in *Technical Papers, Nineteenth Metallography Group Meeting, Held April 20–22, 1965, at Oak Ridge National Laboratory, Oak Ridge, Tennessee*, ORNL-TM-1161, pp 159–73 (February 1966).

[10] Abstract of paper presented at the Fifteenth Annual USAEC Corrosion Symposium, ORNL, May 23–25, 1966 To be submitted for publication.

Part IV.

Reactor Development Support

page blank

24. BONUS Fuel Element Development

G. M. Slaughter G. M. Adamson, Jr.

At the request of the U.S. Atomic Energy Commission, a modest effort has been under way for the past 1.5 years in support of the Boiling Nuclear Superheat (BONUS) Reactor.[1] This metallurgical support effort has the following objectives: (1) to provide assistance and consultation services for the present BONUS core and operations, (2) to develop specifications and provide assistance pertaining to advanced fuel assemblies for this reactor, and (3) to obtain pertinent information on the suitability of advanced alloys for use as BONUS superheater fuel cladding. The last item is required to supplement the somewhat limited existing data that have been acquired on reference and improved alloys under normal and severe BONUS operating conditions.

REBUILDING OF BONUS SUPERHEATER FUEL ASSEMBLY NO. 29

E. A. Franco-Ferreira G. M. Tolson[2]
E. L. Long

To assist in the failure analysis of a superheater fuel assembly from the BONUS Reactor, a spare unirradiated unit was obtained and examined.[3] This examination provided base-line information on the characteristics of a typical fuel assembly in the initial core loading in the as-fabricated state.

We subsequently rebuilt the unit using manufacturing procedures that provided significant improvements over those used for the original core loading.[4] The rebuilding of this assembly satisfied two requirements: (1) replacing the spare element at the BONUS site and (2) proving out the suitability of the proposed fabrication modifications on an actual fuel assembly.

The major improvements in design of this fuel assembly were related to making the fuel rod end closures (i.e., the socket-type weld joints were replaced with the more easily made edge-weld joints and the vent-hole plug welds were eliminated). A view of a typical end cap weld of the new design and its microstructure are shown in Fig. 24.1. The fabrication procedure was significantly changed to assure the retention of a relatively small grain size in the cladding and avoid the large grain size present in the tubes of the initial core loading. Two specific measures were taken to obtain this control: the fuel cladding had a $\frac{1}{4}$-hard mill temper before brazing and spacers were brazed on the fuel tubes before they were loaded with fuel.

During the fabrication of this assembly, an unusual and unexpected cracking problem was encountered in the vicinity of welds in a few fuel rods. Extremely small cracks were found; these were pinpointed with the aid of dye penetrants and helium leak testing. Metallographic sections were made through the tube-to-end-cap welds of these rejected rods, and the specimens were carefully polished until the defects were located.

---

[1] J. E. Cunningham, *Metals and Ceramics Div. Ann. Progr. Rept. June 30, 1965*, ORNL-3870, pp. 293–99.

[2] Now at Oak Ridge Gaseous Diffusion Plant.

[3] J. E. Cunningham, E. L. Long, Jr., E. A. Franco-Ferreira, and D. G. Harman, *BONUS Reactor Superheater Fuel Assemblies — An Investigation of Failure and Method of Correction*, ORNL-3910 (December 1965).

[4] G. M. Slaughter *et al.*, *Fabrication of Rebuilt BONUS Superheater Fuel Assembly No. 29* (in preparation).

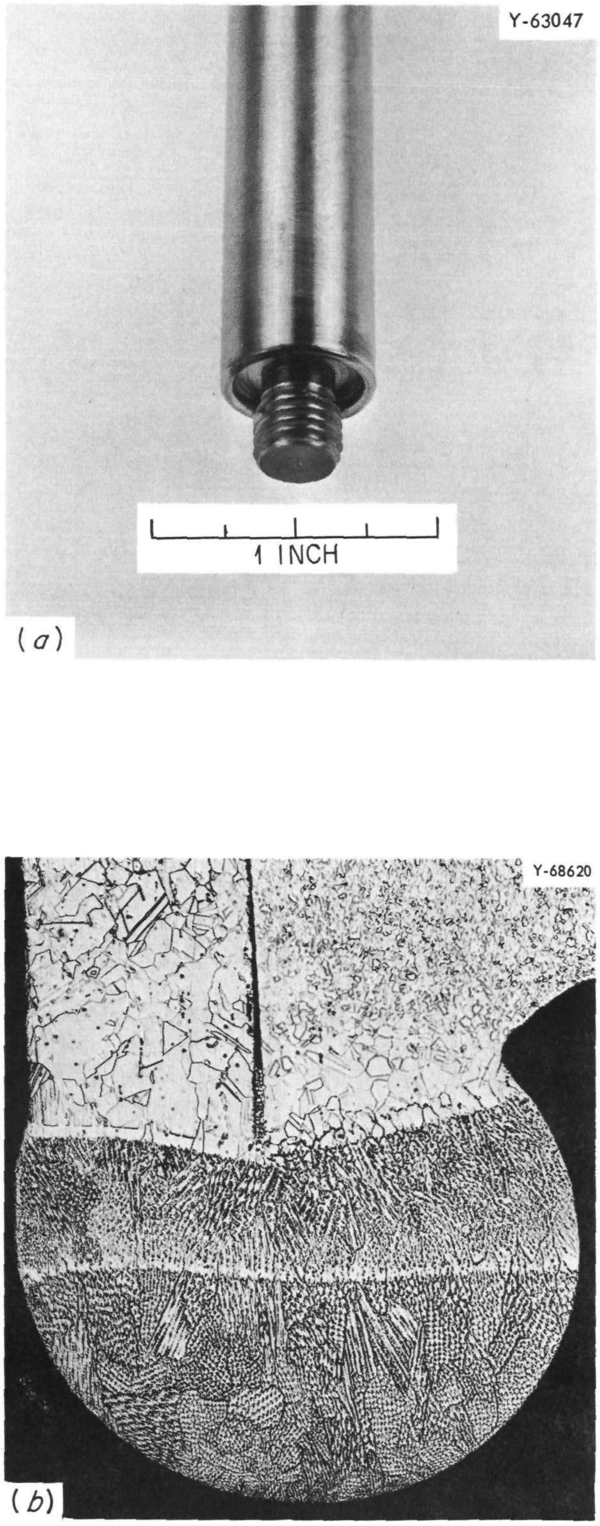

Fig. 24.1. (a) Typical Top End Cap Weld. 1.5×. (b) Cross Section of This Weld. 75×, reduced 22%. Etchant: glyceria regia.

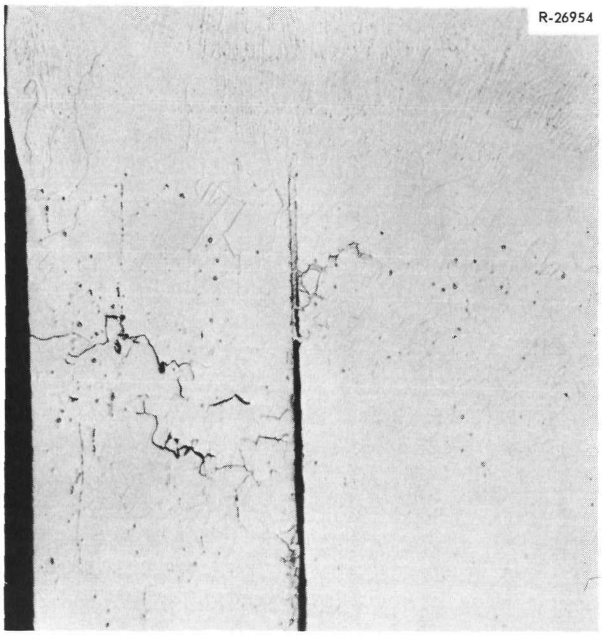

Fig. 24.2. Appearance of a Longitudinal Section Through the Defective Region of Fuel Rod O-28. Note the network of intergranular cracks in the cladding and the wide grain boundary in the end cap. Etched lightly with aqua regia. 100×. Reduced 27%.

A typical area of cracking is shown in Fig. 24.2. A network of intergranular cracks is apparent in the cladding. These cracks probably began at the inner surface and continued through the wall of the cladding. Figure 24.3, a higher magnification view of this weld, shows several areas with wide grain boundaries and distinct evidence of a second phase. Apparently, this second phase was low melting and emanated from the weld deposit, flowed down the cladding–end-cap interface, and wetted a few grain boundaries. Electron microprobe analysis of this second phase showed it to be very high in phosphorus; the mechanism by which a concentration of this magnitude occurred is still being investigated.

The necessary 32 leak-tight fuel rods were successfully constructed, welded into their coolant tubes, and shipped to ORGDP for installation into the standpipe portion of the fuel assembly. The completed assembly has been sent to the reactor site in Puerto Rico.

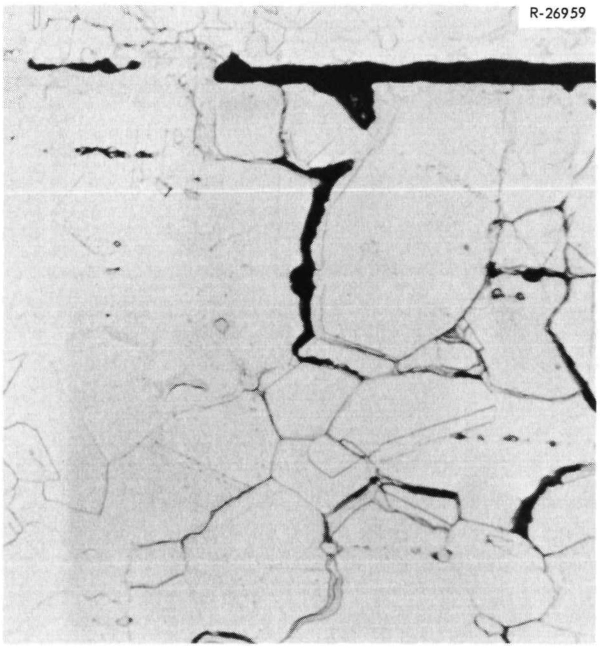

Fig. 24.3. Same Weld as Fig. 24.2 at Higher Magnification. Some of the intergranular cracks in the cladding and the associated second-phase "rivers" show. Note that some of the lower-melting compounds from the weld metal filled a portion of the gap between the cladding and end cap and wetted several grain boundaries. Etchant: copper regia; 500×. Reduced 25.5%.

ASSISTANCE IN FABRICATING ADVANCED FUEL ASSEMBLIES

G. M. Tolson[2]

Technical assistance was given to ORGDP in developing specifications, procuring material, and selecting inspection procedures for eight advanced assemblies to be fabricated for the BONUS Reactor. We selected Incoloy 800 as the fuel cladding material for these assemblies, primarily because it resists corrosion by superheated steam better than the Inconel 600 used for core I. The whole fabrication operation, from initial specifications to final inspection, will also be updated to reflect obvious improvements in manufacturing technology.

Typical results of this liaison program are the following specifications:

Specification	Title
NRS-12	Uranium Dioxide Pellets
NRS-15	Fuel Tubing for BONUS Superheater Element
NRS-16	Rod for BONUS Superheater Element
NRS-17	Special Superheater Fuel Rods for the BONUS Reactor
NRS-18	Leak Testing BONUS Fuel Elements
NRS-19	Clad Tubes Subassemblies for the BONUS Superheater Fuel Element
NRS-20	Triangular Tubing for BONUS Superheater Clad Spacers

MECHANICAL PROPERTIES OF ADVANCED ALLOYS

D. G. Harman

Mechanical properties studies have concentrated on the collapse behavior of fuel tubes made from alloys being considered for advanced BONUS applications. Design considerations do not require the fuel tube to be free-standing, and creep collapse is expected.

An analysis of the Inconel 600 fuel cladding presently in BONUS indicated the times required to collapse the fuel cladding under various reactor operating conditions. At fuel cladding temperatures of 1000, 1100, 1200, and 1300°F, collapse would be expected in 4000 hr, 400 hr, 30 min, and 3 min respectively. These collapse times would be reduced by any tube ovality or wall thickness variations. Tube wrinkling is not expected to be a problem because of the small ratio of diametral gap to tube wall thickness in this fuel loading. This analysis was based on data from a previous ORNL tube-collapse study as well as from extensive Inconel 600 creep data generated at ORNL.

Preliminary tube-collapse studies on Incoloy 800 have shown no tube wrinkling when the diametral gap between fuel and inside tube wall is about 0.002 in. This is the largest gap expected at normal BONUS operating temperatures. These initial Incoloy 800 collapse studies were made on the only lot of tubes of the correct size that was readily available. This tubing, which possessed very low aluminum and titanium contents, will be used only to study geometric variations; specific data (i.e., collapse time vs test temperature) will be obtained with tubing of a composition more nearly conforming to that to be used in the actual assemblies.

NONDESTRUCTIVE TESTING DEVELOPMENT

K. V. Cook

Nondestructive testing studies are being conducted to develop improved techniques for inspecting the BONUS fuel elements. The problem areas include evaluation of the fuel cladding, the spacer-to-cladding braze bonds, and the several welds in the fuel, coolant, and pressure tubes.

Brazes

We are evaluating techniques for inspecting the spacer-to-cladding braze bonds. Radiographs have been made on 15 different spacer brazes; these revealed the presence of a few scattered voids in the brazed joints. These same 15 joints were used as test joints for feasibility studies with ultrasonic testing methods. Through-transmission two-transducer methods were investigated that incorporated a standard transducer and an interior probe, which we fabricated. The probe was fixed in position, and the tube passed longitudinally over it. We masked the external transducer to vary the ultrasound beam in size and shape so that braze bonds could be evaluated with different scanning procedures. For *x-y* scanning of the braze joint, appropriate masking was used to get the mandatory small-diameter beam of ultrasound.

Results showed that this method of evaluation (*x-y* scanning) was not feasible for the particular specimen geometry involved. Another scanning procedure that we tried on the 15 original joints required a very narrow rectangular beam of ultrasound to inspect the entire bond width in incremental steps along its length. The ultrasonic data correlated with the voids detected by radiography; however, no destructive testing has been done to establish the sensitivity of the test. A number of samples containing poor bonds of predetermined shapes and sizes have been received and will be used to further develop the technique.

Tubes

Eleven Incoloy 800 tubes, 0.452 in. OD × 0.020 in. wall, were also evaluated with fluorescent-penetrant and ultrasonic techniques (both resonant and pulse echo). The pulse-echo method was applied with a 0.002-in.-deep × $\frac{1}{4}$-in.-long reference notch (depth 10% of wall). Based on the results for these 11 tubes, Incoloy 800 tubing can apparently be inspected with a more sensitive test or by using a smaller reference notch.

INFLUENCE OF BRAZING CYCLE ON GRAIN SIZE AND PROPERTIES OF CLADDING

G. M. Slaughter

The influence of a braze cycle upon the grain-coarsening tendencies of two heats of Incoloy 800 was determined. Samples of each heat with five different amounts of cold work were prepared and subjected to brazing cycles at 1800, 1850, and 1900°F. Times at temperature of 10, 20, 30, and 60 min were investigated.

At 1800°F grain coarsening did not appear to be a serious problem, although some grain growth did occur after 60 min. Prior cold work was very beneficial in creating a fine grain size after brazing.

Grain growth is a potential problem in Incoloy 800 tubing at a brazing temperature of 1850°F. Some growth was observed in grains on the outer surface of as-received tubes after holding at 1850°F for only 20 min. Since this effect was not noted in the rest of the tube wall, it may be related to the tube-straightening operation normally given the finished product. The slight amount of cold work used in the straightening operation apparently gives rise to germination.

Similar studies at 1850°F on Incoloy 800 sheet showed that grain coarsening was not a problem at a brazing time of 20 min; however, some coarsening was observed after holding for times in the 30- to 60-min range. Prior cold work was very beneficial in creating and ensuring a fine grain size after brazing both heats of material. A 22 to 25% reduction in area seems to be optimum for this temperature.

At a brazing temperature of 1900°F, extensive grain growth in both as-received tubing and sheet was encountered in 20- to 30-min braze cycles. A reduction in area of 22 to 25% appeared to eliminate the problem, except at the 60-min braze time.

Hardness changes were measured to determine the annealing response of 25%-cold-worked Incoloy 800 at a typical brazing temperature of 1850°F.

Brazing times of 1, 2, 4, 6, 10, and 20 min were investigated. The hardness of the cold-worked tubing was 247 DPH. After only 1 min at 1850°F, the hardness was reduced to 142 DPH; after 20 min, no further reduction was evident. This study indicated, as was expected, that thin-walled material anneals completely very rapidly.

Welding studies were conducted on this annealed material, and no cracking difficulties were encountered. We thus conclude that the high-temperature brazing operation will remove all vestiges of cold work from the tubing and that cracking difficulties associated with residual cold work should not be a problem.

25. Desalination

D. A. Douglas, Jr.

The desalination program consists of two main areas of interest. One concerns the reactor and the other the distillation plant. The problems relating to the heat source are under the cognizance of the AEC, while the evaporator-condenser is under the direction of the Office of Saline Water in the Department of the Interior. In the past year we have analyzed the cost of fabricating a number of different fuel elements in an effort to develop the optimum design for producing low-cost steam. We also developed specially shaped tubing for heat-transfer tests in an attempt to reduce the cost of the evaporation and condensing steps in converting salt water to fresh water.

COST ESTIMATES FOR FUEL FABRICATION

T. N. Washburn A. L. Lotts

The consideration being given to the desalting of seawater by nuclear power makes very large single-purpose fuel fabrication plants a distinct possibility. Such large fabrication plants would effect substantial economies in the fabrication of fuel and would accordingly lower fuel-cycle costs.

Large Nuclear Steam Generators [3500 Mw (thermal)]

There is an inherent interest in the potential use in nuclear desalination plants of low-temperature (315°F) reactors that produce heat for water processing only. We have assisted the Reactor Division in the evaluation of the effect of temperature level on the selection of fuel and cladding materials for the Large Nuclear Steam Generator Parameter Study. Fuel fabrication costs were estimated for four different cases. Three of these cases were for fuel elements with the same physical design of three nested annular rings but with different combinations of fuel and cladding materials: UC with SAP, uranium with zirconium, and uranium with aluminum. In the fourth case the design consisted of four nested annular rings with uranium fuel and aluminum cladding. These designs are illustrated in Figs. 25.1 and 25.2, and the calculated fabrication costs as a function of production rate are shown in Fig. 25.3.

Joint U.S.-Mexico Desalination Study

A comparative study of four reactor types was performed by the Reactor Division for the Joint

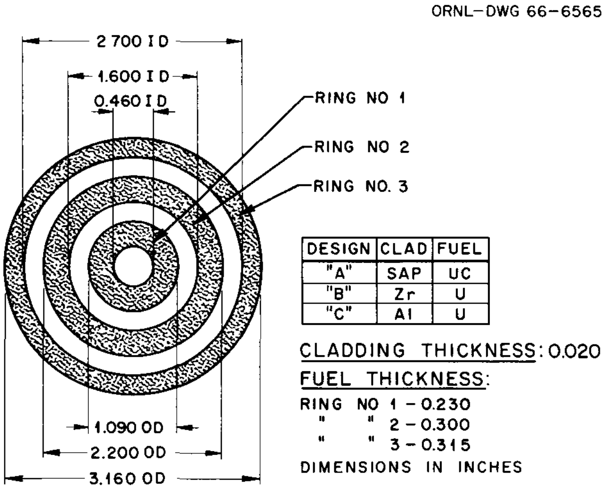

Fig. 25.1. Design of Three-Ring Fuel Elements for Large Nuclear Steam Generator.

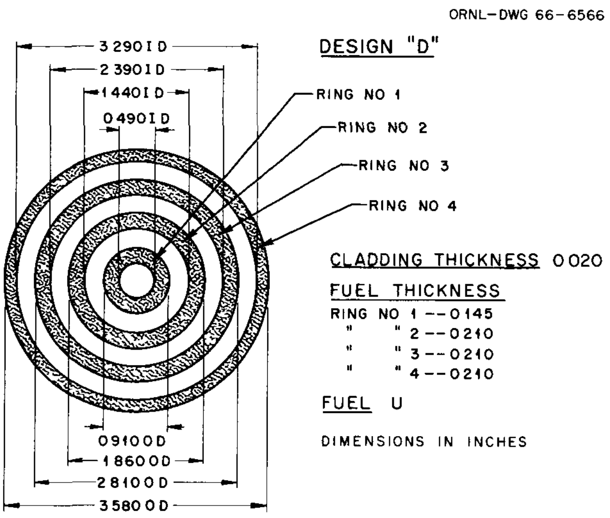

Fig. 25.2. Design of Four-Ring Fuel Elements for Large Nuclear Steam Generator.

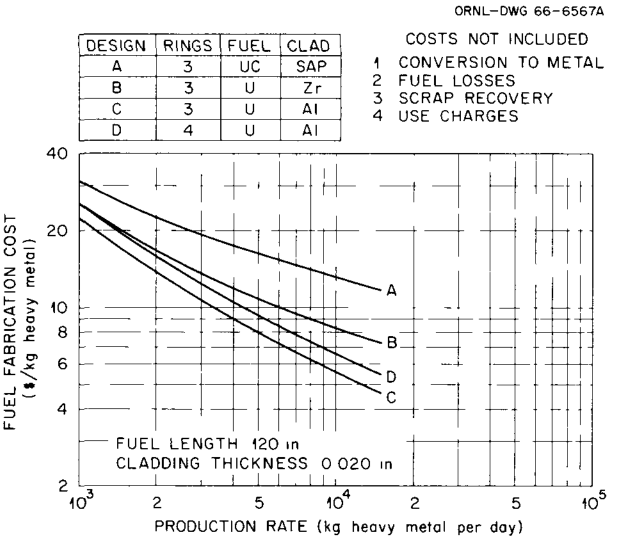

Fig. 25.3. Fabrication Cost Comparison of Fuel Elements for Large Nuclear Steam Generator.

U.S.-Mexico Desalination Study. These reactors would serve as dual-purpose sources of energy for combined electric and water-desalination facilities. These four reactors were a modification of the Hanford New Production Reactor (NPR) with oxide fuel,[1] a similar reactor with metal fuel,[1] a boiling water reactor (BWR) with oxide fuel,[2] and a heavy-water organic-cooled reactor (HWOCR) with carbide fuel.[3] Table 25.1 contains results of the calculations. Each of these fuel element designs was described previously in detail.[1-3]

TUBING FABRICATION

J. M. Jones

In the proposed nuclear desalination plants, extensive use of thin-walled tubing in the evaporator-condenser is necessary. Several methods have been conceived to enhance boiling and condensation characteristics along these tubes; one of these concerns the incorporation of small longitudinal flutes.

Since tubing of this design is not commercially available, we started to develop satisfactory procedures for fabricating a small amount out of aluminum for basic heat-transfer studies. The fabrication process included the machining of flutes on flat aluminum sheets, the forming of these sheets into tubing, and the welding of the formed tubing.

Two tubes $8\frac{1}{2}$ ft long by 1 in. OD were fabricated from 0.065-in.-thick type 6061 aluminum sheet. One tube was fluted only internally; the other tube was fluted both internally and externally. The flutes had a 0.013-in. radius and extended the entire length of the tube except for 3- and 6-in.-long smooth sections at the ends, which were required for installation in the heat-transfer loop. Figure 25.4 shows the internally fluted tube after forming. The flutes were not damaged during the forming process, and the curvature of the tube was very good.

An elaborate jig was necessary to adequately align this long tubing for welding. The optimum welding conditions were: current, 25 to 28 amp; travel speed, $1\frac{1}{2}$ in./min; total time, 68 min for each tube. A typical weld is shown in Fig. 25.5;

---

[1] R. K. Robinson (ed.), *US-Mexico Desalting Plant Study — Graphite Moderated Reactor with Oxide or Metallic Fuel*, RL-GEN-925 (Apr. 15, 1966).

[2] Letter from R. W. Lockhart, GE-APD, to I. Spiewak, ORNL, "Information on Advanced BWR Concepts," Apr. 15, 1966.

[3] *Heavy Water Organic Cooled Reactor, 1000 Mwe Nuclear Power Plant Preliminary Conceptual Design*, AI-CE Memo-6, vols. 1 and 2 (Oct. 1, 1965).

Table 25.1. Fuel Fabrication Cost Summary for Desalination Reactors in Joint U.S.-Mexico Study

Industry Size [Mw (thermal)]	Fuel Exposure (Mwd per Metric ton of U)	Production Rate (kg/day)	Fuel Fabrication Cost ($/kg metal)			
			BWR	HWOCR	NPR	
					Oxide	Metal
25,000	36,450	867	70.20	53.04	22.70	
25,000	30,600	1,032	66.39	49.39	20.96	23.63
25,000	25,000	1,263	62.33	45.67	19.18	
25,000	17,500	1,805	56.03	39.67	16.62	
25,000	15,000	2,106	53.60	37.71	15.66	16.31
25,000	7,700	4,102				11.63
75,000	36,450	2,601	50.63	35.29	14.47	
75,000	30,600	3,096	48.40	33.48	13.60	13.34
75,000	25,000	3,789	46.00	31.56	12.74	
75,000	17,500	5,415	42.36	28.59	11.35	
75,000	15,000	6,318	40.97	27.45	10.84	
75,000	7,700	12,306				7.93

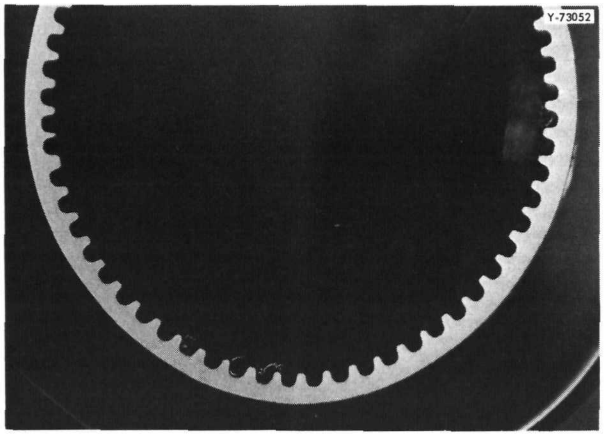

Fig. 25.4. Typical Internally Fluted Tube Showing Excellent Uniformity of Flutes. 5×. Reduced 43%.

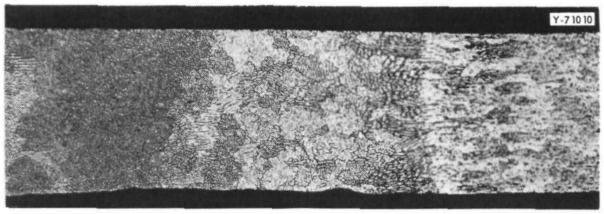

Fig. 25.5. Sound Weld in Fluted Tubing. 40×. Etch: mixed acids. Reduced 47.5%.

the weld was sound with no excess penetration. About three flutes were absorbed into the weld metal of each tube; this represents only 5% of the total number of flutes per tube.

ADHESIVE BONDING STUDIES

J. M. Jones

Construction of evaporators for a nuclear desalination plant would require an enormous number of tube-to-header joints. The processes currently used for making such joints in large heat exchangers are welding, brazing, and mechanical rolling. The potential cost advantage of adhesive bonding made a small feasibility program desirable, particularly in view of the large amount of technical information on this subject that has appeared during the past two years.

Several adhesives that might be suitable for long-time operation in a desalination application were procured and given a cursory evaluation. Since one of the most important of the necessary properties is that the joint withstand temperatures up to 250°F, the initial study involved determination of shear properties. We studied lap joints using type 304L stainless steel sheets $\frac{1}{2}$ in. wide × $2\frac{1}{2}$ in. long. The adhesives acquired for this study and the resulting shear strength prop-

Table 25.2. Results of Shear Tests on Adhesively Bonded Joints

Adhesive	Vendor	Type and Cure	Shear Strength[a] (psi)					
			Room Temperature	100°F	150°F	200°F	250°F	300°F
Tube sealant	Loctite Corporation	Single component, liquid, cures at room temperature in 4 to 6 hr	410	140				
Ceramabond 503	Aremco Products, Inc.	Single component, paste, cures at 250°F in 1 hr	352	420	180	127		
CE-23	U.S. Steel	Two component, paste, cures at room temperature in 48 hr	1825	1248	237	157		
EC-1838 B/A	3M Company	Two component, paste, cures at room temperature in 48 hr	2742	2520	681	258		
FM-1000	Bloomingdale Rubber Co.	Film, cures at 350°F in 1 hr	3560	2615	2260	1405	490	370
Imidite 850	Whittaker Corporation	Film, cures at 300°F in 1 hr	1423	1792	1398	1127	1513	1065

[a] Average of three tests

erties are listed in Table 25.2. The cure cycles listed in the table are those recommended by the manufacturers of the respective adhesives. Only two of the tested adhesives retained appreciable strengths at 250°F, FM-1000 and Imidite 850. Future work should therefore be aimed primarily at further evaluation of the corrosion resistance of these two adhesives and should include the acquisition and evaluation of a number of other adhesives.

26. Gas-Cooled Reactor Program

J. H. Coobs W. O. Harms

Our materials effort in support of the Gas-Cooled Reactor Program is directed principally toward development of unclad ceramic fuel elements for high-temperature gas-cooled converter reactors (HTGR's) such as that being designed by General Atomic and the Public Services of Colorado. Other activities consist in support for the EGCR and other associated research. The significant contributions in these two categories are presented below along with pertinent background information.

All-ceramic nuclear fuel elements offer the distinct advantages of high-temperature operation and good neutron economy. However, the escape of fission-product activity from them into the coolant system of a power reactor may complicate operation and maintenance. Our program on all-ceramic fuels consists mainly in developing the technology for depositing pyrolytic carbon coatings and preparing and testing pyrolytic-carbon-coated oxide and carbide fuel particles. Irradiation testing of unsupported coated particles and fueled-graphite elements containing such particles is included in the program. A smaller effort has involved the preparation and testing of unclad fueled-graphite bodies. Such fuels are designed to release large fractions of the noble-gas fission products and thereby increase fuel lifetime and the conversion ratio by avoiding parasitic capture of neutrons. The results of some related efforts on thorium-containing fuels are reported in Chap. 32 of this report.

Supporting research includes the irradiation creep of moderator-grade graphites, correlation of thermodynamic properties of ceramic fuel materials, and several investigations conducted in support of the Experimental Gas-Cooled Reactor (EGCR) before it was canceled in January 1966. In addition to the investigations presented below, the specifications, procedures, and problems encountered in manufacturing the control rods for the EGCR were documented.[1]

PYROLYTIC CARBON COATING STUDIES

Coatings Deposited from Methane in a 2-in.-diam Fluidized Bed

D. M. Hewette R. L. Beatty

A 2-in.-diam coating apparatus was built for use in depositing pyrolytic carbon coatings on large batches of fuel particles and for study of problems involved in extending coating technology to larger equipment. The apparatus consists of a resistance-heated graphite reaction chamber similar to but larger than that described previously.[2]

We completed a systematic study of the effects of deposition conditions on the properties of coatings deposited from methane in the 2-in.-diam coater.[3] The deposition temperature and the rate of supply of methane relative to the initial surface area of the fluidized bed were considered to be controllable variables as in the previous work. The results of this study are summarized in Fig. 26.1, in which the coating density, plotted as contour lines as functions of these two variables, is compared with the density contour map obtained

---

[1] G. M. Tolson, *The Manufacture of the Control Rods for the Experimental Gas-Cooled Reactor,* ORNL-3932 (April 1966).

[2] R. L. Beatty, F. L. Carlsen, and J. L. Cook, *Nucl. Appl.* 1(6), 560–66 (December 1965).

[3] D. M. Hewette and R. L. Beatty, *GCR Program Semiann. Progr. Rept. Mar. 31, 1966,* ORNL-3951, pp. 3–6.

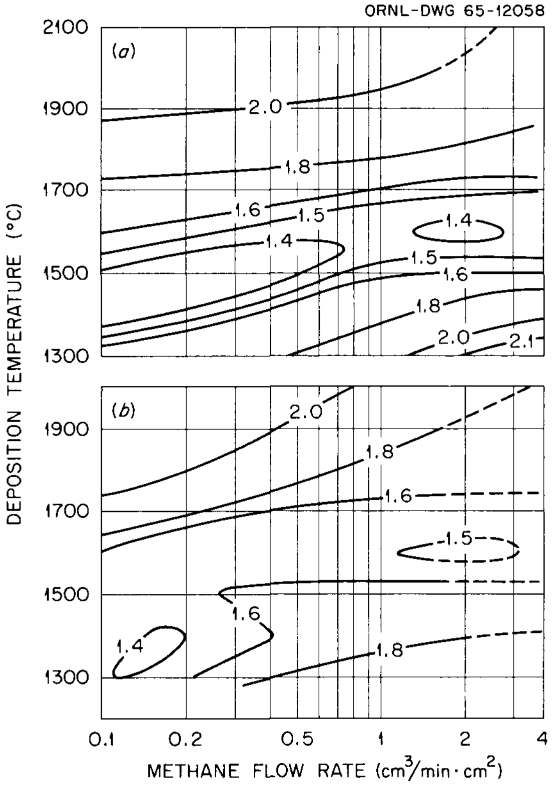

Fig. 26.1. Effect of Deposition Conditions on the Density of 50-μ-thick Pyrolytic Carbon Coatings Deposited on 200-μ-diam Particles in (*a*) a 2-in.-diam and (*b*) a 1-in.-diam Fluidized Bed. The flow rates are in cubic centimeters per minute per square centimeter of particle surface.

with a 1-in.-diam coater. Although slight differences were found in the pattern of densities and the maximum and minimum values, the similarity of the contour maps is striking. We also found excellent correlation between the apparent crystallite size (L_c) of coatings deposited under the same conditions of temperature and supply rate in the two coaters and noted that the anisotropy factors of the deposits followed the same pattern as shown previously.[2]

Coating of Large Particles in a 1-in.-diam Fluidized Bed

H. Beutler[4] R. L. Beatty

Since fuel particles with diameters of 200 to more than 500 μ are being considered in HTGR fuel

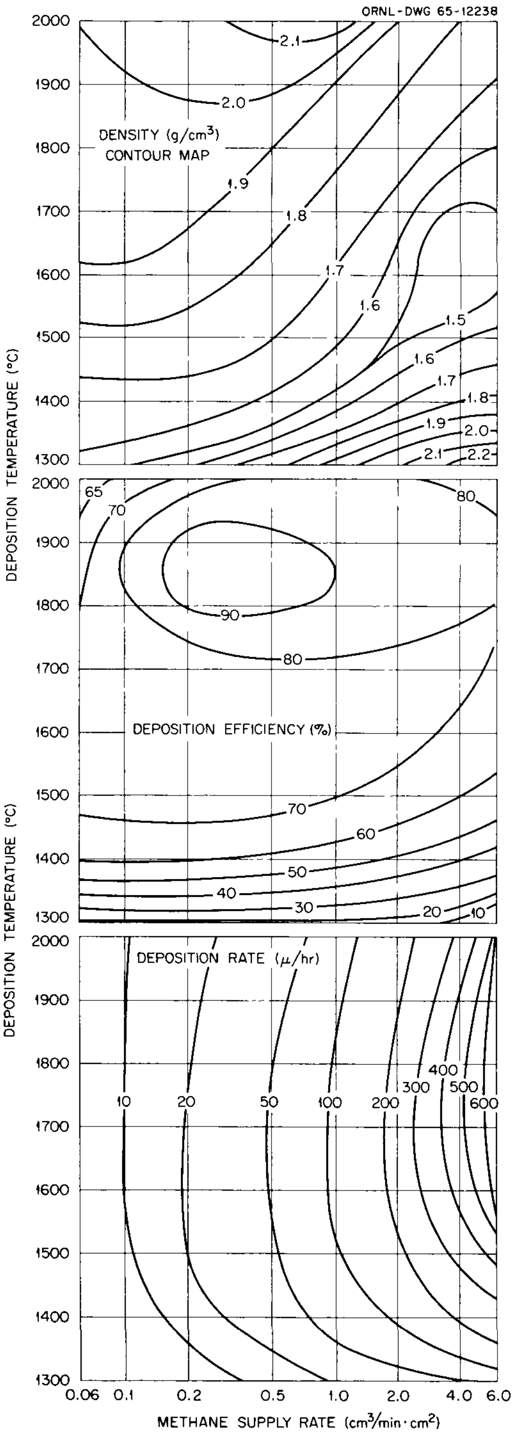

Fig. 26.2. Effect of Methane Supply Rate and Deposition Temperature on Deposition Rate and Efficiency and on Density of Pyrolytic Carbon Coatings Deposited on 530-μ-diam UC_2 Particles in a 1-in.-diam Fluidized Bed. The supply rates are in cubic centimeters per minute per square centimeter of particle surface.

---

[4] Noncitizen employee from Switzerland.

element design studies, we extended[5] our systematic investigation of coating techniques to particles having a nominal diameter of 530 μ. Such particles have much less surface area and require much greater gas flow to maintain fluidization. The charge size and flow rate were adjusted to approximate the surface area and bed volume of the previous study on 200-μ-diam particles,[2] and the higher flow rates actually smoothed the axial temperature gradient in the fluidized bed. However, at 1300°C the cooling effect of the inlet gases reduced coating efficiencies drastically, making methane impractical as a source of hydrocarbon for coating large particles. Results as summarized in Fig. 26.2 show that at higher temperatures the coatings were quite similar to those deposited on smaller particles. The higher flow rates required with large particles permitted deposition of isotropic coatings at rates as high as 650 μ/hr, which is much higher than was possible with the smaller particles.

Deposition and Characterization of Porous Coatings

H. Beutler[4] R. L. Beatty

Pyrolytic-carbon-coated particles with two- and three-layer coatings including a porous inner layer deposited from acetylene have shown remarkably good irradiation behavior.[6] The porous inner layer accommodates fuel swelling, provides volume for storage of gaseous fission products, and protects the outer coating from fission recoil damage. The desired properties of the inner layer are, therefore, a high degree of porosity and low mechanical strength.

We studied systematically the properties of porous coatings deposited from acetylene in a fluidized bed.[7] We made a complete series of coating runs using 460-μ-diam ThO_2 microspheres and some additional runs with smaller UO_2 and UC_2 particles to prepare special samples. Very high acetylene partial pressures and supply rates were clearly essential for producing low-density coatings. The lowest density, 0.6 g/cm^3, was obtained with undiluted acetylene at a supply rate of 6.2 cm^3/min per square centimeter of particle surface, while with an acetylene supply rate of 4 cm^3/min-cm^2 (partial pressure of 490 torrs) the minimum density was 1.1 g/cm^3. Furthermore, the effect of deposition temperature on coating density was insignificant with undiluted acetylene at temperatures from 950 to 1150°C.

When coatings were deposited from acetylene at these high supply rates, the exothermic pyrolysis of the acetylene caused a rapid temperature increase in the fluidizing bed. This transient sometimes exceeded 200°C but did not adversely affect the coating operation. Close control of the temperature was not possible due to the short coating time (<5 min). We correlated our results on the basis of the equilibrium temperature of the fluidized bed at the beginning of the experiment. We could satisfactorily control the thickness of porous coatings; with proper control of conditions we attained a deposition efficiency of 80% or more and avoided soot formation. We also determined, with a mercury porosimeter, that the total accessible porosity was 65% or greater in coatings having a density of 0.6 g/cm^3 and decreased linearly with increasing density, as shown in Fig. 26.3.

We studied the strength and deformation properties of porous coatings as well. When the average crushing load per particle was plotted against the

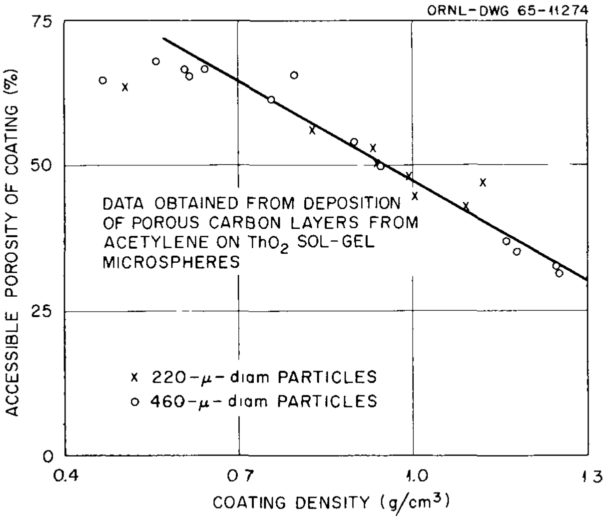

Fig. 26.3. Accessible Mercury Porosity of Low-Density Coatings vs Coating Density.

---

[5] H. Beutler and R. L. Beatty, *GCR Program Semiann. Progr. Rept. Sept. 30, 1965*, ORNL-3885, pp. 3–14.

[6] W. O. Harms, R. W. Dayton, and W. V. Goeddel, "Ceramic Coated-Particle Nuclear Fuels," *Proc. Intern. Conf. Peaceful Uses At. Energy, 3rd, Geneva, 1964*, **11**, 538–46 (1965).

[7] H. Beutler and R. L. Beatty, *GCR Program Semiann. Progr. Rept. Sept. 30, 1965*, ORNL-3885, pp. 14–28.

density, only a wide scatter band of data was obtained. However, the data selected were from batches containing both large (460-μ) and small (200-μ) microspheres, which varied widely in total coating thickness. When the data were expressed as the crushing load per unit of coating thickness, the correlation was much more evident. A plot of this quantity against the density could be fitted to a least-squares line having a base intercept (zero strength) at a density of about 0.5 g/cm^3.

In an attempt to assess the compressibility of porous coatings, we determined stress-strain relationships of coatings of different densities by measuring the change in diameter of a single coated particle as a function of the applied load. The dimensional change was measured with a dial gage as the load was applied. We found that low-density porous coatings (0.6 g/cm^3) deformed as much as 35% before crushing, whereas coatings with intermediate or high densities showed maximum deformations of about 15%. This behavior certainly contributes to the demonstrated capability of porous coatings for protecting high-density outer coatings from internal mechanical damage during irradiation.

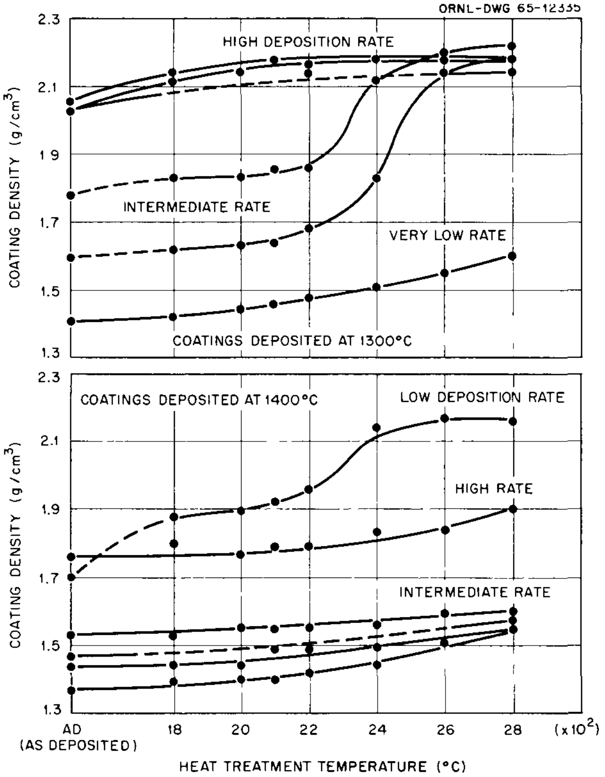

Fig. 26.4. Effect of Heat Treatment on the Density of Pyrolytic Carbon Coatings Deposited at 1300 and 1400°C from Methane.

Effects of Heat Treatment on Pyrolytic Carbon

F. L. Carlsen, Jr.[8]

We conducted a series of heat treatments on pyrolytic carbon coatings to study the effects on physical properties.[9] These coatings were stripped from carbon disks that had been coated along with particles in a fluidized bed at temperatures of 1300 to 2000°C. The specimens were heated in graphite holders in a resistance-heated vacuum furnace for 2 hr at temperatures from 1800 to 2800°C. Densities were measured on the disk coatings by the sink-float method, and apparent crystallite sizes and Bacon anisotropy factors were measured by x-ray diffraction techniques.

Isotropic coatings remained isotropic even when heated to 2800°C, while anisotropic coatings deposited at low rates at 1300 and 1400°C became more anisotropic during heating. Most coatings deposited at 1300°C increased greatly in density when heat treated, as shown in Fig. 26.4, while coatings deposited at 1400°C responded with slight increases except in one case. The crystallite sizes of the specimens deposited at 1300 and 1400°C displayed similar behavior, and in other work[10] we observed that the microhardness of high-density inner coatings deposited on particles at 1300°C was reduced greatly during overcoating at 2000°C. The properties of all coatings deposited at higher temperatures showed little if any change during annealing.

DEVELOPMENT OF UNCLAD FUELS

Thermal Stability of Pyrolytic-Carbon-Coated Oxide Fuel Particles

R. L. Hamner R. L. Beatty H. Beutler[4]

We continued[11] our studies of the thermal stability of coated UO_2 by heating several batches

---

[8] Now at Stellite Division, Union Carbide Corp., Kokomo, Ind.

[9] F. L. Carlsen, Jr., *GCR Program Semiann. Progr. Rept. Sept. 30, 1965*, ORNL-3885, pp. 28–33.

[10] T. M. Kegley, *GCR Program Semiann. Progr. Rept. Mar. 31, 1966*, ORNL-3951, pp. 38–41.

[11] R. L. Hamner, R. L. Beatty, and H. Beutler, *GCR Program Semiann. Progr. Rept. Sept. 30, 1965*, ORNL-3885, pp. 43–50.

either at 1900°C for 680 hr or at 2000°C for 500 hr. The 220-μ-diam sintered UO_2 particles had coatings 110 to 130 μ thick deposited at temperatures of 1300 to 2000°C. No ruptured coatings were observed after these heat treatments, and fuel migration into the coatings was slight or even undetectable except in one batch that had been coated at 1800°C over a porous inner coating layer. Particles in this batch developed a layer of graphite at the UO_2-carbon interface, and fuel migrated as much as 10 μ into the inner coating. This phenomenon must be attributed to a slight permeability of the outer coating, which had a density of 1.59 g/cm^3, or to the formation of small amounts of UC_2 during deposition of the outer coating.

Mathematical Simulation of Coated-Particle Behavior

J. W. Prados[12] J. L. Scott

Our mathematical model for predicting coated-particle behavior, described in earlier reports,[13–17] has been used increasingly in the planning and interpretation of coated-particle irradiation tests and in the investigation of potential improvements in coated-particle design. We have recently completed the first irradiation experiment of a series planned to test our model's predictions, to aid in establishing values for poorly known model parameters, and to identify coated particles with a high degree of irradiation stability. This experiment utilized a static capsule designed for simultaneous high- and low-temperature irradiation of multiple batches of coated particles in an ETR X-basket facility; its description has appeared elsewhere.[18,19]

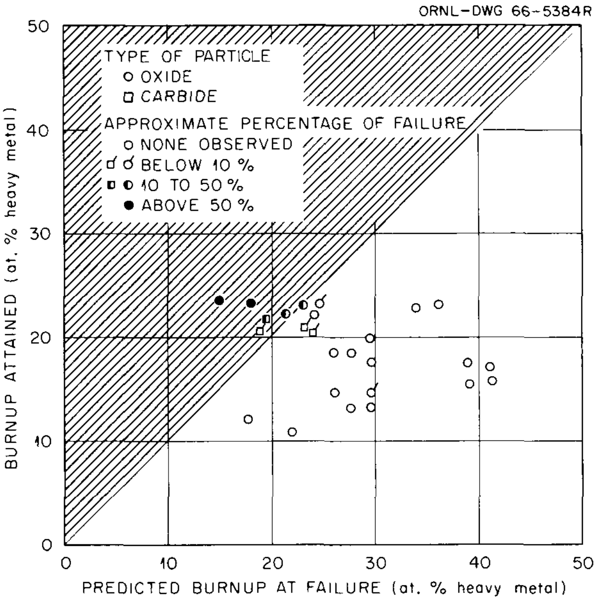

Predicted Burnup Based on: 30,000 psi Rupture Stress, 100 % Release of Fission Gas from Particles, 25 % of Total Inner Coating Porosity Available as Free Volume (Except 50 % for Porous Inner Coatings).

Fig. 26.5. Comparison of Mathematical Model Predictions with Observed Coated-Particle Failures in ETR X-Basket Irradiation Experiment.

Ten different lots of experimental two-layer coated particles were prepared at ORNL for irradiation in this capsule along with two control lots supplied by commercial vendors. Both UO_2 and UC_2 fuel particles were employed; detailed information on coating dimensions and properties[20,21] and irradiation conditions[21] has been previously presented.

In Fig. 26.5 we compare the actual fuel burnup (percent of initial heavy metal atoms fissioned) attained by each lot of experimental particles at high and low temperature with the burnup at failure predicted by our model. Note that each point represents an individual lot of coated particles in either a high- or low-temperature capsule container.

---

[12] On leave from the University of Tennessee.

[13] J. W. Prados and J. L. Scott, *Mathematical Model for Predicting Coated-Particle Behavior*, ORNL-TM-1405 (March 1966); also to be published in *Nuclear Applications*.

[14] J. W. Prados, *A Computer Program for Predicting Coated-Particle Behavior*, ORNL-TM-1385 (March 1966).

[15] J. W. Prados and J. L. Scott, *GCR Program Semiann. Progr. Rept. Sept. 30, 1965*, ORNL-3885, pp. 53–59.

[16] J. W. Prados and J. L. Scott, *Metals and Ceramics Div. Ann. Progr. Rept. June 30, 1965*, ORNL-3870, p. 202.

[17] J. W. Prados and J. L. Scott, *Analysis of Stress and Strain in Spherical Shells of Pyrolytic Carbon*, ORNL-3553 (June 1964).

[18] J. L. Scott and J. W. Prados, *GCR Program Semiann. Progr. Rept. Sept. 30, 1965*, ORNL-3885, pp. 59–62.

[19] E. E. Bloom, J. L. Scott, and J. H. Coobs, *Metals and Ceramics Div. Ann. Progr. Rept. June 30, 1965*, ORNL-3870, pp. 202–3.

[20] J. H. Coobs, *GCR Program Semiann. Progr. Rept. Sept. 30, 1965*, ORNL-3885, pp. 50–52.

[21] J. W. Prados, R. L. Beatty, H. Beutler, J. H. Coobs, A. R. Olsen, and J. L. Scott, "Development of Coated Particle Fuels for Advanced Gas-Cooled Reactors," paper presented at Second International Thorium Fuel Cycle Symposium, Gatlinburg, Tenn., May 3–6, 1966.

The figure legend permits identification of the type of fuel particle employed and the approximate percentage of failed particles found in a given lot on postirradiation examination. The experimental results agreed satisfactorily with our mathematical predictions using the model parameters indicated below the figure.

In evaluating these results one should keep in mind that predictions are based on average coated-particle properties, and the natural variation of these would lead to failures at higher and lower burnups than predicted. The only really unreasonable-looking point represents a lot in which one failed coating was found out of approximately 100 examined metallographically. The failure appeared to result from severe fragmentation of the inner coating, thus allowing direct fission-recoil damage to the outer layer, even though a significant free volume remained.

To aid in identifying improved coated-particle designs, we calculated the optimum distribution of inner and outer coating layer thicknesses for typical coated particles with a fixed ratio of total coating thickness to fuel-particle diameter. This ratio (frequently designated *t/d*) is limited in many power-reactor applications by nuclear restrictions on minimum fuel volume loadings. We have performed these calculations for fully dense (Th,U)C_2 fuel particles with 93% enrichment of uranium in ^{235}U and thorium-to-uranium ratios of 0 and 7. The inner coating is taken to be a porous pyrocarbon with initial density of 0.6 g/cm^3 and is assumed to provide 50% of its total porosity as free volume. The outer coating is taken to be a high-density ($\sim$2 g/cm^3) moderately anisotropic material (anisotropy factor $\sim$1.5) with a rupture stress of 30,000 psi. The ratio of fast (>0.18 Mev) to thermal neutron flux is taken as unity. Complete release of fission gas from the fuel particle is assumed, and the ratio of total coating thickness to fuel particle diameter is held at $\frac{1}{3}$. Results of our calculations for these conditions are given in Fig. 26.6. Here we have plotted the expected thermal-neutron exposure at failure against the ratio of inner coating thickness to total coating thickness for the two thorium-to-uranium ratios in the fuel. Note that the expected coated-particle life is almost doubled if the inner coating occupies 60 to 70% of the total coating thickness rather than the 20 to 30% employed in many current coated-particle designs. Calculations based on other values of coating rupture stress and inner coating density have shown that the locations of these optima along the abscissa are quite insensitive to the values assumed for these coating properties, although the absolute curve heights can be shifted significantly. We feel that these predictions may be highly significant for future coated-particle design and are presently initiating irradiation tests to determine whether the predicted improvements can be obtained in practice.

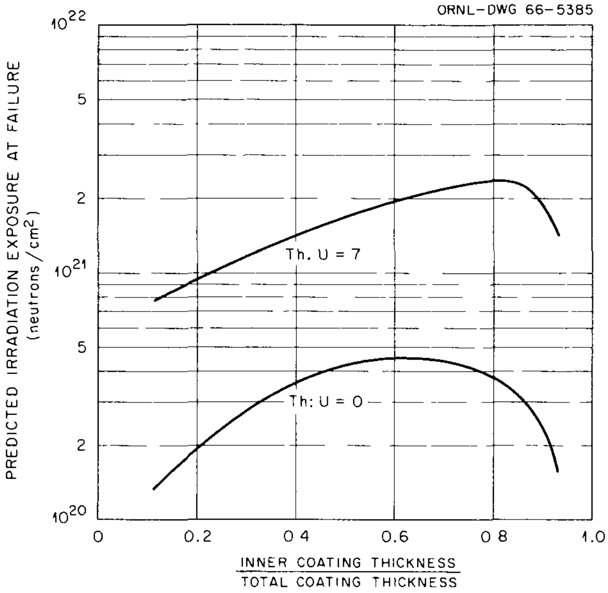

Fig. 26.6. Determination of Optimum Ratio of Inner Coating Thickness to Total Coating Thickness for Coated Particles with Total Coating Thickness Equal to One-Third the Fuel Particle Diameter.

Coated-Particle Survey Irradiation Experiments

J. H. Coobs H. L. Krautweidel[22]
A. R. Olsen J. W. Prados[12]
J. L. Scott

We completed an irradiation experiment designed to provide a relatively simple method of evaluating the effects of coating properties and configurations on irradiation stability by testing a large number of batches of pyrolytic-carbon-coated fuel particles simultaneously.[18,19] The experiment used a static capsule designed for high- and low-temperature testing of coated particles in 28 individual con-

---

[22] On assignment from Karlsruhe Kernforschungszentrum (Nuclear Research Center), Karlsruhe, West Germany.

tainers, as illustrated in Fig. 26.7. Our mathematical model for predicting stresses and strains in pyrolytic carbon coatings under irradiation (see previous section) has proven to be a valuable tool for planning this and other experiments and interpreting the results.

In this experiment we irradiated ten different batches of highly enriched fuel particles prepared at ORNL with two-layer coatings. Coating density, anisotropy, crystallite size, and microstructure were systematically varied between batches by controlling the deposition conditions as we have previously reported.[23,24] Inner coatings nominally 50 μ thick consisted of low-density isotropic, porous, or low- or high-density laminar deposits. High-density granular or isotropic deposits about 70 μ thick were used as outer coatings. Eight of these coating combinations were deposited on 220-μ-diam sintered UO_2 spheroids and two on 200-μ-diam melted UC_2 particles. The capsule was irradiated in an ETR X-basket facility at nominal irradiation temperatures of 1000°C in the high-temperature compartment and 400°C in the low-temperature compartments. Fuel burnup in the experiment ranged from 11 to 23 at. % heavy metal fissioning.

The performance of the various coated particles was evaluated by visual and metallographic examination.[25] The predicted behavior was compared with the observed results in Fig. 26.5 and discussed in the previous section. The results confirm that coated particles must incorporate at least three features to ensure adequate irradiation stability:

1. adequate void volume within the inner coating and/or the fuel particle to accommodate fuel swelling, fission-gas release, and fast-neutron-induced shrinkage of the outer coating;
2. provision for shielding the outer coating from direct fission recoil damage;
3. mechanical decoupling, or a distinct physical separation, between inner and outer coating layers so that recoil-induced shrinkage of the inner layer does not impose excessive stresses and lead to cracking that propagates through both layers.

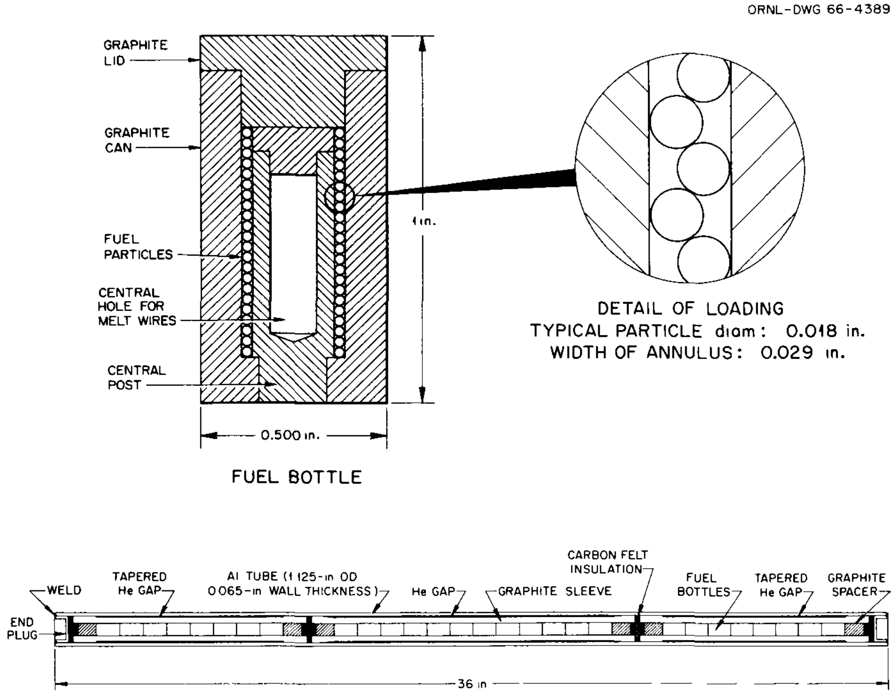

Fig. 26.7. Schematic Drawing of Components for ETR X-Basket Capsule No. 1.

---

[23] R. L. Beatty, F. L. Carlsen, and J. L. Cook, *Nucl. Appl.* 1(6), 560–66 (December 1965).

[24] H. Beutler and R. L. Beatty, *GCR Program Semiann. Progr. Rept. Sept. 30, 1965*, ORNL-3885, pp. 14–28.

[25] A. R. Olsen *et al.*, *GCR Program Semiann. Progr. Rept. Mar. 31, 1966*, ORNL-3951, pp. 41–53.

As predicted by our mathematical model, the most successful types of coated particles in this first X-basket experiment consisted of porous inner coating layers with relatively isotropic outer coatings on UO_2 fuel particles. The appearance of typical coated particles from one of these two batches both before and after irradiation at 1000°C to 23 at. % burnup is illustrated in Fig. 26.8. The only difference is the presence of second-phase material in the UO_2 and partial densification of the porous coating layer by recoil fragments and by swelling of the fuel particle. No evidence of damage to any outer coatings was observed.

A second such experiment, containing sol-gel-derived UO_2 microspheres with a similar series of coatings, is in progress.

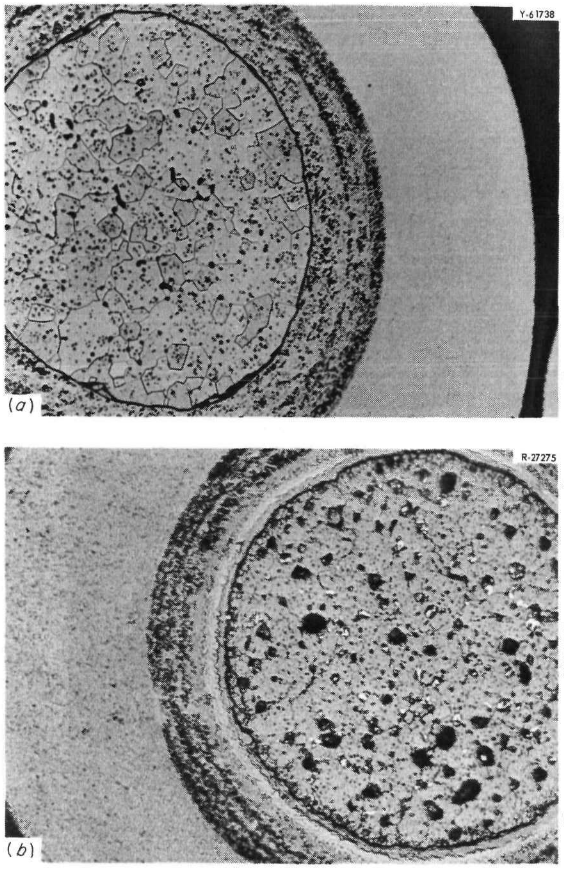

Fig. 26.8. Pyrolytic-Carbon-Coated Particles from an Irradiation-Resistant Batch. Etched. (*a*) Unirradiated. (*b*) Irradiated to 23 at. % burnup at 1000°C.

Coated Fuel Particles for ORNL–Dragon Project Cooperative Irradiation Experiment

R. L. Beatty J. H. Coobs D. M. Hewette

The Dragon Reactor of the OECD Dragon Project is now operating at design power of 20 Mw and maximum fuel temperatures of 1250°C. This reactor has coated-particle fuel in long graphite fuel elements and is cooled with helium. Special arrangements were made with the Project to test our pyrolytic-carbon-coated $(Th,U)O_2$ fuel particles in the experimental fuel elements planned for the second charge. We specified that two ratios of thorium to uranium, 3.5 and 5.0, should be used in the fuel. These ratios are of interest to the HTGR development program of the USAEC and are low enough to allow significant burnup (>5% of heavy metal atoms) during the second charge irradiation.

High-density microspheres of $(Th,U)O_2$ having the above ratios were prepared in the Chemical Technology Division by the ORNL sol-gel process and were coated with pyrolytic carbon in the Ceramics Laboratory. Our mathematical model for coated-particle behavior indicated that performance of the fuel would be adequate with a porous inner coating deposited at about 1100°C and a high-density isotropic outer coating deposited at 2000°C. However, oxide particles must be sealed with a dense coating to prevent reaction during coating at 2000°C. We developed a technique for depositing a thin (~ 10-μ) high-density anisotropic layer within the porous coating, as illustrated in Fig. 26.9. This layer was deposited at low temperature from acetylene by changing the conditions during the porous coating run. Using the modified procedure we prepared about 1.5 kg of coated particles containing about 150 g of ^{235}U, which was sufficient for two fuel rods in the experimental fuel elements. The uniformity of the coating layers is illustrated by the typical coated particle shown in Fig. 26.9. The large equiaxed grains in the fuel are also typical and were developed during deposition of the outer coating at 2000°C.

Thermal Analysis of AVR Poolside Irradiation Experiments

J. W. Prados[26]

To aid in interpreting irradiation effects observed in the 6-cm-diam fueled-graphite spheres (size in-

---

[26] On leave from the University of Tennessee.

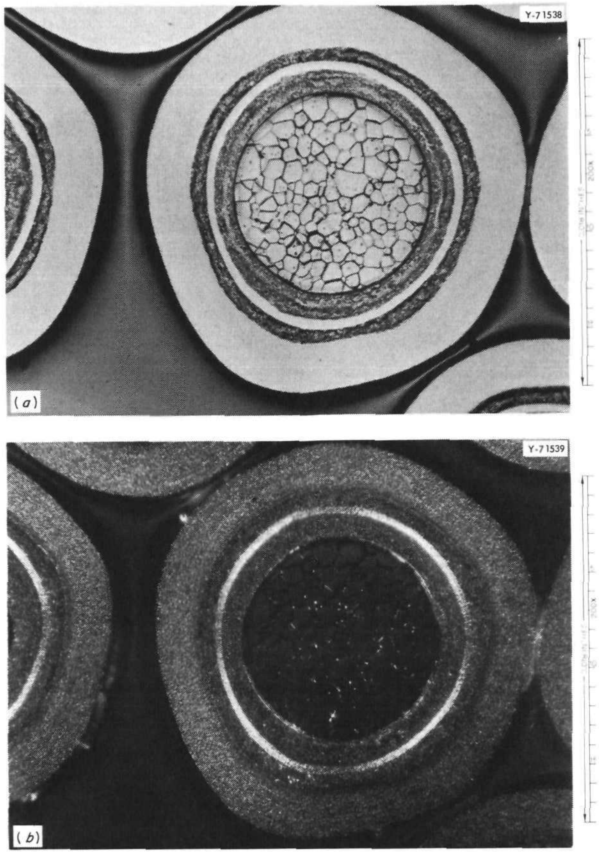

Fig. 26.9. Typical Pyrolytic-Carbon-Coated $(Th,U)O_2$ Fuel Particles for Dragon Irradiation. Thorium-to-uranium ratio = 3.4. (*a*) Bright field illumination. Etched. (*b*) Polarized light.

tended for the German AVR) irradiated in ORR Poolside capsules,[27] we have developed a correlation between fuel element power and measured operating temperatures for these experiments.[28] This correlation has provided a rational basis for smoothing random variations in capsule flux-monitor results, for rejecting flux-monitor results that appeared to be grossly in error, and for determining actual fuel-element heat generation rates at any time, from measured capsule operating temperatures.

Using the correlation and the method described by Prados *et al.*,[29] we determined fuel-matrix thermal conductivities for those fueled-graphite spheres instrumented with a central thermocouple. These conductivities appear to be described satisfactorily as a function of temperature over the range of experimental operation (950 to 1350°C) by the two-constant equation

$$1/k = r + sT\ , \qquad (1)$$

where k is the thermal conductivity in w cm^{-1}(°C)$^{-1}$, T is temperature in °C, and r and s are constants, which appear to depend on the fuel element starting materials and fabrication conditions. Values for the constants r and s are given in Table 26.1 for all instrumented test spheres. Except as noted in the table, these constants did not change significantly during the irradiation period, indicating that in the majority of cases fuel-matrix thermal conductivities as well as the heat transfer resistance between fueled core and unfueled shell were unaffected by irradiation under the conditions of these experiments.[30,31] This is illustrated further in Fig. 26.10, where conductivity data throughout the irradiation period are plotted as a function of temperature for one of the test spheres.

From our power-temperature correlation we were able to determine maximum and average total heat generation rate, fission power, burnup rate, and total heavy-metal burnup for each 6-cm fueled sphere irradiated in the ORR poolside capsules. This information, together with the thermal conductivity

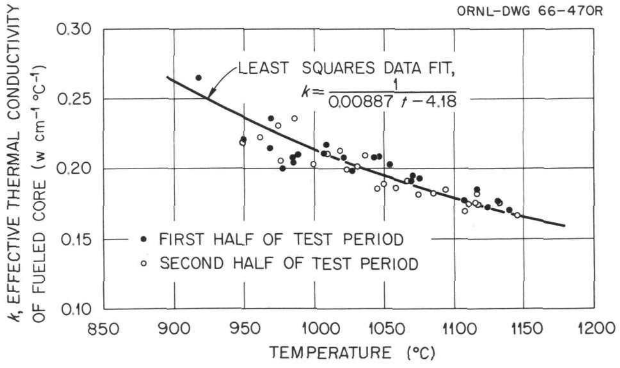

Fig. 26.10. Thermal Conductivity of Fueled-Graphite Core from Irradiation Test Data of Experiment 01A-8.

---

[27] J. L. Scott *et al.*, *GCR Program Semiann. Progr. Rept. Sept. 30, 1963*, ORNL-3523, pp. 326–41.

[28] J. W. Prados *et al.*, *GCR Program Semiann. Progr. Rept. Mar. 31, 1966*, ORNL-3951, pp. 136–44.

[29] J. W. Prados *et al.*, *Trans. Am. Nucl. Soc.* **8**, 37–38 (1965).

[30] J. L. Scott *et al.*, *Trans. Am. Nucl. Soc.* **8**, 426–27 (1965).

[31] J. L. Scott, *GCR Program Semiann. Progr. Rept. Sept. 30, 1965*, ORNL-3885, pp. 186–94.

Table 26.1. Thermal Conductivity Constants for Fueled Cores of 6-cm Fueled-Graphite Spheres

Irradiation Capsule	r ($^\circ$C cm w^{-1})	s (cm/w)	Manufacturer[a] and Type
O1-7	*b*	*b*	NCC; 1.0-cm AGOT shell, no details on core fabrication
O5-7	−2.73[c]	0.00800[c]	GA; 1.1-cm ATJ shell, hot-pressed core, baked at 1800°C
O8-7	−0.975	0.00641	GA; 0.635-cm molded shell, hot-pressed core and shell, baked at 1800°C
O1A-7	*b*	*b*	GA; 0.8-cm ATJ shell, hot-pressed core, baked at 1800°C
O5B-7	−3.83	0.00798	NCC; 1.1-cm ATJ shell, injection-molded core
O8A-7	−3.39	0.00816	GA; 0.8-cm ATJ shell, warm-pressed core, baked at 1800°C
O1-8	0.024[d]	0.00743[d]	ORNL; multihole type
O5-8	−1.52	0.00739	3M; 0.635-cm molded shell, no fabrication data
O8-8	0.666[e]	0.00624[e]	ORNL; 0.8-cm ATJ shell, warm-pressed core, baked at 1000°C
O1A-8	−4.18	0.00887	NCC; 1.0-cm ATJ shell, injection-molded core, baked at 1450°C

[a] Manufacturers: NCC, Carbon Products Division, Union Carbide Corp.; GA, General Atomic Division, General Dynamics Corp.; 3M, Minnesota Mining and Manufacturing Co.

[b] Central thermocouple failed; no conductivity data.

[c] These values apply only during the first 20 days of irradiation; subsequent decrease in conductivity believed due to formation of core-shell gap.

[d] Based on equivalent 1-cm unfueled shell. Apparent conductivity decreased during test to values approximately 50% below those calculated using these constants; decrease believed due to changing gas composition in static compartment.

[e] Results did not cover wide enough range for accurate determination of constants; low conductivity values suggest that gap existed between core and shell throughout test.

values expressed by Eq. (1) and Table 26.1, was used to calculate central fuel temperatures throughout the irradiation period for those spheres not equipped with central thermocouples. The results of these calculations are summarized in Table 26.2.

Fabrication of Fission-Product-Emitting Fuel

J. M. Robbins J. G. Stradley

A process is being developed for fabricating fueled-graphite elements that will allow near-total release of the high-cross-section noble-gas fission products (such as ^{135}Xe and ^{88}Kr) to the primary system and thereby increase fuel lifetime, breeding ratio, or both. For this purpose an element consisting of fuel distributed homogeneously or as networks in a fine-grained graphite matrix with much open porosity would be desirable. Interest in this concept is based upon the potential such a fuel element would have for a high-temperature gas-cooled breeder reactor.[32]

---

[32] R. S. Carlsmith and W. E. Thomas, *GCR Program Semiann. Progr. Rept. Sept. 30, 1965*, ORNL-3885, pp. 236–41.

Table 26.2. Power Levels, Fuel Burnup, and Maximum Central Temperatures for 6-cm Fueled-Graphite Spheres Irradiated in ORR Poolside Capsules

Capsule	Sphere Position[a]	Maximum Total Heat Generation Rate (w)	Average Total Heat Generation Rate (w)	Average Fission Power (w)	Average Burnup Rate[b] (at. % per 100 days)	Irradiation Time (days at 30 Mw)	Fuel Burnup[b] (at. % heavy metal)	Maximum Central Temperature (°C)
O1-7	1	2680	2290	2220	2.68	138.30	3.7	1945[c]
	2	4080	3630	3550	4.26	138.30	5.9	1627
	3	3350	3080	3000	3.59	138.30	5.0	1502
O5-7	1	2720	2630	2560	3.07	91.95	2.8	1638[d]
	2	3820	3620	3530	4.26	91.95	3.9	>1950[c]
	3	3350	3300	3220	3.85	91.95	3.5	1803
O8-7	1	2720	2540	2480	2.97	91.95	2.7	1360[d]
	2	3650	3600	3500	4.19	91.95	3.9	1689
	3	3363	3320	3240	3.88	91.95	3.6	1514
O1A-7	1	3000	2620	2550	3.05	97.30	3.0	1513
	2	3800	3420	3330	3.99	97.30	3.9	1897
	3	2960	2750	2680	3.21	97.30	3.1	1365
O5B-7	1	2750	1920	1870	2.24	95.24	2.1	1444[d]
	2	3660	2330	2260	2.71	95.24	2.6	1841
	3	3330	2180	2120	2.54	95.24	2.4	1534
O8A-7	1	2790	2260	2200	2.64	95.24	2.5	1760[d,e]
	2	3400	2480	2420	2.90	95.24	2.8	1736
	3	3120	2380	2310	2.77	95.24	2.6	1269
O1-8	1	2420	2140	2090	2.45	42.53	1.0	1371[d]
	2	3470	2940	2860	3.45	42.53	1.5	1643
	3	2920	2800	2730	3.23	42.53	1.4	1286
O5-8	1	2720	2470	2410	2.95	272.49	8.0	1382[d]
	2	3350	3220	3140	3.84	272.49	10.5	1589
	3	2920	2880	2810	3.44	272.49	9.4	1172
O8-8	1	2400	2270	2210	2.66	66.34	1.8	1210[d]
	2	3460	3210	3130	3.75	66.34	2.5	1578
	3	2900	2520	2450	2.95	66.34	2.0	1449
O1A-8	1	2560	2350	2300	3.79	145.76	5.5	1275[d]
	2	3310	3170	3100	5.11	145.76	7.4	1562
	3	2870	2820	2750	4.54	145.76	6.6	1403

[a] Position 1 is upper position in static compartment, and 2 is lower position in static compartment; sphere 3 is in sweep compartment.

[b] Burnup based on percentage of initial heavy metal atoms fissioned.

[c] Core-shell gap observed in preirradiation radiography incorporated in central temperature calculation.

[d] Measured values; all others in this column are estimated using thermal conductivity data from Table 26.1.

[e] Questionable; central thermocouple reading drifted upward off scale.

The fuel particles should be small, 10 μ in diameter or less, to allow the gases to escape, and the adjoining graphite grains should be small enough to minimize the effects of fission recoils. To accomplish this, several methods of adding the fuel to the graphite were considered, such as using crushed $(Th,U)O_2$ sol-gel oxide, the fine powder resulting from oxidized uranium chips, or the sol from the intermediate step in the ORNL sol-gel process. We developed a process utilizing the sol, since it appeared to be the most convenient means of dispersing the fuel throughout the graphite matrix. This process[33] involves mixing ThO_2-UO_2 sol with graphite flour, evaporating, adding phenolic resin, drying, sizing the mix, and finally pressing the specimens. These are then heat treated to carbonize the binder.

Specimens prepared by this process appear to possess properties desirable for an emitting fuel element. We prepared specimens containing 40% fuel that was indeed finely divided and dispersed throughout the graphite matrix, as demonstrated by radiographic and metallographic examination.[33] The specimens ranged in density from 1.70 to 2.1 g/cm^3 and contained pores of 0.3 μ average size in porosities as great as 45%. Some of these specimens emitted nearly 90% of the fission gas generated in neutron-activation tests. An irradiation capsule experiment is presently being designed to further verify the emitting properties of specimens made by this process.

SUPPORTING ACTIVITIES

The Internal Stress Problem in Graphite Moderator Blocks

C. R. Kennedy

One of the major concerns in the use of graphite-moderated reactors is the stress generation caused by differential growth. The stress generation is moderated considerably and generally maintained at safe levels by the ability of the graphite to creep under irradiation. The problem resolves itself to a determination of the balance between the differential growth rate producing stress and the creep reducing the stress. Although the creep-rate coefficient may be such that the stress level does not exceed the fracture strength, a second concern is the ability of the graphite to absorb the creep strain indefinitely without failure. Certainly, a failure criterion based upon the fracture stress of the material is accurate. Therefore, it is of great importance to know both the restrained growth rate and the creep coefficient for the material under the operating conditions. Our purpose has been to determine the general creep behavior of graphite under irradiation.

Creep experiments were performed at 700 and 1000°C for comparison to the previous data[34] obtained at lower temperatures. The high-temperature experiments were again similar to the previous experiments in that cantilevered parabolic-beam specimens were used. The main difference was in the use of four-zone furnaces to obtain the desired temperatures. The number of specimens was reduced from nine to six because of the space requirements of the furnaces.

Results from all creep experiments performed from 150 to 1000°C do demonstrate a generalized creep behavior, as shown in Fig. 26.11. This type of behavior strongly supports a Cottrell model for irradiation creep, which allows extrapolation of these data to most reactor grades of graphite. The Cottrell model for irradiation creep, as given by Anderson and Bishop,[35] is

$$K = A\dot{\gamma}/\sigma_y , \tag{2}$$

where

K = creep coefficient,

A = accommodation factor,

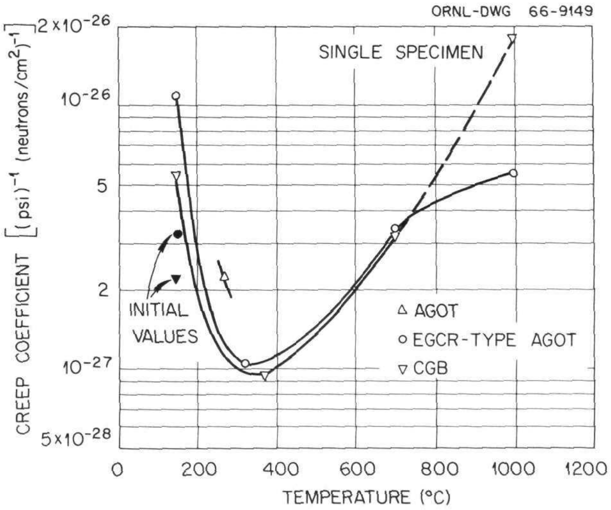

Fig. 26.11. The Effect of Temperature on the Creep Coefficient of Graphite Under Irradiation.

---

[33] J. G. Stradley and J. M. Robbins, *GCR Program Semiann. Progr. Rept. Mar. 31, 1966*, ORNL-3951, pp. 53–56.

[34] C. R. Kennedy, *Metals and Ceramics Div. Ann. Progr. Rept. June 30, 1965*, ORNL-3870, pp. 194–97.

[35] R. G. Anderson and J. F. W. Bishop, "The Effect of Neutron Irradiation and Thermal Cycling on Permanent Deformations in Uranium Under Load," pp. 17–23 in *Uranium and Graphite*, Monograph 27, The Institute of Metals, London, 1962.

$\dot{\gamma}$ = shear rate due to anisotropic growth ($\dot{G}_c - \dot{G}_a$),

σ_y = yield strength of the crystallites,

$\dot{G}_c$ and $\dot{G}_a$ are the growth rates in the *c* and *a* directions.

The shear rate $\dot{\gamma}$ of graphite can be derived from measurements made on pyrolytic graphites through estimates of polycrystalline graphite growth rates. The accommodation factor *A* primarily reflects the degree of accommodation by microcracks and in general the void volume in the graphite. It is not necessarily constant and is expected to vary with temperature and neutron exposure. The variation of *A* with temperature should not be very large; however, *A* should exhibit a rather significant increase as microcrack closure occurs. The closure of microcracks requires a dose of approximately 10^{22} neutrons/cm^2; thus, the value of *A* will be essentially constant for at least half this dose. The value of the yield strength or flow stress σ_y of the crystallites will undoubtedly vary under irradiation and with irradiation temperature. The value of σ_y, like that of *A*, will not vary with temperature, however, as significantly as $\dot{\gamma}$, the shear rate.

The creep-rate coefficient should therefore strongly reflect the variation of $\dot{\gamma}$ with temperature. This is demonstrated in Fig. 26.11, where the creep-rate coefficient exhibits a minimum around 350°C. The creep-rate coefficient *K* is not exactly proportional to the shear rate $\dot{\gamma}$ because of the variations of *A* and σ_y. The value of *A* would be essentially independent of the graphite grade; thus the effect of σ_y on the creep-rate coefficient can be demonstrated by a comparison of various grades at the same temperature. This was demonstrated previously[34] by comparing the modulus of elasticity of six grades of graphite to their creep-rate coefficients at 400°C. Although this correlation strongly supports Eq. (1) or the Cottrell model for the creep of graphite, one glaring discrepancy in the correlation is the test result at 1000°C for the CGB grade of graphite. It should be noted that this particular material demonstrated a one-third decrease in its modulus of elasticity, which is also unlike the behavior of previously tested grades. This particular test result requires confirming data before specific conclusions can be reached.

One should recognize that the Cottrell model for creep does not suggest an actual mechanism by which the graphite deforms plastically. It does describe the creep as actually a process of continuous yielding, which is not thermally activated as the term "creep" generally infers. Also the manifestation of the creep deformation is actually nothing more than a stress-induced imbalance of the internal straining occurring in all polycrystalline graphites due to anisotropic growth. This infers that the limit of creep deformation can be as large as the internal strains that must occur in polycrystalline graphites irradiated without stress. Polycrystalline graphite can accommodate 16% shear strain and polycrystalline carbons 160% shear strain[36] without a loss of mechanical integrity. The obvious conclusion is that as long as the stress acting on the graphite does not exceed the fracture stress, the graphite will continue to absorb the creep deformation without loss of mechanical integrity.

Correlation of Thermodynamic Properties of Nuclear Fuel Materials

J. M. Leitnaker T. G. Godfrey

Thermodynamic Properties of Uranium Carbides.[37] – Thermodynamic and phase information relative to the uranium-carbon system were analyzed and shown to be consistent. The anomalously high heat capacity of UC_2 is justified in the analysis. Thermal functions are calculated for UC and UC_2, using a nonzero S_0° (0.60 eu) for the dicarbide. The standard heat of vaporization of uranium is calculated to be 123.7 ± 1.3 kcal/mole.

Thermodynamic Properties of Uranium Carbides via the U-C-O System.[38] – Equilibrium data of Piazza and Sinnott in the systems UO_2-"UC_2"-C-CO and UO_2-"UC_2"-UC-CO have been recalculated using both second and third law treatments. Internal consistency is excellent for the first system and acceptable for the second. Third law treatments predict the heats of formation, ΔH°_{298}, of "UC_2" and UC to be −20.5 and −23.2

---

[36] J. C. Bokros and R. J. Price, *Radiation-Induced Dimensional Changes in Pyrolytic Carbons Deposited in a Fluidized Bed*, GA-6736 (November 1965) (to be published in *Journal of Applied Physics*).

[37] Abstract of paper submitted for publication to *Journal of Nuclear Materials* and presented in part at 21st Annual Calorimetry Conference, Boulder, Colo., June 22–24, 1966.

[38] Abstract of *J. Chem. Eng. Data* **11**, 392–94 (1966).

kcal/mole, respectively, in excellent agreement with combustion measurements. The "best" value of $\Delta H^\circ_{f,298}$ of "UC_2" is -20.8 ± 0.7 kcal/mole.

A Computer Program to Calculate High-Temperature Thermodynamic Functions.[39] – A computer program, PLOTHEAT, has been written which fits, analytically by least squares, raw high-temperature heat-content data to one of several selected functions. From the generated equation the heat capacity C_p, the heat content $H_T - H_{298}$, the entropy S_T, and the free energy function $(F_T - H_{298})/T$ are calculated and tabulated at 100°C increments. (The last two quantities assume a knowledge of the entropy at 298.15°K, S_{298}.) A subroutine of the program also plots the raw data together with the computed equation using different symbols for different investigators.

Thermodynamic Functions of UC, UC_2, UO_2, ThO_2, and UN.[40] – Thermodynamic functions of five compounds of interest for gas-cooled reactors (UC, UC_2, UO_2, ThO_2, and UN) have been calculated from literature data and tabulated at 100°C increments. Estimates of accuracy are included. The fit of the raw data to the calculated curve is shown graphically in each case.

Evaluation of Pneumatic Temperature-Measuring (PTM) Nozzles

N. C. Cole C. S. Walker[41] B. Fleischer

We investigated the stability of nitrided (malcolmized) type 304 stainless steel nozzles under consideration[42] as primary sensors for coolant-channel temperature measurements in gas-cooled reactors. The nozzles were exposed to slowly flowing impure helium (simulated EGCR helium mixture) at 1050°F. Three nozzles were thermally cycled in a furnace from 1050°F to room temperature every 100 hr. During the first 2000 hr the nozzles were removed from the furnace, measured for throat diameter, and calibrated for flow coefficient at 200-hr intervals. For the last 2200 hr, the nozzles were measured and calibrated only after 400-hr intervals. Two nozzles, one fabricated from Inconel, also were tested for 14,700 hr in a sonic flow loop.

Examination of the type 304 stainless steel nozzles showed gradual oxidation of the nozzle as the result of test conditions. This oxidation reduced the throat diameter of the nozzle by as much as 2.6 mils. In reactor service, dimensional changes of this magnitude would result in registering a temperature significantly higher than the actual temperature of the system. The conversion of the nitride layer was accompanied by a drastic reduction in its hardness: from 925 to 450 DPH after 4200 hr and 300 DPH after 14,700 hr. The base metal hardness remained unchanged. The Inconel nozzle exhibited a small degree of nonuniform oxidation, which proceeded along grain boundaries. The maximum penetration found was 0.8 mil. Complete details on this work have been reported.[43] We concluded that PTM systems of the type tested would be unsatisfactory for GCR service.

Examination of Failed Expansion Bellows Between EGCR Containment Shell and Experimenters Cell 6[44]

T. M. Kegley, Jr. G. M. Tolson

A horizontal 42-in.-diam × 0.039-in.-thick expansion bellows of type 304 stainless steel that connected Experimenters Cell 6 to the EGCR containment shell failed because of several leaks at the bottom of the bellows. Examination of the bellows to determine the cause of the failure indicated (1) severe pitting attack, which occurred predominantly from the inside of the bellows, and (2) the presence of 4.44% Cl^- in scale removed from the inside of the bellows. The failure by severe pitting attack most probably was due to the presence of chloride and to the stagnant condition of the liquid in the bottom of the bellows.

---

[39] Abstract of ORNL-TM report (in press).

[40] Additional author, J. A. Woolley, summer employee 1965. Abstract of report in preparation.

[41] Instrumentation and Controls Division.

[42] T. L. McLean, *Nucl. Safety* 2(1), 30–32 (September 1960).

[43] C. S. Walker, N. C. Cole, and B. Fleischer, *GCR Program Semiann. Progr. Rept. Mar. 31, 1966*, ORNL-3951, pp. 209–16.

[44] Abstract of ORNL-TM-1380 (February 1966).

27. High Flux Isotope Reactor

G. M. Adamson, Jr.

The High Flux Isotope Reactor (HFIR) was constructed at ORNL to provide a high flux density to produce research quantities of the transplutonium elements.[1] The reactor is designed to produce 5×10^{15} neutrons cm^{-2} sec^{-1} with an average power density of 2000 kw/liter and a total power of 100,000 kw. In spite of the high power density, aluminum is being used as the structural material for both the fuel element and the control rod.

The fuel core consists of only two fuel elements containing 171 and 369 involute-shaped plates 0.050 in. thick. Each plate contains a dispersion of U_3O_8 in aluminum, with the quantity of uranium varying nonlinearly across the plate width.

We fabricated both the first fuel element and the first control rod for use in this reactor.[2] With these components, the reactor has achieved criticality and power operation. Elements for future use are being obtained commercially under our supervision. Our efforts are now being directed toward improvements for longer lives.

FUEL ELEMENT MANUFACTURE

G. M. Adamson, Jr. R. W. Knight
J. W. Tackett[3]

Through the past year, assistance has been provided to Metals and Controls, Inc.,[4] in developing manufacturing procedures for the HFIR fuel element that are adaptable to a production basis. These procedures had to be relatively foolproof and insensitive to normal variations in production processes. Thus, the fabrication and inspection procedures for the component parts had to be reviewed and modified repeatedly.

In the first half year all final production procedures were set up and proven, and all final procedural qualifications were examined and accepted by ORNL. During this time some minor modifications were made to the HFIR specifications;[5] however, no change was made in these specifications that would downgrade the quality of the finished fuel element. The final fuel plate qualification for the outer fuel plates was completed in October, and in November fuel plate production was begun. The first few fuel plate lots were rejected because of blisters caused by hot rolling at a temperature lower than specified; however, once the furnace was repaired, production continued on a routine basis with no major problems. Since fuel plate production started, 6384 outer-annulus and 2976 inner-annulus fuel plates have been completed. The rejection rate through this period has dropped from over 20% to 10%. A continued effort is being made to improve this rejection rate. The highest single cause of rejection has been poor surface quality from handling defects. Welding parameters for the fuel elements were perfected, and fuel element welding is now progressing with no major problems. Melt-through and porosity have been the major problems encountered. The principal corrective actions have been reductions in preheat temperature and wire feed rate. In no case has melt-through exceeded the specifications.

---

[1] F. T. Binford and E. N. Cramer, *The High Flux Isotope Reactor — A Functional Description*, vol. 1, ORNL-3572 (May 1964).

[2] G. M. Adamson, Jr., *Metals and Ceramics Div. Ann. Progr. Rept. June 30, 1965*, ORNL-3870, pp. 214–29.

[3] Now at Union Carbide Corp., Stellite Division, Kokomo, Ind.

[4] A Division of Texas Instruments, Inc., Attleboro, Mass.

[5] G. M. Adamson, Jr., and J. R. McWherter, *Specifications for High Flux Isotope Reactor Fuel Element (HFIR-FE-1)*, ORNL-TM-902 (August 1964).

The "B"-type weld porosity has exceeded and is continuing on occasions to exceed the specifications; however, in most cases, good fusion has been achieved and the fuel elements have been accepted without repair. Development work is continuing to achieve "B"-type weld parameters that will decrease porosity without affecting fusion.

Another welding problem requiring development was that of the fuel plates becoming progressively unseated during welding. In some cases the fuel plate edges were just visible in the weld groove by the time the outside welds were made. Fuel plate seating during welding was improved measurably by changing the welding sequence. Originally, "A"-type welds were done alternately – first two on the outside tube, then two on the inside tube. This has been changed so that only six inside-tube welds have been made when the welding of the outside tube is complete. This change has stabilized plate protrusion during the welding process. Also, we adopted pinning the side plates to the end trunions to prevent rotation of the element.

Nonuniform weld shrinkage down the length of an element caused difficulty in meeting the dimensional tolerances, especially the one on minimum wall thickness. Both ends of the element shrank much less than the center portions, causing a flaring of the ends. To minimize this difficulty, fixtures were fabricated for both the outside and inside tubes so that when they were attached to the element and heated their respective inside and outside diameters were of such a size that they would either compress or expand the side plates to the desired value. For the outside tube a 100°C rise in temperature would change the diameter of the element about 0.020 in.

The manufacturer required considerable assistance in getting the welding machine working properly. However, once the sources of difficulty were eliminated it has operated with very little interruption or trouble. The most troublesome feature was the wire feed for the outer torch. After several attempts to use "improved" drive rolls, it was necessary to return to rolls similar to those developed at ORNL.

A problem in shape of the weld deposit surface was traced to the angle at which the weld wire was fed into the molten puddle. The weld face would be varied from concave and severely tilted to flat by small modifications of this angle.

Fuel element assembly has become a routine procedure, and few fuel plates are rejected because of curvature. Fuel plate seating, which was a major problem, has been solved by assembling the fuel element on a parts feeder vibrator. After the element is assembled, the vibrator is turned on and the outer side plate is rotated against an inner side plate with a spanner wrench. For both annuli, the Teflon spacer thickness finally adopted was 0.048 in. Average fuel-plate spacings for finished fuel elements are now 0.050 in. for the outer annulus and 0.0489 in. for the inner annulus.

To date, 11 assemblies consisting of both outer- and inner-annulus fuel elements have been manufactured. All fuel plates have met specifications or were accepted by ORNL. Problems are still encountered in final machining of the outer annulus. The finished side plate is so thin that the fuel elements go out of round during machining. To date, there have been several out-of-specification dimensions; most of the deviations were from roundness. None of these out-of-specification dimensions should hamper the operation of the reactor, although it has been necessary to analyze each one individually.

PLATE ROLLING STUDIES FOR THE HFIR

W. J. Werner   C. F. Leitten, Jr.

A series of experimental plates was processed to study the effect of initial compact density on rolled core density and attendant plan dimensions. Outer-annulus plates were chosen for the study. To facilitate the experimental work, we used rectangular fuel compacts rather than the contoured compacts required for the reactor. Compacts were prepared by conventional dry-blending and cold-pressing techniques. Compacts of the same weight but different density and thickness were obtained by cold pressing two compacts at each pressure from 15 through 35 tons/in.^{2} in 5-ton/in.^{2} increments. The billets were then hot rolled and subsequently cold rolled according to established HFIR procedures. Densities of the as-pressed compacts were obtained from weights and dimensions after outgassing. Rolled core density, length, and width data were obtained on all the hot-rolled plates and on one plate each at each pressing pressure after cold rolling.

Figure 27.1 shows core density (as pressed, as hot rolled, and as hot rolled plus 20% cold reduction) as a function of cold-pressing pressure. A statistical analysis showed that the as-hot-rolled density increased slightly with initial pressing pressure or initial core density. The density after cold reduction, however, was independent of initial compact density; it decreased during cold rolling due to oxide degradation. Practically speaking, the data show that core density in a finished outer-annulus plate is independent of the density of the as-pressed compact in the range studied at a total reduction ratio of approximately 11. Because hot-rolled density does not change appreciably with compact density, we believe the core density is also independent of compact density for both inner- and outer-annulus production plates, for which the total reduction ratio is approximately 10.

The core length and width data for the experimental plates are presented in Table 27.1. Interestingly, both core length and width became relatively constant for compacts pressed at 25 tons/in.^{2}

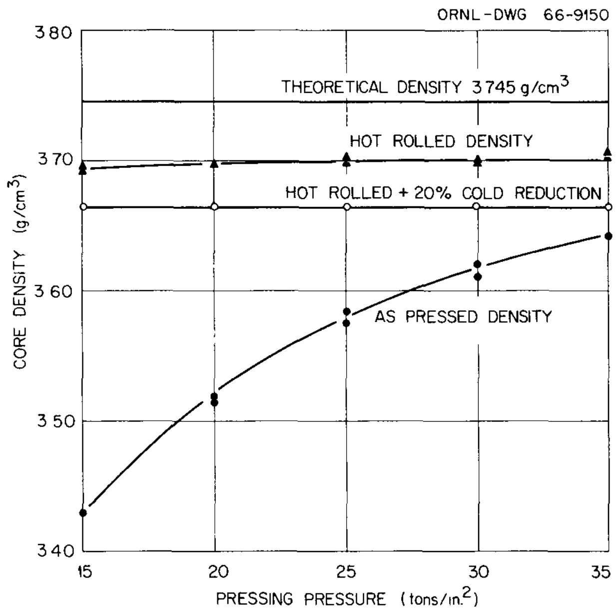

Fig. 27.1. Core Density at Different Process Stages as a Function of Pressing Pressure.

Table 27.1. Effect of Initial Compact Density on Core Dimensions of Rolled Experimental HFIR Outer-Annulus Plates

Compacting Pressure (tons/in.^{2})	Average Compact Thickness (in.)	As-Pressed Density[a] (g/cm^3)	Core Width[b] (in.)		Core Length[c] (in.)	
			Hot Rolled	Cold Rolled[d]	Hot Rolled	Cold Rolled[d]
15	0.333	3.429	2.719	2.736	15.50	19.56
15	0.333	3.429	2.711		15.53	
20	0.325	3.519	2.729		15.75	
20	0.325	3.514	2.730	2.751	15.69	19.75
25	0.318	3.483	2.751	2.766	15.75	19.84
25	0.319	3.575	2.750		15.81	
30	0.316	3.610	2.757		15.84	
30	0.315	3.620	2.752	2.770	15.91	19.94
35	0.313	3.642	2.753	2.778	15.91	19.97
35	0.313	3.641	2.755		15.88	

[a] Obtained from compact weights and dimensions.

[b] Average of three measurements: one at plate center line and two at midpoints between center line and plate ends (initial width = 2.645 in.).

[c] Average of three measurements, measured at center line and $\frac{1}{4}$ in. in from plate edges (initial length = 1.800 in.).

[d] Hot rolled and then cold reduced 20%.

and above. This correlates quite well with the as-pressed density, which depends less on pressing pressure in this region than at the lower pressures.

OXIDE CHARACTERIZATION FOR THE HFIR

W. J. Werner C. F. Leitten, Jr.

Studies were continued on the homogeneity bias caused by oxide comminution during rolling.[6] In general, plates containing vendor oxide exhibited an apparent fuel excess when examined for fuel homogeneity by x-ray attenuation. Additionally, oxide comminution caused higher and more variable attenuation of ultrasound, thereby increasing the spurious fuel plate rejection rate through reduced nonbond detection sensitivity.

The vendor oxide was thoroughly examined and subsequently rejected for not meeting the 0.05 m^2/g static BET krypton surface area specification. Metallographic examination showed that the oxide was a low-grade product, which was highly stressed and/or full of microcracks. The differences in particle morphology and microstructure are quite readily detected by differences in the static BET krypton surface area measurement. Consequently, 312.6 kg of U_3O_8 was prepared for the HFIR fuel element subcontract by the Y-12 Uranium Chemistry Group. Because of the geometry restrictions imposed by nuclear safety and the availability of the equipment from other oxide production programs, the material was produced in approximately 16-kg batches in laboratory-type equipment. These batches were subsequently cross blended into two master blends for further product uniformity. Table 27.2 shows the chemical and physical data obtained on the two master blends. All specifications were met, including surface area.

A report is currently being prepared[7] to document the characterization of both the Y-12 and vendor oxides and the oxide preparation method used by the Y-12 facility.

URANIUM HOMOGENEITY

M. M. Martin C. F. Leitten, Jr.

The design of the HFIR requires very tight and complex specifications on uranium homogeneity. We investigated the uranium distribution in the fuel plate for the dual purpose of elucidating any undesirable periodic effects and defining the degree of uranium homogeneity. As described previously[6] 25 inner and 50 outer plates, randomly selected from the first reactor production, were inspected on our homogeneity scanner. The instrument completely scanned each plate with a $^5/_{64}$-in.-diam x-ray beam and monitored the instantaneous (spot) and 0.16-sec *RC* time constant (average) attenuations at 0.048-in. increments along the length of the fuel core. We recorded about 38,000 of these observations per plate and then subjected them to detailed analyses with the aid of an electronic computer.

For each $^5/_{64}$-in.-wide scan along the length of the fuel core, we obtained from the computer the following readouts: (1) the mean spot, mean average, and their associated standard deviations; (2) the maximum spot and maximum and minimum averages, expressed in percent from the specified nominal uranium content; (3) the approximate lengthwise location of the maximum spot and maximum and minimum averages; and (4) the maximum mean from averaging ten concurrent spots, again expressed in percent. The latter output adequately represented the maximum average and demonstrated the feasibility of eliminating the averaging circuit in digital analysis. Additionally, the computer tabulated for each plate the number of spot rejects per scan at tolerances of 15, 20, 25, 30, 35, and 40%; the number of average rejects per scan at tolerances of ±5, ±10, ±15, and ±20%; and the statistical tolerance limits per scan calculated at the 95 and 99% confidence level to include 95, 99, and 99.9% of the observations.

The statistical interpretation of the calculated tolerance limits is depicted in Fig. 27.2. The plots show the percentage rejection of plates for a very rigid homogeneity specification that rejects plates for a single observation greater than or equal to positive spot and plus and minus average tolerances. The curves for average variations of ±5, ±10, ±15, and ±20% and infinity are surprisingly steep for both annuli and indicate sharp homogeneity

---

[6] M. M. Martin, B. E. Foster, and S. D. Snyder, *Metals and Ceramics Div. Ann. Progr. Rept. June 30, 1965,* ORNL-3870, pp. 221–23.

[7] W. J. Werner and J. R. Barkman, technical memorandum in preparation.

Table 27.2. Chemical and Physical Data of HFIR U_3O_8

	Blend 1	Blend 2	Specification
Total mass, kg	148.1	164.5	
Uranium content, wt %	84.614	84.602	$\geqq 84.5$
Isotopic analysis, wt %			
^{234}U	1.00	1.00	*a*
^{235}U	93.18	93.16	>93%
^{236}U	0.35	0.33	*a*
^{238}U	5.47	5.51	*a*
Surface area (krypton BET determination), m^2/g	0.050	0.047	<0.05
Density (toluene pycnometer), g/cm^3	8.23	8.24	>8.29
UO_2 (x-ray diffraction), %	<1	<1	<1
Fluorine (ppm)	<1	<1	<10
Spectrographic, ppm on U_3O_8 basis			
Al	2	7	10
B	<0.1	<0.1	0.2
Ba	<2	<2	10
Be	<0.01	<0.01	0.2
Ca	<10	<10	50
Cd	<0.1	<0.1	0.5
Co	<1	<1	3
Cr	<2	4	15
Cu	10	8	20
Fe	20	20	100
K	<6	<6	20
Li	<0.2	<0.2	1.0
Mg	3	8	100
Mn	<1	<1	5
Na	<1	<1	5
Ni	5	4	20
P	<100	<100	<100
Si	<10	<10	50
V	<1	<1	2
Stoichiometry (by difference calculation)	$U_3O_{8.015}$	$U_3O_{8.021}$	*a*
Syntron sieve analysis (100-g sample), %			
+170	0.0	0.2	*a*
−170 +200	18.9	14.2	*a*
−200 +230	14.1	14.2	*a*
−230 +270	30.1	15.6	*a*
−270 +325	32.5	35.8	*a*
−325	4.4	5.5	<10%

[a] Not specified.

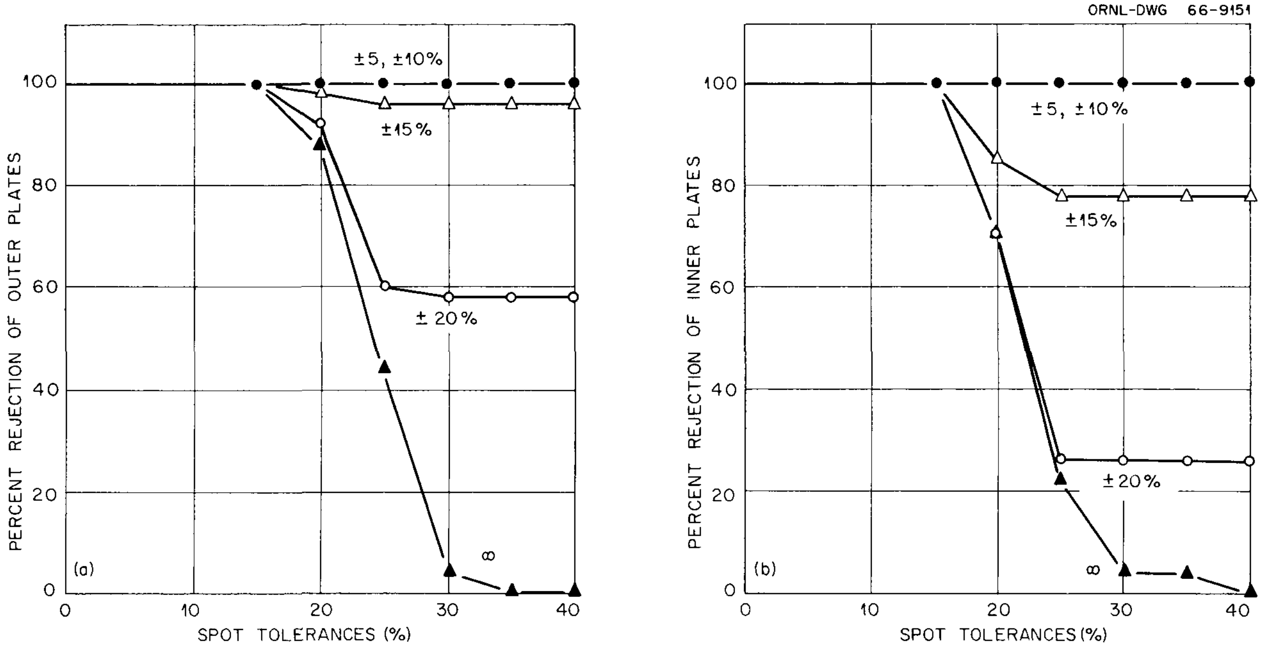

Fig. 27.2. Relationship Between Spot and Average Tolerance Limits and Rejection Rates of (*a*) Outer- and (*b*) Inner-Annulus Fuel Plates. Curves calculated at the 95% confidence level to include 99% of the actual observations.

boundaries for the fabrication process. In both cases the percentage rejection of plates was less than 5% for a 30% spot tolerance. When an average requirement of ±20% was included, however, the number of rejects increased significantly to 26% for the inner- and 57% for the outer-annulus plates. A reduction in the permissible average specification to ±15% resulted in rejection rates greater than 75%. The higher rejection rate for outer plates at the 20% tolerance is attributed to inadequate moisture control during blending of the fuel compacts.

An example of the computer output from digital homogeneity data, which presumably would permit a more sophisticated analysis of a fuel plate's ability to sustain a particular average heat flux, is shown in Table 27.3. A review of this immense quantity of data for the 75 plates showed no periodicity of uranium segregation. In most plates the observed maximum average did not cover a significant portion of the fueled area and the maximum spot was not at the outlet end of the plates nor near the maximum average. For these reasons a digital analysis technique would probably reduce the fraction of rejects in HFIR plates, since it is capable of considering the actual concentration, size, and location of uranium segregation.

PULSED-ARC WELDING DEVELOPMENT

R. G. Donnelly

A new welding technique has recently been developed and is known as pulsed-arc welding. This technique has several potential advantages over other types of gas metal-arc welding. These include (1) lower total heat input, which tends to minimize shrinkage and distortion; (2) better arc controllability; and (3) the ability to use larger diameter wires which, in turn, reduces problems in wire feeding.

Because these advantages would be attractive for welding HFIR core assemblies, a welding system of this type was assembled by combining and modifying existing welding power supplies. Test welds with 0.045-in.-diam wire instead of the 0.030-in.-diam wire now being used demonstrated the potential of this technique. However, to make

Table 27.3. Excerpts of Digital Output for an Inner-Annulus Reactor Plate

Scan	Distance from Reference Edge (in.)	Theoretical Uranium Content (mg)	Spot				Average						Maximum Average of Ten Concurrent Spots (%)
			Mean (mg)	Standard Deviation (mg)	Maximum (%)	Distance from Top of Plate (in.)	Mean (mg)	Standard Deviation (mg)	Maximum (%)	Distance from Top of Plate (in.)	Minimum (%)	Distance from Top of Plate (in.)	
3	0.286	0.673	0.661	0.0532	18.7	17.0	0.668	0.0314	7.4	11.0	−12.0	19.7	7.5
4	0.347	0.722	0.719	0.0530	21.5	8.3	0.725	0.0304	8.3	8.3	−11.8	21.7	9.0
5	0.408	0.772	0.788	0.0500	22.4	6.1	0.791	0.0264	8.8	8.3	−6.1	19.8	10.4
6	0.469	0.819	0.837	0.0546	19.6	13.7	0.843	0.0287	9.8	14.8	−9.3	21.4	9.9
7	0.530	0.868	0.906	0.0526	21.8	14.6	0.908	0.0311	11.7	13.6	−5.1	21.4	13.0
.													
.													
.													
28	1.811	1.511	1.525	0.0551	10.0	11.0	1.528	0.0280	4.3	11.3	−3.1	21.4	5.9
29	1.872	1.516	1.540	0.0621	12.6	13.8	1.547	0.0332	7.6	15.4	−3.2	20.2	7.0
30	1.933	1.518	1.546	0.0619	12.2	15.3	1.548	0.0389	7.5	15.5	−4.1	21.2	7.3
31	1.994	1.517	1.548	0.0700	13.7	13.1	1.552	0.0444	6.7	9.1	−4.2	2.5	6.9
32	2.055	1.515	1.533	0.0710	14.9	6.4	1.538	0.0471	6.8	12.1	−7.4	21.4	7.7
.													
.													
.													
47	2.970	1.266	1.328	0.0583	17.8	15.6	1.331	0.0386	11.3	11.5	−1.2	21.4	11.7
48	3.031	1.242	1.300	0.0577	15.5	9.5	1.302	0.0360	9.5	9.9	−3.2	21.7	9.8
49	3.092	1.215	1.269	0.0556	17.6	10.5	1.271	0.0351	9.7	10.2	−2.8	2.4	10.0
50	3.153	1.188	1.235	0.0679	16.4	12.3	1.240	0.0387	10.1	12.6	−3.5	3.2	11.6
51	3.214	1.159	1.234	0.0587	20.3	16.0	1.236	0.0388	13.5	16.9	+0.2	3.7	14.6

the welding variables developed in future studies directly transferable to production, we feel we need a commercial pulsed-arc power supply, the first models of which have just become available.

ATTACHMENT OF COOLANT CHANNEL SPACERS

G. M. Adamson, Jr.

At one stage of the development of the HFIR fuel element, a doubt was raised that the element could run at the design power of 100,000 kw without additional water channel spacers. It was speculated that bowing and similar deforming of the channels would be encountered. As a preventive measure, while these design problems were being studied, ways of adding such spacers were to be sought. If such spacers should not be required for the present element, they undoubtedly would be for an advanced element. Studies show they are not required for the 100,000-kw operation; so they are not being added to the present production elements.

Two methods of attaching such spacers were studied. In the first, wires are to be drawn through the channels of completed elements. To eliminate abrasion during use, the wires would be larger than the channels and fit into grooves. Such a technique might be difficult on a production basis but could be used with the stockpile of existing elements. The second technique consisted in attaching wires to the plates before assembly into an element. Such wires would be machined to close tolerances after welding. The shrinkage of the element during welding would be used to obtain contact with the adjacent plate and prevent galling during operation.

Welded Wires

C. H. Wodtke J. W. Tackett

Development studies were conducted in cooperation with the Plant and Equipment Division Fabrication Department to determine suitable means for attaching welded wire spacers to the HFIR fuel plates. Wire was selected for ribs because its simple geometry was desirable for considerations of heat transfer and coolant flow.

The ultrasonic welding process was believed advantageous for this application because joining could be accomplished without gross heating and melting of the fuel cladding. Thus, exposure of fuel in the core might be avoided. During the program, we developed a unique welding tip and an ultrasonic welding procedure to join the wire ribs to simulated fuel plates.

In the test assembly, plates were 6061-O aluminum, 0.050 × 3.3 × 24 in. Ribs were 6061-O aluminum wire, 0.063 in. in diameter and 24 in. long. Two ribs were attached 1 in. apart on each plate. They were joined by ultrasonic spot welds on $\frac{1}{2}$-in. centers and subsequently machined to desired height (0.050 in., ideally) above the plate surface.

We encountered various problems initially when using a "standard" welding tip having a groove matching the contour of the wire. These were mashing the wire, embedding the wire into the plate, inconsistent bonding or complete loss of bonding resulting from loss of energy transfer to the work, and fatigue cracking of the wire. These problems were solved by use of a special welding tip with a V-groove. This tip facilitated welding under low clamping force and thereby prevented mashing or embedding of the wire.

The fixture for positioning plate and wire is shown in Fig. 27.3 mounted on the welding head. The plate is held down by vacuum. A mechanical clamp ring applied added hold-down force around the welding tip during the welding cycle. The wire is held under light spring tension. The upper part of the fixture is movable and is indexed at $\frac{1}{2}$-in. stops along the plate.

The success of the development was demonstrated by the welding of spacers onto plates and assembling them into a flow test rig, shown partly assembled in Fig. 27.4 and completed in Fig. 27.5. Several such rigs will be made to determine if such an element is subject to abrasion during flow. In the completed element, the plates are gas tungsten-arc welded to side supports and the ends of the plates and wires are also welded together. The flow testing of this first element has been satisfactorily completed. All bonds between rib and plate appeared sound under visual examination. Detailed evaluation of the plates is now being conducted.

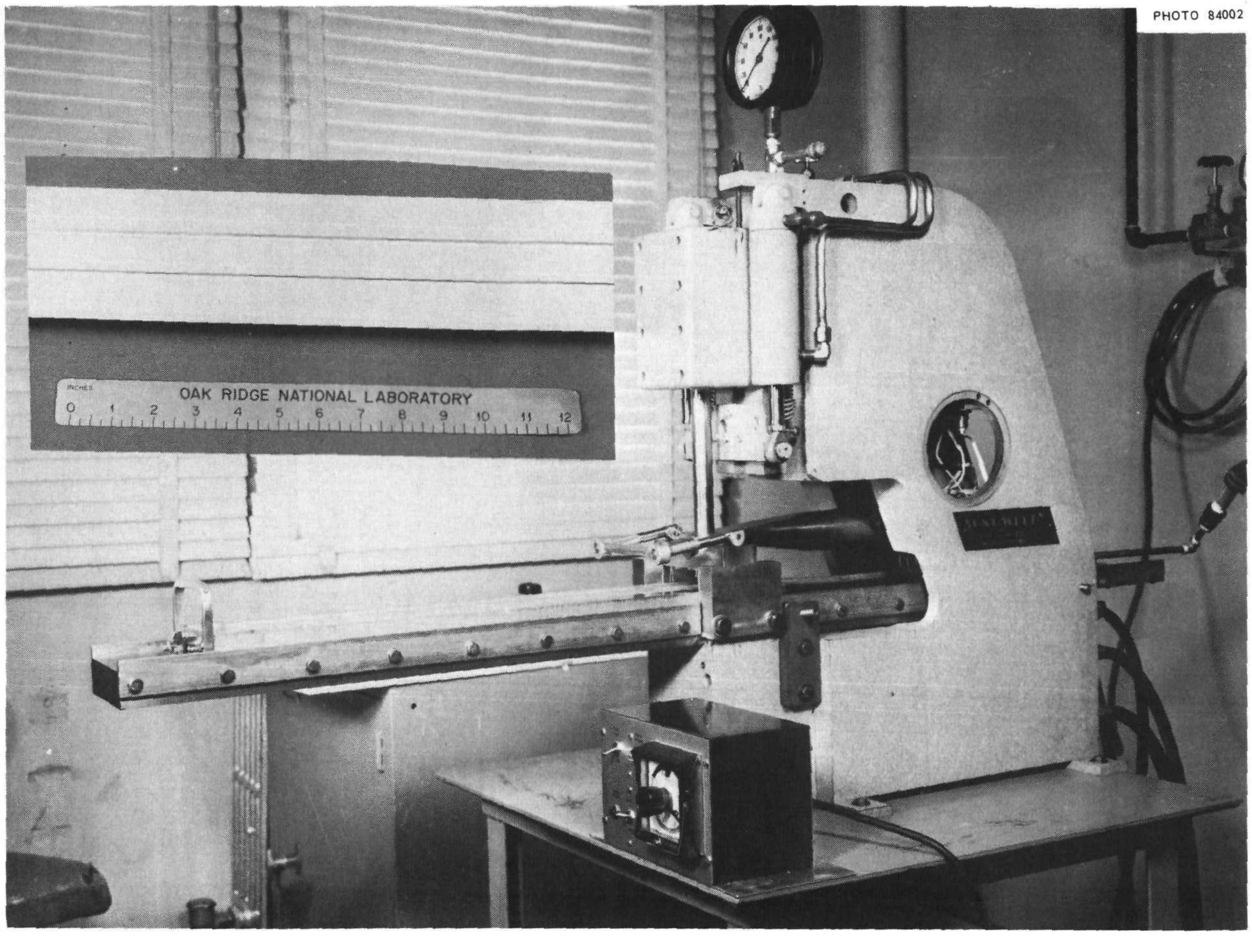

Fig. 27.3. Ultrasonic Welding Machine and Fixture for Positioning Plate and Wire. Insert shows fuel plate with spacers attached.

The plates, with wires attached, can be formed with conventional HFIR dies and techniques. No failure of the welds or cracking of the cladding under a weld was encountered. Sufficient plates have not yet been formed to furnish data on the reproducibility of the process.

Drawn Wires

G. A. Reimann C. F. Leitten, Jr.

Early work entailed feasibility studies in which grooving the fuel plates to accept the restraining wires, insertion of the wires, lubricants, and the establishment of fabrication parameters were of prime concern. Results of these studies assisted in the construction of a flow-test element, which is currently in test to demonstrate this spacing method.

The most practical method of forming the grooves was drawing carbon steel wires through the coolant channel. It was necessary, however, to use spacer shims to support the plates against the forming pressure and help to maintain the proper groove alignment. The smoothest groove was obtained by pulling tungsten carbide balls through the channels, using a metal strip in which small holes were drilled to hold the balls. Unfortunately, this procedure proved inadequate, since it did not permit the use of spacer shims between the plates to minimize distortion.

We established the feasibility of forming longitudinal grooves in the plates, although the minimum and/or optimum depth still remains to be determined. A groove greater than 3 mils deep was formed in

Fig. 27.4. Flow-Test Element Partially Assembled.

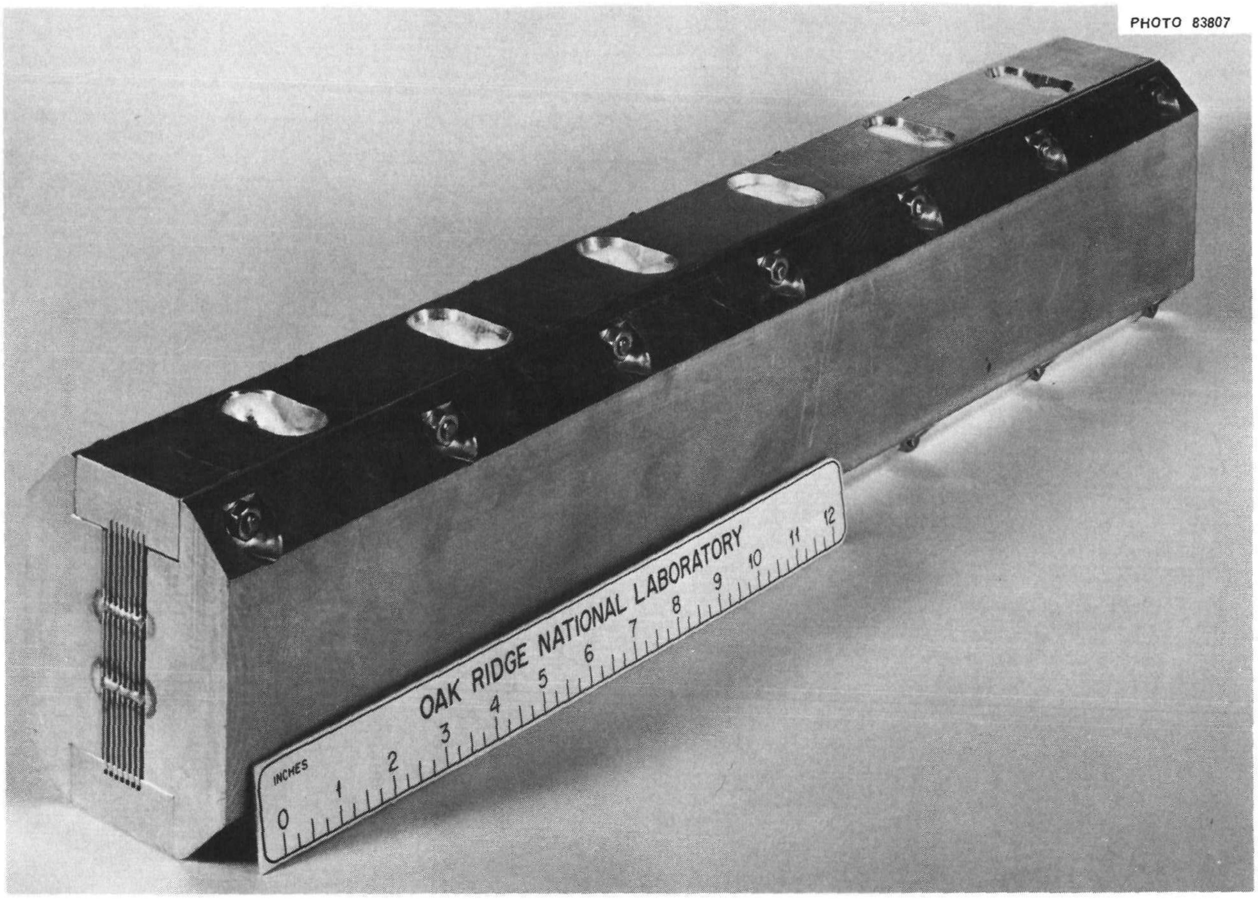

Fig. 27.5. Completed Flow-Test Element.

the plates with little difficulty and permitted the easy insertion of 55-mil aluminum wires in a 50-mil coolant channel. During the forming step, considerable metal was displaced on both sides of the groove and increased its effective depth. This feature of forming could allow the restraining wires to be guided with shallower grooves and avoid drastic thinning of the fuel-plate cladding.

The success of pulling type 6061 aluminum restraining wires into the grooves depended mainly upon lubrication and sufficient diametral clearance. The results of pull tests, presented in Table 27.4 for a single 50-mil channel, showed that the aluminum wire should be at least 0.0015 in. less in diameter than the preceding forming wire. When the clearance was only 0.001 in., the drawing force always exceeded 40 lb and broke the wire. In the test, SAE-30 machine oil lubricated the grooves and aluminum wire. Lubricants of camphor in alcohol and stearic acid in CCl_4 were also investigated, but severe galling eliminated them from further consideration.

The flow-test element comprised nine plates that gave eight 0.050-in.-gap channels into each of which two aluminum restraining wires were pulled. To prepare the grooves, eight forming wires were pulled simultaneously into one side of the rig at a time, lubricated with SAE-30 oil. The additional drawing force, however, necessitated successive passes with 55- and 58-mil wires to form the grooves without breaking the steel wires. The resulting grooves were of sufficient depth to permit insertion of 57-mil aluminum restraining wires. To complete the assembly, the wires were fused to the ends of the plate. The direction of further development in this area will depend upon the performance of this element in the flow test.

Table 27.4. Force Required to Pull Aluminum Wires of Various Diameters into a 50-mil Channel[a]

Diameter of Aluminum Wire (mils)	Pull Force (lb)	
	Start	Finish
54[b]	<1	<1
55[b]	<1	<1
56	15	25
56	15	30
56	12	20
56	12	25
57[c]	45	0
57[c]	47	0
57[c]	40	0

[a] The grooves were formed to a depth of 2.8 to 3.1 mils by drawing a 58-mil-diam steel wire through the channel with a force of 40 to 50 lb.

[b] Wire pulled through by hand.

[c] Wire broke after 1.5 to 2.0 in. of travel.

CONTROL PLATE FABRICATION

J. H. Erwin W. J. Werner
M. M. Martin

Our work has been directed toward manufacturing the third and fourth sets of control plates for use in the reactor. We successfully fabricated these plates to the same specifications and with the established procedures that were reported for the first and second loadings.[8]

In the fabrication of the earlier plates, we frequently observed severe bowing during the initial stages of hot rolling. The poison sections of Al–33 vol % Eu_2O_3 and Al–40 vol % Ta usually met the dimensional requirements in these plates but always showed an abnormal amount of tapered ends (flash) and out-of-squareness. Two equipment innovations for the third and fourth sets resulted in an improvement in core end effects: additions to our 20-in.-diam rolling mill of pressure lubricators and an adjustable-height feed table reduced the amount of flash from 0.18 to 0.14 in. and out-of-squareness from 0.48 to 0.19 in. We attributed the improved quality of the rolled core sections to equalization of rolling lubricant on the top and bottom rolls and to our new ability to center the control plate billet precisely midway between the top and bottom rolls on every pass.

The third set of plates was transferred to Y-12 and successfully fabricated by explosive forming into control cylinders. All dimensions met specifications.

IRRADIATION TESTING OF DISPERSIONS OF EUROPIUM OXIDE AND EUROPIUM MOLYBDATE IN ALUMINUM

R. J. Beaver A. E. Richt

During the past year we completed our evaluation of three HFIR-type control rod specimens that were irradiated in the ORR at 60°C. As reported previously,[9] two of the aluminum-clad test specimens contained cores composed of 33 vol % Eu_2O_3 dispersed in aluminum (the reference neutron absorber material for the "black" regions of the HFIR control rods). The core of the third specimen also contained an equivalent europium loading; however, in this specimen the poison material was incorporated as 38 vol % $Eu_{5.3}MoO_{11}$ dispersed in aluminum. All three test specimens had the same nominal cladding-core-cladding thicknesses (0.031-0.188-0.031 in.) as the full-size HFIR control rod plates.

The test specimens were irradiated at process-water temperature (60°C) for periods ranging up to one year of full-power operation, resulting in estimated unperturbed doses of up to 2.9×10^{21} neutrons/cm^2 (thermal) and 1.1×10^{21} neutrons/cm^2 (fast). After irradiation the specimens were examined closely for evidence of dimensional changes and then sectioned for metallographic examinations, analytical burnup determinations, and corrosion tests.

Postirradiation examination indicated that both the Al–33 vol % Eu_2O_3 and Al–38 vol % $Eu_{5.3}MoO_{11}$ were quite stable during irradiation. Figure 27.6,

---

[8] M. M. Martin, *Metals and Ceramics Div. Ann. Progr. Rept. June 30, 1965*, ORNL-3870, p. 224.

[9] R. J. Beaver and A. E. Richt, *Metals and Ceramics Div. Ann. Progr. Rept. June 30, 1965*, ORNL-3870, pp. 227–28.

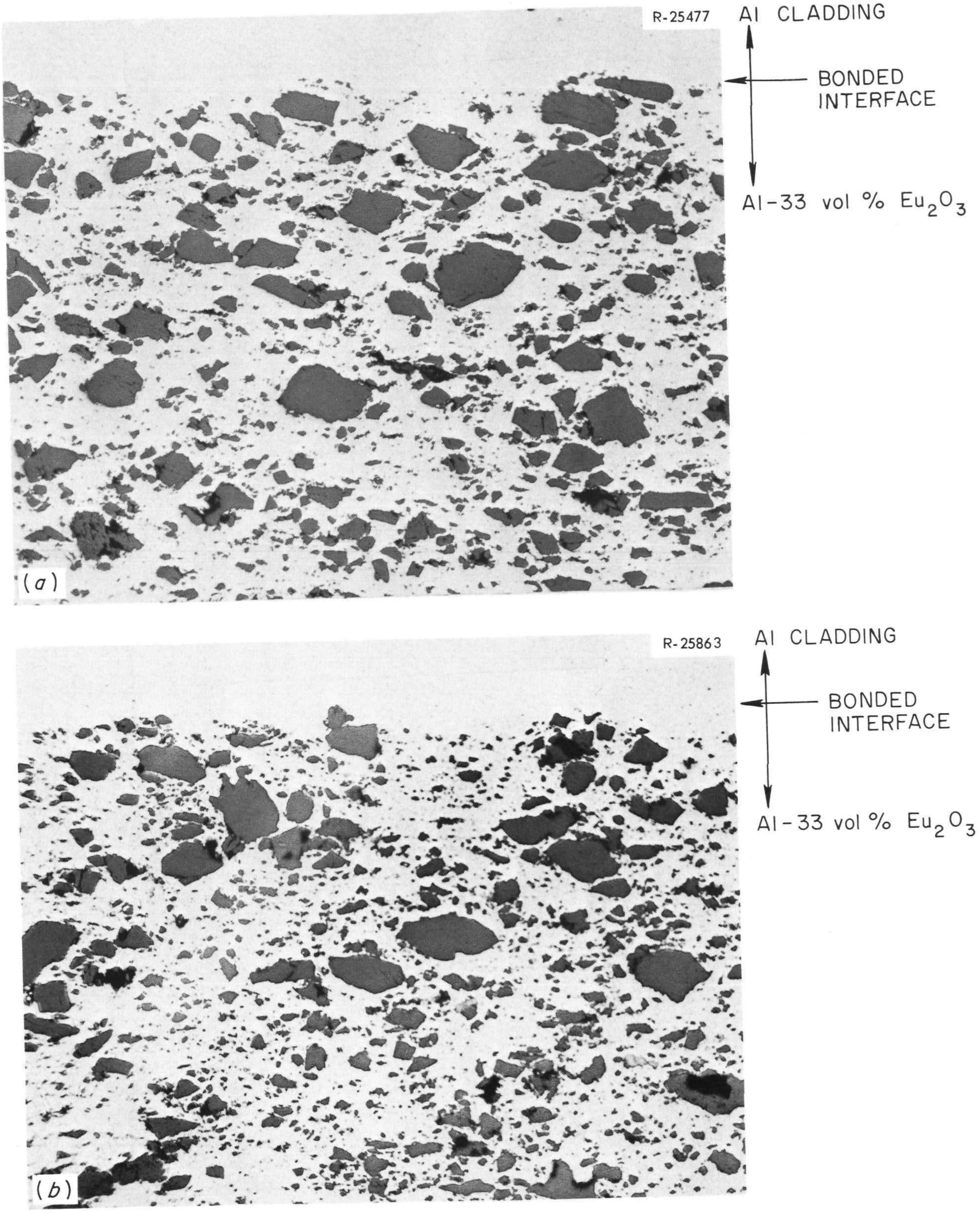

Fig. 27.6. Typical Microstructures of Al–33 vol % Eu_2O_3 Dispersions. As polished. 250×. (*a*) Unirradiated. (*b*) After absorbing 4.1×10^{21} neutrons/cm^3.

Table 27.5. Dimensional Stability of Eu_2O_3-Al and $Eu_{5.3}MoO_{11}$-Al Dispersions After Irradiation in the ORR at 60°C

Specimen	Dispersion Concentration (vol %)	Specimen Burnup		Volume Change (%)
		(neutrons absorbed per original europium atom)	(neutron absorptions/cm^3)	
			$\times 10^{21}$	
4	33 Eu_2O_3	0.19	1.6	+0.17
2	33 Eu_2O_3	0.48	4.1	−0.03
10	38 $Eu_{5.3}MoO_{11}$	0.34	2.9	+0.60

Table 27.6. Corrosion of Irradiated and Control HFIR-Type Neutron Absorber Plates

Specimen	Poison Loading (vol %)	Specimen Burnup (neutron absorptions/cm^3)	Weight Change (%)	Thickness Change (%)
		$\times 10^{21}$		
5	33 Eu_2O_3	Unirradiated	+2.03	+15.2
4	33 Eu_2O_3	1.6	+0.43	+5.1
2	33 Eu_2O_3	4.1	+0.32	+3.2
9	38 $Eu_{5.3}MoO_{11}$	Unirradiated	+0.02	0
10	38 $Eu_{5.3}MoO_{11}$	2.9	+0.06	0

which illustrates the microstructure of the europium oxide dispersed in aluminum, is clear evidence of the chemical compatibility after absorption of 4.1 × 10^{21} neutrons/cm^3. This exposure is quite high and is comparable to 90% burnup of ^{10}B in a 1 wt % ^{10}B–stainless steel alloy. The same microstructural stability was observed for europium molybdate dispersions. Dimensional changes, as evidenced by the volume measurements listed in Table 27.5, do not show any significant changes for the europium oxide dispersoid. The 0.60% change for the europium molybdate dispersion is thought to be an experimental error, since this change was recorded the first time the samples were removed and checked and no further change was noted in the latter removals; however, even if true it is low and not a detriment to use of this corrosion-resistant compound for control rod applications.

We compared the behavior of irradiated and unirradiated material in water at 100°C for 100 hr. The samples were sections cut from the unirradiated control specimens and the irradiated test specimens. Weight and thickness changes were used to judge the degree of attack by the water. The results listed in Table 27.6 demonstrate the corrosion resistance of the $Eu_{5.3}MoO_{11}$ compound. As expected, Eu_2O_3 hydrolyzed. The comparative results on the europium oxide dispersions should not be interpreted that irradiation improves the corrosion resistance of Eu_2O_3 per se. We attribute the difference to the fast-neutron-induced hardening of the aluminum matrix. The increase in strength probably acts to retard cracking when the hydrolyzed Eu_2O_3 swells, thus decreasing corrosion penetration into the interior.

28. High Flux Isotope Reactor Target Development

D. A. Douglas, Jr.

The Transuranium Project is to produce gram quantities of the heavier transuranium elements for research purposes by successive neutron captures in ^{239}Pu. The first part of the production path – that is, the conversion of ^{239}Pu to ^{242}Pu, ^{243}Am, and ^{244}Cm – was carried out in large reactors at Savannah River. Facilities and equipment at ORNL will be used to further irradiate these products and recover the isotopes produced. Target elements containing principally these three nuclides will be fabricated and then irradiated in the High Flux Isotope Reactor (HFIR) at a flux of approximately 3×10^{15} neutrons cm^{-2} sec^{-1}. After they are irradiated the target elements will be reprocessed in the Transuranium Processing Facility (TRU) to recover the product actinides and to recycle the target actinides to the HFIR. Recycle target elements must be remotely manufactured because of the high gamma and neutron radiation associated with the contained nuclides.

Our tasks have involved the development of suitable HFIR targets, the development of procedures for fabricating these target elements under various conditions, and the testing and confirmation of design of the target element.

At this point, we have almost completed the irradiation program for confirmation of the HFIR target element design, we have fabricated the necessary ^{242}Pu targets, and we have completed the development of the target fabrication equipment for the TRU. This equipment is now undergoing final testing prior to "hot" operation in the TRU. A movie[1] in sound and color was made during the latter part of the year to document the HFIR target development work and to describe the unique procedures and equipment employed in target fabrication.

TRANSURANIUM TARGET FABRICATION EQUIPMENT

M. K. Preston, Jr.[2]　J. D. Sease
J. E. Van Cleve　A. L. Lotts

For irradiation in the HFIR, the target actinide oxides are encased in an assembly consisting of 31 individual elements. High-purity water flowing at a rate of 40 ft/sec through the target extracts a maximum of 29 kw of heat from each target element. The calculated peak heat flux in the target elements is 1×10^6 Btu hr^{-1} ft^{-2}, which leads to a maximum metal surface temperature of 265°F. To meet these service conditions we designed a target element consisting of 35 individually jacketed pressed pellets, each composed of a mixture of approximately 12 vol % actinide oxide dispersed in aluminum. The pellets are then contained in a type X8001 aluminum tube with discontinuous fins. These fins are subsequently attached to a target rod sheath, which is used for channeling of the water in the target region of the reactor. Details of the target design, shown in Fig. 28.1, were reported previously.[3] Target elements of this design have been tested thoroughly at the service conditions expected in HFIR and performed very satisfactorily.

The preeminent concern in selecting a fabrication flowsheet for producing these target elements was the fact that these rods must be fabricated remotely in the TRU. Considerable attention was given to the process simplification and adaptability of the process to remote operation. Concurrently, we were careful not to compromise the

---

[1] *Development and Fabrication of HFIR Target Elements*, motion picture produced by ORNL, 1966.

[2] On loan from General Engineering and Construction Division.

[3] M. K. Preston, Jr., J. E. Van Cleve, R. I. Deaderick, and A. L. Lotts, *Metals and Ceramics Div. Ann. Progr. Rept. June 30, 1965*, ORNL-3870, pp. 230–35.

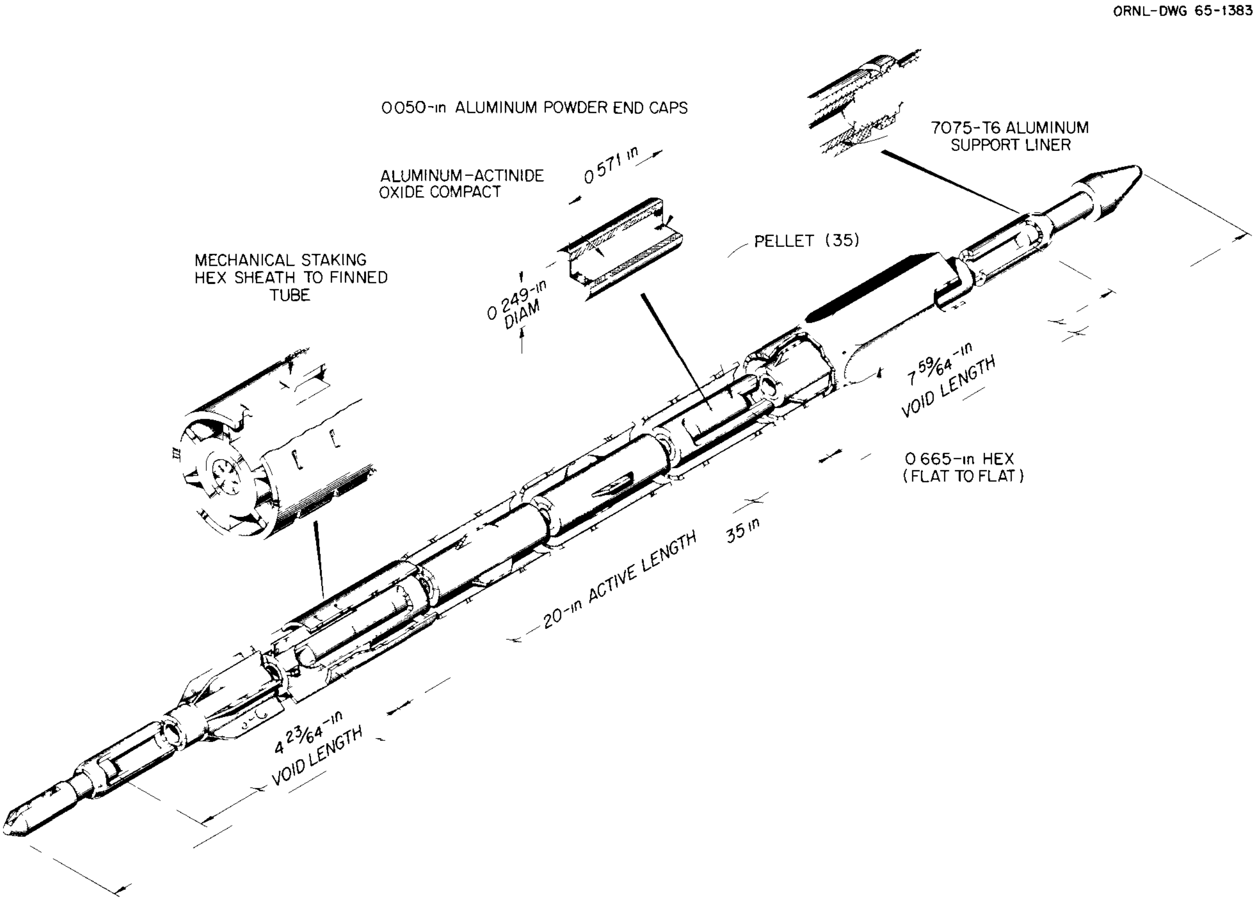

Fig. 28.1. Design of HFIR Target Assembly.

process in any way that would sacrifice the required absolute integrity of the target elements. The procedure for manufacturing the targets consists in powder metallurgical steps, welding, metal forming, and various inspection techniques, such as helium leak testing, radiography, and dimensional inspection.

We completed the development of equipment to remotely fabricate these targets in the heavily shielded TRU. The basic criteria and methods of operation to be used in fabrication were not changed substantially from those established previously.[4]

All equipment has been designed, fabricated, and installed in TRU. The equipment requires minimum use of the master-slave manipulators and can be removed from the cubicle through the 18 × 35 in. equipment transfer opening in the roof. In addition, many components, such as motors, air and water cylinders, valve clusters, electrical and instrument wiring jumpers, and some supporting equipment, can be introduced or removed by the 8-in.-diam × 8-in.-deep intercell conveyor.

A résumé of the design, fabrication, and mockup activities follows; more detailed information on the progress during the last year is reported elsewhere.[5]

Design and Fabrication

Approximately 54 items of equipment have been designed, fabricated, and installed in the three cubicles to fabricate and inspect the HFIR target

---

[4] M. K. Preston, *Metals and Ceramics Div. Ann. Progr. Rept. May 31, 1962*, ORNL-3313, pp. 108–11.

[5] M. K. Preston, Jr., R. I. Deaderick, J. E. Van Cleve, and A. L. Lotts, *Transuranium Quart. Progr. Rept. Oct. 31, 1965*, ORNL-3965 (in press).

4

elements. Primary tasks in design and fabrication during the report period were equipment modifications indicated by the mockup operations. Typical modifications were a new calcining furnace for operation at a temperature of 1250°F (a change necessitated by changes in the oxide preparation procedure), the installation of positive steps for horizontal and vertical positions on the cubicle 2 transfer arm to accurately control and position the transfer arm at the various process stations, changes in the electrical controls and contacts on the pellet inspection and loading equipment to permit semiautomatic operation, and modification of the assembly machine to introduce through the electrode holder the helium gas that is used to purge the chamber and blanket the welding operation. The latter change led to better arc control and cleaner weld surfaces. Other modifications included installing horizontal positive stops and limit switches for the vertical positions of the transfer arm.

The instrument and electrical control panels were designed and fabricated to incorporate the mode of operation derived from the mockup phase of the program. All in-cell electrical jumper lines and drop boxes from the ceiling to the side wall were designed and fabricated for installation with the equipment in the cubicles.

In-cell piping was fabricated at the mockup and transferred with the equipment for installation in the cubicles. Pipe connections from the equipment located in the chemical makeup area of TRU were installed after the equipment was removed from the mockup.

Equipment Mockup and Installation in TRU

A mockup was used effectively to develop satisfactory operating procedures, to test and modify the equipment in an accessible environment, and to locate for fabrication the electrical jumpers and in-cell piping. From our experience the operating and maintenance manuals were started and are now being completed.

Removal of equipment from the mockup and installation in TRU started in February 1966 and is now complete.

All equipment has operated satisfactorily, but a few items still require undue attention to keep them in operating condition. These components include the three scale systems in cubicle 3, which will not stay calibrated for a sufficient length of time, and the dimensional inspection equipment, which also has given us problems in maintenance of calibration.

PLUTONIUM TARGET FABRICATION

J. D. Sease A. L. Lotts

Fabrication of ^{242}Pu-Containing Target Elements for Initial HFIR Loading

We fabricated 36 HFIR target elements, 3 of which are currently being irradiated in the HFIR as the initial target loading. Each of these target elements (Fig. 28.2) contained 8 g of ^{242}Pu in the form of PuO_2. The loading was dictated primarily by heat-generation considerations and by the quantity of available ^{242}Pu. Essentially the same procedure was used to fabricate these elements as to fabricate the prototype irradiation target elements[6] and the target elements made for irradiation at Savannah River.[7] The fabrication procedure, which was carried out in a gloved-box fabrication line, consisted in pressing pellets containing $^{242}PuO_2$ in an aluminum matrix (35 separate pellets per element), inserting the pellets into an aluminum tube, end-closure welding, helium leak testing, cold hydrostatic collapse of the cladding onto the pellets, and mechanical attachment of the cover can to the finned cladding tube.

The fabrication of the elements was completed without any major problems. In previous fabrication we had experienced considerable difficulty in obtaining a homogeneous dispersion of the PuO_2 powder in the aluminum matrix; however, the use of a new blending and dispersing system eliminated this problem. This system was subsequently incorporated into the TRU fabrication line. Again, the collapse fabrication step bowed the rods; some required hand straightening.

The preirradiation data included measurements of the rod diameter, rod bow, rod weight, and rod-to-can spacing. Radiographs were taken of

---

[6] J. D. Sease and D. M. Hewette II, *Fabrication and Preirradiation Data for High Flux Isotope Reactor Prototype Target Rods*, ORNL-TM-811 (June 1964).

[7] J. D. Sease, *Fabrication and Preirradiation Data of HFIR Target Elements for Savannah River Irradiations*, ORNL-TM-1095 (June 1965).

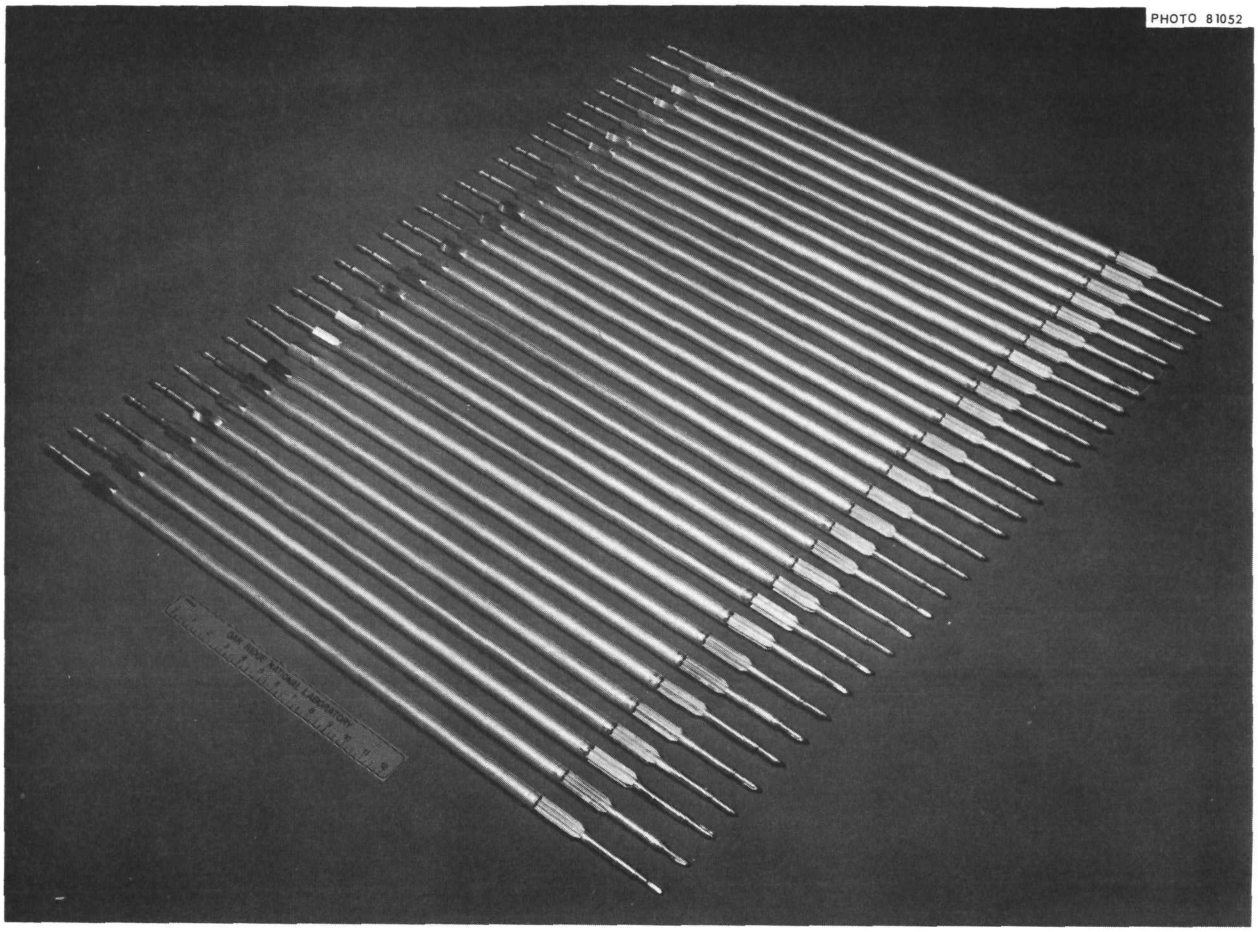

Fig. 28.2. Plutonium Targets Fabricated for Use in HFIR.

the welds (three places) and the entire rod assemblies. In addition, the rods were leak checked and the assembled elements were photographed. Complete preirradiation data are reported elsewhere.[8]

Fabrication of Simulated HFIR Target Elements

We fabricated 38 simulated HFIR target elements, and they are currently being used by the reactor operators in initial power testing. The simulated elements each contained 0.300 g of tantalum and 0.083 g of 10%-enriched UO_2 to match the heat generation and cross section of the ^{242}Pu target elements. These elements were fabricated in a manner identical to the elements containing the ^{242}Pu. The same preirradiation data were taken, except the rod-to-can spacing was not determined. Fabrication details and preirradiation data are reported elsewhere.[8]

IRRADIATION TESTING

A. R. Olsen J. D. Sease
A. E. Richt J. W. Ullmann[9]

Four prototype target elements have successfully completed the planned irradiations in the Engineering Test Reactor. Three have been examined, and the fourth is currently under examination.

---

[8] J. D. Sease, *The Fabrication and Preirradiation Data for ^{242}Pu and Simulated Target Element for the High-Flux Isotope Reactor* (in preparation).

[9] Chemical Technology Division.

Table 28.1. Irradiation Data for HFIR Target Prototypes

Rod No.	Equivalent Reactor Full-Power Days	Time-Average Surface Heat Flux (Btu hr^{-1} ft^{-2})	Advertised Time-Integrated Peak Unperturbed Exposure (neutrons/cm^2)	^{239}Pu Burnup (at. %)	Plutonium Fissioned (at. %)	Plutonium Fissioned (fissions/cm^3)
			$\times 10^{21}$			$\times 10^{21}$
TRU-1	108	640,000	1.7	44	31	1.02
TRU-2	205	640,000	3.2			
	30	1,000,000	0.9	90	64	2.10
TRU-3	293	640,000	4.3	84	62	2.04
TRU-4	376	640,000	7.2	(99)[a]	(74)[a]	(2.40)[a]

[a] Not available at this time. Rod presently undergoing postirradiation examination. The values are computer-calculated anticipated burnups.

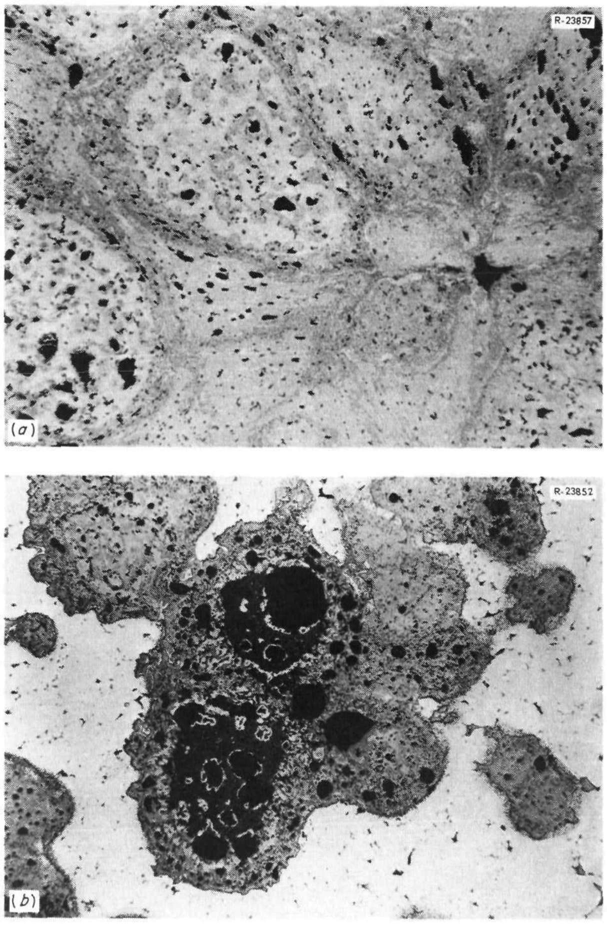

Fig. 28.3. Microstructures of HFIR Prototype Target Rod TRU-2 Exposed at a Maximum Surface Heat Flux of 1,000,000 Btu hr^{-1} ft^{-2} During the Final 30 Days of Irradiation. 250×. (*a*) Typical central fueled region. (*b*) Typical outer fueled region.

The findings on these rods have been reported.[10–13]

Table 28.1 summarizes the irradiation data on these prototype rods. There was no evidence of gross swelling on any of these rods. Essentially all the fission product gas was retained in the pellet matrix; less than 5% was recovered from the end plenums of the rod subjected to the higher heat rating.

Oxide film on the exterior of the tube will influence heat transfer characteristics. This is not expected to be a serious limitation, since the maximum thicknesses, which were found on

---

[10] A. R. Olsen, J. W. Ullmann, and S. D. Clinton, *Transuranium Quart. Progr. Rept. Aug. 25, 1964*, ORNL-3739, pp. 49–52.

[11] A. R. Olsen, J. W. Ullmann, and S. D. Clinton, *Transuranium Quart. Progr. Rept. Nov. 30, 1964*, ORNL-3847, p. 42.

[12] A. R. Olsen, S. D. Clinton, J. W. Ullmann, and A. E. Richt, *Transuranium Quart. Progr. Rept. Oct. 31, 1965*, ORNL-3965 (in press).

[13] A. R. Olsen, J. D. Sease, A. E. Richt, J. W. Ullmann, and S. D. Clinton, *Trans. Am. Nucl. Soc.* 9(1), 66 (1966).

TRU-2, were only 0.0016 in. over the fueled regions and 0.0013 over the unfueled regions; approximately 0.0005 in. of this thickness had apparently accumulated during storage in the pool following irradiation.

The fuel dispersions, as reported last year, showed some reaction between the aluminum matrix and the plutonium dioxide under irradiation. Although this has not been duplicated out of irradiation, comparison of TRU-2 and TRU-3, which had similar burnup levels, clearly indicates that temperature is the predominant rate-controlling factor. Figure 28.3 is a pair of typical photomicrographs from TRU-2. The limited extent of reaction shown for the outer fueled region, where the temperature was lower, is typical of the entire fueled regions of prototype rods TRU-1 and TRU-2, which operated only at the anticipated HFIR target heat ratings. These reactions did not cause swelling. The performance of these rods clearly indicates that the HFIR target should provide satisfactory performance at the anticipated operating conditions.

THERMAL CONDUCTIVITY OF ALUMINUM-UO$_2$ CERMETS

J. P. Moore

Central melting of the dispersion should be avoided during irradiation of targets in the HFIR. Consequently, we are investigating the effects of oxide volume and particle size on the dispersion thermal conductivity using UO$_2$ to simulate the actinide oxides.

Thermal conductivity was measured on a series of aluminum-UO$_2$ cermets with various proportions of the constituents. The temperature dependence of the thermal conductivity appears to be controlled by the aluminum. The variation of conductivity with UO$_2$ content up to 20% obeys theoretical predictions with the aluminum assumed to be the continuous phase.

29. Medium-Power Reactor Experiment

G. M. Adamson, Jr.

Our purpose has been to provide materials support for the Medium-Power Reactor Experiment. This reactor was being designed and developed at ORNL; however, during this year the project was terminated by the AEC. The MPRE was to have been a single-loop Rankine-cycle system employing boiling potassium as the reactor coolant and thermodynamic working fluid. The reactor system was to be constructed of conventional materials, primarily stainless steel, and was to operate in the temperature range of 870°C or lower.

The principal materials assistance has been in the investigation of various materials exposed in the liquid metal or its vapor. Components have also been fabricated for many of the engineering and critical tests. We prepared and issued a series of papers[1–4] discussing various materials problems in the MPRE.

A joint program to determine the effect of fast-neutron exposure on the mechanical properties of stainless steel has been conducted with support from this project, the mechanical property program, and Los Alamos Scientific Laboratory. The results of this program are reported in Part III, Chap. 20 of this report.

FORCED-CIRCULATION BOILING-POTASSIUM LOOP TESTS

J. H. DeVan R. E. MacPherson[5]
D. H. Jansen L. W. Fuller[5]

Candidate materials for high-temperature liquid-metals turbine nozzles and blades are being tested over a range of temperatures, vapor velocities, and vapor quality levels in forced-circulation boiling-potassium systems.[6] The basic test loop and potassium conditions are shown in Fig. 29.1. To date the following tests have been completed:

Test Section Nozzle and Blade Material	Operating Time (hr)
Type 316 stainless steel	750
Haynes alloy No. 25	1679
TZM	544
TZM	2067
TZM	1000
TZM	1000
TZM	3600

The last of these is still operating; it is scheduled for 10,000 hr.

Examinations of these loops revealed the maximum erosion damage at the middle nozzle-blade position with the lowest vapor quality (82%). The first three tests of the TZM alloy resulted in unusually heavy reaction layers and cratering at the impingement areas of the first- and second-stage blades; however, this attack was eliminated

---

[1] S. C. Weaver and J. L. Scott, *Comparison of Reactor Fuels for High Temperature Applications*, ORNL-TM-1360 (Dec. 30, 1965) (classified).

[2] J. H. DeVan, *Compatibility of Structural Materials with Boiling Potassium*, ORNL-TM-1361 (April 1966) (classified).

[3] W. R. Martin, *Factors Affecting the Mechanical Properties of Stainless Steels at MPRE Operating Temperatures*, ORNL-TM-1362 (February 1966) (classified).

[4] R. W. Swindeman, *Fatigue of Austenitic Stainless Steels in the Low and Intermediate Cycle Range*, ORNL-TM-1363 (January 1966).

[5] Reactor Division.

[6] C. W. Cunningham *et al.*, *Trans. Am. Nucl. Soc.* 8(2), 401 (1965).

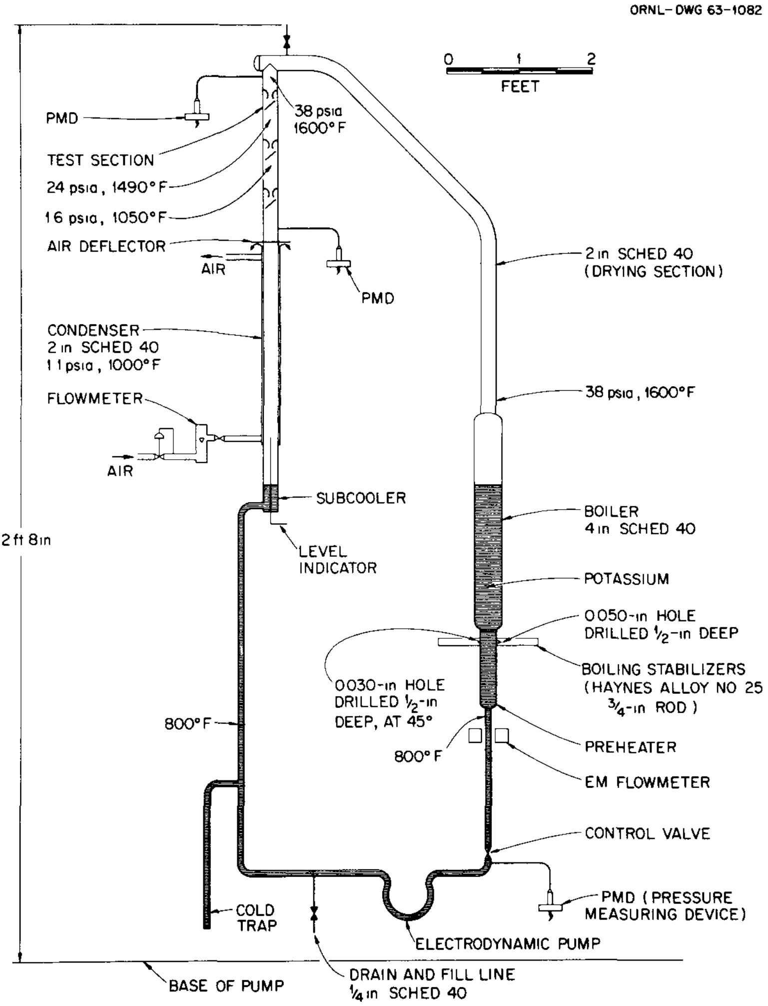

Fig. 29.1. Type 316 Stainless Steel–Boiling Potassium Nozzle and Turbine Blade Corrosion Loop.

in a fourth test by the incorporation of an in-line zirconium hot trap in the boiler preheater.[7] Tests of the other alloys revealed little damage beyond formation of a smooth shallow depression at the second-stage blade impingement area.

NATURAL-CIRCULATION BOILING-POTASSIUM LOOP TESTS

J. H. DeVan D. H. Jansen

Evaluation of TZM test sections discussed above showed that impurities present in boiling potassium could be transported with potassium vapor to cause oxidation of the TZM alloy.

To evaluate the migration of impurities in potassium vapor, a series of natural-circulation stainless steel loops was initiated with potassium intentionally contaminated with oxygen. The test systems are small loops with pot boilers. Tight-fitting sleeve-type inserts are placed in the condenser-subcooler leg and serve as post-test weight change specimens. One group of loop tests contains alternate inserts of TZM and stainless steel, while another group contains only stainless steel inserts.[8] All systems are being operated with an 870°C boiler-condenser temperature.

---

[7] J. H. DeVan, C. W. Cunningham, D. H. Jansen, L. C. Fuller, and R. E. MacPherson, ORNL-3860, pp. 78–82 (classified).

[8] J. H. DeVan and D. H. Jansen, ORNL-3860, pp. 82–84 (classified).

Type 304 Stainless Steel Loops with TZM Alloy Inserts

A base-line loop of type 304 stainless steel that contained alternate inserts of TZM alloy and type 304 stainless steel in the condenser-subcooler leg completed a scheduled 3000-hr test with high-purity (99.97%) potassium. Spectrographic results indicated that small amounts of stainless steel components, principally chromium, had mass transferred to the TZM alloy inserts. Intergranular attack 1 to 2 mils in depth was observed metallographically on the boiler wall adjacent to the boiling nucleation sites. No other loop components showed metallographic evidence of damage or dissolutive attack, and weight changes of insert specimens were correspondingly small. Two other loop tests of this type are currently in operation with potassium containing 3100 and 4500 ppm oxygen.

Types 316 and 347 Stainless Steel Loops

Concurrent with the stainless steel–refractory metal loop tests, we are also operating loops containing various types of stainless steel inserts. One such test,[9,10] a type 316 stainless steel loop containing types 316 and 347 stainless steel inserts, was operated for 3000 hr with potassium containing 3400 ppm oxygen. Examination of this loop revealed heavy corrosion on the boiler wall adjacent to boiling nucleation sites, and the insert weight changes were considerably greater than for loops containing pure potassium. A companion loop[11,12] to this test, containing pure potassium, was terminated by a tubing failure after 2700 hr, and a replacement loop is being fabricated.

CORROSION OF SOME HIGH-TEMPERATURE BRAZING ALLOYS IN BOILING POTASSIUM

N. C. Cole C. W. Fox
G. M. Tolson[13]

The compatibility of six high-temperature brazing alloys, described in Table 29.1, was evaluated in boiling potassium at temperatures of 1540°F for 6500 hr and 1600°F for 4500 hr. Braze samples of each of the six alloys joining type 316 stainless steel tubes were placed in a capsule partially filled with potassium, which was then heated to boiling with a Firerod heater. One specimen of each brazing alloy was placed in the liquid potassium, one at the calculated liquid-vapor (boiling) interface, and one in the vapor region. In some tests samples were also brazed onto the cartridge heater with Nicrobraz 50. We have run 21 tests, and over 800 samples have been examined metallographically.

Table 29.1. Brazing Alloys Examined in Boiling Potassium

Alloy	Composition (wt %)	Brazing Temperature (°F)
General Electric J8100	71 Ni, 19 Cr, 10 Si, 0.15 C	2125
General Electric J8300	61 Ni, 19 Cr, 10 Si, 10 Mn	2100
Coast Metals No. 50	93.4 Ni, 3.5 Si, 1.6 B, 1.5 Fe	2000
Coast Metals No. 52	90.5 Ni, 4.5 Si, 3.25 B, 1.5 Fe	1950
Nicrobraz 50	77 Ni, 13 Cr, 10 P	1850
Nicrobraz 10	89 Ni, 11 P, 0.15 C	1850

---

[9] J. H. DeVan and D. H. Jansen, ORNL-3897, pp. 94–96 (classified).

[10] J. H. DeVan and D. H. Jansen, ORNL-3937, pp. 94–101 (classified).

[11] J. H. DeVan and D. H. Jansen, ORNL-3976, pp. 59–64 (classified).

[12] J. H. DeVan and D. H. Jansen (in press) (classified).

[13] Now at Oak Ridge Gaseous Diffusion Plant.

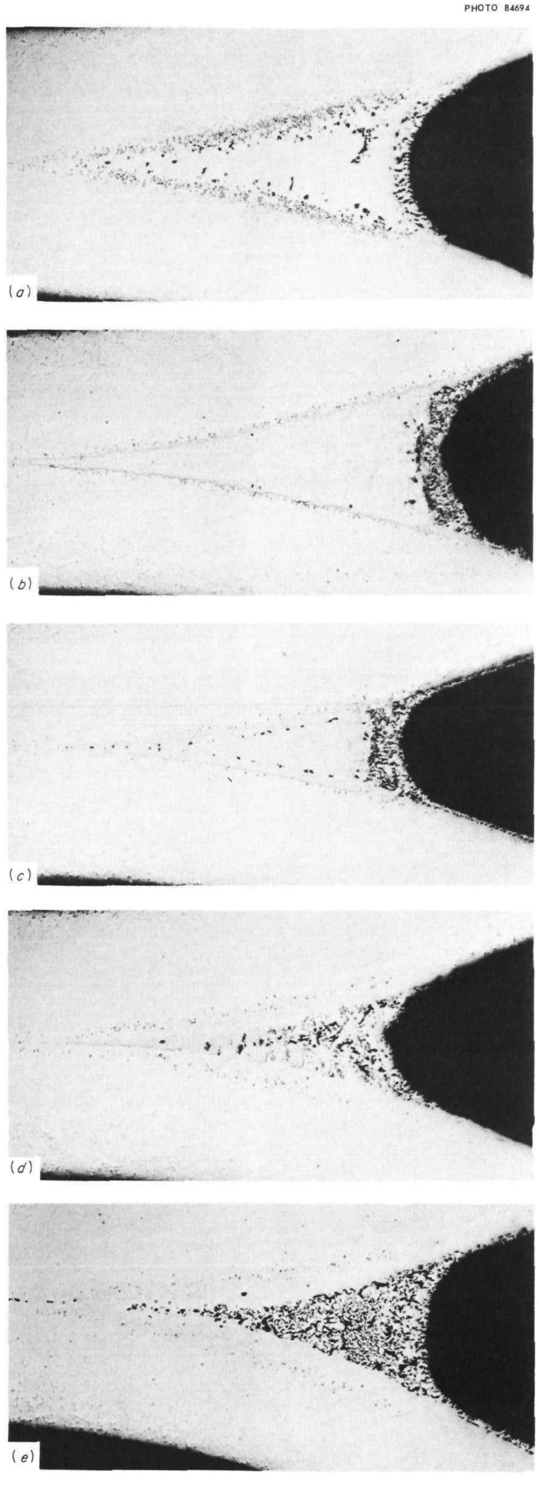

Fig. 29.2. Microstructure of the Five Brazing Alloys Tested in Boiling Potassium at 1540°C for 6575 hr. As polished. 75×. (*a*) Coast Metals 50. (*b*) General Electric J8100. (*c*) General Electric J8300. (*d*) Nicrobraz 50. (*e*) Nicrobraz 10. Reduced 53.5%.

In general, potassium leached material from the specimen, forming subsurface voids. Preliminary microprobe analyses indicate that silicon and phosphorus are the constituents that migrate to form the void. Figure 29.2 compares the metallographic appearance of the test alloys after residence in the boiling liquid for more than 6500 hr. We rate the brazing alloys in suffering increasing amount of attack as follows: Coast Metals Nos. 50 and 52, General Electric J8100, General Electric J8300, Nicrobraz 50, and Nicrobraz 10. The General Electric brazing alloys showed deeper surface attack than the Coast Metals brazing alloys, but the diffusion voids in the latter along the tube-to-braze interface may have the same effect on strength after long-time service at temperature. We are currently investigating this point by subjecting specimens to Miller-Peaslee[14] bend tests.

All the brazing alloys with the exception of Nicrobraz 10 are recommended for boiling potassium service at 1540°F, depending on the individual system requirements. For instance, the Coast Metals alloys are not recommended for use in a reactor core, because the boron would transmute to helium, leaving numerous voids. Also, the General Electric alloys must be assigned to service where their high brazing temperatures (Table 29.1) would not cause damaging grain growth in the adjacent base material. Based on the corrosion results to date, we must conclude Nicrobraz 50 is marginal for long-time service. However, meager data from bend tests show that after phosphorus is leached from this brazing alloy, the remaining nickel-chromium alloy tends to be just as strong as the initial alloy.

BORE SEAL DEVELOPMENT

N. C. Cole

One of the major limitations to the development of electric generators for space electric power systems is providing a hermetic division between the vulnerable portions of the machine and the alkali metal working fluid. We have continued to seek a metal-to-ceramic seal corrosion resistant to potassium vapor. Attack on alumina, which is

---

[14] F. M. Miller and R. L. Peaslee, *Welding J.* 37(4), 144s–50s (1958).

relatively compatible with potassium vapor, in prototype joints has been traced to the metallizing treatment used to promote bonding. Either an active metal braze that eliminates the use of metallizing or a 3-mil tungsten vapor plate provided adequate protection for 1000 hr at 1000°F. Complete details of the development and testing program are available elsewhere.[15–17]

ANALYSIS OF INTERMEDIATE POTASSIUM SYSTEM FILTER DEPOSIT

B. Fleischer

A deposit found on routine inspection of the intermediate potassium system feed line filter after 2600 hr service was examined to assess its nature and the reason for its presence. The water-soluble portion of the deposit, 29% of the sample weight, was primarily K_2CO_3 and $KHCO_3$. The water-insoluble portion was composed primarily of Cr, Fe, O, K, and Mo, indicating that oxygen contamination occurred during operation and led to the formation of corrosion product oxides.

BEHAVIOR OF STAINLESS STEEL WELDS UNDER CYCLIC LOADING

D. A. Canonico R. W. Swindeman

A reactor system will normally contain a number of critically located weldments. These may be situated within the reactor proper or be part of the equipment complex associated with it. They will be subjected to cyclic loading due to fluctuations in power level, mechanical vibrations, or both.

Fatigue studies on such stainless steel welds have been conducted on a push-pull specimen that includes weld metal, a heat-affected zone, and base metal in its gage length. In this specimen, failure is not forced to occur in a particular area but may occur in the most fatigue-sensitive portion of the weldment. Each microstructure in the specimen thus tends to behave as it would in a typical joint.

A type 304 stainless steel plate $\frac{1}{2}$ in. thick was welded by the manual tungsten-arc process with type 308 stainless steel filler wire. The welding heat inputs and technique used represented typical welding practices in the nuclear industry. After machining, one-half of the specimens were given a postweld heat treatment of 1800°F for 1 hr in hydrogen. This heat treatment served as a stress relief and also permitted some redistribution of microconstituents in the weld.

Plastic strain is plotted against the number of cycles to failure for both the as-welded and heat-treated specimens in Fig. 29.3. A comparison with data[18] for wrought type 304 stainless steel is also

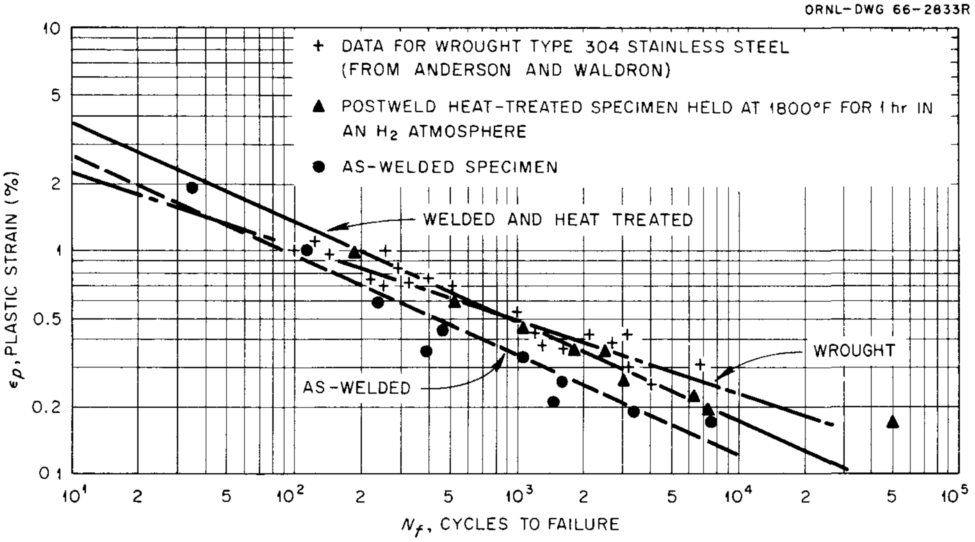

Fig. 29.3. Fatigue Test Data for Type 304 Stainless Steel Weldments.

---

[15] N. C. Cole, ORNL-3860, pp. 84–85 (classified).

[16] N. C. Cole, ORNL-3897, pp. 107–9 (classified).

[17] N. C. Cole, ORNL-3937, pp. 107–10 (classified).

[18] W. F. Anderson and C. R. Waldron, *High-Temperature Strain-Fatigue Testing with a Modified Direct Stress Fatigue Machine*, NAA-SR-4051 (October 1959).

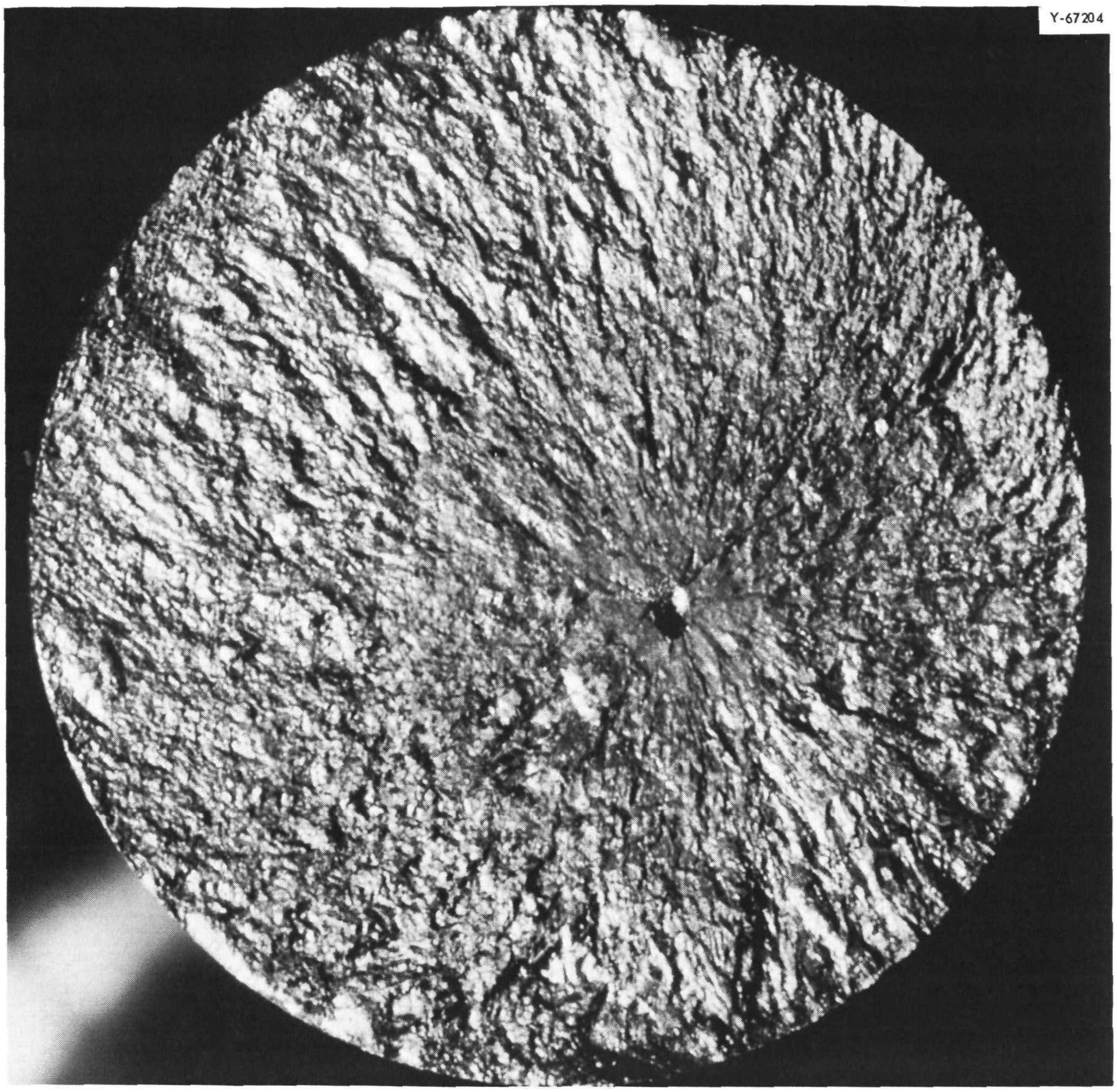

Fig. 29.4. Fracture Interface in Weld Metal. Notice that failure initiated at a pore.

presented for reference. For a given strain level, the postweld heat-treated specimens have a consistently greater life expectancy than the as-welded specimens. Although exact comparisons cannot be made since the material may not be comparable, the wrought material and heat-treated welds are about the same. The fracture specimens have been submitted for evaluation by both light microscopy and electron fractography. We hope that these investigations will provide data relevant to the morphology of fracture and its relation to the thermal history and strain level of the test specimens. A similar set of data is being obtained for the base metal.

An interesting sidelight of this study was found in a heat-treated specimen that had a life of 496,530 cycles at a strain of 0.0017. It contained a very small pore in the weld metal, shown in Fig. 29.4, where failure initiated. The influence of small defects on weld behavior will be studied further as the investigation proceeds.

TURBINE PUMP FABRICATION

C. W. Fox

We are continuing to fabricate refractory-metal turbine pumps with cermet bearings for operation in liquid-metal systems. We fabricated nine additional turbine wheels and impellers during this year, using procedures previously reported[19] although the cermet was changed to WC–6% Co from WC–12% Co.

A modified pump is being designed with a higher capacity than the previous one. Five impellers for this larger pump have been fabricated to date. Figure 29.5 shows one of these impellers after successful brazing.

One feature of the new pump design that posed a problem stemmed from a desire to carburize certain of the TZM (Mo–0.5% Ti–0.08% Zr) components. The proposed carburizing treatment occurs at a temperature above the melting point of the brazing alloy. Therefore, a series of tests was run to determine the effect of such a treatment on the integrity of the braze joint. The first test consisted of four tungsten carbide-to-TZM joints brazed with different nickel-base brazing alloys and carburized 24 hr at 1230°C in 2% CH_4. Although the temperature was 50°C above the melting point of the alloys, all joints were intact after the treatment. However, metallographic examination showed all joints to have large voids and cracks, which would make them unacceptable.

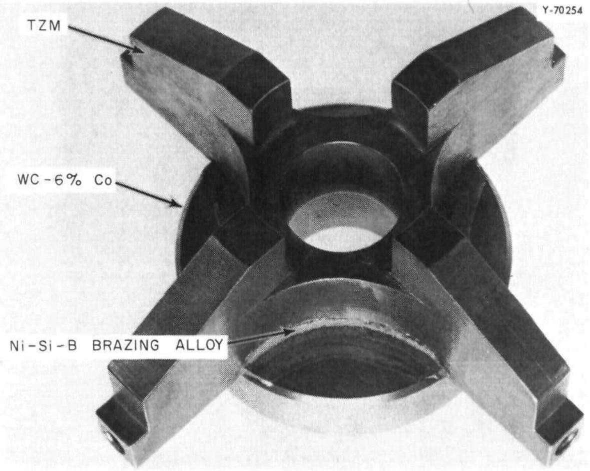

Fig. 29.5. Turbine Pump Impeller After Brazing.

A second test was conducted at a lower carburizing temperature. Four tungsten carbide-to-TZM joints were brazed as in the first test and carburized at 1093°C for 24 hr in 2% CH_4. Two of the specimens had large voids and cracks in the braze alloy, but the other two joints were in better condition. These joints used General Electric alloy J8100 (Ni–20% Cr–10% Si) and Coast Metals No. 60 (Ni–20% Cr–10% Si–3% Fe), which if used with the lower carburizing temperature should perform satisfactorily.

INVESTIGATION OF HIGH-EMITTANCE COATINGS FOR METALS

C. W. Fox T. G. Kollie

A program was undertaken to determine a method of raising the thermal emittance of metal components associated with the MPRE system. The investigation has included treatments for both aluminum and stainless steel.

The first treatment investigated involved a commercial product that can be sprayed or painted onto metal components. It is a silicone material dissolved in xylene. The coating appeared suitable for use on aluminum components up to 600°F for at least 1000 hr in air. On stainless steel specimens results were unfavorable at the temperatures of interest (1000 to 1500°F). The coating began to flake and spall when subjected to temperatures of 1000°F and higher in air for even short lengths of time.

Previous measurements[20] established that this coating increased the total hemispherical emittance E_t of type 316 stainless steel to above 0.88. The effects of time at temperature and thermal cycling on E_t revealed that specimens heated above 1200°F had a positive temperature coefficient of E_t, whereas those heated to 1040°F or lower had a negative coefficient. The exposure temperature dominates any thermal cycling effect up to 60 cycles. An E_t greater than 0.88 can be obtained by treatment for 2 hr at 1200°C, but a value no higher than 0.93 will result for treatments at 1600°F.

---

[19] C. W. Fox, *Metals and Ceramics Div. Ann. Progr. Rept. June 30, 1964,* ORNL-3670, p. 225.

[20] T. G. Kollie and R. S. Graves, *Metals and Ceramics Div. Ann. Progr. Rept. June 30, 1965,* ORNL-3870, p. 242.

Another commercial treatment for stainless steel components, phosphate coating applied by painting or dipping, is under investigation. Preliminary results indicate that the coating is stable to 1500°F in air for at least 1000 hr.

Conventional black anodizing was found to be unsuitable for raising the emissivity of aluminum components. The specimen changed in color from black to gold upon exposure to elevated temperatures (300 to 600°F). However, a modified anodizing technique that is used for hard-facing of aluminum components appears to give a very stable coating. Hard-faced samples were exposed for 3000 hr at 600°F in air and showed no visible change, but the emissivity characteristics of the coating have not yet been measured.

30. Molten-Salt Reactor Program

G. M. Adamson, Jr. A. Taboada[1]

The Molten-Salt Reactor Program is an ORNL program aimed at thermal breeder development. The major effort has been in the development, construction, and operation of the Molten-Salt Reactor Experiment (MSRE). The purpose of this experiment is to test fuels and materials that might be used in a larger thermal breeder and to obtain experience with the operation and maintenance of a molten-salt reactor. The MSRE is a nominally 10-Mw, 1200°F experimental reactor in which the fuel is contained in and circulates as a molten fluoride salt.[2,3] The reactor has now achieved full-power operation.

Our effort during this past year has been primarily the solving of materials problems as they have arisen during the reactor testing and startup. Major emphasis has been on determining the expected lifetime of the system at the predicted radiation levels and on providing adequate samples to monitor its performance. Planning and preliminary work have been aimed at the next step, a Molten-Salt Breeder Experiment (MSBE).

MSRE MATERIALS SURVEILLANCE TESTING

W. H. Cook A. Taboada[1]

The fabrication of surveillance specimens from the moderator graphite, grade CGB, and the structural material, Hastelloy N (also known as INOR-8), of the MSRE were reported in the previous annual report.[4] These have been assembled and placed in the reactor and the control unit.[5] Those in the MSRE have had more than 1350 hr exposure to molten fluoride salts and neutrons. They will be used to survey the effects of the reactor operations on these materials to provide information for monitoring the MSRE and for designing advanced molten-salt reactors.

There are three groups of specimens. Two groups consist of both graphite and Hastelloy N specimens: the reactor core specimens near the center of the core and a matching group (reactor control specimens) in a control unit. In the control unit, specimens are exposed to molten salt under a temperature gradient matching that of the moderator graphite and are controlled to follow the reactor temperatures. The third group of specimens, not previously reported, consist only of Hastelloy N; these are suspended just outside the reactor vessel in a nitrogen atmosphere; they are called reactor vessel specimens. Each of the three groups consists of three sets of specimens. As significant amounts of radiation are accumulated, one or more sets from a group will be removed for examination and new sets will replace them. The new sets will be made from more MSRE graphite and Hastelloy N or advanced materials. The combinations of old and new sets will be returned to the reactor.

As reported, the graphite specimens are multiples of the smallest shape, 0.11 × 0.47 × 2.25 in. These are bound to make 64-in.-long sets or stringers that have cross sections 0.47 × 0.660

---

[1] Present address, Division of Reactor Technology and Development, USAEC, Washington, D.C.

[2] R. B. Briggs *et al.*, *MSR Program Semiann. Progr. Rept. July 31, 1964*, ORNL-3708.

[3] R. B. Briggs *et al.*, *MSR Program Semiann. Progr. Rept. Feb. 28, 1966*, ORNL-3936.

[4] W. H. Cook and A. Taboada, *Metals and Ceramics Div. Ann. Progr. Rept. June 30, 1965*, ORNL-3870, pp. 256–57.

[5] R. B. Briggs *et al.*, *MSR Program Semiann. Progr. Rept. Aug. 31, 1965*, ORNL-3872, pp. 87–92.

in. Each set has two rods of Hastelloy N specimens. Each rod consists of 27 tensile bars welded end to end; each bar is approximately 2 in. long with a 0.125-in. gage diameter. Figure 30.1 shows the three sets of specimens that make up the group. Figure 30.2 shows how these were assembled, sealed into a basket, and placed near the center of the reactor moderator core.

A full-scale mockup of the reactor core specimens, exclusive of the basket (Fig. 30.2), was made out of MSRE graphite, Hastelloy N, and type 304L stainless steel. The assembled unit was given to the Hot Cells Operations for them to develop handling techniques and holding jigs for the surveillance specimens that are to be removed from the MSRE.

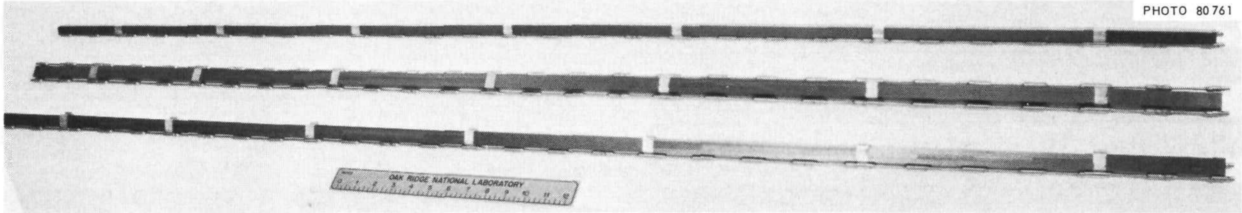

Fig. 30.1. Three Stringers of CGB Graphite and Hastelloy N Surveillance Specimens.

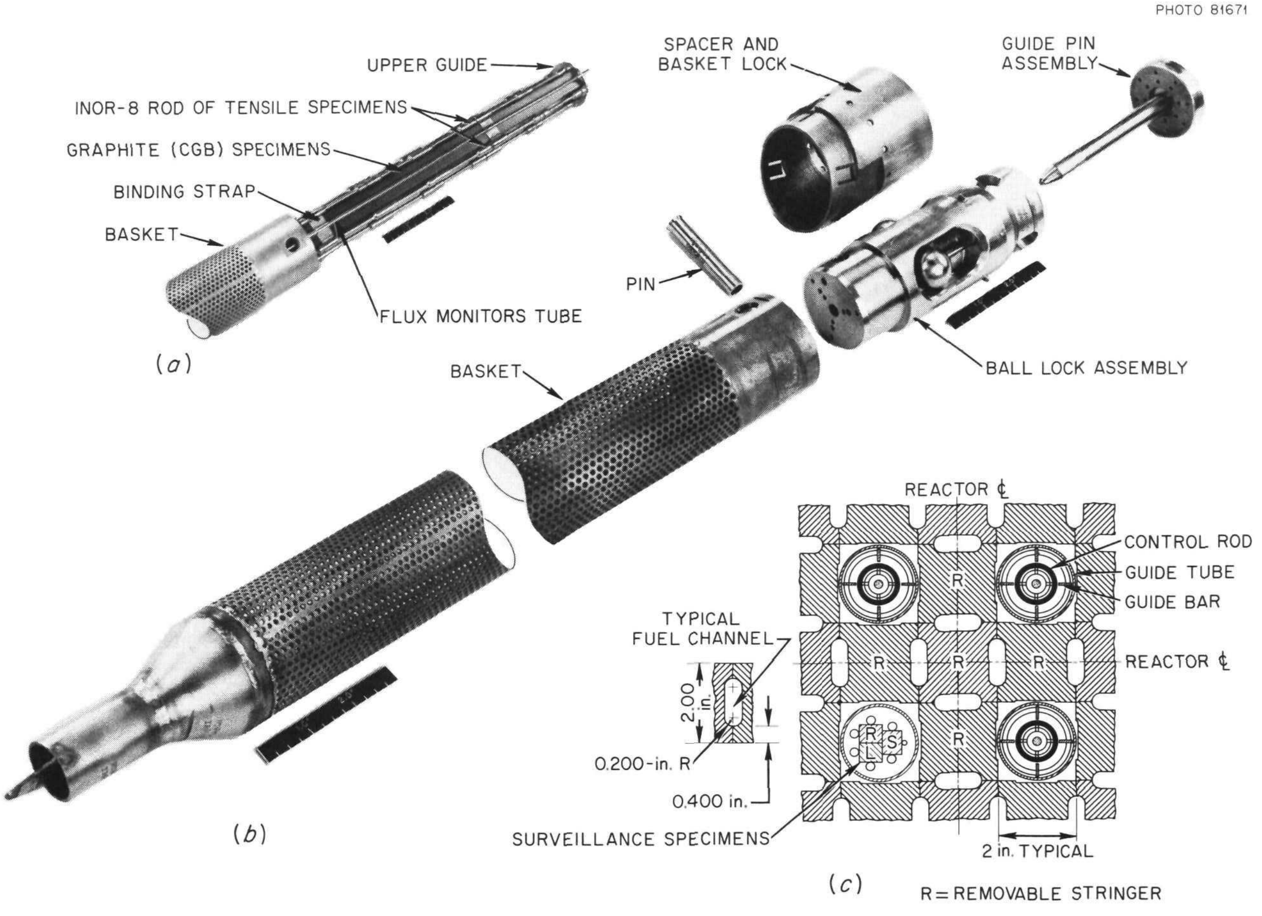

Fig. 30.2. Hastelloy N and Grade CGB Graphite Surveillance Specimens and Container Basket. (*a*) Specimens partly inserted into the container. (*b*) Container and its lock assemblies. (*c*) Location of surveillance specimens in the MSRE.

Table 30.1. Sampling Schedule for the MSRE Surveillance Specimens

Sampling	Reactor Operation[a] (Mwhr)	Stringer[b]		Thermal-Neutron Dose on Stringer (neutrons/cm^2)	Equivalent Operating Time for Vessel at 10 Mw (hr)	Actual Dose on Vessel (neutrons/cm^2)
		Core[c]	Vessel			
1	10,000	S		1.7×10^{20}	20,000	8.3×10^{18}
2	50,000	R		8.5×10^{20}	100,000	4.1×10^{19}
			V-1	4.1×10^{19}	5,000	4.1×10^{19}
		S-1		6.6×10^{20}	80,000	4.1×10^{19}

[a] The integrated power levels at which specimens are pulled can vary ±5% from the indicated figure.

[b] S and R denote two of the three stringers originally in the reactor core. V-1 is one of the three stringers on the reactor vessel. S-1 replaces S when S is removed.

[c] A matching control stringer is also removed from the control test rig with each reactor core specimens sampling.

The first significant property changes produced in the MSRE materials by radiation will be in the Hastelloy N; therefore, these changes control the rate of sampling. The current sampling schedule[6] is shown in Table 30.1. This sampling schedule has the desirable feature that the thermal dose accumulates faster in the Hastelloy N surveillance specimens than it does in the reactor vessel. For this reason we have shown only two samplings. We believe that future sampling schedules should be guided by the data obtained under this current schedule. This means that the first sampling should be made during the early part of August 1966. The S-1 sets removed from the reactor core and controls will be replaced with MSRE graphite and modifications of Hastelloy N that should be more resistant to irradiation. Future sets will include specimens of advanced grades of graphite.

POSTIRRADIATION CREEP AND STRESS RUPTURE OF HASTELLOY N[7]

W. R. Martin J. R. Weir

The postirradiation stress rupture and creep ductilities of irradiated Hastelloy N at 650°C have been determined for several neutron exposures up to 5×10^{20} neutrons/cm^2.

The postirradiation stress-rupture properties of Hastelloy N are highly sensitive to neutron dose. The reduction in rupture life is more severe at the higher levels. At a given neutron dose a stress level exists below which no embrittlement is observed. This threshold stress level is approximately proportional to the one-third power of the neutron dose, or possibly the helium content. This observation is consistent with the idea that helium bubbles serve as crack nuclei whose critical diameter is related to stress. The reduction in stress-rupture life is due to a reduction in ductility, and the absolute value of ductility is lower at the lower-strain-rate tests. The reduction in ductility to values as low as 0.4% is due to the effect of irradiation on intergranular fracture.

The rate of decrease in time to rupture with helium content corresponds to a power law of ½ predicted by the relationship given by Oliver and Girifalco[8] for stress rupture based on the growth of voids. No consistent or significant variations in the stress-strain relationship were observed. The reduction in stress-rupture life and, in many cases, the ductility is accompanied by a lower density of grain-boundary cracks of a size visible in the optical microscope. Intergranular cracks, once formed, propagate with greater ease the

---

[6] Private communication from H. E. McCoy and W. H. Cook of the Metals and Ceramics Division.

[7] Condensed from paper submitted to *Nuclear Applications*.

[8] P. R. Oliver and L. A. Girifalco, *Acta Met.* **10**, 765 (1962).

greater the radiation exposure. This evidence supports the hypothesis for elevated-temperature irradiation embrittlement being related to an effect of helium on intergranular fracture.

HASTELLOY N WELDING STUDIES

H. E. McCoy D. A. Canonico

Our weld studies on Hastelloy N have two main objectives: (1) to improve the weldability so that welds have greater strength and ductility and (2) to study the effects of irradiation on the properties of welds and to investigate ways of improving their resistance to irradiation damage. Our findings can be summarized as follows.

1. Welds in commercial Hastelloy N had poorer stress-rupture properties than did the base metal, as shown in Fig. 30.3. The properties could be improved by postweld heat treatments, as shown in Fig. 30.4. Rate curves were determined for stress-relief temperatures of 1200, 1400, and 1600°F. The annealing schedules determined from this study were used to heat treat the welds in the MSRE.
2. Postirradiation tensile properties of welds were only slightly worse than those of the base metal. Hence, the properties of the welds were degraded less by irradiation than those of the base metal.
3. Several techniques have been tried for improving the postirradiation properties of welds. These include the use of low-boron filler wire and Al_2O_3-coated filler wire. These methods were not significantly effective.

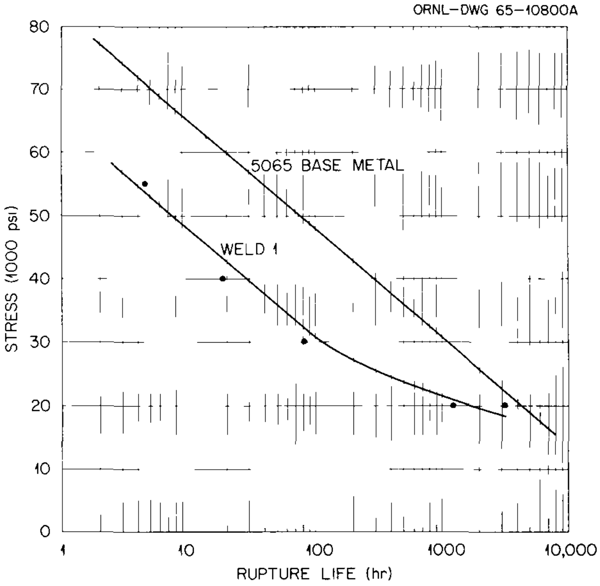

Fig. 30.3. Influence of Welding on the Creep-Rupture Properties of Hastelloy N at 650°C.

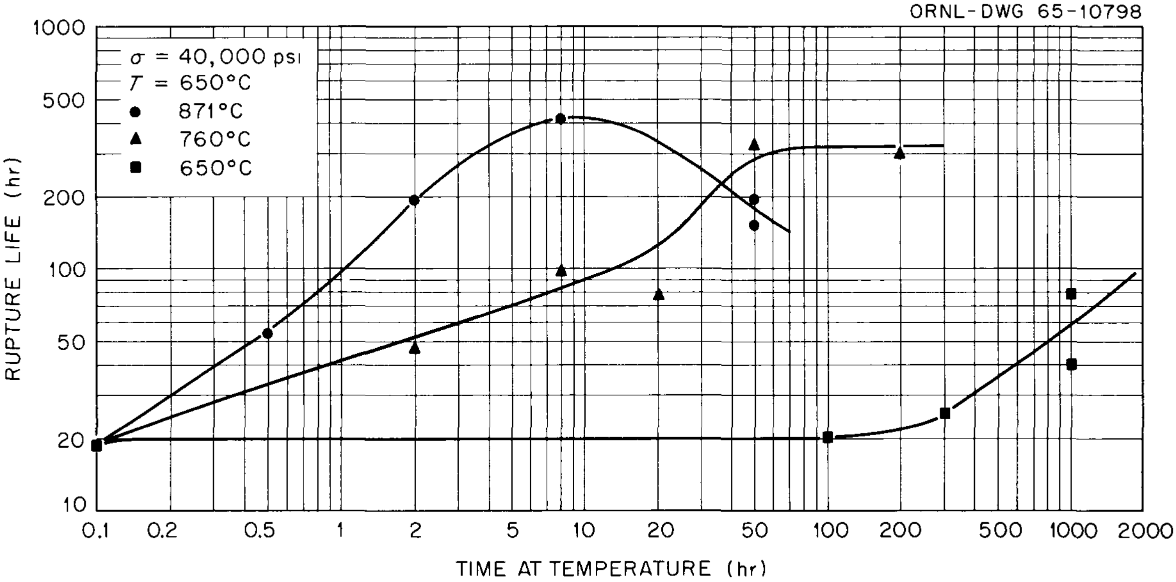

Fig. 30.4. Influence of Stress Relieving on the Rupture Life of a Weld in Hastelloy N. The rupture life of the base metal was 298 hr.

DYNAMIC CORROSION STUDIES

G. M Tolson[9] A. Taboada[1]
A. P. Litman

We are continuing to study the compatibility of coolants with structural materials of interest for molten-salt reactors in thermal convection loops Current loop operation is summarized in Table 30.2. One loop has operated over 37,000 hr under MSRE conditions

To evaluate the compatibility of the proposed secondary coolant for the reference design Molten-Salt Breeder Reactor, two thermal convection loops were fabricated. One listed in Table 30.2 was made from Hastelloy N and is operating with a boron-containing molten fluoride proposed as a coolant The other loop was fabricated from Croloy 2¼ and was terminated because flow could not be established in the loop We are investigating the cause of this failure

Using a new loop design[10] and more rigid purity control, we are investigating the compatibility of circulating lead with selected construction materials. Lead has attractive properties as a coolant for molten fluoride systems. An interim report has been issued on work to date.[11] This report discusses the findings that carbon, low-alloy, and stainless steels tend to plug due to the formation of dendritic crystals of iron and chromium in the cold regions of uninhibited lead systems.

The alloy Nb–1% Zr is known to have good resistance to attack by uninhibited liquid lead.[12] Further examination of a loop listed in Table 30.2 revealed the presence of mass-transfer crystals in the cold portion of the system, shown in Fig. 30.5. Electron microprobe study showed the crystals were almost pure niobium. The mass transfer of niobium in systems of this type has not been reported by other investigators.

The effect of magnesium additions to inhibit liquid lead corrosion by preferentially combining with system oxygen is also under study. A Croloy 2¼ thermal convection loop, which held lead

Table 30.2. Thermal Convection Loops

Loop Material	Fluid	Maximum Temperature (°F)	Temperature Difference (°F)	Time Operated (hr)
Hastelloy N	Simulated MSRE fuel salt[a]	1300	160	37,195
Type 304 stainless steel	Simulated MSRE fuel salt[a]	1250	180	25,915
Nb–1% Zr[b]	Simulated MSRE fuel salt[a]	1400	300	3,025
Hastelloy N	Proposed secondary coolant for reference design MSBR	1125	265	1,005
Nb–1% Zr	Lead	1400	400	5,280[c]
Croloy 2¼	Lead[d]	1100	200	2,952[e]

[a] $LiF-BeF_2-ZrF_4-UF_4$ (65-29.1-5-0.9 mole %).
[b] Exterior cladding of type 446 stainless steel.
[c] Loop plugged on July 26, 1965
[d] 230 ppm Mg inhibitor added.
[e] Loop plugged on June 9, 1966

---

[9] Now at Oak Ridge Gaseous Diffusion Plant.

[10] G. M. Tolson and A. Taboada, *Metals and Ceramics Div Ann Progr Rept June 30, 1965*, ORNL-3870, pp. 259–60.

[11] G. M. Tolson and A Taboada, *A Study of Lead and Lead-Salt Corrosion in Thermal Convection Loops*, ORNL-TM-1437 (April 1966).

[12] G. M. Tolson and A. Taboada, *Metals and Ceramics Div Ann Progr Rept June 30, 1965*, ORNL-3870, pp. 258–59

Y-67208

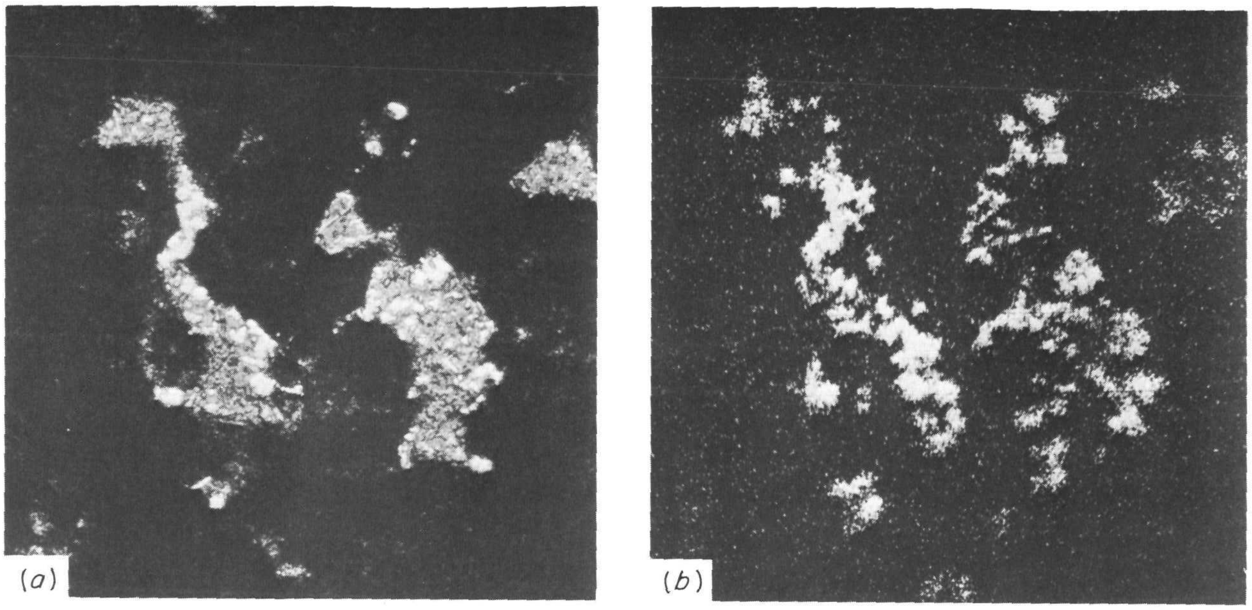

Fig. 30.5. Niobium Crystals Formed in the Cold Leg of an Nb–1% Zr Thermal Convection Loop Operated with the Hot Leg at 1400°F and a 400°F Temperature Difference. 250×. (*a*) Light optics. (*b*) Niobium $L\alpha$ x-ray image.

containing 230 ppm Mg, operated for almost 2952 hr at 1100°F and a ΔT of 200°F before plugging. Removable hot-leg specimens showed an average weight loss of approximately 0.7 mg/month after 800 hr. Analysis of this loop is now in progress.

BRAZING OF GRAPHITE

J. M. Jones R. G. Donnelly

The joining of graphite to structural metals such as Hastelloy N is of interest for advanced molten-salt reactors. Two basic difficulties are encountered in making such joints: (1) graphite is not easily wetted by conventional brazing alloys, and (2) there is a large difference between the thermal expansion coefficients of graphite and many metals, causing cracking of the joint during temperature cycling.

Brazing Alloy Development

The ORNL-developed brazing alloy Au–35% Ni–30% Mo is very useful for brazing graphite; however, its application in a high-neutron-flux area is limited by gold transmutation. Consequently, a study was undertaken to develop gold-free brazing alloys that are compatible with molten salts, contain a carbide former, and have reasonably low melting points. The nickel-palladium-chromium system was selected for further study for the following reasons: (1) noble-metal alloys would be expected to be corrosion-resistant to fused fluoride, (2) palladium has a lower thermal-neutron cross section than gold (8 barns vs 99 barns), and (3) chromium is a carbide former, which helps it wet the graphite.

After a cursory screening study, the following alloys were selected for further examination: Pd–35% Ni–5% Cr, Pd–35% Ni–10% Cr, Pd–40% Ni–5% Cr, and Pd–40% Ni–10% Cr. These four alloys were used to make lap-joint braze specimens of graphite to molybdenum. The specimens were brazed at two temperatures (1250 and 1300°C) and were subjected to thermal cycling conditions similar to those expected in a typical service application. The Pd–35% Ni–5% Cr alloy brazed at 1250°C for 10 min appeared to be the best. Microstructures of this alloy before and after thermal cycling are compared in Fig. 30.6. We plan to evaluate alloys of this type for long-time service in molten-salt environments.

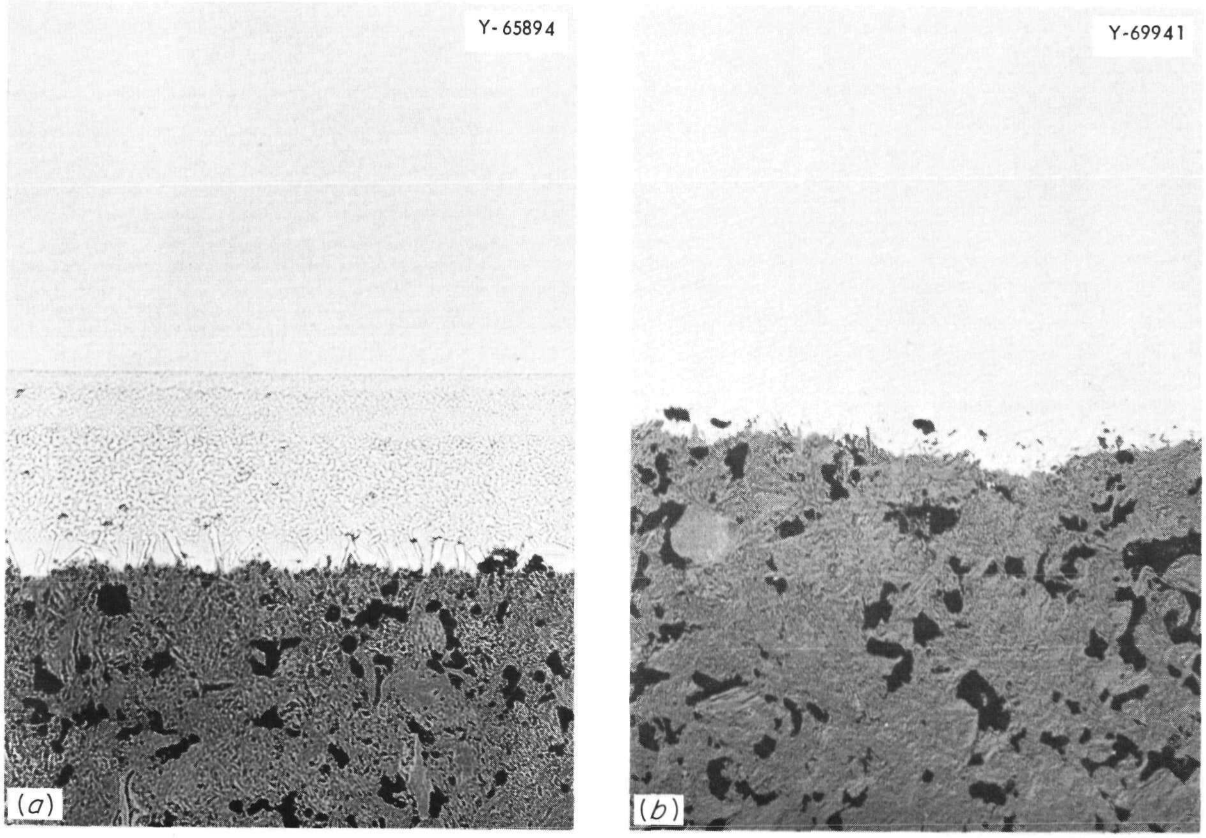

Fig. 30.6. Graphite-to-Molybdenum Joints Brazed with the Pd–35% Ni–5% Cr Developmental Alloy at 1250°C. 100×. (*a*) As brazed. (*b*) After cycling ten times from 700°C to ambient.

Vapor Coating to Enhance Overall Wetting Behavior

Vapor coating of graphite with titanium is being investigated as a means of enhancing its wetting properties. This technique was suggested by C. M. Adams, consultant from Massachusetts Institute of Technology, and initial samples were coated there. Using this technique, a much wider range of brazing alloys can be considered.

In the first experiments we brazed with copper, which resists corrosion by molten fluorides and does not wet graphite in conventional brazing procedures. We obtained moderate wetting with heating either in a vacuum furnace or in an electron-beam welder. Further work is planned to more systematically study the contribution of titanium coatings.

Transition Joints

One attractive method of circumventing the thermal expansion problem in graphite-to-metal joints is to make the transition with one or more materials with expansion coefficients intermediate between those of the graphite and Hastelloy N. This makes the stress concentration between the two less severe. Thus, we undertook development of potential transition pieces.

Molybdenum and tungsten are two metals that have expansion coefficients intermediate between those of graphite and Hastelloy N and were selected for further study. However, due to cost and availability, nearly all work was performed on molybdenum. This decision was further justified by the fact that nearly all alloys that braze molybdenum will also braze tungsten.

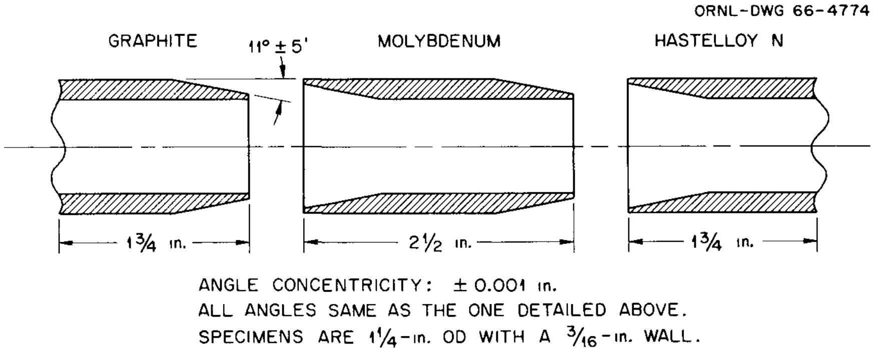

Fig. 30.7. Schematic Drawing of Tapered Graphite-to-Hastelloy N Joint Using Molybdenum as a Transition Piece.

We used the transition joint presented in Fig. 30.7, which incorporates an 11° tapered edge to reduce shear stresses arising from thermal expansion differences. This configuration has enabled us to join graphite to molybdenum with the nickel-palladium-chromium alloy and molybdenum to Hastelloy N with copper sheet. All brazing was performed in a vertical vacuum furnace. Visual inspection of sectioned joints revealed no flaws, and the sections are now being prepared for metallographic evaluation.

COMPATIBILITY OF GRAPHITE-MOLYBDENUM BRAZED JOINTS WITH MOLTEN FLUORIDE SALTS

W. H. Cook

The current Molten-Salt Breeder Reactor (MSBR) design[13] is predicated on joining graphite to the structural material, Hastelloy N. One of the more promising techniques is to use molybdenum as a transition material and braze the joints. A short section of graphite pipe with graphite-to-molybdenum joints brazed with gold-nickel alloy successfully contained molten fluoride salts at 700°C and a pressure of 150 psig during a 500-hr test period.[14] The graphite pipe was machined to $1\frac{1}{4}$ in. OD × $\frac{3}{4}$ in. ID from a bar of MSRE graphite, grade CGB. Molybdenum end caps were brazed to the ends of the pipe[15] with Au–35% Ni–30% Mo, ANM-16.

The test configuration is shown in Fig. 30.8. No leaks occurred during the 500-hr test period. The appearance of the pipe and joints before and after test is shown in Fig. 30.9. Post-test radiographic examination indicated that the salt was contained as planned and no salt penetrated the graphite. No corrosion of the braze was detected by metallographic examination or chemical analyses.

Although metal-to-graphite joining requires much additional development, this test, which operated satisfactorily despite a primitive joint design and a relatively small thin-walled graphite pipe, emphasized the potential application of the larger graphite-to-metal joints under consideration for the MSBR.

Joints of graphite to molybdenum brazed with Pd–35% Ni–5% Cr survived a 700°C corrosion test in $LiF\text{-}BeF_2\text{-}ZrF_4\text{-}ThF_4\text{-}UF_4$ for 1000 hr with only a slight surface roughening (less than 0.5 mil) of the brazing alloy, as shown in Fig. 30.10. Chemical analyses show no evidence of corrosion. Similar joints are currently in test to obtain corrosion data for exposures of 5000, 10,000, and 20,000 hr.

---

[13] E. S. Bettis *et al., Summary of Molten-Salt Breeder Reactor Design Studies*, ORNL-TM-1467 (Mar. 24, 1966).

[14] R. B. Briggs *et al., MSR Program Semiann. Progr. Rept. Feb. 28, 1966*, ORNL-3936, pp. 104–7.

[15] R. B. Briggs *et al., MSR Program Semiann. Progr. Rept. Feb. 28, 1965*, ORNL-3812, pp. 73–76.

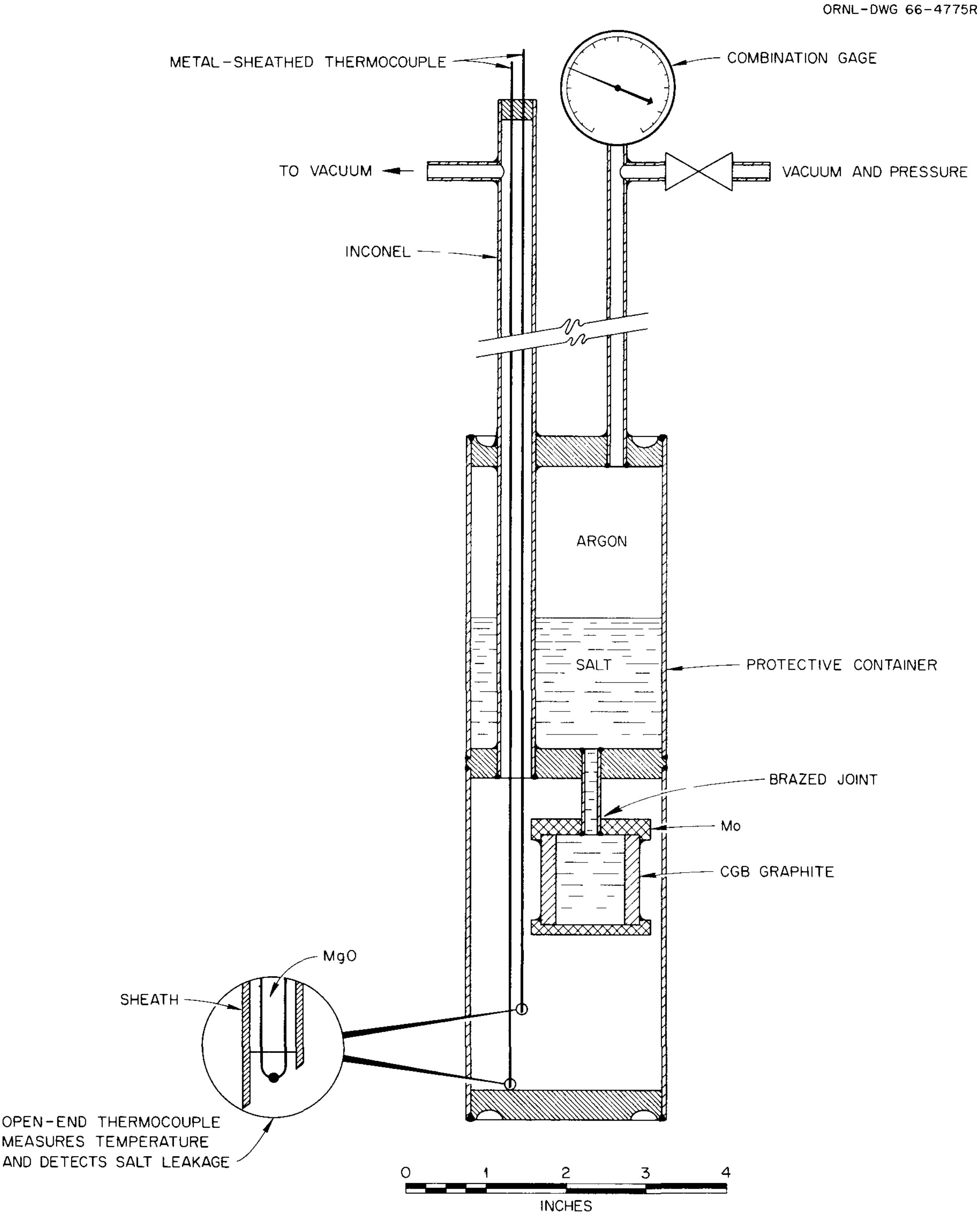

Fig. 30.8. Test for Small Graphite Pipe and Graphite-to-Metal Joints.

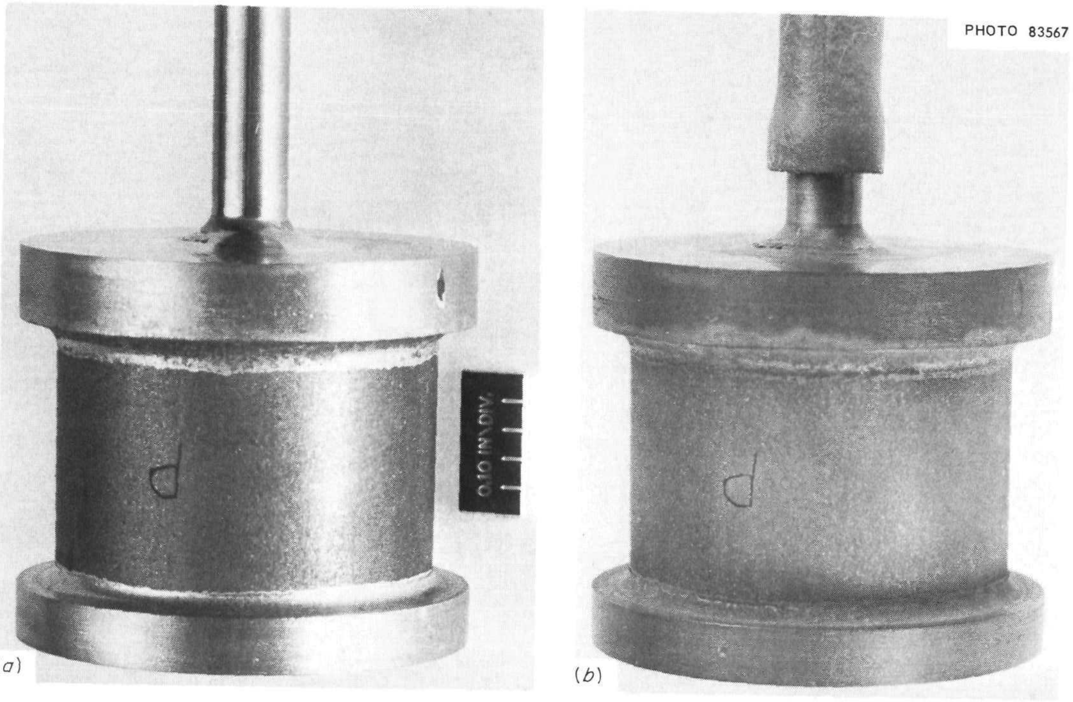

Fig. 30.9. Grade CGB Graphite Pipe Brazed to Molybdenum End Caps (*a*) Before Test and (*b*) After Containing Molten Fluoride Salts at 700°C Under Pressure of 150 psig for 500 hr.

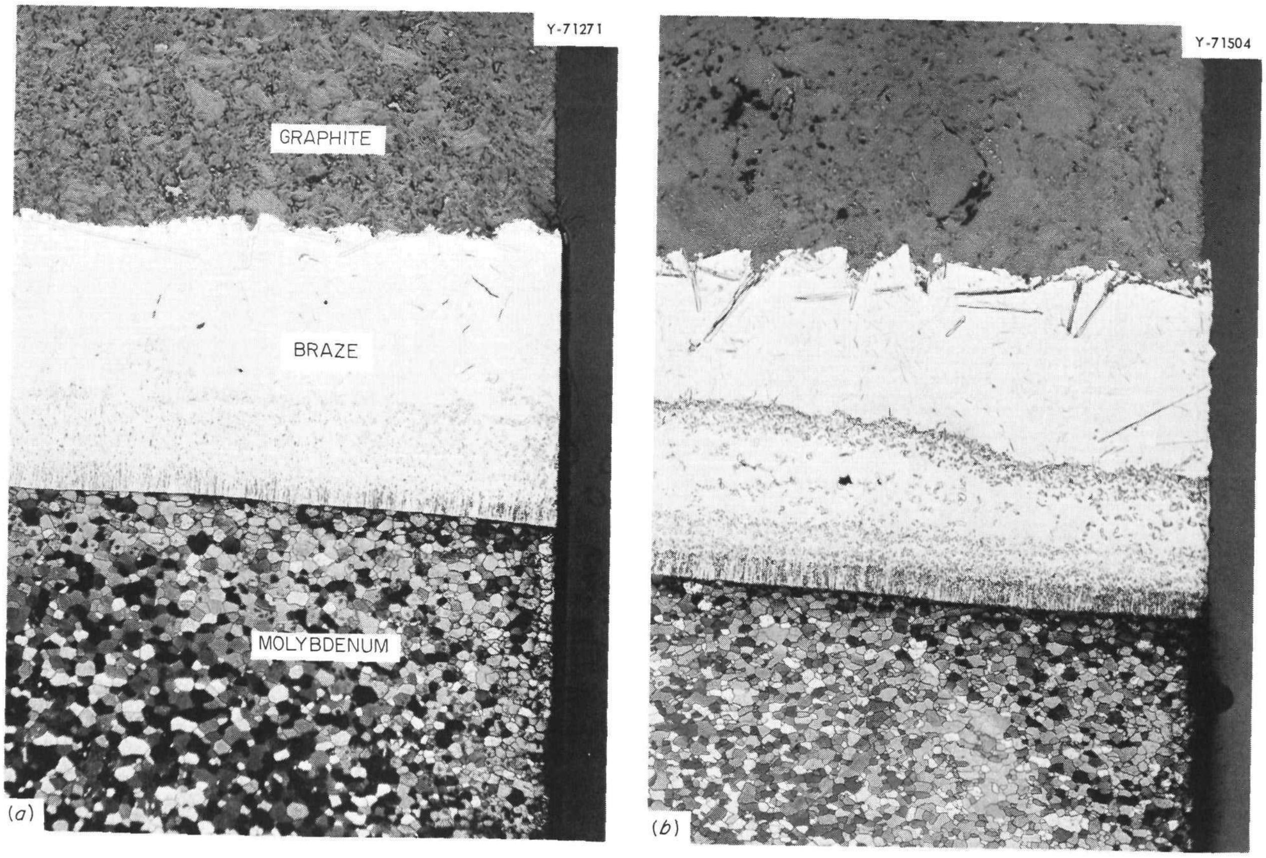

Fig. 30.10. Grade CGB Graphite Brazed to Molybdenum with Pd–35% Ni–5% Cr Alloy. Etched in 10% solution of oxalic acid. 100×. (*a*) Untested. (*b*) After 1000-hr exposure to $LiF\text{-}BeF_2\text{-}ZrF_4\text{-}ThF_4\text{-}UF_4$ at 700°C during which slight attack roughened the exposed surface of the brazing alloy. Reduced 27%.

EVALUATION OF NEW GRADES OF GRAPHITE

W. H. Cook

Six new grades of graphite are being evaluated for physical properties that are related to use in the MSBR. Four are isotropic, and two are anisotropic needle-coke graphite. One isotropic grade and one needle-coke grade were in the form of pipe.

Specimens from the six grades were subjected to the MSRE standard salt impregnation screening test; that is, the specimens were evacuated and subsequently exposed for 100 hr to molten fluoride salt at 700°C under a pressure of 150 psig. The average penetrations by salt were 0.3, 0.5, 4.0, 7.1, 13.5, and 14.0%. The two lowest values were obtained on specimens from the two anisotropic needle-coke graphite grades. The 7.1 value was obtained on specimens from the isotropic pipe grade. Since the value for the MSRE core graphite was 0.2 in such tests, none of the six new grades of graphite is of the quality required for the MSBR.

Pore entrance diameter spectra, gas permeabilities, and strength measurements are being made on the six grades of graphite to determine what potential they may have for additional development to make them suitable for MSBR requirements.

31. Reactor Evaluation

D. A. Douglas, Jr.

The total cost of producing heat or power by nuclear energy is composed of a multitude of interacting relationships. Capital costs, operating costs, and fuel cycle costs are some of the general terms used to collectively identify categories. To achieve a meaningful reduction in cost, one must consider the problem in its entirety and recognize the effect that changes made in one area may have on others. ORNL is engaged in studying this general problem, and our role is to examine fabrication costs and fuel element performance as they relate to fuel cycle and other cost areas. Accordingly, we work in conjunction with chemical processing personnel in the Chemical Technology Division and the physicists and design engineers in the Reactor Division. Thus, we report here fragments of much broader studies.

COMPUTER PROGRAM DEVELOPMENT

T. N. Washburn　　A. L. Lotts

An indispensable factor in the evaluation and comparison of various proposed reactor systems is the cost of fuel element fabrication. Accordingly, we have assisted the evaluation of reactor concepts by providing extensive studies of the cost of fuel fabrication.

The prediction of fabrication costs involves the selection of the fabrication procedures and of flowsheets and the calculation of operating costs, capital costs, and the costs of materials used in the processes. Also, one must apply certain factors such as the fabrication environment, the prospects of success for the process, and the method of financing. Because a large number of variables are involved in calculating fabrication costs, we previously[1] developed three computer programs to perform the calculations on a limited number of fuel element types.

The programs work in the following way. All the information concerning the process and the costs involved in the process are stored in the computer program. When the fuel element, the plant in which it is to be fabricated, and the manner in which the plant is to be operated and financed are described, fuel fabrication costs can be calculated for a number of production rates.

We have continued to expand the types of fuel elements and flowsheets that can be handled by our computer programs for calculation of fuel fabrication costs. Table 31.1 shows the different fuel element types for which we can now calculate fuel fabrication costs.

During this year we have added three fuel element fabrication procedures to the computer programs. These are the ceramic extrusion of oxide fuel bodies, the low-energy vibratory compaction of oxide microspheres, and the hot swaging of cermet fuel rods. Each of these is applicable to rod-bundle fuel elements. In addition, the computer programs have been modified such that either gas or sodium is optional for core-to-cladding bonds except for elements with metallurgical or diffusion bonding.

The table also reflects the capability of calculating the cost of fabricating fueled graphite elements for high-temperature gas-cooled reactors.

---

[1] A. L. Lotts, *Metals and Ceramics Div. Ann. Progr. Rept. June 30, 1964*, ORNL-3670, pp. 254–55.

Table 31.1. Fuel Element Types for Which a Fabrication-Cost Computer Program Is Available

Type of Fuel Element	Fuel Material	Fabrication Process	Type of Core-to-Cladding Bonding
Rod bundle	Oxide shards	Vibratory compaction	Gas or sodium
Rod bundle	Oxide microspheres	Vibratory compaction (low energy)	Gas or sodium
Rod bundle	Oxide	Pelletization	Gas or sodium
Rod bundle	Oxide	Ceramic extrusion	Gas or sodium
Rod bundle	Carbide	Slugs	Gas or sodium
Rod bundle	Cermet	Hot swaging	Metallurgical
Rod bundle	Metal	Extrusion	Diffusion (Ni)
Rod bundle	Metal	Coextrusion	Metallurgical
Nested tubes	Oxide	Vibratory compaction	Gas or sodium
Nested tubes	Oxide	Pelletization	Gas or sodium
Nested tubes	Carbide	Slugs	Gas or sodium
Nested tubes	Metal	Extrusion	Diffusion (Ni)
Nested tubes	Metal	Coextrusion	Metallurgical
Fueled graphite	Oxide	Carbon coating, compaction	Gas
Fueled graphite	Carbide	Carbon coating, compaction	Gas

HWOCR FUEL FABRICATION COST ESTIMATES

T. N. Washburn A. L. Lotts

One of the principal tasks undertaken during the year was to assist in the Heavy-Water Organic-Cooled Reactor (HWOCR) evaluation.[2] Three fuel element designs were evaluated: the low-enrichment uranium monocarbide with SAP cladding proposed by Atomics International and Combustion Engineering (AI-CE) and the two thorium-fueled designs submitted by the Babcock and Wilcox Co. (B&W). One of these consisted of thorium-uranium oxide loaded in SAP cladding by vibratory compaction and the other of thorium-uranium alloy coextruded with Zircaloy cladding as annular rings. The details of each design have been described.[2]

The method of estimating fuel fabrication costs for this evaluation is consistent with and similar to that used in the Advanced Converter Evaluation.[3] Both operating and capital costs are stored in the computer program for performing each step of the fabrication process over a wide range of production rates. Costs of tubing, end caps, and other items of fuel element hardware are specified, with values covering the ranges of physical dimensions, quality level, and procurement rates required for different evaluations. Input data for each particular case include a specification of the fuel element parameters, the fabrication process selected, rate of capital amortization, an estimated reject rate, plant utilization factor, and the production rates of interest. The computer program then selects the appropriate cost for each step of the process and accumulates and manipulates these costs for each specified set of conditions to calculate the fuel fabrication cost in dollars per kilogram of heavy metal.

Input material to the fabrication plant for the uranium monocarbide design is ceramic grade UO_2; the output of the fabrication plant would be fuel assemblies packaged for shipment. The fuel production rate required in the fabrication plant for reference conditions is 3475 kg of uranium per day; this corresponds to a fuel exposure of 15,000 Mwd per metric ton of uranium, a reactor on-line factor of 80%, operation of the fabrication plant 260 days/year, and furnishing the fueling needs of a 15,000 Mw (electrical) industry. This scale of

---

[2] P. R. Kasten, *An Evaluation of Heavy-Water Moderated Organic-Cooled Reactors*, ORNL-3921 (to be published).

[3] M. W. Rosenthal *et al.*, *A Comparative Evaluation of Advanced Converters*, ORNL-3686 (January 1965).

production is a large extrapolation of existing technology and experience; thus, the cost estimates obtained are based primarily on engineering estimates and judgments. For the above production rate and a 22%/year amortization rate, the fabrication cost breakdown (in dollars per kilogram of uranium) is given below.

Capital charges	8.50
Operating expenses	13.46
Hardware costs	6.46
Total	28.41

Material fed to the fabrication plant is sol-gel-produced high-density thoria-urania fragments for the oxide case and thorium powder briquettes with fully enriched uranium metal for the metallic fuel case. For both fuels, output of the fabrication plant consists of fuel assemblies packaged for shipment. The fuel fabrication rate required for the reference conditions is 2590 kg of heavy metal per day; this is based on a fuel exposure of 20,000 Mwd per metric ton of heavy metal, a reactor load factor of 80%, operation of the fabrication plant for 260 operating days/year, and furnishing the fueling needs of a 15,000 Mw (electrical) industry.

The above production rate, if virgin material is fabricated, is not as large an extrapolation of current experience as that for the carbide fuel. The major area of extrapolation for fabrication of the thorium cores is the large-scale application of remote operations required for recycle fuel. While vibratory compaction of sol-gel thoria-urania fuel has been performed at the ORNL Kilorod Facility[4–6] and B&W has evaluated the process on a pilot-plant scale in a hooded facility,[7] there is no experience to date on operation of a remotely operated fabrication plant as envisioned. However, a detailed engineering design of both facilities and equipment for remote fabrication has been accomplished[8] for the Thorium-Uranium Recycle Facility (TURF) at ORNL. In addition, design studies and evaluation of factors involved in plant extrapolations have been done extensively in other work at ORNL. Thus, the projection of fabrication costs in remotely operated large-scale plants for oxide fuels is reasonably well founded.

Uranium has been coextruded with Zircaloy cladding successfully on a production basis for a number of years. Also, thorium-uranium alloys have been coextruded with Zircaloy cladding at Hanford,[9] Savannah River,[10] and Nuclear Metals, Inc. There is no experience, however, relative to remote fabrication by this process. Therefore, the accuracy of the cost estimate for the metallic fuel assembly is probably less than that for the oxide pin assembly.

Table 31.2 compares the estimated fabrication costs per kilogram of heavy metal for the three designs, based on reference conditions and the specific design parameters associated with the different fuel assemblies. On a relative basis, the oxide pin design is penalized by its small fuel diameter and low fuel density. The metal fuel design is likewise penalized by its thin fuel section and low density relative to uranium carbide. The carbide fuel design has relative cost advantages due to the high fuel density and large pin diameter; both these factors contribute to a high fuel loading per unit length, which decreases the number of fuel-bearing components per unit weight of fuel material.

The above results show that for the three fuel assembly designs evaluated, the fabrication cost per kilogram of heavy metal is least for the carbide ($28.41), intermediate for the metal ($42.14), and greatest for the oxide ($63.50). However, when converted to a fabrication cost per reactor core, the spread in cost is relatively insignificant at

---

[4] J. D. Sease, F. C. Davis, and A. L. Lotts, *Thorium–Uranium-233 Oxide (Kilorod) Facility – Rod Fabrication Process and Equipment,* ORNL-3539 (April 1964).

[5] C. C. Haws, J. L. Matherne, F. W. Miles, and J. E. Van Cleve, Jr., *Summary of the Kilorod Project – A Semiremote 10-kg/day Demonstration of* $^{233}UO_2$*-*ThO_2 *Fuel-Element Fabrication by the ORNL Sol-Gel Vibratory-Compaction Method,* ORNL-3681 (August 1965).

[6] J. E. Van Cleve, Jr., J. J. Varagona, and A. L. Lotts, *Time Study of Fuel Rod Fabrication in the Kilorod Facility,* ORNL-3740 (October 1965).

[7] G. Schileo and L. R. Weissert, "A Pilot Plant for the Production of Th-U^{233} Recycle Fuels," paper presented at the VIII Congresso Nucleare of the Comitato Nazionale per L'Energia Nucleare, Rome, Italy, June 17–23, 1963.

[8] A. R. Irvine, A. L. Lotts, and A. R. Olsen, "The Thorium-Uranium Recycle Facility," *Proceedings of the 13th Conference on Remote Systems Technology, 1965,* American Nuclear Society, Hinsdale, Ill., 1966.

[9] R. S. Kemper *et al., Fabrication of Zircaloy-2 Clad Thorium-Uranium Alloy Fuel Elements,* HW-79843 (March 1964).

[10] S. R. Nemeth, ed., *Thorium–1.4 wt %* ^{235}*Uranium Metal Fuel Tubes – Fabrication and Irradiation in HWCTR,* DP-943, suppl. (April 1965).

Table 31.2. Comparison of Fuel Element Parameters and Fuel Fabrication Costs

	AI-CE		B&W	B&W Metal				
	Large Rods	Small Rods	Oxide	Ring 1	Ring 2	Ring 3	Ring 4	Ring 5
Fuel type	UC	UC	$(Th,U)O_2$	Th-U alloy				
Fuel dimensions, in.								
Outside diameter	0.472	0.275	0.316	2.606	3.116	3.638	4.176	4.750
Inside diameter				2.406	2.916	3.438	3.976	4.550
Length	41.5	41.5	44	48	48	48	48	48
Thickness				0.100	0.100	0.100	0.100	0.100
Fuel density								
Theoretical, g/cm^3	13.4	13.4	10.0	11.85				
Attained, %	100	100	88	100				
Rods (rings) per assembly	31	6	66	1	1	1	1	1
Fuel, kg of heavy metal								
Per piece	1.52	0.52	0.44	7.34	8.83	10.36	11.94	13.62
Per foot	0.44	0.15	0.12	1.84	2.21	2.59	2.99	3.41
Per assembly	50.09		29.07	52.09				
Fuel element autoclaved	No		No	Yes				
Type fabrication	Hooded		Remote	Remote				
Fuel fabrication cost, dollars per kilogram of heavy metal	28.41		63.50	42.14				

Table 31.3. Fuel Fabrication Cost per Core for Different Burnup Levels (HWOCR)

Fuel Material	Burnup (Mwd/metric ton)	Fuel per Core (kg of heavy metal)	Fabrication Cost	
			($/kg heavy metal)	($/core)
				$\times 10^6$
Uranium carbide	15,000[a]	123,000	28.41	3.5
(Th-U) metal	20,000[a]	93,400	42.14	3.9
(Th-U) oxide	20,000[a]	58,160	63.50	3.7
Uranium carbide	15,000[a]	123,000	28.41	3.5
(Th-U) metal	15,000	93,400	37.25	3.5
(Th-U) oxide	15,000	58,160	60.00	3.5
Uranium carbide	20,000	123,000	30.50	3.8
(Th-U) metal	20,000[a]	93,400	42.14	3.9
(Th-U) oxide	20,000[a]	58,160	63.50	3.7

[a] Burnup specified by sponsors.

reference design conditions because of the large differences in quantity of fuel for the different cores, as shown in Table 31.3.

The ultimate significance of these evaluations is the estimate of the total cost of producing energy, which is composed of numerous interactions of costs and design parameters. Fuel fabrication cost is only one of many contributors to the total cost, but it can become a substantial segment of the whole, and its influence must not be neglected in any evaluation.

EVALUATION OF FUELS FOR THE HWOCR

R. E. Adams A. L. Lotts

As part of ORNL's assistance to the AEC in analyzing the technical and economic potential of reactor systems, we evaluated the potential of heavy-water-moderated organic-cooled reactors (HWOCR). The study was based on three preliminary designs of 1000-Mw (electrical) reactors. Pressure tubes of SAP containing fuel and coolant extend through Zircaloy-2 calandria tubes in the heavy-water moderator tank. Core-outlet coolant temperatures and maximum cladding temperatures were specified at 750 and 850°F respectively. The uranium cycle HWOCR was designed by AI-CE. Two similar reactor cores, based on ThO_2-UO_2 and thorium-uranium alloy fuel, were designed by B&W to permit evaluation of the thorium cycle in this type of reactor. We have analyzed fuel performance and core materials problems of these three systems.

The uranium cycle HWOCR uses SAP-clad UC fuel slugs. Five 37-rod fuel assemblies are stacked in each fuel channel. Maximum burnup is about 20,000 Mwd/metric ton, and maximum heat ratings were 28.7 kw/ft. An analysis of the fuel element performance in view of available data indicates that the fuel element design is reasonable. Burnup limitations cannot yet be defined, and additional research will be necessary to determine that fuel swelling and cracking at proposed burnups will not exceed what can be tolerated by the SAP cladding.

The thorium-metal-fueled reactor has five concentric fuel tubes of coextruded Zircaloy-4-clad thorium-uranium alloy, and six elements are stacked in each pressure tube. The tubes have 0.100-in.-thick alloy fuel and 0.025-in.-thick Zircaloy-4 cladding; their outer diameters range between 2.6 and 4.8 in., and coolant channels range between 0.078 and 0.137 in. thick.

Proposed burnups (about 20,000 Mwd/metric ton) have not yet been achieved with annular fuel elements, and the tubes are considerably larger in diameter than any as yet tested. The rather high cladding-to-fuel ratio of the tube should help restrain stresses induced by fuel swelling. Temperatures and thermal gradients in the fuel tubes appear to be acceptable, but fuel assemblies must be tested to determine whether the thin annuli between fuel tubes can accommodate distortions that may develop during the life of the fuel element.

The fuel assembly for the thorium oxide reactor contains 66 pins, each 4 ft long. Fuel rods are fabricated by vibratorily compacting ThO_2-UO_2 fuel into finned SAP tubes. Although prototype rods have not been tested, experimental tests have shown ThO_2 to be somewhat superior to UO_2 in fuel performance. Controlled fabrication conditions have yielded vibratorily compacted UO_2 elements that perform comparably to pelletized fuel. Successful performance of UO_2 fuels has been demonstrated at heat ratings and burnups that exceed those proposed for the HWOCR. Vibratory compaction in SAP cans must be demonstrated to yield fuel tubes that will tolerate the required exposures under HWOCR conditions.

Compatibility of core materials was also evaluated. The principal compatibility problem of concern is hydriding of the Zircaloy-4 cladding of the thorium metal fuel elements. The hydriding rate of Zircaloy in organic coolant is significantly dependent on coolant impurities. Experimental testing will be required to define the importance of hydriding in limiting fuel element life. All fuel materials are compatible with the organic coolant. Reactions can occur between fuel and cladding materials at temperatures slightly above the normal operating temperature, but available data do not indicate that such reactions will proceed to the point that serious cladding failure will result.

Of particular concern in these reactors are the mechanical properties of SAP, since it is a relatively new material for which specifications and information on design stresses have not been completely developed. Its principal deficiency is the low ductility at low strain rates. On the basis of the limited data available we concluded that the use of SAP cladding would be satisfactory for both designs. The use of SAP pressure tubes may also be feasible; however, stresses proposed for the process tubes are subject to code interpretation for the 30-year life. Additional information will be required before the effects of low ductility and brittleness on performance of SAP for this application can be evaluated. An extensive backup program is recommended for the development of satisfactory zirconium alloy pressure tubes.

32. Thorium Utilization

D. A. Douglas, Jr.

For several years the simplification and cost reduction of the thorium fuel cycle as it pertains to the processing of bred fuels has been the aim of a joint effort of the Chemical Technology and Metals and Ceramics Divisions. The problems encountered in recycling bred fuels and the technical alternatives that are available may be reviewed in more detailed discussions.[1–3]

Since the recent evaluations of reactors that would use the thorium-^{233}U cycle have shown that the high-temperature gas-cooled reactor (HTGR) has the greatest potential for utilization of this cycle, the direction of our program has changed to place more emphasis on the fueled-graphite elements required for such reactors. In the Metals and Ceramics Division, we are comprehensively developing pilot-scale processes and equipment for recycle of advanced HTGR fuels. Our work is in three parts: process development, engineering development and demonstration, and product evaluation and irradiation testing. Irradiation testing of coated-particle fuels, done jointly with the Gas-Cooled Reactor Project, is described in Chap. 26 of this report.

THORIUM-URANIUM RECYCLE FACILITY

A. L. Lotts

Reliable economic analyses of the reprocessing and refabrication techniques for various fuel elements in the thorium fuel cycle is an essential part of the development. The reliability of such analyses is improved if data are provided at pilot-scale production levels for the recycle processes. Evaluations have indicated that there may be economic advantage in recycling fuel through low-decontamination processes and then remotely refabricating fuel elements. Also, the ^{232}U decay in recycle fuel produces increasing radioactivity, which necessitates biological protection. Consequently, a heavily shielded facility, the Thorium-Uranium Recycle Facility (TURF), is being constructed to permit the development and evaluation of a variety of integrated fuel processing and refabrication schemes at the necessary pilot-scale production levels.

Concurrently with the construction of the facility, research and development are proceeding on the first fabrication line for the TURF, which will prepare sol-gel microspheres and refabricate prototype high-temperature gas-cooled reactor fuel elements.

Building

A. R. Irvine[4] A. L. Lotts
A. R. Olsen

A heavily shielded facility for virtually any phase of pilot-scale development for the Th-^{233}U fuel cycle is under construction in the Melton

---

[1] A. B. Shuck, A. L. Lotts, and K. Drumheller, "The Remote Fabrication of Reactor Fuels," *Reactor Technology—Selected Reviews, 1965*, TID-8541, pp. 71–148.

[2] A. L. Lotts and D. A. Douglas, Jr., "Refabrication Technology for the Thorium–Uranium-233 Fuel Cycle," pp. 212–45 in *Utilization of Thorium in Power Reactors, Report of a Panel Held in Vienna 14–18 June 1965*, International Atomic Energy Agency, Vienna, 1966.

[3] A. L. Lotts, D. A. Douglas, Jr., and R. L. Pilloton, "Refabrication Technology and Costs for High-Temperature Gas-Cooled Reactor Fuels," to be published in *Proceedings of the EURATOM Symposium on Fuel Cycles of High-Temperature Gas-Cooled Reactors, June 10–11, 1965, Brussels, Belgium.*

[4] Chemical Technology Division.

Valley area of ORNL. Details of its design have been reported previously.[5–9] Construction started in May 1965 and is currently on schedule; the construction contractor's work is to be completed in December 1966.

Approximately 70% of the work is complete. The building shell is essentially complete, and work is progressing on the cell complex. All major items of building equipment have been purchased; only the large shielding doors that isolate the remote fabrication cells from the decontamination cell and the shielding door between the decontamination cell and the maintenance area are slightly behind schedule. This is not expected to delay the scheduled completion date.

Fueled Graphite Fabrication Equipment

T. N. Washburn R. L. Pilloton

We are currently conceptually designing equipment to be used for demonstration of refabrication technology for HTGR fuel elements. The flowsheet that is being used for conceptual design is shown in Fig. 32.1. Production-type equipment will be used, so that information gained will be applicable both technically and economically to a full-scale production facility.

The coating and particle-consolidation steps appear to be the limiting factors of the fabrication process. We are currently evaluating means for minimizing time requirements in these areas. The production capability of the TURF line will be determined by the fuel element design and the fabrication process selected. We anticipate that the fuel element will have physical dimensions similar to that of the Peach Bottom Reactor[10] but will probably be hexagonal, with fuel and coolant channels similar to the proposed Public Service of Colorado HTGR fuel element design.[11]

A pneumatic conveyance system has been designed for handling loose particles in the TURF fabrication line up to the point of particle consolidation. This closed system of material transfer should minimize airborne contamination, losses, inventory difficulties, and fuel material contamination by extraneous materials. All items of equipment for processing and transfer are being designed for geometrical control of criticality. This concept is deemed advisable due to the high ^{235}U content of the fissile fuel particles.

Design of this equipment is being closely coordinated with process development and irradiation testing to assure the maximum practicable level of process and product flexibility in the fabrication line.

FUELED-GRAPHITE DEVELOPMENT

A. L. Lotts

In our development of the fueled-graphite process, the primary aim is to optimize the various steps in the process and to obtain engineering data that can be used in the design of the refabrication line for TURF. Emphasis has been placed on the most complicated processes from the standpoint of remote fabrication technology, on those parts of the process that are the principal contributors to the fabrication costs, and on suitable techniques for process evaluation and inspection of the components made in the processes. Accordingly, the principal work has involved pyrolytic carbon coating processes, a process for conversion of oxide to carbide, and nondestructive techniques for process control.

Coated-Particle Development Laboratory

R. B. Pratt R. L. Pilloton

A pilot-scale microsphere fabrication line in the Coated-Particle Development Laboratory started operating during the past year. Objectives of

---

[5] A. R. Irvine and A. L. Lotts, "The Thorium Fuel Cycle Development Facility Conceptual Design," pp. 333–50 in *Proceedings of the Thorium Fuel Cycle Symposium, Gatlinburg, Tennessee, December 5–7, 1962*, TID-7650, book 1 (July 1963).

[6] A. R. Irvine and A. L. Lotts, *Metals and Ceramics Div. Ann. Progr. Rept. May 31, 1963*, ORNL-3470, pp. 198–201.

[7] A. R. Irvine, A. L. Lotts, and A. R. Olsen, *Metals and Ceramics Div. Ann. Progr. Rept. June 30, 1964*, ORNL-3670, pp. 230–31.

[8] A. R. Irvine, A. L. Lotts, and A. R. Olsen, *Metals and Ceramics Div. Ann. Progr. Rept. June 30, 1965*, ORNL-3870, pp. 267–68.

[9] A. R. Irvine, A. L. Lotts, and A. R. Olsen, "The Thorium-Uranium Recycle Facility," pp. 19–24 in *Proceedings of the 13th Conference on Remote Systems Technology, 1965*, American Nuclear Society, Hinsdale, Ill., 1966.

[10] S. L. Koutz, *Nucl. News* 8(8), 21–23 (August 1966).

[11] R. F. Turner and W. V. Goeddel, *Trans. Am. Nucl. Soc.* 9(1), 314–15 (June 20–23, 1966).

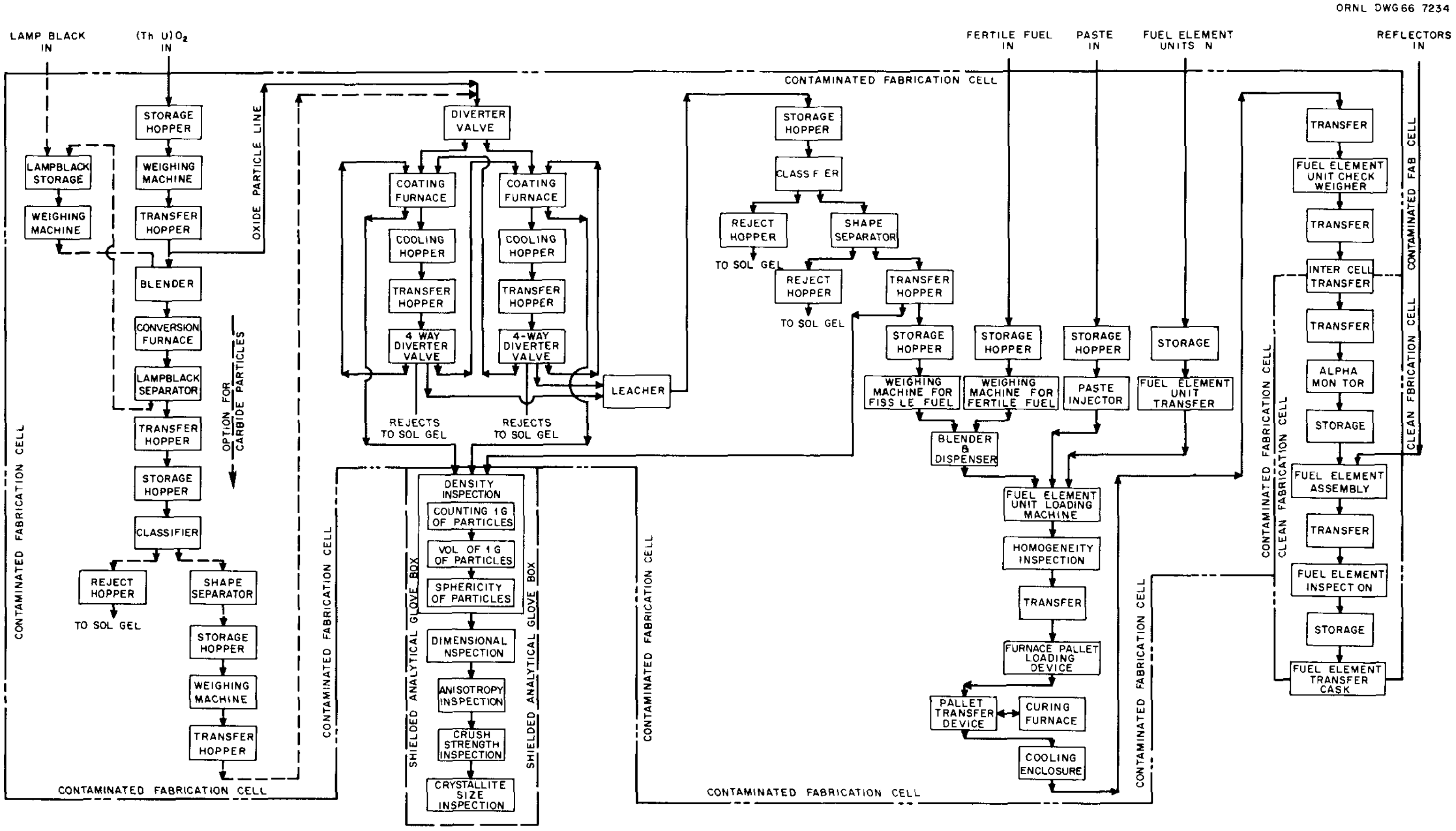

Fig. 32.1. Flowsheet for Refabrication of HTGR Fuel Elements.

our work include to scale up the process, to achieve an ability to prepare specific types of coatings, to assure coating reproducibility, to develop low-maintenance equipment, and to develop equipment and procedures suitable for future remote fabrication in TURF. Development work has included microsphere preparation, coating of particles with pyrolytic carbon, development of auxiliary particle processing equipment, and development of operating and analytical procedures. Conversion of oxide to carbide will begin when equipment is available. Although work to date has been concerned with natural thorium compounds, future work will include uranium of various enrichments.

Principal efforts have been toward equipment startup, component evaluation, and production of specific coatings in batches up to 3 kg. The process flowsheet remains essentially the same as shown in Fig. 32.2.

Fluidized Bed

R. B. Pratt R. L. Pilloton

The fluidized-bed process is the principal method investigated for coating nuclear fuel particles with pyrolytic carbon in TURF. In this process microspheres are suspended by an upward flow of helium and hydrocarbon in a heated column. The cracking of the hydrocarbon produces the coating.

The design of the nozzle used to introduce the gases into the fluidizing column was extremely important to ensure proper particle motion and gas-solid contact and to minimize carbon deposition on the nozzle itself. The nozzle of Fig. 32.3 met most requirements under many conditions. It consists of a dual gas flow graphite plate resting on a water-cooled base.

Our experiments using a 5-in.-ID coating furnace indicated that the main factors affecting

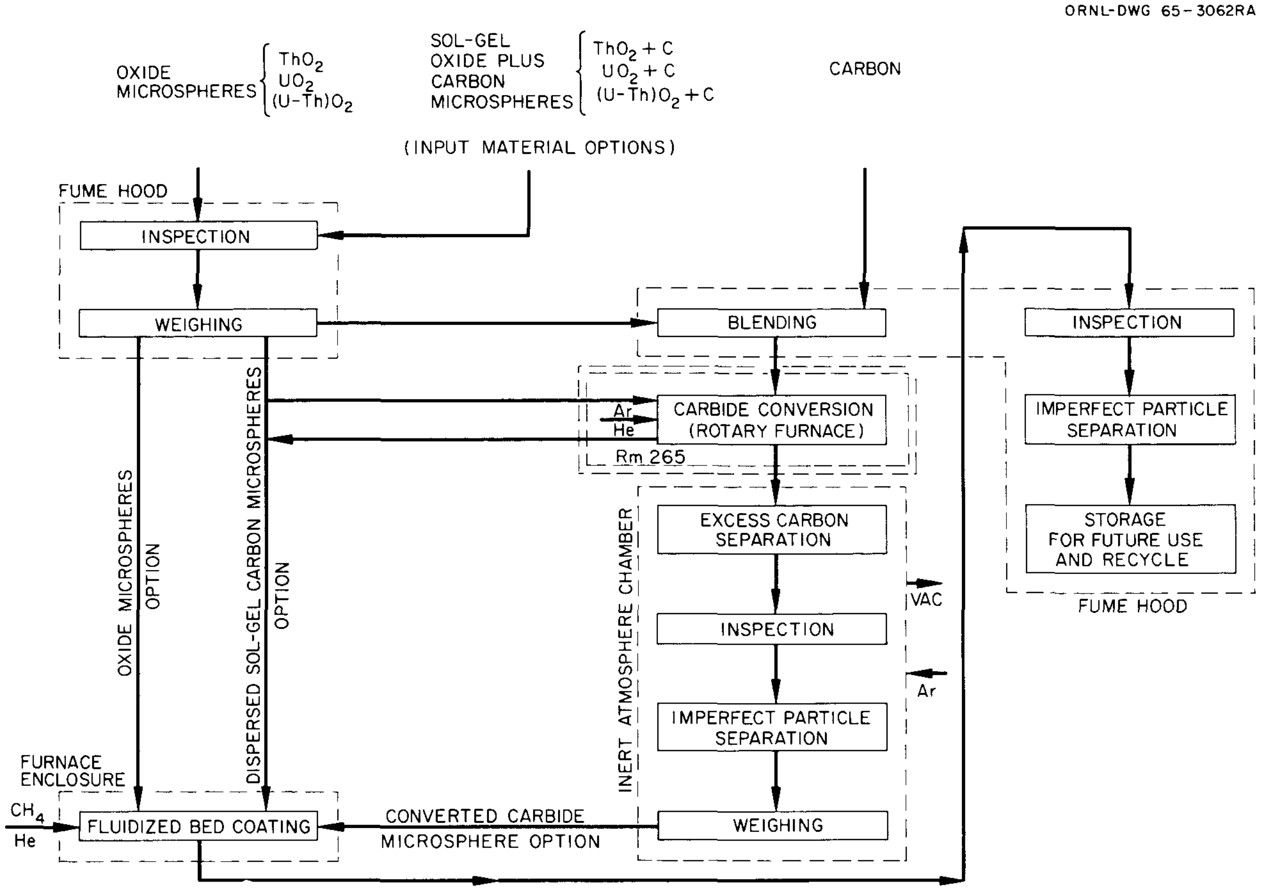

Fig. 32.2. Coated Particle Development Laboratory Microsphere Coating Process Flow Diagram.

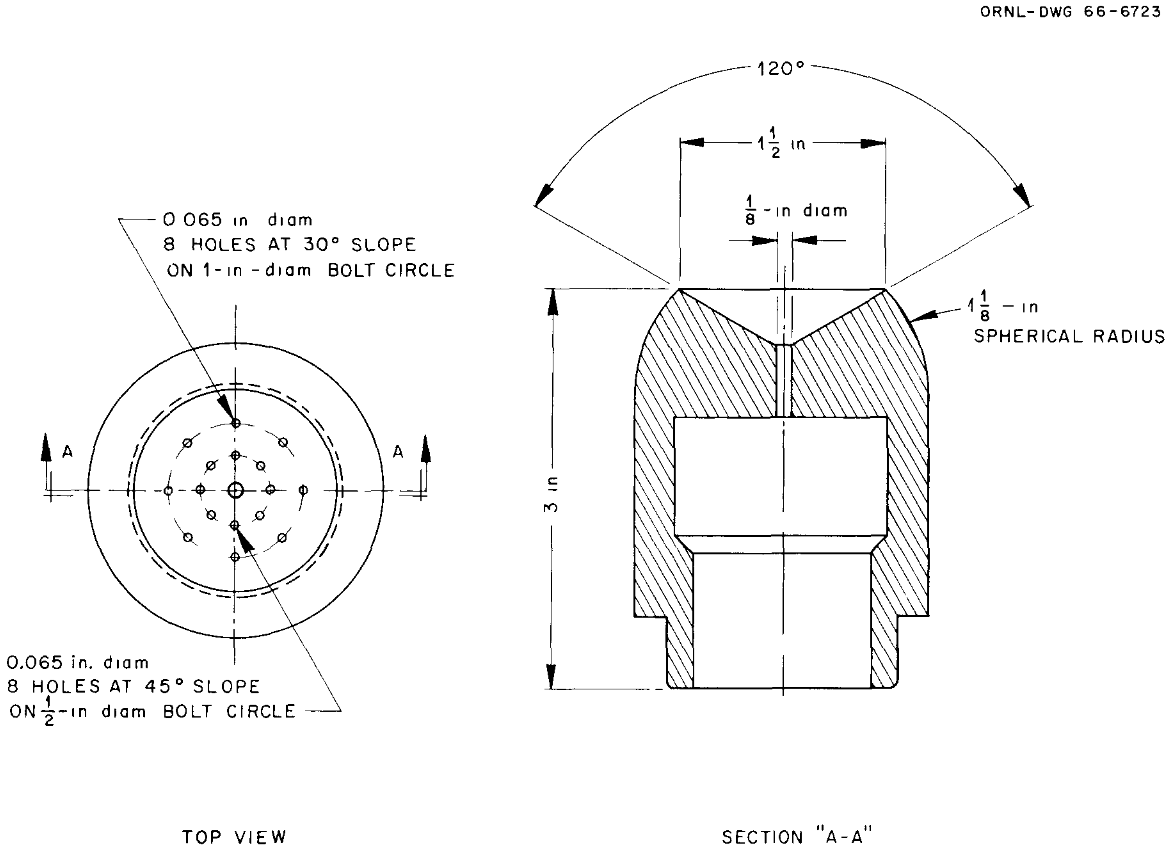

Fig. 32.3. Reference Nozzle for Fluidized-Bed Coater.

the coating characteristics were the bed and nozzle temperatures, the charge weight, the particle size, and the flow of gas per unit of bed surface area (gas flux).

With batches of 0.5 to 3 kg of 230-μ-diam microspheres we obtained the coating densities listed in Table 32.1. These results are in agreement with generally accepted nuclear particle coating densities of less than 1.2 g/cm^3 for the inner porous layer and greater than 2.0 g/cm^3 for the outer dense coating.

Entrained Bed

S. E. Bolt[12] H. J. Flamm[13]
R. B. Pratt

As an alternate to the fluidized bed described above, we have developed an entrained-bed system for coating ThO$_2$ microspheres. The experimental apparatus is shown in Fig. 32.4. The particles are entrained by the coating gas stream and carried up through the insert, recirculated

Table 32.1. Typical Results from Fluidized-Bed Coater

Coating Gas	Bed Temperature (°C)	Gas Flux[a]	Coating Density (g/cm^3)
Acetylene	1100	6.0	0.54
	1130	2.0	1.2
Methane	1550	0.2–0.7	1.5–1.8
	> 2000	0.25	1.9–2.1

[a] Gas flux measured in cm^3/sec per square centimeter of particle surface.

---

[12] On loan from the Reactor Division.

[13] Euratom employee on temporary assignment at ORNL from Dragon Project, AEE Winfrith, Dorchester, Dorset, England.

down through the packed bed, and then reentrained in the entrainment region. This technique ensures uniform gas-solid contact through repeated forced recirculation of particles through this coating zone. We have conducted 30 coating runs in this coater over a wall temperature range of 1650 to 2250°C with charge weights of 1000 to 3000 g of ThO_2, achieving coating densities up to 1.94 g/cm^3.

Rotary Drum Coater

S. E. Bolt[12] H. J. Flamm[13]
R. B. Pratt

The rotary drum coater described previously[14] and shown in Fig. 32.5 was completed and placed

ORNL-DWG 66-9152

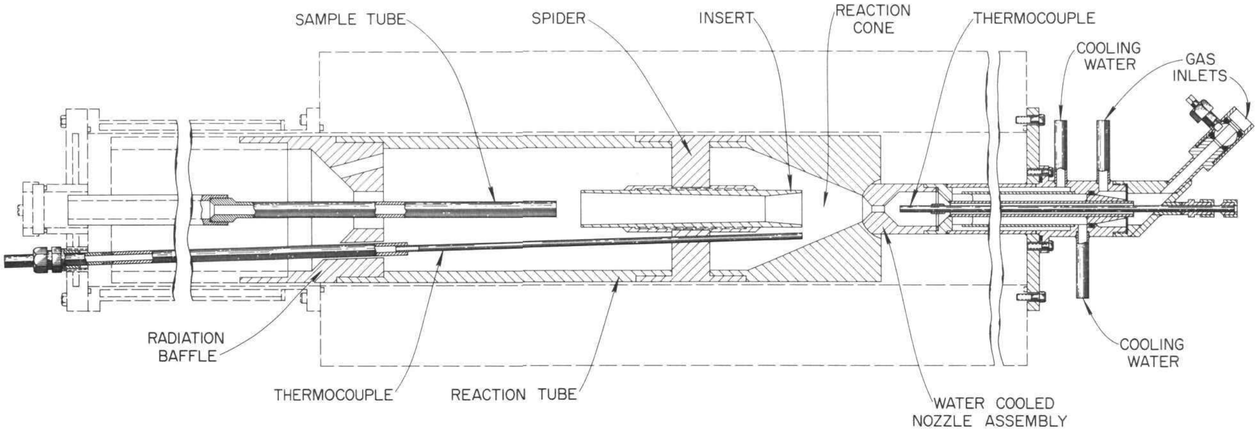

Fig. 32.4. Entrained Bed Coater Assembly.

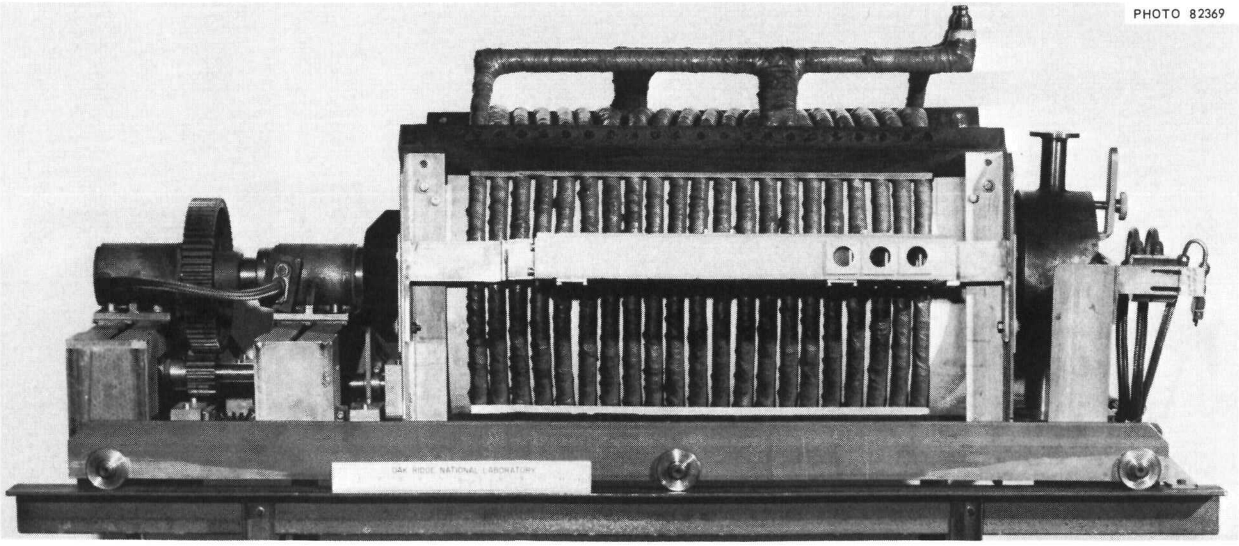

Fig. 32.5. Rotary Drum Coater.

---

[14] H. J. Flamm and R. B. Pratt, *Metals and Ceramics Div. Ann. Progr. Rept. June 30, 1965*, ORNL-3870, p. 280.

in operation with only minor modifications being required. Fourteen coating runs were conducted with irregular silicon carbide chips substituted for the sol-gel microspheres. The particles were coated, but evaluation of the data is somewhat difficult due to their irregular shape. We could not achieve the design operating temperature of 2200°C because of insufficient power. In the present configuration, 1750°C is the maximum temperature that has been reached during a coating run. An improved insulation is being fabricated to alleviate this problem.

Three coating runs using ThO_2 microspheres were conducted. Very low coating efficiencies indicated that the particles were not adequately contacted by the methane. Current efforts to better distribute the coating gas, to increase the residence time of the gas, and to increase the drum wall temperature should improve the coating conditions in future experiments.

Conversion of Sol-Gel Microspheres from Oxides to Carbides

R. B. Pratt R. L. Pilloton

The carbon-diffusion process[15,16] for one-step conversion of sol-gel oxides into dense carbides was used to make gross quantities of ThC_2, $(Th,U)C_2$ (example shown in Fig. 32.6), and UC_2 microspheres. Carbide has been produced by heating oxide microspheres to 2100°C under argon in a bed of carbon flour in a rotary crucible. The resulting carbide microspheres are very dense as long as the initial oxide particles are practically free of carbon. The presence of carbon in the oxide causes porosity in the final product.

The design of the crucible and its rotational speed were studied in detail because of their importance for complete oxide-carbide conversion and for avoiding agglomeration or sticking of the particles to the wall. These observations have now been used to design and to build the continuous rotary conversion furnace prototype shown in Fig. 32.7.

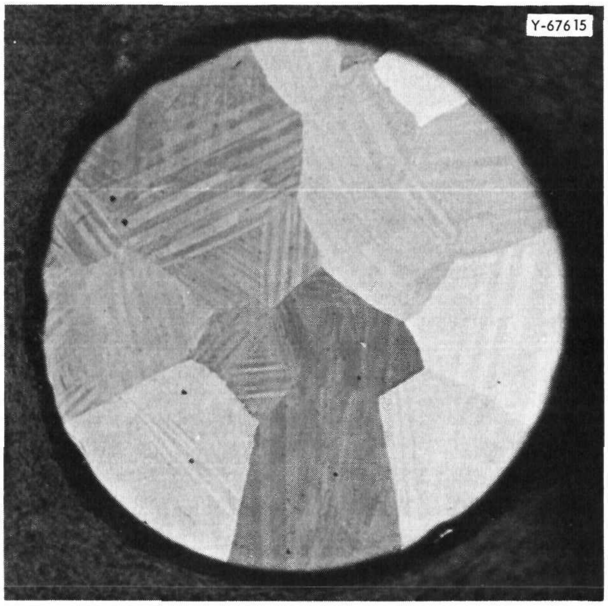

Fig. 32.6. Microstructure of a (Th–25% U)C_2 Microsphere Obtained by Heating a (Th–25% U)O_2 Microsphere in a Bed of Lampblack for 3 hr at 2100°C. Etchant: dilute HNO_3. Bright field illumination. 500×. Reduced 24%.

This furnace essentially consists of a 6-in.-ID, 58-in.-long graphite tube heated by induction and rotated in an inert atmosphere chamber. Mechanisms have been designed for continuous feeding of the oxide microspheres and carbon flour at one end of the tube and for the discharge of the carbide microspheres and excess carbon at the other end. The equipment is now ready for process development.

IRRADIATION OF POWDER-PACKED SOL-GEL OXIDES

A. R. Olsen Y. Hirose[18]
J. W. Ullmann[17] E. J. Manthos

The irradiation testing and evaluation of sol-gel-derived oxide as a nuclear fuel is continuing.

---

[15] R. L. Pilloton and R. L. Hamner, "A Method for Preparing Dense Spherical Particles of Thorium and Uranium Dicarbides," paper presented at the 11th Annual American Nuclear Society Meeting, Gatlinburg, Tenn., June 21–24, 1965 (to be published).

[16] R. L. Pilloton, R. L. Hamner, and E. S. Bomar, *Metals and Ceramics Div. Ann. Progr. Rept. June 30, 1965*, ORNL-3870, p. 275.

[17] Chemical Technology Division.

[18] Noncitizen guest from Hitachi, Ltd., Japan.

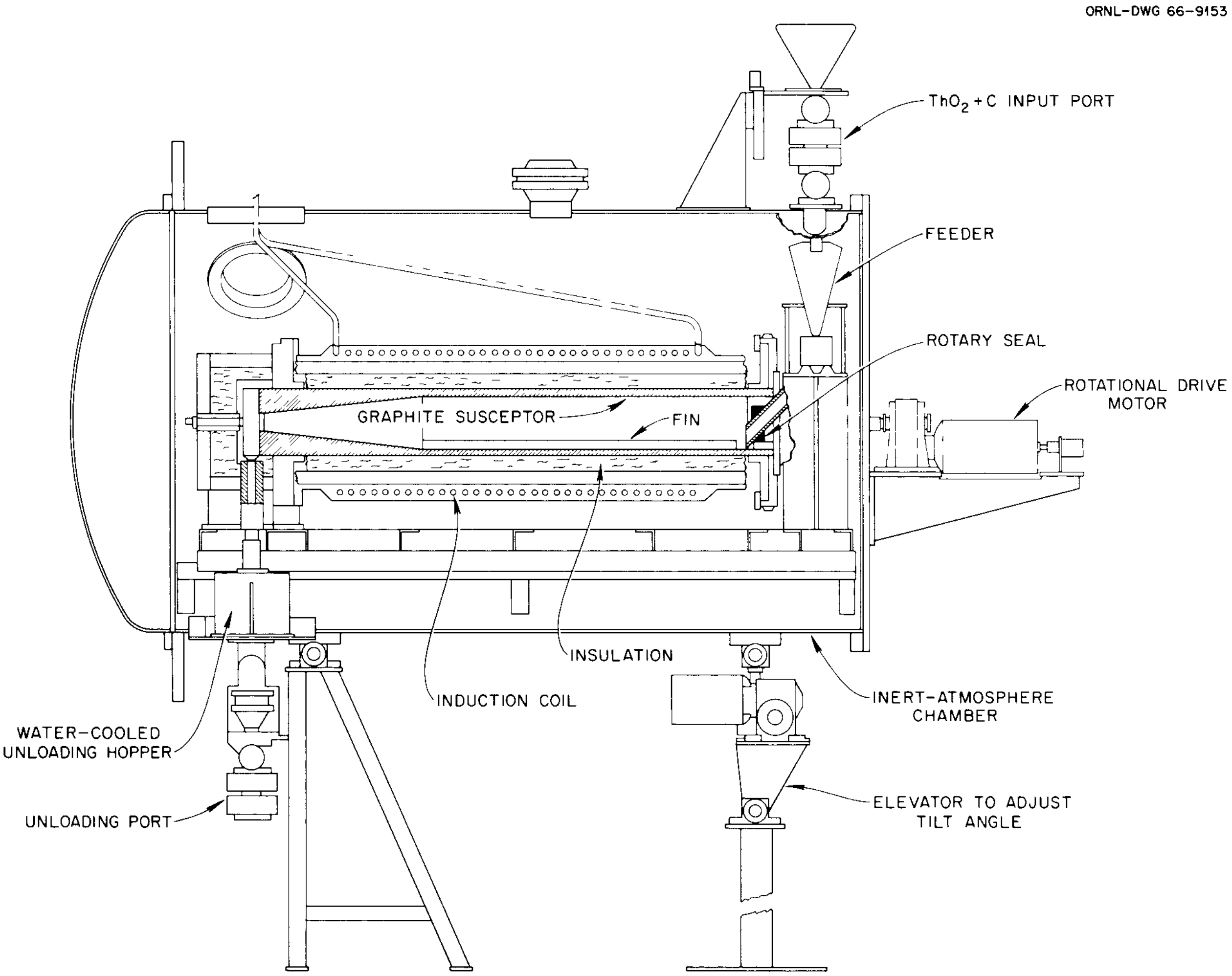

Fig. 32.7. Schematic Assembly of Rotary Furnace Prototype for the Conversion of Oxide Sol-Gel Microspheres into Dense Carbide Microspheres by the Carbon Diffusion Process.

Previously reported results[19–25] have shown that metal-clad fuel rods containing vibratorily compacted sol-gel-derived thoria-base fuels with less than 5% fissile additions perform satisfactorily under irradiation. These fuel rods, in lengths up to 36 in., can operate at current water-reactor linear heat ratings of 10 to 14 kw/ft to burnup levels in excess of 100,000 Mwd per metric ton of Th + U with no evidence of breakaway swelling or sudden increases in fission-gas release. The

---

[19] S. A. Rabin, *Metals and Ceramics Div. Ann. Progr. Rept. May 31, 1963*, ORNL-3470, pp. 205–9.

[20] S. A. Rabin, J. W. Ullmann, and D. A. Douglas, *Metals and Ceramics Div. Ann. Progr. Rept. June 30, 1964*, ORNL-3670, pp. 238–45.

[21] R. G. Wymer and D. A. Douglas, Jr., (compilers), *Status and Progress Report for Thorium Fuel Cycle Development Dec. 31, 1963*, ORNL-3611, pp. 96–102.

[22] A. R. Olsen, J. W. Ullmann, Y. Hirose, and E. J. Manthos, *Metals and Ceramics Div. Ann. Progr. Rept. June 30, 1965*, ORNL-3870, pp. 283–88.

[23] R. G. Wymer and D. A. Douglas, Jr. (compilers), *Status and Progress Report for Thorium Fuel Cycle Development Dec. 31, 1964*, ORNL-3831, pp. 82–116.

[24] A. R. Olsen, J. W. Ullmann, and E. J. Manthos, chap. 7 in *Status and Progress Report for Thorium Fuel Cycle Development Dec. 31, 1965*, ORNL-4001 (in press).

[25] S. A. Rabin, J. W. Ullmann, E. L. Long, Jr., M. F. Osborne, and A. E. Goldman, *Irradiation Behavior of High Burnup ThO_2–4.45% UO_2 Fuel Rods*, ORNL-3837 (October 1965).

fission-gas release rates were less than 20% and the swelling rates less than 0.5 vol % per 10^{20} fissions/cm^3. We are currently investigating the effects of extended burnup, varying heat ratings, and sol-gel processing variables, such as calcining atmospheres, on the fuel material. Table 32.2 summarizes the experimental conditions of the tests under irradiation.

During the past year only two rods have been removed from the reactor for examination. One of these is a sol-gel powder-packed rod from experimental group MTR-I. Although the examination is not complete, the rod was exposed for 1107 reactor full-power days to a peak unperturbed advertised dose of 1.5×10^{22} neutrons/cm^2. This should provide a burnup of approximately 120,000 Mwd per metric ton of Th + U. There were no appreciable changes in rod diameter or length and thus no excessive swelling. The precise fission-gas release rate cannot be determined until the burnup analyses are completed, but we already know it will certainly be less than 5%. This low release percentage indicates a lower than anticipated fuel temperature during irradiation, a parameter that cannot be evaluated without the burnup analyses.

The second test rod removed this year has not yet been examined. It was one of the semiremotely fabricated (ThO_2-$^{233}UO_2$) ETR-II group, and it operated at a peak linear heat rating of 20 kw/ft. The rod failed at a peak unperturbed dose of 20.3×10^{20} neutrons/cm^2, approximately 17,000 Mwd per metric ton of U + Th. This is the second failure in the entire irradiation program to date. Both failures have occurred in Zircaloy-clad rods. The first failure occurred in the ORR loop group, which operated at 1750 psi with 260°C water coolant. The failure occurred in the plenum area and was attributed[21] to an undetected flaw in the

Table 32.2. Summary of Thorium Fuel Cycle Program Test Rods[a] Under Irradiation in June 1966

Designation	Number of Rods	Type of Oxide	Density (% of theoretical)	Linear Heat Rating (w/cm)	Peak Burnup (Mwd per metric ton of metal)	Objective
MTR-II	2	Sol-gel S	88–89	600	100,000	Obtain higher heat rating by increasing enrichment
MTR-III	6	Sol-gel 35	86–89	820	100,000	Compare oxide calcining atmospheres and higher heat ratings obtained by increasing diameter
MTR-P	3	Pellets	95	400	150,000	Study effects of extended burnup on swelling and fission-gas release
ETR-II	5	BNL Sol-gel	90	630	30,000–100,000	Study effects of remote fabrication and oxide recalcining
ETR-III	7	Sol-gel ThO_2	88	770	10,000–70,000	Study ThO_2 blanket material with gradually increasing heat rating and provide high-protactinium low-fission-product material for chemical processing

[a] All MTR rods were clad with type 304 stainless steel; all ETR rods were clad with Zircaloy-2.

tubing. Underwater examinations of the second failure indicate that it occurred in the plenum area also. Detailed examination is scheduled to begin in July.

Having completed the evaluation of some of the phases in the irradiation program, we have been able not only to report the status[26–28] but also in part to analyze the prospects of the thoria-base fuels.[27–28] These analyses have shown that thoria-base fuels are unique and not simply a substitute for urania. Thoria can operate at higher linear heat ratings, up to at least 1000 w/cm, without central melting.

Under similar exposure conditions, vibratorily compacted sol-gel-derived thoria can sustain approximately 40% higher power ratings than similar urania fuel while undergoing similar microstructural changes and fission-gas release rates. The available experimental evidence on fuel swelling agrees well with semitheoretical calculations and indicates at least a 20% lower swelling rate for bred ^{233}U fissions than for bred ^{239}Pu fissions. The sol-gel process does not lead to gas entrapment within the particles, but the surface sorption characteristics are not fully defined. Postirradiation analyses agree well with calculated levels of fissile atom content up to 120,000 Mwd per metric ton of Th + U burnup and indicate relatively small changes in fuel reactivity with burnup, even at flux levels as high as 1.0×10^{14} neutrons/cm^2. The reduced control problems, structural stability, and higher thermal capability of thoria-base fuels, thus defined, indicate potential savings in inventory and fabrication costs, which might make thoria fuels competitive with low-enrichment urania fuels in reactors specifically designed to take advantage of the thoria fuel performance characteristics. With the recent development of a sol-gel process for producing PuO_2 and $(Th,Pu)O_2$ and the potential fabrication cost savings of low-energy vibratory compaction of microspheres (discussed elsewhere in this chapter), future irradiation tests will be directed toward the evaluation of the crossed-progeny fuels and the packed microspheres.

THERMAL CONDUCTIVITY OF $(Th,U)O_2$

J. P. Moore

The irradiation performance evaluation of sol-gel-derived thoria-base fuels requires knowledge of the thermal conductivity as a function of process variables and composition. We are investigating these parameters, starting with pelletized bodies. To date only the low-temperature regime has been investigated.

Table 32.3 contains thermal conductivity (λ) data obtained between 30 and 120°C on sol-gel ThO_2, oxalate-derived ThO_2, ThO_2–5% UO_2, and ThO_2–8% UO_2. The last two materials were sintered either in hydrogen or in air. The following conclusions were indicated.

1. For equivalent densities, λ of oxalate ThO_2 is approximately 30% higher than λ of sol-gel ThO_2.
2. Air- or hydrogen-sintered specimens of sol-gel ThO_2 have essentially the same λ.
3. The sintering environment used during the preparation of the ThO_2–5% UO_2 and ThO_2–8% UO_2 has a marked effect on λ. The ThO_2 and UO_2 mixtures sintered in hydrogen have a λ twice that of the air-sintered material.
4. The ThO_2–8% UO_2 sintered in hydrogen has essentially the same λ as pure ThO_2.

ADVANCED FUEL CYCLE PROCESS DEVELOPMENT

A. L. Lotts

We have attempted to use the unique properties of the various states of sol-gel advantageously to simplify processes for making various fuels and to more economically recycle fuels from various reactors. Primarily this effect has involved the fabrication of suitable ceramic bodies from sol-gel material in a sufficiently plastic state to allow

---

[26] A. R. Olsen, W. O. Harms, D. B. Trauger, R. E. Adams, and D. A. Douglas, "Irradiation Behavior of Thorium-Uranium Alloys and Compounds," pp. 246–91 in *Utilization of Thorium in Power Reactors, Report of a Panel Held in Vienna 14–18 June 1965*, International Atomic Energy Agency, Vienna, 1966.

[27] A. R. Olsen, J. H. Coobs, and J. W. Ullmann, "Current Status of Irradiation Testing of Thorium Fuels at Oak Ridge National Laboratory," paper presented at the Second International Thorium Fuel Cycle Symposium May 3–6, 1966, to be printed in the Transactions.

[28] A. R. Olsen, D. A. Douglas, Jr., Y. Hirose, J. L. Scott, and J. W. Ullmann, "Properties and Prospects of Thoria-Base Nuclear Fuels," paper presented at The British Ceramic Society Meeting on Nuclear and Engineering Ceramics, Oct. 25–27, 1965, to be published in the Transactions.

Table 32.3. Thermal Conductivity of ThO_2 and ThO_2-UO_2

UO_2 Content (%)	Source	Density (g/cm^3)	Sintering Conditions[a]	Thermal Conductivity (w cm^{-1} °C^{-1})		
				30°C	75°C	120°C
5[b]	Sol-gel	9.067	Air, 1650°C	0.0411	0.0396	0.0380
8[b]	Sol-gel	9 043	Air, 1650°C	0.0332	0.0325	0.0317
5	Sol-gel	8.733	H_2, 1750°C	0.0852	0.0769	0.0683
0	Sol-gel	8.950	H_2, 1750°C	0.0892	0.0787	0.0680
0	Sol-gel	8.968	Air, 1650°C	0.0925	0.0813	0.0702
0	Oxalate	9.525	Air, 1650°C	0.1460	0.1292	0.1125
0	Oxalate	8.582	Air, 1650°C	0.0999	0.0893	0.0788
0	Oxalate	8.116	Air, 1650°C	0.0834	0.0749	0.0662

[a] For 1 hr.

[b] Results of two samples of each material agreed to within ±0.5%.

the forming and packing of microspheres, which are so easily produced in the sol-gel process.

Extrusion Studies

R B. Fitts J D. Sease

Extrusion, which is a low-cost high-production method of forming ceramics, even in complex shapes, is being investigated as a means of forming sol-gel-derived fuels. Besides their low sintering temperature and inherent homogeneity, sol-gel materials are attractive for extrusion because the plasticity of the semisolid gel state may allow fabrication by extrusion without the addition of extraneous organic binders or plasticizers. Initial results indicate that extrusion of pure sol-gel materials is possible.

We used 10 to 12 *M* ThO_2 and ThO_2–5% UO_2 sols and sol-gel-produced powders as basic starting materials. We extruded $\frac{1}{8}$- to $\frac{3}{8}$-in.-diam rods using primarily sigma mixers and ceramic extrusion presses. Extrusions of pure clays exhibit high density and high shrinkage. A network of fine cracks, shown in Fig. 32.8, occurred during drying and firing. Despite these cracks, $\frac{1}{4}$-in.-diam × 1-in.-long extrusions may be produced with 99% of theoretical density and reasonable strength.

Additions of powder to the clay prior to extrusion lower the density but also lower the shrinkage. This technique promotes dimensional control and reduces or eliminates cracking. Powder additions also improve the economy of the fuel cycle by utilizing scrap material for the powder. Samples have been produced with 75 to 98% of theoretical density and microstructures similar to those of high-quality pressed-and-sintered UO_2 pellets. In some cases the as-fired extrusions exhibit variation of less than 0.0005 in. in a $\frac{1}{4}$-in. diameter. We are presently investigating the effects of various powder particle sizes and preaddition heat treatment of the powder on the quality of the extrusions. Preliminary results indicate that addition to the sol clay of a mixture of fired (1150°C) and lightly calcined (200 to 500°C) powders will produce the best extruded product.

In conclusion, the results to date indicate that pure thoria and thoria-urania sol-gel materials can be extruded to produce nuclear fuels of various densities. Pure clay extrusions are of high density with some fine internal cracking. Clay with powder additions will produce 75- to 98%-dense extrusions with good microstructure and excellent potential for dimensional control.

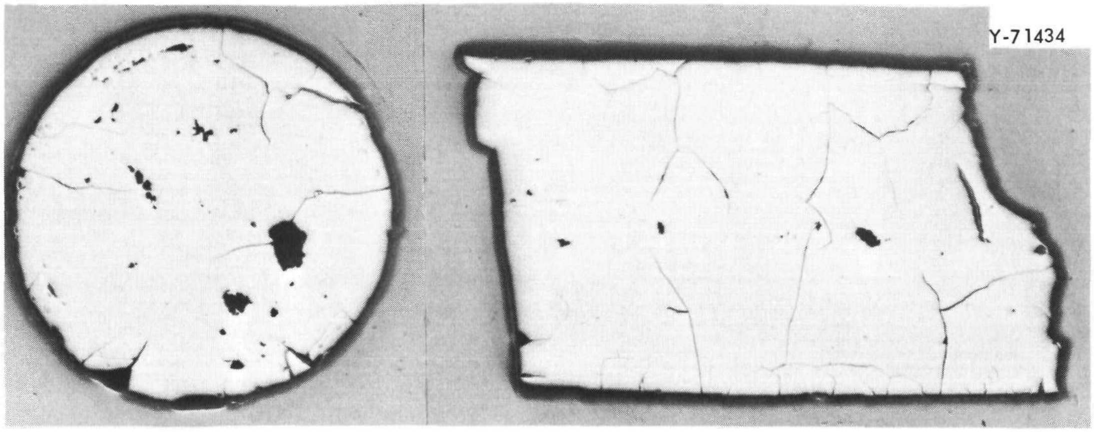

Fig. 32.8. Pure ThO_2 Sol Clay Extrusion Sintered at 1150°C for 3 hr. Approximately 9×.

Low-Energy Microsphere Packing

A. R. Olsen J. D. Sease

The high-energy vibratory compaction of sol-gel-derived fuel fragments appears to offer potential economic advantages for the remote fabrication of metal-clad bulk oxide fuel elements, but this process includes a variety of crushing, grinding, and sizing operations, which complicate the remote handling equipment requirements. The development of the sol-gel microsphere-forming process for coated-particle fuels coupled with reported studies[29-30] on low-energy vibratory compaction of spherical particles appears to offer an alternate approach.

Limited laboratory experiments using available sol-gel microspheres have been completed. Two size fractions were used in the initial tests. The coarse size fraction was −35 +40 mesh (500- to 420-μ-diam) microspheres produced by the sol-gel column forming technique, while the fine fraction was −325 mesh (less than 44-μ-diam) microspheres produced by the sol-gel "stirred pot" forming technique. All attempts at mechanical blending or simultaneous separate feeding resulted in gross segregation and low packing densities. Sequential loading, in which the coarse fraction is first loaded into the tube and the fine fraction then infiltrated from the top, produces the highest density and most uniform packing. The tests indicate that a vibrational frequency of 60 cps provides the best loading rates with no loss in final pack density. A light follower rod will increase the packing density from 82.5% of theoretical to 83.5% and permit extended vibration without segregation.

Although not all the variables have been optimized, as long as the tube diameter is at least ten times the coarse-fraction microsphere diameter and the size ratio of the coarse to fine microspheres is approximately 10, pack densities of approximately 83% are readily attained. The volume ratio of coarse to fine particles, which in the case of sol-gel thoria microspheres is the same as the weight ratio, is 2.73 for maximum pack density. Both larger and smaller microsphere diameter and volume ratios adversely affect either the loading time or the final pack densities.

Equipment is being set up in a glove box to fabricate irradiation test rods by this technique.

BASIC PHYSICAL STUDIES ON SOL-GEL-PREPARED CERAMIC MATERIAL

Sintering and Grain Growth of Sol-Gel Thoria and Urania

M. J. Bannister[31] H. Beutler[32]
J. W. Prados[33]

We continued our study of the sintering kinetics and concurrent grain growth of sol-gel-derived

---

[29] R. K. McGeary, *J. Am. Ceram. Soc.* **44**(10), 513–22 (October 1961).

[30] J. E. Ayer and F. E. Soppet, *J. Am. Ceram. Soc.* **48**(4), 180–83 (April 1965).

[31] On loan from AAEC Research Establishment, Lucas Heights, Australia.

[32] Noncitizen employee from Switzerland.

[33] On leave from the University of Tennessee.

thoria. The release of surface enthalpy during sintering was determined by differential thermal analyses, as reported earlier.[34] Quantitative calibration of the DTA apparatus, using the heats of transformation for barium carbonate (at 800°C) and zirconium dioxide (at 1124°C), enabled the surface enthalpy to be measured quantitatively. This produced a value of 1060 ± 220 ergs/cm^2 for the surface enthalpy of the thoria gel at an average temperature of 970°C. Although the crystal faces present in the thoria gel are not known, we expect that low-energy faces would predominate. Predicted values for a (111) plane (the lowest energy surface in thoria) range from 810 to 1290 ergs/cm^2.

Changes in crystallite size and BET surface area during sintering have been determined. From the broadening of (111), (220), and (311) reflections, the x-ray crystallite size increased and the BET surface area decreased with increase in both time and temperature. The experimental results are shown in Fig. 32.9. No simple laws described this behavior. However, the fact that both crystallite size and surface area could be related directly to shrinkage, despite variation in sintering time and temperature, indicates that the processes of shrinkage, crystal growth, and surface area change respond in the same way to changes in temperature.

The shrinkage rates of thoria sol-gel microspheres were determined by hot-stage microscopy. Individual microspheres were held at carefully concontrolled temperatures, and the process of shrinkage was followed by sequence photography. An initial linear shrinkage of 4% was consistently observed as the volatile content of the gel was removed during heating; after this period the additional shrinkage followed a power law,

$$\Delta L/L_0 \propto t^n ,$$

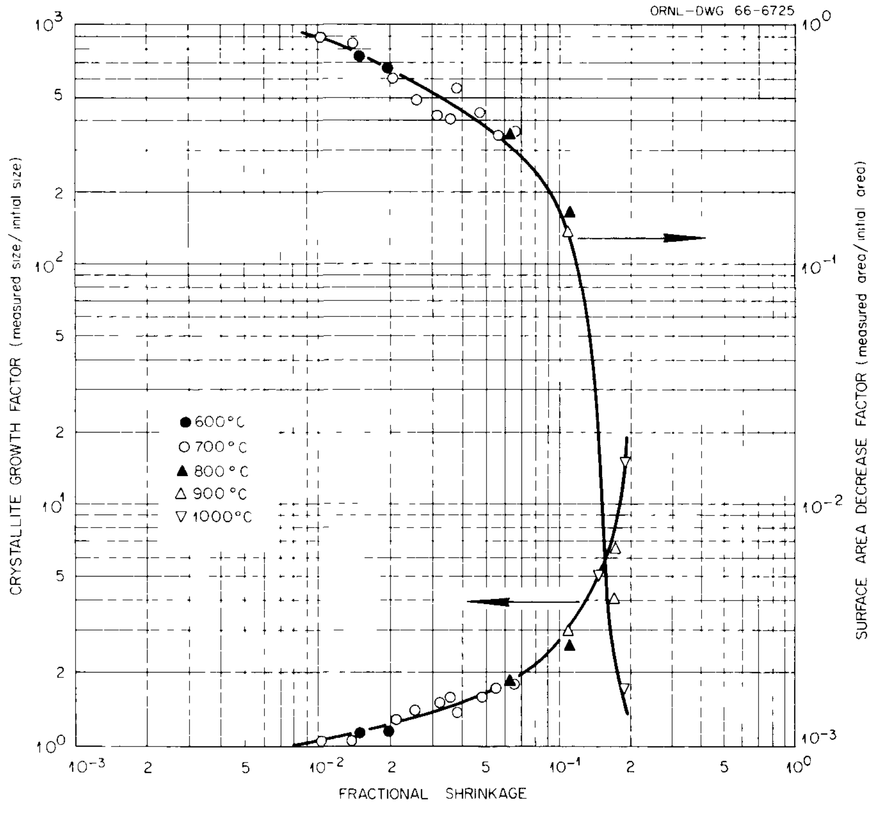

Fig. 32.9. The Relationship Between Crystallite Size, BET Surface Area, and Fractional Linear Shrinkage on Heating to Various Temperatures.

---

[34] M. J. Bannister, *Metals and Ceramics Div. Ann. Progr. Rept. June 30, 1965*, ORNL-3870, pp. 281–82.

at constant temperature, where *n* decreased from 0.3 at $\Delta L/L_0$ values of 0.01 to 0.02 to about 0.2 at $\Delta L/L_0$ values around 0.1. The maximum fractional shrinkage observed during the experiments was 0.26 after 85 min at 1138°C, compared with a predicted value of 0.27 for shrinkage to theoretical density. The activation energy of the process responsible for shrinkage was determined by measuring the effect of temperature changes on shrinkage rates. We derived a mean value of 63 kcal/mole (standard deviation of a single determination was 9 kcal/mole) and found that within experimental accuracy the activation energy did not vary with shrinkage or with magnitude or direction of the temperature changes.

Using hot-stage microscopy, we also began investigation of the sintering behavior of sol-gel-derived urania microspheres. Preliminary shrinkage measurements indicate that complete densification of the UO_2 microspheres is obtained in dry hydrogen after 10 min at 1060°C and within 25 hr at 800°C. The total fractional linear shrinkage was 0.34, compared with a maximum of 0.35 for shrinkage to theoretical density. We have confirmed that the presence of moisture in hydrogen enhances the sintering of UO_2 sol-gel considerably; however, the water vapor also promotes oxidation of UO_2, as evidenced by the presence of nonstoichiometric phases in the composition range UO_2 to $UO_{2.2}$.

Drying of Gel

H. Beutler[32]

Recently we studied the merits of various drying and sintering procedures for sol-gel thoria and urania microspheres. This work is in direct support of the program aimed at establishing suitable remote fuel fabrication procedures. Sol-gel microspheres, as extracted from the spheroidizing column, contain considerable quantities of residual volatiles, particularly water, nitrates, organic solvents, and surfactants. Most of these volatiles can be easily removed by heat treatments either in air or in an inert atmosphere up to 600°C. However, the removal of the residual organics proved to be more difficult. In air the rapid oxidation of released organic compounds led to severe temperature excursions in bulk charges of microspheres and caused severe cracking. If the oxidation was suppressed by heat treating in an inert atmosphere, the removal of organic materials was incomplete, leading to high residual carbon contents in the fully sintered product. Both these problems were successfully eliminated by heat treating wet sol-gel particles in superheated steam. We determined the removal of organics by steam from thoria and urania microspheres as a function of time at 200 and 400°C. These results are shown in Fig. 32.10, together with the results of alternate treatments for comparison. The mechanism of the steam-organic reaction is not known; however, the data indicated that the reaction is strongly temperature dependent in the region investigated. The removal of residual organics from UO_2 sol-gel microspheres by steam was less complete than from thoria. We attribute this to the more rapid sintering of UO_2, which occurs to a measurable extent even at temperatures as low as 400°C. The sintering inhibits the escape of volatile organics or carbon produced from them.

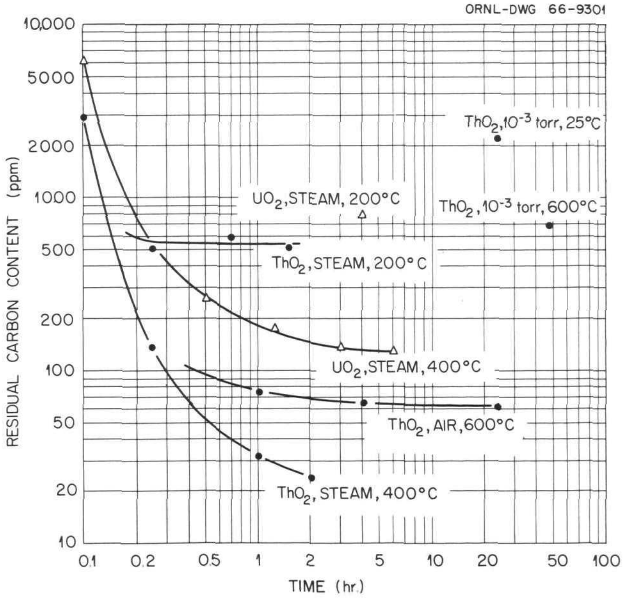

Fig. 32.10. Effect of Various Drying Procedures on Residual Carbon Content of Thoria and Urania Sol-Gel Microspheres.

Part V.

Other Program Activities

page blank

33. Isotopic Heat Source Development

R. J. Beaver

A program was inaugurated with the Isotopes Division to investigate materials of current and future interest for encapsulating isotopes to be used as heat sources. The value of these sources rests primarily on their ability to operate unattended for relatively long periods of time at elevated temperature for powering thermoelectric and thermionic devices. Our attention during the past year has been directed mainly at electron-beam welding techniques for sealing refractory-metal containers and at the evaluation of the mechanical properties of the tantalum-base alloys T-111 and T-222 as encapsulating materials for alpha-emitting isotopes. We also examined compatibility in iridium brazed with platinum to a W–2% Mo alloy.

In addition, we assisted in design evaluations by calculating thermal conductivities of a bed of PuO_2 spheroids in various inert atmospheres and of solid and liquid promethium.

WELDING OF REFRACTORY-ALLOY CAPSULES

R. G. Donnelly

A major problem in encapsulating alpha-emitting isotopic heat sources for high-temperature applications is the requirement that crack-free full-penetration welds be produced in tungsten-, molybdenum-, and tantalum-base alloys by remote operation. These containers are basically pressure vessels, since helium is continuously generated by the sources, therefore, high-strength ductile joints are required. The electron-beam welding process is attractive for this application because (1) an excellent welding atmosphere (a vacuum of 10^{-4} to 10^{-5} torr) is inherent with this process, (2) generally superior results are obtained on refractory alloys due to minimum heat input and contamination, and (3) the modular equipment required for the process is available commercially.

With the assistance of the Isotopes Division personnel, we adapted electron-beam welding equipment for remote operation in a hot cell. Figure 33.1 illustrates the electron-beam welding assembly, its power supply, and its accessories prior to installation in the cell. The unique features of this apparatus are its compactness and its maneuvering ability as a unit within the hot cell. The vacuum welding chamber incorporates a rotating chuck for making welds, and the entire setup was designed with programmed welding in mind.

The welding of caps to W–2% Mo containers with 0.090-in.-thick walls was investigated using this equipment. The alloy had been arc-cast and extruded into a bar, from which containers approximately 1 in. in diameter had been machined. Full-penetration, crack-free welds were obtained using 240 ma at 30 kv and 20 in./min travel speed. A typical result is illustrated in Fig. 33.2. The very coarse grain size in the weld region is characteristic of this alloy. Notable is the lack of porosity and the small amount of excess weld metal or "overhang" associated with this weldment. Overhang for this alloy was maintained to less than 0.020 in. of the original diameter.

The weldability of W–26% Re alloy using the same design was also evaluated. Most of the W–26% Re was a powder-metallurgy product, extruded into bar by the filled-billet technique. Some of the caps that were welded to the containers were an arc-cast and extruded product. The problem associated with welding the W–26% Re alloy was the development of fusion-line

R-25658

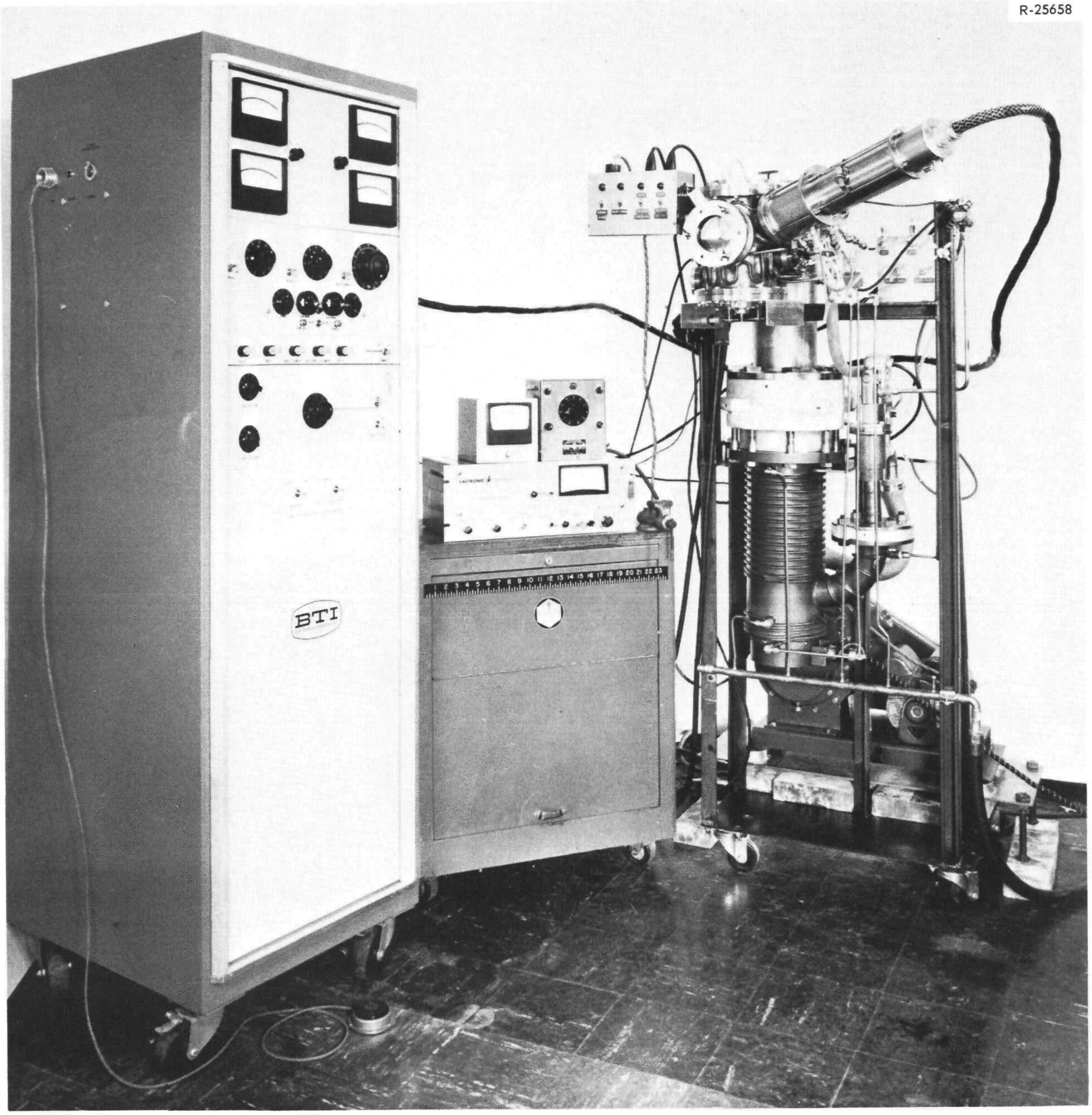

Fig. 33.1. Modular Electron-Beam Welding Equipment with Power Supply and Controls at Left and Electron Gun Mounted on Vacuum System at Right.

porosity of appreciable magnitude. Figure 33.3 compares a joint in which both cap and container were powder-metallurgy products with one in which the cap was from arc-melted and extruded stock. In the latter case porosity was observed only in the fusion line near the capsule body. The welding conditions were 220 ma at 30 kv and 20 in./min travel speed. Figure 33.3 also illustrates the greater overhang in welding these capsules compared to the W–3% Mo containers, although the power input was less. This result may be due to the lower melting point of the W–26% Re alloy and possibly to its greater fluidity.

Fig. 33.2. Section of Electron-Beam Weld in W–2% Mo Alloy. 16×. Notice the larger grain size but absence of porosity and weld metal overhang. Reduced 25%.

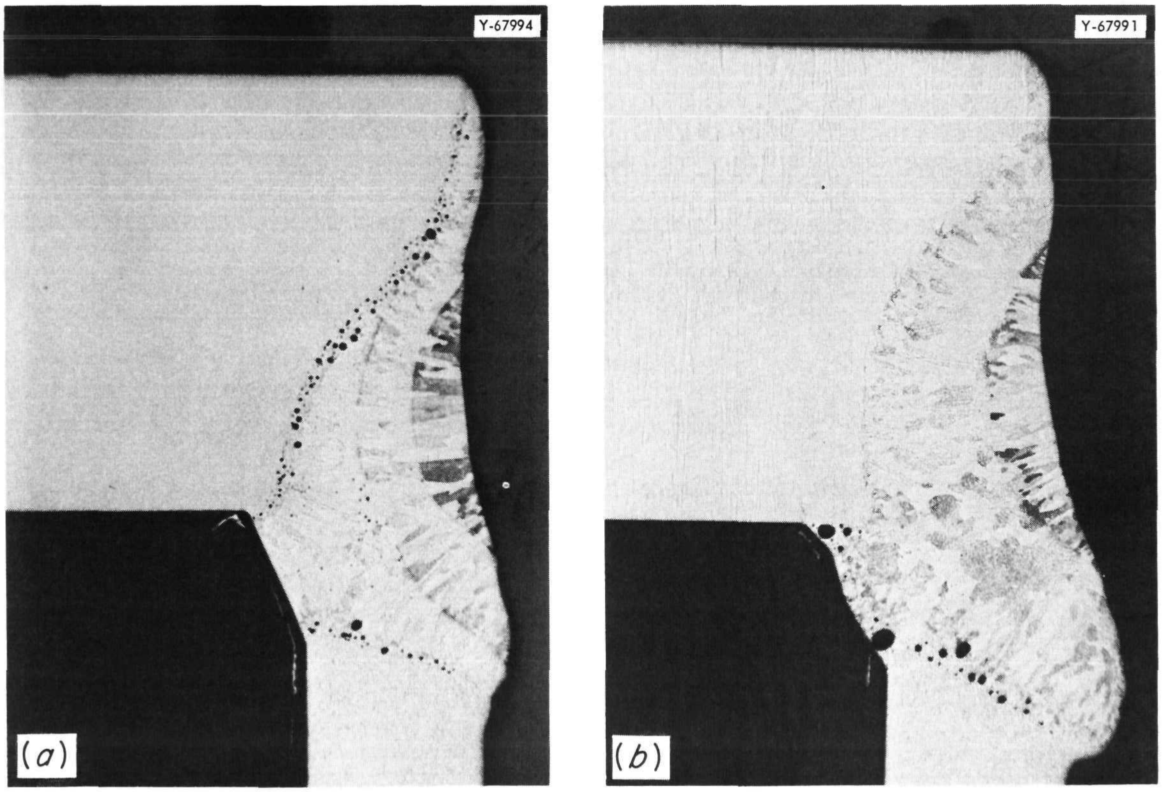

Fig. 33.3. Electron-Beam Welds *in* W–26% Re Alloy. 16×. *Etched with solution* of hydrogen peroxide and ammonia. (*a*) Both parts powder-metallurgy product; porosity shows at both fusion lines; wall thickness of smallest section is 90 mils. (*b*) Arc-cast cap (heavy section) and powder-metallurgy capsule body; porosity shows only at the capsule body fusion line. Reduced 25%.

CREEP BEHAVIOR OF REFRACTORY-ALLOY CAPSULES

H. E. McCoy R. L. Stephenson

The decay of an isotopic heat source is often accompanied by the release of alpha particles, and hence one must contain not only the isotope but also the gas that is released. The gas release will continue with time, but the temperature will decrease as a significant portion of the isotope decays. This reduction in temperature will also tend to decrease the gas pressure. Hence, the encapsulating material will have a complex history of temperature and internal pressure, which must be taken into account in the design.

An analytical technique was developed for obtaining reasonable design values for an isotopic source container.[1] First, one must obtain constant-load creep data at several temperatures. At each temperature these data must be described by an equation of the form

$$t_\epsilon = (A/\sigma)^n \, , \tag{1}$$

where t_ϵ is the time in hours to a particular strain ϵ, σ is the stress in psi, and A and n are constants for the material in question.

Through the use of the materials constants derived in this manner, the time for a given amount of strain t_ϵ under a constant rate $\dot{\sigma}$ of stress increase can be calculated using the expression

$$A^n = \dot{\sigma}^n t_\epsilon^{n+1}/(n+1) \tag{2}$$

developed by Kennedy.[2]

The temperature T of the isotope container will vary with time t according to the equation

$$T = (T_0 - T_a) \exp(-0.693t/\tau_{1/2}) + T_a \, , \tag{3}$$

where T_0 is the initial temperature, T_a is the ambient temperature, and $\tau_{1/2}$ is the half-life of the isotope.

To determine the creep properties under constant load at variable temperature, the Larson-Miller parameter P is used. This parameter is defined by

$$P = T(C + \log t_\epsilon) \, , \tag{4}$$

where T is the absolute temperature and C is a constant. The raw constant-load creep data are plotted as log σ vs P. For any temperature it is possible to obtain the information to make a plot of log σ vs log t_ϵ and to determine values for the materials constants A and n. Then Eq. (2) can be used to predict the creep behavior at a constant stress rate.

A computer program has been used to combine these steps to derive a plot of log t_ϵ vs log $\dot{\sigma}$ that is temperature compensated to match the history of the capsule. A plot of this type is shown in Fig. 33.4 for a T-111 capsule containing ^{238}Pu. This plot could be used by taking the original stress rate in the capsule and reading vertically to obtain the time to failure. This procedure should be used cautiously because (1) the stress rate is assumed constant, whereas it actually decreases with time, and (2) the temperature at the point of intersection is assumed to apply during the entire life. These effects tend to be compensating, and in many instances the predicted life will probably be shorter than the life actually observed.

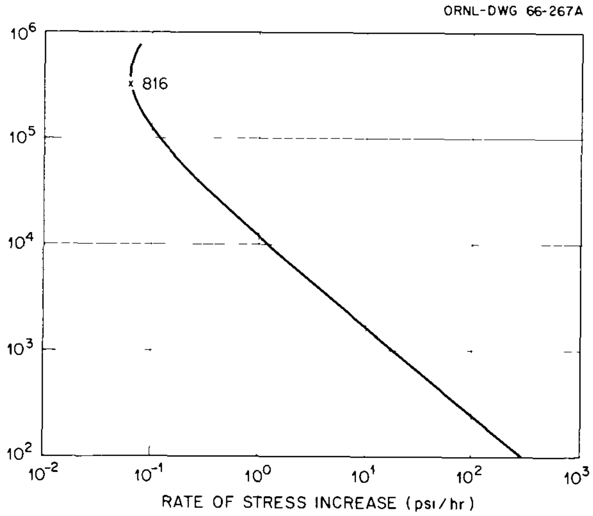

Fig. 33.4. Stress Rate Envelope for T-111 Capsule Containing ^{238}Pu.

---

[1] R. L. Stephenson, *An Approximate Method for Determining Allowable Stress Rates for Capsules Containing Helium-Producing Isotopes*, ORNL-TM-1436 (May 1966).

[2] C. R. Kennedy, *Metals and Ceramics Div. Ann. Progr. Rept. May 31, 1962*, ORNL-3313, pp. 44–45.

Also, we have measured[3] creep-rupture properties of T-222 (Ta–9.6% W–2.4% Hf–0.01% C), a candidate material for such capsules, over the temperature range 980 to 1650°C. The data obeyed Eq. (1). Stress-rate tests were also performed to establish the applicability of Eq. (2) to this alloy.

A generally accepted practice when alpha-emitting isotopes are sealed within a container is to specify full-penetration weldments to the capsule body. Since substantial internal helium pressures are generated throughout the life of the capsule, the joint should be as strong and ductile as the base metal. We tested T-222 welded joints to assess joint efficiency.[3] Sheet specimens 0.060 in. thick containing a transverse weld consistently failed in the base metal. However, a limited number of specimens taken from a weld in $\frac{1}{4}$-in.-thick plate failed in the weld with very low elongation. The effect of section size and heat input on the weldability of this alloy must be studied further before it is used for this application.

BRAZEMENT COMPATIBILITY STUDIES

R. J. Beaver T. K. Roche[4]

In thermoelectric and thermionic applications it is desirable to have efficient and oftentimes directional heat transfer. Brazement between two materials is a common method employed for this purpose. We have evaluated the compatibility of brazements of iridium joined to W–2% Mo alloy with platinum after heat treatments of 200 hr at 1500 and 1725°C in a vacuum of 10^{-8} torr. As illustrated in Fig. 33.5, Kirkendall diffusion voids are formed, the deterioration of the heat-transfer efficiency is obvious. Measurements of the hardness impressions shown in this illustration revealed an increase from 300 to 550 DPH, indicative of the formation of a hard, probably brittle, phase in the braze region.

THERMAL-CONDUCTIVITY CALCULATIONS

D. L. McElroy

The compound $^{238}PuO_2$ is a promising isotopic heat source. A method for preparing a heat source of this type is to pack spheroids of the oxide into a container. In this case, the effective thermal conductivity is an important design parameter. The effective thermal conductivity between 1000 and 1500°C was calculated for a powder consisting of PuO_2 spheres with an average diameter of 150 μ packed to give a 20% void volume. In three cases calculated, the void was vacuum and helium at 1 and 10 atm. This estimate involved a semiempirical method for obtaining the contribution of solid contacts, continuous-phase conduction, and radiation heat transfer. At 1500°C the three cases considered yielded thermal-conductivity values of 0.00176, 0.01345, and 0.01745 $w\ cm^{-1}\ {}^{\circ}C^{-1}$, respectively.

Promethium-147 is also a candidate isotopic heat source, but the physical properties of this isotope are almost completely unknown. To assist design studies involving this isotope, we estimated the thermal conductivity of both solid and liquid promethium.[5] This work is summarized in Part I, Chap. 8 of this report.

---

[3] H. E. McCoy, *Creep-Rupture Properties of the Tantalum-Base Alloy T-222*, ORNL-TM-1576 (in preparation).

[4] Now with Union Carbide Corporation, Stellite Division, Kokomo, Ind.

[5] R. K. Williams and D. L. McElroy, *Estimated Thermal Conductivity Values for Solid and Liquid Promethium*, ORNL-TM-1424 (March 1966).

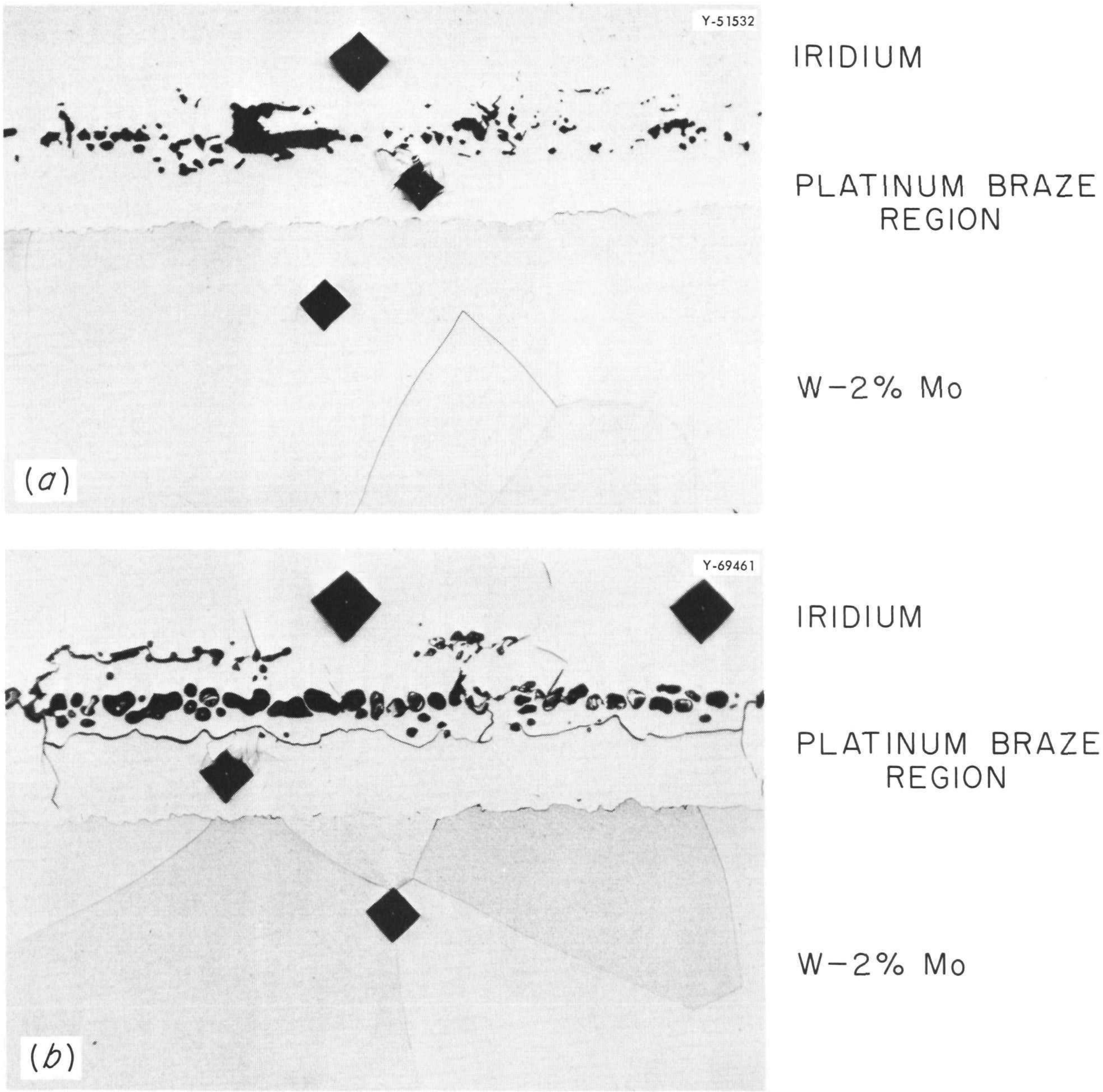

Fig. 33.5. Effects of 200-hr Heat Treatments on Iridium Brazed to W–2% Mo Alloy with Platinum. 200×. (*a*) 1500°C. (*b*) 1725°C. Reduced 21%.

34. Metallography

R. J. Gray

This group operates principally in a service capacity, providing metallographic assistance to the Metals and Ceramics Division and other divisions. We prepare, examine, and interpret ceramic and metal microstructures, and obtain, assemble, and transmit data to requesters. Evidence of our work is found throughout this report, as well as in most of the other reports originating in the Metals and Ceramics Division, in the form of photomicrographs and macrophotographs. Also, we did all of the postirradiation metallographic examinations and most of the electron-beam microprobe analyses.

In addition to providing direct service, we try to stay abreast of new techniques and equipment and develop our own as well. Some of the more pertinent developments of the past year are reported below.

MICROSTRUCTURAL DISCRIMINATION BY DEPOSITION OF SURFACE FILMS

J. O. Stiegler[1] R. J. Gray

Phase distinction from the appearance of surface films formed by heat tinting, stain etching, and anodizing has been successfully used for many years, because the film thickness produced by oxidation or anodization depends on the composition of the underlying phase. As a result, each phase shows a characteristic interference color. The technique, unfortunately, is limited to the very few alloy systems that form suitable surface films. In 1960, Pepperhoff[2] observed that surface films of uniform thickness deposited by vacuum evaporation also distinguish different phases by an optical phase shift at the film-metal interface, which depends on the optical constants of the film and the underlying metal. This extends the range of phase identification by surface films to all metal-alloy systems. Experimental details for employing this technique, which we call deposition etching, have been reported[3] along with some examples of the use of the technique in resolving fine structures and in determining the amounts and distributions of phases.

THE PRESENT STATUS OF METALLOGRAPHY[4]

R. J. Gray

The metallographer has a prime responsibility as a member of a metallurgical or, in many laboratories, a materials team. In addition to his duties of specimen preparation and of assistance in interpretation of microstructures, he must keep abreast of new techniques and developments in his field or develop his own as they are needed.

The nuclear and space ages have created new problems for the metallographer. The daily remote handling of highly radioactive and toxic materials, which only a few years ago were textbook curiosities, has removed the "touch" formerly considered

---

[1] Electron Microscopy Group.

[2] W. Pepperhoff, *Naturwissenschaften* **16**, 375 (1960).

[3] J. O. Stiegler and R. J. Gray, *Proceedings of the 20th AEC Metallographic Group Meeting Held May 18–20, 1966, Denver, Colorado,* to be published by The Dow Chemical Company, Rocky Flats Division, Golden, Colo.

[4] Presented at the Sixty-Ninth Annual Meeting of the American Society for Testing and Materials held in Atlantic City, N.J., June 27–July 1, 1966.

an essential part of metallography. Almost all the preparational and investigational steps performed in a conventional laboratory can be carried out by remote operations.

New techniques to reveal the microstructure by staining, anodizing, and vacuum evaporation are becoming very useful. Autoradiographic and microradiographic techniques complement the standard methods of observing the microstructure. Some techniques that produce color in the microstructure have enhanced the art tremendously. This enhancement is not confined to an aesthetic appeal. Many reaction mechanisms, such as corrosion and diffusion, and crystallographic orientations have been understood more clearly and can be communicated with less confusion by referring to areas of distinctive colors. This information can be photographically recorded and processed in the laboratory by following rigid procedures.

The development of certain commercial equipment allied to the responsibilities of the metallographer has been a big help. The electron microscope has been a valuable tool in surface studies by replication techniques and is even more valuable in transmission studies. The many attachments available for the electron microscope today make it useful for numerous applications. The pressing need for chemical analyses of minute areas has been relieved with the laser in emission spectroscopy, the ion-microprobe mass spectrometer, and especially the electron-beam microprobe analyzer. Hot-stage microscopy allows us to view grain-boundary movements and many other features formerly confined to the imagination. Qualitative data are obtainable now in a fraction of the time formerly required. Along with this development of commercial equipment, many "in-lab" developments and modifications show great promise.

The availability of technical metallographers is a problem today. Current trends in metallurgy and materials science curricula seem to be decreasing the amount of metallographic training. If this trend continues, we may have a serious shortage of metallographers and a subsequent equally serious shortage of metallographic technicians, who must depend on technical metallographers for instruction and guidance.

Our responsibilities are to keep raising our standards of preparation and methods of examination, never to be content with "the way it is done today," and to try to pass this working philosophy to our co-workers of today and tomorrow.

AN EFFECT OF CURING STRESSES IN EPOXY MOUNTING RESINS

R. S. Crouse

The Welding and Brazing Group prepared T-joint test brazes of tantalum with a series of experimental titanium-zirconium alloys. Prior to submission to the Metallography Group, the joints were dye-penetrant inspected, and some of the joints were subjected to a severe mechanical test in which the leg of the "T" was hammered flat. Tests that showed no cracks on inspection and/or survived the "hammer test" were mounted in Araldite 502 epoxy resin[5] for metallographic preparation.

Even though no indication of cracking had been revealed by previous tests, the joints all showed cracks in the braze upon examination after polishing. The cracks appeared to be related to the shrinkage that takes place in mounting material as it cures. Figure 34.1 shows a typical crack. The shrinkage is not confined to the Araldite 502, for several other brands of epoxy resins were used for mounting with similar results.

To visualize the stresses in a metallographic mount, an entire mount was photographed in polarized light: Fig. 34.2. A small sharp loop can be seen at the fillet of the braze joint. A larger loop, which is indicated by an arrow, was caused by a set screw used to hold the mount in a weight for polishing on a vibratory polisher. We also tried[6] to determine the magnitude of stresses developed in the curing of the epoxy by attaching micro strain gages to a T-joint prior to mounting. Although some strain was recorded, the T-joint did not fracture before the test was terminated.

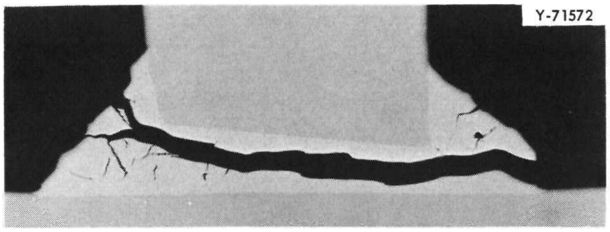

Fig. 34.1. Typical Crack in Brazed T-Joint. 100×. Reduced 24.5%.

---

[5] Ciba Products, Summit, N.J.

[6] This work was done by J. H. Smith of the Metallurgical Services Group at Y-12.

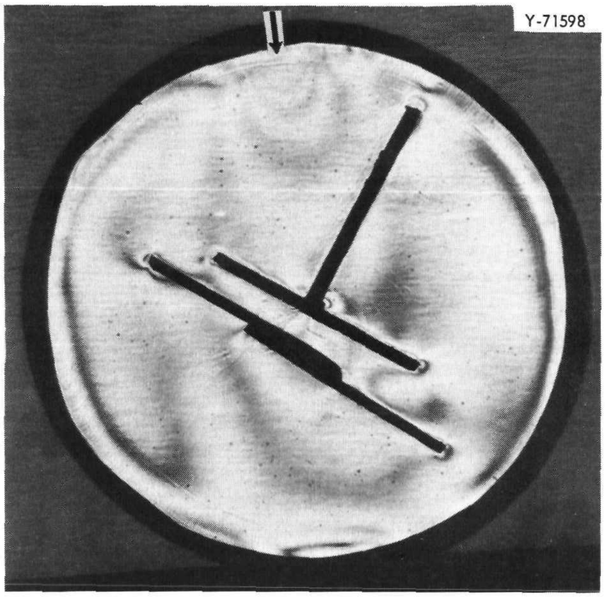

Fig. 34.2. Stress Lines in an Epoxy-Mounted Specimen.

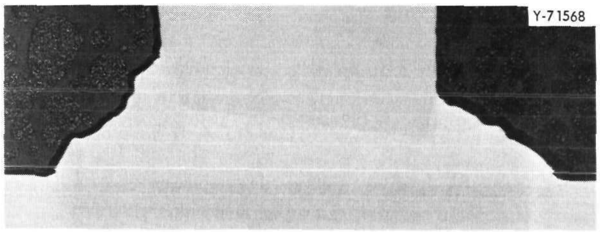

Fig. 34.3. Brazed T-Joint Mounted in Pelletized-Alumina-Filled Epoxy Resin. 100×. Reduced 27%.

Cracking can be prevented in unbent samples by mounting them in epoxy resin filled with pelletized alumina. Figure 34.3 shows the results of this technique. Nickel plating will also preserve the sample without cracking. Bent T-joints will eventually develop cracks even in filled epoxy, but we feel that modifications of the mounting technique may eliminate them.

More complete details of this investigation have been reported.[7]

INFLUENCE OF PREPARATION OF METAL SPECIMENS ON THE PRECISION OF ELECTRON-BEAM MICROPROBE ANALYSIS[8]

M. L. Picklesimer[9]   G. Hallerman

The preparation of the surfaces of metal specimens for electron-beam microprobe analysis has been the subject of much discussion, yet there has been no definitive study of the matter. Some of the factors that could affect the accuracy of the analysis are (1) surface roughness due to scratching, rumpling, polishing relief, and etching relief; (2) preferential leaching of one element from the matrix during etching, pitting during etching, and deposition of extraneous or reacted elements from the etchants; (3) smearing of the surface and deep cold working during polishing; and (4) surface films formed by low-temperature oxidation, anodization, and electrolytic polishing and etching. Most of these factors have been examined in controlled experiments for their effects on the precision of the microprobe analysis.

Traverse analyses made on pure copper grids of thicknesses ranging from 50 to less than 2 μ showed no loss of signal from a 2-μ thickness when the takeoff angle was 35° but a loss of 10% when the takeoff angle was 15.5°. The losses increased with grid thickness.

Traverse analyses made on a heavily segregated 50% Cu–50% Ni alloy in the conditions of lightly etched, heavily etched, and ground on 3/0 paper showed no loss of signal at a takeoff angle of 35° and a 2% loss of signal at a takeoff angle of 15.5°, when the as-polished condition was used as a standard. Elevation differences in the heavily etched and in the ground conditions were 1 to 2.5 μ.

Anodically formed oxide films on zirconium and on an Nb–33% Zr alloy had no effect on the operation of the electron beam and caused only a small loss of signal (and error in the analysis) when the zirconium standard specimen was anodized to the same film thickness.

Intercomparison of traverse data for an Al–40% U alloy in the conditions as-polished, lightly etched,

---

[7] R. J. Gray and R. S. Crouse, "An Effect of Curing Stresses in Epoxy Resins," *Proceedings of the 20th Metallographic Group Meeting Held May 18–20, 1966, Denver, Colorado*, to be published by The Dow Chemical Company, Rocky Flats Division, Golden, Colo.

[8] Abstract of paper presented at The First National Conference on Electron Probe Microanalysis, University of Maryland, May 3–6, 1966. Submitted for publication.

[9] Zirconium Alloy Development Group.

and heavily etched showed no loss of accuracy in the analysis at a takeoff angle of 35° whether the analysis was for aluminum or uranium. The differences in elevation in the heavily etched specimen were estimated to be between 1 and 2 μ.

Smearing of one phase over another, leaching during etching, and deposition of an element during etching (either from the components of the etchant or from the reacted components of the specimen) can each cause an error in the accuracy of the analysis when the affected layers are only 10 to 200 A in thickness. The critical layer thickness depends partly on the element concerned, the sensitivity of the analysis, and whether or not the layer is one of the phases present in the specimen. Estimates of critical layer thicknesses can be obtained from the equations presented.

The general problems discussed are those of selecting the section of the specimen to be cut, the type of surface preparation to be used, the interpretation of the effects of preparation, and the type of information that can be obtained from the specimen.

CERIUM DICARBIDE METALLOGRAPHY

T. M. Kegley, Jr.

Previously[10,11] we reported on the preparation of thorium and thorium-uranium dicarbides, which required special metallographic procedures because of their reactivity with moisture. Cerium carbides exhibit similar reactivity with moisture and also require special procedures.

We developed the following procedure. The cerium dicarbide specimen was mounted in epoxy resin, ground successively on 600-, 400-, and 300-grit silicon carbide papers with ethyl alcohol as the lubricant, and mechanically polished on a Metcloth-covered wheel with Linde A abrasive and ethyl alcohol. The specimen was then chemically polished by swabbing in a mixture of equal parts of concentrated lactic, acetic, and nitric acids, washed with ethyl alcohol, and electrolytically etched at 5 v for 10 sec in a solution of equal parts of concentrated lactic, acetic, and sulfuric acids. The etchant colors the dicarbide specimen a golden brown and passivates the polished surface to retard reaction and moisture. Figure 34.4 shows the cerium dicarbide microstructure developed by this procedure. The twinned structure is probably related to the cubic-tetragonal transformation that occurs in cerium dicarbide.[12]

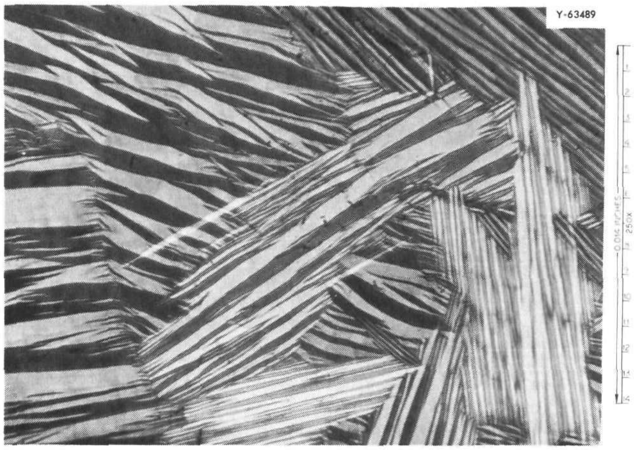

Fig. 34.4. Microstructure of Cerium Dicarbide Under Polarized Light. Etched electrolytically with equal parts concd lactic, acetic, and sulfuric acids. 250×. Reduced 48%.

MICROSTRUCTURES OF PYROLYTIC CARBON COATINGS

B. C. Leslie T. M. Kegley, Jr.

Pyrolytic-carbon-coated UC_2 particles from two different batches vibratorily polished 6 hr on a nylon cloth with a Linde A alumina–silicone oil slurry are contrasted in Figs. 34.5 and 34.6 with particles from the same batches vibratorily polished 4 hr on a nylon cloth with 0.5-μ diamond compound and water. These figures show the dependence of the structural appearance of pyrolytic carbon coatings upon the polishing method employed. In Fig. 34.5 the Linde A–silicone oil method reveals the laminar characteristic of the outer coating much better than the diamond-water method. Yet the dense character of this coating appears to be better shown by the diamond-water method.

---

[10] T. M. Kegley, Jr., and B. C. Leslie, *Metals and Ceramics Div. Ann. Progr. Rept. June 30, 1964*, ORNL-3670, pp. 185–87.

[11] T. M. Kegley, Jr., and B. C. Leslie, *Metals and Ceramics Div. Ann. Progr. Rept. June 30, 1965*, ORNL-3870, pp. 301–2.

[12] N. H. Krikorian, T. C. Wallace, and M. G. Bowman, *Phase Relationships of the High Carbon Portion of the Lanthanide Dicarbides*, LA-DC-6814 (1964).

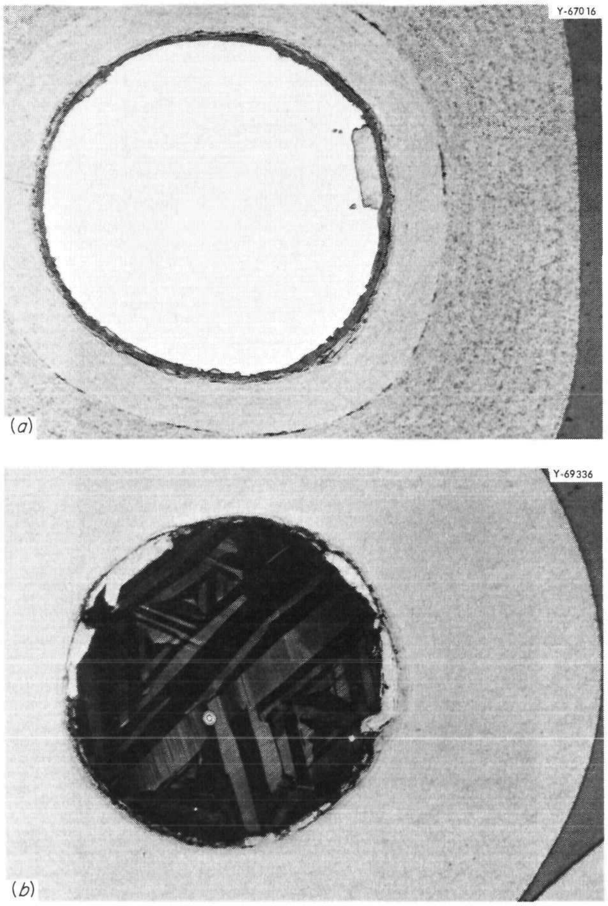

Fig. 34.5. Effect of Polishing Method on Appearance of Pyrolytic Carbon Coating Microstructures. (*a*) Linde A alumina–silicone oil method. (*b*) 0.5-μ-diamond–water method. 500×. Reduced 47.5%.

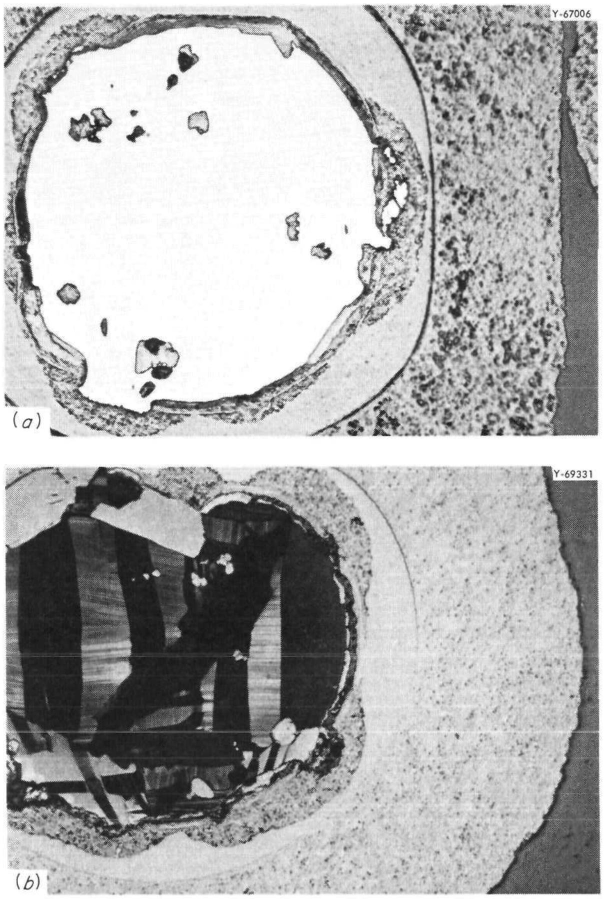

Fig. 34.6. Effect of Polishing Method on Appearance of Pyrolytic Carbon Coating Microstructures. (*a*) Linde A alumina–silicone oil method. (*b*) 0.5-μ-diamond–water method. 500×. Reduced 48%.

35. Rover Rocket Nozzle Materials

E. A. Franco-Ferreira

We are continuing to provide materials and fabrication support to the AEC-NASA Space Nuclear Propulsion Office on the Rover Nuclear Rocket Program. In general, we are providing technical liaison between NASA and its contractors, and, where necessary, performing appropriate experimental studies. This assistance has been directed toward the fabrication of nozzles to be used in static reactor test firings at the Nevada test site. Two types of nozzles are involved: NERVA nozzles for a 1000-Mw, 50,000-lb-thrust system and Phoebus nozzles for a 5000-Mw, 250,000-lb-thrust system. The work may be divided into two broad categories: studies in direct support of NASA contractor operations and studies aimed at developing a generalized rocket materials technology. Some aspects of the general experimental program will be discussed below.

MATERIALS EVALUATION

We evaluated a number of materials for the fabrication of nuclear nozzles. The alloys studied and their compositions are listed in Table 35.1. These alloys may be grouped into two general classifications: precipitation-hardened alloys and solid-solution-strengthened alloys. Two broad areas were covered in detail; these were mechanical properties and joinability. The mechanical-properties work included experimental determinations of the elevated-temperature short-time tensile behavior of the candidate materials. In the joinability studies, both the weldability and brazeability of the alloys were measured. The weldability determination was based on the use of a hot-ductility test, which measures the resistance of weld-heat-affected zones to hot cracking. The brazeability work used small sample T-joints to measure the wettability of the base metal by different brazing alloys under various furnace conditions.

Mechanical Properties

D. G. Harman

Short-time tensile tests were performed on the alloys listed in Table 35.1 at temperatures ranging from room temperature through 1800°F, using strain rates of 1.0, 0.1, and 0.01/min. Tests allowing a 30-min soak at temperature immediately before testing were also performed to determine the short-time stability of these alloys.

All alloys were tested in sheet form ranging from 0.053 to 0.064 in. in thickness except Inconel 625, which was tested as $^5\!/_{16}$-in.-diam rod swaged from $^1\!/_2$-in.-diam stock. All alloys were fully heat treated as prescribed by the supplier. We received IN-102 at a later date and are currently testing it.

The short-time tensile properties of these alloys were significantly affected by temperature and strain rate. Figure 35.1 shows the effect of temperature on mechanical properties measured at a strain rate of 0.1/min. The range of each property is shown for all alloys in each group. Note the convergence of properties at high temperatures.

In general, we observed higher strength and ductility values at the higher strain rate and lower values at the lower strain rate than those given in Fig. 35.1. An example of the effect of strain rate is shown by the change in the properties when the strain rate was changed from 0.1 to 0.01/min. The total elongation of Inconel X-750 at 1400°F decreased from 6 to 1.5%; the ultimate tensile strength of Inconel 625 at 1800°F decreased from 34,300 to 11,600 psi. Similar strain-rate effects were noted also at other temperatures and with the other alloys.

The 30-min soak at temperature had no effect on the mechanical properties of these alloys.

Table 35.1. Nominal Compositions of Candidate Nuclear Nozzle Materials

Alloy	Content (%)							
	C	Cr	Ni	Fe	Mo	Mn	Nb + Ta	Other
Precipitation-Hardened Alloys								
Inconel X-750	0.08	14–17	70 min	5–9		1.0	0.7–1.2	Al: 0.4–1.0 Ti: 2.25–2.75 Cu: 0.5
Inconel 718	0.10	17–21	50–55	Bal	2.8–3.3	0.5	4.5–5.75	Al: 0.2–1.0 Ti: 0.3–1.3 Cu: 0.75
René 62	0.05	15	Bal	22.5	9.0		2.25	Al: 1.25 Ti: 2.50 B: 0.01
Solid-Solution-Strengthened Alloys								
Hastelloy X	0.15	22	Bal	20	9.0			
Hastelloy N	0.04–0.08	6–8	Bal	5.0	15–18	1.0		Al + Ti: 0.5 Si: 1.0 W: 0.5
Inconel 625	0.05	22	Bal	3.0	9.0	0.15	4.0	
IN-102	0.06	15	Bal	7.0	3.0		3.0	Al: 0.5 Ti: 0.5 W: 3.0
Type 347 SS	0.08	17–19	9–13	Bal			10 × C min	

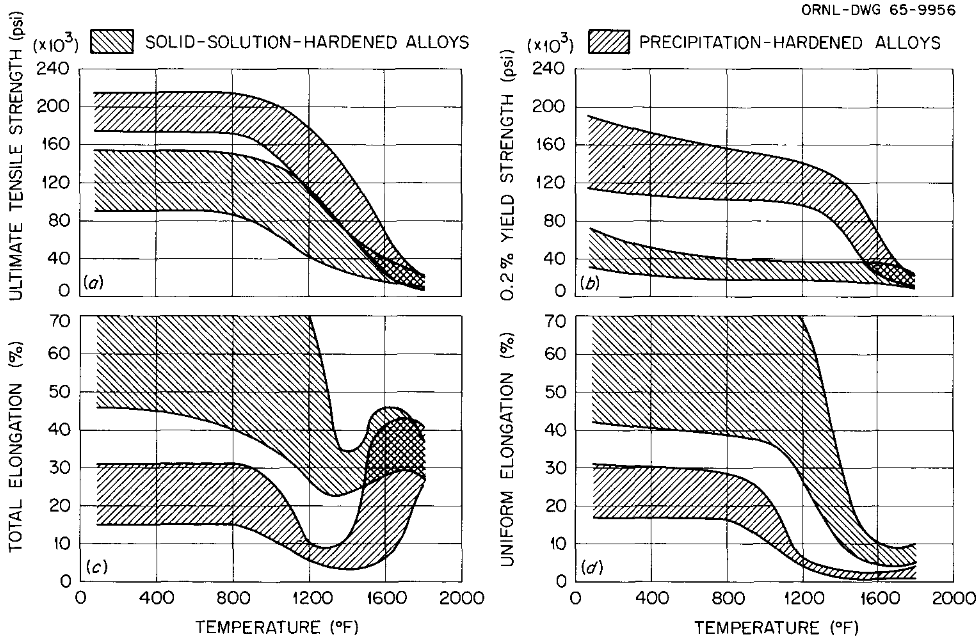

Fig. 35.1. The Effect of Temperature on the Short-Time Tensile Properties at 0.1/min.

Hot-Ductility Testing

J. M. Jones H. H. Scott[1]
E. A. Franco-Ferreira

The hot-ductility test, as developed by Nippes and Savage[2] was used to evaluate the weldability of several alloys. Weldability is determined from the behavior of the base metal in the weld heat-affected zone under a generalized welding thermal treatment. No inferences are made regarding the response of the bulk weld metal itself.

The method of application of the hot-ductility test has been discussed before.[3] An example of

---

[1] Co-op student from Missouri School of Mines.

[2] E. F. Nippes, W. K. Savage, and G. Grotke, *Further Studies of the Hot Ductility of High Temperature Alloys*, Rensselear Polytechnic Institute, Troy, N.Y. (June 1956).

[3] R. G. Gilliland, *Metals and Ceramics Div. Ann. Progr. Rept. June 30, 1964*, ORNL-3670, pp. 259–61.

ORNL-DWG 65-2496

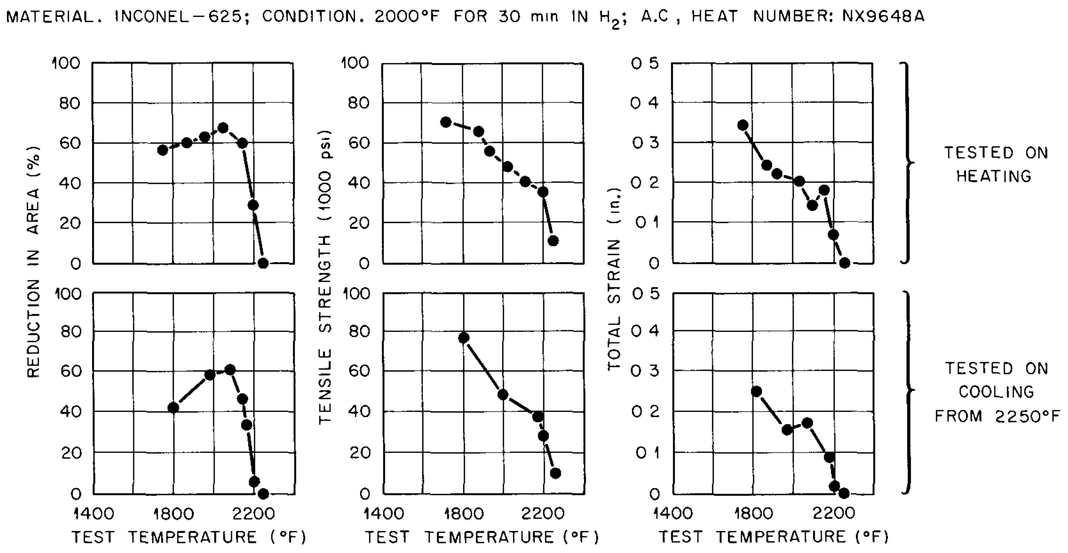

Fig. 35.2. Hot-Ductility Test Data for Inconel 625.

ORNL DWG 65-2491

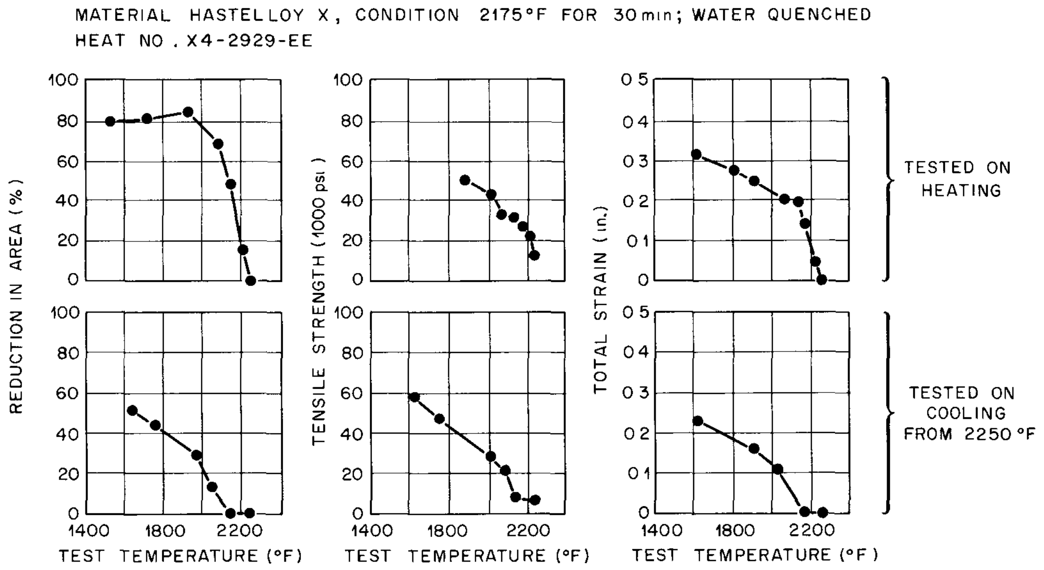

Fig. 35.3. Hot-Ductility Test Data for Hastelloy X.

the data obtained is shown in Fig. 35.2 for Inconel 625. The data for the "on cooling" tests show good recovery of the "on heating" properties and thus indicate good weldability. In contrast, Fig. 35.3 shows the poor recovery of the "on heating" properties for Heat X42929EE of Hastelloy X during the "on cooling" tests. This type of behavior usually indicates poor or marginal weldability. On the other hand, the behavior of three additional heats of Hastelloy X predicted satisfactory weldability. The results of the hot-ductility testing are summarized in Table 35.2.

Brazeability

L. C. Williams E. A. Franco-Ferreira

We determined the brazeability of the alloys listed in Table 35.1 by performing T-joint wettability tests using three powdered brazing alloys in different brazing atmospheres. Each completed T-joint was examined to assess the amount by which the brazing alloy wet and flowed on the base metal.

The brazing test conditions and results are presented in Table 35.3. These results lead to

Table 35.2. Results of Hot-Ductility Testing

Material	Vendor	Heat No.	Heat Treatment[a]	Peak Temperature on Heating (°F)	Nil-Ductility Temperature (°F)	Results
Type 347 SS	Unknown	Unknown	Mill annealed	2400	2400	Weldable
Hastelloy N	Stellite Division	Reactor grade	2150°F – ½ hr, AC	2400	2295	Weldable
Hastelloy X	Stellite Division	X42929EE	2175°F – ½ hr, WQ	2400	2250	Not weldable
Hastelloy X	Stellite Division	X52722EE	2175°F – ½ hr, WQ	2400	2250	Weldable
Hastelloy X	Stellite Division	X52731	2175°F – ½ hr, WQ	2400	2250	Weldable
Hastelloy X	Stellite Division	X52741	2175°F – ½ hr, WQ	2400	2250	Weldable
Inconel 625	International Nickel[b]	NX9648A	2000°F – ½ hr, AC	2400	2250	Weldable
IN 102	International Nickel	04528	1800°F – 1 hr, AC	2400	2250	Weldable
Inconel X-750	International Nickel	9699A	2100°F – 4 hr, AC 1550°F – 16 hr, AC	2400	2300	Weldable
Inconel X-750	International Nickel	3977X	2100°F – 4 hr, AC 1550°F – 16 hr, AC	2400	2300	Weldable
Inconel 718	International Nickel	4478EV	1750°F – 20 min, AC 1325°F – 8 hr, AC at 100°F/hr to 1150°F, 8 hr at 1150°F, AC	2400	2200	Weldable
René 62	General Electric	F507794	2175°F – ½ hr, WQ	2400	2250	Weldable

[a] AC = air cooled; WQ = water quenched.

[b] Huntington Alloy Products Division, International Nickel Co.

Table 35.3. Brazing Conditions[a] and Results[b]

Brazing alloy	Nioro[c]	Nioro	Nioro	J8600[d]	J8600	Premabraze 750[e]
Atmosphere	Vacuum	H_2	He	Vacuum	H_2	Vacuum
Temperature, °C	1010	1010	1010	1170	1170	1160
Results						
Inconel X-750	1		4	1	3	2
Inconel 718	2	1	4	1	3	
René 62	2		4	1	3	3
Hastelloy X	1	1		1	2	1
Hastelloy N	1	1		1	2	
Inconel 625	1	1		1	2	1
IN-102	1	3		1	3	
Type 347 stainless steel	1	1		1	2	3

[a] All times at temperature were 5 min.

[b] Class 1, very good wetting and flow; 2, fair wetting and flow; 3, wetting but no flow; 4, no wetting, no flow.

[c] Au–18% Ni.

[d] Ni–33% Cr–24% Pd–4% Si.

[e] Ag–20% Pd–5% Mn.

the following conclusions. Solid-solution-strengthened alloys have high brazeability. They are wettable by most brazing alloys and can be brazed in a variety of atmospheres. The brazing alloys flow well into tight joints. These materials do not require heat treatment after brazing. Precipitation-hardened alloys, on the other hand, have less brazeability. They are not highly wettable by all brazing alloys even in a vacuum. If they must be brazed in a gaseous atmosphere, the complication of protective coating of the base metal is added. The brazing cycle must also incorporate the specified precipitation-hardening heat treatment.

PHOEBUS NOZZLE FABRICATION STUDIES

In support of the Phoebus nozzle fabrication program, we are evaluating the mechanical properties of welds made in heavy section plates of Hastelloy X, Hastelloy N, and Inconel 625. To date, the work has been limited to Hastelloy X and Inconel 625.

Welding of Hastelloy X and Inconel 625 in Heavy Sections

E. A. Franco-Ferreira

Three heats of Hastelloy X and one heat of Inconel 625 plate 1 in. thick have been welded in a highly restrained configuration. These welds are being used to verify the weldability of the material and to provide specimens for subsequent mechanical-property tests. A view of the typical test weld setup with welding partially completed is shown in Fig. 35.4. As illustrated, the plates are highly restrained by being welded to a heavy steel strongback before the joint in the plates is welded. To date, plates from Hastelloy X heats X52722EE, X52731, and X52741 and Inconel 625 heat NX2172A have been welded. Careful manual welding procedures were used, which have generally resulted in high-quality welds.

The welds were x rayed, and sections were taken for metallographic examination. Hot-ductility tests were also run on the base metal. The metallographic examinations of the weld samples correlated quite well with the hot-ductility test results shown in Table 35.2. The freedom of the weld deposits from microcracking has also been verified.

Mechanical-Property Testing of Hastelloy X and Inconel 625 Welds

D. G. Harman

We are testing longitudinal and transverse mechanical properties of Hastelloy X and Inconel 625 welded plate at temperatures ranging from −321

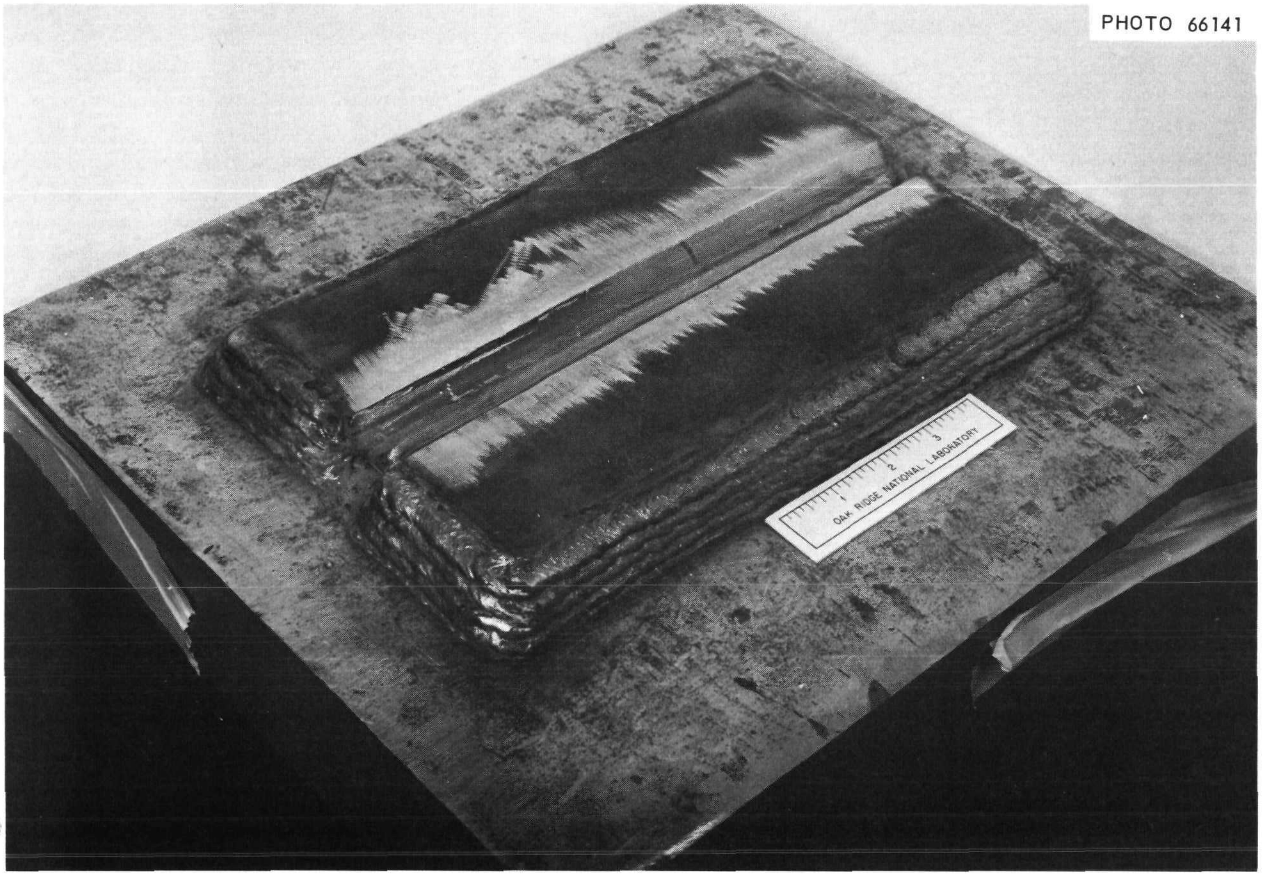

Fig. 35.4. Arrangement for Welding 1-in.-thick Plates of Hastelloy X.

to 1200°F. We tested longitudinal all-weld-metal specimens and transverse weld-joint specimens, including the effects of specimen location, strain rate, and postweld heat treatments. To date, short-time tensile tests of both notched and unnotched specimens have been conducted on welds from four heats of Hastelloy X plate and from one heat of Inconel 625 plate. These results are shown in Figs. 35.5 and 35.6. Both the Hastelloy X and Inconel 625 welds showed increasing strength at the cryogenic temperatures, and the as-welded ductility remained fairly high.

Since porosity was noted in the weld metal of some Hastelloy X welds, its effect on strength properties was studied. The presence of porosity lowered the ductility at cryogenic temperatures; one test showed only 3.5% elongation at −196°C compared with 20% for a sound specimen. Metallographic sectioning of these specimens revealed

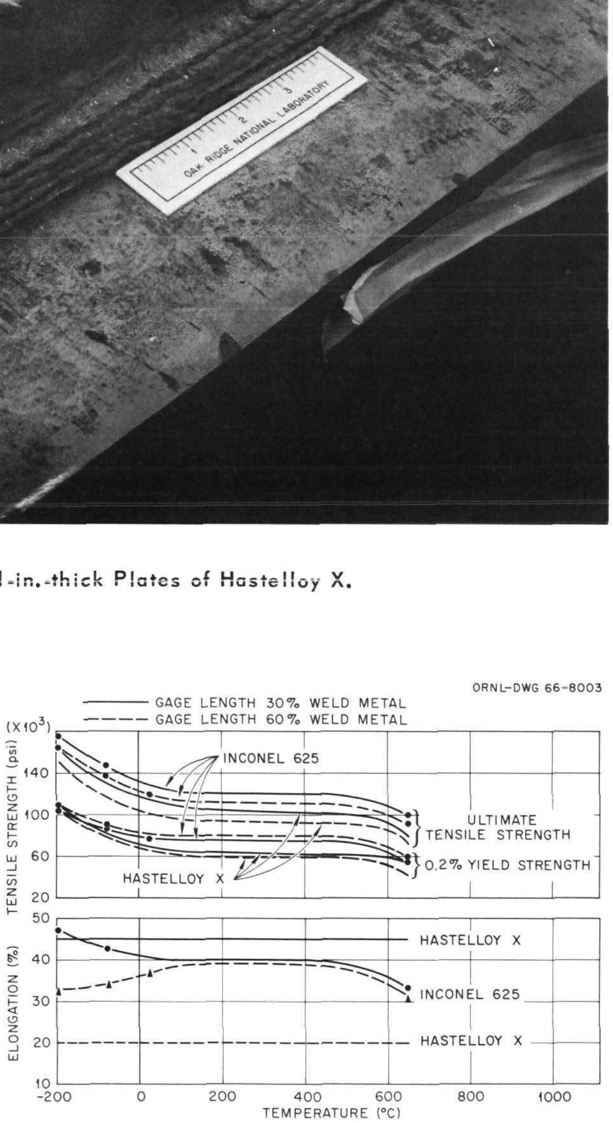

Fig. 35.5. Transverse Strength Properties of Hastelloy X and Inconel 625 Welds. Hastelloy X curves show average values from four heats of 1-in. plate butt welded with the same heat of weld rod. Inconel 625 data are on a single heat. Specimens tested as welded.

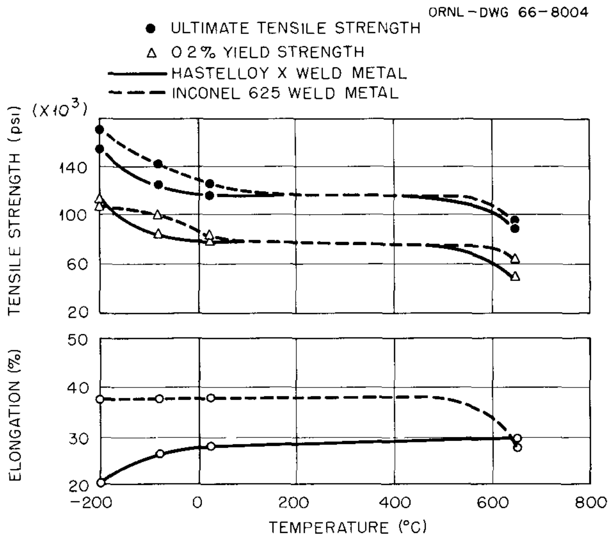

Fig. 35.6. Longitudinal Strength Properties of Hastelloy X and Inconel 625 Welds. Hastelloy X curves show average values from three butt welds on 1-in. plate welded with the same heat of weld rod. Inconel 625 data are from a single weld. Specimens tested as welded.

spherical pores ranging in diameter from less than 1 to 30 mils; many of the smaller pores had initiated cracks along weld-metal grain boundaries. Many pores were observed on the fracture surfaces.

Specimens with a $\frac{1}{16}$-in.-deep V-notch with a root radius of 1.5 to 2.4 mils (K_t, of 5.2 to 6.4) showed notch strengthening at all temperatures for both materials. Notches were located in the weld metal, the base metal, and the heat-affected zone.

PHYSICAL PROPERTIES OF NICKEL-BASE ALLOYS[4]

D. L. McElroy J. P. Moore
T. G. Kollie

The physical properties of four nickel-base alloys (Hastelloy N, Hastelloy X, Inconel 625, and Inconel 702) were estimated between −270 and 1000°C, based on λ and ρ measurements within this range. The thermal properties of Inconel 702 have been measured by three laboratories[5–7] with agreement better than 1% between 50 and 1000°C. The electronic component λ_E was calculated using $L_0 T/\rho$ and measured ρ values. This was subtracted from the measured λ to yield the lattice thermal conductivity λ_L. The lattice thermal resistivity $1/\lambda_L$ of Inconel 702 increased linearly to 100°C, was constant between 100 and 700°C, and increased linearly above 700°C. Extensions of the linear portions allowed prediction of λ_L and λ outside the range of λ measurements. A similar behavior was noted for Hastelloy N data[8] treated in this manner. Assuming this behavior to be typical of nickel-base alloys that exhibit short-range ordering, the limited data available on Hastelloy X and Inconel 625 were used to establish λ for these alloys by this process. Table 35.4 shows the estimated λ values for all four alloys. The estimates for Inconel 702 and Hastelloy N are within 1% of the measured values, and the deviations for Hastelloy X and Inconel 625 are less than 4% in the regions where measured values exist.

NONDESTRUCTIVE TEST DEVELOPMENT

K. V. Cook R. W. McClung

Since very-thin-walled tapered tubing is usually used for the fabrication of regeneratively cooled rocket nozzles, a sensitive method of determining the quality of this tubing was needed. We have developed a technique for the immersed ultrasonic inspection of tapered tubing and demonstrated the applicability of the technique for detecting longitudinal cracks on both the inner and outer surfaces of such tubing. The technique has been shown to be capable of detecting discontinuities with a depth less than 0.001 in.

Commercial pulsed ultrasonic instrumentation with an associated *B*-scan display system was used to generate, detect, and display the signals associated with the ultrasonic test. A 5-Mc lithium

---

[4] See Part I, chap. 8 of this report for explanation of mathematical symbols.

[5] M. J. Laubitz and K. D. Cotman, *Can. J. Phys.* **42**, 131–52 (1964).

[6] D. R. Flynn, National Bureau of Standards, private communication, 1963.

[7] J. P. Moore, W. P. Murray, and W. Fulkerson, *Metals and Ceramics Div. Ann. Progr. Rept. June 30, 1965*, ORNL-3870, p. 44.

[8] D. L. McElroy, T. G. Godfrey, and T. G. Kollie, *Am. Soc. Metals, Trans. Quart.* **55**, 740–51 (1962).

Table 35.4. Estimated Total Thermal Conductivity of Nickel-Base Alloys

Temperature ($^\circ$C)	Estimated Total Thermal Conductivity (w cm^{-1} $^\circ$C^{-1})			
	Hastelloy X	Inconel 625	Hastelloy N	Inconel 702
−270	0.020	0.020	0.020	0.020
−260	0.0295	0.0295	0.0295	0.0295
−250	0.0500	0.0532	0.0614	0.0876
−200	0.0594	0.0614	0.0690	0.0926
−100	0.0779	0.0777	0.0828	0.1031
0	0.0966	0.0937	0.0980	0.1171
100	0.1146	0.1103	0.1131	0.1290
200	0.1319	0.1259	0.1296	0.1467
300	0.1505	0.1422	0.1425	0.1644
400	0.1664	0.1593	0.1550	0.1821
500	0.1830	0.1731	0.1729	0.2000
600	0.2015	0.1926	0.1944	0.2209
700	0.2212	0.2132	0.2169	0.2433
800	0.2410	0.2342	0.2379	0.2606
900	0.2596	0.2539	0.2574	0.2815
1000	0.2772	0.2731	0.2758	0.3025

sulfate transducer was used to transmit and receive the ultrasonic pulses. The basic mechanical equipment was the same that we originally developed for the immersed ultrasonic inspection of conventional (nontapered) tubing.[9] The original equipment included an immersion tank and a scanner dolly to hold the search tube and transducer and maintain the tubing in proper alignment during the examination. A motor and gear reducer assembly rotated the tubing and simultaneously translated the scanner dolly longitudinally, accomplishing a helical scan. The ultrasonic beam is adjusted so that it is incident upon the tubing at an appropriate angle to allow the sound to travel circumferentially around the tube wall, as illustrated in Fig. 35.7. The optimum incident angle is critical and can vary with the ultrasonic frequency, tubing material, and wall thickness. In practice, it is usually determined empirically with a standard tube that contains reference discontinuities of known size on both inner and outer surfaces. Figure 35.8 is a block diagram of our system.

The tapered tubing of concern had a constant nominal wall thickness, so a fixed angle of sound entry was required for optimum inspection as the tubing diameter varied. As mentioned earlier, the scanner dolly maintains the conventional tubing in proper alignment with the sound beam during the helical scan. This is accomplished with two face plates containing Teflon bushings that are machined to fit the inspected tubing and are mounted on either side of the search tube. For

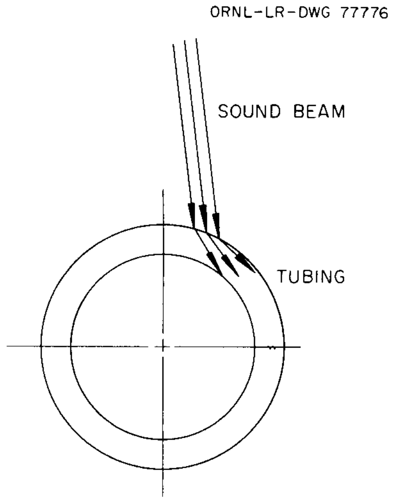

Fig. 35.7. Propagation of Sound in Tube Wall.

---

[9] R. B. Oliver, R. W. McClung, and J. K. White, *Nondestructive Testing* 15, 14D (1957).

ORNL-DWG 65-4738

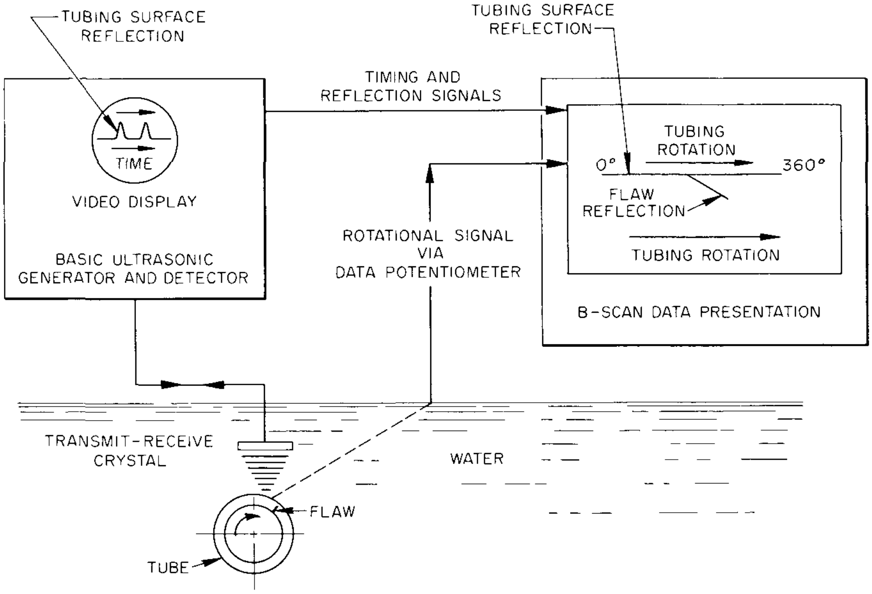

Fig. 35.8. Block Diagram of System for Ultrasonic Inspection of Tubing.

the tapered tubing inspection, the face-plate bushings were machined to fit the maximum diameter of the tapered tube. The search tube was adjusted and fixed in a constant position relative to the face plates to achieve optimum response to longitudinal notches placed on the inner and outer surfaces at or near the maximum diameter. As the tubing was traversed, two spring-loaded V-block devices held the tubing at a constant point of tangency that coincided with the proper incident angle of the sound beam for inspection. The V-blocks were adjusted for optimum response to notches at or near the minimum diameter. Thus, the incident angle of the sound beam on the tube wall did not vary as the diameter changed. Figure 35.9 is a cross-sectional drawing showing how the axis of the tube was shifted along a radius at the appropriate angle to maintain a constant angle of incidence at the point of tangency. Since the tubing was not coaxial with the chuck, a universal joint connection from the chuck allowed it to rotate. Hence, we could with this system maintain the ultrasonic inspection setup despite the tapering of the tube.

ORNL-DWG 64-9378

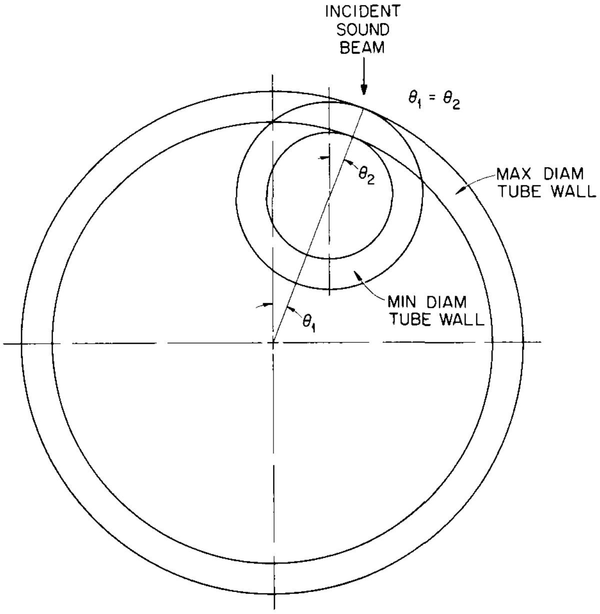

Fig. 35.9. Tapered Tube Cross Sections Showing Constant Incident Angle at Common Points of Tangency.

36. SNAP-8 and SNAP-50 Corrosion Studies

A. P. Litman   A. Taboada[1]

Corrosion support programs for SNAP-8 and SNAP-50 space-power electrical-generating systems have continued as a joint effort between the Metals and Ceramics Division and the Reactor Division.[2,3] These *Systems for Nuclear Auxiliary Power* are being developed by NASA and the AEC for use in future space vehicles.

SNAP-8 PRIMARY SYSTEM COMPATIBILITY STUDIES

B. Fleischer   A. Taboada[1]

The SNAP-8 primary system incorporates four different structural alloys and a reactor cooled with NaK, fueled with zirconium hydride containing ^{235}U, and reflected with beryllium. The reactor is designed to operate with surface temperatures in the range of 590 to 775°C and to supply 35 kw of electricity through a boiling-mercury Rankine power-conversion system. All systems are designed for 10,000 hr unattended operation.

A loop program was conducted that entailed operation of $\frac{1}{45}$th-scale forced-flow loops that closely simulated important features of the SNAP-8 primary system. The structural materials involved in the test systems were chromized Hastelloy N, types 347 and 316 stainless steel, Hastelloy C, and Croloy 9M. Eutectic NaK (78% K) was the heat-transfer medium. The most pronounced performance-deteriorating corrosion phenomenon found was carbon migration from the Croloy 9M to all other portions of the system. This result and other observations have been reported in detail.[4]

CORROSION STUDIES ON SNAP-50 BIMETALLIC HEAT-REJECTION SYSTEMS

A. P. Litman   B. Fleischer
A. Taboada[1]

Our compatibility program on the SNAP-50 electrical generating system has, to date, been in support of bimetallic heat-rejection systems. A loop, consisting of a radiator fabricated from type 316 stainless steel and a heated section made from Nb–1% Zr, was built and operated for a portion of its scheduled lifetime during the previous reporting period.[2] The test loop, containing eutectic NaK (78% K), operated with a heater outlet temperature of 680°C and a temperature difference of approximately 100°C. The system completed its scheduled 6000-hr operation on March 14, 1966, was dismantled, and is presently being subjected to metallurgical examination.

Removable and permanent specimens had been installed in the heated portion of this loop to provide information on corrosion and mass-transfer rates. After 6000 hr both types of type 316 stainless steel specimens showed no significant weight change. The removable and permanent Nb–1% Zr specimens exhibited very small weight losses, approximately 0.1 mg cm^{-2} month^{-1} average, even though this system was not hot trapped. Interestingly, the refractory-alloy specimens in the inlet portion of the heated section at about 600°C exhibited the maximum weight loss. This probably indicates that these specimens were in the most suitable position to interact with impurities in this non-hot-trapped test system.

---

[1] Present address, Division of Reactor Development and Technology, USAEC, Washington, D.C.

[2] A. Taboada, *Metals and Ceramics Div. Ann. Progr. Rept. June 30, 1965*, ORNL-3870, pp. 305–11.

[3] ORNL-3772 (classified).

[4] H. W. Savage *et al.*, *SNAP-8 Corrosion Program Summary Report*, ORNL-3898 (December 1965).

37. Thermonuclear Project

W. J. Leonard

Controlled thermonuclear research is primarily concerned with extracting useful energy from the fusion of certain light elements. The process would occur in a dense high-temperature plasma contained by magnetic fields. Thus, in complex and diverse plasma physics experiments, ORNL is studying and evaluating the problems associated with the creation of such a plasma. The control of metallurgical variables affecting the quality and operation of present equipment and the advisability or possibility of construction of new equipment are items that consume the major portion of the metallurgical support effort.

FAILURE OF COPPER TUBING ON DCX-1

W. J. Leonard

Pinhole defects develop in oxygen-free copper tubing connected to the DCX-1 working space. This tubing carries liquid nitrogen and then turbulent high-pressure steam during preparation for experiments; during experiments it must hold a 10^{-9}-torr vacuum. Metallographic examination of these defects showed intergranular oxidation had formed microcracks that extended across the tubing wall. The alloy Cu–30% Ni appears to be a satisfactory replacement for copper in this use.

PRODUCTION OF LEAD-LITHIUM ALLOY SHIELDING MATERIAL

W. J. Leonard

Lead-lithium alloys as rich in lithium as possible are desired for simultaneous attenuation of both gamma radiation and neutrons. Commercial alloys contain up to 0.1% Li, and a shielding alloy containing 0.72% Li has been reported.[1] We have prepared alloys ranging from 0.01 to 3.2% Li in

Fig. 37.1. Microstructure of Near-Eutectic Pb–0.7% Li Alloy.

---

[1] D. H. Jansen, E. E. Hoffman, and D. M. Shepherd, *J. Nucl. Mater.* 3, 249–58 (1959).

Fig. 37.2. Microstructure of Hypereutectic Pb–0.9% Li Alloy.

1-lb batches from high-purity metals. Microstructures of near-eutectic and hypereutectic alloys are shown in Figs. 37.1 and 37.2 respectively. Table 37.1 shows the hardening of lead by alloying. Melting of large batches of the alloys is complicated by the exothermic formation of the intermetallic compound PbLi. Nevertheless, we have successfully cast a 680-lb melt of Pb–1.25% Li without serious segregation. Dissolution of lithium in lead started at 800°F; without further heating, the alloy temperature reached 1500°F before dissolution was complete.

Table 37.1. Hardening of Lead by Lithium Addition

Lithium Content (%)	Hardness (DPH)
0	4
0.1	12
0.7	14
0.9	16
3.2[a]	40

[a] Near composition of intermetallic compound PbLi.

FABRICATION OF TUNGSTEN–BORON NITRIDE PROBES

R. L. Heestand W. J. Leonard

The Thermonuclear Division needs better probes for electrical field measurement in plasma. Usable upper limits of existing dielectrics are presently around 1300°K for the application, whereas measurement of voltages at 3000°K is desired. To attain this higher temperature, we are fabricating probes from tungsten and boron nitride by vapor deposition. The probe consists of a 0.005-in.-diam tungsten wire insulated with 0.015-in.-thick boron nitride clad with 0.003-in.-thick tungsten. High-quality boron nitride can be deposited by reaction of boron trichloride with ammonia. Differential contraction on cooling led to cracking when boron nitride was deposited directly on tungsten wire. To overcome this difficulty, we plated on spring-loaded Pt–40% Rh wire; creep of the wire compensated for thermal expansion. On cooling, the wire could be removed and tungsten wire could be inserted into the resulting BN tube. Tungsten cannot be directly deposited on the BN from WF_6, since this compound converts BN to BF_3. To obtain the outer tungsten layer, we first flash coated the BN with tungsten by decomposition of $W(CO)_6$. Then sufficient tungsten was deposited by reduction of WF_6 to complete the 0.003-in. coating.

Several probes have been fabricated by the above technique and are being evaluated for electrical characteristics.

page blank

Papers and Publications

page blank

Papers and Oral Presentations

Quarterly Meeting of the Southeastern Section of the American Ceramic Society, Gatlinburg, Tenn., July 8–10, 1965

F. L. Carlsen, Jr.,* "Microstructure of Pyrolytic-Carbon-Coated Fuel Particles"

Gordon Research Conference on Physical Metallurgy, Meriden, N.H., July 19–23, 1965

R. J. Arsenault,* "The Energy of Formation of a Double Kink"

IAEA Symposium on Thermodynamics with Emphasis on Nuclear Materials and Atomic Transport in Solids, Vienna, Austria, July 22–27, 1965

T. S. Lundy and F. R. Winslow,* "Atomic Transport Problems of Interest in Nuclear Systems"

Gordon Research Conference on Corrosion, New London, N.H., Aug. 9–13, 1965

J. V. Cathcart* and G. F. Petersen, "Oxide Lattice Disregistry and the Kinetics of Oxidation of Copper"

R. E. Pawel,* "Oxygen Solution in Tantalum and Niobium During Oxidation at Low Temperatures"

IAEA Symposium on Nuclear Materials Management, Vienna, Austria, Aug. 30–Sept. 3, 1965

Roy G. Cardwell, Jr.,* "Materials Control in the Fabrication of Enriched Uranium Fuels"

Gordon Research Conference, Molten Salt Session, Meriden, N.H., Aug. 30–Sept. 3, 1965

N. J. Bjerrum* and C. R. Boston, "Spectra Resulting from the Combination of Bi and Bi^{3+} in Molten Solvents Containing $AlCl_3$"

Institution of Electrical Engineers International Conference on Thermionic Electrical Power Generation, London, England, Sept. 20–24, 1965

J. I. Federer,* R. L. Heestand, F. H. Patterson, and C. F. Leitten, Jr., "Thermochemical Deposition of Refractory Metals, Alloys, and Compounds for Application in Thermionic Devices"

Twelfth National Vacuum Symposium, New York, N.Y., Sept. 29–Oct. 1, 1965

D. S. Easton* and J. O. Betterton, "High-Purity Zirconium Single Crystals Produced in an Ion-Pumped Zone Refiner"

Fourth Symposium on Refractory Metals, Institute of Metals Division, The Metallurgical Society of AIME, French Lick, Ind., Oct. 3–5, 1965

H. Inouye,* "Equilibrium Solid Solutions of Nitrogen in Cb–1% Zr Between 1200 to 1800°C"

R. L. Stephenson,* "Comparative Creep-Rupture Properties of B-66 and D-43 Alloys"

---

*Speaker

1965 American Welding Society National Fall Meeting, Birmingham, Ala., Oct. 4–7, 1965

R. G. Gilliland and J. T. Venard,* "Elevated-Temperature Mechanical Properties of Welds in a Ni-Mo-Cr-Fe Alloy"

R. G. Gilliland and G. M. Slaughter,* "The Welding of New Solution-Strengthened Nickel-Base Alloys"

1965 Fall Meeting of the Electrochemical Society, Buffalo, N.Y., Oct. 10–14, 1965

J. C. Banter,* "Effects of Neutron Irradiation and Vacuum Annealing on Oxide Films on Zirconium"

M. L. Picklesimer,* "Deformation, Creep, and Fracture in Alpha-Zirconium Alloys"

P. L. Rittenhouse* and M. L. Picklesimer, "Research on the Mechanical Anisotropy of Zircaloy-2"

Symposium on Stainless Copper Alloys, Sponsored by International Copper Research Association, Tarrytown, N Y., Oct. 14–15, 1965

J. V. Cathcart,* "Effect of Lattice Disregistry on the Oxidation of Copper"

ASM Seminar, Recrystallization, Grain Growth, and Textures, Detroit, Mich., Oct. 16–17, 1965

Paul Gordon and R. A. Vandemeer,* "Grain Boundary Migration"

Fall Meeting of the American Institute of Mining, Metallurgical, and Petroleum Engineers, Detroit, Mich., Oct. 17–21, 1965

R. J. Arsenault,* "An Investigation of Solid Solution Effects and Work Hardening in Tantalum and Tantalum-Base Alloys"

John Askill* and T. S. Lundy, "Environmental Effects on the Diffusion of Tantalum-182 in Bcc Titanium"

J. F. Murdock* and T. S. Lundy, "Diffusion of Titanium-44 in Vanadium-Titanium Alloys"

F. R. Winslow* and T. S. Lundy, "Diffusion of Hafnium-181 in Bcc Hafnium"

25th National Convention of the Society for Nondestructive Testing, Detroit, Mich., Oct. 18–22, 1965

K. V. Cook and R. W. McClung,* "Development of Ultrasonic Inspection Techniques for Tapered Tubing"

Fifth Conference on Thermal Conductivity, Denver, Colo., Oct. 20–22, 1965

T. G. Kollie, "A Pulse Heating Calorimetric Technique for Measuring the Specific Heat of Electrical Conductors and Its Application to Pure Iron from 100 to 1400°C" (presented by J. P. Moore)

J. P. Moore, R. S. Graves, W. Fulkerson,* and D. L. McElroy, "The Physical Properties of Tungsten"

Physical Properties Group, D. L. McElroy,* "Progress Report: Oak Ridge National Laboratory"

British Ceramic Society Meeting on Nuclear and Engineering Ceramics, Harwell, England, Oct. 25–27, 1965

A. R. Olsen, D. A. Douglas, Y. Hirose, J. L. Scott, and J. W. Ullmann, "Properties and Prospects of Thoria-Based Nuclear Fuels" (presented by A. E. Goldman)

R. G. Wymer* and J H. Coobs, "Preparation, Coating, Evaluation, and Irradiation Testing of Sol-Gel Oxide Microspheres"

Annual Meeting of the American Physical Society, Chicago, Ill., Oct. 28–30, 1965

Gordon Czjzek, J. L. C. Ford, Jr.,* Felix E. Obenshain, and Dietrich Seyboth, "Observation of the Mössbauer Effect Following Coulomb Excitation of ^{73}Ge"

---

*Speaker

Southeastern Section of American Physical Society, Charlottesville, Va., Nov. 1–3, 1965

G. Czjzek,* "Recoilless Gamma Ray Emission Following Coulomb Excitation"

J. S. Faulkner,* "Developments in the Bend Theory of Disordered Systems"

Ad-Hoc Forum of Scientific and Technical Information Analysis Center Managers, Directors, and Professional Analysts, Battelle Memorial Institute, Columbus, Ohio, Nov. 9–11, 1965

R. L. Pilloton,* "Organization of a New Information Center on Nuclear Fuel Technology"

1965 Winter Meeting of the American Nuclear Society, Washington, D.C., Nov. 15–18, 1965

J. W. Prados* and J. L. Scott, "Mathematical Model for Predicting Coated-Particle Behavior"

J. H. DeVan, J. R. DiStefano, and D. H. Jansen,* "Compatibility of Refractory Metals with Boiling Alkali Metals"

C. W. Cunningham, J. H. DeVan, L. E. Fuller, D. H. Jansen, and R. E. McPherson,* "Screening Tests of Turbine Nozzle and Blade Materials"

J. L. Scott,* J. G. Morgan, and V. A. DeCarlo, "Irradiation Evaluation of Fuel Elements for the PBRE and AVR Reactors"

A. C. Schaffhauser,* "Low-Temperature Ductility and Strength of Vapor-Deposited Tungsten"

A. R. Irvine,* A. L. Lotts, and A. R. Olsen, "The Thorium-Uranium Recycle Facility Design"

Tungsten and Tungsten Alloy Fabrication at Argonne National Laboratory, Argonne, Ill., Dec. 2, 1965

W. O. Harms* and C. F. Leitten, Jr., "Status of Programs on Fabrication and Evaluation of Tungsten and Tungsten-Base Alloys at the Oak Ridge National Laboratory"

Tenth AEC Coated-Particle Working Group Meeting, Battelle Memorial Institute, Columbus, Ohio, Dec. 7–8, 1965

J. H. Coobs* and O. Sisman, "Coated-Particle Fuels Development at Oak Ridge National Laboratory for Period May 15, 1965, to November 15, 1965"

21st High-Temperature Fuels Committee Meeting, Battelle Northwest, Richland, Wash., Dec. 14–16, 1965

Staffs of the Metals and Ceramics, Reactor Chemistry, and Reactor Divisions of ORNL, "High-Temperature Fuel Work at the Oak Ridge National Laboratory" (presented by J. L. Scott)

1966 Small Angle X-Ray Scattering Conference, New York, N.Y., Jan. 25–26, 1966

R. W. Hendricks,* "Some Considerations for the Use of Proportional Counters in X-Ray Analysis"

P. W. Schmidt* and R. W. Hendricks, "Weighting Functions for Collimation Corrections in Small-Angle X-Ray Scattering"

11th Meeting of the Refractory Composites Working Group, Los Angeles, Calif., Jan. 25–27, 1966

A. C. Schaffhauser,* "Low-Temperature Ductility and Strength of Thermochemically Deposited Tungsten and Effects of Heat Treatment"

US/UK Exchange on Nuclear Fuels, Harwell, England, Feb. 21–24, 1966

J. L. Scott,* "Nuclear Fuels Development at the Oak Ridge National Laboratory"

American Institute of Mining, Metallurgical, and Petroleum Engineers Annual Meeting, New York, N.Y., Feb. 27–Mar. 3, 1966

H. E. McCoy, W. R. Martin,* and J. R. Weir, "Radiation Effects on the Mechanical Properties of Nickel-Base Alloys"

---

*Speaker

US/EURATOM Exchange on Nuclear Fuels, Brussels, Belgium, Feb. 28–Mar. 2, 1966

J. L. Scott,* "Nuclear Fuels Development at the Oak Ridge National Laboratory"

Fast Flux Test Facility Driver Fuels Meeting, Richland, Wash., Mar. 8–10, 1966

J. E. Cunningham,* "Cladding and Dispersion Fuel Development at ORNL"

Middle Tennessee Section of the Society for Nondestructive Testing, Tullahoma, Tenn., Apr. 15–16, 1966

R. W. McClung,* "Nondestructive Testing at the Oak Ridge National Laboratory"

Cleveland Meeting of the Electrochemical Society, Cleveland, Ohio, May 1–5, 1966

H. Beutler,* R. L. Beatty, and J. H. Coobs, "Pyrolytic-Carbon Coatings on Nuclear Fuel Particles"

International Symposium on Capsule Irradiation Experiments, Pleasanton, Calif., May 3–5, 1966

J. W. Woods,* "In-Reactor Mechanical Properties Experiments"

Second International Thorium Fuel Cycle Symposium, Gatlinburg, Tenn., May 3–6, 1966

A. R. Olsen,* R. E. Adams, and J. H. Coobs, "Current Status of Irradiation Testing of Thorium Fuels at Oak Ridge National Laboratory"

J. W. Prados,* R. L. Beatty, H. Beutler, J. H. Coobs, A. R. Olsen, and J. L. Scott, "Development of Coated-Particle Fuels for Advanced Gas-Cooled Reactors"

J. D. Sease,* R. B. Pratt, and A. L. Lotts, "Remote Fabrication of Thorium Fuels"

First National Conference on Electron Probe Microanalysis, College Park, Md., May 4–6, 1966

M. L. Picklesimer* and G. Hallerman, "The Influence of the Preparation of Metal Specimens on the Precision of Electron Microprobe Analysis"

68th Annual Meeting of American Ceramic Society, Washington, D. C., May 7–12, 1966

L. E. Poteat* and C. S. Yust, "Deformation Mechanisms in Thoria at Elevated Temperatures"

Conference on Nuclear Applications of Nonfissionable Ceramics, Washington, D.C., May 9–11, 1966

C. F. Leitten, Jr.,* "Application of Nonfissionable Ceramics as Neutron Absorber Materials"

Vanadium Alloy Working Group Meeting, Pittsburgh, Pa., May 10, 1966

J. F. Murdock,* "Diffusion in V-Ti Binary Alloys"

20th Metallography Group Meeting, Denver, Colo., May 18–20, 1966

R. S. Crouse,* "Modifications to the Bausch and Lomb Research Metallograph"

C. K. H. DuBose* and J. O. Stiegler, "Semi-Automatic Preparation of Specimens for Transmission Electron Microscopy"

R. J. Gray and R. S. Crouse,* "An Effect of Curing Stresses in Epoxy Resins"

J. O. Stiegler and R. J. Gray,* "Phase Identification by Deposition of Surface Films"

15th Annual U.S.A.E.C. Corrosion Symposium, Oak Ridge, Tenn., May 23–25, 1966

N. C. Cole, C. W. Fox, and G. M. Tolson,* "The Corrosion of Some High-Temperature Brazing Alloys in Boiling Potassium"

J. H. DeVan,* "Compatibility of Structural Materials with Boiling Potassium"

J. C. Wilson,* "Anisotropy of Oxidation in Zirconium"

---

*Speaker

22nd High-Temperature Fuels Committee Meeting, Pittsburgh, Pa., May 24–26, 1966

J. L. Scott,* "Highlights of Coated-Particle Fuel Development at the Oak Ridge National Laboratory"

Tungsten and Tungsten Alloy Tubing Development Meeting, AEC, Washington, D.C., May 26, 1966

W. O. Harms,* "Tungsten and Tungsten Alloy Tubing Development Meeting – a Summary of Progress by Metals and Ceramics Division, ORNL"

Eleventh AEC Coated-Particle Working Group Meeting, Los Alamos, N.M., June 1–2, 1966

J. H. Coobs and J. G. Morgan,* "Coated-Particle Fuels Development at Oak Ridge National Laboratory"

Third International Materials Symposium, Berkeley, Calif., June 13–16, 1966

L. E. Poteat* and C. S. Yust, "Grain-Boundary Reactions During Deformation"

12th Annual American Nuclear Society Meeting, Denver, Colo., June 19–23, 1966

J. E. Cunningham* and E. L. Long, "Failure of BONUS Reactor Superheater Fuel Assembly Traced to Faulty Weld Practice"

C. F. Leitten, Jr.* and R. J. Beaver, "Technology and Performance of Lanthanide Oxide Neutron Absorbers"

W. R. Martin,* J. R. Weir, Jr., J. A. Basmajian, and L. D. Kirkbride, "Fast-Reactor Irradiation Effects on Type 316L and 17-4 PH Steels"

R. E. McDonald, G. A. Reimann,* and C. F. Leitten, Jr., "The Extrusion of Tungsten and Tungsten-Alloy Tubing"

A. R. Olsen,* J. D. Sease, A. E. Richt, J. W. Ullmann, and S. D. Clinton, "Irradiation of High Flux Isotope Reactor Target Prototypes"

International Conference on Crystal Growth, Boston, Mass., June 20–24, 1966

A. T. Chapman, G. W. Clark,* and D. E. Hendrix, "Modified Floating-Zone Technique for Growth of Uranium Dioxide"

21st Annual Calorimetry Conference, Boulder, Colo., June 22–24, 1966

T. G. Godfrey* and J. M. Leitnaker, "An Explanation of the Anomalous Heat Capacity of Uranium Dicarbide"

US/UK Libby-Cockcroft Irradiation Effects Meeting, Long Island, N.Y., June 23–24, 1966

E. E. Bloom, W. R. Martin, J. O. Stiegler, and J. R. Weir,* "Comparison of Displacement Damage and Strength for Stainless Steel Irradiated at Intermediate Temperatures"

W. R. Martin and J. R. Weir, Jr.,* "Irradiation Embrittlement of Low- and High-Carbon Stainless Steels at 700, 800, and 900°C"

W. R. Martin and J. R. Weir,* "Postirradiation Creep and Stress Rupture of Hastelloy N"

69th Annual Meeting of the American Society for Testing and Materials, Atlantic City, N.J., June 27–July 1, 1966

R. J. Gray,* "Present Status of Metallography"

W. R. Martin and J. R. Weir,* "Solutions to the Problems of Elevated-Temperature Irradiation Embrittlement"

---

*Speaker

Publications

Arsenault, R. J., *The Energy of Formation of a Double Kink and an Examination of Low-Temperature Deformation*, ORNL-3862 (September 1965). Available from CFSTI.

Arsenault, R. J., "Stress-Induced Ordering of Interstitial Atoms Due to Dislocation Motion," *Phil. Mag.* **13**(121), 31 (January 1966).

Askill, J., *A Bibliography on Tracer Diffusion in Metals. Part II. Impurity Diffusion in Pure Metals*, ORNL-3795, Part II (November 1965).

Askill, J., *A Bibliography on Tracer Diffusion in Metals. Part I. Self-Diffusion in Pure Metals. Part II. Impurity Diffusion in Pure Metals*, ORNL-3795, Supplement to Parts I and II (June 1966).

Askill, J., and T. S. Lundy, "Discussion of 'Correlation of Diffusion in Fcc Metals as a Function of Atomic Volume,' by R. H. Moore," *Trans. Met. Soc. AIME* **233**, 2125 (December 1965).

Banter, J. C., "Effects of Neutron Irradiation and Vacuum Annealing on Oxide Films on Zirconium," *Electrochem. Technol.* **4**(5–6), 237–39 (May–June 1966).

Barrett, Lida K., *Mathematical Models of Diffusion in Grain Boundaries*, ORNL-TM-1224 (August 1965). Available from CFSTI.

Beatty, R. L., F. L. Carlsen, Jr., and J. L. Cook, "Pyrolytic-Carbon Coatings on Ceramic Fuel Particles," *Nucl. Appl.* **1**(6), 560–66 (December 1965).

Bjerrum, N. J., C. R. Boston, G. P. Smith, and H. L. Davis, "Unusual Oxidation States of Bismuth Produced by the Reaction Between Bismuth Metal and Bi(III) in Acid Chloride Media," *Inorg. Nucl. Chem. Letters* **1**, 141–43 (1965).

Bloom, E. E., J. O. Stiegler, W. R. Martin, and J. R. Weir, *Comparison of Displacement Damage and Strength for Stainless Steel Irradiated at Intermediate Temperatures*, ORNL-TM-1535 (June 1966).

Boston, C. R., "Densities of Molten $AlCl_3$ and $NaCl$-$AlCl_3$ Mixtures," *J. Chem. Eng. Data* **11**(2), 262–63 (April 1966).

Bourgette, D. T., *Design and Evaluation of Special Purpose High-Vacuum High-Temperature Equipment for Refractory-Metal Research*, ORNL-TM-1426 (April 1966). Available from CFSTI.

Bourgette, D. T., *High-Temperature Chemical Stability of Refractory-Base Alloys in High Vacuum*, ORNL-TM-1431 (April 1966). Available from CFSTI.

Bourgette, D. T., and H. E. McCoy, "A Study of the Vaporization and Creep-Rupture Behavior of Type 316 Stainless Steel," *ASM (Am. Soc. Metals) Trans. Quart.* **59**(2), 324–39 (June 1966).

Bridges, W. H., and R. L. Pilloton, *A Thesaurus of Keywords on Nuclear Fuel Technology*, ORNL-TM-1285 (November 1965).

Cardwell, R. G., Jr., "Materials Control in the Fabrication of Enriched Uranium Fuels," pp. 65–87 in *Nuclear Materials Management*, International Atomic Energy Agency, Vienna, 1966.

Cathcart, J. V., G. F. Petersen, and C. J. Sparks, Jr., "Lattice Disregistry in Very Thin Oxide Films on Copper," *Mem. Sci. Rev. Met.* **62**, 11–16 (May 1965).

Chapman, A. T., and G. W. Clark, "Growth of UO_2 Single Crystals Using the Floating-Zone Technique," *J. Am. Ceram. Soc.* **48**(9), 494–95 (September 1965).

Chernock, W. P., R. M. Mayfield, and J. R. Weir, Jr., "Cladding Materials for Nuclear Fuels," *Proc. Intern. Conf. Peaceful Uses At. Energy, 3rd, Geneva, 1964* **9**, 35–43 (1965).

Clausing, R. E., *Exploratory Experiments Concerning the Desorption of Gases by Bombardment with Electrons,* ORNL-TM-1166 (Nov. 3, 1965). Available from CFSTI.

Coobs, J. H., and J. G. Morgan, *Coated-Particle Fuels Development at Oak Ridge National Laboratory for Period November 15, 1965 to May 15, 1966,* ORNL-TM-1528 (May 1966). Available from CFSTI.

Coobs, J. H., and O. Sisman, *Coated-Particle Fuels Development at Oak Ridge National Laboratory for Period May 15, 1965 to November 15, 1965,* ORNL-TM-1331 (December 1965). Available from CFSTI.

Cook, J. L., *Studies of the Thorium-Uranium Dicarbide Pseudobinary System in the Presence of Excess Graphite* (thesis), ORNL-TM-1188 (September 1965). Available from CFSTI.

Cook, K. V., and R. W. McClung, "An Ultrasonic Technique for Evaluation of Heat-Exchanger Brazed Joints," *Mater. Evaluation* **24**(2), 97–100 (February 1966).

Crouse, R. S., "Accelerated Epoxy Mounting Using a Radio Frequency Furnace," pp. 98–102 in *Technical Papers, Nineteenth Metallographic Group Meeting, Held April 20–22, 1965, Oak Ridge National Laboratory, Oak Ridge, Tennessee,* ORNL-TM-1161 (February 1966). Available from CFSTI.

Crouse, R. S., *Identification of Carbides, Nitrides, and Oxides of Niobium and Niobium Alloys by Anodic Staining,* ORNL-3821 (July 1965). Available from CFSTI.

Cunningham, J. E., E. L. Long, Jr., E. A. Franco-Ferreira, and D. G. Harman, *BONUS Reactor Superheater Fuel Assemblies – an Investigation of Failure and Method of Correction,* ORNL-3910 (December 1965). Available from CFSTI.

Czjzek, G., J. L. C. Ford, Jr., F. E. Obenshain, and D. Seyboth, "Observation of the Mössbauer Effect Following Coulomb Excitation of ^{73}Ge," *Phys. Letters* **19**(8), 673–75 (Jan. 1, 1966).

Dayton, R. W., W. V. Goeddel, and W. O. Harms, "Ceramic Coated-Particle Nuclear Fuels," *Proc. Intern. Conf. Peaceful Uses At. Energy, 3rd, Geneva, 1964* **11**, 538–46 (1965).

DeVan, J. H., *Compatibility of Structural Materials with Boiling Potassium,* ORNL-TM-1361 (April 1966) (classified).

Dodd, C. V., *A Solution to Electromagnetic Induction Problems* (thesis), ORNL-TM-1185 (August 1965). Available from CFSTI.

Donnelly, R. G., *Brazing Flanges to Sintered, Stainless Steel Filters for High-Temperature Service,* ORNL-TM-1252 (October 1965). Available from CFSTI.

Donnelly, R. G., and G. M. Slaughter, "Weldability Evaluation of Advanced Refractory Alloys," *Welding J. (N.Y.)* **45**(6), 250-s–257-s (June 1966).

Donnelly, R. G., W. C. Thurber, and G. M. Slaughter, "Fabrication Procedures for Enrico Fermi Fast Breeder Reactor Fuel Elements," *Welding J. (N.Y.)* **44**(12), 1027–34 (December 1965).

Douglas, D. A., Jr., R. W. McClung, B. E. Foster, and C. V. Dodd, "Non-Destructive Testing Techniques for Research and Process Control," pp. 247–64 in *Non-Destructive Testing in Nuclear Technology, Vol. II,* International Atomic Energy Agency, Vienna, 1965.

DuBose, C. K. H., and J. O. Stiegler, "Electron Metallography of Pyrolytic Carbon Coating on Fuel Particles," pp. 159–71 in *Technical Papers of the Eighteenth Metallographic Group Meeting, Held June 22–24, 1964, Atomics International, Canoga Park, Calif.,* NMI-5025 (Pt. I), Nuclear Metals, West Concord, Mass., August 1965.

Federer, J. I., and C. F. Leitten, Jr., "Vapor Deposition and Characterization of Tungsten-Rhenium Alloys," *Nucl. Appl.* **1**(6), 575–80 (December 1965).

Federer, J. I., and R. A. Padgett, Jr., "Diffusion Studies of ^{95}Nb in Polycrystalline UO_2 Between 1100 and 2100°C," *J. Nucl. Mater.* **17**(4), 294–304 (1965).

Ferguson, D. E., O. C. Dean, and D. A. Douglas, "The Sol-Gel Process for the Remote Preparation and Fabrication of Recycle Fuels," *Proc. Intern. Conf. Peaceful Uses At. Energy, 3rd, Geneva, 1964* **10**, 307–15 (1965).

Finch, C. B., and G. W. Clark, "Single-Crystal Growth of Thorium Dioxide from Lithium Ditungstate Solvent," *J. Appl. Phys.* **36**(7), 2143–45 (July 1965).

Finch, C. B., L. A. Harris, and G. W. Clark, "Single Crystal Synthesis and Properties of Lanthanide Germano-Molybdates," pp. 107–15 in *Proc. Conf. Rare Earth Res., 4th, Phoenix, Ariz., 1964* (1965).

Foster, B. E., *Measurement of Mass Attenuation Coefficients Using 50- to 150-kvp X Rays* (thesis), ORNL-TM-1457 (June 1966). Available from CFSTI.

Franco-Ferreira, E. A., "The Fabrication of a Large Columbium–1% Zirconium Pumped Loop for Boiling-Potassium Service," pp. 623–631 in *Refractory Metals and Alloys III: Applied Aspects,* Vol. 30, ed. by Robert I. Jaffee (Proceedings of the Third Technical Conference, AIME), Gordon and Breach Science Publishers, New York, 1966.

Fulkerson, W., J. P. Moore, and D. L. McElroy, "Comparison of the Thermal Conductivity, Electrical Resistivity, and Seebeck Coefficient of a High-Purity Iron and an Armco Iron to 1000°C," *J. Appl. Phys.* **37**(7), 2639–53 (June 1966).

Gilliland, R. G., "The Development of Refractory-Metal Brazing Alloys for Elevated-Temperature Service," pp. 227–38 in *Refractory Metals and Alloys III: Applied Aspects,* Vol. 30, ed. by Robert I. Jaffee (Proceedings of the Third Technical Conference, AIME), Gordon and Breach Science Publishers, New York, 1966.

Gilliland, R. G., and G. M. Slaughter, *The Welding of New Solution-Strengthened Nickel-Base Alloys,* ORNL-TM-1408 (April 1966).

Gilliland, R. G., and J. T. Venard, "Elevated-Temperature Mechanical Properties of Welds in a Ni-Mo-Cr-Fe Alloy," *Welding J. (N.Y.)* **45**(3), 103-s–110-s (March 1966); ORNL-TM-1341 (January 1966).

Gray, R. J., and J. V. Cathcart, "Polarized Light Microscopy of Pyrolytic Carbon Deposits," *J. Nucl. Mater.* **19**(1), 81–89 (April 1966).

Gray, R. J., and R. S. Crouse, "Experience with Color in Metallography," pp. 112–29 in *Technical Papers, Nineteenth Metallographic Group Meeting, Held April 20–22, 1965, Oak Ridge National Laboratory, Oak Ridge, Tennessee,* ORNL-TM-1161 (February 1966). Available from CFSTI.

Gurinsky, D. H., J. R. Weeks, C. J. Klamut, L. Rosenblum, and J. H. DeVan, "Corrosion in Liquid Metals," *Proc. Intern. Conf. Peaceful Uses At. Energy, 3rd, Geneva, 1964* **9**, 550–58 (1965).

Hammond, J. P., and G. M. Adamson, Jr., "Activated Sintering of Uranium Monocarbide," pp. 3–25 in *Modern Developments in Powder Metallurgy, Vol. 3, Development and Future Prospects* (ed. by H. H. Hausner), Plenum Press, New York, 1966.

Harms, W. O., "Carbon-Coated Carbide Particles as Nuclear Fuels," pp. 290–313 in *Modern Ceramics – Some Principles and Concepts,* ed. by J. E. Hove and W. C. Riley, John Wiley & Sons, Inc., New York, 1965.

Harris, L. A., and H. L. Yakel, "The Crystal Structure of Calcium Beryllate, $Ca_{12}Be_{17}O_{29}$," *Acta Cryst.* **20**(2), 295–301 (February 1966).

Haws, C. C., J. L. Matherne, F. W. Miles, and J. E. Van Cleve, *Summary of the Kilorod Project – a Semiremote 10-kg/day Demonstration of $^{233}UO_2$-ThO_2 Fuel-Element Fabrication by the ORNL Sol-Gel Vibratory-Compaction Method,* ORNL-3681 (August 1965) . Available from CFSTI.

Heestand, R. L., and C. F. Leitten, Jr., "Parameters for the Production of Refractory-Metal Tubing by the Vapor Deposition Process," pp. 113–23 in *Refractory Metals and Alloys III: Applied Aspects,* Vol. 30, ed. by Robert I. Jaffee (Proceedings of the Third Technical Conference, AIME), Gordon and Breach Science Publishers, New York, 1966.

Heestand, R. L., and C. F. Leitten, Jr., "Thermochemical Reduction of Uranium Hexafluoride for the Direct Fabrication of Uranium Dioxide Ceramic Fuels," *Nucl. Appl.* **1**(6), 584–88 (December 1965).

Holden, A. N., B. Weidenbaum, and C. F. Leitten, Jr., "Control Rod Materials," *Proc. Intern. Conf. Peaceful Uses At. Energy, 3rd, Geneva, 1964* **9**, 419–27 (1965).

Inouye, H., "The Contamination of Refractory Metals in Vacua Below 10^{-6} Torr," pp. 871–83 in *Refractory Metals and Alloys III: Applied Aspects,* Vol. 30, ed. by Robert I. Jaffee (Proceedings of the Third Technical Conference, AIME), Gordon and Breach Science Publishers, New York, 1966.

Inouye, H., *Equilibrium Solid Solutions of Nitrogen in Cb–1% Zr Between 1200–1800°C,* ORNL-TM-1355 (February 1966). Available from CFSTI.

Irvine, A. R., A. L. Lotts, and A. R. Olsen, "The Thorium-Uranium Recycle Facility," pp. 19–24, *Proceedings of the 13th Conference on Remote Systems Technology, 1965,* American Nuclear Society, Hinsdale, Ill., 1966.

James, D. W., "Structure of Molten Nitrates. I. Estimation of Effective Interionic Distances," *Australian J. Chem.* **19**(6), 993–98 (June 1966).

Joy, H. W., and G. S. Handler, "Convergence in One-Center Expansions. H_2^+," *J. Chem. Phys.* **43**(10), S252–53 (Nov. 15, 1965).

Kegley, T. M., *Evaluation of Aluminum Fuel Element Corrosion Sample from Pakistan Research Reactor,* ORNL-TM-1507 (June 1966). Available from CFSTI.

Kegley, T. M., Jr., and B. C. Leslie, "Metallographic Preparation of Dicarbides of Thorium and Thorium-Uranium," pp. 71–83 in *Technical Papers of the Eighteenth Metallographic Group Meeting, Held June 22–24, 1964, Atomics International, Canoga Park, California,* NMI-5025 (Pt. I), Nuclear Metals, West Concord, Mass., August 1965.

Kegley, T. M., Jr., and B. C. Leslie, "Metallographic Preparation of Thorium Carbides," pp. 193–207 in *Technical Papers, Nineteenth Metallographic Group Meeting, Held April 20–22, 1965, Oak Ridge National Laboratory, Oak Ridge, Tennessee,* ORNL-TM-1161 (February 1966). Available from CFSTI.

Kegley, T. M., Jr., and G. M. Tolson, *Examination of Failed Expansion Bellows Between EGCR Containment Shell and Experimenters Cell 6,* ORNL-TM-1380 (February 1966). Available from CFSTI.

King, E. M., and E. L. Long, "BONUS Superheater Failure," *Nucl. Safety* **7**(1), 113–18 (Fall 1965).

Kittel, J. H., T. K. Bierlein, B. R. Hayward, and W. C. Thurber, "Irradiation Behavior of Metallic Fuels," *Proc. Intern. Conf. Peaceful Uses At. Energy, 3rd, Geneva, 1964* **11**, 227–34 (1965).

Kollie, T. G., *The Development of a Pulse Heating Calorimetric Technique for Measuring the Specific Heat of Electrical Conductors and Its Application to Pure Iron from 100 to 1400°C* (thesis), ORNL-TM-1187 (August 1965). Available from CFSTI.

Kopp, O. C., and G. W. Clark, "Split Autoclave for Hydrothermal Experiments," *Rev. Sci. Instr.* **37**(3), 372–73 (March 1966).

Koppenaal, T. J., and R. J. Arsenault, "A Rate Controlling Mechanism for Slip in Neutron Irradiated Copper Single Crystals," *Phil. Mag.* **12**, 951–61 (November 1965).

LaValle, D. E., R. M. Steele, and W. T. Smith, Jr., "Rhenium Nitrogen Fluoride and Rhenium Tetrafluoride," *J. Inorg. Nucl. Chem.* **28**(1), 260 (January 1966).

Leitten, C. F., Jr., "Nuclear Poisons and Control Applications of Ceramic Materials," pp. 435–51 in *Proceedings of the Conference on Nuclear Applications of Nonfissionable Ceramics, Washington, D.C., May 9–11, 1966,* American Nuclear Society, Hinsdale, Ill., June, 1966.

Litman, A. P., "Diffusion of Oxygen in Niobium," *Phys. Status Solidi* 11, K47–K48 (1965).

Litman, A. P., *The Effect of Oxygen on the Corrosion of Niobium by Liquid Potassium* (thesis), ORNL-3751 (July 1965). Available from CFSTI.

Litman, A. P., and J. W. Prados, "The Partitioning of Oxygen Between Zirconium and Liquid Potassium," *Electrochem. Technol.* **3**(9–10), 228–33 (September–October 1965).

Long, E. L., Jr., *Examination of BONUS Preheater-Dryer Piping*, ORNL-TM-1282 (October 1965). Available from CFSTI.

Long, E. L., Jr., and R. J. Gray, "Radiation Metallography in the High-Radiation-Level Examination Laboratory," p. 131 in *Technical Papers, Nineteenth Metallographic Group Meeting, Held April 20–22, 1965, Oak Ridge National Laboratory, Oak Ridge, Tennessee*, ORNL-TM-1161 (February 1966). Available from CFSTI.

Lotts, A. L., and D. A. Douglas, Jr., "Refabrication Technology for the Thorium–Uranium-233 Fuel Cycle," pp. 212–45 in *Utilization of Thorium in Power Reactors, Report of a Panel Held in Vienna 14–18 June 1965*, International Atomic Energy Agency, Vienna, 1966; ORNL-TM-1141 (June 1965).

Love, G. R., *Near-Surface Effects in Superconducting Niobium-Zirconium Alloys*, ORNL-TM-1276 (December 1965).

Love, G. R., and M. L. Picklesimer, "The Kinetics of Beta-Phase Decomposition in Niobium (Columbium)-Zirconium," *Trans. Met. Soc. AIME* **236**(4), 430–35 (April 1966).

Lundy, T. S., J. I. Federer, R. E. Pawel, and F. R. Winslow, "A Summary of ORNL Work on Diffusion in Beta Zirconium, Vanadium, Columbium, and Tantalum," pp. 35–49 in *Diffusion in Body-Centered Cubic Metals*, American Society for Metals, Metals Park, Ohio, 1965.

Lundy, T. S., F. R. Winslow, R. E. Pawel, and C. J. McHargue, "Diffusion of Nb-95 and Ta-182 in Niobium (Columbium)," *Trans. Met. Soc. AIME* **233**(8), 1533–38 (August 1965).

Martin, M. M., W. J. Werner, and C. F. Leitten, Jr., *Fabrication of Aluminum-Base Irradiation Test Plates*, ORNL-TM-1377 (February 1966). Available from CFSTI.

Martin, W. R., *Factors Affecting the Mechanical Properties of Stainless Steels at MPRE Operating Temperatures*, ORNL-TM-1362 (February 1966) (classified).

Martin, W. R., and J. R. Weir, "The Effect of Irradiation Temperature on the Post-Irradiation Stress-Strain Behavior of Stainless Steel," pp. 251–67 in *Flow and Fracture of Metals and Alloys in Nuclear Environments, Spec. Tech. Publ. No. 380*, American Society for Testing and Materials, Philadelphia, Pa., 1965.

Martin, W. R., and J. R. Weir, "Influence of Grain Size on the Irradiation Embrittlement of Stainless Steel at Elevated Temperatures," *J. Nucl. Mater.* **18**(2), 108–18 (February 1966).

Martin, W. R., and J. R. Weir, "Influence of Preirradiation Heat Treatment on the Postirradiation Ductility of Stainless Steels," *Nucl. Appl.* **1**, 478–83 (October 1965).

Martin, W. R., and J. R. Weir, *Postirradiation Creep and Stress Rupture of Hastelloy N*, ORNL-TM-1515 (June 1966).

Martin, W. R., and J. R. Weir, *Solutions to the Problems of High-Temperature Irradiation Embrittlement*, ORNL-TM-1544 (June 1966). Available from CFSTI.

Martin, W. R., J. R. Weir, R. E. McDonald, and J. C. Franklin, "Irradiation Embrittlement of Low-Boron Type Stainless Steel," *Nature* **208**(5005), 73–74 (Oct. 2, 1965).

Martin, W. R., and J. R. Weir, Jr., "Irradiation Effects in Stainless Steels at High Temperatures," pp. 36–46 in *Proceedings of Sodium Components Development Program* (Information Meeting held in Chicago, Illinois, June 16–17, 1965), Conf-650620 (1966).

Martin, W. R., and J. R. Weir, Jr., *Irradiation Embrittlement of Low- and High-Carbon Stainless Steels at 700, 800, and 900°C*, ORNL-TM-1516 (June 1966). Available from CFSTI.

McClung, R. W., "Factors in Radiography at Energies Below 400 kvp," *Mater. Evaluation* **24**(5), 263–68 (1966).

McClung, R. W., and D. A. Douglas, "Non-Destructive Testing of Irradiated Materials in the United States," pp. 179–202 in *High Activity Hot Laboratories Working Methods,* Vol. 1, Proceedings of an International Symposium Organized by ENEA and EURATOM, McGraw-Hill, New York, 1965.

McCoy, H. E., *Studies of the Carbon Distribution in Hastelloy N,* ORNL-TM-1353 (February 1966).

McCoy, H. E., and J. R. Weir, "Effect of Irradiation on Bend Transition Temperatures of Molybdenum- and Columbium-Base Alloys," pp. 131–55 in *Flow and Fracture of Metals and Alloys in Nuclear Environments, Spec. Tech. Publ. No. 380,* American Society for Testing and Materials, Philadelphia, Pa., 1965.

McCoy, H. E., Jr., *An Evaluation of the Creep Properties of Cb-753 and a Comparison of This Alloy with Several Other Niobium-Base Alloys,* ORNL-TM-1347 (January 1966); *ASM (Am. Soc. Metals) Trans. Quart.* **59**(2), 277–87 (June 1966).

McCoy, H. E., Jr., and J. R. Weir, Jr., *Influence of Irradiation on the Tensile Properties of the Aluminum Alloy 6061,* ORNL-TM-1348 (January 1966). Available from CFSTI.

McDonald, R. E., and C. F. Leitten, Jr., "Production of Refractory-Metal Tube Shells by Extrusion and Flow-Turning Techniques," pp. 85–98 in *Refractory Metals and Alloys III: Applied Aspects,* Vol. 30, ed. by Robert I. Jaffee (Proceedings of the Third Technical Conference, AIME), Gordon and Breach Science Publishers, New York, 1966.

McQuilkin, F. R., D. R. Cuneo, J. W. Prados, E. L. Long, Jr., and J. H. Coobs, *An Irradiation Test of AVR Production Fuel Spheres in the Oak Ridge Research Reactor,* ORNL-TM-1512 (June 1966).

Melton, C. E., and H. W. Joy, "Ionization Potentials of Alkyl Free Radicals and *n*-Alkanes Through $C_{17}H_{36}$ by Energy-Calibrated Molecular Orbital Methods," *Can. J. Chem.* **44**(12), 1455–62 (June 1966).

Michelson, C., J. L. Scott, and E. L. Long, Jr., *An Evaluation of UO_2 Irradiated at 1600 to 2400°C,* ORNL-3930 (May 1966). Available from CFSTI.

Morgan, C. S., and D. H. Bowen, *Inert Gas Bubbles in Neutron Irradiated Magnesium Oxide,* AERE-R-5223 (June 1966).

Morgan, C. S., and L. L. Hall, "The Creep of ThO_2 and ThO_2-CaO Solid Solutions," *Proc. Brit. Ceram. Soc.* **6**, 233–38 (June 1966).

Morgan, C. S., C. J. McHargue, and C. S. Yust, "Material Transport in Sintering," *Proc. Brit. Ceram. Soc.* **3**, 177–84 (October 1965).

Morgan, J. G., M. F. Osborne, and E. L. Long, Jr., *Postirradiation Examination of EGCR Prototype Capsule O3A-6,* ORNL-TM-1378 (February 1966). Available from CFSTI.

Morgan, J. G., P. E. Reagan, and E. L. Long, Jr., *Evaluation and Irradiation Effects Studies on Pyrolytic Carbon Coated Fuel Particles,* ORNL-3923 (March 1966). Available from CFSTI.

Murdock, J. F., "Diffusion of Titanium-44 and Vanadium-48 in Titanium," pp. 261–67 in *Diffusion in Body-Centered Cubic Metals,* American Society for Metals, Metals Park, Ohio, 1965.

Ogle, J. C., and C. J. McHargue, "The Annealing of Deformation Twins in Columbium," *Trans. Met. Soc. AIME* **236**(5), 686–94 (May 1966).

Olsen, A. R., D. A. Douglas, Y. Hirose, J. L. Scott, and J. W. Ullmann, *Properties and Prospects of Thoria-Base Nuclear Fuels,* ORNL-TM-1297 (November 1965). Available from CFSTI.

Olsen, A. R., W. O. Harms, D. B. Trauger, R. E. Adams, and D. A. Douglas, "Irradiation Behavior of Thorium-Uranium Alloys and Compounds," pp. 246–91 in *Utilization of Thorium in Power Reactors, Report of a Panel Held in Vienna 14–18 June 1965,* International Atomic Energy Agency, Vienna, 1966.

Olsen, A. R., S. A. Rabin, J. W. Snider, W. S. Ernst, and J. W. Tackett, *Fabrication and Preirradiation Information on Vibratorily Compacted ThO_2-UO_2 Fuel Rods for Experiments ETR-I and MTR-III,* ORNL-TM-1322 (January 1966). Available from CFSTI.

Osborne, M. F., E. L. Long, Jr., and J. G. Morgan, "Performance of Prototype Experimental Gas-Cooled Reactor Fuel Under Extreme Conditions," *Nucl. Sci. Eng.* **22**(4), 420–33 (August 1965).

Osborne, M. F., E. L. Long, Jr., and J. G. Morgan, *Postirradiation Examination of High Burnup EGCR Prototype Fuel Capsules,* ORNL-TM-1511 (June 1966). Available from CFSTI.

Pawel, R. E., and E. E. Stansbury, "Contributions to the Vibrational Specific Heat of Metals," *J. Appl. Phys.* **36**(7), 2330–31 (July 1965).

Peterson, S., "Ignition and Combustion of Reactor Materials Under Accident Conditions," *Nucl. Safety* **7**(2), 169–72 (Winter 1965–66).

Peterson, S., "Integrity of Reactor Fuels," *Nucl. Safety* **6**(4), 398–403 (Summer 1965).

Peterson, S., R. E. Adams, and D. A. Douglas, "Properties of Thorium, Its Alloys, and Its Compounds," pp. 292–312 in *Utilization of Thorium in Power Reactors, Report of a Panel Held in Vienna 14–18 June 1965,* International Atomic Energy Agency, Vienna, 1966.

Picklesimer, M. L., *Microstructural Examination,* ORNL-TM-1338 (January 1966). Available from CFSTI.

Picklesimer, M. L., and P. L. Rittenhouse, "Hydride and Basal Pole Figures in Zircaloy-2 by Quantitative Metallography," pp. 55–64 in *Technical Papers, Nineteenth Metallographic Group Meeting, Held April 20–22, 1965, Oak Ridge National Laboratory, Oak Ridge, Tennessee,* ORNL-TM-1161 (February 1966). Available from CFSTI.

Pilloton, R. L., *Machine-Assembled Reviews on Coated Nuclear Fuel Particles,* ORNL-TM-1335 (December 1965). Available from CFSTI.

Pilloton, R. L., *NUFTIC, an Information Center on Nuclear Fuel Technology,* ORNL-TM-1358 (March 1966). Available from CFSTI.

Pilloton, R. L., "Organization of a New Information Center on Nuclear Fuel Technology," pp. 35–52 in *Proceedings of 1st Ad-Hoc Forum of Scientific and Technical Information Analysis Center Managers, Directors, and Professional Analysts Held at Battelle Memorial Institute, Columbus, Ohio, November 9–11, 1965,* CONF-651131.

Pilloton, R. L., and J. A. Carpenter, *Motion of Particles in Fluidized Beds and Implications for the Preparation of Coated Nuclear Fuel Particles,* ORNL-TM-1170 (August 1965). Available from CFSTI.

Pilloton, R. L., and H. J. Flamm, *Motion of Spheres in Smooth Rotating Drums and Applications to the Coating of Nuclear Fuel Particles,* ORNL-3819 (August 1965).

Prados, J. W., *A Computer Program for Predicting Coated-Particle Behavior,* ORNL-TM-1385 (March 1966). Available from CFSTI.

Prados, J. W., and J. L. Scott, *Mathematical Model for Predicting Coated Particle Behavior,* ORNL-TM-1405 (March 1966).

Rabin, S. A., J. W. Ullmann, E. L. Long, Jr., M. F. Osborne, and A. E. Goldman, *Irradiation Behavior of High Burnup ThO_2–4.45% UO_2 Fuel Rods,* ORNL-3837 (October 1965). Available from CFSTI.

Richt, A. E., *Interim Postirradiation Examination of a Europium-Bearing Control Rod from the Stationary Medium Power Reactor,* ORNL-TM-1407 (March 1966). Available from CFSTI.

Rittenhouse, P. L., and M. L. Picklesimer, "Comparison of Pole Figure Data Obtained by X-Ray Diffraction and Microhardness Measurements on Zircaloy-2," pp. 16–28 in *Papers and Proceedings of the Meeting on X-Ray Diffraction in the Atomic Energy Field, Hanford Atomic Products Operation, Richland, Washington,* RL-REA-2595 (October 1965); *Trans. Met. Soc. AIME* **236**(4), 496–501 (April 1966).

Rittenhouse, P. L., and M. L. Picklesimer, "The Effect of Preferred Orientation and Stress on the Directional Precipitation of Hydrides in Zircaloy-2," pp. 79–102 in *Papers Presented at the X-Ray Preferred Orientation Meeting Held at National Lead Company of Ohio, December 5 and 6, 1963*, ed. by J. W. Colby, NLCO-946 (December 15, 1965).

Rittenhouse, P. L., and M. L. Picklesimer, *Precipitation of Hydrides in Zircaloy-2 as Affected by Preferred Orientation, Elastic Stress, and Hydrogen Content*, ORNL-TM-1239 (September 1965). Available from CFSTI.

Rittenhouse, P. L., and M. L. Picklesimer, *Strain Behavior in Zircaloy-2 Sheet-Type Tensile Specimens*, ORNL-TM-1226 (September 1965). Available from CFSTI.

Roche, T. K., "Effect of Degree of Vacuum on the Slow-Bend Creep Behavior of Columbium–0.6% Zirconium at 1000°C," pp. 901–16 in *Refractory Metals and Alloys III: Applied Aspects*, Vol. 30, ed. by Robert I. Jaffee (Proceedings of the Third Technical Conference, AIME), Gordon and Breach Science Publishers, New York, 1966.

Roche, T. K., *Procurement and Quality Evaluation of Nb–1% Zr Stock for Boiling Alkali Metal Corrosion Studies*, ORNL-TM-1179 (August 1965). Available from CFSTI.

Roche, T. K. (compiler), *Evaluation of Niobium-Vanadium Alloys for Application in High-Temperature Reactor Systems*, ORNL-TM-1131 (October 1965). Available from CFSTI.

Rutledge, R. M., and A. F. Saturno, "One-Center-Expansion–Configuration-Interaction Studies on CH_4 and NH_3," *J. Chem. Phys.* **44**(3), 977–85 (February 1966).

Scott, J. L., "Fuel Element Performance Limitations," *Nucl. Safety* **7**(3), 302–13 (Spring 1966).

Sears, M. B., L. M. Ferris, and R. J. Gray, "High-Temperature Immiscibility of Uranium Mono- and Dicarbides," *J. Electrochem. Soc.* **113**(3), 269–74 (March 1966).

Sease, J. D., and A. R. Olsen, *Fabrication Procedures and Preirradiation Data for* $(Th,{}^{233}U)O_2$*-Bearing Irradiation Rods*, ORNL-TM-1461 (May 1966). Available from CFSTI.

Sease, J. D., R. B. Pratt, and A. L. Lotts, *Remote Fabrication of Thorium Fuels*, ORNL-TM-1501 (April 1966). Available from CFSTI.

Shuck, A. B., A. L. Lotts, and K. Drumheller, "The Remote Fabrication of Reactor Fuels," pp. 71–148 in *Reactor Technology – Selected Reviews – 1965*, USAEC (1965).

Silverstone, H. J., H. W. Joy, and M. K. Orloff, "Toward a Better $2p\pi$-Atomic Orbital for π-Electron Theory," *J. Am. Chem. Soc.* **88**(6), 1325–27 (March 1966).

Smith, G. P., and C. R. Boston, "Influence of Rare-Gas-Configuration Cations on the Absorption Spectra of Nickel(II) Centers in Liquid Chloride and Bromide Salts," *J. Chem. Phys.* **43**(11), 4051–56 (December 1965).

Smith, G. P., and S. von Winbush, "Optical Spectra and Densities of Molten Chloride Salts Having Large Nickel Chloride Concentrations. Nickel Chloride–Tri-*n*-butylbenzylphosphonium Chloride Systems Up to 33.3 Mole % Nickel Chloride," *J. Am. Chem. Soc.* **88**(10), 2127–31 (May 1966).

Stephenson, R. L., *An Approximate Method for Determining Allowable Stress Rates for Capsules Containing Helium-Producing Isotopes*, ORNL-TM-1436 (May 1966). Available from CFSTI.

Swindeman, R. W., *Fatigue of Austenitic Stainless Steels in the Low and Intermediate Cycle Range*, ORNL-TM-1363 (January 1966).

Tolson, G. M., *The Manufacture of the Control Rods for the Experimental Gas-Cooled Reactor*, ORNL-3932 (April 1966). Available from CFSTI.

Tolson, G. M., *MPRE Fuel Elements: Manufacture, Inspection, Drawings, and Specifications*, ORNL-3902 (January 1966) (classified).

Tolson, G. M., and A. Taboada, *A Study of Lead and Lead-Salt Corrosion in Thermal-Convection Loops*, ORNL-TM-1437 (April 1966). Available from CFSTI.

Van Cleve, J. E., Jr., J. J. Varagona, and A. L. Lotts, *Time Study of Fuel Rod Fabrication in the Kilorod Facility,* ORNL-3740 (October 1965). Available from CFSTI.

Venard, J. T., C. R. Kennedy, and J. R. Weir, *Effect of Irradiation on the Mechanical Properties of Stainless Steel at 750°C Under Constant Stress Rate Conditions,* ORNL-TM-1216 (September 1965). Available from CFSTI.

Venard, J. T., and J. R. Weir, *Effect of Irradiation on the Stress-Rupture Characteristics of a 20% Cr–25% Ni Niobium-Stabilized Stainless Steel,* ORNL-TM-1359 (February 1966). Available from CFSTI.

Venard, J. T., and J. R. Weir, "In-Reactor Stress-Rupture Properties of a 20 Cr–25 Ni, Columbium-Stabilized Stainless Steel," p. 269 in *Flow and Fracture of Metals and Alloys in Nuclear Environments, Spec. Tech. Publ. No. 380,* American Society for Testing and Materials, Philadelphia, Pa., 1965.

Watts, T. D., W. J. Werner, and J. P. Hammond, *Calculations of Charge and Contour Dimensions of Powder-Loading Assembly Used in the Production of HFIR Composite Fuel Compacts,* ORNL-TM-1193 (September 1965). Available from CFSTI.

Weaver, S. C., and J. L. Scott, *Comparison of Reactor Fuels for High-Temperature Application,* ORNL-TM-1360 (December 1965) (classified).

Williams, R. K., and D. L. McElroy, *Estimated Thermal Conductivity Values for Solid and Liquid Promethium,* ORNL-TM-1424 (March 1966). Available from CFSTI.

Williams, R. O., "High Precision Gas Volumeter," *Rev. Sci. Instr.* **36**(10), 1441–43 (October 1965).

Wilson, J. C., "Electrical Discharge Machining in the Metallurgical Laboratory," pp. 159–72 in *Technical Papers, Nineteenth Metallographic Group Meeting, Held April 20–22, 1965, Oak Ridge National Laboratory, Oak Ridge, Tennessee,* ORNL-TM-1161 (February 1966). Available from CFSTI.

Winslow, F. R., and T. S. Lundy, "Diffusion of Hf^{181} in Bcc Hafnium," *Trans. Met. Soc. AIME* **233**, 1790 (September 1965).

Wymer, R. G., and D. A. Douglas, Jr. (compilers), *Status and Progress Report for Thorium Fuel Cycle Development for Period Ending December 31, 1964,* ORNL-3831 (May 1966). Available from CFSTI.

Young, J. P., and G. W. Clark, "Apparatus for the Spectrophotometric Study of Small Crystals," *Rev. Sci. Instr.* **37**(2), 234–35 (February 1966).

The following quarterly progress reports have been issued during this reporting period:

Patriarca, P., *Fuels and Materials Development Program Quart. Progr. Rept. June 30, 1965,* ORNL-TM-1200; *Sept. 30, 1965,* ORNL-TM-1270; *Dec. 31, 1965,* ORNL-TM-1400; *Mar. 31, 1966,* ORNL-TM-1500 (Official Use Only).

Harms, W. O., *High-Temperature Materials Program Quart. Progr. Rept. July 31, 1965,* ORNL-TM-1300 (classified); *Oct. 31, 1965,* ORNL-TM-1350 (classified); *Jan. 31, 1966,* ORNL-TM-1455 (Official Use Only).

page blank

METALS AND CERAMICS DIVISION

JUNE 30, 1966

DIRECTOR J. H FRYE, JR.
BERTIE BY

ASSISTANT DIRECTOR J. E. CUNNINGHAM
MARGE WHITE

STAFF ASSIGNMENTS

A R OLSEN[1,2]
S PETERSON

ADMINISTRATIVE ASSISTANT

L. E. BANKER
MARY YAGGI

FUNDAMENTAL RESEARCH

B. S. BORIE[2]
WILMA MASON

CRYSTAL PHYSICS

G W CLARK
C B FINCH
S D FULKERSON
D E HENDRIX
H M SMITH

DEFORMATION OF CRYSTALLINE SOLIDS

R O WILLIAMS
R ARSENAULT[3]
A WOLFENDEN

REACTIONS AT METAL SURFACES

J. V. CATHCART
R. E. PAWEL
G. F. PETERSEN
J. J. CAMPBELL

SPECTROSCOPY OF IONIC MEDIA

G P SMITH, JR
N N BJERRUM[7]
C R BOSTON
J BRYNESTAD[3]
F C GILMORE[4]
W E SMITH[3]
W M EWING

STRUCTURE OF METALS

C. J. McHARGUE[2]
J C. OGLE
R. A. VANDERMEER

THEORY OF ALLOYING

J. O BETTERTON, JR.
G. V CZJZEK
D. S. EASTON
J C. LOVE[12]
J. O. SCARBROUGH

X-RAY DIFFRACTION

H L YAKEL, JR
B S BORIE[2]
O B CAVIN
L A HARRIS
R W HENDRICKS
C J SPARKS, JR
R M STEELE

THEORETICAL RESEARCH

J S FAULKNER
H L DAVIS
H W JOY
R M RUTLEDGE[5]

APPLIED RESEARCH

C J McHARGUE[2]
MARY COMBS
DOLORES POE

ELECTRON MICROSCOPY

J O STIEGLER
K FARRELL
R GEHLBACH
B T LOH[3]
C K H DuBOSE
J T HOUSTON

METALLOGRAPHY

R J GRAY
R S CROUSE
E L LONG, JR
G HALLERMAN
T M KEGLEY, JR
H L KRAUTWEDEL[7]
A E RICHT
M D ALLEN
L A AMBURN
N M ATCHLEY
E D BOLLING
E R BOYD
W E DENNY
W H FARMER
H R GADDIS[6]
J C GOWER
E P GRIGGS
C P HALTOM
T J HENSON
C W HOUCK[6]
E H LEE
B C LESLIE
R J LOCKETT
Z R McNUTT
L G SHRADER
E D SIMS
S E SPENCER
H R TINCH
R M WALLACE
M A WHEELER
C E ZACHARY

METALLURGY OF SUPERCONDUCTING MATERIALS

M L PICKLESIMER[2]
C C KOCH
G R LOVE

PHYSICAL PROPERTIES

D L McELROY
W FULKERSON
T G KOLLIE
J P MOORE
R K WILLIAMS
R S GRAVES

PHYSICAL CERAMIC STUDIES

C S MORGAN, JR
C S YUST
L L HALL

SOLID REACTION STUDIES

T S LUNDY[3]
J ASKILL
J F MURDOCK
F R WINSLOW
L C MANLEY
R A PADGETT, JR

ZIRCONIUM ALLOY DEVELOPMENT

M L PICKLESIMER[2]
J C BANTER
D O HOBSON
P L RITTENHOUSE
J C WILSON
P J JONES
G C NELSON

SPECIAL ASSIGNMENT

R E CLAUSING

RESEARCH AND DEVELOPMENT

P PATRIARCA
W O HARMS
R M EVANS
ANN HOBBS
EDITH TAYLOR

PROJECT COORDINATION

GCR, HTM, SNPO-C

W. O HARMS[2]
J. H. COOBS[2]
E. A. FRANCO-FERREIRA[2]

CERAMICS LABORATORY

J L SCOTT
R L BEATTY
H BEUTLER[3]
E S BOMAR
J H COOBS[2]
W S ERNST, JR
T G GODFREY, JR
R L HAMNER
D M HEWETTE II
J M LEITNAKER
D MATKIN[7]
R E MEADOWS
R A POTTER
J W PRADOS
J M ROBBINS
J G STRADLEY
S C WEAVER
B R CHILCOAT
C M FITZPATRICK
F P JEFFERS
H KEETING[13]
D V KIPLINGER[6]
J E POPE
W W PROAPS
D E ROSSON
W H SMITH, JR

MATERIALS COMPATIBILITY

J H DeVAN
W H COOK
J R DISTEFANO
D H JANSEN
R L KLUEH
C E SESSIONS
J L GRIFFITH
J W HENDRICKS
B W McCOLLUM
R E POTTER
L R TROTTER

PHYSICAL METALLURGY

H INOUYE
D T BOURGETTE
A SCHAFFHAUSER
J F NEWSOME
R L TAYLOR
S H WHEELER

DISPERSIONS IN SOLIDS

J P HAMMOND
C HAMBY

SPECIAL ASSIGNMENT

A E GOLDMAN
W J LEONARD
J J PRISLINGER
S J ACRES

COST, BUDGET, AND NUCLEAR MATERIALS

R G CARDWELL, JR
H W HOOVER[2]

RESEARCH AND DEVELOPMENT

G M ADAMSON, JR[2]
NANCY BOWMAN
FREDA FINN

PROJECT COORDINATION

TRU HFIR, MSRP, MPRE
BONUS

G M ADAMSON, JR[2]
G M SLAUGHTER[2]

TRU OPERATIONS

A L LOTTS[2]
E J MANTHOS
M K PRESTON[11]
J E VANCLEVE, JR
K P BAYNE
J T EAST
J E EVE
C L JOHNSON
B J STRADER

CORROSION ENGINEERING

A P LITMAN
B FLEISCHER
F D HARVEY
E J LAWRENCE
J B PHILLIPS

MATERIALS PROCESSING

C F LEITTEN, JR
G L COPELAND
D COWGILL[10]
J H ERWIN
J I FEDERER
R L HEESTAND
M M MARTIN
R E McDONALD
F H PATTERSON
G A REIMANN
W C ROBINSON
J T VENARD
W J WERNER
L A ALLEN[9]
J K ALLEY[6]
G E ANGEL
T W COFFEY
C E DUNN
J B FLYNN
J W GEER
G D GOLDSTON
J N HIX
C W HOLLAND, JR
R J HUNTER
W R JOHNSON
L QUEENER
H E REESOR
E R TURNBILL
H J WALLACE
W H WARWICK[6]

WELDING AND BRAZING

G M SLAUGHTER[2]
D A CANONICO
R G DONNELLY
C W FOX
E A FRANCO-FERREIRA[2]
J M JONES
W R MILLER[13]
J W TACKETT
L G BRYSON
J D HUDSON
R G SHOOSTER
L C WILLIAMS
J J WOODHOUSE, JR

AL ASSIGNMENT

A ABOADA
R G GILLILAND
R W KNIGHT
C H WODTKE
J P DURR[8]
R J SAWYERS[8]

RESEARCH AND DEVELOPMENT

D A DOUGLAS, JR[2]
JANE MORRISON
LOUIE MAE PYATT

PROJECT COORDINATION

DESALINATION, SAP, THORIUM UTILIZATION, ISOTOPES, STUDIES AND EVALUATIONS, INFORMATION CENTER

D. A. DOUGLAS, JR.[2]
R. J. BEAVER

INFORMATION CENTER

R L PILLOTON[2]
W H BRIDGES[2]
GENEVA HARRIS
SALLY MOONEY[6]

MECHANICAL PROPERTIES

J R WEIR, JR
E E BLOOM
W W DAVIS
C W DOLLINS
D G HARMAN
C R KENNEDY
R T KING
W R MARTIN
H E McCOY, JR
R L STEPHENSON
R W SWINDEMAN
J W WOODS
F L BEELER
K W BOLING
E BOLLING
V R BULLINGTON
D G GATES
L L HEATHERLY[6]
H W KLINE
V G LANE
B McNABB, JR
E B PATTON, JR
C K THOMAS
E M THOMAS
R D WADDELL, JR
C W WALKER
B C WILLIAMS

NONDESTRUCTIVE TESTING

R W McCLUNG
W H BRIDGES[2]
K V COOK
C V DODD III
B E FOSTER
S D SNYDER
L SNYDERS[7]
R R WAMORKAR[7]
L D CHITWOOD
O E CONNER
R A CUNNINGHAM, JR
R L FITZGERALD
D P GODSEY
W J MASON

REMOTE FABRICATION

A L LOTTS[2]
R E ADAMS
R B FITTS
A R OLSEN
R L PILLOTON[2]
R B PRATT
J D SEASE
T N WASHBURN
R A BOWMAN
T L BOSWELL
R A BUHL[6]
H R LIVESEY
W H MILLER, JR
H G MOORE
C F SANDERS

DIVISION SERVICES

PROCUREMENT AND MAINTENANCE

R J STEERE
RUTH HENGSTLER
H W HOOVER[2]

REPORTS OFFICE

M R HILL
MARJORIE CLARY
FRANCES LOVING
THELMA REEDY
FRANCES SCARBORO
BETTE THOMAS

---

[1] RADIATION CONTROL OFFICER
[2] DUAL CAPACITY
[3] NONCITIZEN EMPLOYEE
[4] GRADUATE RESEARCH STUDENT
[5] POSTDOCTORATE FELLOW
[6] TEMPORARY EMPLOYEE
[7] NONCITIZEN VISITOR
[8] U S ARMY PERSONNEL
[9] ON LOAN FROM INSPECTION ENGINEERING DEPARTMENT
[10] ON LOAN FROM ATOMICS INTERNATIONAL
[11] ON LOAN FROM GENERAL ENGINEERING AND CONSTRUCTION DIVISION
[12] NATIONAL SCIENCE FOUNDATION FELLOW
[13] ON LOAN FROM INSTRUMENTATION AND CONTROLS DIVISION

ORNL-3970
UC-25 – Metals, Ceramics, and Materials

INTERNAL DISTRIBUTION

1.	Biology Library
2–4.	Central Research Library
5.	Reactor Division Library
6–7.	ORNL – Y-12 Technical Library, Document Reference Section
8–57.	Laboratory Records Department
58.	Laboratory Records, ORNL R.C.
59.	ORNL Patent Office
60.	Laboratory Shift Supervisor
61.	G. M. Adamson, Jr.
62.	L. G. Alexander
63.	R. J. Beaver
64.	J. O. Betterton, Jr.
65.	D. S. Billington
66.	A. L. Boch
67.	E. G. Bohlmann
68.	E. S. Bomar
69.	B. S. Borie
70.	G. E. Boyd
71.	E. J. Breeding
72.	R. B. Briggs
73.	J. V. Cathcart
74.	C. E. Center
75.	G. W. Clark
76.	J. H. Coobs
77.	J. A. Cox
78.	F. L. Culler
79.	J. E. Cunningham
80.	G. V. Czjzek
81.	J. H. DeVan
82.	J. H. Erwin
83.	G. W. Flack
84.	A. P. Fraas
85.	J. H Frye, Jr.
86.	J. H. Gillette
87.	A. E. Goldman
88.	R. J. Gray
89.	W. R. Grimes
90.	J. P. Hammond
91.	W. O. Harms
92.	C. S. Harrill
93–98.	M. R. Hill
99.	N. E. Hinkle
100.	A. Hollaender
101.	A. S. Householder
102.	A. P. Huber (K-25)
103.	H. Inouye
104.	R. G. Jordan (K-25)
105.	M. T. Kelley
106.	E. M. King
107.	R. B. Korsmeyer
108.	J. A. Lane
109.	C. E. Larson
110.	A. P. Litman
111.	R. S. Livingston
112.	A. L. Lotts
113.	T. S. Lundy
114.	H. G. MacPherson
115.	R. W. McClung
116.	H. C. McCurdy
117.	D. L. McElroy
118.	C. J. McHargue
119.	A. J. Miller
120.	E. C. Miller
121.	C. S. Morgan
122.	K. Z. Morgan
123.	M. L. Nelson
124.	S. M. Ohr
125.	A. R. Olsen
126–127.	R. B. Parker
128.	P. Patriarca
129.	S. Peterson
130.	M. L. Picklesimer
131.	J. W. Prados
132.	A. W. Savolainen
133.	J. L. Scott
134.	H. E. Seagren
135.	G. M. Slaughter
136.	G. P. Smith, Jr.
137.	J. T. Stanley
138.	P. E. Stein (K-25)
139.	J. O. Stiegler
140.	E. H. Taylor
141.	D. B. Trauger
142.	A. M. Weinberg
143.	J. R. Weir, Jr.
144.	G. D. Whitman
145.	G. C. Williams
146.	R. O. Williams
147.	J. C. Wilson
148.	H. L. Yakel
149.	M. B. Bever (consultant)
150.	A. R. Kaufmann (consultant)
151.	J. A. Krumhansl (consultant)
152.	T. A. Read (consultant)

EXTERNAL DISTRIBUTION

153. C. M. Adams, Jr., MIT
154. M. J. Bannister, MIT
155. R. B. Burlin, AEC, Washington
156. E. D. Calvert, U.S. Bureau of Mines, P.O. Box 492, Albany, Oregon
157. G. Champier, E.N.S.M.I.M. Laboratoire de Physique, Parc de Saurupt, Nancy (M.-&-M.), France

158–159. D. F. Cope, AEC, ORO

160. J. F. Elliott, MIT
161. N. Engel, Georgia Institute of Technology
162. H. B. Finger, AEC, Washington
163. J. D. Fleming, Georgia Institute of Technology
164. V. D. Frechette, Alfred Univ.
165. Angelo Giambusso, AEC, Washington
166. R. G. Gilliland, MIT
167. J. L. Gregg, Bard Hall, Cornell Univ.
168. W. W. Grigorieff, Assistant to the Execuitve Director, Oak Ridge Associated Universities
169. E. G. Haas, Dept. of the Navy, Washington
170. R. F. Hehemann, Case Institute of Technology
171. E. E. Hoffman, GE, Cincinnati
172. O. C. Kopp, Univ. of Tenn.
173. J. Korringa, Ohio State Univ.
174. J. J. Lombardo, NASA, Lewis Research Center
175. W. D. Manly, Stellite Division, Kokomo, Ind.
176. R. S. Mateer, Univ. of Kentucky
177. P. W. McDaniel, AEC, Washington
178. Peter Murray, AERE, Harwell
179. R. R. Nash, NASA, Washington
180. E. F. Nippes, Rensselaer Polytechnic Inst.
181. H. M. Otte, Martin Company, Mail Point No. 105, Orlando, Florida
182. R. E. Pahler, AEC, Washington
183. R. M. Parke, MAB, National Academy of Science, Washington
184. J. Pheline, Centre d'Etudes Nucleaires de Saclay
185. J. M. Prosser, AEC, Washington
186. H. B. Rahner, Savannah River Operations
187. T. A. Read, Univ. of Illinois
188. R. E. Reed-Hill, Univ. of Florida
189. F. N. Rhines, Univ. of Florida
190. A. F. Saturno, Univ. of Tenn.
191. R. W. Schroeder, NASA, Lewis Research Center
192. F. C. Schwenk, AEC, Washington
193. A. A. Shoudy, Atomic Power Development Associate, Inc.
194. J. Simmons, AEC, Washington
195. E. E. Sinclair, AEC, Washington
196. L. M. Slifkin, Univ. of N.C.
197. E. E. Stansbury, Univ. of Tenn.
198. D. K. Stevens, AEC, Washington
199. Dorothy Smith, AEC, Washington
200. J. A. Swartout, Union Carbide Corp., New York
201. A. Van Echo, AEC, Washington
202. J. B. Wagner, Massachusetts Institute of Technology
203. Watt Webb, Union Carbide Metals

204. J. Weertman, Northwestern Univ.
205. G. W. Wench, AEC, Washington
206. M. J. Whitman, AEC, Washington
207. C .H. T. Wilkins, Univ. of Ala.
208. Research and Development Division, AEC, ORO
209–477. Given distribution as shown in TID-4500 under Metals, Ceramics, and Materials category (25 copies – CFSTI)